



The  
University  
Of  
Sheffield.

**A Study of the Dissolution of Nuclear Waste Glasses in Highly-  
Alkaline Conditions**

**By:**

Daniel John Backhouse

A thesis submitted in partial fulfilment of the requirements for the degree of  
Doctor of Philosophy

The University of Sheffield  
Faculty of Engineering  
Department of Materials Science and Engineering

March 2017

# Abstract

Long-term disposal of nuclear waste is a problem for the world's nuclear energy industry. The preferred option for the UK for Intermediate- and High-Level Waste (ILW & HLW) is for long-term emplacement in a Geological Disposal Facility (GDF), which requires a robust safety case based on the long-term behaviour of the waste. This work investigates one aspect of the long-term behaviour: the dissolution of the waste in highly-alkaline conditions, in the case of the formation of a highly-alkaline plume within the GDF by the interaction of groundwater with cementitious materials.

Dissolution experiments were performed on a range of glass compositions with varying CaO and MgO contents and B/Al ratios to analyse their effects on glass dissolution at high-pH. Ca and Mg are expected to be present in the GDF and in UK HLW, and are known to significantly affect glass dissolution. The effect of varying B/Al ratio is relevant to the comparison of natural glasses (B/Al = 0), with nuclear waste glasses (B/Al ~ 1 – 10). Magic-Angle Spinning Nuclear Magnetic Resonance (MAS-NMR) spectroscopy was performed to identify the effects of composition on glass structure. Dissolution experiments were also performed on existing glasses pertinent to UK nuclear waste disposal to determine their performance.

The addition of CaO and MgO, in replacement for Na<sub>2</sub>O, was found to lead to a decrease in <sup>IV</sup>B units, due to the inability of the divalent Ca<sup>2+</sup> and Mg<sup>2+</sup> cations to charge-compensate for two <sup>IV</sup>B tetrahedra each. The increased strength of this effect in the Mg-containing glasses suggests that Mg may be behaving as an intermediate oxide. Increasing the ratio of B/Al in aluminoborosilicate glasses was found to lead to an increase in the proportion of <sup>IV</sup>B units.

Glass dissolution resistance was found to correlate with replacement of Na<sub>2</sub>O for CaO and MgO. Ca-containing glasses displayed a higher dissolution resistance than those containing Mg, due to a combination of structural and solution factors. Increasing the B/Al ratio of the glasses led to a decrease in dissolution resistance, believed to be due to the greater resistance of Si – O – Al bonds to hydrolysis compared to Si – O – B bonds. The leachant cation (Ca or K) was found to have a significant effect on dissolution behaviour.

The International Simple Glass (ISG) was found to behave differently to MW-25% (UK simulant HLW glass) in Ca-rich, high-pH solutions, suggesting that it is not helpful as an analogue for the dissolution of UK nuclear waste glasses. The dissolution of a laboratory-made basaltic glass was found to be partially comparable to that of natural basaltic glasses, indicating that care must be taken when comparing the dissolution resistance of natural basaltic glasses with nuclear waste glasses. Significant localisation of elements in alteration layers during dissolution, e.g. Zr for ISG, suggests that the mechanism of dissolution in these experiments was coupled dissolution-precipitation.

# Acknowledgements

I'd like to start by thanking my supervisors Prof. Russell Hand, Dr. Claire Corkhill, Prof. Neil Hyatt and Dr. Mike Harrison, without whom I would not have been able to complete this work. Thank you for answering my questions, both theoretical and practical, and keeping me on track when I've veered off on occasion.

I would also like to thank all of the people who have contributed to the research presented in this work. Thank you to Dr. David Apperley and the EPSRC MAS-NMR service at Durham University for carrying out all of the MAS-NMR presented here and his help with analysis. Thanks also to Dr. Peng Zeng at the Sorby Centre for carrying out the FIB and TEM work for this research. Thanks to Dr. Daniel Grolimund for use of the X05 micro-focus beamline at SLS, and to Prof. Neil Hyatt, Dr. Claire Corkhill, Dr. Daniel Crean and Daniel Bailey for running the micro-focus XRD experiments. Thank you again to Dr. Claire Corkhill for training and help on the ICP-OES. Thanks to Dr. Neil Bramall for ICP-AES and ICP-MS compositional analysis of the glass samples. Thank you to Dr. Claire Utton and Dr. Paul Heath for their help and willingness to answer my questions, which prevented me from making too many mistakes early on in the project.

Thank you to Dr. Mike Harrison and NNL for their provision of base glass and calcine for the production of MW-25% glass, and to Dr. Joe Ryan at PNNL for provision of the ISG. A big thank you to Rob Ashurst and Alan Smalley in the Department of Geography for helping me to use the large Tema mill there, which significantly reduced the time and effort required in producing powdered glass samples. Also a big thank you to Ian Watts, Dr. Lisa Hollands and Dean Haylock for their help with glass-melting. I'm sorry that my glass set fire to the floor! Thanks also to Andrew Fairburn in the Kroto Institute for help in qualifying test vessels for the dissolution experiments. Thanks to Frank Fletcher and Richard Kangley for being patient while I took up a quarter of G06 with my glovebox for over 3 years. A big thank you to Dr. Martin Stennett for all the training and help in use of the labs. Thanks to EPSRC for funding this project, and to the Nuclear FiRST DTC for training and support. Thanks to the MIDAS project for use of equipment, and to DECC and the University of Sheffield for providing the funding for MIDAS.

Thanks to my cohort from the DTC for their friendship and some fun trips; Ian, Ashleigh, Ross and Ben at Sheffield, and Billy, Jen, Greg, Rob and Craig at Manchester. Thanks to all the other students in the ISL for their help (and chat when I got bored) over the years, particularly to (King) Dan for a fiercely-fought King of the Dans competition; Colleen, for lots of interesting dissolution chat and help when I got into a flap with the ICP; Laura, for knowing how to do and organise everything; Sam, for being a walking encyclopaedia; Kris, for some fun lunches; and Dan for lots of help and advice.

Huge thanks to all of my friends, particularly Alex, Kate, Elliot, Chris and Sophie, for actually wanting to hang out with me, and for putting up with me going AWOL while writing up. Thanks to my brothers and sisters at The Crowded House for love and support throughout my time with them, particularly; the Johnsons, Goodwins, Palmers and Carrie. And especially massive thanks to Martin and Val for their tremendous support of me, both spiritual and practical, particularly in letting me stay with them while writing up. And thank you to Zach for being (mostly) lovely while I was there.

An immeasurably big thank you to my Mum and Dad for shaping me into the person I am today, and for always loving and supporting me. Thanks to David for generally being a good, and not-annoying, brother.

I thank God for his provision of this opportunity to me, and for instilling in me a love of the world He has created.

Last, but certainly not least, thank you to Rachel. Thank you for your love, and support, and understanding, and help and for all the amazing times we've had together. I'm looking forward to spending the rest of our lives together. I dedicate this to you.

## **Publications and Conferences from Thesis**

### **Contributions to Conferences and Meetings – Proceedings**

D. J. Backhouse, C. L. Corkhill, N. C. Hyatt, M. L. Harrison and R. J. Hand, *Effect of Ca and Mg Addition on the Aqueous Durability of Glasses in High-pH Environments*, Proceedings of the 34<sup>th</sup> Annual Cement and Concrete Science Conference, and Workshop on Waste Cementation, September 2014, p443.

### **Contributions to Conferences and Meetings – Posters**

D. J. Backhouse\*, C. L. Corkhill, N. C. Hyatt and R. J. Hand, *Effect of Ca on the Aqueous Durability of Glasses in High-pH Environments*, GeoRepNet 2/RATE Conference, Nottingham, 2014.

D. J. Backhouse\*, C. L. Corkhill, N. C. Hyatt and R. J. Hand, *Effect of Ca on the Aqueous Durability of Glasses in High-pH Environments*, Thermal Treatment of Radioactive Wastes 2015, Risley, 2015.

D. J. Backhouse, C. L. Corkhill\*, N. C. Hyatt and R. J. Hand, *Characterisation of glass alteration layers using a microscopic, spectroscopic and diffraction approach*, Glass & Optical Materials Division of the American Ceramic Society (GOMD) Annual Meeting, Madison, 2016.

### **Contributions to Conferences and Meetings – Talks**

D. J. Backhouse\*, N. C. Hyatt, M. L. Harrison and R. J. Hand, *Aqueous Alteration of Nuclear Waste Glasses in High-pH Conditions*, Society of Glass Technology Annual Conference, Cambridge, 2013.

D. J. Backhouse\*, C. L. Corkhill, N. C. Hyatt, M. L. Harrison and R. J. Hand, *Effect of Ca and Mg Addition on the Aqueous Durability of Glasses in High-pH Environments*, Nuclear Waste Research Forum Meeting, Lancaster, 2014.

D. J. Backhouse\*, C. L. Corkhill, N. C. Hyatt, M. L. Harrison and R. J. Hand, *Effect of Ca and Mg Addition on the Aqueous Durability of Glasses in High-pH*

*Environments*, Glass & Optical Materials Division and Deutsche Glastechnische Gesellschaft (GOMD-DGG) Joint Annual Meeting, Miami, 2015.

D. J. Backhouse\*, C. L. Corkhill, N. C. Hyatt, M. L. Harrison and R. J. Hand, *Aqueous Durability of Nuclear Waste Glasses in High-pH Environments*, 25<sup>th</sup> Goldschmidt Conference, Prague, 2015.

D. J. Backhouse\*, C. L. Corkhill, N. C. Hyatt, M. L. Harrison and R. J. Hand, *Is the International Simple Glass a Valid Analogue for the Dissolution of UK High-Level Waste Glass at High-pH?*, Joint Society of Glass Technology Centenary Conference and European Society of Glass Conference, Sheffield, 2016.



# Contents

<b>1. Introduction .....</b>	<b>14</b>
<b>2. Literature Review .....</b>	<b>18</b>
2.1 Geological Disposal of Nuclear Waste .....	18
2.1.1 Introduction .....	18
2.1.2 Geological Disposal in the United Kingdom.....	18
2.1.3 Glass as a Nuclear Waste Matrix.....	20
2.2 Glass Structure .....	20
2.2.1 Silicates and Alkali/Alkaline Earth Silicates.....	20
2.2.2 Borates, Borosilicates and Alkali/Alkaline Earth Borosilicates .....	24
2.2.3 Aluminosilicates and Alkali/Alkaline Earth Aluminosilicates.....	27
2.2.4 Aluminoborosilicates and Alkali/Alkaline Earth Aluminoborosilicates .....	28
2.3 Glass Dissolution.....	29
2.3.1 Introduction .....	29
2.3.2 Dissolution in Aqueous Solutions .....	29
2.3.3 Dissolution at High-pH.....	33
2.3.4 Gel and Alteration Layer Production.....	36
2.3.5 Natural Glasses as Analogues for Nuclear Waste Glass Dissolution .....	38
2.3.6 State of Knowledge of UK Nuclear Waste Glass Dissolution .....	38
2.4 Summary .....	40
<b>3. Experimental Methods .....</b>	<b>42</b>
3.1 Sample Production .....	42
3.1.1 Glass-Making.....	42
3.1.2 Preparation of Samples for Dissolution Experiments.....	48
3.2 Dissolution Testing .....	49
3.2.1 Product Consistency Test B (PCT-B).....	49
3.2.2 Materials Characterisation Center Test 1 (MCC-1) .....	51
3.3 Inductively-Coupled Plasma Optical Emission Spectrometry (ICP-OES) .....	53
3.4 Electron Microscopy .....	56
3.4.1 Scanning Electron Microscopy (SEM).....	57
3.4.2 Transmission Electron Microscopy (TEM).....	60

3.4.3 Energy-Dispersive X-ray Spectroscopy (EDS).....	62
3.5 Solid-State Nuclear Magnetic Resonance Spectroscopy (SSNMR).....	63
3.6 X-Ray Diffraction (XRD).....	68
3.8 Geochemical Modelling using PHREEQC.....	69
<b>4. Structural Analysis of Simple Glass Compositions by Magic-Angle Spinning Nuclear Magnetic Resonance (MAS-NMR) Spectroscopy.....</b>	<b>70</b>
4.1 Introduction.....	70
4.2 Results.....	71
4.2.1 <sup>11</sup> B MAS-NMR.....	71
4.2.1.1 <i>NCxBS Glasses</i> .....	71
4.2.1.2 <i>NMxBS Glasses</i> .....	73
4.2.1.3 <i>NCABxS Glasses</i> .....	74
4.2.1.4 <i>NMABxS Glasses</i> .....	76
4.2.2 <sup>29</sup> Si MAS-NMR.....	77
4.2.2.1 <i>NCxBS Glasses</i> .....	77
4.2.2.2 <i>NMxBS Glasses</i> .....	78
4.2.2.3 <i>NCABxS Glasses</i> .....	79
4.2.2.4 <i>NMABxS Glasses</i> .....	80
4.2.3 <sup>27</sup> Al MAS-NMR.....	81
4.2.3.1 <i>NCABxS Glasses</i> .....	81
4.2.3.2 <i>NMABxS Glasses</i> .....	83
4.3 Discussion of Results.....	84
4.3.1 <sup>11</sup> B MAS-NMR.....	84
4.3.2 <sup>29</sup> Si MAS-NMR.....	89
4.3.3 <sup>27</sup> Al MAS-NMR.....	92
4.4 Summary.....	93
<b>5. Effect of Varying Glass Composition on Dissolution at High-pH96</b>	
5.1 Introduction.....	96
5.2 Experimental Procedure.....	96
5.3 Elemental Leaching Results.....	96
5.3.1 Leaching in Calcium Hydroxide.....	96
5.3.1.1 <i>NCxBS Glasses</i> .....	97

5.3.1.2 <i>NMxBS Glasses</i> .....	100
5.3.1.3 <i>NCABxS Glasses</i> .....	104
5.3.1.4 <i>NMABxS Glasses</i> .....	109
5.3.2 Leaching in Potassium Hydroxide.....	114
5.3.2.1 <i>NCxBS Glasses</i> .....	114
5.3.2.2 <i>NMxBS Glasses</i> .....	119
5.3.2.3 <i>NCABxS Glasses</i> .....	122
5.3.2.4 <i>NMABxS Glasses</i> .....	128
5.4 Analysis of Alteration Product Formation.....	133
5.4.1 Ca(OH) <sub>2</sub> -leached Samples.....	133
5.4.1.1 <i>NCxBS Glasses</i> .....	133
5.4.1.2 <i>NMxBS Glasses</i> .....	138
5.4.1.3 <i>NCABxS Glasses</i> .....	142
5.4.1.3 <i>NMABxS Glasses</i> .....	147
5.4.2 KOH-leached Samples.....	152
5.4.2.1 <i>NCxBS Glasses</i> .....	152
5.4.2.2 <i>NMxBS Glasses</i> .....	156
5.4.2.3 <i>NCABxS Glasses</i> .....	160
5.4.2.4 <i>NMABxS Glasses</i> .....	162
5.5 Discussion of Results.....	164
5.5.1. <i>NCxBS Glasses</i> .....	164
5.5.2 <i>NMxBS Glasses</i> .....	168
5.5.3 <i>NCABxS Glasses</i> .....	171
5.5.4 <i>NMABxS Glasses</i> .....	176
5.5.5 Effect of Ca vs Mg Addition on Glass Durability.....	182
5.5.6 Summary.....	188
<b>6. Dissolution Experiments on Literature Glass Compositions.....</b>	<b>192</b>
6.1 Introduction.....	192
6.2 Experimental Procedure.....	192
6.3 Elemental Leaching Results.....	194
6.3.1 MCC-1 Leaching Results.....	194
6.3.2 PCT-B Leaching Results.....	200
6.4 SEM-EDS Analysis of Alteration Product Formation.....	209

6.4.1 Monoliths from MCC-1 Experiments .....	209
6.4.1.1 ISG .....	209
6.4.1.2 MW-25%.....	218
6.4.1.3 BAS .....	226
6.4.1.2 G73 .....	234
6.5 Discussion of Results .....	242
6.5.1 Elemental Leaching Data .....	242
6.5.2 Alteration Layer Analysis .....	247
6.5.2.1 ISG.....	247
6.5.2.2 MW-25%.....	254
6.5.2.3 BAS .....	265
6.5.2.4 G73 .....	267
6.5.2.5 Alteration Layer Thickness .....	270
6.5.3 Summary .....	271
<b>7. Discussion .....</b>	<b>274</b>
7.1 Introduction.....	274
7.2 Effect of Glass Composition on Structure .....	274
7.2.1 Effect of Composition on B Coordination .....	274
7.2.2 Effect of Composition on Si Coordination.....	276
7.2.3 Summary .....	277
7.3 Effect of Glass Composition on Durability in High-pH Environments.....	278
7.3.1 Effect of Alkaline-Earth Oxide Replacement for Soda.....	278
7.3.2 Effect of Varying B/Al Ratio .....	281
7.4 Effect of Glass Structure on Durability in High-pH Environments.....	283
7.5 Effect of Leachant Cation on Dissolution in High-pH Environments .....	285
7.6 Dissolution Congruency in High-pH Environments.....	287
7.7 Dissolution Performance of Current and Proposed UK Nuclear Waste and Reference Glasses .....	291
7.7.1 Validity of ISG as an Analogue for the Dissolution of UK HLW Vitrified Product.....	292
7.7.2 Validity of Basaltic Glasses as Natural Analogues for the Dissolution of Nuclear Waste Glasses .....	293
7.7.3 Roles of Different Elements During High-pH Dissolution .....	293
7.7.4 Mechanism of Dissolution in High-pH Environments.....	293

7.7.5 Precipitation of B-containing Phases During Dissolution.....	294
<b>8. Conclusions and Further Work.....</b>	<b>296</b>
8.1 Conclusions .....	296
8.2 Further Work.....	297
<b>Appendix A – XRD of Pristine Glasses.....</b>	<b>300</b>
<b>Appendix B – Fitting of NMR Spectra.....</b>	<b>304</b>
<b>Appendix C – ICP-OES Data (Chap. 5) .....</b>	<b>310</b>
<b>Appendix D – ICP-OES Data (Chap. 6) .....</b>	<b>314</b>
<b>Appendix E – PHREEQC Phases.....</b>	<b>318</b>
<b>Bibliography .....</b>	<b>322</b>



# 1. Introduction

The UK Government's 2014 White Paper, entitled 'Implementing Geological Disposal', outlines its desire for geological disposal, with co-location of Intermediate-Level Waste (ILW) and High-Level Waste (HLW), to be the final option for the UK (excluding Scotland) nuclear waste legacy [1]. Co-location refers to the emplacement of the two waste categories within the same facility, but in separate vaults. The safety case for the repository is based on the multi-barrier concept; a set of engineered and natural barriers working in concert to ensure the isolation of the waste from the environment. One of these barriers is the buffer material around the waste canisters which separates the waste from the host geology, acting as a buffer for radionuclide migration. In the case of the ILW vault, a high-pH cementitious buffer containing a significant amount of portlandite ( $\text{Ca(OH)}_2$ ) is proposed, whereas for the HLW vault it is likely to be a clay material. UK HLW (from Magnox and oxide fuel reprocessing, but excluding some spent nuclear fuel and exotic fuels), is being immobilised within a mixed-alkali borosilicate glass (the MW base glass). The immobilisation of problematic ILW waste streams, in addition to decommissioning wastes, through vitrification is also being considered [2]. With groundwater ingress into a repository inevitable on extended timescales, co-location of the wastes may therefore result in the interaction of a Ca-rich, alkaline plume, with a pH potentially greater than 12.5, with the glass wasteforms. Previous studies [3]–[7] have shown that the dissolution rate of silicate and borosilicate glasses increases as the pH moves from neutral to more alkaline. An increased rate of dissolution may result in a greater release of radionuclides to the repository and thus, eventually, into the geosphere and biosphere. It is therefore of great importance to obtain a clearer understanding of the performance of nuclear waste glasses in highly-alkaline conditions (pH of 12 – 14), as well as the mechanisms of dissolution, and which elements play important roles, in such conditions.

Ca and Mg are known to play important roles in the glass dissolution process, and are important elements in the specific case of UK geological disposal. The UK's vitrified HLW from its Magnox reactors contains 5.6 wt.% MgO [8]. As previous workers [9]–[12] have suggested a link between Mg and a reduction in the glass dissolution rate, the confirmation or refutation of this link is important to our understanding of the dissolution of UK nuclear waste glasses. There are also similar

claimed links between Ca [3], [13] and B [3] and changes in the dissolution rate of borosilicate glasses, which were investigated during the course of this project.

Much of the work performed on the dissolution of nuclear waste glasses has concerned either: French nuclear waste glasses [4], [9], [10], [12], [14], [15], or American nuclear waste glasses [7], [16]–[18]. Whilst France and the US also use borosilicate glass as an immobilisation matrix, there are differences between the base glass and waste stream compositions of these countries compared to those in the UK, as well as in the likely conditions of disposal; thus, although useful in the general understanding of borosilicate glass dissolution, the outcomes of much of the reported research do not necessarily apply directly to the specific issues facing the UK. This project aimed to improve this situation, by looking at an inactive simulant of the UK's vitrified HLW product, MW-25%, and G73, proposed as an immobilisation matrix for some UK ILW [2].

To fully understand the dissolution behaviour of these glasses, there are two parameters that must be considered: i) the intrinsic resistance of the glass to dissolution, which is dependent on its structure and composition; and ii) the formation of secondary phases, such as alteration layers and crystalline precipitates, which is dependent on the composition of the glass and the chemical conditions of the leachant. For long-term dissolution expected within a geological disposal facility (GDF), the formation of secondary phases is expected to dominate. This is especially true when considering dissolution in high-pH conditions; several authors, including Corkhill *et al.* [19], Gin *et al.* [20] and Debure *et al.* [21], have observed the formation of significant alteration layers on glass in alkaline, Ca-rich conditions after time periods of less than one year.

Research conducted in this project was performed to assess: the variations in structure and durability of glasses in the  $\text{Na}_2\text{O}\cdot\text{CaO}\cdot\text{B}_2\text{O}_3\cdot\text{Al}_2\text{O}_3\cdot\text{SiO}_2$  and  $\text{Na}_2\text{O}\cdot\text{MgO}\cdot\text{B}_2\text{O}_3\cdot\text{Al}_2\text{O}_3\cdot\text{SiO}_2$  systems; the durability performance of UK nuclear waste and reference glasses; the formation of alteration layers and secondary phases on glass samples during dissolution in high-pH conditions, and how these alteration products affect the dissolution behaviour of the glasses.

In Chapter 4, the variations in structure of glasses in the  $\text{Na}_2\text{O}\cdot\text{CaO}\cdot\text{B}_2\text{O}_3\cdot\text{Al}_2\text{O}_3\cdot\text{SiO}_2$  and  $\text{Na}_2\text{O}\cdot\text{MgO}\cdot\text{B}_2\text{O}_3\cdot\text{Al}_2\text{O}_3\cdot\text{SiO}_2$  systems were investigated through the use of Nuclear Magnetic Resonance (NMR) spectroscopy. Static dissolution tests utilising the PCT-B protocol carried out on the glasses in the

$\text{Na}_2\text{O}\cdot\text{CaO}\cdot\text{B}_2\text{O}_3\cdot\text{Al}_2\text{O}_3\cdot\text{SiO}_2$  and  $\text{Na}_2\text{O}\cdot\text{MgO}\cdot\text{B}_2\text{O}_3\cdot\text{Al}_2\text{O}_3\cdot\text{SiO}_2$  systems are described in Chapter 5, with the formation and composition of alteration products investigated by Scanning Electron Microscopy (SEM), Energy Dispersive X-ray Spectroscopy (EDS) and X-Ray Diffraction (XRD). Chapter 6 investigated the dissolution performance of UK nuclear waste glasses and reference glasses, utilising both the PCT-B protocol and the MCC-1 protocol. The formation and composition of alteration products were investigated through SEM, EDS, Transmission Electron Microscopy (TEM) and micro-focus XRD.

By combining dissolution studies on UK nuclear waste glasses with those on series of simple glasses and structural studies of the simple glasses, this work aims to increase the knowledge base on the dissolution of nuclear waste glasses in Ca-rich high-pH conditions, such as those that might be found in a UK Geological Disposal Facility.



## 2. Literature Review

### 2.1 Geological Disposal of Nuclear Waste

#### 2.1.1 Introduction

Since the advent of nuclear fission as a source for energy production in the 1950s, many countries have implemented nuclear programmes as part of their energy portfolios, e.g. the U.S.A., the U.K., Japan, France, Germany, etc. As a result of this each of these countries now has a legacy of nuclear waste produced over the last 60 years. There is a general consensus amongst the governments of these nations that a long-term plan is needed for this legacy. The favoured strategy for many of these governments is that of geological disposal, i.e. the placement of nuclear waste in a facility 500 – 1000 m underground.

#### 2.1.2 Geological Disposal in the United Kingdom

In 2003, the U.K. Government set up the Committee on Radioactive Waste Management (CoRWM) in order to review the options for managing its radioactive waste inventory safely. CoRWM released its recommendations in a report to the government in July of 2006 [22]. This report identified geological disposal as being the best long-term solution to the U.K.'s radioactive waste inventory, as opposed to long-term storage. Due to the risks of war, terrorist actions, loss of institutional control or severe environmental change associated with long-term storage, the committee felt that geological disposal represented the lowest-risk option, in terms of non-proliferation of radioactive material and the safety of the public.

In 2014, the U.K. Government's Department of Energy and Climate Change (DECC) released a white paper entitled 'Implementing Geological Disposal: A Framework for the long-term management of higher activity radioactive waste' [1]. This paper sets out the framework for the government to manage its higher level waste (intermediate-level waste (ILW) and high-level waste (HLW)) inventory in the long-term through geological disposal.

Among the proposals put forward was the idea of co-disposal of ILW and HLW. Co-disposal involves the emplacement of ILW and HLW within the same facility. The safety case for the repository is based on the multi-barrier concept; a set of engineered

and natural barriers working in concert to ensure the isolation of the waste from the environment [23], [24]. These barriers are, from the waste outwards:

**Wasteform** – acts to reduce the rate at which radionuclides can be leached from waste. UK HLW is vitrified in a mixed-alkali borosilicate glass and UK ILW is encapsulated in cement.

**Waste container** – facilitates ease of handling and transport of radioactive waste. Both HLW and ILW wasteforms are stored in steel containers.

**Overpack** – waste containers will be placed into larger, ‘overpack’ containers, 3 or 4 waste containers to an overpack container. The purpose of the overpack is to prevent the waste containers from coming into contact with water in the repository over long timescales. These overpack containers will likely be made from thick steel, or from a corrosion resistant metal or alloy, such as copper. Each overpack container is referred to as a waste package.

**Buffer/Backfill** – fills the space between the waste packages and the host rock. Its purpose is to protect the waste packages from the chemical and physical processes occurring in the surrounding geology. It is likely to be a clay or clay-like material, such as bentonite, for HLW, and likely to be a high-pH cementitious material, such as Nirex reference vault backfill (NRVB) material, for ILW.

**Host Geology** – the environment surrounding the repository. This is dependent on the location of the repository.

The first four barriers are engineered barriers, while the host geology is a natural barrier. The potential use of a high-pH cementitious backfill could lead, through water ingress into the repository, to an alkaline plume forming that could come into contact with vitrified HLW. The potential implications of this are covered in Section 2.3.3.

### **2.1.3 Glass as a Nuclear Waste Matrix**

Vitrification is the process of transforming a material into a glass. One application of vitrification is the immobilisation of waste. Waste is immobilised through the creation of a vitreous wasteform which contains the waste as part of its structure, thereby rendering it passively safe, i.e. safe to be left in its current state without interference. The first investigation into using glass for the immobilisation of nuclear waste occurred in Canada in the 1950s. Subsequently, a pilot vitrification plant was established at Chalk River Nuclear Laboratories (CRNL) in Ontario, in order to establish the feasibility of large scale production. This facility produced blocks of radioactive glass between 1958 and 1960 [25]. Eventually, in the 1970s and 1980s, France, the U.S. and the U.K. made the decision to begin vitrifying their high-level wastes in borosilicate glasses, due to their increasingly large inventories of defence and civil nuclear wastes [2].

The choice of borosilicate glass for vitrification was made for reasons of cost, ease of processing, waste retention and durability [26]. If durability was the sole motivator for the choice, then pure silica glass would be ideal due to its high chemical and physical durability. However, this durability comes at a cost; its glass transition temperature is 1200 °C, meaning that temperatures of around 2200 °C are required for the glass to homogenise and fine (removal of bubbles). These temperatures are not feasible on an industrial scale due to the associated high costs, and the ease of volatilisation of important species, such as Cs-137. While numerous oxides (Li<sub>2</sub>O, Na<sub>2</sub>O, K<sub>2</sub>O, CaO, MgO, BaO etc.) can be added to silica to create glasses with reasonable processing temperatures, they have a large deleterious effect on the chemical durability of the product. However, the addition of boron oxide to a silicate glass to form a borosilicate glass leads to a significant reduction in the melting point of the glass to around 1100-1300 °C, depending on other additives, whilst maintaining a high chemical durability.

## **2.2 Glass Structure**

### **2.2.1 Silicates and Alkali/Alkaline Earth Silicates**

As the vast majority of glasses that have been produced through history have been silicates, the earliest discussions about structural theory in glasses concentrated on vitreous silica and alkali silicates. The first theory of glass structure was the crystallite

theory, formulated by Lebedev [27]. This theory postulates that glasses consist of crystallites which are microscopic, deformed versions of crystals of the same composition as the glass [28]. However, this theory has been widely dismissed, in favour of the ‘random network theory’ theory (see below) [29].

In 1932, Norwegian-American physicist, William H. Zachariasen, released a paper entitled ‘The Atomic Arrangement in Glass’, which postulated a theory of glass formation [30]. Zachariasen stated that, as the crystallite theory of glass structure fails to explain all the observed phenomena and properties for vitreous silica, e.g. density and thermal properties, it could not be a satisfactory description of the general atomic structure of glasses. He proposed that glass structure is ‘characterized by an extended three-dimensional network which lacks symmetry and periodicity’. He also proposed four rules that describe the requirements for the formation of a glass:

- (1) Each oxygen atom is linked to no more than two cations
- (2) The number of oxygen atoms surrounding each cation must be small
- (3) Oxygen polyhedra must share corners, not edges or faces
- (4) At least three corners of each oxygen polyhedron must be shared

Rule (4) only applies if the network is required to be 3-dimensional. The first three rules give rise to a glass structure as shown in Figure 2.1. An  $\text{MO}_4$  tetrahedron, as described by the rules, is labelled. The characteristic ‘rings’ of a glass structure are composed of several of these tetrahedra bonded together. These rules were developed for glasses made from simple oxides, so three more rules have been devised for more complex glasses [28]:

- (5) The sample must contain a high percentage of network cations which are surrounded by oxygen tetrahedra or triangles
- (6) The tetrahedra or triangles share only corners with each other
- (7) Some oxygen atoms are linked to only two network cations, and do not form further bonds with any other cations

Zachariasen’s rules were formulated to describe the conditions required for glass formation, but they are the basis for many glass structural models today, which are grouped under the term ‘random network theory’ [28]. The use of the term ‘random’ in any model of glass structure is controversial, as there is only a finite range of angles that can exist between  $\text{MO}_4$  tetrahedra within an  $\text{MO}_2$  structure.

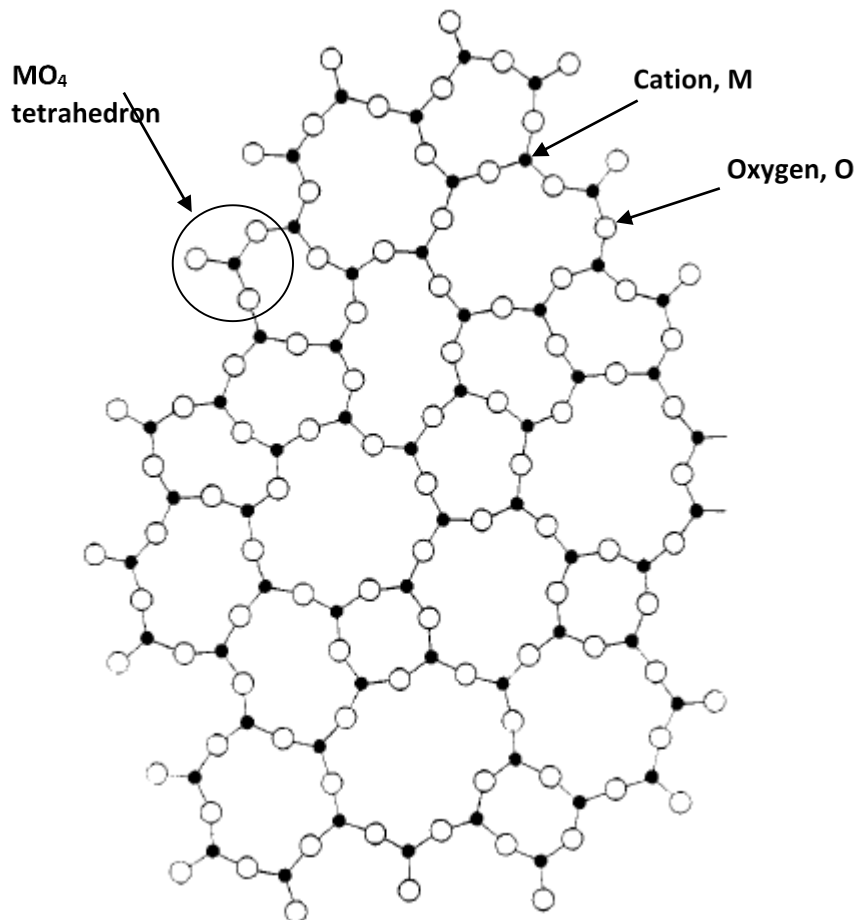
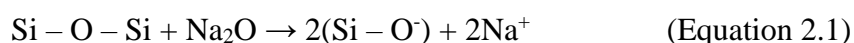


**Figure 2.1.** Proposed structure of a simple oxide glass in two dimensions.  
Adapted from Zachariasen [30].

Although Zachariasen's model, dubbed the 'Continuous Random Network' (CRN) model, readily explains the structure of vitreous silica, an extension was proposed by Warren in 1941 to describe the structure of alkali silicates (although it can also be applied to alkaline earth silicates) [31]. This is known as the Zachariasen-Warren model, and it postulates that the alkali cations randomly occupy the spaces within the rings of tetrahedra in the glass (Figure 2.2). As monovalent alkali cations (A) are added, each one causes a bridging oxygen (BO) bond (Si – O – Si) to become a non-bridging oxygen (NBO) bond (Si – O<sup>-</sup>). These NBOs are charge-balanced by the alkali cations, for example:



Due to this effect on the glass network, alkali and alkaline earth metals are known as network modifiers. In 1981, Greaves & co-workers proposed a modification to the

Zachariasen-Warren model, dubbed the ‘modified random network’ (MRN), based on EXAFS data obtained on alkali silicates [32], [33]. In the MRN, the glass structure is comprised of two separate, interlinking, regions, or ‘sublattices’; a network region comprised of network formers, and inter-network regions containing the network modifying cations. Figure 2.3 shows a two-dimensional illustration of this for a glass of approximate composition  $A_2O_3(G_2O_3)_2$ , where A is a network modifying cation, and G is a network former. There are two types of oxygen site in this model; a site bonded to two glass forming cations (a bridging oxygen), and a site bonded to one glass forming cation and two glass modifying cations (a non-bridging oxygen). This model of structure utilises Smekal’s idea that glasses only form when there is bond mixing, i.e. when both covalent and ionic bonds are present [34]. In this case, the bonding in the network regions is mostly covalent (solid lines in Figure 2.3) and the bonding in the inter-network regions is ionic (dashed lines). This theory of glass structure is supported by nuclear magnetic resonance (NMR) data obtained by Voigt et al. [35] as well as data from molecular dynamics simulations carried out by Huang and Cormack [36].

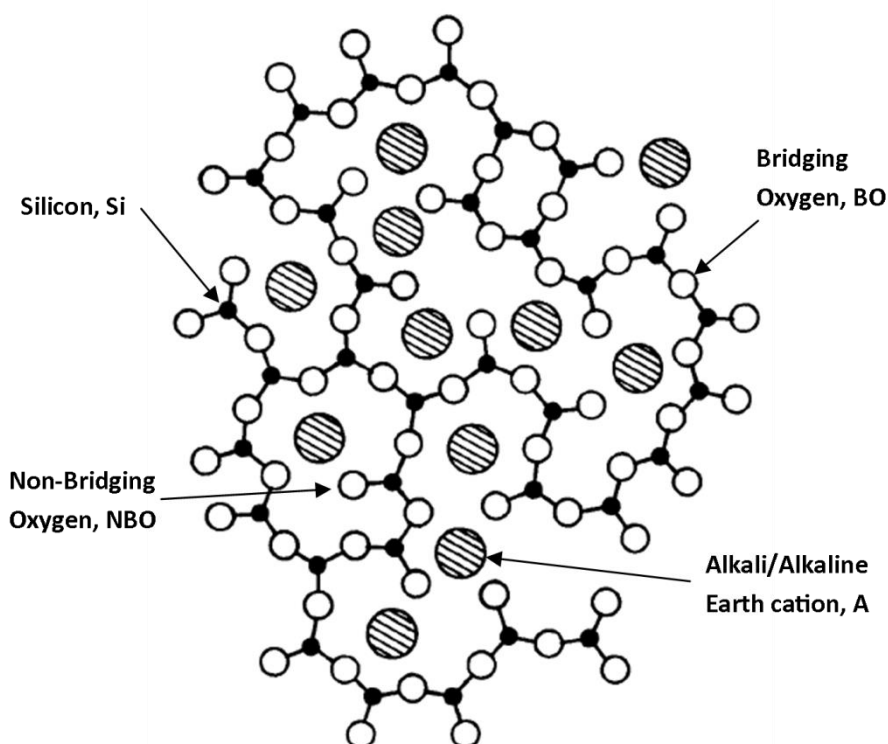


**Figure 2.2.** Structure of an alkali silicate in 2-d, as described by the Zachariasen-Warren model. Adapted from Warren [31].

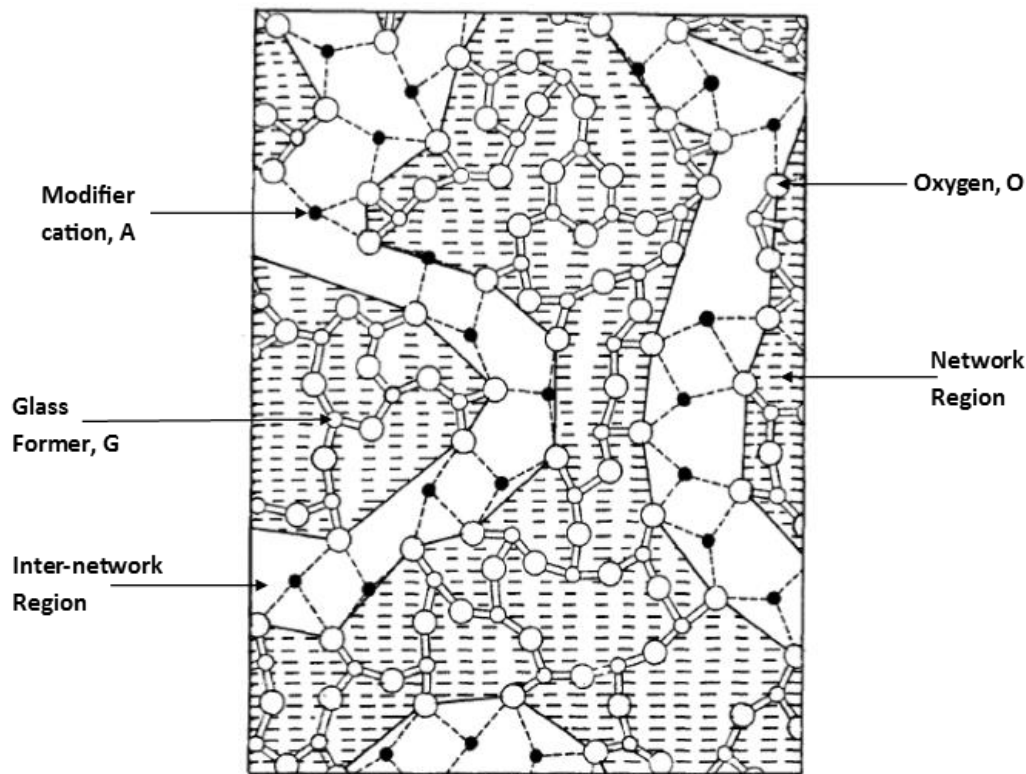


**Figure 2.3.** Two-dimensional representation of a modified random network (MRN) in the model glass  $A_2O_3(G_2O_3)_2$ . Adapted from Greaves [33].

### 2.2.2 Borates, Borosilicates and Alkali/Alkaline Earth Borosilicates

The structural theories for silicate glasses cannot be applied to borosilicate glasses, as boron can exist in both 3-coordinate trigonal ( $^{III}B$ ) units and 4-coordinate tetrahedral ( $^{IV}B$ ) units within the glass network, whereas silicon only exists in a 4-coordinated state ( $^{IV}Si$ ).

To understand the structure of borosilicate glasses, it is helpful to consider the structure of borate glasses. A brief overview is presented here, focusing on alkali borates, but for a more thorough treatment, see the review by Wright [37]. The first structural model of borate glasses was developed by Abe in 1952 [38], and had three rules:

- i) Tetrahedral  $^{IV}B$  units cannot be immediate neighbours
- ii) Trigonal  $^{III}B$  units cannot be bound to more than one  $^{IV}B$  tetrahedral unit
- iii) NBOs only occur on trigonal  $^{III}B$  units

However, this model predicted peak values of the fraction of four-fold coordinated boron ( $^{IV}B$ ) which were too low and were at too low values of added alkali fraction. Beekenkamp therefore proposed that Rule ii) of Abe's model must be violated [39],

but, despite this, the model still predicted <sup>IV</sup>B fraction values which were too low. In 1986, Gupta proposed a model which suggested that Rule i) from Abe's model is also violated [40]. To do this, he proposed the Random Pair Model, which has three rules:

- i) <sup>IV</sup>B units occur in pairs joined by an unconstrained <sup>IV</sup>B – O – <sup>IV</sup>B bond
- ii) No <sup>IV</sup>B – <sup>IV</sup>B pair can be bound to another such pair
- iii) NBOs only occur on trigonal <sup>III</sup>B units

These models all assume that borate glasses only contain structural units. However, there is mounting evidence to suggest that superstructural units, that is, units made up of more than one <sup>III/IV</sup>B structural unit with no internal degrees of freedom with respect to bond and torsion angles, are the primary 'building blocks' of borate glasses [41]. A model of borate glass structure based on superstructural units was first proposed by Krogh-Moe in 1962 [42]. The primary difference between this model and that of Gupta is that in the Gupta model, the <sup>IV</sup>B – O – <sup>IV</sup>B pair bonds are unconstrained, whereas the <sup>IV</sup>B – O – <sup>IV</sup>B bonds within superstructural units have fixed bond and torsion angles. The Krogh-Moe model predicts the borate structure through the relative proportions of boroxol (three <sup>III</sup>B units interlinked, B<sub>3</sub>O<sub>6</sub>), tetraborate (6 <sup>III</sup>B and 2 <sup>IV</sup>B units, B<sub>8</sub>O<sub>16</sub>) and diborate (2 <sup>III</sup>B and 2 <sup>IV</sup>B units, B<sub>4</sub>O<sub>9</sub>) superstructural units, and uses the Zachariasen-Warren rules (see Section 2.2.1), which are applied to the superstructural units rather than individual <sup>III</sup>B and <sup>IV</sup>B units. In 1978, Griscom utilised Krogh-Moe's predictions to form a model of borate glass structure [43]. However, this model has two main issues:

- i) It assumes that pure vitreous B<sub>2</sub>O<sub>3</sub> is composed entirely of boroxol rings, but evidence from NMR spectroscopy and neutron diffraction suggest that this is not the case
- ii) It involves the substitution of NBOs for <sup>IV</sup>B units in diborate groups, but this would also require the inclusion of <sup>III</sup>B units to maintain the correct stoichiometry

In general, it appears that models taking into account superstructural units are required to fully describe borate glass structure.

Some of the early work on a structural model for borosilicate glasses was carried out on Na<sub>2</sub>O – B<sub>2</sub>O<sub>3</sub> – SiO<sub>2</sub> glasses by Yun and Bray in 1978 [44], which was then corrected by Yun et al. in 1979 [45]. Dell, Bray and Xiao then furthered this work to form the theory known as the Dell-Bray model, which was applied to all single alkali borosilicates [46]. This model states that for a constant K ratio ( $[\text{SiO}_2]/[\text{B}_2\text{O}_3]$ ), the

glass structure passes through 4 distinct regions with increasing R ratio ( $[M_2O]/[B_2O_3]$  where M is an alkali ion). The four regions are:

- 1)  $R < 0.5$ : The alkali ions cause 3-coordinated  $^{III}B$  to become 4-coordinated  $^{IV}B$ . The ratio of  $^{IV}B/(^{III}B + ^{IV}B)$  is equal to R.
- 2)  $0.5 \leq R \leq R_{Max}$  ( $R_{Max} = 1/2 + 1/16K$ ): The additional alkali ions cause the formation of reedmergnerite groups, which are boron tetrahedra with each oxygen bridging to a silicate tetrahedron (formula =  $1/2(Na_2O.B_2O_3.8SiO_2)$ ).
- 3)  $R_{Max} \leq R \leq R_{D1}$  ( $R_{D1} = 1/2 + 1/4K$ ): All the additional alkali ions go to creating non-bridging oxygens on the silicate tetrahedra of the reedmergnerite groups.
- 4)  $R_{D1} \leq R \leq R_{D3}$  ( $R_{D3} = 2 - K$ ):  $((K - K/4)/(2 + K))$  of the additional alkali ions combine with diborate groups (consist of  $2 ^{III}B$  groups +  $2 ^{IV}B$  groups) to form borate units with two non-bridging oxygens (pyroborate groups). The  $((K + K/4)/(2 + K))$  remaining alkali ions combine with reedmergnerite groups.

As the number of four-coordinated boron groups increases in regions 2 and 3, the connectivity of the network increases. This leads to an increase in the glass transition temperature. However, as the number of four-coordinated boron groups reaches a maximum in region 3, and then decreases in region 4, the connectivity of the network decreases to its original level.

In more recent years, the Dell-Bray model has been criticised a number of times, e.g. by Sen [47] and Martens & Müller-Warmuth [48]. The general consensus seems to be that the Dell-Bray model gives a good description of the structural changes in a borosilicate with the addition of alkali ions, but that the alkali cations are more randomly distributed between the borate and silicate networks than is assumed in the model [49].

### 2.2.3 Aluminosilicates and Alkali/Alkaline Earth Aluminosilicates

As with borosilicates, structural models for silicates cannot be applied to aluminosilicates as aluminium can be present in three different forms; 4-coordinate  $^{\text{IV}}\text{Al}$ , 5-coordinate  $^{\text{V}}\text{Al}$  and 6-coordinate  $^{\text{VI}}\text{Al}$ .

The role of Al in the glass structure is dependent on the glass composition [50]. The conventional view of this is that for a binary  $\text{Al}_2\text{O}_3 - \text{SiO}_2$  glass, Al is only present in 6-coordinated octahedral sites, and thus acts as a network modifier, producing non-bridging oxygens (NBOs) [28]. However, when alkali or alkaline earth network-modifying cations are added to the glass, they act to convert the  $^{\text{VI}}\text{Al}$  octahedra into  $^{\text{IV}}\text{Al}$  tetrahedra which are singly-charged anions. Each alkali cation can produce one  $^{\text{IV}}\text{Al}$  tetrahedron, while, theoretically, each alkaline earth cation can produce two such groups. In this model, for a given value of K ( $\text{SiO}_2/\text{Al}_2\text{O}_3$ ), there are three distinct regions of network formation when the ratio of alkali oxide to alumina ( $\text{R}_2\text{O}/\text{Al}_2\text{O}_3$ ),  $\text{R}_1$ , or the ratio of alkaline earth oxide to alumina ( $\text{RO}/\text{Al}_2\text{O}_3$ ),  $\text{R}_2$ , varies [51]:

- 1)  $\text{R}_1 < 1$ ,  $\text{R}_2 < 0.5$ : A fraction ( $\text{R}_1$ ,  $2\text{R}_2$ ) of the Al ions are present in tetrahedral sites, while the other fraction,  $((1 - \text{R}_1), (1 - 2\text{R}_2))$  are present in octahedral sites.
- 2)  $\text{R}_1 = 1$ ,  $\text{R}_2 = 0.5$ : All of the Al ions are present in tetrahedral sites, and all of the alkali/alkaline earth cations are used in this process.
- 3)  $\text{R}_1 > 1$ ,  $\text{R}_2 > 0.5$ : All of the Al ions are present in tetrahedral sites, and the excess alkali/alkaline earth cations go to creating NBOs on the silica tetrahedra.

As the R ratios increase from zero, the network connectivity of the glass will increase, as the number of network-modifying Al octahedra reduces. The network connectivity will reach a maximum at  $\text{R}_1 = 1$  or  $\text{R}_2 = 0.5$ , and will then decrease with increasing R, due to the formation of NBOs by the excess alkali/alkaline earth cations.

The conventional view of aluminosilicate structure is challenged by data reported by Stebbins & Xu, who found NBOs present in a  $\text{CaAl}_2\text{Si}_2\text{O}_8$  glass ( $\text{R}_2 = 0.5$ ) using NMR [52]. However, Huang & Behrman [53] and Cormier et al. [54] have also presented data that suggests that Al is only present in tetrahedra in calcium

aluminosilicates, so there should be no NBOs associated with the presence of Al. It is possible that the NBOs reported by Stebbins and Xu are associated with the silica tetrahedra rather than the Al tetrahedra, as they suggest, reconciling these different datasets.

#### 2.2.4 Aluminoborosilicates and Alkali/Alkaline Earth Aluminoborosilicates

As well as borosilicate and aluminosilicate glasses, aluminoborosilicate glasses containing both intermediate oxides are relevant to nuclear waste glasses, e.g. France HLW glasses are aluminoborosilicates, and the waste-loaded UK glasses also contain  $Al_2O_3$ . One important feature in the structure of aluminoborosilicates is that tetrahedral  $^{IV}Al$  units are preferentially charge-compensated by  $M_2O$  (generally  $Na_2O$ ) and  $MO$  (where  $M = Ca, Mg, Ba, Sr$ ) over tetrahedral  $^{IV}B$  units, as discovered by Yamashita *et al.* [55], [56]. As such, when  $[Na_2O] < [Al_2O_3]$ , all available sodium is used in charge-compensating for  $^{IV}Al$  tetrahedra, but the deficiency in sodium concentration leads to the presence of  $^{V}Al$  units, which are coordinated to three non-bridging oxygens and two bridging oxygens, and thus act as network modifiers. When  $[Na_2O] > [Al_2O_3]$ , all of the aluminium is charge-compensated and present in  $^{IV}Al$  tetrahedra, and the excess sodium is used in the charge-compensation of  $^{IV}B$  tetrahedra, or the generation of NBOs on silicate or borate tetrahedra [57]. The proportion of  $^{IV}B$  units to the total boron content, known as  $N_4$ , has been shown to correlate well with  $r/(1 - r)$ , where [55]:

$$r = \frac{[Na_2O - Al_2O_3]}{[Na_2O - Al_2O_3 + B_2O_3]} \quad (\text{Equation 2.2})$$

Thus,  $r/(1 - r)$  can be simplified to:

$$r' = \frac{[Na_2O - Al_2O_3]}{[B_2O_3]} \quad (\text{Equation 2.3})$$

This provides evidence that the  $^{IV}Al$  tetrahedra are preferentially charge-compensated over  $^{IV}B$  tetrahedra.

## 2.3 Glass Dissolution

### 2.3.1 Introduction

The dissolution behaviour of glass has been a topic of interest for scientists for over a hundred years, not least because of the near-universal application of glass as the material of choice for many pieces of standard laboratory equipment, such as beakers and measuring cylinders.

Studies of the dissolution behaviour of glasses have typically involved exposing the glass to an attacking solution, to obtain data from commercially, or scientifically, important glass compositions [58]–[63]. The test methods used generally fall into one of two categories: static and dynamic. In a static dissolution test, e.g. the Materials Characterisation Center (MCC-1) test [64], the sample to be tested is placed within a reaction vessel with the attacking solution, or *leachant*, and kept sealed for the remainder of the test. In a dynamic test, such as Single-Pass Flow-Through (SPFT) [65], the leachant is passed through the reaction vessel at a constant rate, so that the solution within the vessel is constantly replenished. In both categories, parameters such as sample composition, duration of test, composition of leachant, and temperature can be adjusted.

### 2.3.2 Dissolution in Aqueous Solutions

The dissolution of glasses in aqueous solutions is a complex, and not fully-understood, process. Many parameters are known to affect the chemical durability of glasses in aqueous solutions: glass composition [3], [12], [66]; composition of the attacking solution [13], [67]; temperature [7], [68]; pH [3]–[5]; and sample-surface-area-to-attacking-volume (S/V) ratio [69]. As the area of glass dissolution is so wide, and as glass composition has an effect on glass dissolution, only the dissolution of nuclear waste glasses (and analogues), particularly boro- and aluminosilicates, will be discussed here.

The research done on the dissolution of HLW glasses has been distilled into a five-stage phenomenological description by several previous works [70], [71]. A schematic for this description is shown in Figure 2.4. The five phenomenological regimes are:

Stage I: Ion exchange (or interdiffusion) of alkali ions

Stage II: Hydrolysis of the silicate network

Stage III: The rate-drop regime

Stage IV: The residual rate (also saturation) regime

Stage V: Precipitation of alteration products, possibly leading to resumption of dissolution

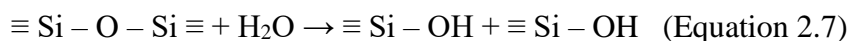
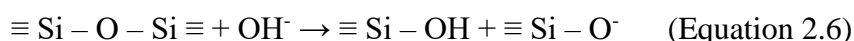
Stages I and II together are referred to as the initial rate regime. In nuclear waste glasses, which contain alkali ions, ion exchange with positively-charged species from the aqueous solution ( $H^+$  and  $H_3O^+$ ) leads to preferential leaching of the alkali ions from the glass [72]:



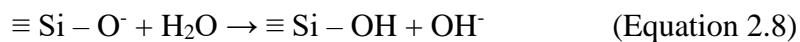
or



where  $R$  is an alkali ion. Most authors think that Equation 2.5 is more likely, e.g. Gelder & Fearn [73]. This process is also referred to as interdiffusion, as the flux of alkali ions out of the glass is opposed by the flux of the positive species from the solution into the glass. A general theory for this process was outlined by Doremus [74]. Interdiffusion results in hydrolysis of the silica network, which also takes place through direct water attack:



The  $OH^-$  ions are formed to charge-balance the alkali ions released into solution, which leads to an increase in the pH of the solution, if the solution is static. The non-bridging oxygen from Equation 2.6 can then react with another molecule of water:



producing another hydroxyl ion that can hydrolyse another siloxane bond [51]. Once each of the four bonds on a  $\text{SiO}_4$  tetrahedron have been hydrolysed, then a silicic acid monomer,  $\text{Si}(\text{OH})_4$ , is released into the solution. This process results in congruent dissolution of the glass.

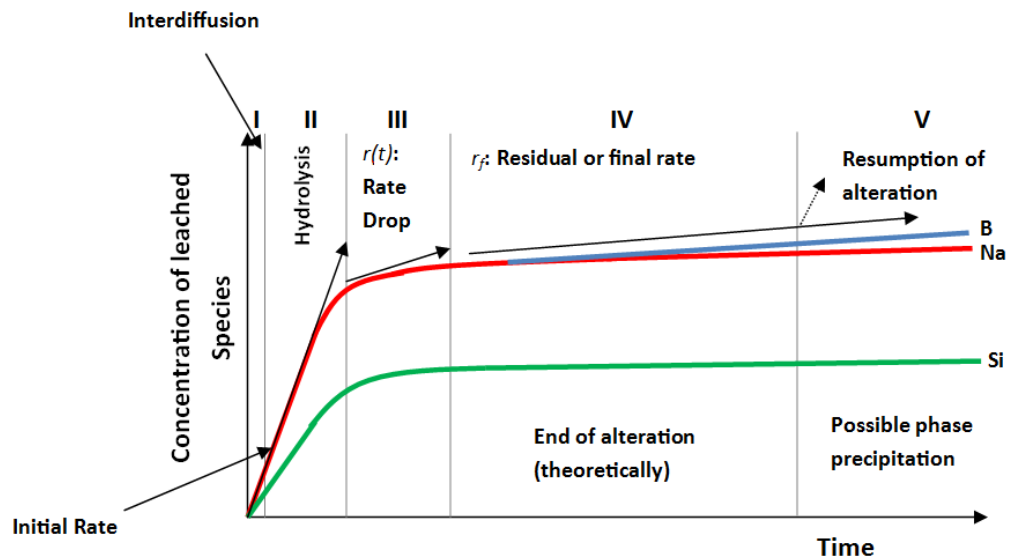


**Figure 2.4.** Schematic of five-stage phenomenological description of nuclear waste glass dissolution. Adapted from Utton et al. [170].

The initial rate of dissolution, before the solution is modified by ions leaching into it, is the maximum rate of dissolution for each glass. In a static system, with no replenishment of the attacking solution, the rate of alteration decreases. This is the rate drop regime (Stage III). There are two main theories that purport to describe this:

- 1) The increase in silicic acid activity in the solution, due to the congruent dissolution of the glass matrix, reduces the chemical affinity for further dissolution; i.e. a thermodynamic ‘steady-state’ is achieved. N.B. True thermodynamic equilibrium cannot be achieved in a glass-solution system as the glass itself is not thermodynamically stable [75].
- 2) The formation of a gel-layer on the surface of the glass acts as a kinetic barrier to further ion exchange of species between the glass and the solution [59], [60], [71].

It is also possible that the rate drop is due to a combination of these effects. There are researchers who favour the chemical affinity theory, e.g. Jantzen et al. [18] and Grambow [76], whilst others, such as Rajmohan et al [66] and Chave et al. [13], prefer the protective gel layer theory. Gin et al., state that both processes are important, and that they are coupled [14]. Abraitis et al. state that the silicic acid activity is the main influence on the rate, but only at high pH, due to its effect on Si release through network hydrolysis (which is dominant at high pH) [5]. Recently, Icenhower and Steefel reported dissolution experiments where an increase in Si added to the solution led to a non-linear decrease in the rate of dissolution, which is not consistent with current models for glass dissolution using chemical affinity [67]. So far, there is no general consensus on this subject.

The residual regime is the fourth stage of this description of glass dissolution. Dissolution continues at a very low rate, several orders of magnitude below the initial rate. This stage is tied-in with the rate drop regime, as it occurs where the system reaches a 'steady-state' between the dissolution processes and the rate-limiting processes.

In stage V, saturation of leached species in the solution can lead to the precipitation of mineral phases, referred to as 'alteration products'. It has been suggested by Gin & Mestre that the precipitation of these phases pulls elements from the alteration layer on the surface of the glass, leading to a degradation in its protective capabilities, and hence a resumption of a higher rate of alteration [4]. This theory is also endorsed by Frugier, who again suggested that it is the competition between the formation of a protective gel layer and the formation of the secondary precipitates which is responsible for an increase in the alteration rate [12]. Work by Gin et al. has also shown that precipitation does not necessarily occur for every glass composition; out of 10 compositions studied, only 3 had formed secondary precipitates [14]. Out of these 3 samples, two (CJ1 and CJ8) had been significantly altered, whilst the other was more durable (SON68). Whether this was due to the effect of the precipitates is not clear. This compositional dependence was also noted by Curti et al., who studied the dissolution of the UK's simulant nuclear waste glass, MW-25%, and France's simulant nuclear waste glass, SON68, over 12 years, and found that the MW produced many more secondary crystalline phases, and was more significantly altered, than the SON68 glass [77]. This is attributed to the presence of Mg in MW, which is replaced with Ca in SON68.

This model of glass dissolution is not the only one in the literature. Geisler *et al.* [61] and Hellmann *et al.* [78] proposed a model based on congruent dissolution of the glass matrix, followed by supersaturation of the leachate with respect to solid phases in an interfacial region next to the glass surface, which leads to the reprecipitation of glass components from solution. This mechanism is discussed further in Section 2.3.4.

A recent advance in describing the dissolution behaviour of nuclear waste glasses is the Glass Reactivity with Allowance for the Alteration Layer, or GRAAL, model developed by Frugier *et al.* [71]. This model has been developed through analysis of the dissolution of SON 68, the inactive simulant of French nuclear waste glass, and was created in response to discrepancies in the literature with regards to the mechanisms relating to the rate drop and residual rate regimes (Stages III & IV in Figure 2.4). The GRAAL model depends on a set of simplified hypotheses, namely:

- The amorphous alteration layer can be divided into 3 parts: the glass hydration zone, the Passive Reactive Interphase (PRI) and the gel zone depleted in network-forming elements. However, only the PRI, which acts as a limiter to diffusion, is described by the model.
- Diffusion of water and hydrated and solvated glass constituents in the PRI are described by a single apparent diffusion coefficient.
- A thermodynamic equilibrium is used to describe the reactivity of the PRI with the leaching solution.

As of the present day, the GRAAL model has been primarily applied to the French SON68 and R7T7 glasses [79]–[81]. Further work is required for it to be validated against a range of glass compositions.

### 2.3.3 Dissolution at High-pH

It is commonly known that the dissolution of silicate glasses (and borosilicates) has a dependence on the pH of the attacking solution [28], [51], [72], [82]. In general, as the pH moves away from 6-7, the dissolution rate of the glass increases. For example, Figure 2.5 shows the Si release for a Magnox glass (UK HLW simulant) at  $18 \pm 4$  °C, over a pH range of 2 – 12 (figure adapted from Abraitis *et al.* [5]). Si release is an indicator of the overall dissolution rate of the glass, as Si loss from the glass implies network hydrolysis, and thus, dissolution of the glass matrix. Below pH 6, the release rate rapidly increases, as it does above pH 7, although not as rapidly. This pH-

dependence has been shown for a range of nuclear waste glasses [3]–[5], [7], as well as other compositions not earmarked for waste immobilisation [6], [83].

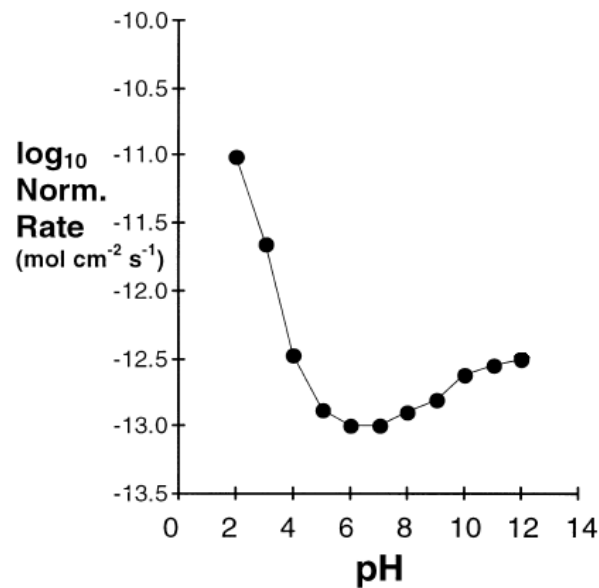


**Figure 2.5.** Si release rate from Magnox glass at  $18 \pm 4$  °C, over a pH range 2 – 12. Adapted from Abraitis et al. [5].

As mentioned in Section 1.1.2, there is a risk of UK HLW glass coming into contact with a high-pH solution, due to possible implementation of an alkaline cement backfill within the proposed Geological Disposal Facility (GDF). At high pH, there is a greater concentration of hydroxyl ions in the attacking solution, leading to a greater rate of network hydrolysis, and thus matrix dissolution [51]. In this case, one would expect to see congruent dissolution of the glass, as is reported by Pierce et al. [7] and Abraitis et al. [5]. However, Utton et al. recorded incongruent dissolution at high pH [3]. No reason is given for this result in the work, but it is likely that all elements are being leached equally, i.e. the leaching is non-selective, but some of the elements are being consumed by the gel layer or secondary precipitates, drawing them out of solution.

One important factor in the dissolution of nuclear waste glasses at high-pH is the precipitation of secondary phases. The solubility of many mineral phases decreases significantly with increasing pH, and so these secondary phases are a common sight in experiments of this nature. Several different types of secondary phase have been observed in high-pH experiments, from calcium silicate hydrates (C-S-H) [21], [84] and calcium aluminium silicate hydrates (C-A-S-H) [85], to Mg-bearing smectites [84] and crystalline Mg silicates [21], [81], [86]. Along with these observations of

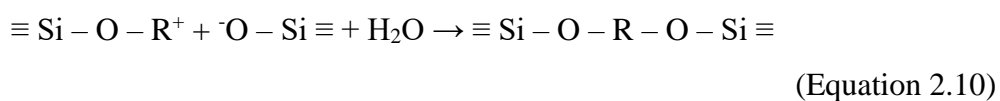
secondary precipitates, a resumption of alteration after reaching the residual regime (discussed below) was observed by Utton et al., Ferrand et al. and Fleury et al. [84]–[86].

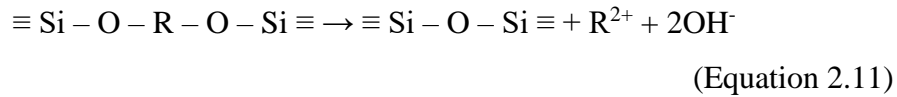
Obviously, it is desirable to keep the dissolution of vitrified wastes in a GDF as low as possible. However, Gin & Mestre reported total alteration of a sample of SON68 at pH 11.5 after only 240 days [4]. These experiments were carried out at elevated temperature (90 °C) and with a high S/V ratio of 5000 m<sup>-1</sup>, which are both significantly higher than one would expect in repository conditions. As mentioned in Section 2.3.2, the authors suggest that the precipitation of aluminosilicate minerals is responsible for the degradation of the gel layer that led to a high rate of dissolution even after the residual regime had been entered. Although Utton et al. [3], Pierce et al. [7] and Abraitis et al. [5] have carried out dissolution tests at high pH without observing the same extensive alteration, it is very difficult to compare their results to those of Gin & Mestre, due to differences in test method, duration, temperature, pH and S/V. Gin and Ribet [87], following on from [4], altered SON68 powder in pH 11.5 solutions until the formation of precipitates and resumption of rapid alteration, then the pH was artificially dropped to 9.5, whereupon the aluminosilicate precipitates dissolved back into solution and the alteration rate greatly decreased. Fournier et al., in their review of the resumption of alteration in nuclear waste glasses, note that this pH-dependence exists across many different investigations [88]. The three investigations which previously saw a resumption of alteration (Utton et al., Ferrand et al. and Fleury et al.; see above) used leachants with a pH > 10.5, which is a threshold supported by the data analysed in the review by Fournier et al.; precipitation of these secondary phases does not seem to occur at lower pH values. A particularly relevant factor in this mechanism is the presence of Al in the system. Depending on the concentrations of Al and other elements in solution, the Al can sorb to silanol sites, precipitate as surface aluminium oxyhydroxides, or precipitate as zeolites. Whilst the first two options lead to a decrease in silica solubility, and hence a decrease in glass dissolution rate, the precipitation of zeolites has been systematically linked to the resumption of an increased rate of dissolution. This is suggested to be due to the consumption of Si and Al from the glass alteration layer by the zeolites, as zeolites are more thermodynamically favourable than a poorly-crystalline gel phase. This illustrates the importance of analysing the performance of vitreous waste forms in conditions, in this case high-pH, that are thought possible in a given disposal scenario.

Previous works by Andriambololona et al. [89] and Utton et al. [3] have shown results that suggest that the presence of Ca, in the glass or in solution, at pH 12.5 acts to reduce the dissolution rate of some glass compositions. A similar role for Ca in solution at pH 9 was reported by Chave et al. [13]. However, while Utton et al. suggest that this is due to the formation of Ca-rich precipitates that act as a protective layer, Chave et al. attribute this to Ca incorporation into the gel-layer of the glass. Corkhill et al. postulated that, rather than the Ca concentration in solution being key, it is the synergy between Ca and Si [19]. Above a certain Ca concentration, all Si leached from the glass precipitates as calcium-silicate-based phases, whereas below this critical level, Si remains in solution after leaching. These results have relevance to a possible UK disposal scenario, as the high pH cement is likely to contain significant amounts of Ca(OH)<sub>2</sub>. Utton et al. also reported an ‘incubation period’, i.e. a period of low dissolution rate before the onset of the initial rate, for their lab simulant glass. This was suggested be due to the formation of a short-lived calcium borate phase, which acted as a protective layer on the glass. If true, this may pose a problem for dissolution measurement, as B is often used as a dissolution tracer, precisely because it is not incorporated into the alteration layer or precipitated phases [7].

### 2.3.4 Gel and Alteration Layer Production

During the dissolution of glass a gel (or alteration) layer forms. The mechanism for this formation in nuclear waste glasses is under debate. At present there are two theories purported to explain the formation of alteration layers. The first of these centres around the diffusion of mobile species (alkalis, alkaline earths, boron, etc.) from the glass surface, a process termed ‘de-alkalisation’. This proceeds in accordance with Equations 2.4 and 2.5, leaving a porous silica gel layer, which can recondense in-situ to form a layer which can act as a partial barrier to further diffusion [20]. The recondensation process can be aided by the presence of divalent cations, such as Ca<sup>2+</sup> and Mg<sup>2+</sup>, through the following reactions:





Where  $\text{R}^{+/2+}$  are singly- and doubly-charged alkaline earth cations [13]. Firstly, an alkaline earth cation links with a negatively charged silanol (Equation 2.9). The resulting positively-charged complex then attracts another negatively-charged silanol, which causes the two silicate species to be linked by the divalent cation (Equation 2.10). However, this arrangement is unstable, resulting in the ejection of the cation and two hydroxyl ions and the formation of a siloxane group, increasing the connectivity of the gel.

The second hypothesis, as postulated by Geisler et al. [61] and Hellmann et al. [90], is a mechanism based on dissolution and reprecipitation (see Section 2.3.2). The glass network dissolves congruently, leading to an increase of the glass elements in solution in the vicinity of the glass. This results in the solution becoming supersaturated with respect to solid phases, which then precipitate onto the surface of the glass, forming the alteration layer. Evidence exists in support of both of these mechanisms:

- The diffusion-based model is supported by Time-Of-Flight Secondary Ion Mass Spectrometry (TOF-SIMS) measurements of alteration layers, which show depth profiles of elements in the alteration layer which are consistent with diffusion processes [13], [91].
- Dissolution experiments with a leachant containing  $^{29}\text{Si}$  showed that the Si in the alteration layer was  $^{28}\text{Si}$ , suggesting that it originated in the glass, which also supports diffusion over dissolution-reprecipitation [20].
- Dissolution-reprecipitation is supported by energy-filtered transmission electron microscopy and atom-probe tomography of silicate glass alteration layers showing nanometre-scale changes in elemental depth profiles not consistent with a diffusion-based model [92].
- Experiments utilising an  $^{18}\text{O}$ -enriched leachant that was added midway through a leaching experiment on a  $^{30}\text{Si}$ -enriched glass yielded isotopic profiles in the alteration layer that are inconsistent with a diffusion-based model [93].
- The observation of banding in alteration layers on archaeological and nuclear glasses, which is thought to be due to local fluctuations in solution chemistry,

is more consistent with a dissolution-precipitation model than a diffusion-based one [94]–[96]

Both mechanisms appear to explain the results of specific experiments. The mechanism of alteration layer formation is dependent on the conditions involved in dissolution. The dissolution-precipitation model applies when hydrolysis is the primary mode for dissolution, i.e. high-pH and low-pH, whereas the diffusion model is prevalent where diffusion is the dominant dissolution reaction, closer to neutral pH [20]. It might therefore be expected that the experiments carried out in this investigation would show evidence of a dissolution-precipitation mechanism.

### **2.3.5 Natural Glasses as Analogues for Nuclear Waste Glass Dissolution**

One of the primary issues with the study of the dissolution of nuclear waste glasses with regards to their behaviour during geological disposal is the very long timescales that are involved. These could be as long as 1 million years, and it is not possible to even approximate these timescales in a laboratory. As a potential solution to this, it has been suggested since the late 1970s that natural glasses can be used as analogues of the dissolution behaviour of nuclear waste glasses over geological timescales [97]–[104]. Glasses proposed as analogues have generally fallen into one of two categories: rhyolitic glasses with high silica content (> 65 wt.%) [98], [105]; or, more commonly, basaltic glasses, which are aluminosilicates [15], [103], [106]–[109]. The consensus in the literature appears to be that basaltic glasses are valid analogues for the dissolution of nuclear waste glasses, however there are few investigations with direct comparison of basaltic and nuclear waste glasses. One exception is Techer et al. [15], who saw comparable dissolution behaviour in the laboratory between a basaltic glass and SON 68, a French simulant waste glass. One significant difference between aluminoborosilicate nuclear waste glasses and basaltic glasses is that natural basaltic glasses contain no boron oxide. Further investigations are needed, with direct experimental comparison between basaltic glasses and nuclear waste glasses, in order to fully understand the similarities and differences in dissolution behaviour of natural glasses compared to nuclear aluminoborosilicates.

### **2.3.6 State of Knowledge of UK Nuclear Waste Glass Dissolution**

The dissolution behaviour of UK nuclear waste glasses has not been the subject of as extensive study as French nuclear waste glasses. However, a number of studies have

been carried out on various aspects of UK nuclear waste glass dissolution [3], [5], [11], [19], [77], [84], [110]–[112]. Abraitis et al. [5] looked at the dissolution of Magnox waste glass as a function of pH and silicic acid activity, and found a significant dependence on dissolution rate with pH. They suggest that the mechanism of dissolution depends on pH, with proton-promoted hydrolysis of B – O and Al – O bonds, hydration and ion exchange processes being prevalent at low pH, and hydrolysis of siloxane bonds being the rate-limiting step at high-pH, leading to congruent dissolution of the glass network.

Curti et al. studied the relative dissolution performance of MW-25% (referred to as ‘MW’), an inactive simulant of UK HLW vitrified product, compared to SON68, the French equivalent, in pure water at 90 °C. They found that the MW glass dissolved at a rate around 10 times higher than that of the SON68 glass. They postulated that this was due to the presence of Mg in the MW glass leading to the formation of secondary clay minerals which enhanced the dissolution of the glass by consuming silica from its network. Two further investigations were carried out by Curti et al. into the speciation of Na, Mg, Ni and Cs in the altered MW sample [11] and Ce<sup>3+/4+</sup> speciation of the sample and its relevance to the behaviour of Pu during dissolution [112]. In the former, they found that Mg was retained in Mg-smectite clays formed during dissolution, and that there was significant retention of both Ni and Cs in alteration layers. In the latter investigation it was found that the Ce<sup>4+</sup> in the glass became partially reduced to Ce<sup>3+</sup> when leached, and that this Ce<sup>3+</sup> was associated with the Mg-smectite precipitates. They compared the redox behaviour in the Eh – pH conditions of the leaching experiment with that of Pu, and found that the Pu<sup>4+</sup> would be unlikely to be reduced in these conditions, suggesting that Ce<sup>4+</sup> is not a good surrogate for Pu<sup>4+</sup>.

Harrison et al. [110] investigated the dependence of the dissolution behaviour of nuclear waste glass with waste-loading. They looked at waste-loadings of two types of waste, Magnox and Blend, between 25 and 38 wt.% for Magnox and between 17 and 38 wt.% for Blend. They also looked at varying the amount of oxide waste to Magnox waste in the Blend from 75%-25% to 25%-75%. They found that, in general, the chemical durability of the glass increased with waste-loading, and that the durability of the Blend-containing glasses increased with increasing oxide waste to Magnox waste ratio.

Several more recent studies have focussed on the alteration of UK nuclear waste glasses at high-pH [3], [19], [84]. Two studies by Utton et al. investigated the

dissolution behaviour of proposed UK ILW glasses in a saturated  $\text{Ca}(\text{OH})_2$  leachant [3], and the formation of alteration products during the dissolution of these glasses [84]. The former work found that the leaching rate was lower than expected which was explained through the action of Ca in solution (see 2.4.3). It also found that the durability of the waste-loaded samples was higher than for the base glasses, in agreement with the findings of Harrison et al. The latter study by Utton et al. found that Mg and Ca tended to be found in distinct alteration phases, and generally were not found in a mixed phase. Ca was found in calcium silicate hydrate (C-S-H) phases, whereas Mg was found in a smectite clay, postulated to be saponite  $(\text{Ca}_{0.25}(\text{Mg,Fe})_3((\text{Si,Al})_4\text{O}_{10})(\text{OH})_2 \cdot n(\text{H}_2\text{O}))$ . They found that Zr, Fe, and Mg accumulated in the alteration layer along with Ca and Si and lesser amounts of Al. The high S/V experiments saw a resumption of alteration (see Section 2.4.3) after around 56 days, which is likely due to the formation of these crystalline precipitates which consume Si from the alteration layer and glass network, enhancing dissolution. Corkhill et al. [19] reported an incubation period during dissolution which they linked to the ratio of Ca to Si in solution; Si was not seen in solution until the Ca/Si ratio was  $< 2$ .

## 2.4 Summary

The dissolution behaviour of glasses is still not fully understood. The mechanisms of dissolution, the mechanisms of formation of alteration layers and the effects of many elements on the dissolution behaviour of glasses are still the subject of significant debate. The complexity of the dissolution of a thermodynamically metastable material, possibly consisting of 30 different oxides, cannot be overestimated. This has been seen on many occasions in the literature, when seemingly similar experiments with similar samples yield wildly different results. This investigation aims to provide more clarity in this area, with particular regard to the dissolution of UK nuclear waste glasses at high-pH, the mechanisms of dissolution at high-pH, and the effects of elements such as Ca, Mg, Al and B in these conditions.



## 3. Experimental Methods

### 3.1 Sample Production

#### 3.1.1 Glass-Making

Two general categories of glass compositions were produced for testing and analysis in the course of this work; four compositions selected from the literature, and a set of simpler glass compositions containing 3- to 5-oxides – hence forward referred to as ‘simple glasses’ – designed specifically for this project. The literature glasses are as follows:

**MW-25%** - This glass is a simulant of the UK’s vitrified HLW. It consists of an alkali borosilicate base glass (MW) loaded with 25 wt. % simulated Magnox waste, i.e. waste coming from the UK’s Magnox reactors, which is high in magnesium and aluminium. This composition was chosen for this project due to its relevance in regards to UK wasteforms. The glass was produced at the University by melting of appropriate amounts of MW0.5Li base glass frit (MW frit with half the usual amount of Li) and WRW17 calcine (an inactive simulant of HLW calcine), provided by Dr Mike Harrison of NNL, who is the industrial supervisor for this project.

**International Simple Glass (ISG)** – This composition has been developed by the International Glass Corrosion working group as a reference glass for dissolution experiments. It is a mixed-alkali borosilicate based on the French R7T7 base glass. This composition was chosen to provide a frame of reference for the other glasses. A 500 g ingot of this glass was provided by the working group.

**G73** – This glass was designed at the University of Sheffield as a potential immobilisation matrix for ILW [2]. It is a barium silicate, which for the purposes of this project has been waste-loaded with 35 wt. % of simulant ‘waste permutation B’ from Hinkley Point A, a mixture of different ILWs (ion exchange (IEX) resin, active effluent treatment plant (AETP) sludge, pond water treatment plant (PWTF) sludge and sand pressure filter (SPF)

sand) [2]. The G73 base glass frit and the waste permutation B material were provided by Dr Paul Bingham.

**Basaltic Glass (BAS)** – This is a synthetic version of a natural basaltic glass, a calcium-iron aluminosilicate, as produced by Techer et al. [106]. The reasons for this glass being chosen are twofold; firstly, there is a significant amount of literature [98], [103], [105], [108] on the use of natural basaltic glasses as analogues for nuclear aluminoborosilicate glass dissolution, and secondly, borosilicate glasses containing alumina have been found to have a greater chemical durability than those not containing alumina. The sample for this project was melted from the batched raw materials.

The melting/processing conditions are shown in Table 3.1, except for ISG which was provided by an external source. Table 3.2 gives the nominal compositions for these literature glasses. Analysed compositions are given in Chapter 6.

The MW-25% glass was produced by mixing the appropriate amounts of MW0.5Li frit and WRW17 calcine to obtain a 25 wt.% waste-loading of the simulant calcine. This mixture was then mixed by hand for approximately 2 minutes. This mixture was placed in an alumina crucible and heated to 1050 °C in a muffle furnace. Once the batch had reached 1050 °C, it was transferred to a top-loading furnace and kept at 1050 °C for 4 hours, with stirring of the melt occurring for the last 3 hours, using an alumina stirrer. After 4 hours, the melt was poured into a pre-heated iron mould, and then annealed at 500 °C for 1 hour. The temperature of the furnace was then reduced to room temperature at the rate of 1 °C min<sup>-1</sup>, and the glass ingot was removed when this was completed.

**Table 3.1.** Melt conditions for the MW-25%, BAS and G73 glasses.

<b>Glass</b>	<b>MW-25%</b>	<b>BAS</b>	<b>G73</b>
<b>Melt Temp. (°C)</b>	1050	1550	1200
<b>Melt Duration /h</b>	4	4	8
<b>Cooling Rate (°C min<sup>-1</sup>)</b>	0.5	1	1
<b>Anneal. Temp. (°C)</b>	500	670	550
<b>Anneal. Duration /h</b>	3	1	1
<b>Furnace Type</b>	Electric	Gas	Electric
<b>Stirred</b>	Yes	No	No

**Table 3.2.** Nominal compositions of the four literature glasses in mol. %.

<b>Oxide</b>	<b>MW-25%</b>	<b>BAS</b>	<b>G73</b>	<b>ISG</b>
<b>SiO<sub>2</sub></b>	50.02	53.66	51.45	60.10
<b>B<sub>2</sub>O<sub>3</sub></b>	15.80	–	2.22	15.97
<b>Al<sub>2</sub>O<sub>3</sub></b>	3.17	9.48	0.38	3.84
<b>Fe<sub>2</sub>O<sub>3</sub></b>	1.37	4.44	2.91	–
<b>Na<sub>2</sub>O</b>	8.72	2.81	5.61	12.65
<b>Li<sub>2</sub>O</b>	8.88	2.19	7.76	–
<b>CaO</b>	–	12.64	11.03	5.73
<b>MgO</b>	7.85	12.79	0.40	–
<b>BaO</b>	0.26	–	18.14	–
<b>ZrO<sub>2</sub></b>	0.80	–	–	1.72
<b>P<sub>2</sub>O<sub>5</sub></b>	–	0.05	0.01	–
<b>SrO</b>	0.19	0.23	–	–
<b>MnO</b>	–	0.14	–	–
<b>K<sub>2</sub>O</b>	–	0.13	0.02	–
<b>TiO<sub>2</sub></b>	–	1.45	–	–
<b>Cs<sub>2</sub>O</b>	0.24	–	0.03	–
<b>TeO<sub>2</sub></b>	0.07	–	–	–
<b>Other</b>	2.65	–	0.04	–
<b>Oxides</b>				
<b>Total</b>	100.02	100.01	100.00	100.01

The G73 glass was produced by batching appropriate amounts of silica ( $\text{SiO}_2$ , Loch Aline sand), aluminium hydroxide ( $\text{Al}(\text{OH})_3$ , Sigma-Aldrich reagent grade), barium carbonate ( $\text{BaCO}_3$ , Sigma-Aldrich >99%), iron (II, III) oxide ( $\text{Fe}_3\text{O}_4$ , Sigma-Aldrich >99.9%), boric acid ( $\text{H}_3\text{BO}_3$ , Sigma-Aldrich 99.9%), sodium carbonate ( $\text{Na}_2\text{CO}_3$ , Sigma-Aldrich 99.9%), lithium carbonate ( $\text{Li}_2\text{CO}_3$ , Sigma-Aldrich ACS reagent), calcium carbonate ( $\text{CaCO}_3$ , Sigma-Aldrich 99.9%). To this base glass mixture was added 35 wt.% of waste permutation B, a simulant of wet intermediate level waste (WILW) from the Hinkley Point A nuclear power station [113]. The simulant was dried in an oven at 90 °C for 24 hours before mixing with the glass batch. The melt was carried out for 8 hours at 1400 °C. However, this did not produce a homogeneous product (by visual examination), so a second batch was made using the same conditions, and then both batches were milled together. This mixed batch was remelted at 1400 °C for 5 hours, producing a homogeneous product. After this, the melt was poured into a pre-heated iron ingot mould and allowed to cool until it could sustain the ingot shape. It was then transferred to a furnace for annealing at 550 °C for 1 hour, before the temperature was reduced to room temperature at 1 °C  $\text{min}^{-1}$ . The ingot of glass was then removed from the furnace.

The BAS glass was produced by batching the appropriate amounts of silica ( $\text{SiO}_2$ , Loch Aline sand), aluminium hydroxide ( $\text{Al}(\text{OH})_3$ , Sigma-Aldrich reagent grade), iron (II, III) oxide ( $\text{Fe}_3\text{O}_4$ , Sigma-Aldrich >99.9%), sodium carbonate ( $\text{Na}_2\text{CO}_3$ , Sigma-Aldrich 99.9%), lithium carbonate ( $\text{Li}_2\text{CO}_3$ , Sigma-Aldrich ACS reagent), calcium carbonate ( $\text{CaCO}_3$ , Sigma-Aldrich 99.9%), magnesium oxide ( $\text{MgO}$ , Sigma 99%), ammonium dihydrogen phosphate ( $\text{NH}_4\text{H}_2\text{PO}_4$ , Alfa Aesar), strontium nitrate ( $\text{Sr}(\text{NO}_3)_2$ , Sigma >98%), manganese oxide ( $\text{MnO}_2$ , Sigma-Aldrich >99%), potassium carbonate ( $\text{K}_2\text{CO}_3$ , Alfa Aesar >99%) and titanium dioxide ( $\text{TiO}_2$ , Sigma-Aldrich, >99%). The batched reagents were then mixed by hand within a sealed bag for approximately 5 minutes. The resulting mixture was placed in an alumina crucible and pre-heated overnight to 1100 °C. It was then transferred to a gas furnace at 1100 °C. The temperature was increased from 1100 °C to 1550 °C in increments of 20 °C every 2 minutes. The temperature was increased in this fashion due to the lag between the temperature controller and the temperature within the furnace. Once the furnace reached 1550 °C, it was held at this temperature for 4 hours. At the end of the 4 hours, the melt was poured into a pre-heated iron ingot mould. Once the glass had cooled sufficiently, the still-hot ingot was transferred to an annealing furnace. The annealing

furnace was set at 670 °C, held there for an hour and then ramped down to room temperature at 1 °C min<sup>-1</sup>.

The 3- to 5-oxide glasses fall into 4 different series; NC<sub>x</sub>BS, NM<sub>x</sub>BS, NCAB<sub>x</sub>S and NMAB<sub>x</sub>S. The melt conditions for each glass are shown in Table 3.3, and the nominal compositions for these series are shown in Table 3.4. Analysed compositions are given in Chapter 4, Table 4.1. The NC<sub>x</sub>BS and NM<sub>x</sub>BS series are base 20Na<sub>2</sub>O·15B<sub>2</sub>O<sub>3</sub>·65SiO<sub>2</sub> glasses, with the Na<sub>2</sub>O replaced by  $x = 5$  and 10 mol. % of CaO and MgO, respectively. Initially, glasses with  $x = 15$  mol. % were also planned, but they could not be produced without significant phase separation. These two series were studied in order to ascertain the impact of the addition of CaO and MgO to the dissolution rate of the Na-borosilicate base glass. The NCAB<sub>x</sub>S and NMAB<sub>x</sub>S series are base 10Na<sub>2</sub>O·10CaO·15Al<sub>2</sub>O<sub>3</sub>·65SiO<sub>2</sub> and 10Na<sub>2</sub>O·10MgO·15Al<sub>2</sub>O<sub>3</sub>·65SiO<sub>2</sub> glasses, respectively. In both series, the Al<sub>2</sub>O<sub>3</sub> is replaced by  $x = 5$  and 10 mol. % B<sub>2</sub>O<sub>3</sub> in order to study the effect of the addition of B to the glass on the dissolution rate.

All of the simple glasses were batched by mixing the appropriate amounts of the sodium bicarbonate (NaHCO<sub>3</sub>, Sigma-Aldrich 99.9%), calcium carbonate (CaCO<sub>3</sub>, Sigma-Aldrich 99.9%), magnesium carbonate hydroxide hydrate (C<sub>4</sub>Mg<sub>4</sub>O<sub>12</sub>·H<sub>2</sub>MgO<sub>2</sub>·5H<sub>2</sub>O, Sigma-Aldrich 99%), aluminium hydroxide (Al(OH)<sub>3</sub>, Sigma-Aldrich 99.9%), boric acid (H<sub>3</sub>BO<sub>3</sub>, Sigma-Aldrich 99.9%) and silica (SiO<sub>2</sub>, Loch Aline sand). The batch was then mixed by hand in a sealed bag for approximately 5 minutes. In the cases of NC5BS, NC10BS, NM5BS and NM10BS, as much batch as would fit was then placed in a platinum crucible, which was then placed in an electric furnace at the required temperature. Once the batch volume had reduced due to melting, more batch was added and the crucible returned to the furnace, with the process repeated if necessary. The batches were kept at the required temperature for 4 hours, with a platinum stirrer used for the last 3 hours. The melts were then poured into a bucket of water, producing a 'frit'. NC0BS was produced in the same way but using an alumina crucible rather than a platinum one.

The NCAB<sub>x</sub>S and NMAB<sub>x</sub>S series were batched in the same fashion as the NC<sub>x</sub>BS and NM<sub>x</sub>BS series. After mixing, as much of each batch that would fit was placed in an alumina crucible. These crucibles were then heated to 1100 °C in an electric furnace, before being transferred to a gas furnace at 1100 °C. The rest of each batch was placed in the crucibles at this point. The gas furnace temperature was then ramped to the required melt temperature at a rate of 20 °C every 2 minutes. Once at

the appropriate temperature, the crucibles were kept in the furnace for a further 4 hours. At the end of the 4 hours, each of the glasses was fritted in a bucket of cold water.

All glasses were analysed by X-ray Diffraction (XRD) (see Section 3.6) to determine whether they were amorphous. The data are shown in Appendix A.

**Table 3.3.** Processing conditions for production of simple glasses. The NCAB<sub>x</sub>S, NMAB<sub>x</sub>S and NC0BS samples were melted in alumina crucibles, the other samples were melted in Pt crucibles.

<b>Glass</b>	<b>Melt Temp. (°C)</b>	<b>Melt Durat. (Hrs)</b>	<b>Anneal. Temp. (°C)</b>	<b>Anneal. Durat. (Hrs)</b>	<b>Cool. Rate (°C min<sup>-1</sup>)</b>	<b>Stirred</b>
<b>NC0BS</b>	1400	5	620	1	1	Yes
<b>NC5BS</b>	1350	5	600	1	1	Yes
<b>NC10BS</b>	1400	5	600	1	1	Yes
<b>NM5BS</b>	1300	5	550	1	1	Yes
<b>NM10BS</b>	1300	5	550	1	1	Yes
<b>NCAB0S</b>	1550	4	N/A	N/A	N/A	No
<b>NCAB5S</b>	1550	5	N/A	N/A	N/A	No
<b>NCAB10S</b>	1450	5	N/A	N/A	N/A	Yes
<b>NMAB0S</b>	1550	4	N/A	N/A	N/A	No
<b>NMAB5S</b>	1550	4	N/A	N/A	N/A	No
<b>NMAB10S</b>	1550	4	N/A	N/A	N/A	No

**Table 3.4.** Nominal compositions (mol. %) for simple glasses.

<b>Glass</b>	<b>Na<sub>2</sub>O</b>	<b>CaO</b>	<b>MgO</b>	<b>Al<sub>2</sub>O<sub>3</sub></b>	<b>B<sub>2</sub>O<sub>3</sub></b>	<b>SiO<sub>2</sub></b>
<b>NC0BS</b>	20	0	–	–	15	65
<b>NC5BS</b>	15	5	–	–	15	65
<b>NC10BS</b>	10	10	–	–	15	65
<b>NM5BS</b>	15	–	5	–	15	65
<b>NM10BS</b>	10	–	10	–	15	65
<b>NCAB0S</b>	10	10	–	15	0	65
<b>NCAB5S</b>	10	10	–	10	5	65
<b>NCAB10S</b>	10	10	–	5	10	65
<b>NMAB0S</b>	10	–	10	15	0	65
<b>NMAB5S</b>	10	–	10	10	5	65
<b>NMAB10S</b>	10	–	10	5	10	65

### 3.1.2 Preparation of Samples for Dissolution Experiments

Two types of samples were used for dissolution experiments; powders (PCT-B experiments) and monoliths (MCC-1 experiments). Powdered samples were produced by first crushing the glasses (if not already in frit form) in a benchtop vice. The crushed glasses were milled using a Tema T100 Disc Mill. Small amounts of glass were placed in the sample holder, and the mill was turned on for 1 – 3 seconds, depending on the particle size of the unmilled glass. The milled glass was then sieved using 75 and 150  $\mu\text{m}$  steel sieves to obtain the 149 – 75  $\mu\text{m}$  particle size fraction. A magnet was passed over the milled samples to check for any iron contamination from the vice and mill. The powders were then washed in order to remove any adhered fines. They were first rinsed 3 times in ultra-high quality (UHQ) water produced by a Millipore Direct-Q (UV) 3 water purification system. After this, the powders were cleaned ultrasonically in UHQ water for 5 minutes, 4 times. They were then washed ultrasonically in isopropanol for 5 minutes, 3 times, placed in an oven at 100 °C to dry for at least 1 hour and then stored in a desiccator until use.

Monolithic samples were produced from glass ingots. The ingots were first sectioned using a Buehler IsoMet<sup>®</sup> 5000 precision saw. From these sections, coupons

were cut to the required size (approx.  $10 \times 10 \times 5$  mm) using a Buehler IsoMet<sup>®</sup> Low-speed Saw with a Buehler Series 15 LC wafering blade, lubricated with Buehler IsoCut<sup>®</sup> fluid. The coupons were then ground to a standard finish using a Buehler EcoMet 250 Pro, with Buehler P800 SiC abrasive paper. The ground coupons were then cleaned ultrasonically for 5 min in UHQ water. They were cleaned ultrasonically in isopropanol for 3 periods of 5 min, with fresh isopropanol used for each period. After cleaning, the coupons were stored in a desiccator until required.

## 3.2 Dissolution Testing

### 3.2.1 Product Consistency Test B (PCT-B)

The product consistency test (PCT) is a static leaching test designed for the assessment of the durability of nuclear, hazardous and mixed waste glasses, and multiphase glass ceramics. It uses powdered samples and is defined by ASTM International [114]. There are two variations of PCT, A and B. PCT-A is a 7-day test at 90 °C, with very specific requirements of particle size distribution, leachant composition and test vessel material. PCT-B allows for a range of temperatures, durations, particle size distributions and test vessel materials. PCT-B is the test method that was used in this project, and was carried out on the four literature glass compositions, as well as on the simple borosilicate and aluminoborosilicate series.

All tests were carried out in a positive pressure glovebox, where the pressure was maintained by an N<sub>2</sub> flow (Figure 3.1), to prevent carbonation of the leachants and hence reductions in pH. Each test was carried out at 50 °C in a 500 mL HDPE vessel, with 400 mL of leachant and an appropriate amount of 150 – 75 μm powder (20 – 23 g, varying with glass density) to produce a glass-surface area-to-leachant-volume of  $1200 \pm 200 \text{ m}^{-1}$ . The powdered glasses were produced using the method detailed in Section 3.1.2. Two leachants were used; saturated Ca(OH)<sub>2</sub> solution and 0.021/0.21 M KOH/KCl solution, which were prepared to give approximately the same pH value, in order to isolate the change in cation as the only variable to affect the dissolution rate. The pH of a saturated Ca(OH)<sub>2</sub> solution at 50 °C is approximately 11.6. To achieve the same pH using KOH/KCl requires a 0.021/0.21 M solution. KCl is added to the solution in order to buffer the pH. The Ca(OH)<sub>2</sub> leachant was produced by adding an excess of Ca(OH)<sub>2</sub> powder ( $>0.92 \text{ g L}^{-1}$ ) to UHQ water in a HDPE vessel. Unlike the UHQ water for the MCC-1 experiments (see Section 3.2.2), the UHQ water

for the PCT-B experiments did not have  $N_2$  bubbled through it prior to the addition of the hydroxide. It was shaken vigorously in order to achieve full dissolution of the  $Ca(OH)_2$ , and allowed to sit for several hours in order for the excess  $Ca(OH)_2$  to settle to the bottom of the vessel. The KOH/KCl solution was prepared in the same manner as the  $Ca(OH)_2$  solution. The concentrations of KOH and KCl used in the solution were  $1.18 \text{ g L}^{-1}$  and  $15.66 \text{ g L}^{-1}$ , respectively. The preparation of all leachants was carried out in a glovebox with a nitrogen atmosphere in order to prevent carbonation, and hence a reduction in pH. Before the start of the experiments, the HDPE vessels were cleaned using the method outlined in the ASTM standard. For the tests using the  $Ca(OH)_2$  leachant, an Advantec USY-1 ultrafilter unit filled with a slurry of  $Ca(OH)_2$  powder and UHQ water, was added to the test vessel in order to maintain the pH of the leachant. The experimental setups for the PCT experiments are shown in Figure 3.2. The test vessels were placed in a LT Scientific OP39-UF oven in the glovebox at  $50 \text{ }^\circ\text{C}$ . For each glass composition, duplicate tests were run, as well as two blanks.



**Figure 3.1.** Image of glovebox with  $N_2$  cylinder used for high-pH dissolution experiments.

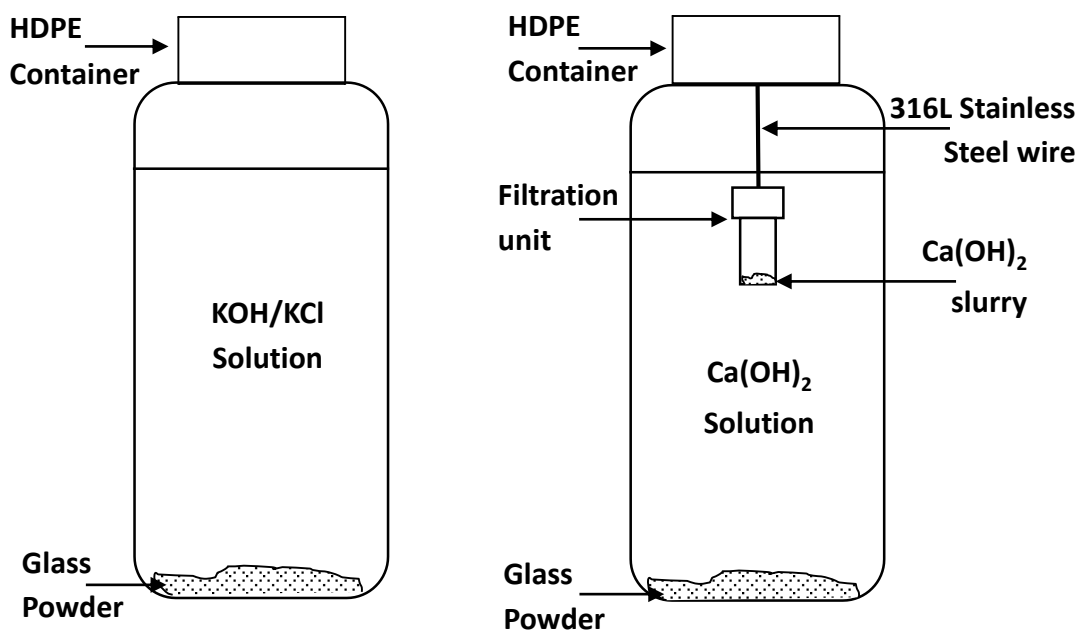


**Figure 3.2.** Schematic diagrams of experimental setup for PCT experiments using KOH/KCl (left) and Ca(OH)<sub>2</sub> (right) leachants.

For analysis, 5 ml aliquots of the solution were taken at designated intervals; 1 day, 3, 7, 14, 28, 56 and 112 days. Before and after the removal of each aliquot, the vessels were weighed to determine the amount of solution which had been lost or removed. This was taken into account in terms of a change in S/V. The 5 ml aliquots were removed using a FinnPipette F1 variable-volume pipettor, and then filtered using a 0.22  $\mu\text{m}$  polyethersulphone (PES) syringe filter. The filtered solution was allowed to cool, before 4 ml was removed and acidified with 1 vol. % 69 % nitric acid, and analysed by Inductively-Coupled Plasma Optical Emission Spectroscopy (ICP-OES, see Section 3.3). This determined the release rates of elements from the glasses. The last 1 ml of filtered solution was used for measuring the pH of the leachate. After the final aliquot was taken, the remaining solution was disposed of, and the glass powder dried in the oven in the glovebox. The glass powder was analysed using X-Ray Diffraction (XRD), to identify any secondary precipitates. Scanning Electron Microscopy with Energy Dispersive X-ray Spectroscopy (SEM-EDS) was also used to look at the morphology and composition of the precipitates.

### 3.2.2 Materials Characterisation Center Test 1 (MCC-1)

The Materials Characterisation Center Test 1 (MCC-1) is a static leaching test designed for the assessment of the durability of monolithic wasteforms for the disposal

of radioactive waste. It is defined by ASTM International [64]. The standard specifies that the test should have a surface-area-to-leachant-volume ( $S/V$ ) ratio of  $10 \pm 0.5 \text{ m}^{-1}$  and a temperature of  $40 \text{ }^\circ\text{C}$ ,  $70 \text{ }^\circ\text{C}$  or  $90 \text{ }^\circ\text{C}$ , but allows for a variety of leachant solutions and test durations.

The tests in this project were carried out at  $50 \text{ }^\circ\text{C}$ , with a  $\text{Ca}(\text{OH})_2$  leachant, a monolith surface area of  $400 \pm 20 \text{ mm}^2$  and a leachant volume of 40 ml (giving the required  $S/V$ ). The vessels used for these tests were Savillex 60 ml perfluoralkoxy (PFA) Teflon standard jars, with 53 mm closures and 46 mm support screens. Figure 3.3 shows a schematic diagram of the experimental setup. These tests were carried out within the glovebox shown in Figure 3.1 (as with the PCT experiments). The glass compositions that were used for these tests were the four literature glasses, and the monoliths used were prepared using the method described in Section 3.1.2.

In order to prepare the  $\text{Ca}(\text{OH})_2$  solution, nitrogen is first bubbled through the UHQ water for  $>24$  hrs to ensure the removal of  $\text{CO}_2$ . This solution was then transferred to the glovebox, where an excess of reagent grade  $\text{Ca}(\text{OH})_2$  powder was added. The water/powder mixture was then placed in the oven at the required temperature overnight to let the undissolved  $\text{Ca}(\text{OH})_2$  powder settle at the bottom of the container.

Each monolith was placed onto a PFA Teflon basket in a vessel, with 40 ml of the  $\text{Ca}(\text{OH})_2$  solution, added with a FinnPipette F1 variable-volume pipettor, with 10 ml FinnPipette tips. The lids of the vessels were replaced, and the vessels placed into the LT Scientific OP39-UF oven at  $50 \text{ }^\circ\text{C}$  for 30, 90, 180, 360, 540 or 720 days. Two tests were run for each of the four glass compositions for each test duration, along with two blanks.

Once the tests were finished, 5 mL aliquots of leachate were taken. 4 mL of this were acidified with 1 vol. % 69 %  $\text{HNO}_3$  and analysed by ICP-OES, whilst the remaining 1 mL was used for pH measurement. The altered coupons were gently rinsed with  $\sim 2$  mL UHQ water, in order to remove any remaining  $\text{Ca}(\text{OH})_2$  without washing off precipitates. Each altered coupon was mounted in epoxy resin, ground to a P1200 grit finish on a Buehler EcoMet 250 Pro, then polished using 6, 3 and 1  $\mu\text{m}$  diamond paste, and analysed using scanning electron microscopy (SEM), to obtain morphological data on precipitates and measure the thickness of the alteration layer, and energy dispersive x-ray spectroscopy (EDS), in order to obtain data on the elemental composition of the precipitates and alteration layer.

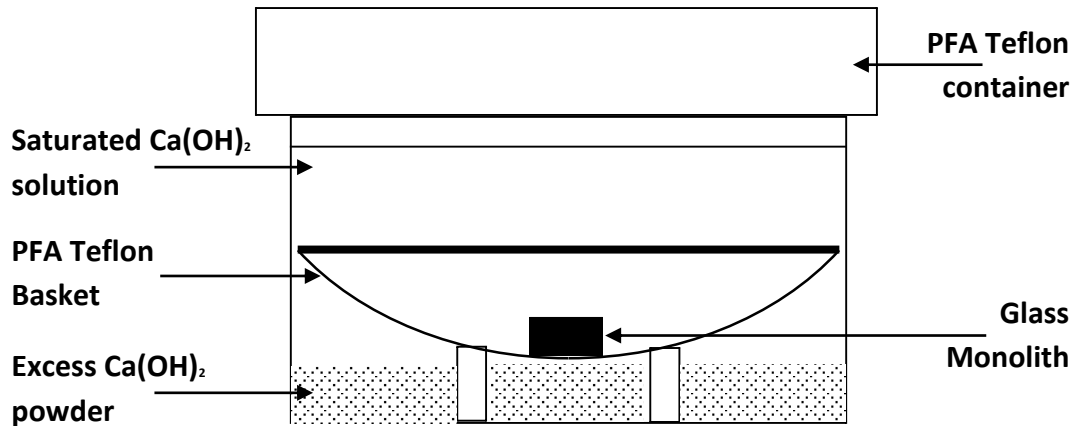


**Figure 3.3.** Schematic of experimental setup for MCC-1 dissolution tests.

### 3.3 Inductively-Coupled Plasma Optical Emission Spectrometry (ICP-OES)

Inductively-Coupled Plasma Optical Emission Spectrometry (ICP-OES) is a technique that can be used to measure the concentration of elements in solution, down to low levels ( $\sim 0.1$  ppm) [115]. This type of spectrometer uses an argon plasma torch to atomise and ionise the sample. This causes the atoms to be excited, through two main interactions; inelastic scattering of an electron off the atom,  $M$ , (equation 3.1) and the radiative-recombination of an ion,  $M^+$ , with an electron (equation 3.2) [115]:



This leads to the emission of photons,  $h\nu$ , with wavelengths that are characteristic of each element, with the intensity of the emission recorded being proportional to the amount of the element present. A schematic of a standard ICP-OES setup is shown in Figure 3.5. Before introduction to the instrument, samples must first be in solution and acidified. The sample introduction system consists of a peristaltic pump, which pumps the sample and an Au standard solution into a nebuliser. The Au standard solution is an internal standard used to correct for any systematic issues in the instrument. In the nebuliser, the sample and Au standard are mixed with Ar gas to form a liquid aerosol. The aerosol is fed into the plasma torch which atomises and ionises it. The signal from the excited sample is carried from the torch through a radial

route and an axial route. This signal then passes through the transfer optics to the spectrometer itself. The spectrometer collects the signal through charge-coupled devices (CCDs) and calculates the concentration of each element by measuring the intensity of the characteristic emission peaks. This information is then output to a computer. In order to generate accurate results, the instrument must be calibrated before use [116]. This was done by using a set of 5 standards with known concentrations of the elements to be analysed. In order to do this, high-quality Fluka elemental standards (B, Al, Si, Na, Ca, Mg, Zr, Ba, Fe, and a Rare-Earth multiple standard) were purchased from Sigma-Aldrich, and used to make the calibration standards. Using the software on the computer, a calibration curve can be produced which the instrument then uses to produce accurate data.

The elemental concentration data collected from the ICP-OES, measured in ppm, were subsequently converted to normalised mass loss values, using:

$$NL_i = \frac{(C_i - C_{i,b})}{x_i \times \frac{S}{V}} \quad (\text{Equation 3.3})$$

where:  $NL_i$  is the normalised mass loss for element,  $i$ , in  $\text{g m}^{-2}$ ;  $C_i$  is the average concentration of  $i$  in solution in the duplicate tests, in  $\text{mg L}^{-1}$ ;  $C_{i,b}$  is the average concentration of  $i$  in the blank tests, in  $\text{mg L}^{-1}$ ;  $x_i$  is the mass fraction of  $i$  in the glass monolith;  $S$  is the surface area of the glass monolith, in  $\text{m}^2$ ; and  $V$  is the volume of leachant, in  $\text{m}^3$ . Using normalised mass loss values makes comparisons between the releases of different elements from the samples possible, and also allows the surface area to volume variation of the tests to be taken into account. The normalised mass loss values were plotted against time for each of the glasses. The uncertainty in the normalised mass loss,  $NL_i$ , for each element,  $i$ , was calculated through the following equation:

$$\sigma_{NL_i} = NL_i \times \sqrt{\frac{(\hat{\sigma}_{C_i} \times C_i)^2 + (\hat{\sigma}_{\bar{C}_{i,b}} \times \bar{C}_{i,b})^2}{(C_i - \bar{C}_{i,b})^2} + \hat{\sigma}_{x_i}^2 + \hat{\sigma}_S^2 + \hat{\sigma}_V^2}$$

$$(\text{Equation 3.4})$$

where:  $\hat{\sigma}_{C_i}$  is the relative uncertainty in  $C_i$ , the concentration of element,  $i$ , in the leachate;  $\hat{\sigma}_{\bar{C}_{i,b}}$  is the relative uncertainty in  $\bar{C}_{i,b}$ , the average concentration of element,  $i$ , in the blanks; and  $\hat{\sigma}_{x_i}$ ,  $\hat{\sigma}_S$  and  $\hat{\sigma}_V$  are the relative uncertainties in  $x_i$ , the mass fraction

of element,  $i$ , in the glass,  $S$ , the surface area of the glass sample, and  $V$ , the volume of the leachate, respectively. Relative uncertainties were calculated by dividing the absolute uncertainty in the measurement by the value of that measurement, e.g.  $\hat{\sigma}_S = \frac{\sigma_S}{S}$ .

In addition to the normalised mass losses, mass loss rates were also calculated. An apparent initial rate was calculated from the gradient of the dissolution data from 0 days, to either 1, 3 or 7 days. The greatest possible number of datapoints was used, with the caveat that they must follow a linear trend. For most samples this was 3-4 datapoints (up to 3 or 7 days), but for some glasses this was only possible for 2 datapoints. Apparent residual mass loss rates were calculated from the gradient of the dissolution data between the last 3 or 4 datapoints, depending on the linearity of the fit, i.e. 14 – 112 days or 28 – 112 days for PCT experiments, and 180 – 720 days or 360 – 720 days for MCC-1 experiments. It should be noted that these ‘apparent’ rates are not true initial and residual rates. Calculation of true initial rates would require dynamic dissolution experiments (e.g. Single-Pass Flow-Through), whereas true residual rates would require experimental proof that the samples had reached the residual dissolution regime. The uncertainty in these rates was estimated at 15%.

All of the ICP-OES analysis in this work was carried out using a Thermo iCAP 6300 instrument. Analysis was carried out on all of the aliquots taken from the PCT-B and MCC-1 experiments. Before use, the samples were filtered using 0.22  $\mu\text{m}$  filters, and acidified with 1 % v/v 69%  $\text{HNO}_3$ , as described in Section 3.2.1. This analysis was carried out in order to determine the leach rates of different elements from each glass.

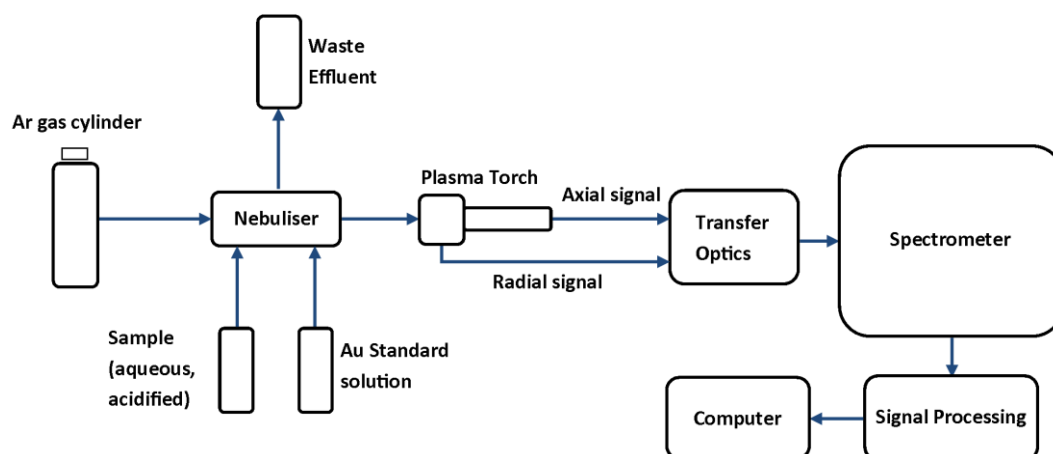


**Figure 3.5.** Schematic of a standard ICP-OES.

### 3.4 Electron Microscopy

Microscopes are an essential piece of equipment in innumerable scientific, and other, fields, from microbiology to materials science and many more. However, the resolution of an optical system is fundamentally limited by the wavelength of the source, per Rayleigh's criterion:

$$\theta = 1.220 \frac{\lambda}{D} \quad (\text{Equation 3.5})$$

where  $\theta$  is the angular resolution of the system in radians,  $\lambda$  is the wavelength of the source and  $D$  is the diameter of the aperture of the lens. The specific case for a microscope is given by:

$$R = \frac{1.22\lambda}{2NA} \quad (\text{Equation 3.6})$$

where  $R$  is the spatial resolution of the system and  $NA$ , the numerical aperture of the lenses, is given by:

$$NA = \eta \sin \theta \quad (\text{Equation 3.7})$$

where  $\eta$  is the refractive index of the medium between the lens and the object and  $\theta$  is half of the angular aperture of the microscope,  $\alpha$ . Given that it is difficult to exceed values of 1.45 and 0.95 for the  $NA$  of the condenser and objective lenses, respectively, and that the shortest wavelength for visible light is around 400 nm for violet, this gives a resolution limit of approximately 200 nm for optical microscopes. Many objects of interest, e.g. atomic structures within materials, are smaller than this so a higher resolution technique is required. Due to the wave-particle duality of electrons, they can be used as an alternative to photons in microscopy systems. The wavelength of an electron is given by the De Broglie equation:

$$\lambda = \frac{h}{p} \quad (\text{Equation 3.8})$$

where  $h$  is Planck's constant and  $p$  is the relativistic momentum of the electron. By accelerating electrons through an electric field, one can attain wavelengths tens of thousands of times shorter than for visible-light photons. For example, an electron microscope using an accelerating voltage of 10 kV produces electrons with a wavelength of approximately 12 pm. This enables even very small objects to be resolved. There are two main types of electron microscopy; scanning electron

microscopy (SEM) and transmission electron microscopy (TEM).

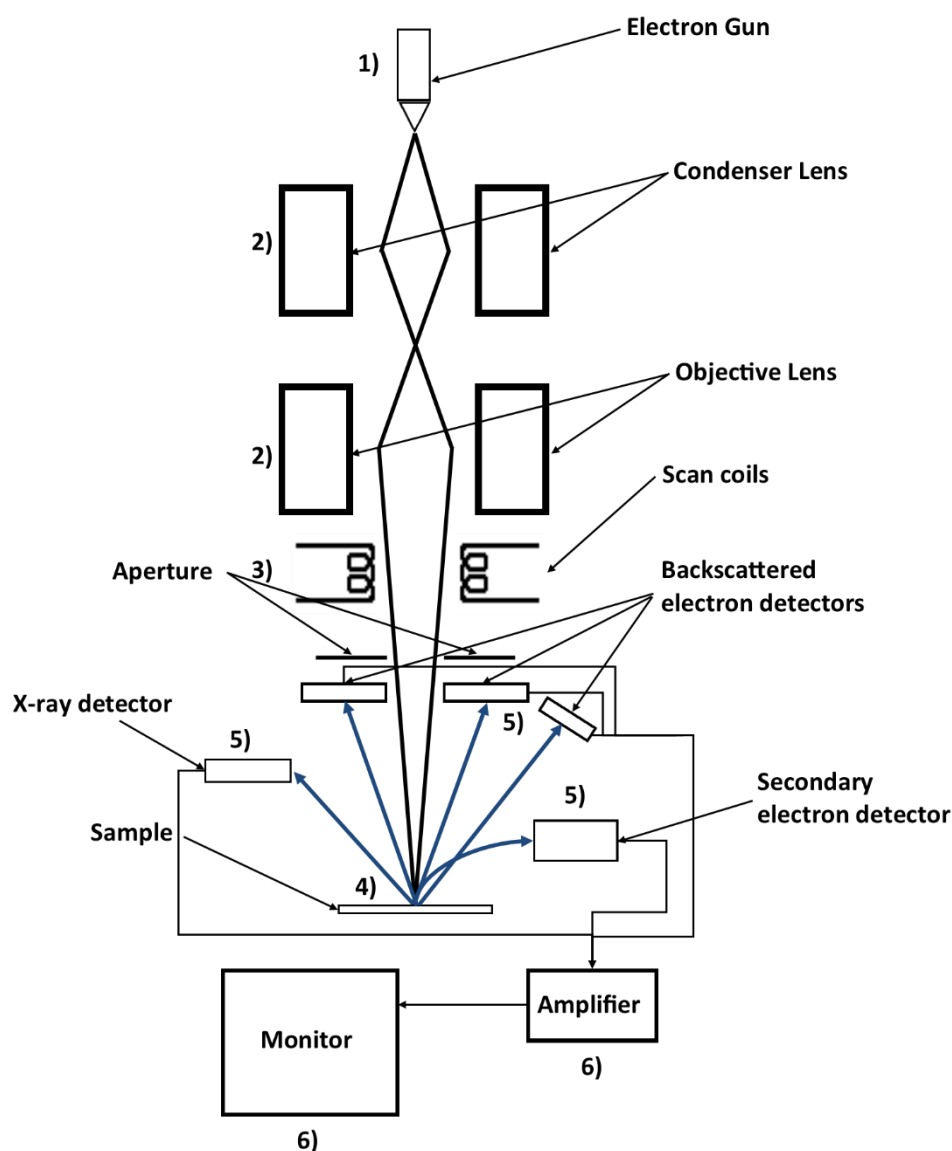
### 3.4.1 Scanning Electron Microscopy (SEM)

Figure 3.6 shows a schematic of a scanning electron microscope (SEM). The principle of a scanning electron microscope is as follows:

- 1) The electron source, or 'electron gun', produces electrons which are then accelerated towards an anode through a voltage difference of between 0.1 and 50 kV.
- 2) The beam of accelerated electrons is then shaped by a set of electromagnetic lenses, which focus the beam onto the sample.
- 3) The beam can be rastered across the sample, using scan coils.
- 4) As the beam of electrons hits the sample, they interact, both elastically and inelastically, to produce backscattered electrons, Auger electrons, X-ray photons and secondary electrons.
- 5) The backscattered electrons, secondary electrons and X-rays are collected by detectors arranged around the sample.
- 6) The signal from the detector is then amplified and converted into an image on a monitor; different images can be obtained by using signals from different detectors.

As mentioned, the primary electron beam can interact with the sample in a number of different ways. This is illustrated by Figure 3.6. The part of the sample which is penetrated by the primary electron beam is called the interaction volume [117]. Some of the primary electrons are scattered through  $\sim 180^\circ$  (backscattered electrons (BSE)) and are collected by detectors near to the beam aperture. The number of backscattered electrons generated by each incident electron is dependent on the atomic number of the particular region of the sample; a higher  $Z$  means more backscattered electrons, and a lower  $Z$  means fewer. Thus, using BSE imaging, one can obtain data on the relative  $Z$  values for different regions. Primary electrons that are scattered less strongly, but still escape the sample, are known as secondary electrons (SE). Secondary electrons only escape from within the sample from a relatively small region, due to having lower energy than BSE. This means that greater spatial resolution can be achieved in images using SE [118]. The primary electrons are also susceptible to inelastic scattering within the sample, generating radiation, most of which is reabsorbed within the sample. However, X-rays are not readily reabsorbed,

and so these can be detected. This will be expanded upon in Section 3.4.3.



**Figure 3.6.** Schematic of a scanning electron microscope. Adapted from Goodhew et al [118].

SEM was used to analyse altered and unaltered glass samples in this work. BSE images were collected in order to gain information on the structure of any alteration layers formed, i.e. whether the layer consisted of a single band, or several. SE images were collected in order to determine the depth of any alteration layer present. For SEM analysis, monolithic samples were first mounted in an epoxy resin. They were then ground using P1200 SiC abrasive paper to produce a flat surface. Each sample was then polished using 6, 3 and 1  $\mu\text{m}$  diamond paste for 5, 10 and 30 minutes, respectively, using isopropanol as a lubricant. The polished samples were coated with a layer of carbon using an Edwards Speedivac coating unit, in order to facilitate the flow of electrons from the sample to ground. This is to prevent issues with ‘charging’, where electrons build up on the surface of the sample, causing issues with contrast

and image stability. After carbon-coating, a conductive silver paint was used to electrically connect the top and bottom surfaces of the resin mount (Figure 3.7, picture of finished sample). Powdered samples were attached to adhesive carbon tabs on aluminium stubs (Figure 3.8), in order to look at any alteration products formed on the outside of the particles. Powdered glass samples were also mounted in resin and ground and polished in order to examine cross-sections of the particles (Figure 3.9). It should be noted that alteration layer thicknesses were not measured for any glass particles. This is due to the potential biasing of the thickness measurements by the random orientation of the particle surfaces with respect to the electron beam. Images were taken using 2 Microscopes; a Hitachi TM3030 desktop microscope and an FEI Inspect F, using voltages of 5 - 15kV and a working distance of 7-9 mm (Hitachi) or 10 mm (FEI).

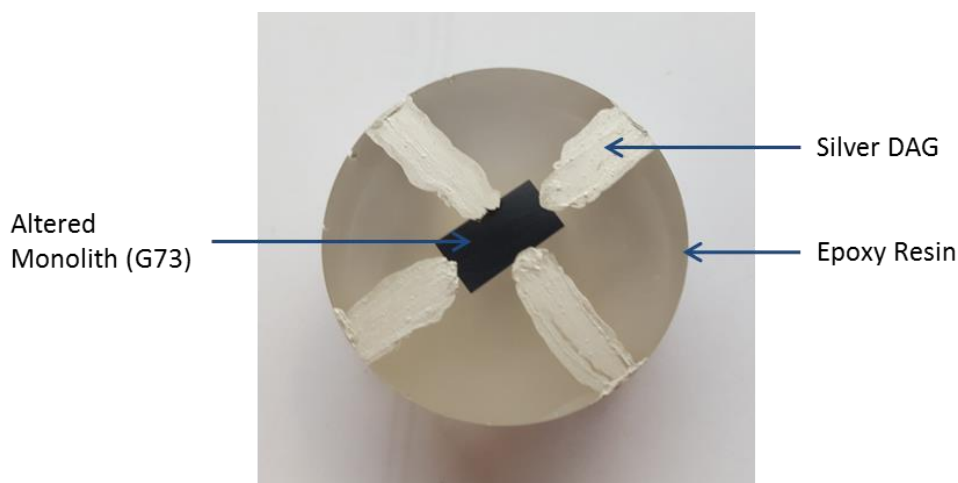


**Figure 3.7.** Image of altered monolith of G73, mounted in epoxy resin and prepared for analysis by SEM-EDX.

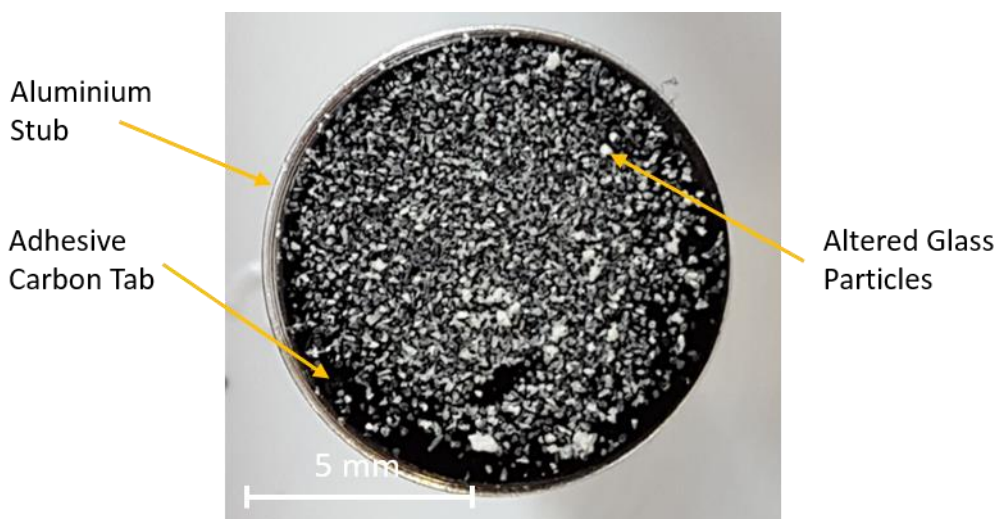


**Figure 3.8.** Particles of altered NM5BS glass attached to adhesive carbon tab on an aluminium stub for SEM-EDS analysis.

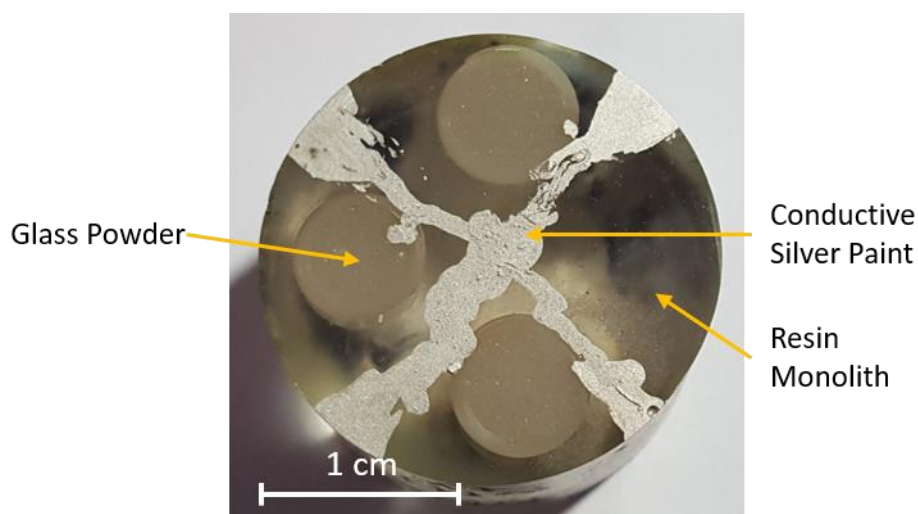


**Figure 3.9.** Particles of three altered glass mounted in epoxy resin for cross-sectional SEM-EDS analysis.

### 3.4.2 Transmission Electron Microscopy (TEM)

Transmission Electron Microscopy (TEM) utilises the same techniques and phenomena as SEM, but the electrons are detected after they have passed through a very thin sample, rather than being detected after being scattered from the sample surface. Figure 3.10 shows a schematic of a TEM. A TEM operates as follows:

- 1) Electrons are produced by an electron source, as with an SEM, albeit with generally higher potential differences (50 kV - ~ 1 MV) [118]
- 2) The accelerated electron beam is focused onto the sample by a condenser lens.
- 3) After the electrons pass through the sample, they go through a further set of

lenses: the objective lens, the intermediate lens, and the projector lens. The projector lens guides the beam onto a set of image collection apparatus.

- 4) The first image collection method is a fluorescent screen which allows the user to view images generated by the TEM in real time. Below this is a slot for photographic film, for the collection of electron diffraction patterns. The final detector is a CCD camera for the collection of digital electron images.

It is also possible to attach an x-ray detector near to the sample, in order to perform x-ray spectroscopy (see Section 3.4.3).

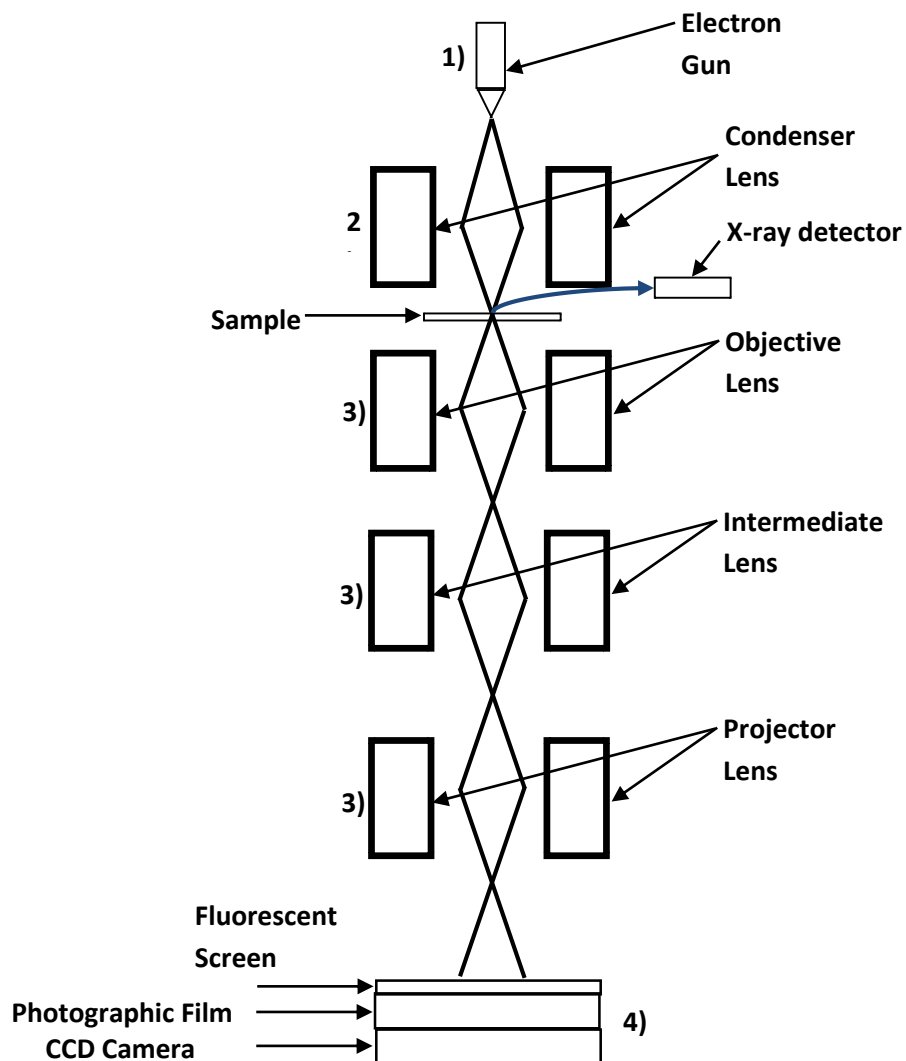


**Figure 3.10.** Schematic of a transmission electron microscope. Adapted from image at

[http://intranet.tdmu.edu.ua/data/kafedra/internal/histolog/classes\\_stud/en/stomat/ptn/1/01%20Microscope.%20Microscopic%20equipment.%20Histologic%20technique.%20Cytology.%20General%20structure%20of%20the%20cell.%20Superficial%20complex.htm](http://intranet.tdmu.edu.ua/data/kafedra/internal/histolog/classes_stud/en/stomat/ptn/1/01%20Microscope.%20Microscopic%20equipment.%20Histologic%20technique.%20Cytology.%20General%20structure%20of%20the%20cell.%20Superficial%20complex.htm)

The use of transmitted electrons requires that the sample be very thin, on the order of microns or smaller. This can be achieved by several methods: Chemical or electropolishing, mechanical polishing, and ion-beam milling [118]. Due to the fragile nature of the altered glass monoliths that were studied in this project, only the latter method was used, and so will be the only method discussed here. Samples were prepared using an FEI Quanta 200 3D focused ion beam (FIB) microscope. The microscope uses a gallium source, to which an electric field is applied to create a very fine tip, generating a narrow beam of  $\text{Ga}^+$  ions. When the beam impinges on the sample, it causes sputtering, leading to the ejection of sample material. By scanning the beam across the surface, trenches can be cut into the sample, allowing small pieces to be removed. These pieces are further thinned using the  $\text{Ga}^+$  beam, until they are electron-transparent and are ready to be examined in a TEM. SEM-ready samples, prepared by the method detailed in Section 3.4.1, were placed in the FIB microscope and TEM samples were prepared in this fashion. TEM analysis was carried out on a FEI Tecnai 20 at 200 kV.

### **3.4.3 Energy-Dispersive X-ray Spectroscopy (EDS)**

A complementary technique to SEM and TEM is energy-dispersive x-ray spectroscopy (EDS). This utilises the x-rays produced within the interaction volume, as mentioned in Section 3.4.1, to obtain elemental spatial distribution and concentration data. When a primary electron enters the sample with the correct energy, it ejects an electron from the 1s shell of an atom. This causes an electron from a higher shell (2p) to drop down into the resulting hole, releasing a photon with an energy equivalent to the energy difference between the two electron shells [119]. This energy falls within the x-ray range, and is characteristic of the element of the atom which emits the photon. EDS was carried out in conjunction with SEM imaging using a Bruker Quantax 70 spectrometer on the Hitachi TM3030. EDS was collected over a range of times, from 5 minutes for preliminary investigations, up to 10 minutes for detailed mapping. EDS data were obtained in order to gain information on the chemical composition of the alteration layers formed on different glass samples.

### 3.5 Solid-State Nuclear Magnetic Resonance Spectroscopy (SSNMR)

Nuclear magnetic resonance spectroscopy (NMR) is a technique which exploits the electromagnetic properties of nuclei in order to provide information on their chemical environment. Each nucleus has an associated intrinsic spin, denoted  $I$ . This spin leads to the production of a nuclear magnetic moment,  $\mu_I$ , given by [120]:

$$\mu_I = \frac{ge\hbar I}{2m_p} \quad (\text{Equation 3.9})$$

where  $g$  is the Landé splitting factor,  $e$  is the charge of the electron in coulombs,  $\hbar$  is the reduced Planck's constant in J s, and  $m_p$  is the proton mass. In an externally applied, static, magnetic field,  $B_0$ , the magnetic moment can exist in a range of states depending on the orientation of the moment with the external field. The component of  $\mu_i$  parallel to the field has values of  $m\hbar$ , where  $m$  ranges from  $-I$  to  $+I$  in integer steps. The energy,  $E$ , of a magnetic moment in an external magnetic field,  $B$ , can be calculated by:

$$E = -\mu \cdot B \quad (\text{Equation 3.10})$$

Thus, energy of the  $m$ th state of the nuclear magnetic moment is:

$$E = -\frac{ge\hbar I}{2m_p} \cdot B \quad (\text{Equation 3.11})$$

which can be simplified to:

$$E = -\gamma m \hbar B \quad (\text{Equation 3.12})$$

where  $\gamma$  is the magnetogyric ratio, equal to  $-\frac{ge}{2m_p}$ . The energy difference between two adjacent states is given by:

$$\Delta E = \hbar \gamma B \quad (\text{Equation 3.13})$$

which means that radiation with frequency  $\gamma B$  would excite the transition between the two states. For nuclear moments, this frequency lies in the radio frequency (RF) range ( $10^6 - 10^9$  Hz) [120], and so many NMR experiments are carried out by irradiating samples with RF radiation within a magnetic field, and then measuring the resonance response from the sample.

The total energy of a system exhibiting nuclear magnetic resonance,  $E_{NMR}$ , is the sum over various different contributions:

$$E_{NMR} = E_Z + E_{RF} + E_S + E_J + E_D + E_Q \quad (\text{Equation 3.14})$$

where:  $E_Z$  is the contribution from the Zeeman effect (Equation 3.12);  $E_{RF}$  is the contribution from the interaction of the spins and the applied RF;  $E_S$  is the shielding effect, which modifies the Zeeman contribution;  $E_J$  is the contribution from indirect

spin coupling;  $E_D$  is the contribution from dipolar spin coupling; and  $E_Q$  is the quadrupolar spin coupling [121]. The latter four contributions depend on the orientation of the spins in the magnetic field, and thus for solid samples, where the molecules are mostly static, these contributions are large and lead to line-broadening in the resonance spectra. In order to isolate the shielding contribution, which gives information on the chemical environment of the nuclei, these contributions can be averaged out by spinning the sample at an angle of  $54^\circ 44'$  to the external magnetic field, known as ‘magic-angle spinning’ [121].

All spectroscopy was carried out on powdered glass with a particle size fraction of 75 – 149  $\mu\text{m}$ . Solid-state NMR spectra were obtained at the EPSRC UK National Solid-state NMR Service at Durham University. The nuclei studied were  $^{11}\text{B}$ ,  $^{27}\text{Al}$  and  $^{29}\text{Si}$ .

The spectra were collected using a Varian VNMRS operating at 128.301 MHz for  $^{11}\text{B}$ , 104.199 MHz for  $^{27}\text{Al}$  and 79.438 MHz for  $^{29}\text{Si}$ .  $^{11}\text{B}$  and  $^{27}\text{Al}$  spectra were collected with a 4 mm (rotor outer diameter) probe, while the  $^{29}\text{Si}$  spectra used a 6 mm probe. Spinning rates were 11 kHz for  $^{11}\text{B}$  and  $^{27}\text{Al}$ , and 6 kHz for  $^{29}\text{Si}$ . All spectra were acquired using a pulse-acquire experiment. Recycle delays were 5 s for  $^{11}\text{B}$ , 0.2 s for  $^{27}\text{Al}$  and 120 s for  $^{29}\text{Si}$ . The  $^{11}\text{B}$ ,  $^{27}\text{Al}$  and  $^{29}\text{Si}$  spectra were referenced to  $\text{BF}_3/\text{OEt}_2$ , 1M aq.  $\text{Al}(\text{NO}_3)_3$  and neat tetramethylsilane (TMS), respectively.

The  $^{11}\text{B}$  multiple-quantum (MQ) MAS-NMR experiment was carried out on the Varian VNMRS operating at 128.295 MHz with a 4 mm probe spinning at 12 kHz. The data were referenced to  $\text{BF}_3/\text{OEt}_2$ . The  $^{27}\text{Al}$  triple-quantum (3Q) MAS-NMR experiment was carried out on a Bruker Avance III HD operating at 140 MHz, with a 1.9 mm probe spinning at 15 kHz, with frequencies referenced to 1M aq.  $\text{Al}(\text{NO}_3)_3$ .

The data obtained were used to analyse the structure of the glasses through identification of the fractions of different silicate  $\text{Q}_n$  species, the proportions of  $^{\text{III}}\text{B}$  and  $^{\text{IV}}\text{B}$  structural units, and the coordination environment of Al.

The peaks seen in NMR spectra of glass samples are composed of contributions from a range of different chemical environments within the glass. This varies with the isotope being studied, and so the fitting procedure is isotope-dependent. All of the peak-fitting was performed using the DMFit software developed by Massiot *et al.* [122]. All of the spectra in this study were normalised to a peak height of 100.

$^{29}\text{Si}$  MAS-NMR spectra can provide important information on the structure of silicate glasses. It is often possible to differentiate between different Q-species (i.e.

silicate tetrahedra with different numbers of bridging and non-bridging oxygens), e.g.  $Q_3$  and  $Q_4$ , and thus a measure of the connectivity of the network can be obtained. The spectra are also sensitive to the nearest-neighbour species bonded to the silicate tetrahedra, e.g. Si – O – Si compared to Si – O – Al. However, due to the disordered nature of glasses there are a wide range of different Si environments contributing to the spectra – different Q-species, different nearest neighbours, a range of bond angles and lengths – and so it can be difficult to ascertain which parts of the spectrum are due to which contributions. The spectra were fitted with Gaussian peaks. The central peak was fitted with either one or two Gaussian peaks, which correspond to asymmetric (Peak 1) and symmetric (Peak 2) contributions. Asymmetric contributions come from  $Q_3$  tetrahedra and  $Q_4$  tetrahedra that are connected to one non-silicate tetrahedron, e.g.  $Q_4(1B, 3Si)$  or  $Q_4(1Al, 3Si)$ , henceforth referred to as  $Q_4(X)$ . Symmetric contributions come from  $Q_4$  tetrahedra linked to only other silicate tetrahedra, i.e.  $Q_4(4Si)$ . Spinning sidebands were also fitted with Gaussian peaks, and their position was used to fix the position of the asymmetric contribution peak (it was placed in the centre of the two sidebands). In this case, the position of the asymmetric peak was fixed but its amplitude and width were allowed to refine, and the position, amplitude and width of the symmetric contribution peak were allowed to freely refine. Where spinning sidebands were not visible, all parameters were allowed to refine freely. It was difficult to obtain unique fits of the NCAB $_x$ S and NMAB $_x$ S spectra due to the presence of both B and Al causing a further blurring of the distinctions between different contributions, and so deconvolutions of these spectra are not reported here. Example fits are shown in Figure 3.11. All spectra fits can be found in Appendix B.

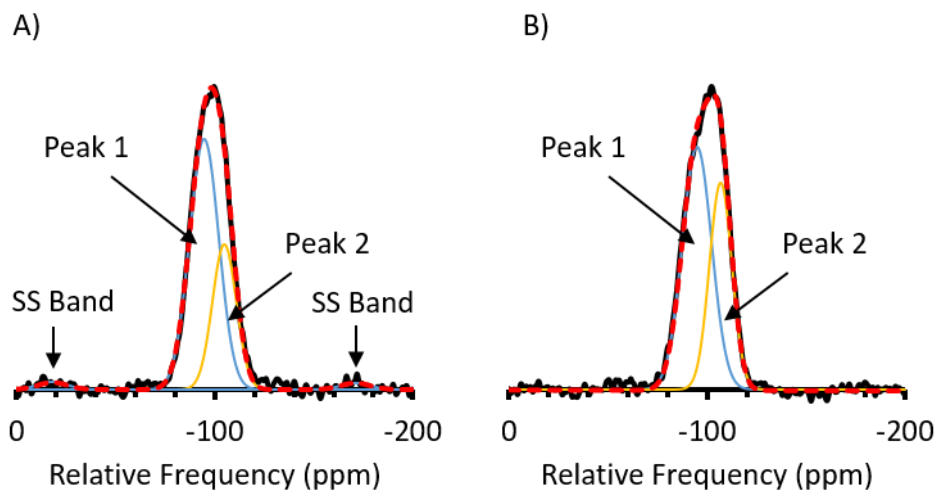


**Figure 3.11.**  $^{29}\text{Si}$  MAS-NMR example fits: A) NC5BS Glass with spinning sidebands; B) NC10BS glass without spinning sidebands.

Due to the quadrupolar nature of  $^{11}\text{B}$  (spin  $> 1/2$ ), fitting of  $^{11}\text{B}$  spectra is treated significantly differently to that for  $^{29}\text{Si}$  spectra. In the spectra in this study, there are two primary contributions to the spectra: one from  $^{\text{IV}}\text{B}$  units ( $\text{BO}_4$  tetrahedra) and one from  $^{\text{III}}\text{B}$  units ( $\text{BO}_3$  units). For the borosilicate glasses, each of these is the sum of two separate contributions, as shown in Table 3.5. These assignments are based on those used by Parkinson et al. [123], as the glasses studied are similar, particularly with regards to K-values. Evidence for the presence of two  $^{\text{IV}}\text{B}$  sites was seen in the  $^{11}\text{B}$  MQMAS-NMR spectrum for NM10BS, where a ‘shoulder’ in the  $^{\text{IV}}\text{B}$  peak suggests the presence of a second  $^{\text{IV}}\text{B}$  contribution (Figure 3.12). However, although these peaks are assigned in order to lend robustness to the methodology of the fit, the primary data extracted from these spectra are the overall contributions from  $^{\text{III}}\text{B}$  and  $^{\text{IV}}\text{B}$  species, due to complications with the fitting of aluminoborosilicate glasses. For the aluminoborosilicate glasses, two peaks were used to fit the  $^{\text{III}}\text{B}$  contribution, while either one or two peaks was used for the  $^{\text{IV}}\text{B}$  contribution, depending on which was able to produce an adequate fit. For all samples, the two peaks fitted to the  $^{\text{III}}\text{B}$  contribution were  $Q_{\text{mas}} 1/2$  curves. The parameters for these curves were: amplitude, position, apodisation of the theoretical lineshape (EM), quadrupolar frequency ( $\nu_Q$ ) and the asymmetry parameter ( $\eta_Q$ ).  $\eta_Q$  values were fixed at 0.28, but all other parameters were allowed to refine. The peaks fitted to the  $^{\text{IV}}\text{B}$  contribution were Gaussian profiles. Their amplitude, width and position were allowed to refine. Example fits of  $^{11}\text{B}$  spectra are shown in Figure 3.13. Fits for the other spectra can be

found in Appendix A.

**Table 3.5** Peak assignments for  $^{11}\text{B}$  MAS-NMR spectra on borosilicate glasses [123]

Coordination	Peak	Assignment
$^{\text{IV}}\text{B}$	$^{\text{IV}}\text{B}$ Peak 1	$^{\text{IV}}\text{B}$ (1B, 3Si)
	$^{\text{IV}}\text{B}$ Peak 2	$^{\text{IV}}\text{B}$ (0B, 4Si)
$^{\text{III}}\text{B}$	$^{\text{III}}\text{B}$ Peak 1	Symmetric ( $^{\text{III}}\text{B}(\text{O}_{1/2})_3$ )
	$^{\text{III}}\text{B}$ Peak 2	Asymmetric ( $^{\text{III}}\text{B}(\text{O}_{1/2})_2(\text{O}^-)$ )

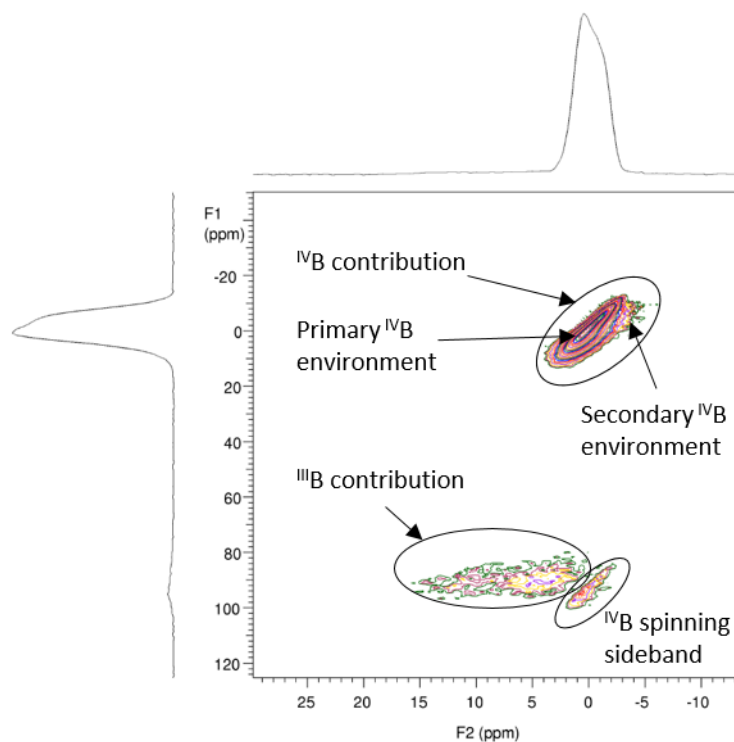


**Figure 3.12.**  $^{11}\text{B}$  MQMAS-NMR spectrum for NM10BS. A shoulder in the  $^{\text{IV}}\text{B}$  contribution suggests a secondary  $^{\text{IV}}\text{B}$  environment.

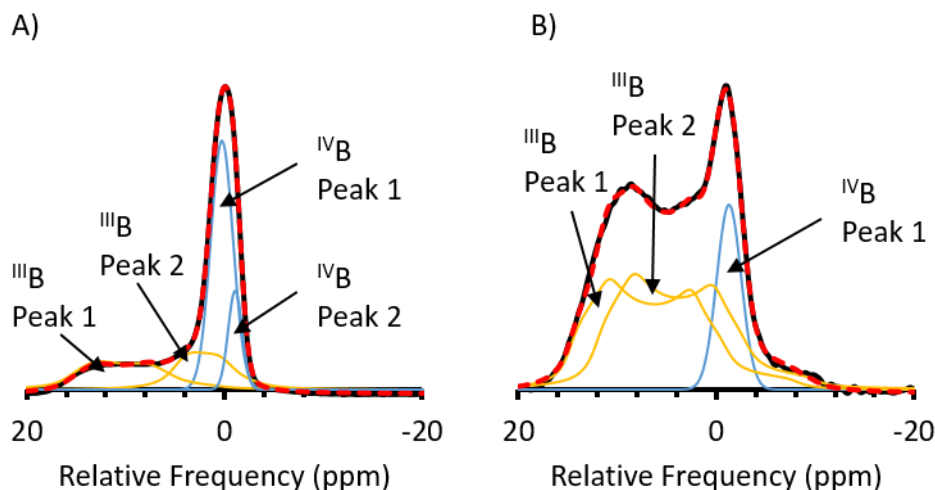


**Figure 3.13.**  $^{11}\text{B}$  MAS-NMR example fits: A) NM5BS Glass with two  $^{\text{III}}\text{B}$  peaks and two  $^{\text{IV}}\text{B}$  peaks; B) NMAB10S glass with two  $^{\text{III}}\text{B}$  peaks and one  $^{\text{IV}}\text{B}$

The  $^{27}\text{Al}$  spectra fits were attempted using either one or two peaks, with the primary peak corresponding to  $^{\text{IV}}\text{Al}$  and the other corresponding to  $^{\text{V}}\text{Al}$ . These contributions were simulated using peaks which utilised a simplified version of the Czjzek model. The Czjzek model was developed by Czjzek et al. in order to be able to model contributions from quadrupolar nuclei in amorphous solids during Mössbauer spectroscopy [124]. The implementation of this model to MAS-NMR spectroscopy of amorphous solids is detailed by d’Espinoze de Lacaillerie et al. [125]. The peaks utilise six parameters: amplitude, position, Full-Width at Half-Maximum of the chemical shift Gaussian distribution (FWHM CS), apodisation of the lineshape (EM au), quadrupolar coupling ( $\nu_Q$ ) and the critical exponent of the Czjzek distribution,  $d$ .  $d$  was fixed at 5 for each peak, but the other parameters were allowed to refine. However, it was not possible to obtain reasonable fits of the  $^{27}\text{Al}$  spectra. The one-peak fits were unable to simulate the spectra appropriately, and although a two-peak fit was able to recreate the experimental spectra, the peak positions did not correspond to known contributions. Thus, fits of the spectra are not presented in this work.

### 3.6 X-Ray Diffraction (XRD)

X-ray diffraction is an analytical technique where a beam of x-rays is incident on a sample, causing them to be diffracted by the atomic structure of the sample. Bragg’s Law states that:

$$n\lambda = 2d \sin \theta \quad (\text{Equation 3.15})$$

where  $\lambda$  is the wavelength of the x-rays,  $d$  is the spacing between adjacent crystallographic planes,  $\theta$  is the angle of incidence of the x-rays and  $n$  is the diffraction order. By varying  $\theta$ , and measuring the number of electrons being diffracted through that angle, the structure of a sample can be elucidated [126]. It is most associated with the study of crystalline materials, where the structure produces characteristic peaks depending on structure type and composition. It generally provides less information on amorphous materials, such as glass, and so has been used in this work as a crude indicator of whether the glass samples were amorphous or not (Diffraction patterns for each glass are shown in Appendix A). When a sample is amorphous, no sharp peaks are observed. However, as the detection limits for crystalline phases are high (~ 5 wt. %), this is an indicator, rather than a definitive measurement of amorphousness.

XRD was used to analyse the structure, of powdered samples of each glass, i.e. whether the samples were X-ray amorphous. It was also used in an attempt to detect any crystalline phases that precipitated during the alteration of the samples through PCT-B experiments. The diffraction spectra were collected using a Bruker D2 Phaser diffractometer, with Cu K $\alpha$ 1 radiation ( $\lambda = 1.54056 \text{ \AA}$ ), an angular range of  $10 - 65^\circ 2\theta$ , and a working voltage of 30 kV.

### 3.8 Geochemical Modelling using PHREEQC

The PHREEQC geochemical modelling package was created by Parkhurst and Appelo [127]. Version 3 of the software was used in this work. This software was used to calculate the saturation indices of various phases in the leachates during glass dissolution, in order to ascertain whether their formation was possible during the dissolution experiments. The concentrations of the elements in the leachate, as measured by ICP-OES, were input into PHREEQC, which then calculated the saturation indices of a range of phases present in the thermodynamic database used, in this case the Lawrence Livermore National Laboratory (LLNL) database. A full list of phases included, along with the thermodynamic constants used, is shown in Appendix E. Where mentioned in the text, other starting elemental concentrations were also used. These saturation indices were then used to inform identification of phases precipitating during dissolution, in support of other techniques, such as SEM, EDS and XRD.

## 4. Structural Analysis of Simple Glass Compositions by Magic-Angle Spinning Nuclear Magnetic Resonance (MAS-NMR) Spectroscopy

### 4.1 Introduction

Magic-Angle Spinning Nuclear Magnetic Resonance (MAS-NMR) spectroscopy was performed on the simple glasses. The normalised compositions of these glasses, analysed by HF digestion and Inductively-Coupled Plasma Atomic Emission Spectroscopy (ICP-AES), along with their densities (measured by gas pycnometry), are shown in Table 4.1. The analysed compositions were found to be generally similar to the nominal compositions of these glasses (see Table 3.4), within an error of ~12%. However, there were a few exceptions to this:

- The analysed  $\text{Al}_2\text{O}_3$  content of NC0BS was 3.60 mol.%, compared to a nominal content of 0.00 mol.%. This was likely due to contamination from the use of an alumina crucible.
- The MgO content of NM5BS was 3.18 mol.% compared to a nominal value of 5.00 mol.%. This could be due to the volatilisation of MgO from the melt, or due to thermal updrafts in the furnace blowing away some of the magnesium carbonate precursor, which had a very small particle size.
- The analysed CaO content of NCAB5S was 5.31 mol.% compared to a nominal content of 10.00 mol.%. The reason for this discrepancy is unknown, but could be due to a batching error, or other human error.
- The analysed  $\text{Al}_2\text{O}_3$  content of NMAB10S was 9.45 mol.% compared to a nominal value of 5.00 mol.%. This could again be due to human error.

**Table 4.1.** Normalised compositions of simple glasses in molar %, based on analysis by HF digestion and ICP-AES. Glass density values from gas pycnometry.

	Al <sub>2</sub> O <sub>3</sub> (mol. %)	B <sub>2</sub> O <sub>3</sub> (mol. %)	CaO (mol. %)	MgO (mol. %)	Na <sub>2</sub> O (mol. %)	SiO <sub>2</sub> (mol. %)	Total (mol. %)	Density (g cm <sup>-3</sup> )
<b>NC0BS</b>	3.60	15.09	0.05	0.00	19.66	61.60	100.00	2.497
<b>NC5BS</b>	0.00	16.10	5.36	0.00	16.09	62.46	100.00	2.510
<b>NC10BS</b>	0.00	16.28	10.59	0.09	10.35	62.68	100.00	2.497
<b>NM5BS</b>	0.00	16.66	0.06	3.18	16.22	63.88	100.00	2.472
<b>NM10BS</b>	0.00	16.38	0.14	11.35	10.40	61.73	100.00	2.415
<b>NCAB0S</b>	14.63	0.00	10.11	0.22	10.93	64.11	100.00	2.515
<b>NCAB5S</b>	11.08	5.31	5.31	0.18	11.01	67.11	100.00	2.471
<b>NCAB10S</b>	4.57	11.35	11.02	0.08	10.79	62.04	99.85	2.495
<b>NMAB0S</b>	13.89	0.00	0.31	9.13	11.36	65.30	100.00	2.487
<b>NMAB5S</b>	11.25	5.59	0.18	9.21	11.01	62.76	100.00	2.410
<b>NMAB10S</b>	9.45	9.82	0.14	8.91	9.92	61.76	100.00	2.382

## 4.2 Results

### 4.2.1 <sup>11</sup>B MAS-NMR

#### 4.2.1.1 NC<sub>x</sub>BS Glasses

The <sup>11</sup>B MAS-NMR spectra for the NC<sub>x</sub>BS glasses are shown in Figure 4.1. There are two general trends observable in these data: 1) The peak corresponding to the <sup>IV</sup>B contribution at around -1.5 ppm became more asymmetric as the CaO content increased, and shifted to more positive values (-1.0 ppm for NC10BS); 2) The wide region between 2 and 16 ppm, which corresponds to <sup>III</sup>B contributions, increased in intensity with increasing CaO content. These trends are borne out in calculated contributions from each of the four different environments to the three spectra (Table 4.2). The total <sup>III</sup>B and <sup>IV</sup>B contents were corrected to account for loss of intensity from the <sup>III</sup>B contributions to the spinning sidebands, which does not occur for the <sup>IV</sup>B contributions [128]. This correction took the form of a 4% increase to the <sup>III</sup>B contributions. The former trend appears to have been due to a decrease in the amount of <sup>IV</sup>B tetrahedra that are linked to one other <sup>IV</sup>B tetrahedron and three SiO<sub>4</sub> tetrahedra (<sup>IV</sup>B(1B, 3Si), <sup>IV</sup>B Peak 1), compared to <sup>IV</sup>B tetrahedra which are linked to four SiO<sub>4</sub> tetrahedra (<sup>IV</sup>B(0B, 4Si), <sup>IV</sup>B Peak 2). The former <sup>IV</sup>B environment can be assigned to danburite superstructural units, while the latter environment can be assigned to

reedmergnerite superstructural units [123]. This could suggest that increasing the CaO content of the glasses led to an increase in boron clustering. The second trend was due to a decrease in  $N_4$ , the ratio of  $^{IV}B$  units to total B units. This decreased with CaO content, from  $0.59 \pm 0.01$  for NC0BS, down to  $0.46 \pm 0.002$  for NC10BS.

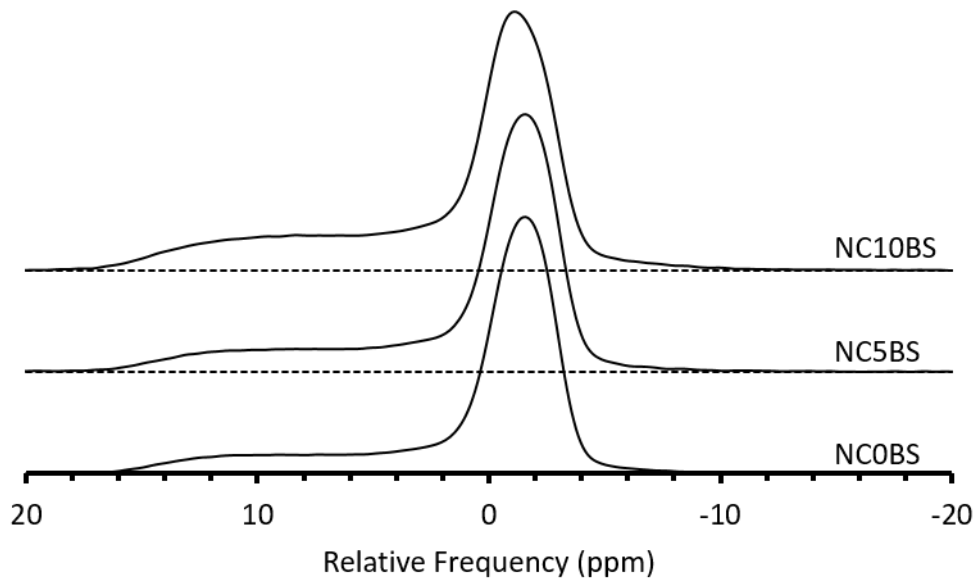


**Figure 4.1.**  $^{11}B$  MAS-NMR spectra obtained on NCxBS glasses.

**Table 4.2.** Calculated peak contributions from deconvolutions of  $^{11}\text{B}$  MAS-NMR spectra from  $\text{NC}_x\text{BS}$  samples. Errors are taken from the standard deviation of deconvolutions repeated 5 times.

Sample	Peak	Peak Area %	Total $^{\text{III}}\text{B}$ (corrected)	Total $^{\text{IV}}\text{B}$ (corrected)	$\text{N}_4$
NC0BS	$^{\text{III}}\text{B}$ Peak 1	$19.8 \pm 0.3$	$41.4 \pm 1.5$	$58.6 \pm 1.5$	$0.59 \pm 0.01$
	$^{\text{III}}\text{B}$ Peak 2	$17.6 \pm 1.2$			
	$^{\text{IV}}\text{B}$ Peak 1	$54.1 \pm 2.4$			
	$^{\text{IV}}\text{B}$ Peak 2	$8.4 \pm 0.9$			
NC5BS	$^{\text{III}}\text{B}$ Peak 1	$18.0 \pm 0.7$	$44.0 \pm 1.0$	$56.0 \pm 1.0$	$0.56 \pm 0.01$
	$^{\text{III}}\text{B}$ Peak 2	$22.0 \pm 1.6$			
	$^{\text{IV}}\text{B}$ Peak 1	$52.7 \pm 1.4$			
	$^{\text{IV}}\text{B}$ Peak 2	$7.3 \pm 0.4$			
NC10BS	$^{\text{III}}\text{B}$ Peak 1	$25.8 \pm 0.6$	$54.2 \pm 0.2$	$45.8 \pm 0.2$	$0.46 \pm 0.002$
	$^{\text{III}}\text{B}$ Peak 2	$24.5 \pm 0.9$			
	$^{\text{IV}}\text{B}$ Peak 1	$38.9 \pm 0.7$			
	$^{\text{IV}}\text{B}$ Peak 2	$10.9 \pm 0.5$			

#### 4.2.1.2 $\text{NM}_x\text{BS}$ Glasses

Figure 4.2 shows the  $^{11}\text{B}$  MAS-NMR spectra for the  $\text{NM}_x\text{BS}$  glasses. These glasses exhibited the same trends as the  $\text{NC}_x\text{BS}$  glasses: an increase in the asymmetry and relative frequency of the  $^{\text{IV}}\text{B}$  peak, and an increase in the  $^{\text{III}}\text{B}$  contribution to the spectra with increasing MgO content. Table 4.3 shows the calculated contributions of each of the four B environments to the spectra. As with the  $\text{NC}_x\text{BS}$  glasses,  $\text{N}_4$  decreased with the addition of alkaline earth oxide, from  $0.54 \pm 0.006$  for  $\text{NM5BS}$  to  $0.37 \pm 0.02$  for  $\text{NM10BS}$ .

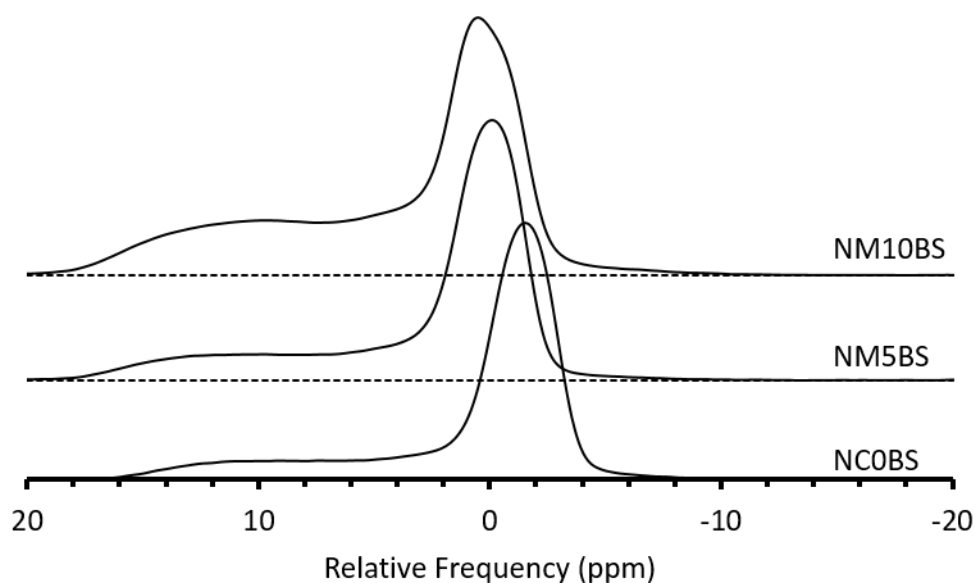


**Figure 4.2.**  $^{11}\text{B}$  MAS-NMR spectra obtained on  $\text{NM}_x\text{BS}$  glasses.

**Table 4.3.** Calculated peak contributions from deconvolutions of  $^{11}\text{B}$  MAS-NMR spectra from  $\text{NM}_x\text{BS}$  samples. Errors are taken from the standard deviation of deconvolutions repeated 5 times.

Sample	Peak	Peak Area %	Total $^{\text{III}}\text{B}$ (corrected)	Total $^{\text{IV}}\text{B}$ (corrected)	$N_4$
NM5BS	$^{\text{III}}\text{B}$ Peak 1	$22.3 \pm 0.3$	$46.1 \pm 0.6$	$53.9 \pm 0.1$	$0.54 \pm 0.01$
	$^{\text{III}}\text{B}$ Peak 2	$19.8 \pm 0.3$			
	$^{\text{IV}}\text{B}$ Peak 1	$46.7 \pm 0.2$			
	$^{\text{IV}}\text{B}$ Peak 2	$11.4 \pm 0.1$			
NM10BS	$^{\text{III}}\text{B}$ Peak 1	$31.3 \pm 3.0$	$62.2 \pm 1.2$	$36.9 \pm 2.4$	$0.37 \pm 0.02$
	$^{\text{III}}\text{B}$ Peak 2	$26.9 \pm 5.1$			
	$^{\text{IV}}\text{B}$ Peak 1	$29.0 \pm 3.0$			
	$^{\text{IV}}\text{B}$ Peak 2	$12.8 \pm 0.8$			

#### 4.2.1.3 NCAB $_x$ S Glasses

Figure 4.3 shows the  $^{11}\text{B}$  MAS-NMR spectra for NCAB5S and NCAB10S (N.B. NCAB0S does not contain any  $\text{B}_2\text{O}_3$ ). The calculated contributions of the different B environments are shown in Table 4.4. The NCAB5S spectrum was fitted with one  $^{\text{IV}}\text{B}$  peak, corresponding to  $^{\text{IV}}\text{B}(1\text{B}, 3\text{Si})$ , as it was not possible to obtain a reasonable fit

with two  $^{IV}B$  peaks. Two observations for these spectra were: 1)  $N_4$  increased significantly with increasing B/Al ratio, from  $0.12 \pm 0.01$  for NCAB5S to  $0.39 \pm 0.001$  for NCAB10S; 2) The  $^{IV}B$  contribution shifted towards more negative relative frequencies with increasing B/Al. The latter trend could be due to an increase in the amount of  $^{IV}B(OB, 4Si)$  units in the glass.

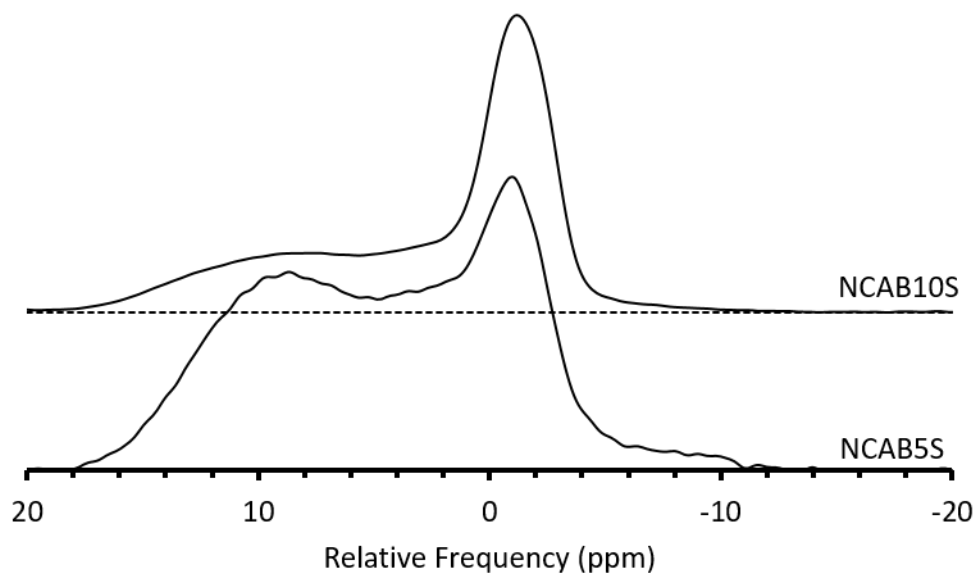


**Figure 4.3.**  $^{11}B$  MAS-NMR spectra obtained on NCAB5S and NCAB10S.

**Table 4.4.** Calculated peak contributions from deconvolutions of  $^{11}B$  MAS-NMR spectra from NCAB $x$ S samples. Errors are taken from the standard deviation of deconvolutions repeated 5 times.

Sample	Peak	Peak Area %	Total $^{III}B$ (corrected)	Total $^{IV}B$ (corrected)	$N_4$
NCAB5S	$^{III}B$ Peak 1	$43.2 \pm 1.2$	$87.5 \pm 0.8$	$12.5 \pm 0.8$	$0.12 \pm 0.01$
	$^{III}B$ Peak 2	$40.3 \pm 1.7$			
	$^{IV}B$ Peak 1	$16.5 \pm 0.8$			
	$^{IV}B$ Peak 2	N/A			
NCAB10S	$^{III}B$ Peak 1	$35.1 \pm 2.3$	$61.1 \pm 0.2$	$38.9 \pm 0.2$	$0.39 \pm 0.001$
	$^{III}B$ Peak 2	$22.1 \pm 2.4$			
	$^{IV}B$ Peak 1	$37.8 \pm 0.6$			
	$^{IV}B$ Peak 2	$5.1 \pm 0.5$			

#### 4.2.1.4 NMAB $x$ S Glasses

The  $^{11}\text{B}$  MAS-NMR spectra for NMAB5S and NMAB10S are shown in Figure 4.4 (N.B. NMAB0S contained no  $\text{B}_2\text{O}_3$ ). As with the NCAB5S spectrum, the NMAB5S spectrum was fitted with only one  $^{\text{IV}}\text{B}$  peak. The calculated total  $^{\text{III}}\text{B}$  and  $^{\text{IV}}\text{B}$  contributions to these spectra are shown in Table 4.5. The contributions from individual peaks are not reported due to lack of consistency of the fits. However, there was appropriate consistency in the overall  $^{\text{III}}\text{B}$  and  $^{\text{IV}}\text{B}$  contributions. As with the NCAB $x$ S glasses, an increase in  $\text{N}_4$  with increasing B/Al ratio was observed, from  $0.09 \pm 0.004$  for NMAB5S to  $0.14 \pm 0.01$  for NMAB10S.

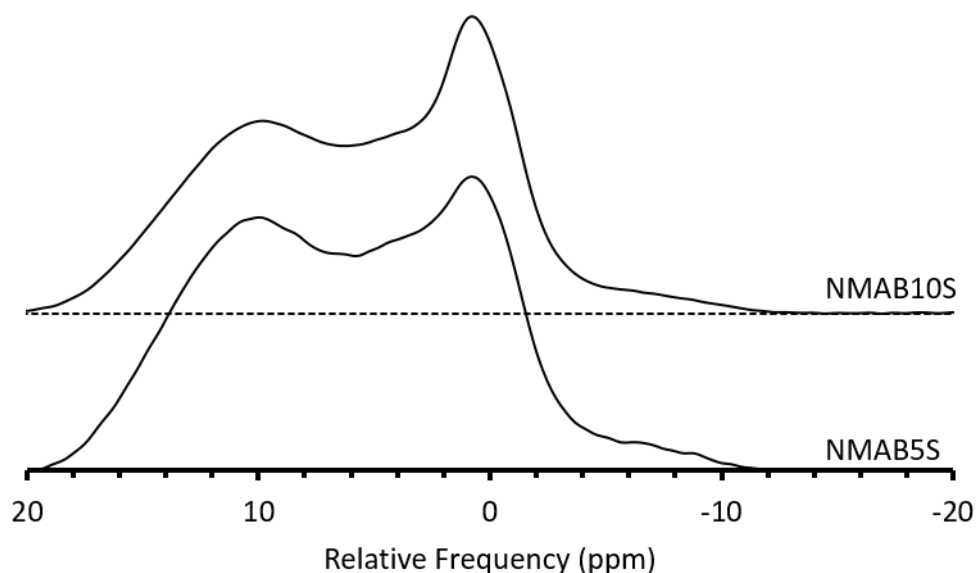


**Figure 4.4.**  $^{11}\text{B}$  MAS-NMR spectra obtained on NMAB5S and NMAB10S.

**Table 4.5.** Calculated total  $^{\text{III}}\text{B}$  and  $^{\text{IV}}\text{B}$  contributions from deconvolutions of  $^{11}\text{B}$  MAS-NMR spectra from NMAB $x$ S samples. Errors are taken from the standard deviation of deconvolutions repeated 5 times.

Sample	Total $^{\text{III}}\text{B}$ (corrected)	Total $^{\text{IV}}\text{B}$ (corrected)	$\text{N}_4$
NMAB5S	$91.2 \pm 0.4$	$8.8 \pm 0.4$	$0.09 \pm 0.004$
NMAB10S	$85.8 \pm 0.7$	$14.2 \pm 0.7$	$0.14 \pm 0.01$

## 4.2.2 $^{29}\text{Si}$ MAS-NMR

### 4.2.2.1 $\text{NC}_x\text{BS}$ Glasses

The  $^{29}\text{Si}$  MAS-NMR spectra for the  $\text{NC}_x\text{BS}$  glasses are shown in Figure 4.5. As the CaO content increases, the frequency of the centre of the spectra moves towards lower values, as shown by the dotted lines in the figure. The ppm positions for the centre of each spectrum are -97.92, -99.84 and -102.38 ppm for  $\text{NC0BS}$ ,  $\text{NC5BS}$  and  $\text{NC10BS}$ , respectively. This suggests that the proportion of symmetric species, i.e.  $\text{Q}_4(0\text{B}, 4\text{Si})$ , increases with increasing CaO content. The calculated contributions from the asymmetric ( $\text{Q}_3 + \text{Q}_4(\text{X})$ ) and symmetric species ( $\text{Q}_4$ ) are shown in Table 4.6. This also suggests that the  $\text{Q}_4$  fraction of the glasses increases with increasing CaO content, from  $0.24 \pm 0.03$  for  $\text{NC0BS}$  to  $0.38 \pm 0.01$  for  $\text{NC10BS}$ .

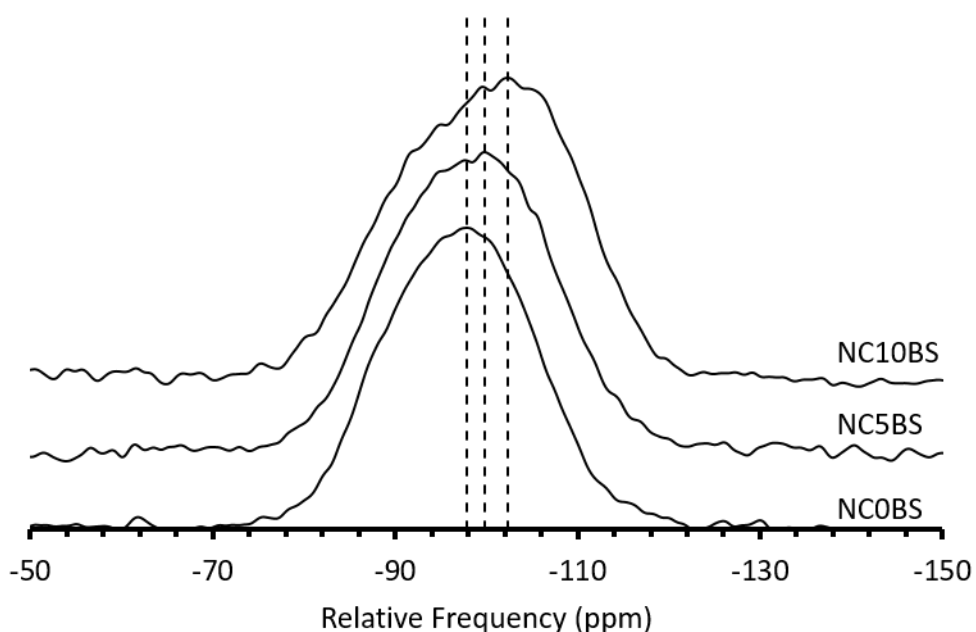


**Figure 4.5.**  $^{29}\text{Si}$  MAS-NMR spectra obtained on  $\text{NC}_x\text{BS}$  glasses. The dotted lines mark the peak of each spectrum.

**Table 4.6.** Calculated total asymmetric ( $Q_3 + Q_4(X)$ ) and symmetric ( $Q_4$ ) contributions from deconvolutions of  $^{29}\text{Si}$  MAS-NMR spectra from  $\text{NC}_x\text{BS}$  samples. Errors are taken from the standard deviation of deconvolutions repeated 5 times.

Sample	Total $Q_3 + Q_4(X)$ (w/ sidebands)	Total $Q_4$	$Q_4$ Fraction
NC0BS	$76.3 \pm 2.6$	$23.7 \pm 2.6$	$0.24 \pm 0.03$
NC5BS	$69.3 \pm 0.7$	$30.7 \pm 0.7$	$0.31 \pm 0.01$
NC10BS	$61.8 \pm 0.9$	$38.2 \pm 0.9$	$0.38 \pm 0.01$

#### 4.2.2.2 $\text{NM}_x\text{BS}$ Glasses

Figure 4.6 shows the  $^{29}\text{Si}$  MAS-NMR spectra for the  $\text{NM}_x\text{BS}$  glasses. The spectra exhibited the same trend as the  $\text{NC}_x\text{BS}$ ; a decrease in the relative frequency of the centre of the spectra with increasing MgO content. The positions of the centre points were -99.87 ppm and -105.79 ppm for  $\text{NM}_5\text{BS}$  and  $\text{NM}_{10}\text{BS}$ , respectively, compared to -97.92 ppm for  $\text{NC}_0\text{BS}$ . This again suggests that the proportion of symmetric species ( $Q_4(0\text{B}, 4\text{Si})$ ) increased with increasing MgO content.. The calculated contributions of the asymmetric and symmetric species are shown in Table 4.7. The  $Q_4$  fraction of the glasses increases with MgO content, as suggested by the relative frequency shift, from  $0.35 \pm 0.01$  for  $\text{NM}_5\text{BS}$  to  $0.41 \pm 0.02$  for  $\text{NM}_{10}\text{BS}$ .

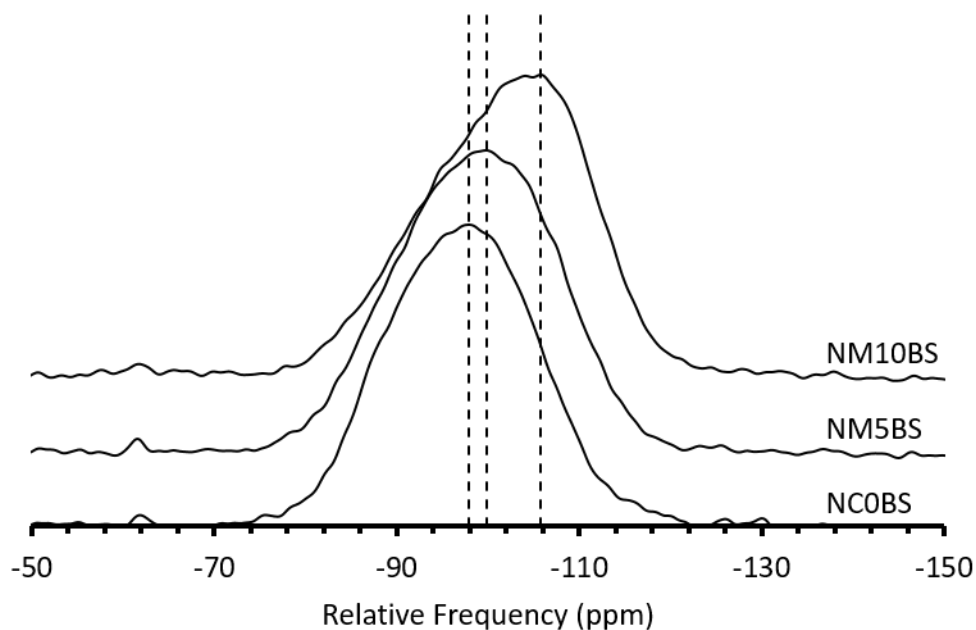


**Figure 4.6.**  $^{29}\text{Si}$  MAS-NMR spectra obtained on  $\text{NM}_x\text{BS}$  glasses. The dotted lines mark the peak of each spectrum.

**Table 4.7.** Calculated total asymmetric ( $\text{Q}_3 + \text{Q}_4(\text{X})$ ) and symmetric ( $\text{Q}_4$ ) contributions from deconvolutions of  $^{29}\text{Si}$  MAS-NMR spectra from  $\text{NM}_x\text{BS}$  samples. Errors are taken from the standard deviation of deconvolutions repeated 5 times.

Sample	Total $\text{Q}_3 + \text{Q}_4(\text{X})$ (w/ sidebands)	Total $\text{Q}_4$	$\text{Q}_4$ Fraction
NM5BS	$65.4 \pm 0.9$	$34.6 \pm 0.9$	$0.35 \pm 0.01$
NM10BS	$59.4 \pm 2.1$	$40.6 \pm 2.1$	$0.41 \pm 0.02$

#### 4.2.2.3 $\text{NCAB}_x\text{S}$ Glasses

Figure 4.7 shows the  $^{29}\text{Si}$  MAS-NMR spectra for the  $\text{NCAB}_x\text{S}$  glasses. The general trend was for a negative shift in the relative frequencies of the spectra peaks with increasing B/Al ratio. The positions were -93.13, -94.82 and -99.68 ppm for  $\text{NCAB}_0\text{S}$ ,  $\text{NCAB}_5\text{S}$  and  $\text{NCAB}_{10}\text{S}$ , respectively. This suggests an increase in the proportion of symmetric species ( $\text{Q}_4(\text{OB}, 4\text{Si})$ ) present.

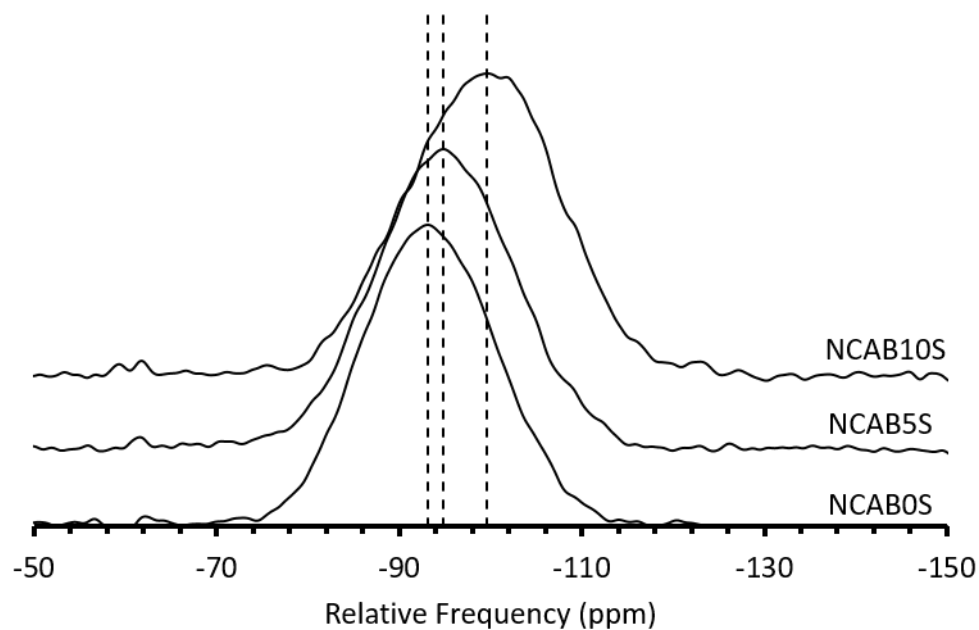


**Figure 4.7.**  $^{29}\text{Si}$  MAS-NMR spectra obtained on NCAB $x$ S glasses. The dotted lines mark the peak of each spectrum.

#### 4.2.2.4 NMAB $x$ S Glasses

The  $^{29}\text{Si}$  MAS-NMR spectra for the NMAB $x$ S glasses are shown in Figure 4.8. The trend observed was the same as for the NCAB $x$ S glasses; a negative shift in the relative frequency of the spectra peaks with increasing B/Al ratio, with peak centre positions at -95.65, -97.55 and -99.97 ppm for NMAB0S, NMAB5S and NMAB10S, respectively. This suggests an increase in the  $\text{Q}_4(4\text{Si})$  contribution to the spectra with increasing B/Al ratio.

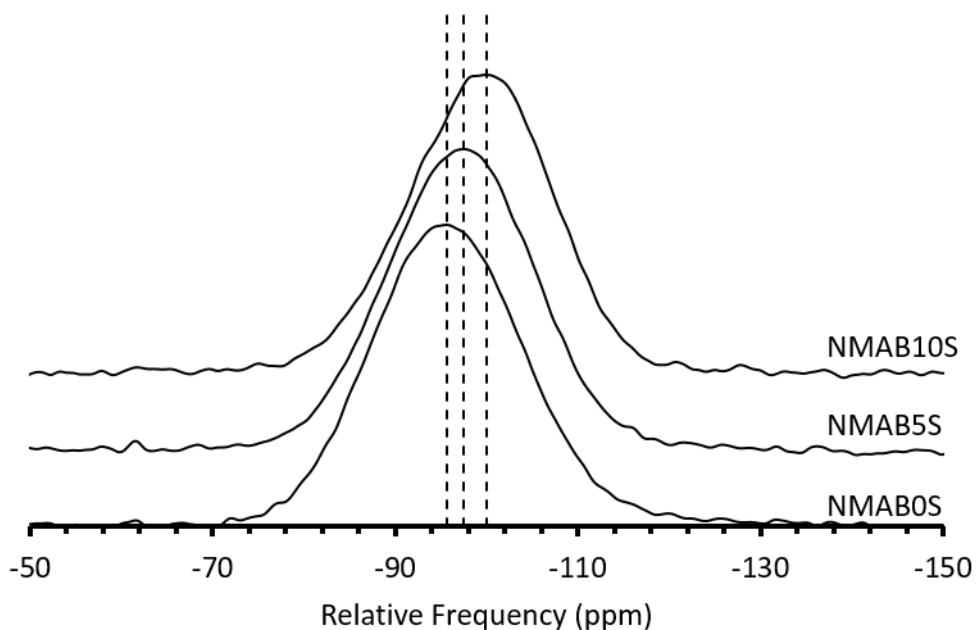


**Figure 4.8.**  $^{29}\text{Si}$  MAS-NMR spectra obtained on  $\text{NMAB}_x\text{S}$  glasses. The dotted lines mark the peak of each spectrum.

### 4.2.3 $^{27}\text{Al}$ MAS-NMR

#### 4.2.3.1 $\text{NCAB}_x\text{S}$ Glasses

The  $^{27}\text{Al}$  MAS-NMR spectra for the  $\text{NCAB}_x\text{S}$  glasses are shown in Figure 4.9. In general, the spectra were fairly similar, but two trends could be observed: 1) the relative frequency of the peak of the spectra decreased with increasing B/Al ratio; 2) the peak became narrower with increasing B/Al ratio.

Due to the difficulty in fitting the  $^{27}\text{Al}$  MAS-NMR spectra, a triple-quantum (3Q) MAS-NMR experiment was carried out on  $\text{NCAB0S}$  in order to determine the coordination of the Al. The spectrum for this is shown in Figure 4.10. The data suggest that Al was only present in tetrahedral coordination in this sample. As the  $\text{NCAB0S}$  1D MAS-NMR spectrum had the most intense tail (joint with  $\text{NCAB5S}$ ) at lower frequencies of the  $\text{NCAB}_x\text{S}$  series, and  $^{\text{V}}\text{Al}$  contributions would be expected to be found around this low-frequency tail, this suggests that the Al in all of the three glasses was present as  $^{\text{IV}}\text{Al}$ . As well as the large primary  $^{\text{IV}}\text{Al}$  contribution in the 3QMAS spectrum (58 – 27 ppm F1, 70 – -20 ppm F2), there appear to be three other features in the spectrum: a small peak at 29 – 23 ppm F1, 85 – 70 ppm F2; a slightly larger peak at 34 – 26 ppm F1, 80 – 60 ppm F2; and a shoulder in the primary contribution at 49 ppm F1, 55 ppm F2. This suggests that there are four different  $^{\text{IV}}\text{Al}$  environments contributing to this spectrum.

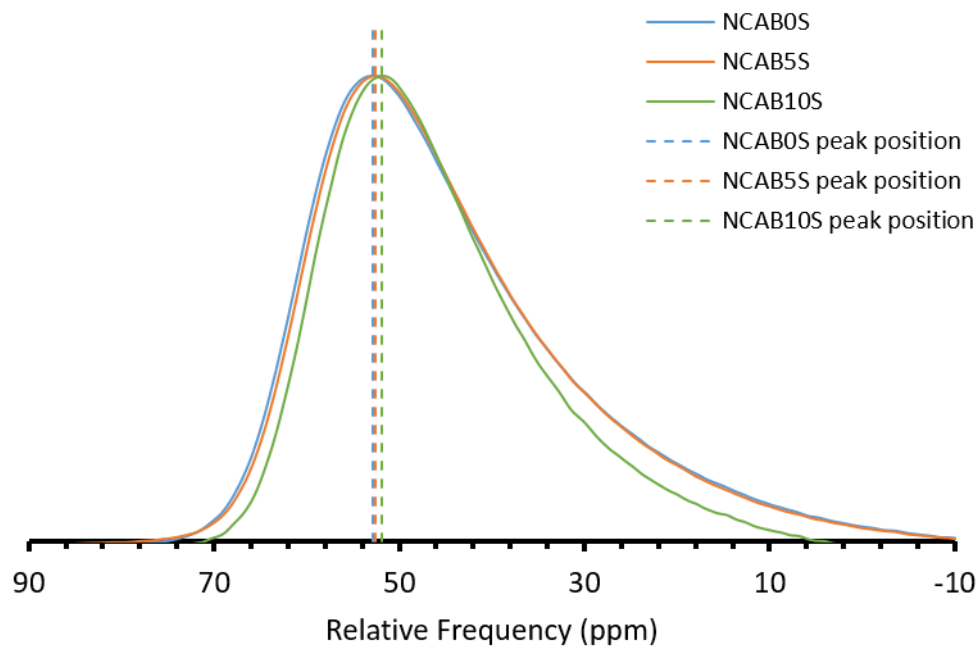


**Figure 4.9.**  $^{27}\text{Al}$  MAS-NMR spectra obtained on NCAB $x$ S glasses. The dotted lines mark the peak of each spectrum.

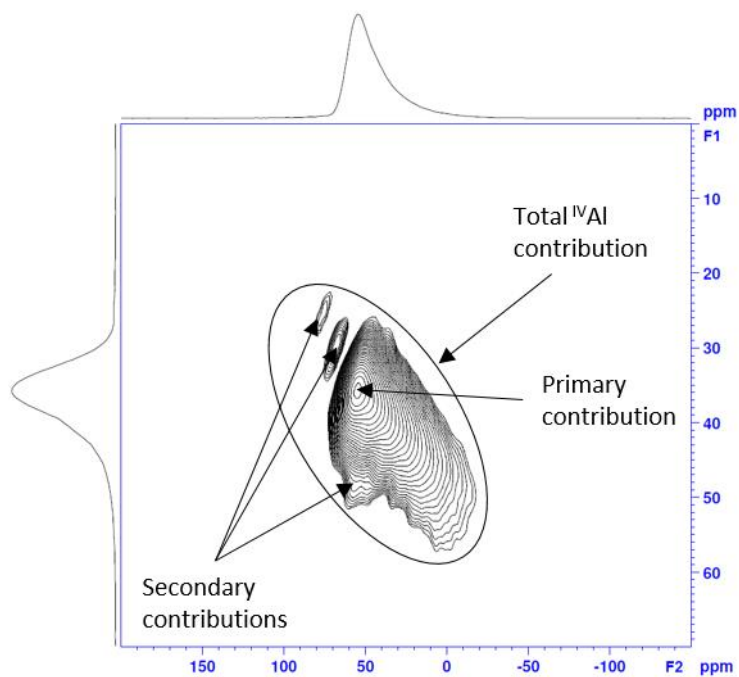


**Figure 4.10.**  $^{27}\text{Al}$  3QMAS-NMR spectrum obtained on NCAB0S glass.

#### 4.2.3.2 NMAB<sub>x</sub>S Glasses

Figure 4.11 shows the  $^{27}\text{Al}$  MAS-NMR spectra for the NMAB<sub>x</sub>S glasses. As with the NCAB<sub>x</sub>S glasses, the spectra are quite similar, although there is a systematic negative shift in the relative frequency of the spectra peaks with increasing B/Al, and also a narrowing of the peaks with increasing B/Al.

As the lineshapes are very similar to those for the NCAB<sub>x</sub>S glasses, it is likely that the Al in these glasses is also in predominantly tetrahedral coordination.

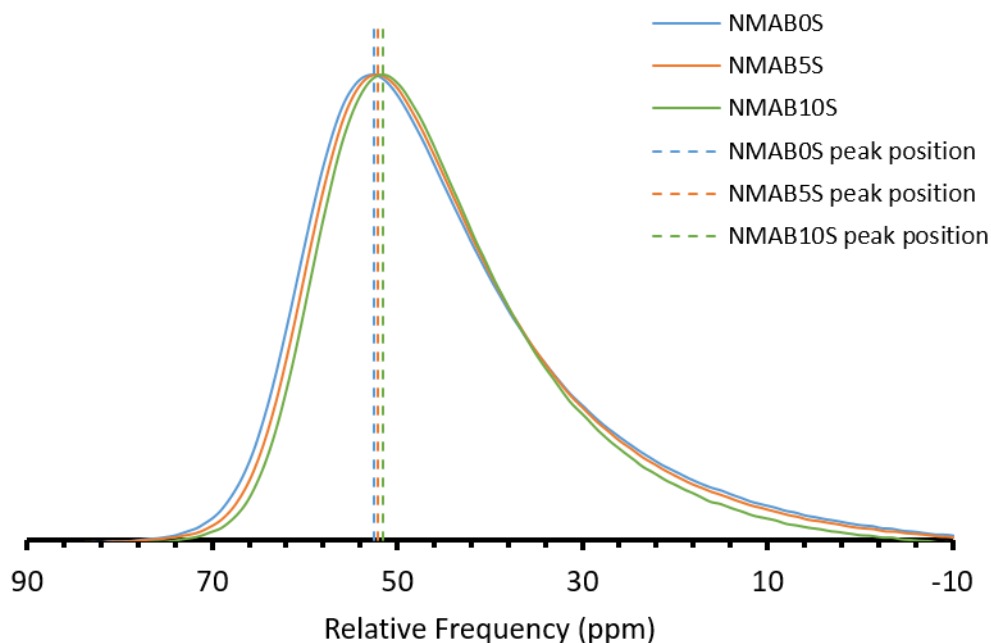


**Figure 4.11.**  $^{27}\text{Al}$  MAS-NMR spectra obtained on NMAB<sub>x</sub>S glasses. The dotted lines mark the peak of each spectrum.

### 4.3 Discussion of Results

Table 4.8 shows a summary of the results from the  $^{11}\text{B}$  and  $^{29}\text{Si}$  MAS-NMR spectroscopy, as well as pertinent data from the glass compositions. As noted in Section 4.1, the CaO content of NCAB5S is around half of the target value (5.31 mol.% compared to 10.00 mol.%). Therefore, the variation in composition between NCAB5S and the rest of the NCABxS series is not simply in the B/Al ratio, and as such, the data from this glass should be considered carefully. This might have a significant effect on the trend for the  $^{11}\text{B}$  data (Figs. 4.13 & 4.14), as only NCAB5S and NCAB10S contain boron. However, the overall trends in the  $^{29}\text{Si}$  and  $^{27}\text{Al}$  data should not be significantly affected.

**Table 4.8.** Summary of results from  $^{11}\text{B}$  and  $^{29}\text{Si}$  MAS-NMR spectroscopy.

	CaO (mol. %)	MgO (mol. %)	B/Al	$^{\text{IV}}\text{B}$ Fraction ( $\text{N}_4$ )	Rel. Freq. $^{29}\text{Si}$ Peak (ppm)	$\text{Q}_4$ Fraction
NC0BS	0.05	0.00	4.19	$0.59 \pm 0.01$	-97.92	$0.24 \pm 0.03$
NC5BS	5.36	0.00	–	$0.56 \pm 0.01$	-99.84	$0.31 \pm 0.01$
NC10BS	10.59	0.09	–	$0.46 \pm 0.002$	-102.38	$0.38 \pm 0.01$
NM5BS	0.06	3.18	–	$0.54 \pm 0.01$	-99.87	$0.35 \pm 0.01$
NM10BS	0.14	11.35	–	$0.37 \pm 0.02$	-105.79	$0.41 \pm 0.02$
NCAB0S	10.11	0.22	0.00	–	-93.13	–
NCAB5S	5.31	0.18	0.48	$0.12 \pm 0.01$	-94.82	–
NCAB10S	11.02	0.08	2.48	$0.39 \pm 0.001$	-99.68	–
NMAB0S	0.31	9.13	0.00	–	-95.65	–
NMAB5S	0.18	9.21	0.50	$0.09 \pm 0.004$	-97.55	–
NMAB10S	0.14	8.91	1.04	$0.14 \pm 0.01$	-99.97	–

#### 4.3.1 $^{11}\text{B}$ MAS-NMR

The addition of alkaline earth oxides (MO) to the glasses in place of  $\text{Na}_2\text{O}$  generally resulted in a decrease in fraction of  $^{\text{IV}}\text{B}$  units ( $\text{N}_4$ ). Figure 4.12 shows the  $^{\text{IV}}\text{B}$  fractions for the  $\text{NC}_x\text{BS}$  and  $\text{NM}_x\text{BS}$  glasses as a function of the ratio of the measured content of MO to the measured content of  $\text{Na}_2\text{O}$  ( $\text{MO}/\text{Na}_2\text{O}$ ). The decrease in  $^{\text{IV}}\text{B}$  fraction has two possible causes:

- the  $\text{Ca}^{2+}$  and  $\text{Mg}^{2+}$  cations are not able to charge-compensate for two  $^{\text{IV}}\text{B}$  tetrahedra each

- the  $\text{Ca}^{2+}$  and  $\text{Mg}^{2+}$  cations are more strongly associated with the silicate network than the borate network

As  $\text{Ca}^{2+}$  and  $\text{Mg}^{2+}$  are divalent cations, they can theoretically charge-compensate for two  $\text{BO}_4$  tetrahedra each. However, this requires each cation to be in the vicinity of two such tetrahedra, or the cations will charge-compensate for fewer than 2 tetrahedra on average, decreasing the fraction of  $^{\text{IV}}\text{B}$  units. Similarly, if a smaller proportion of alkaline earth cations are associated with the borate network, compared to the proportion of  $\text{Na}^+$  cations, fewer cations will be available for the charge-compensation of  $^{\text{IV}}\text{B}$  units and hence  $N_4$  will decrease. However, if the proportion of modifier cations associated with the silicate network increased an increase in the number of non-bridging oxygens (NBOs) and hence an increase in the proportion of  $\text{Q}_3$  with increasing  $\text{CaO}$  and  $\text{MgO}$  would be expected. This was not observed in the  $^{29}\text{Si}$  MAS-NMR data for these glasses (see Section 4.3.2). This suggests that the former explanation is more likely.

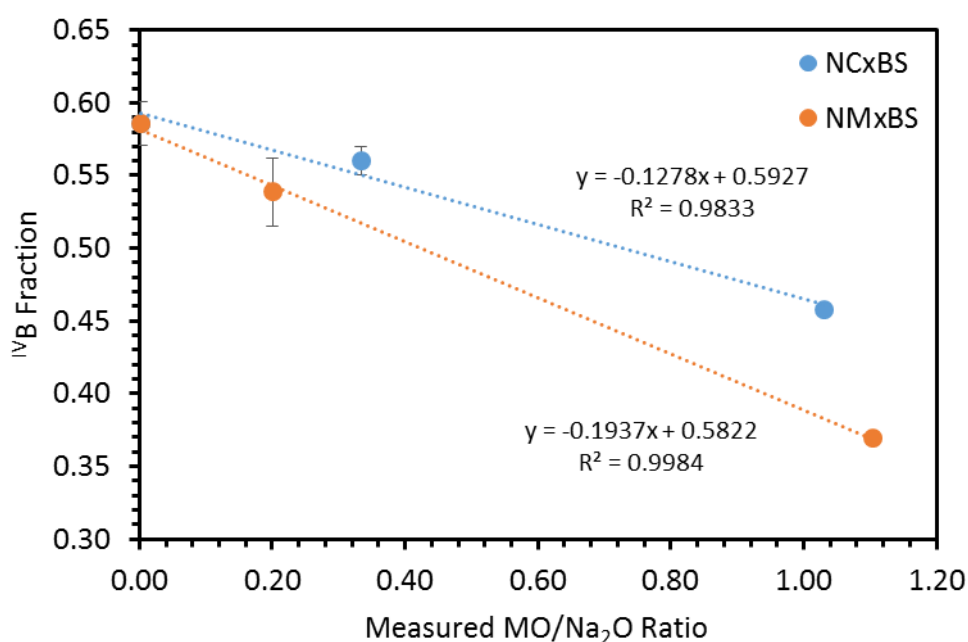


**Figure 4.12.**  $^{\text{IV}}\text{B}$  fraction as a function of measured  $\text{MO}/\text{Na}_2\text{O}$  ratio for the  $\text{NC}_x\text{BS}$  and  $\text{NM}_x\text{BS}$  glasses.

The depression of  $N_4$  with  $\text{MO}$  content was greater for the  $\text{MgO}$ -containing series than for the  $\text{CaO}$ -containing series. A potential explanation for this is that some of the  $\text{Mg}$  in the glass is present in tetrahedral coordination.  $\text{Mg}$  is known to be able to exist in four-fold coordination in glasses, whereas this is not the case for  $\text{Ca}$  [129].  $\text{Mg}$  in

four-fold coordination would not be available for charge-compensation of  $^{IV}B$  units, and would thus lead to a lower value of  $N_4$  than for the equivalent CaO-containing glass. In addition to this, these  $^{IV}Mg$  units would also require charge-compensation by  $Na^+$  cations [130], further reducing the number of cations available to charge-compensate the  $^{IV}B$  units.

Varying the B/Al ratio of the glasses also led to variations in the relative proportions of  $^{III}B$  and  $^{IV}B$  units. Figure 4.13a shows the fraction of  $^{IV}B$  units in the NCAB $x$ S and NMAB $x$ S glasses as a function of their B/Al ratio. Figure 4.13b shows the fraction of  $^{IV}B$  units in all of the aluminoborosilicate glasses (including NC0BS), as a function of their measured B/Al ratios. It is clear that an increase in the B/Al ratio of the glasses resulted in an increase in their  $^{IV}B$  fraction. This effect has been previously observed by Geisinger *et al.* in glasses along the  $NaAlSi_3O_8$ - $NaBSi_3O_8$  join [131]. It is likely due to competition between the  $^{IV}Al$  and  $^{IV}B$  tetrahedra for  $Na^+$  cations for charge-compensation, as the  $^{11}B$  MAS-NMR data for the borosilicate glasses suggest that alkaline-earth cations are not as efficient at charge-compensation as the  $Na^+$  cations. Based on the  $^{27}Al$  3QMAS-NMR experiment on NCAB0S (see Section 4.2.3.1) it appears that the vast majority, if not all, of the Al present in these glasses was in tetrahedral coordination. This implies that the Al tetrahedra are charge-compensated preferentially over the  $^{IV}B$  tetrahedra, as suggested by Yamashita *et al.* [55], [56]. Thus, for the NCAB5S and NMAB5S glasses, the vast majority of the ~10 mol.% of  $Na_2O$  is scavenged by the ~10 mol.% of  $Al_2O_3$ , leaving primarily CaO or MgO for  $^{IV}B$  charge-compensation. However, for the NCAB10S and NMAB10S glasses, some of the  $Na_2O$  would remain after the  $^{IV}Al$  had been charge-compensated, and so could charge-compensate some of the  $^{IV}B$  units. This can be seen more clearly in Figure 4.14a, where the  $^{IV}B$  fraction of all the B-containing glasses is plotted against  $[(Na_2O - Al_2O_3)/B_2O_3]$ , an approximate measure of the proportion of  $^{IV}B$  units that could be charge-compensated by  $Na^+$  cations, assuming preferential  $^{IV}Al$  charge-compensation. Figure 4.14b shows the same data for the NCAB $x$ S and NMAB $x$ S glasses with the data for NC10BS and NM10BS included, as these are effectively the  $B_2O_3$  endmembers of the NCAB $x$ S and NMAB $x$ S series. This shows that the  $^{IV}B$  fraction was lower in the MgO-containing glasses than in the CaO-containing glasses. This could again be due to the presence of  $^{IV}Mg$  units leading to a lower overall ability to charge-compensate the  $^{IV}B$  units.

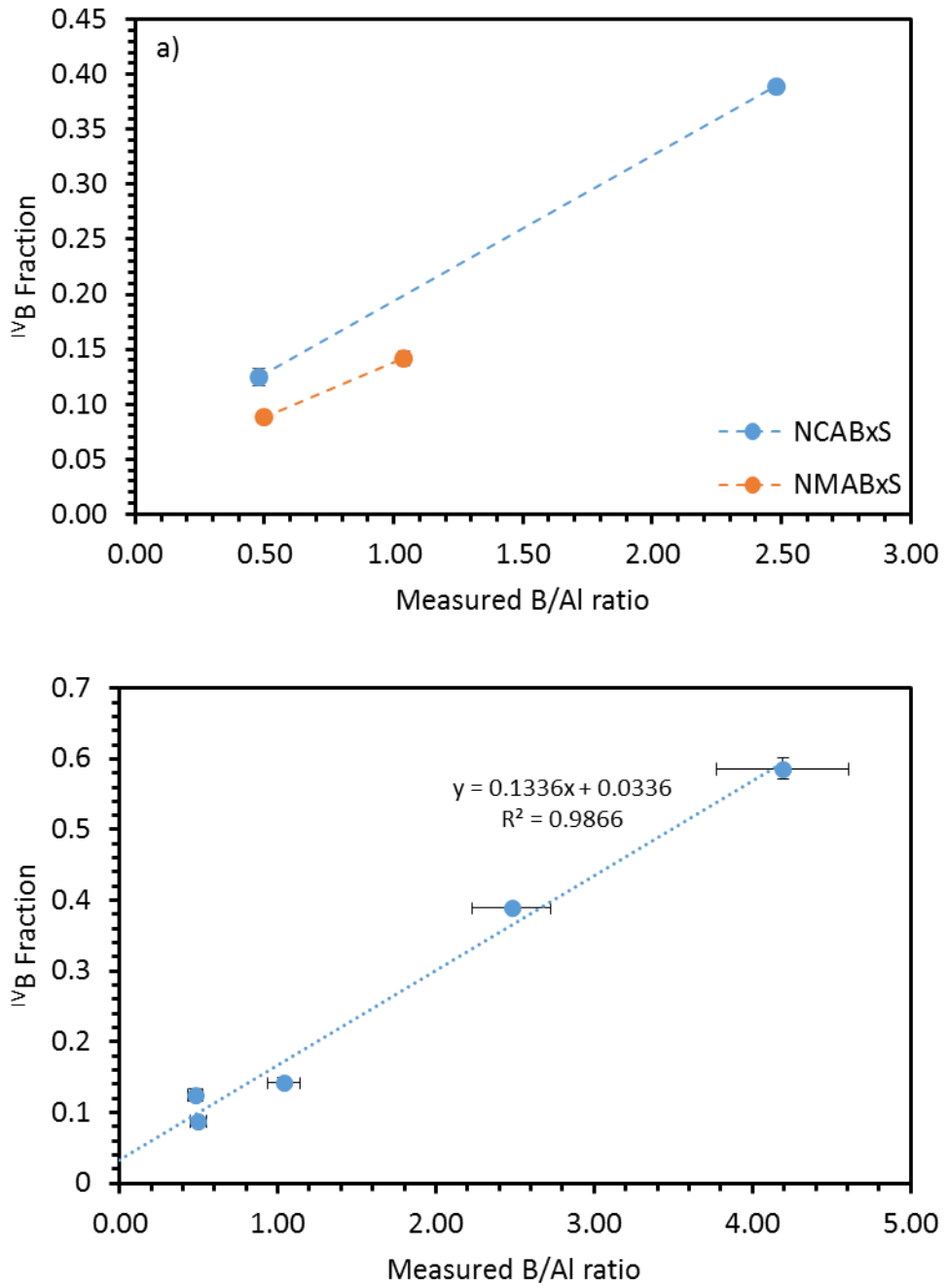


**Figure 4.13.** a) <sup>IV</sup>B fraction as a function of measured B/Al ratio for the NCAB<sub>x</sub>S and NMAB<sub>x</sub>S glasses (lines drawn as a guide for the eye). b) <sup>IV</sup>B fraction as a function of B/Al ratio for all aluminoborosilicate glasses.

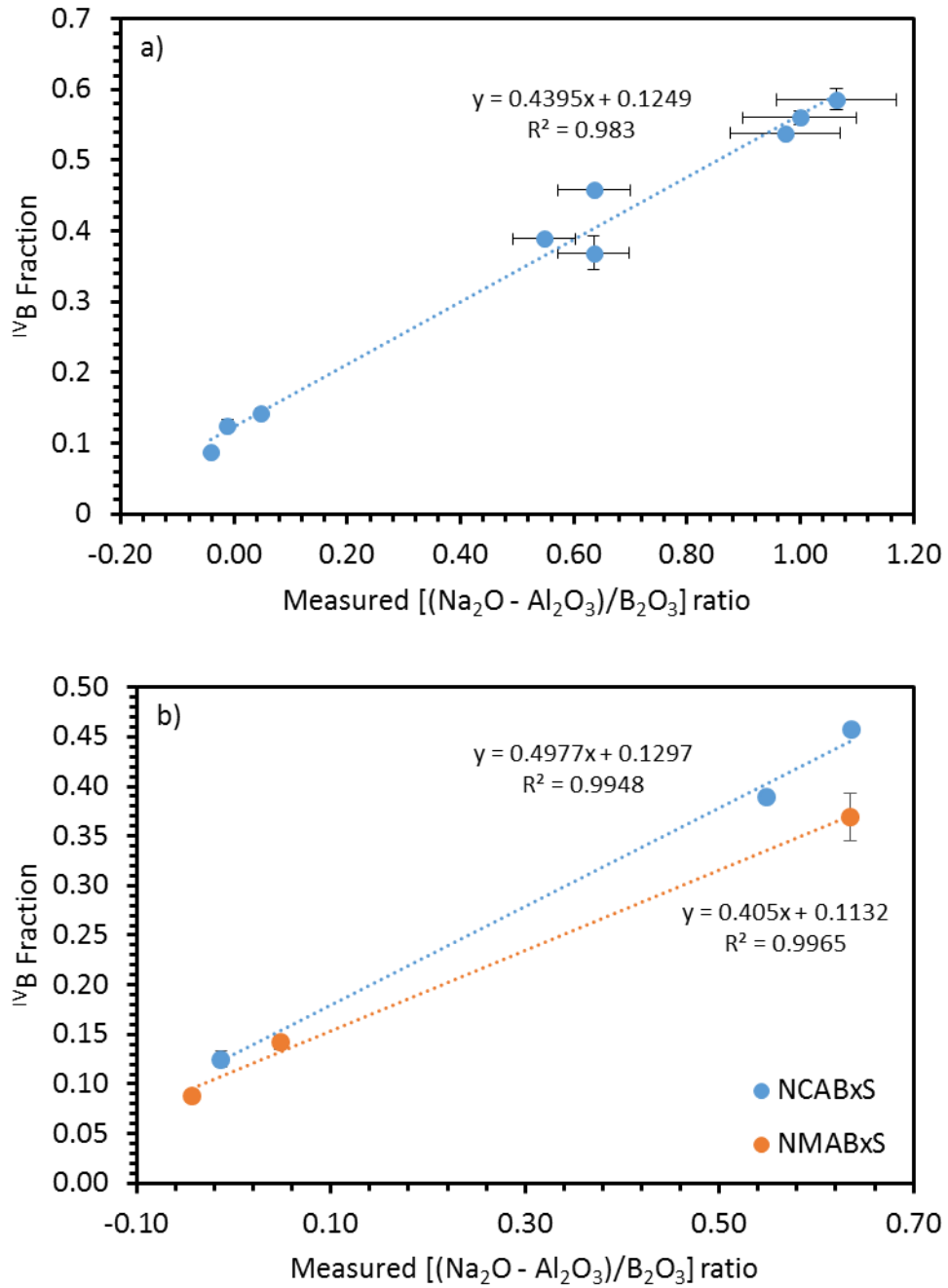


**Figure 4.14.**  $^{\text{IV}}\text{B}$  fraction as a function of available  $\text{Na}_2\text{O}$  for charge-compensation as a proportion of total  $\text{B}_2\text{O}_3$  content for: a) all B-containing glasses; b) the NCAB $x$ S and NMAB $x$ S glasses, including NC10BS and NM10BS.

### 4.3.2 $^{29}\text{Si}$ MAS-NMR

The  $^{29}\text{Si}$  MAS-NMR spectra for the  $\text{NC}_x\text{BS}$  and  $\text{NM}_x\text{BS}$  glasses showed that the fraction of symmetric  $\text{Q}_4$  species increased with increasing MO content. This can be seen in both the shift in the peak of the spectra, and in the deconvolution of the spectra. Figure 4.15 shows the relative frequency of the peaks of the  $\text{NC}_x\text{BS}$  and  $\text{NM}_x\text{BS}$  spectra as a function of the measured alkaline-earth oxide to sodium oxide ( $\text{MO}/\text{Na}_2\text{O}$ ) ratio, while Figure 4.16 shows the  $\text{Q}_4$  fraction, calculated from deconvolution of the spectra, as a function of  $\text{MO}/\text{Na}_2\text{O}$ . The increase in the fraction of symmetric  $\text{Q}_4$  species could be due to:

- A decrease in the number of NBOs in the network, leading to a decrease in  $\text{Q}_3$  species and a commensurate increase in  $\text{Q}_4$  species
- A decrease in the number of Si-O-B bonds, leading to a decrease in  $\text{Q}_4(\text{B})$  units and an increase in symmetric  $\text{Q}_4$  units

The former mechanism is unlikely, as the overall modifier content of the glasses did not vary significantly in these series, and the  $^{11}\text{B}$  MAS-NMR spectra do not suggest an increase in modifiers associated with those species. The more likely cause of the increase in symmetric  $\text{Q}_4$  species is a decrease in the fraction of  $\text{Q}_4(\text{B})$  species. As described in Section 4.3.1, the  $^{11}\text{B}$  MAS-NMR spectra for the  $\text{NC}_x\text{BS}$  and  $\text{NM}_x\text{BS}$  glasses showed a decrease in the fraction of  $^{\text{IV}}\text{B}$  units and an increase in the fraction of  $^{\text{III}}\text{B}$  units.  $^{\text{III}}\text{B}$  units can only bond to three other units, whereas  $^{\text{IV}}\text{B}$  units can bond to four. Thus, as the fraction of  $^{\text{IV}}\text{B}$  units decreases, there are a lower overall number of potential Si-O-B bonds, and so the proportion of  $\text{Q}_4(\text{B})$  units decreases.

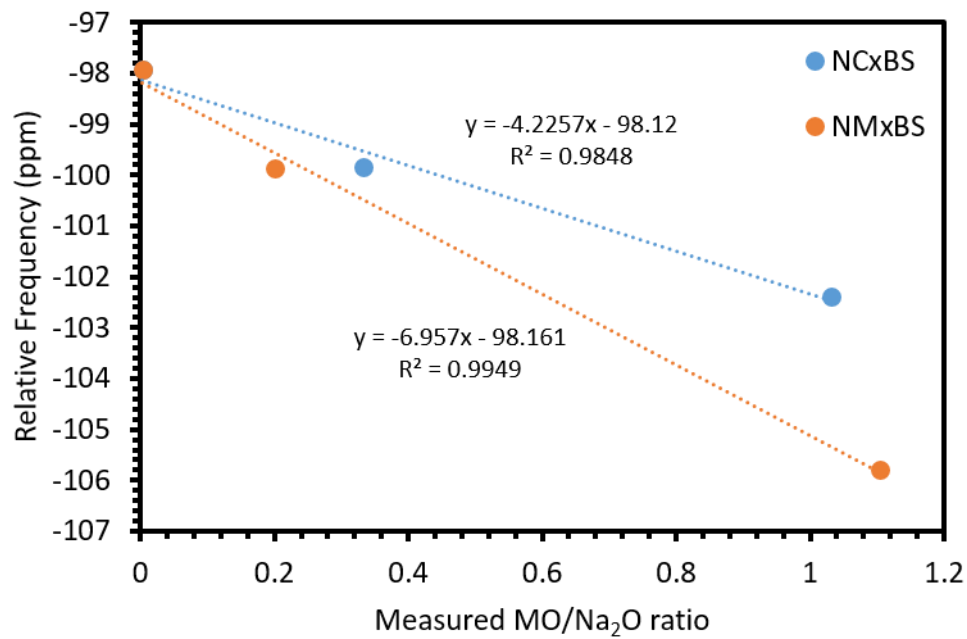


**Figure 4.15.** Relative frequency of spectra peaks as a function of measured MO/Na<sub>2</sub>O ratio for the NCxBS and NMxBS glasses.

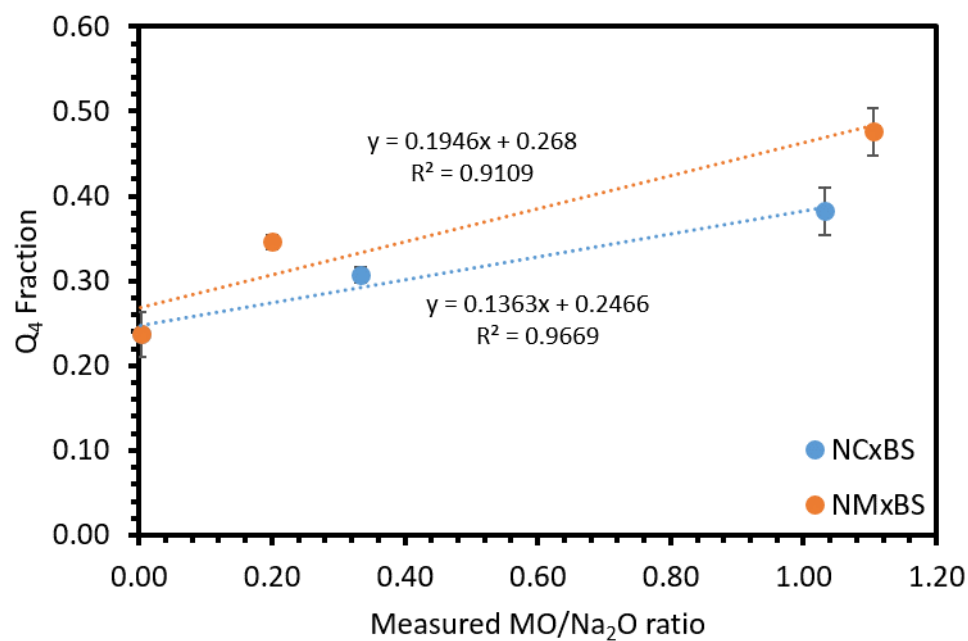


**Figure 4.16.** Q<sub>4</sub> fraction as a function of measured MO/Na<sub>2</sub>O ratio for the NCxBS and NMxBS glasses.

For the variation in peak shift with MO/Na<sub>2</sub>O ratio, the effect of adding MgO was greater than the effect of adding CaO. This trend was also seen in the Q<sub>4</sub> fraction, with addition of MgO leading to greater increases in Q<sub>4</sub> fraction than the additions of CaO. This suggests that the mechanism of Q<sub>4</sub> increase described above might be correct, as the addition of MgO also had a greater effect than the addition of CaO on the decrease in the proportion of <sup>IV</sup>B units in the glass, possibly due to it behaving as an intermediate oxide, with some network-forming capabilities.

Figure 4.17 shows the relative frequency of the spectra peaks as a function of B/Al ratio for the NCAB<sub>x</sub>S and NMAB<sub>x</sub>S series. The relative frequency of the spectra peaks shifted to more negative values with increasing B/Al ratio for both the NCAB<sub>x</sub>S and NMAB<sub>x</sub>S glasses. This is likely to be due to

- formation of fewer Si-O-Al bonds due to the decrease in Al<sub>2</sub>O<sub>3</sub> content
- An increase in the proportion of symmetric Q<sub>4</sub> species over Q<sub>3</sub> and asymmetric Q<sub>4</sub>(X) species

The former causes a decrease in chemical shift as the Si-O-Al bond leads to the Si nuclei in silicate tetrahedra being more deshielded, and thus results in higher chemical shifts than would be the case for equivalent Si-O-Si or Si-O-B bonds [128]. Fewer Si-O-Al bonds would lead to contributions at lower chemical shifts. An increase in the proportion of symmetric Q<sub>4</sub> species is likely to be due to the fact that most of the B in these glasses (at least 60%, per Figure 4.13) was present in trigonal rather than tetrahedral coordination, compared to Al which was mostly present in tetrahedral coordination. This decrease in overall tetrahedral unit content leads to a decrease in the number of potential Si – O – X bonds (X = B, Al), as trigonal <sup>III</sup>B units can only bond to three other units, whereas <sup>IV</sup>B and <sup>IV</sup>Al can bond to four. Thus, the replacement of Al<sub>2</sub>O<sub>3</sub> by B<sub>2</sub>O<sub>3</sub> leads to a decrease in the total number of Q<sub>4</sub>(X) units and an increase in symmetric Q<sub>4</sub>.

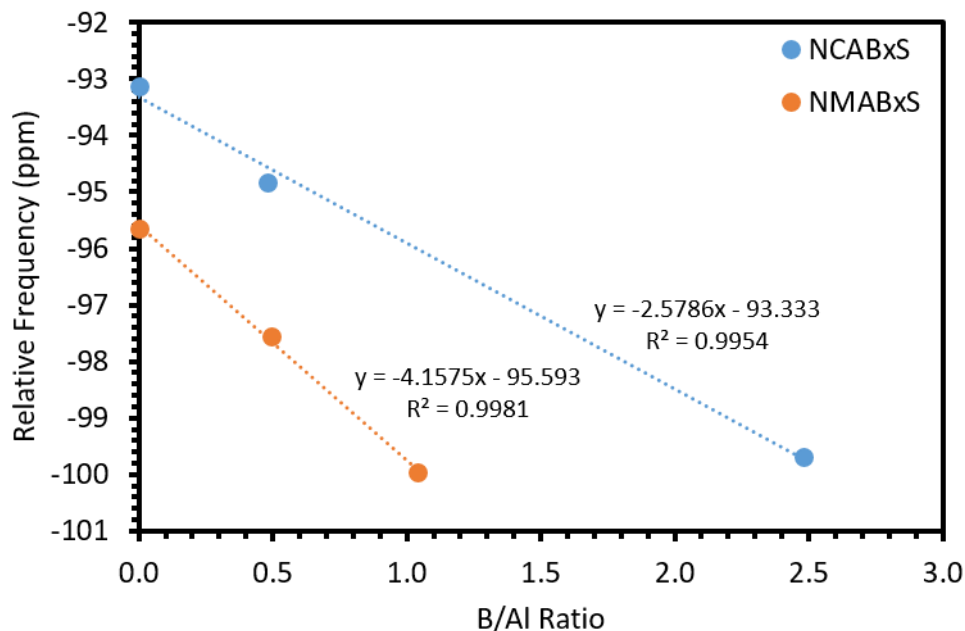


**Figure 4.17.** Relative frequency of spectra peaks as a function of B/Al ratio for the NCAB<sub>x</sub>S and NMAB<sub>x</sub>S glasses.

### 4.3.3 <sup>27</sup>Al MAS-NMR

It was difficult to extract significant structural data from the <sup>27</sup>Al MAS-NMR spectra due to the problems with fitting. However, it appears from both the 1D MAS-NMR and 3QMAS-NMR that Al in the NCAB<sub>x</sub>S and NMAB<sub>x</sub>S glasses was only present as tetrahedral <sup>IV</sup>Al units. This suggests that the modifier cations in the glasses, particularly Na<sup>+</sup>, were preferentially involved in charge-compensation for <sup>IV</sup>Al units, rather than in charge-compensation for <sup>IV</sup>B units or non-bridging oxygen (NBO) formation on SiO<sub>4</sub> tetrahedra.

The 3QMAS-NMR spectrum for NCAB<sub>0</sub>S in Figure 4.12 suggests the presence of 3-4 different <sup>IV</sup>Al environments. These are likely to be due to the number of other SiO<sub>4</sub> and AlO<sub>4</sub> units the <sup>IV</sup>Al tetrahedron is bonded to [132]. The large contribution is likely to be due to <sup>IV</sup>Al units bonded to four SiO<sub>4</sub> tetrahedra, denoted <sup>IV</sup>Al(4Si), due to the preference of <sup>IV</sup>Al units to avoid <sup>IV</sup>Al – O – <sup>IV</sup>Al bonds (known as the Loewenstein Avoidance Principle [133]). The two smaller peaks probably correspond to: <sup>IV</sup>Al(3Si), at 34 – 26 ppm F1, 80 – 60 ppm F2; and <sup>IV</sup>Al(2Si), at 29 – 23 ppm F1, 85 – 70 ppm F2. The former consists of an AlO<sub>4</sub> tetrahedron connected to three SiO<sub>4</sub> units and one AlO<sub>4</sub> while the latter consists of an AlO<sub>4</sub> tetrahedron linked to two SiO<sub>4</sub> and two AlO<sub>4</sub> units. The cause of the shoulder in the primary <sup>IV</sup>Al(4Si) contribution at around 49 ppm F1, 55 ppm F2 is not known, and further experiments would be required to

ascertain this. As further 3QMAS-NMR experiments were not able to be carried out due to equipment issues, it is not known how the proportions of these units vary with B/Al and between the NCAB<sub>x</sub>S and NMAB<sub>x</sub>S glasses.

#### 4.4 Summary

MAS-NMR spectroscopy was performed on 3- to 5-oxide simple glasses to ascertain the effect of varying Na/Ca, Na/Mg and Al/B ratios on the structure of alkali-alkaline earth borosilicate and aluminoborosilicate glasses. The key findings of these experiments are:

- The addition of alkaline earth oxides (CaO and MgO) to sodium borosilicate glasses leads to an increase in the symmetric Q<sub>4</sub> content of the silicate network, due to a decrease in <sup>IV</sup>B content likely caused by the difficulty in CaO and MgO being able to simultaneously charge-compensate two <sup>IV</sup>B tetrahedra.
- The effect of alkaline earth oxide addition is greater for MgO than for CaO, likely due to MgO behaving as an intermediate oxide rather than solely as a modifier.
- Increasing the ratio of B/Al in alkali-alkaline earth aluminoborosilicates leads to an increase in <sup>IV</sup>B content, which is likely due to the competition for Na<sup>+</sup> cations to charge-compensate <sup>IV</sup>B and <sup>IV</sup>Al units.
- Higher values of B/Al lead to the formation of fewer Si-O-X bonds due to the lower proportion of B that is in tetrahedral coordination compared to Al.
- Al was found to be in tetrahedral coordination, independent of the ratio of B/Al, or the nature of the alkaline-earth present, in the glass

In order to advance the knowledge of these structural effects, MAS-NMR experiments at higher magnetic field strengths would be vital. Increasing the field strength from 9.4 T used in these experiments to 18.8 T would significantly increase the resolution of the spectra and allow easier identification of contributions from different isotopic environments, e.g. resolving <sup>[III]</sup>B and <sup>[IV]</sup>B contributions into separate, identifiable peaks. However, multiple quantum MAS-NMR experiments would also be required to fully investigate the contributions from different species, such as <sup>IV</sup>B(3B, 1Si) and asymmetric (<sup>III</sup>B(O<sub>1/2</sub>)<sub>2</sub>(O<sup>-</sup>)). Further <sup>27</sup>Al 3QMAS-NMR experiments would enable the variation of the proportions of different <sup>IV</sup>Al environments with B/Al and alkaline earth oxide to be analysed. Furthermore, <sup>25</sup>Mg and <sup>43</sup>Ca MAS-NMR would elucidate

the isotopic environment of the alkaline earth cations, providing further evidence of the structure of these glasses. These experiments were not carried out in this work as they require access to high magnetic field strength spectrometers, which was not possible within the timeframe of this investigation.



## 5. Effect of Varying Glass Composition on Dissolution at High-pH

### 5.1 Introduction

Dissolution experiments utilising the Product Consistency Test B (PCT-B) protocol were carried out on the ‘Simple Glasses’ that were detailed in Section 3.1.1 and studied by MAS-NMR in Chapter 4.

### 5.2 Experimental Procedure

The glasses were synthesised or obtained as described in Section 3.1.1, and their compositions are detailed in Table 4.1 in Chapter 4. From these glasses, powdered samples were produced, as detailed in Section 3.1.2, and used in PCT-B experiments which were set up as described in Section 3.2.1. Briefly, experiments were carried out for a period of 112 days, in either a saturated  $\text{Ca}(\text{OH})_2$  or a  $\text{KOH}/\text{KCl}$  solution, at a S/V ratio of  $1200 \text{ m}^{-1}$ , at  $50 \text{ }^\circ\text{C}$ , and with sampling points at 1, 3, 7, 14, 28, 56 and 112 days. ICP-OES analysis was used to determine the concentrations of all elements in solution (Data shown in Appendix C). These concentration data were used to calculate normalised mass losses and mass loss rates as described in Section 3.3. All ‘initial’ and ‘residual’ rates are apparent, rather than true rates, as discussed in Section 3.3. Once the experiments were completed, the altered powders were analysed by SEM-EDS and XRD.

As discussed in Section 4.1, NCAB5S has a significantly lower CaO content than targeted (5.31 mol.% compared to a target of 10.00 mol.%). As such, the data produced from this glass are of limited usefulness in comparing to the other NCAB $x$ S glasses. For the sake of completeness, the results for NCAB5S have been included in this chapter, but NCAB5S has been omitted from the discussion of the results.

### 5.3 Elemental Leaching Results

#### 5.3.1 Leaching in Calcium Hydroxide

The simple glasses were leached in a saturated  $\text{Ca}(\text{OH})_2$  solution, as this was taken to be a simplified representative for a solution that has come into contact with a portland cement (PC) based mortar or concrete, which contain significant amounts of portlandite ( $\text{Ca}(\text{OH})_2$ ) (see Chapter 1).

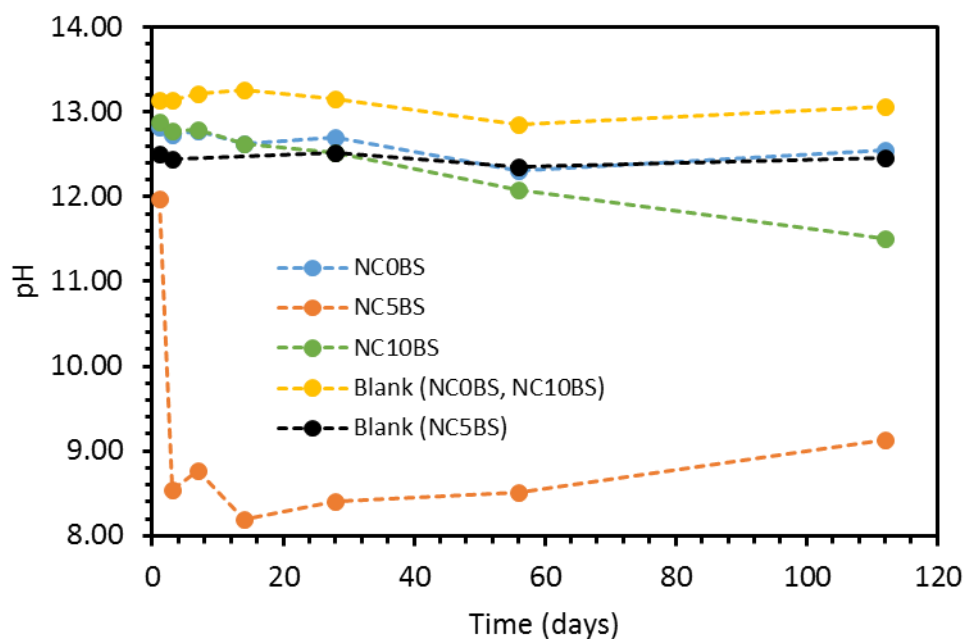
### 5.3.1.1 NCxBS Glasses

Figure 5.1 shows the pH of the leachate for the NCxBS tests. Generally, the leachate pH of the blanks remained consistent across the experiments. The pH of the NC0BS glass decreased slightly from pH 12.8, to pH 12.5, whereas that of the NC10BS leachate dropped from an initial value of ~12.8 to 11.5. The values for the NC5BS leachate dropped sharply from 11.98 at day 1 to 8.54 after day 3 and remained between 8 and 9 for the rest of the experiment. However, these pH values are likely due to the carbonation of the samples. The pH for these samples was not measured immediately, and the samples had to be removed from the glovebox, with its N<sub>2</sub> atmosphere, into a standard air atmosphere before they could be measured. This probably led to the carbonation of these samples due to the ingress of CO<sub>2</sub> from the air into the test tubes. This is true for a number of other samples. This was also observed for other samples. Figure 5.2 shows the normalised mass loss of boron, NL(B), data for the NCxBS glasses after undergoing 112-day PCT-B experiments in a saturated Ca(OH)<sub>2</sub> solution, at 50 °C with an initial S/V of 1200 m<sup>-1</sup>. Initial (R<sub>0</sub>(B)) and residual (R<sub>r</sub>(B)) normalised mass loss rates calculated from these data are shown in Table 5.1. Each of the three glasses had a high initial rate of boron loss, at  $0.100 \pm 0.005$ ,  $0.151 \pm 0.008$  and  $0.125 \pm 0.006$  g m<sup>-2</sup> d<sup>-1</sup> for NC0BS, NC5BS and NC10BS, respectively. This was followed by a significant decrease in the rate between 7 and 56 days. After 112 days, NC10BS had the highest NL(B), followed by NC0BS and NC5BS; the values were  $1.03 \pm 0.21$ ,  $0.66 \pm 0.12$  and  $0.51 \pm 0.09$  g m<sup>-2</sup>, respectively. The residual mass loss rates were significantly lower than the initial rates, at  $(2.0 \pm 1.0) \times 10^{-4}$ ,  $(1.9 \pm 0.1) \times 10^{-3}$  and  $(3.7 \pm 0.2) \times 10^{-3}$  g m<sup>-2</sup> d<sup>-1</sup> for NC0BS, NC5BS and NC10BS. Boron is generally considered to be a good tracer of the dissolution rate of glasses as it is not thought to take part in the formation of an alteration layer, or in the precipitation of secondary crystalline phases. Figure 5.3 shows the NL(Si) data for the same glasses. Unlike B, Si is an integral part of the formation of alteration layers, and is also involved in the precipitation of secondary crystalline phases (see Section 5.4). Thus, the measured concentration of Si in solution is no indicator of the total release of Si from the glass. The silicon release for all three glasses was very low (< 0.04 g m<sup>-2</sup>), suggesting that a significant proportion of the silicon leached from the glass remained in the alteration layer.

The normalised mass loss of Na for these glasses is shown in Figure 5.4. The data

closely followed the trends of the NL(B) data, with each of the glasses undergoing a significant reduction in mass loss rate after 7 days, from initial rates of  $0.389 \pm 0.019$ ,  $0.175 \pm 0.009$  and  $0.499 \pm 0.024 \text{ g m}^{-2} \text{ d}^{-1}$  for NC0BS, NC5BS and NC10BS, respectively. As with the NL(B) data, NC10BS had the highest total mass loss, followed by NC0BS and NC5BS. The values of NL(Na) after 112 days were  $2.80 \pm 0.55$ ,  $1.54 \pm 0.27$  and  $0.69 \pm 0.13 \text{ g m}^{-2}$ , for NC10BS, NC0BS and NC5BS, respectively. NC10BS also had the highest residual mass loss rate,  $R_r(\text{Na})$ , at  $(5.6 \pm 0.3) \times 10^{-3} \text{ g m}^{-2} \text{ d}^{-1}$ , compared to  $(-2.5 \pm 0.1) \times 10^{-3}$  and  $(3.7 \pm 0.2) \times 10^{-3} \text{ g m}^{-2} \text{ d}^{-1}$  for NC0BS and NC5BS, respectively. It is unlikely that the negative rate calculated for NC0BS is significant as it is the result of the final data point. It is possible that this is an anomalous point, although further data points would be required to prove this.

It was not possible to measure NL(Ca) values for these experiments, as the Ca-rich leachant obscured any change in Ca concentration in solution caused by leaching.



**Figure 5.1.** pH values for  $\text{Ca}(\text{OH})_2$  PCT-B experiments on  $\text{NC}_x\text{BS}$  glasses.

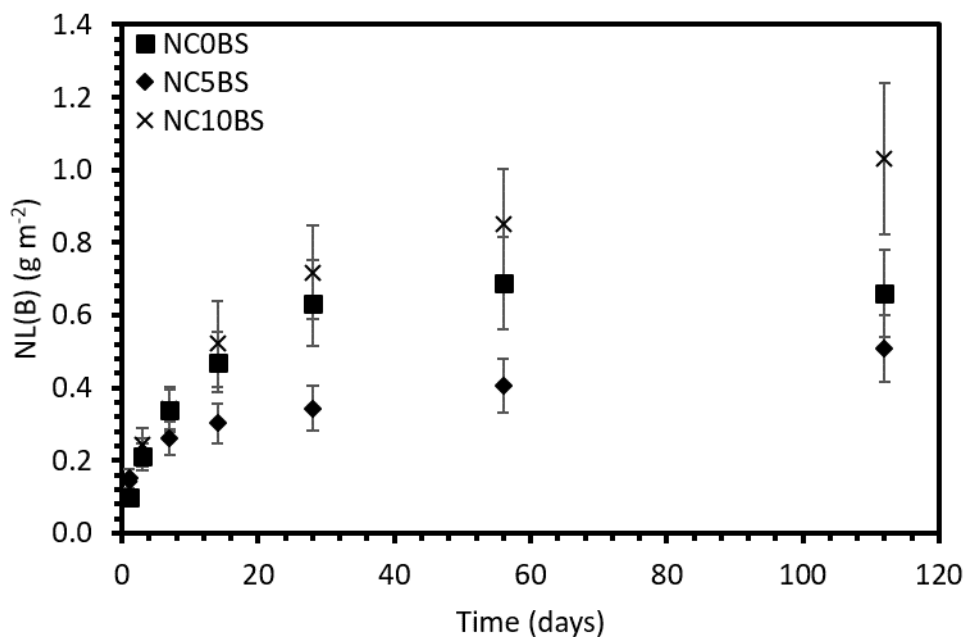


**Figure 5.2.** NL(B) values for Ca(OH)<sub>2</sub> PCT-B experiments on NC<sub>x</sub>BS glasses.

**Table 5.1.** Initial ( $R_0(i)$ ) and residual ( $R_r(i)$ ) normalised mass loss rates for B and Na for the NC<sub>x</sub>BS glasses in Ca(OH)<sub>2</sub>.

Rate (g m <sup>-2</sup> d <sup>-1</sup> )	NC0BS	NC5BS	NC10BS
$R_0(B)$	$0.100 \pm 0.005$	$0.151 \pm 0.008$	$0.125 \pm 0.006$
$R_r(B)$	$(2.0 \pm 1.0) \times 10^{-4}$	$(1.9 \pm 0.1) \times 10^{-3}$	$(3.7 \pm 0.2) \times 10^{-3}$
$R_0(Na)$	$0.389 \pm 0.019$	$0.175 \pm 0.009$	$0.499 \pm 0.024$
$R_r(Na)$	$(-2.5 \pm 0.1) \times 10^{-3}$	$(3.7 \pm 0.2) \times 10^{-3}$	$(5.6 \pm 0.3) \times 10^{-3}$

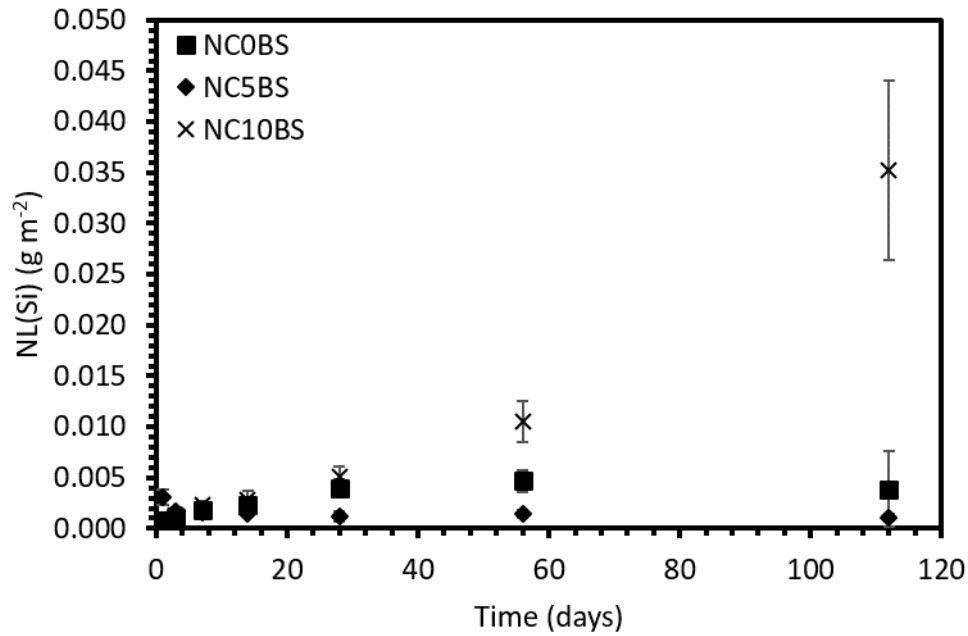


**Figure 5.3.** NL(Si) values for Ca(OH)<sub>2</sub> PCT-B experiments on NC<sub>x</sub>BS glasses.

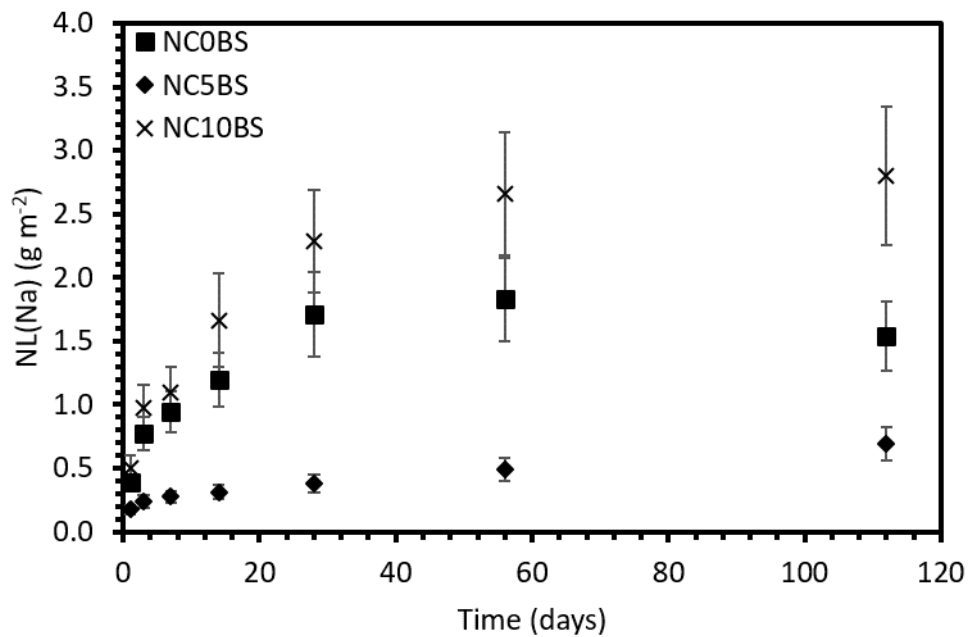


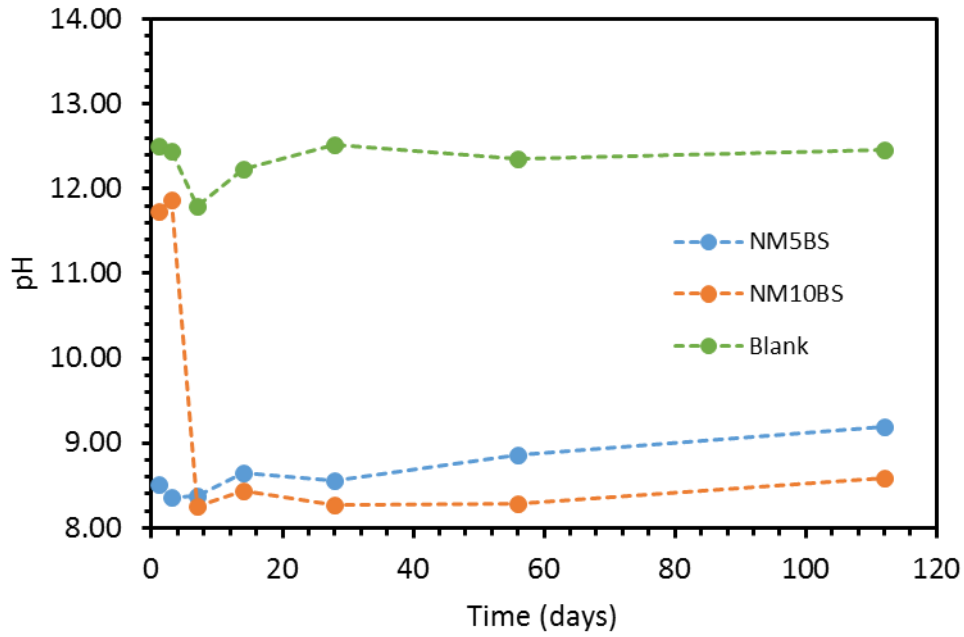
**Figure 5.4.** NL(Na) values for Ca(OH)<sub>2</sub> PCT-B experiments on NC<sub>x</sub>BS glasses.

### 5.3.1.2 NM<sub>x</sub>BS Glasses

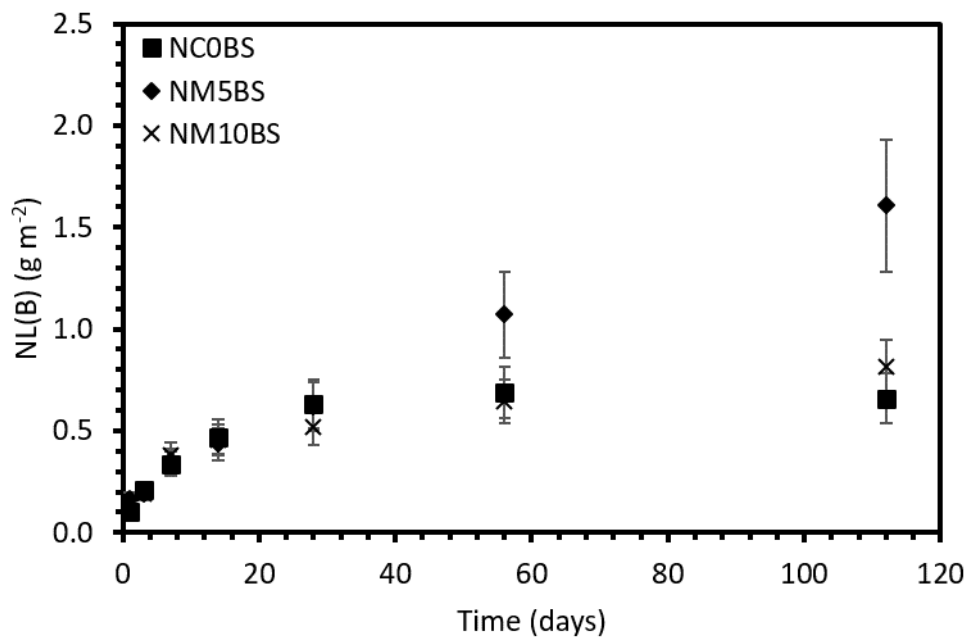
Figure 5.5 shows the pH of the NM<sub>x</sub>BS experiments. The pH of the blanks remained fairly consistent at ~12.5, except for a value of ~11.79 after 7 days, which is assumed to be anomalous. However, the pH values from the NM<sub>x</sub>BS samples were found to be very low (< 9), which is likely due to post-sampling carbonation (see Section 5.3.1.1).

Figure 5.6 shows the NL(B) values for the NM<sub>x</sub>BS glasses. Initial and residual mass loss rates are shown in Table 5.2. As with the NC<sub>x</sub>BS glasses, each of the glasses had a high initial rate of boron loss;  $0.100 \pm 0.005$ ,  $0.165 \pm 0.008$  and  $0.153 \pm 0.008$  g m<sup>-2</sup> d<sup>-1</sup> for NC0BS, NM5BS and NM10BS, respectively, which was followed by a decrease in the rate from 3 – 7 days onwards. This rate reduction was significantly more pronounced for NM10BS and NC0BS, compared to NM5BS; the rate decreased by a factor of ~45 to  $(3.4 \pm 0.2) \times 10^{-3}$  g m<sup>-2</sup> d<sup>-1</sup> for NM10BS, and the rate for NC0BS decreased by a factor of ~500 to  $(2.0 \pm 1.0) \times 10^{-4}$  g m<sup>-2</sup> d<sup>-1</sup>, whereas the rate for NM5BS only decreased by a factor of ~15 to  $0.011 \pm 0.001$  g m<sup>-2</sup> d<sup>-1</sup>. This resulted in final values of NL(B) of  $1.61 \pm 0.32$ ,  $0.81 \pm 0.14$  and  $0.66 \pm 0.12$  g m<sup>-2</sup> for NM5BS, NM10BS and NC0BS, respectively. The values of NL(B) for NM10BS and NC0BS were similar throughout the experiments. Figure 5.7 displays the NL(Si) values for the glasses. The data were 2-3 orders of magnitude lower than the NL(B) values, remaining below 0.01 g m<sup>-2</sup> for all timepoints, which suggests that silicon was retained in the alteration phases. The formation of alteration phases was investigated through SEM-EDS (Section 5.4).

The NL(Na) values for the glasses are shown in Figure 5.8, with initial and residual rates shown in Table 5.2. Up to 56 days, NC0BS had the highest NL(Na), although this was followed by a significant reduction from  $1.83 \pm 0.33$  g m<sup>-2</sup> to  $1.54 \pm 0.27$  g m<sup>-2</sup> at 112 days. This is in agreement with its high initial rate of  $0.389 \pm 0.019$  g m<sup>-2</sup> d<sup>-1</sup>, compared to  $0.206 \pm 0.010$  and  $0.198 \pm 0.010$  g m<sup>-2</sup> d<sup>-1</sup> for NM5BS and NM10BS, respectively. NM5BS and NM10BS had similar values of NL(Na) up to 28 days, but after this NM5BS experienced a significant increase in sodium mass loss, leading to a final value of  $1.91 \pm 0.38$  g m<sup>-2</sup>, compared to a value of  $1.04 \pm 0.18$  g m<sup>-2</sup> for NM10BS, and a residual rate of  $0.015 \pm 0.001$  g m<sup>-2</sup> d<sup>-1</sup> for NM5BS compared to  $(6.1 \pm 0.3) \times 10^{-3}$  g m<sup>-2</sup> d<sup>-1</sup> for NM10BS. Figure 5.9 shows the values of NL(Mg) for the Mg-containing glasses. These values were very low – less than 0.01 g m<sup>-2</sup> across the time period of the experiments – with large uncertainties. This suggests that the Mg was involved in the formation of alteration phases, similar to the behaviour of silicon (see Section 5.4).



**Figure 5.5.** pH values for  $\text{Ca}(\text{OH})_2$  PCT-B experiments on  $\text{NM}_x\text{BS}$  glasses.



**Figure 5.6.**  $\text{NL}(\text{B})$  values for  $\text{NM}_x\text{BS}$  from PCT-B experiments in  $\text{Ca}(\text{OH})_2$  solution.

**Table 5.2.** Initial ( $R_0(i)$ ) and residual ( $R_r(i)$ ) normalised mass loss rates for B and Na for the  $NM_xBS$  glasses in  $Ca(OH)_2$ .

Rate ( $g\ m^{-2}\ d^{-1}$ )	NC0BS	NM5BS	NM10BS
$R_0(B)$	$0.100 \pm 0.005$	$0.165 \pm 0.008$	$0.153 \pm 0.008$
$R_r(B)$	$(2.0 \pm 1.0) \times 10^{-4}$	$0.011 \pm 0.001$	$(3.4 \pm 0.2) \times 10^{-3}$
$R_0(Na)$	$0.389 \pm 0.019$	$0.206 \pm 0.010$	$0.198 \pm 0.010$
$R_r(Na)$	$(-2.5 \pm 0.1) \times 10^{-3}$	$0.015 \pm 0.001$	$(6.1 \pm 0.3) \times 10^{-3}$

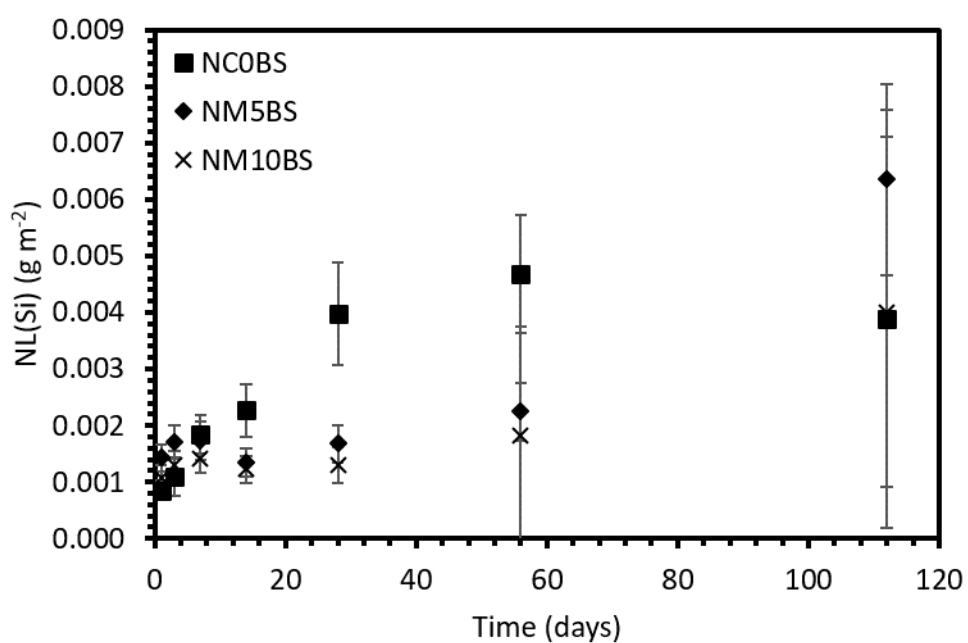


**Figure 5.7.**  $NL(Si)$  values for  $NM_xBS$  from PCT-B experiments in  $Ca(OH)_2$  solution.

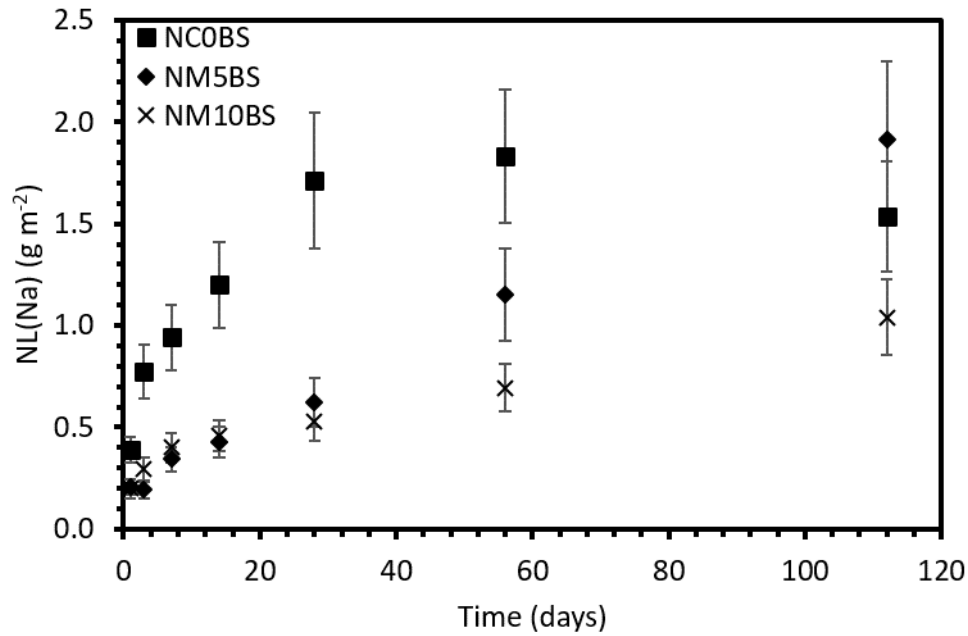


**Figure 5.8.** NL(Na) values for NM<sub>x</sub>BS from PCT-B experiments in  $\text{Ca}(\text{OH})_2$  solution.

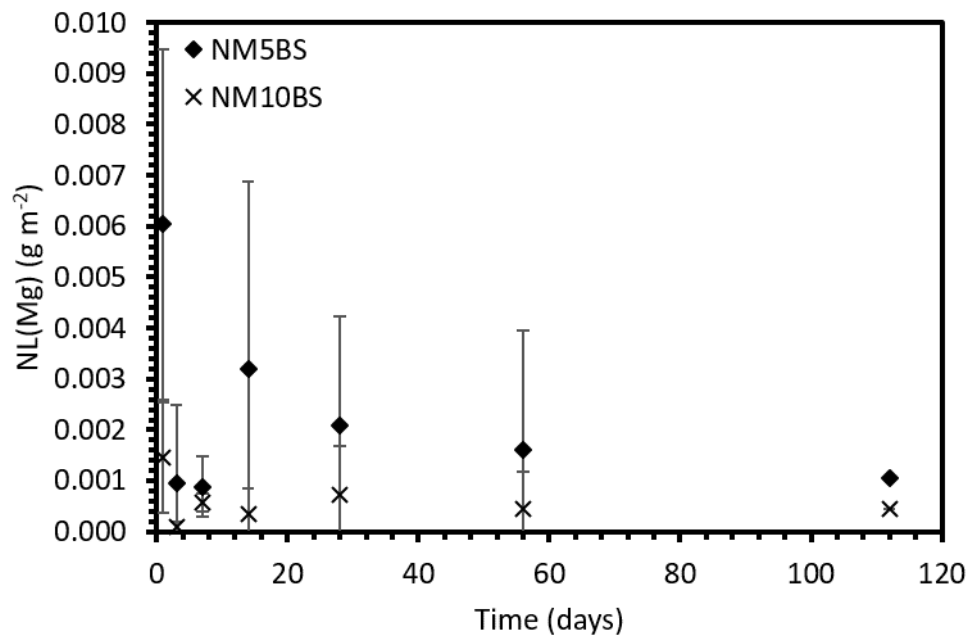


**Figure 5.9.** NL(Mg) values for NM<sub>x</sub>BS from PCT-B experiments in  $\text{Ca}(\text{OH})_2$  solution.

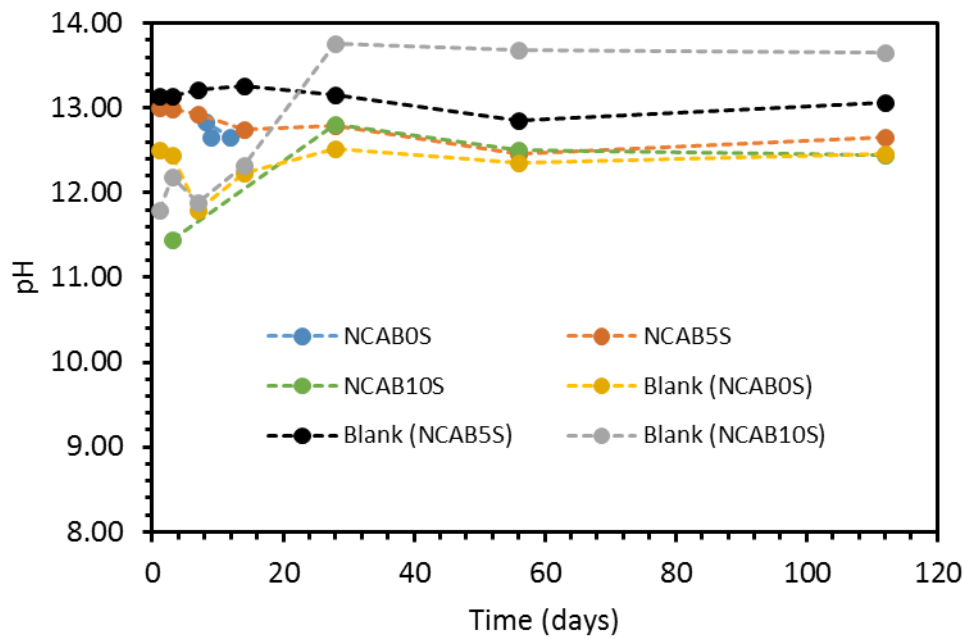
### 5.3.1.3 NCAB<sub>x</sub>S Glasses

Figure 5.10 shows the pH values for the leachates in the NCAB<sub>x</sub>S experiments. The blanks for the NCAB0S and NCAB5S samples had consistent pH values, but the

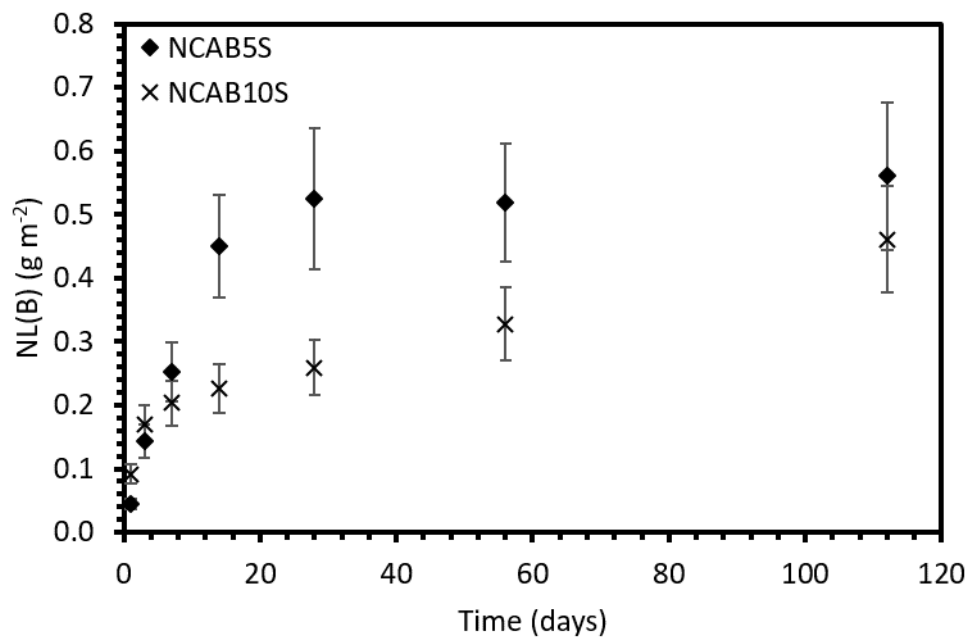
values for the NCAB10S blank started at  $\sim 12$  before increasing to  $\sim 13.7$ . The reason for this discrepancy is unknown. The pH values for the NCAB $x$ S leachates remained consistently high throughout the experiments. Figure 5.11 shows the NL(B) values for the NCAB $x$ S glasses excluding NCAB0S, which contains no boron, with  $R_0(\text{B})$  and  $R_r(\text{B})$  values shown in Table 5.3. NCAB10S had higher values of NL(B) after 1 and 3 days, with a higher value of  $R_0(\text{B})$  of  $0.092 \pm 0.005 \text{ g m}^{-2} \text{ d}^{-1}$ , compared to  $0.048 \pm 0.002 \text{ g m}^{-2} \text{ d}^{-1}$  for NCAB5S. From 7 days onwards, NCAB5S had the greater mass loss of boron. The final values of NL(B) were  $0.56 \pm 0.12$  and  $0.46 \pm 0.08 \text{ g m}^{-2}$  for NCAB5S and NCAB10S, respectively, with respective residual B mass loss rates of  $(5.0 \pm 0.3) \times 10^{-4}$  and  $(2.4 \pm 0.1) \times 10^{-3} \text{ g m}^{-2} \text{ d}^{-1}$ . The normalised mass loss of silicon for these glasses is shown in Figure 5.12. As with the NC $x$ BS and NM $x$ BS series, NL(Si) was significantly lower than that of boron; less than  $0.008 \text{ g m}^{-2}$  over the duration of the experiments. Each of the three glasses appeared to have a different Si mass loss profile; NCAB0S had a steadily descending curve, NCAB5S appeared to have an initial incubation period followed by a steady increase, and NCAB10S had the conventional shape seen in most other samples. However, this pattern was not seen in any other data, and so further work would be required to ascertain whether this was an anomaly or due to the properties of the three glasses.

Figure 5.13 displays the NL(Na) for the NCAB $x$ S glasses. NCAB5S had the highest mass loss of sodium across all sampling times, whereas NCAB0S and NCAB10S had similar, significantly lower, mass losses, with initial mass loss rates of  $0.185 \pm 0.009$ ,  $0.092 \pm 0.005$  and  $0.097 \pm 0.005 \text{ g m}^{-2} \text{ d}^{-1}$  for NCAB5S, NCAB0S and NCAB10S, respectively. The final values for each of the three glasses were  $0.53 \pm 0.12$ ,  $1.51 \pm 0.30$  and  $0.53 \pm 0.10 \text{ g m}^{-2}$  for NCAB0S, NCAB5S and NCAB10S, with residual rates of  $(1.2 \pm 0.1) \times 10^{-3}$ ,  $(3.0 \pm 0.2) \times 10^{-3}$  and  $(-1.7 \pm 0.1) \times 10^{-3} \text{ g m}^{-2} \text{ d}^{-1}$ . It is unlikely that the negative residual rate for NCAB10S is significant, as it is possible to obtain positive residual rates from the data, within error. The normalised mass loss of aluminium for the glasses is shown in Figure 5.14. The  $R_0(\text{Al})$  values for NCAB0S, NCAB5S and NCAB10S were  $0.035 \pm 0.002$ ,  $0.085 \pm 0.004$  and  $0.002 \pm 0.0001 \text{ g m}^{-2} \text{ d}^{-1}$ , respectively. NCAB5S had the highest NL(Al) across each time point, followed by NCAB0S and NCAB10S, with final values of  $0.44 \pm 0.10$ ,  $0.13 \pm 0.02$  and  $0.008 \pm 0.03 \text{ g m}^{-2}$ , respectively, and  $R_r(\text{Al})$  values of  $(1.0 \pm 0.1) \times 10^{-4}$ ,  $(-8.0 \pm 0.4) \times 10^{-4}$  and  $(4.0 \pm 0.2) \times 10^{-5}$ , respectively. Again, the negative residual rate calculated for NCAB5S may or may not be significant as it is possible to calculate a

positive value, within error.



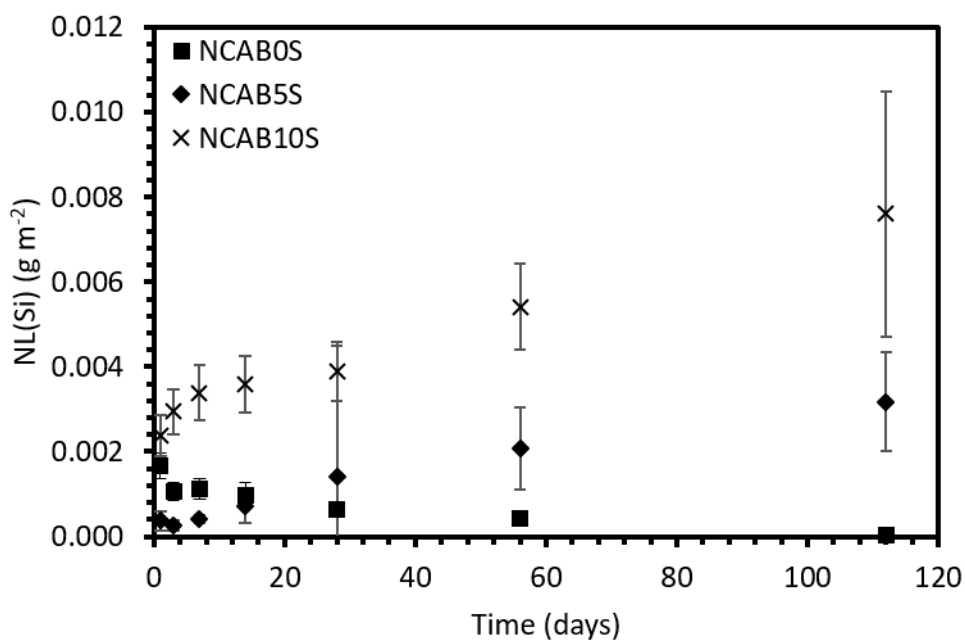
**Figure 5.10.** pH values for  $\text{Ca}(\text{OH})_2$  PCT-B experiments on  $\text{NCAB}_x\text{S}$  glasses.



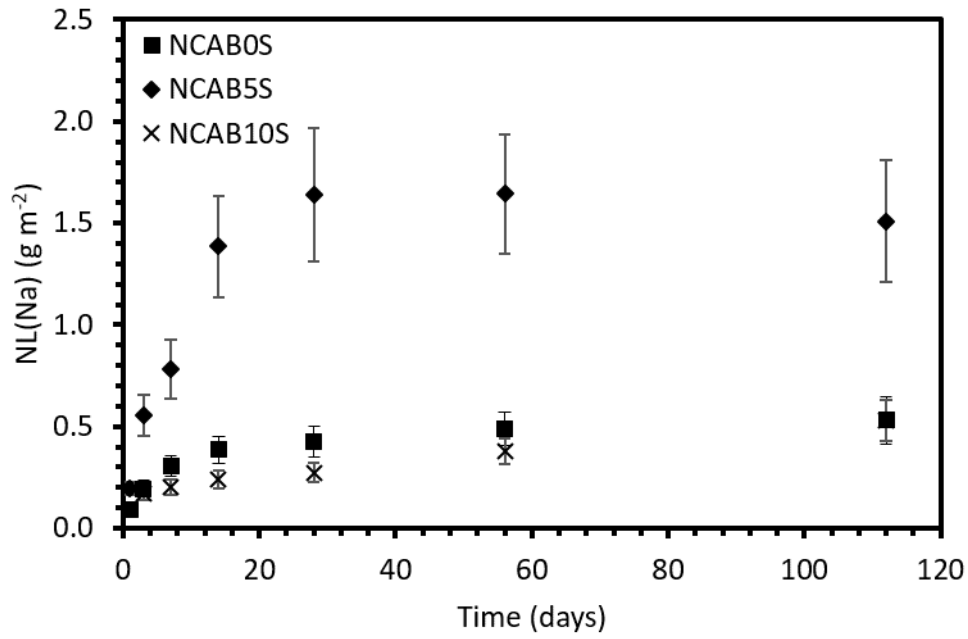
**Figure 5.11.**  $\text{NL}(\text{B})$  for  $\text{NCAB}_x\text{S}$  glasses for PCT-B experiments in  $\text{Ca}(\text{OH})_2$ .

**Table 5.3.** Initial ( $R_0(i)$ ) and residual ( $R_r(i)$ ) normalised mass loss rates for B, Na and Al for the NCAB $x$ S glasses in  $\text{Ca}(\text{OH})_2$ .

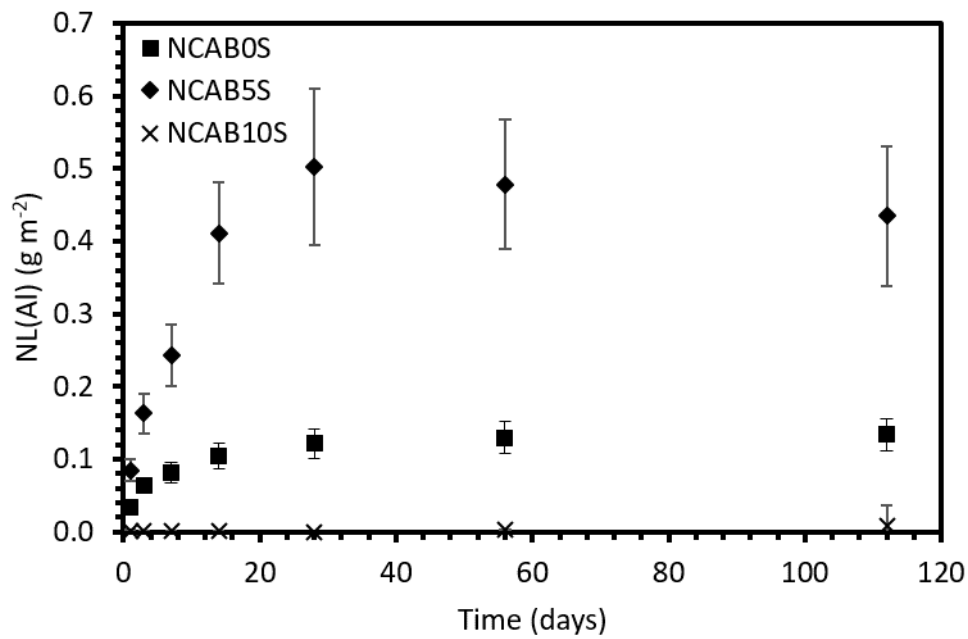
Rate ( $\text{g m}^{-2} \text{d}^{-1}$ )	NCAB0S	NCAB5S	NCAB10S
$R_0(\text{B})$	-	$0.092 \pm 0.005$	$0.048 \pm 0.002$
$R_r(\text{B})$	-	$(5.0 \pm 0.3) \times 10^{-4}$	$(2.4 \pm 0.1) \times 10^{-3}$
$R_0(\text{Na})$	$0.092 \pm 0.005$	$0.185 \pm 0.009$	$0.097 \pm 0.005$
$R_r(\text{Na})$	$(1.2 \pm 0.1) \times 10^{-3}$	$(3.0 \pm 0.2) \times 10^{-3}$	$(-1.7 \pm 0.1) \times 10^{-3}$
$R_0(\text{Al})$	$0.035 \pm 0.002$	$0.085 \pm 0.004$	$0.002 \pm 0.0001$
$R_r(\text{Al})$	$(1.0 \pm 0.1) \times 10^{-4}$	$(-8.0 \pm 0.4) \times 10^{-4}$	$(4.0 \pm 0.2) \times 10^{-5}$



**Figure 5.12.** NL(Si) for NCAB $x$ S glasses for PCT-B experiments in  $\text{Ca}(\text{OH})_2$ .



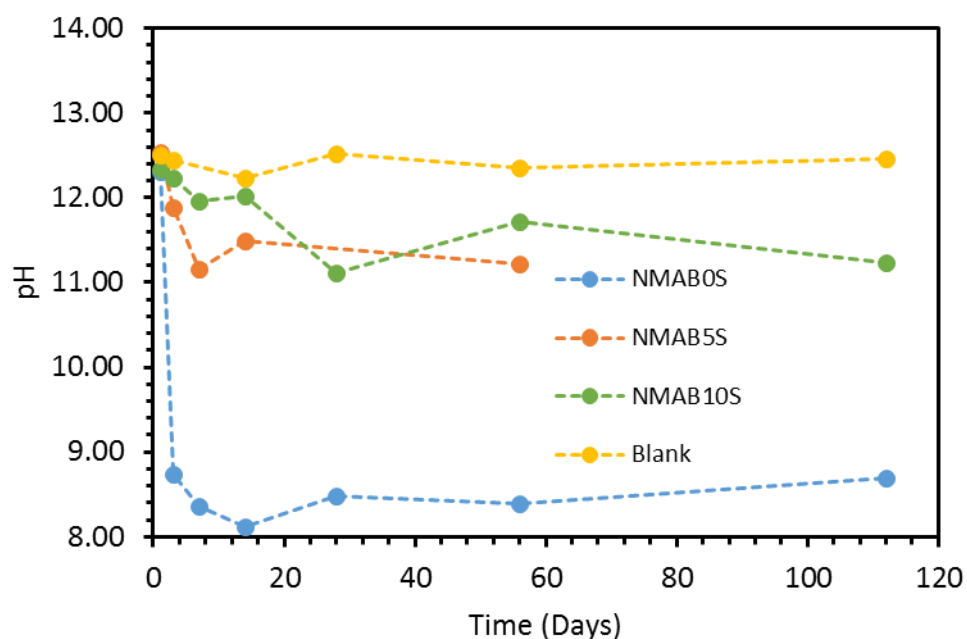
**Figure 5.13.** NL(Na) for NCAB<sub>x</sub>S glasses for PCT-B experiments in Ca(OH)<sub>2</sub>.



**Figure 5.14.** NL(Al) for NCAB<sub>x</sub>S glasses for PCT-B experiments in Ca(OH)<sub>2</sub>.

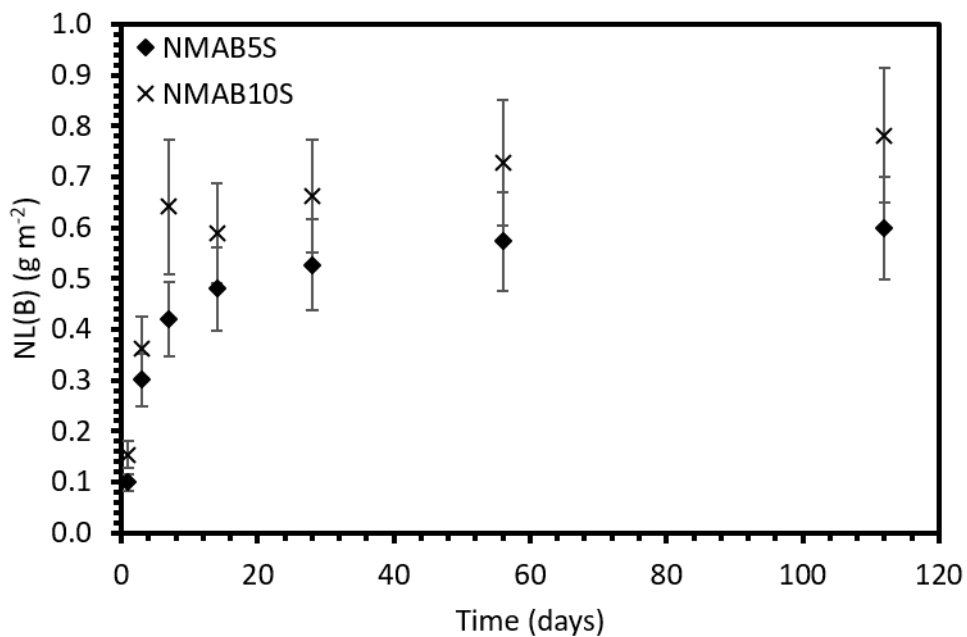
#### 5.3.1.4 NMAB<sub>x</sub>S Glasses

Figure 5.15 shows the pH values for the NMAB<sub>x</sub>S experiments. The blanks remained consistent at approximately pH 12.5. The NMAB5S and NMAB10S samples dropped from pH 12.5 at the beginning of the experiments to pH 11.22 for NMAB5S after 56 days (112 day datum not available) and to pH 11.24 for NMAB10S after 112 days. The pH of the NMAB0S samples dropped rapidly between 1 and 3 days, due to carbonation (see Section 5.3.1.1). The NL(B) data for the NMAB<sub>x</sub>S glasses, excluding NMAB0S, which contains no boron, are shown in Figure 5.16. Initial and residual mass loss rates are shown in Table 5.4. Both glasses followed the same trend as each of the other glass series, i.e. a high initial rate followed by a significant reduction of rate with time. The initial rates for NMAB5S and NMAB10S were  $0.100 \pm 0.005$  and  $0.154 \pm 0.008 \text{ g m}^{-2} \text{ d}^{-1}$ , respectively, whilst the respective residual rates were  $(8.0 \pm 0.4) \times 10^{-4}$  and  $(1.4 \pm 0.1) \times 10^{-3} \text{ g m}^{-2} \text{ d}^{-1}$ . NMAB10S had the highest NL(B) at each time point, with a value after 112 days of  $0.78 \pm 0.13 \text{ g m}^{-2}$ , compared  $0.60 \pm 0.10 \text{ g m}^{-2}$  for NMAB5S at the same time-point. Figure 5.17 shows the NL(Si) data for the NMAB<sub>x</sub>S series. The values for each of the glasses remained below  $1.3 \times 10^{-3} \text{ g m}^{-2}$  throughout the experiments, in common with each of the other 3 glass series, again suggesting that the silicon was involved in the formation of alteration phases in the system.



**Figure 5.15.** pH values for  $\text{Ca}(\text{OH})_2$  PCT-B experiments on NMAB<sub>x</sub>S glasses.

Figure 5.18 shows the NL(Na) values for each of the glasses. The data closely followed the trends observed in the NL(B) data, with NMAB10S having the highest mass loss, followed by NMAB5S and NMAB0S. The  $R_0(\text{Na})$  values for NMAB10S, NMAB5S and NMAB0S were  $0.240 \pm 0.012$ ,  $0.133 \pm 0.007$  and  $0.109 \pm 0.006 \text{ g m}^{-2} \text{ d}^{-1}$ , respectively. The final NL(Na) values for the three glasses were  $1.15 \pm 0.21$ ,  $0.84 \pm 0.16$  and  $0.65 \pm 0.13 \text{ g m}^{-2}$  from greatest (NMAB10S) to least (NMAB0S), with corresponding  $R_r(\text{Na})$  values of  $(3.0 \pm 0.2) \times 10^{-3}$ ,  $(1.8 \pm 0.1) \times 10^{-3}$  and  $(1.5 \pm 0.1) \times 10^{-3} \text{ g m}^{-2} \text{ d}^{-1}$ . Figure 5.19 shows the normalised mass loss of aluminium for each of the glasses. The values for NMAB0S and NMAB5S were similar over the course of the experiments, although that of NMAB10S was significantly lower. The initially fast mass loss seen in each glass -  $0.021 \pm 0.002$ ,  $0.012 \pm 0.001$  and  $0.013 \pm 0.001 \text{ g m}^{-2} \text{ d}^{-1}$  for NMAB0S, NMAB5S and NMAB10S, respectively – decreased earliest and most rapidly in NMAB10S, at 3 days, whereas it decreased more gradually for the other two glasses, between 3 days and 28 days. The final values of NL(Al) were  $0.088 \pm 0.015$ ,  $0.086 \pm 0.015$  and  $0.049 \pm 0.008 \text{ g m}^{-2}$  for NMAB0S, NMAB5S and NMAB10S, and their respective  $R_r(\text{Al})$  values were  $(6.0 \pm 0.3) \times 10^{-5}$ ,  $(1.0 \pm 0.1) \times 10^{-4}$  and  $(2.0 \pm 0.1) \times 10^{-4} \text{ g m}^{-2} \text{ d}^{-1}$ . The normalised mass loss of magnesium is shown in Figure 5.20. Apart from the day 1 samples, all of the magnesium concentrations in solution were below the detection limits of the ICP-OES. This is the same behaviour that was observed in the magnesium-containing borosilicate glasses; any magnesium that was leached does not seem to remain in solution, but rather must be incorporated into alteration phases.



**Figure 5.16.** NL(B) data for NMAB<sub>x</sub>S glasses for PCT-B experiments in Ca(OH)<sub>2</sub>.

**Table 5.4.** Initial ( $R_0(i)$ ) and residual ( $R_r(i)$ ) normalised mass loss rates for B, Na and Al for the NMAB<sub>x</sub>S glasses in Ca(OH)<sub>2</sub>.

Rate (g m <sup>-2</sup> d <sup>-1</sup> )	NMAB0S	NMAB5S	NMAB10S
$R_0(B)$	-	$0.100 \pm 0.005$	$0.154 \pm 0.008$
$R_r(B)$	-	$(8.0 \pm 0.4) \times 10^{-4}$	$(1.4 \pm 0.1) \times 10^{-3}$
$R_0(Na)$	$0.109 \pm 0.006$	$0.133 \pm 0.007$	$0.240 \pm 0.012$
$R_r(Na)$	$(1.5 \pm 0.1) \times 10^{-3}$	$(1.8 \pm 0.1) \times 10^{-3}$	$(3.0 \pm 0.2) \times 10^{-3}$
$R_0(Al)$	$0.021 \pm 0.002$	$0.012 \pm 0.001$	$0.013 \pm 0.001$
$R_r(Al)$	$(6.0 \pm 0.3) \times 10^{-5}$	$(1.0 \pm 0.1) \times 10^{-4}$	$(2.0 \pm 0.1) \times 10^{-4}$

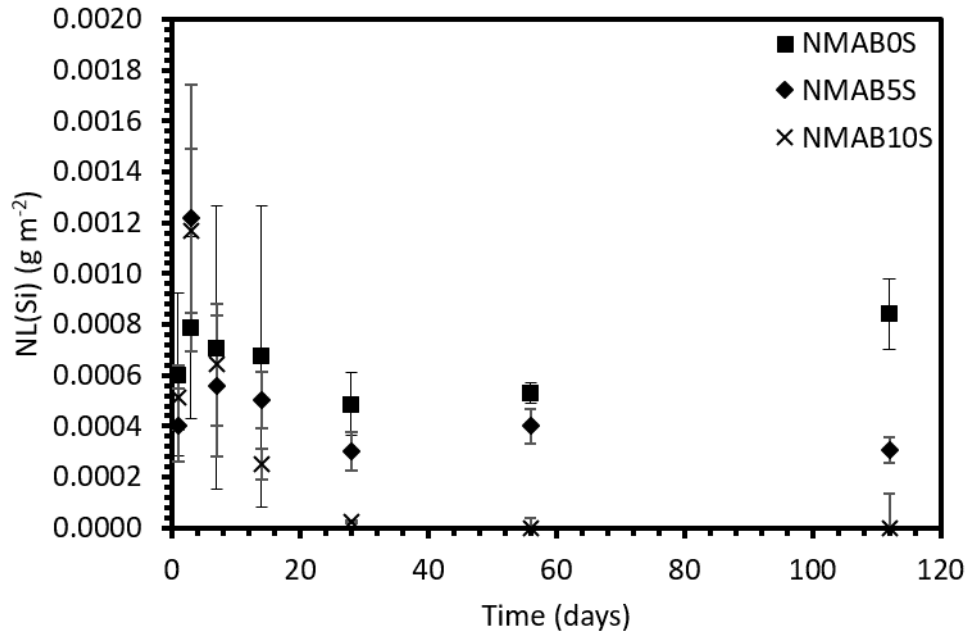


**Figure 5.17.** NL(Si) data for NMAB<sub>x</sub>S glasses for PCT-B experiments in Ca(OH)<sub>2</sub>.

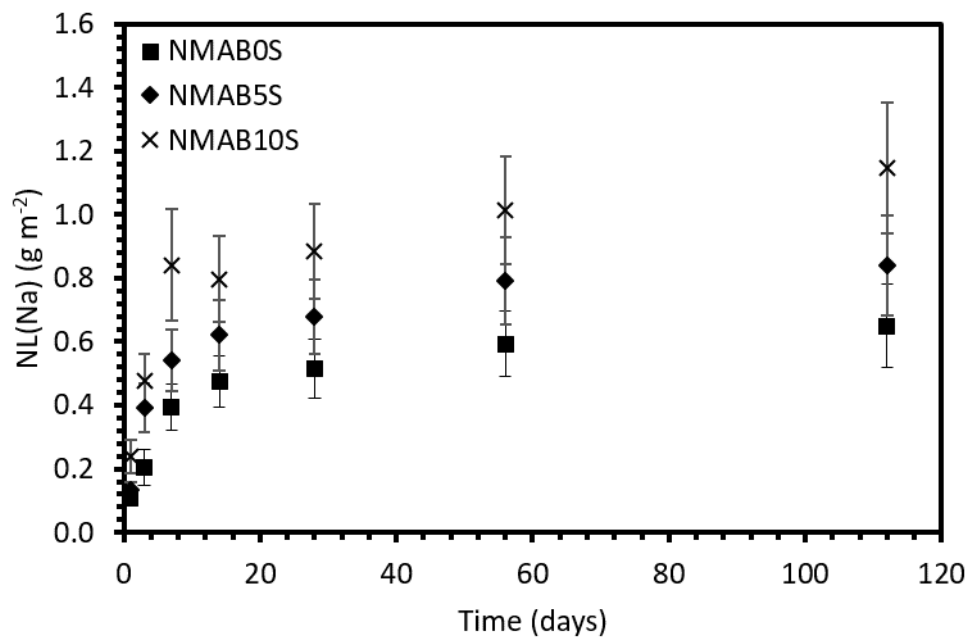


**Figure 5.18.** NL(Na) data for NMAB<sub>x</sub>S glasses for PCT-B experiments in Ca(OH)<sub>2</sub>.

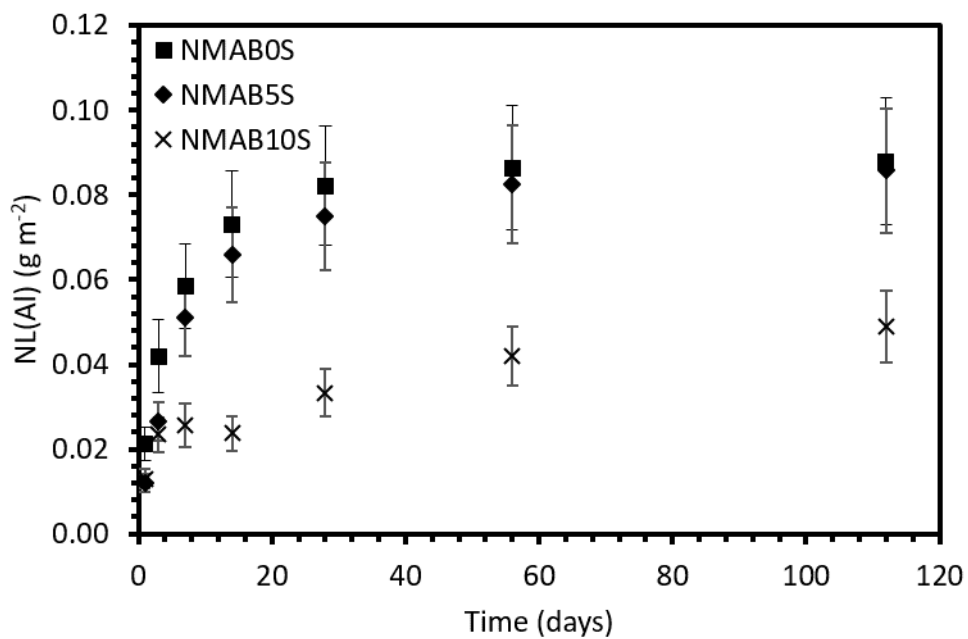


Figure 5.19. NL(Al) data for NMAB<sub>x</sub>S glasses for PCT-B experiments.

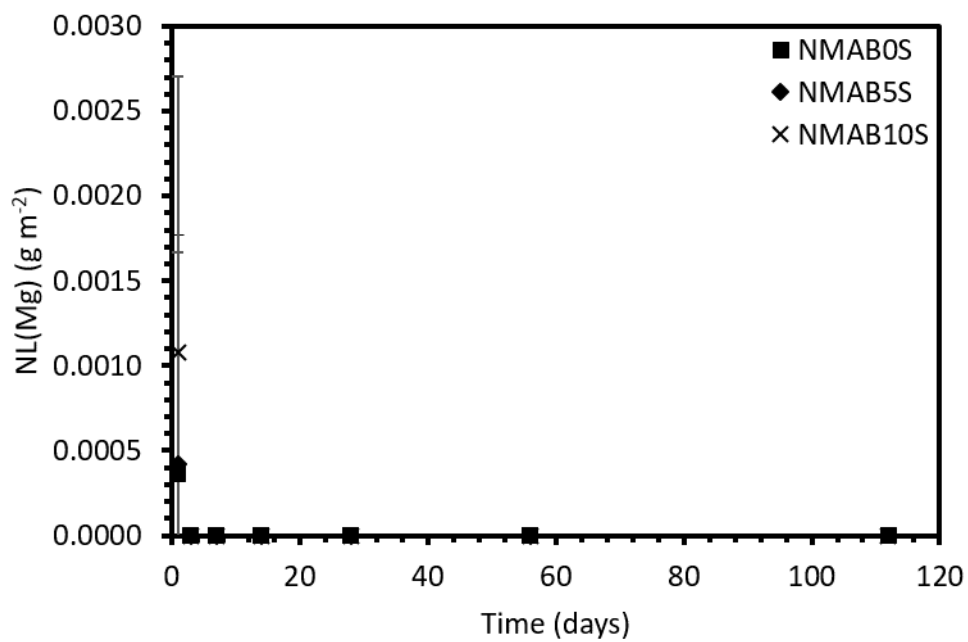


Figure 5.20. NL(Mg) data for NMAB<sub>x</sub>S glasses for PCT-B experiments.

### 5.3.2 Leaching in Potassium Hydroxide

Leaching was performed in a solution of 0.0021/0.021 M KOH/KCl to investigate whether the glass dissolution behaviour in  $\text{Ca}(\text{OH})_2$  is governed only by pH, or whether the cation in solution has an effect. KCl was added as a buffer, in order to maintain the solution pH.

#### 5.3.2.1 NCxBS Glasses

Figure 5.21 shows the pH values for the NCxBS samples in KOH. The blanks maintained consistent pH values of  $\sim 12.6$ , for that associated with NC0BS and NC10BS, and  $\sim 12.8$  for that associated with NC5BS. The pH values for all 3 NCxBS glasses decreased from day 1 values of 12.36, 12.57 and 12.58 for NC0BS, NC5BS and NC10BS, respectively, to corresponding day 112 values of 10.92, 10.88 and 10.76. The decrease was most rapid for NC0BS, which reached a consistent value after 14 days, and least rapid for NC10BS, which reached a consistent value after 28 days. Data were not available for all timepoints for the NC5BS samples, but its decrease between 1 and 3 days matched that of NC0BS. The NL(B) values from PCT-B experiments in KOH on the NCxBS glasses are shown in Figure 5.22. Initial and residual rates of mass loss are shown in Table 5.5. Data were only available for NC10BS up to 28 days, due to a test vessel failure during the experiments, and thus reasonable residual rates could not be determined for NC10BS. The glasses exhibited the same general trends as in  $\text{Ca}(\text{OH})_2$ , with rapid initial mass loss followed by a significant decrease in rate between 3 and 28 days. An analysis of glass dissolution variations between KOH and  $\text{Ca}(\text{OH})_2$  solutions is discussed in Section 5.5.1. The initial B loss rates were  $0.205 \pm 0.010$ ,  $0.206 \pm 0.010$  and  $0.130 \pm 0.007 \text{ g m}^{-2} \text{ d}^{-1}$  for NC0BS, NC5BS and NC10BS, respectively. Up to 14 days, NC5BS had the highest NL(B), followed by NC10BS and NC0BS. However, from 14 days onwards NC5BS undergoes a greater drop in mass loss rate than NC0BS, with the two glasses having respective values of  $R_r(\text{B})$  of  $0.028 \pm 0.001$  and  $(6.6 \pm 0.3) \times 10^{-3} \text{ g m}^{-2} \text{ d}^{-1}$ , and final values of NL(B) of  $2.77 \pm 0.43$  and  $4.75 \pm 1.07 \text{ g m}^{-2}$ . The final value of NL(B) for NC10BS is  $2.97 \pm 0.68 \text{ g m}^{-2}$  after 28 days. Figure 5.23 shows the NL(Si) values for these experiments. There was a significant difference between these values and those of the same glasses in  $\text{Ca}(\text{OH})_2$ . The KOH NL(Si) values were of the order of  $1 \text{ g m}^{-2}$ , whereas those obtained from the  $\text{Ca}(\text{OH})_2$  experiments were of the order of  $0.01 \text{ g}$

$\text{m}^{-2}$ . This implies that more Si was remaining in solution during the experiments using KOH, and did not become incorporated into alteration phases. NC0BS had the highest silicon loss during the experiments, followed by NC10BS and NC5BS. The initial Si loss rates were  $0.255 \pm 0.013$ ,  $0.165 \pm 0.008$  and  $0.123 \pm 0.006 \text{ g m}^{-2} \text{ d}^{-1}$  for NC0BS, NC5BS and NC10BS, respectively. The final mass loss values were  $4.76 \pm 1.05$ ,  $2.15 \pm 0.39$  and  $1.67 \pm 0.28 \text{ g m}^{-2}$  for NC0BS, NC10BS (after 28 days) and NC5BS, with residual rates of  $0.019 \pm 0.001$  and  $(-2.0 \pm 0.1) \times 10^{-4}$  for NC0BS and NC5BS, respectively. The negative residual rate for NC5BS is unlikely to be significant due to the presence of an anomalously low datapoint at 56 days.

Figure 5.24 shows the NL(Na) values for the NCxBS glasses. The trends in these data are similar to those in the NL(B) and NL(Si) data, with NC0BS having the highest NL(Na), followed by NC10BS and NC5BS. The  $R_0(\text{Na})$  values for NC0BS, NC10BS and NC5BS were  $0.837 \pm 0.042$ ,  $0.448 \pm 0.022$  and  $0.195 \pm 0.010 \text{ g m}^{-2} \text{ d}^{-1}$ , respectively. The residual rates for NC0BS and NC5BS were  $0.041 \pm 0.002$  and  $(5.4 \pm 0.3) \times 10^{-3} \text{ g m}^{-2} \text{ d}^{-1}$ , leading to final normalised mass losses of  $8.71 \pm 2.01$ ,  $6.34 \pm 1.24$  and  $2.46 \pm 0.51$  for NC0BS, NC10BS (28 days) and NC5BS, respectively. Figure 5.25 shows the calcium mass loss for these glasses (excluding NC0BS, which doesn't contain Ca). The NL(Ca) values for NC10BS were significantly higher than those for NC5BS. After 28 days, NL(Ca) reached  $0.42 \pm 0.11 \text{ g m}^{-2}$ , whereas the maximum value for NC5BS was  $0.15 \pm 0.04$  after 7 days.

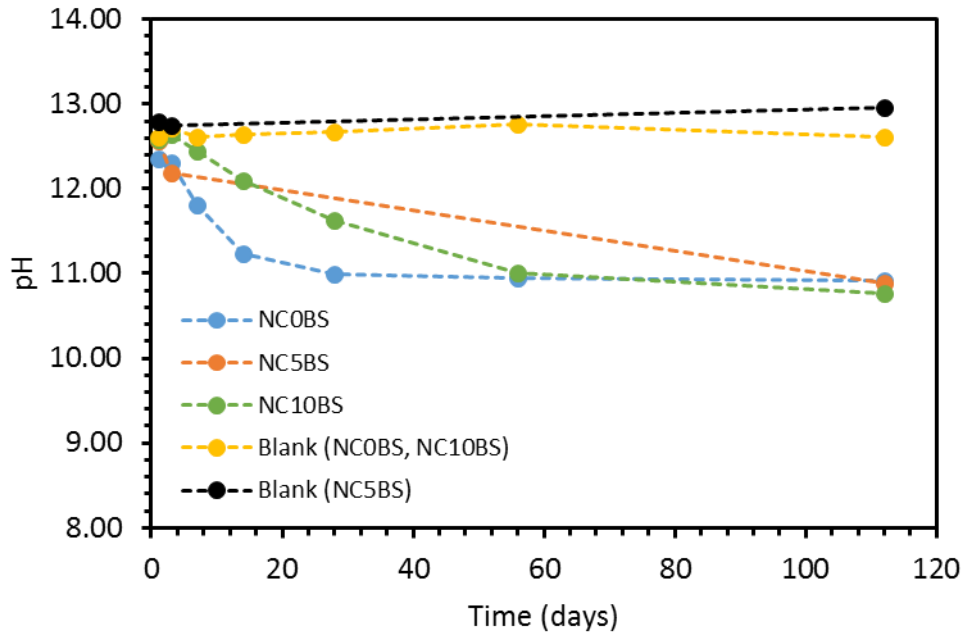


**Figure 5.21.** pH values for KOH PCT-B experiments on NC<sub>x</sub>BS glasses.

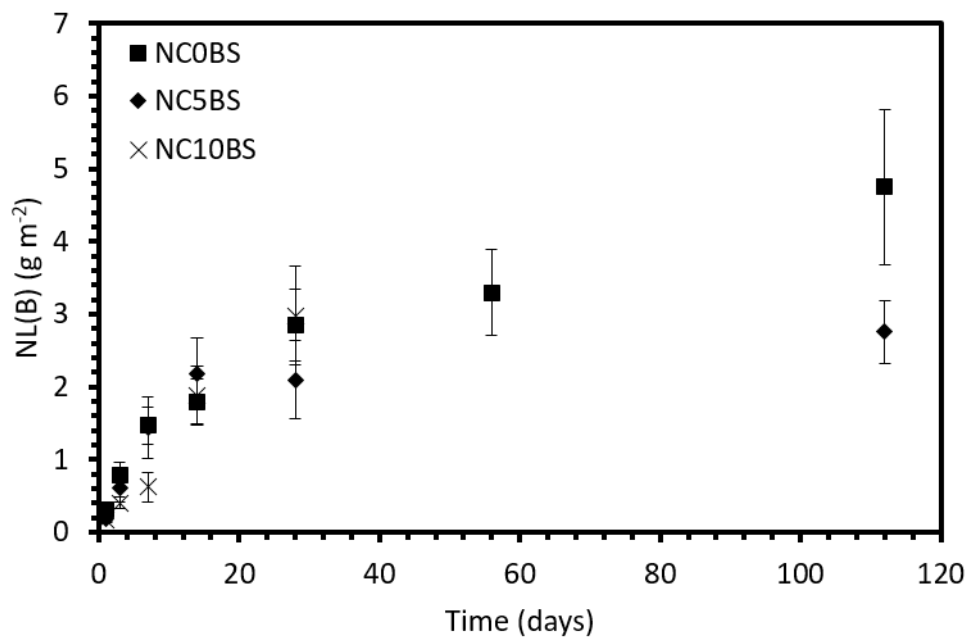


**Figure 5.22.** NL(B) data for NC<sub>x</sub>BS glasses for KOH PCT-B experiments.

**Table 5.5.** Initial ( $R_0(i)$ ) and residual ( $R_r(i)$ ) normalised mass loss rates for B, Na and Si for the NC $x$ BS glasses in KOH.

Rate ( $\text{g m}^{-2} \text{d}^{-1}$ )	NC0BS	NC5BS	NC10BS
$R_0(\text{B})$	$0.205 \pm 0.010$	$0.206 \pm 0.010$	$0.130 \pm 0.007$
$R_r(\text{B})$	$0.028 \pm 0.001$	$(6.6 \pm 0.3) \times 10^{-3}$	-
$R_0(\text{Na})$	$0.837 \pm 0.042$	$0.195 \pm 0.010$	$0.448 \pm 0.022$
$R_r(\text{Na})$	$0.041 \pm 0.002$	$(5.4 \pm 0.3) \times 10^{-3}$	-
$R_0(\text{Si})$	$0.255 \pm 0.013$	$0.165 \pm 0.008$	$0.123 \pm 0.006$
$R_r(\text{Si})$	$0.019 \pm 0.001$	$(-2.0 \pm 0.1) \times 10^{-4}$	-

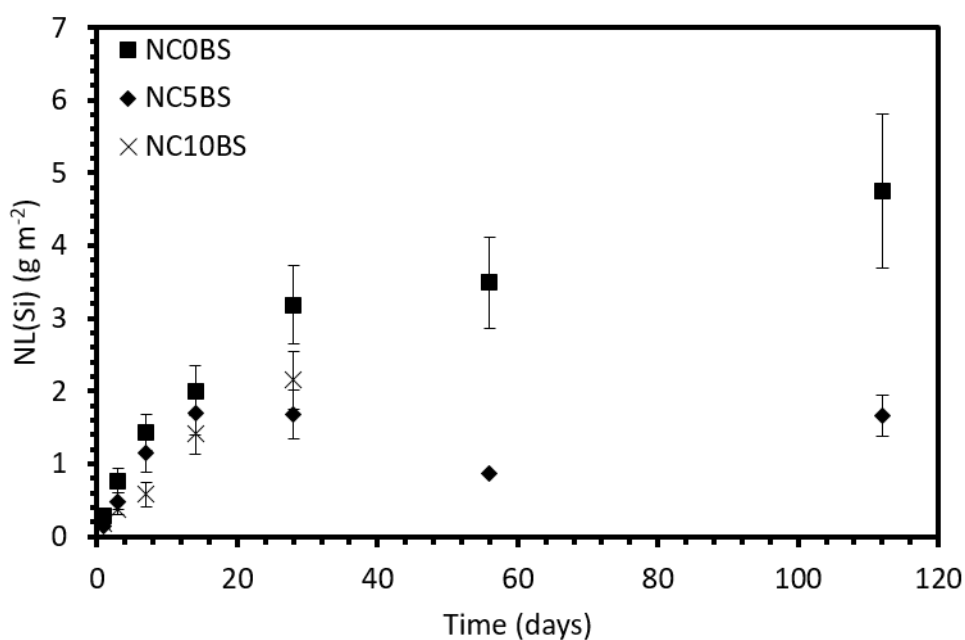


**Figure 5.23.** NL(Si) data for NC $x$ BS glasses for KOH PCT-B experiments.

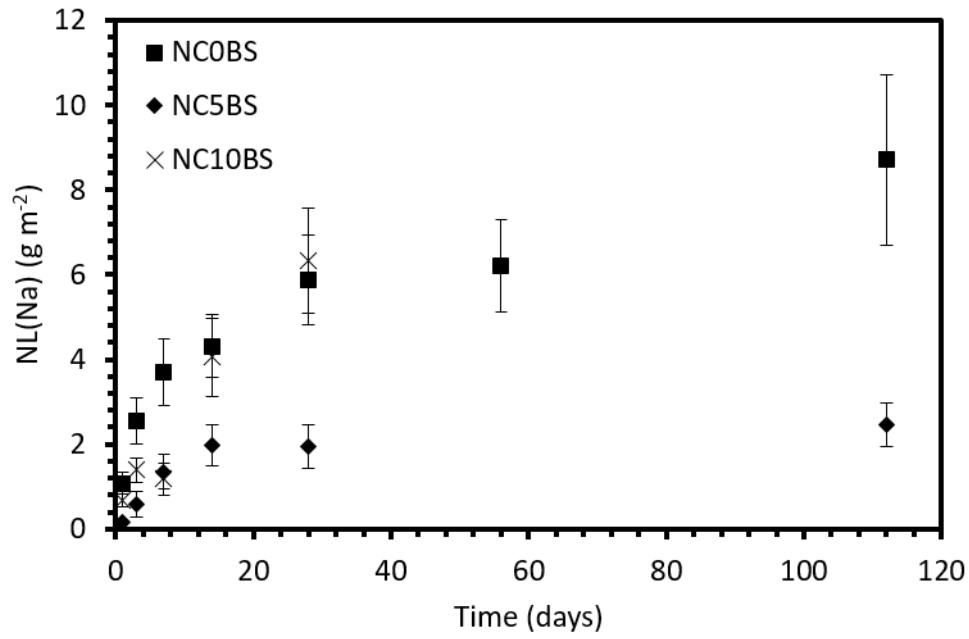


**Figure 5.24.** NL(Na) data for NC $_x$ BS glasses for KOH PCT-B experiments.

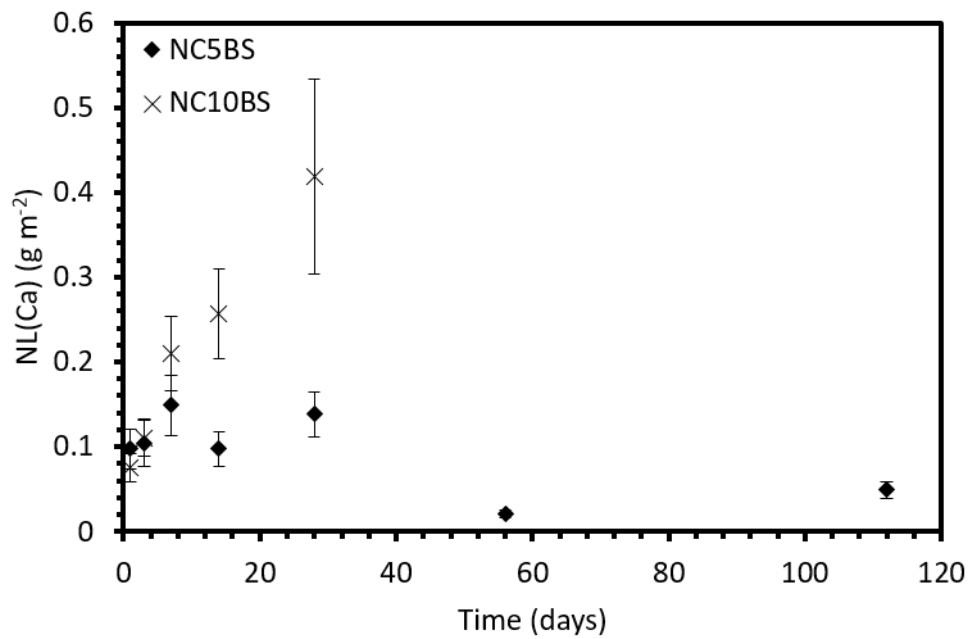


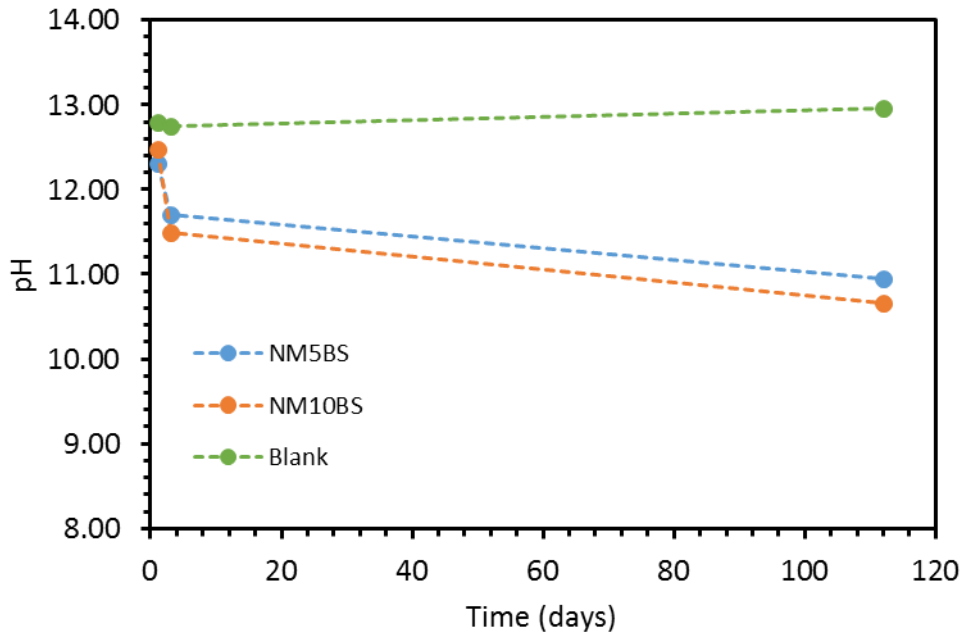
**Figure 5.25.** NL(Ca) data for NC $_x$ BS glasses for KOH PCT-B experiments.

### 5.3.2.2 *NM<sub>x</sub>BS Glasses*

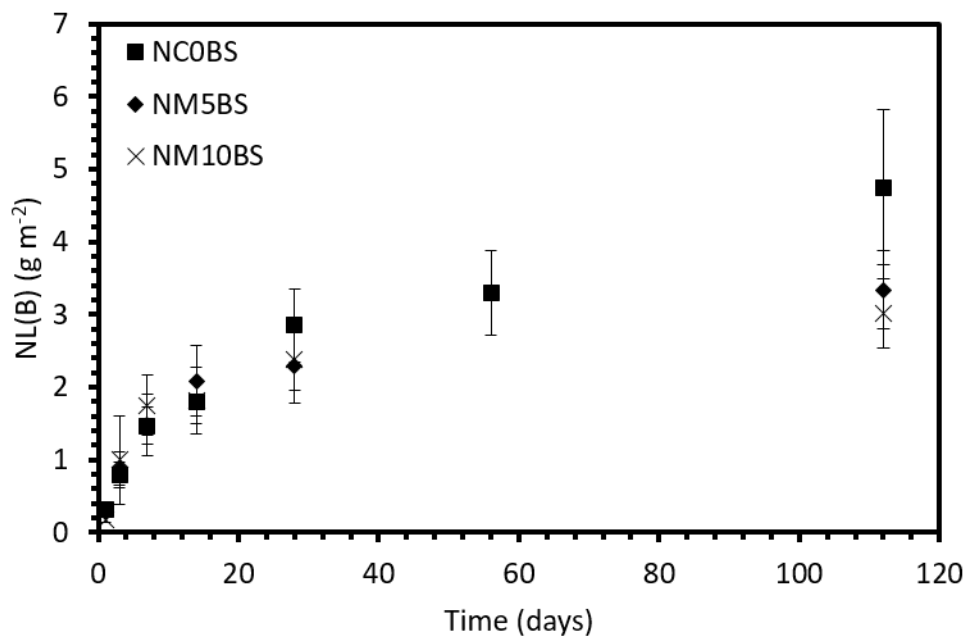
Figure 5.26 shows the pH values for the *NM<sub>x</sub>BS* samples in KOH. Data were only available for the 1, 3 and 112 day sampling times due to issues with carbonation of samples. The pH values for *NM5BS* and *NM10BS* were 12.32 and 12.47, respectively, at day 1 but decreased significantly over the duration of the experiments to 10.95 and 10.66, respectively, after 112 days. The *NL(B)* values for the *NM<sub>x</sub>BS* glasses in KOH are shown in Figure 5.27. Initial and residual rates are shown in Table 5.6. The data followed the trends seen in the  $\text{Ca(OH)}_2$  data; rapid initial release followed by a significant decrease in rate with time. Initially, the two Mg-containing glasses had higher mass losses than *NC0BS*, with  $R_0(\text{B})$  values of  $0.319 \pm 0.016$ ,  $0.295 \pm 0.015$  and  $0.205 \pm 0.010 \text{ g m}^{-2} \text{ d}^{-1}$  for *NM10BS*, *NM5BS* and *NC0BS*, respectively. However, *NM5BS* and *NM10BS* experienced a greater drop in mass loss rate than *NC0BS*, leading to *NC0BS* having the highest mass loss after 14 – 28 days. The final values of *NL(B)* were  $4.75 \pm 1.07$ ,  $3.34 \pm 0.54$  and  $3.01 \pm 0.48 \text{ g m}^{-2}$ , for *NC0BS*, *NM5BS* and *NM10BS*, respectively, with  $R_r(\text{B})$  values of  $0.028 \pm 0.001$ ,  $0.013 \pm 0.001$  and  $0.011 \pm 0.001 \text{ g m}^{-2} \text{ d}^{-1}$ . Figure 5.28 contains the *NL(Si)* data for this series. The initial rates of Si loss were similar for the three glasses, at  $0.255 \pm 0.013$ ,  $0.204 \pm 0.010$  and  $0.262 \pm 0.013 \text{ g m}^{-2} \text{ d}^{-1}$  for *NC0BS*, *NM5BS* and *NM10BS*, respectively. *NL(B)* and *NL(Si)* were very similar for *NC0BS*, but the values of *NL(Si)* were significantly lower than the *NL(B)* values for both of the Mg-containing glasses, due to the Mg-containing glasses having lower residual rates;  $(1.1 \pm 0.1) \times 10^{-3}$  and  $(1.8 \pm 0.1) \times 10^{-3} \text{ g m}^{-2} \text{ d}^{-1}$  for *NM5BS* and *NM10BS* compared to  $0.019 \pm 0.001 \text{ g m}^{-2} \text{ d}^{-1}$  for *NC0BS*. This suggests that some silicon was retained in the alteration phases. This phenomenon was also seen in the *NL(Si)* data for the *NC<sub>x</sub>BS* glasses in KOH (Figure 5.18).

Figure 5.29 contains the *NL(Na)* values for the *NM<sub>x</sub>BS* glasses. *NM5BS* and *NM10BS* had lower *NL(Na)* values than *NC0BS* throughout the experiments, with initial rates of  $0.837 \pm 0.042$ ,  $0.277 \pm 0.014$  and  $0.331 \pm 0.017 \text{ g m}^{-2} \text{ d}^{-1}$  for *NC0BS*, *NM5BS* and *NM10BS*. The two Mg-containing glasses had similar *NL(Na)* values, although *NM10BS* had the lowest at the end of the experiments. The final normalised mass losses were  $8.71 \pm 2.01$ ,  $2.96 \pm 0.70$  and  $2.72 \pm 0.57 \text{ g m}^{-2}$  for *NC0BS*, *NM5BS* and *NM10BS*, respectively, with respective  $R_r(\text{Na})$  values of  $0.041 \pm 0.002$ ,  $0.011 \pm 0.001$  and  $0.008 \pm 0.001 \text{ g m}^{-2} \text{ d}^{-1}$ . The normalised mass loss of magnesium for the glasses is shown in Figure 5.30. In common with the data from the  $\text{Ca(OH)}_2$

experiments, the mass loss of magnesium remained low throughout the experiments – below  $0.025 \text{ g m}^{-2}$ . This level was significantly lower than the calcium release of the equivalent Ca-containing glasses (NC5BS and NC10BS, see Figure 5.25), suggesting that the magnesium is retained in alteration phases at a higher level than calcium (see Section 5.5.5 for further discussion).



**Figure 5.26.** pH values for KOH PCT-B experiments on NMxBS glasses.



**Figure 5.27.** NL(B) data for NMxBS glasses for KOH PCT-B experiments.

**Table 5.6.** Initial ( $R_0(i)$ ) and residual ( $R_r(i)$ ) normalised mass loss rates for B, Na and Si for the  $NM_xBS$  glasses in KOH.

Rate ( $g\ m^{-2}\ d^{-1}$ )	NC0BS	NM5BS	NM10BS
$R_0(B)$	$0.205 \pm 0.010$	$0.295 \pm 0.015$	$0.319 \pm 0.016$
$R_r(B)$	$0.028 \pm 0.001$	$0.013 \pm 0.001$	$0.011 \pm 0.001$
$R_0(Na)$	$0.837 \pm 0.042$	$0.277 \pm 0.014$	$0.331 \pm 0.017$
$R_r(Na)$	$0.041 \pm 0.002$	$0.011 \pm 0.001$	$0.008 \pm 0.001$
$R_0(Si)$	$0.255 \pm 0.013$	$0.204 \pm 0.010$	$0.262 \pm 0.013$
$R_r(Si)$	$0.019 \pm 0.001$	$(1.1 \pm 0.1) \times 10^{-3}$	$(1.8 \pm 0.1) \times 10^{-3}$

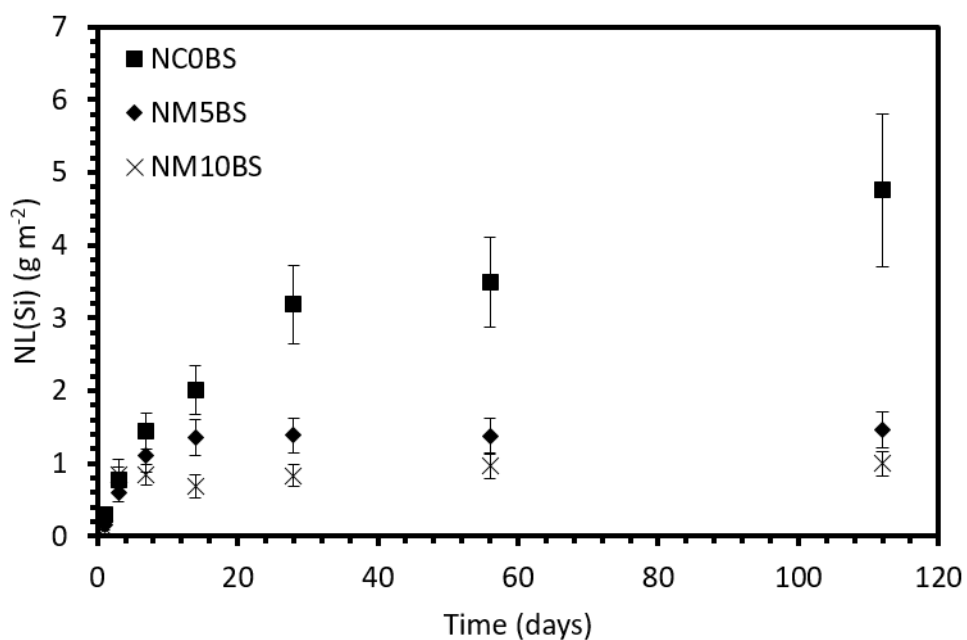


**Figure 5.28.** NL(Si) data for  $NM_xBS$  glasses for KOH PCT-B experiments.

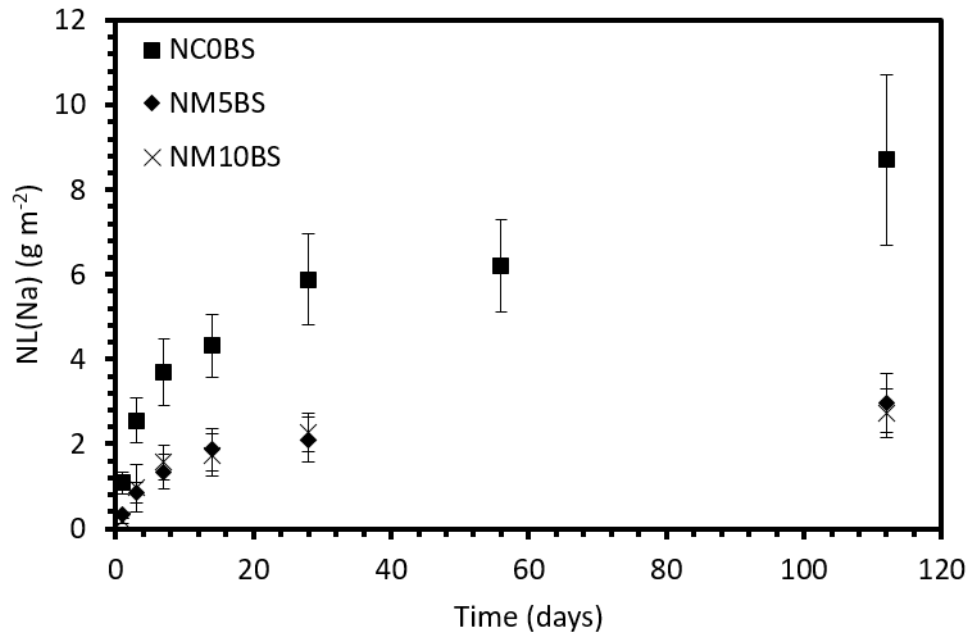


**Figure 5.29.** NL(Na) for NMxBS glasses for KOH PCT-B experiments.

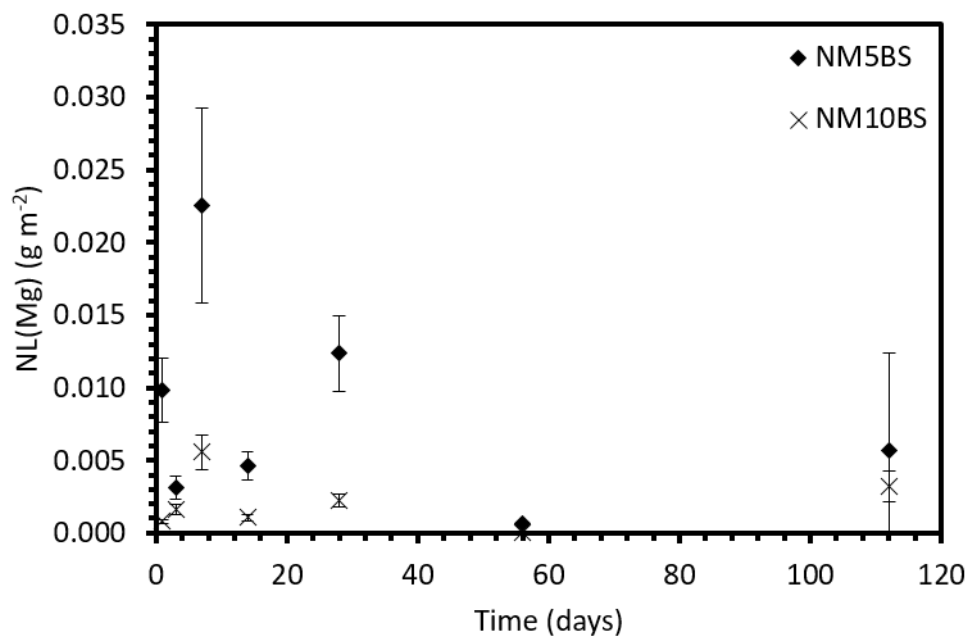


**Figure 5.30.** NL(Mg) for NMxBS glasses for KOH PCT-B experiments.

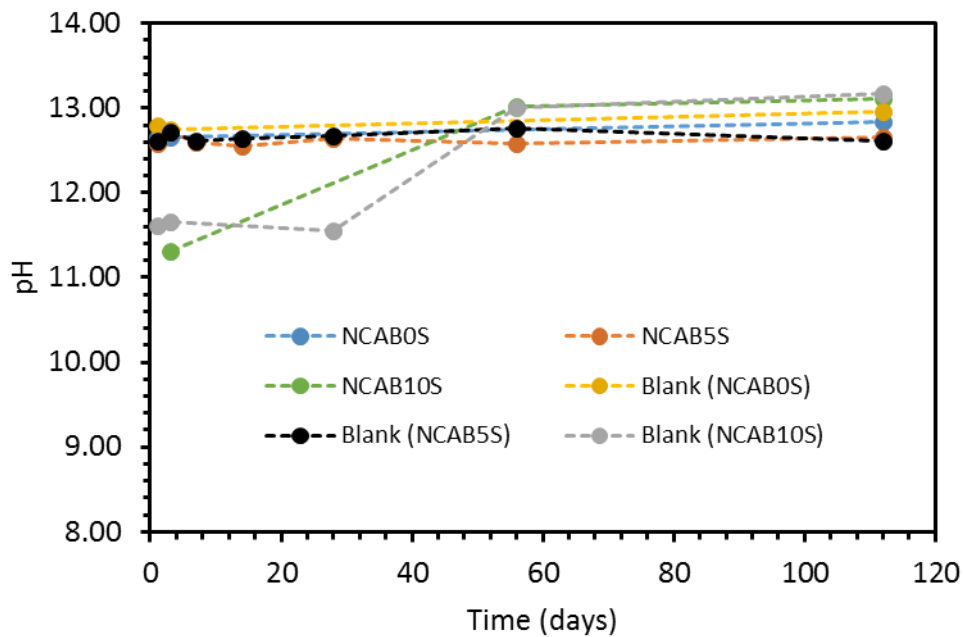
### 5.3.2.3 NCABxS Glasses

Figure 5.31 shows the pH values for these experiments. The blanks corresponding to the NCAB0S and NCAB5S samples maintained a consistent pH throughout the duration of the experiments, with initial and final values of 12.80 and 12.96 for the NCAB0S blank and 12.61 and 12.61 for the NCAB5S blank. The blank corresponding

to NCAB10S had low values ( $\sim 11.5$ ) up to 28 days, before increasing to  $\sim 13.1$ . This is likely due to partial carbonation of the early samples. This same trend can be seen for the NCAB10S samples, which had an average pH value of 11.32 after day 3, but an average value of 13.11 after 112 days. The values for the NCAB0S and NCAB5S samples remained consistent, with respective initial values of 12.65 and 12.58, and final values of 12.84 and 12.65. Figure 5.32 shows the NL(B) data for the NCAB $x$ S glasses, excluding NCAB0S which contains no boron. Initial and residual rates are shown in Table 5.7. Mass loss data are only available up to 28 days for NCAB5S due to test vessel failure during the experiments, and so residual rates are not available for this sample. The initial boron releases for the two glasses were similar up to 14 days, with  $R_0(\text{B})$  values of  $0.016 \pm 0.001$  and  $0.029 \pm 0.001 \text{ g m}^{-2} \text{ d}^{-1}$  for NCAB5S and NCAB10S, respectively, before NCAB5S underwent a significant increase between 14 and 28 days. NCAB10S underwent a significant rate drop between 3 and 14 days, which continued until the end of the experiment at 112 days. Its residual rate was  $(4.0 \pm 0.2) \times 10^{-5} \text{ g m}^{-2} \text{ d}^{-1}$ . The final NL(B) values were  $0.36 \pm 0.06 \text{ g m}^{-2}$  for NCAB5S and  $0.15 \pm 0.02 \text{ g m}^{-2}$  for NCAB10S. These values are approximately an order of magnitude lower than those obtained for the borosilicate series (NC $x$ BS and NM $x$ BS). Figure 5.33 shows the NL(Si) for the three glasses. The data for each glass displayed the characteristic ‘turnover’ in rate seen in all of the data. The initial rates for the three glasses were  $0.021 \pm 0.001$ ,  $0.028 \pm 0.001$  and  $0.037 \pm 0.002 \text{ g m}^{-2} \text{ d}^{-1}$  for NCAB0S, NCAB5S and NCAB10S, respectively. The rate drop occurred at around the same time for NCAB0S and NCAB10S (between 3 and 14 days) and slightly later in NCAB5S (between 7 and 56 days), although this is slightly obscured due to the presence of an apparently anomalous datum at 28 days. The general trend was that NCAB0S has the lowest silicon loss, followed by NCAB10S and NCAB5S, with residual rates of  $(1.0 \pm 0.1) \times 10^{-4}$  and  $(-6.0 \pm 0.3) \times 10^{-5}$  for NCAB0S and NCAB10S, respectively. The negative rate calculated for NCAB10S is unlikely to be significant, as positive values can be calculated from the data within error. The final values of NL(Si) were  $0.32 \pm 0.06$ ,  $0.18 \pm 0.03$  and  $0.12 \pm 0.02 \text{ g m}^{-2}$  for NCAB5S, NCAB10S and NCAB0S, respectively.

The normalised mass loss of sodium for the NCAB $x$ S glasses is shown in Figure 5.34. NCAB5S again had the highest mass loss, followed by NCAB10S and NCAB0S. The 28 day datum for NCAB5S was anomalous, as with the NL(B) and NL(Si) data. The  $R_0(\text{Na})$  values were  $0.021 \pm 0.001$ ,  $0.096 \pm 0.005$  and  $0.036 \pm 0.002 \text{ g m}^{-2} \text{ d}^{-1}$  for

NCAB0S, NCAB5S and NCAB10S, whilst the  $R_r(\text{Na})$  values for NCAB0S and NCAB10S were  $(-2.0 \pm 0.1) \times 10^{-5}$  and  $(1.0 \pm 0.1) \times 10^{-4} \text{ g m}^{-2} \text{ d}^{-1}$ , respectively. The final values of  $\text{NL}(\text{Na})$  for NCAB0S, NCAB5S and NCAB10S were  $0.12 \pm 0.03$ ,  $1.19 \pm 0.20$  and  $0.18 \pm 0.03 \text{ g m}^{-2}$ , respectively. Figure 5.35 shows the normalised mass loss of aluminium for the three glasses. The values for NCAB0S and NCAB10S were similar for the duration of the experiments, whereas those for NCAB5S were significantly higher, starting with the initial rate of Al loss, which was  $0.095 \pm 0.005 \text{ g m}^{-2} \text{ d}^{-1}$  for NCAB5S, compared to  $0.016 \pm 0.001$  and  $0.027 \pm 0.001 \text{ g m}^{-2} \text{ d}^{-1}$  for NCAB0S and NCAB10S. The final values of  $\text{NL}(\text{Al})$  were  $0.72 \pm 0.14$ ,  $0.12 \pm 0.02$  and  $0.11 \pm 0.02 \text{ g m}^{-2}$  for NCAB5S, NCAB10S and NCAB0S. The residual rates of Al loss for NCAB0S and NCAB10S were  $(1.0 \pm 0.1) \times 10^{-4}$  and  $(-1.0 \pm 0.1) \times 10^{-4} \text{ g m}^{-2} \text{ d}^{-1}$ , respectively. Figure 5.36 shows the  $\text{NL}(\text{Ca})$  values for the NCAB $x$ S glasses. The values were very similar for NCAB0S and NCAB10S, but were again far higher for NCAB5S. The final values of  $\text{NL}(\text{Ca})$  for NCAB0S, NCAB5S and NCAB10S were  $0.14 \pm 0.03$ ,  $2.90 \pm 0.51$  and  $0.15 \pm 0.02 \text{ g m}^{-2}$ .



**Figure 5.31.** pH values for KOH PCT-B experiments on NCAB $x$ S glasses.

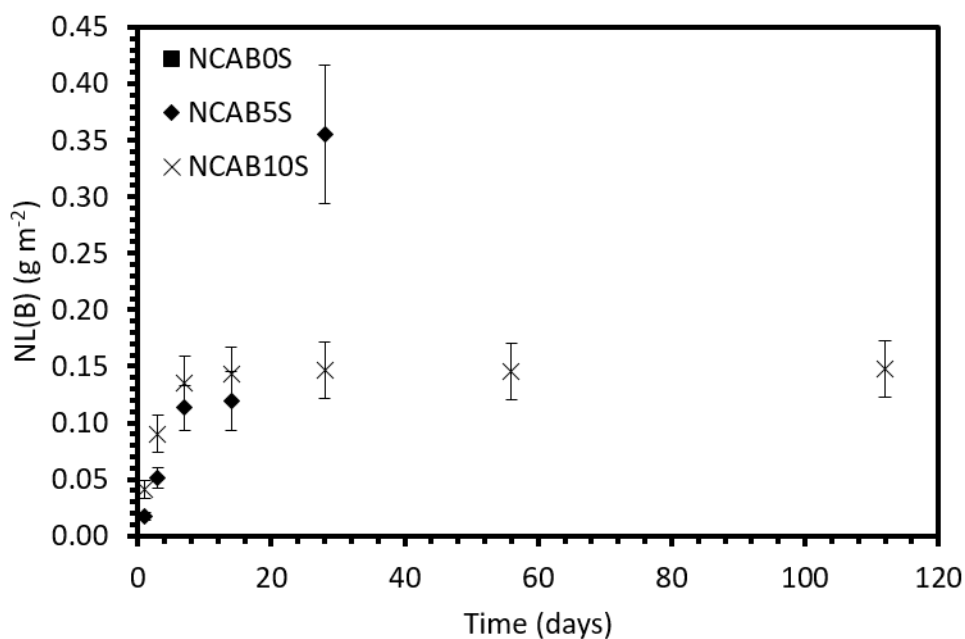


**Figure 5.32.** NL(B) for NCAB<sub>x</sub>S glasses for KOH PCT-B experiments.

**Table 5.7.** Initial ( $R_0(i)$ ) and residual ( $R_r(i)$ ) normalised mass loss rates for B, Na, Al and Si for the NCAB<sub>x</sub>S glasses in KOH.

Rate (g m <sup>-2</sup> d <sup>-1</sup> )	NCAB0S	NCAB5S	NCAB10S
$R_0(B)$	-	$0.016 \pm 0.001$	$0.029 \pm 0.001$
$R_r(B)$	-	-	$(4.0 \pm 0.2) \times 10^{-5}$
$R_0(Na)$	$0.021 \pm 0.001$	$0.096 \pm 0.005$	$0.036 \pm 0.002$
$R_r(Na)$	$(-2.0 \pm 0.1) \times 10^{-5}$	-	$(1.0 \pm 0.1) \times 10^{-4}$
$R_0(Al)$	$0.016 \pm 0.001$	$0.095 \pm 0.005$	$0.027 \pm 0.001$
$R_r(Al)$	$(1.0 \pm 0.1) \times 10^{-4}$	-	$(-1.0 \pm 0.1) \times 10^{-4}$
$R_0(Si)$	$0.021 \pm 0.001$	$0.028 \pm 0.001$	$0.037 \pm 0.002$
$R_r(Si)$	$(1.0 \pm 0.1) \times 10^{-4}$	-	$(-6.0 \pm 0.3) \times 10^{-5}$

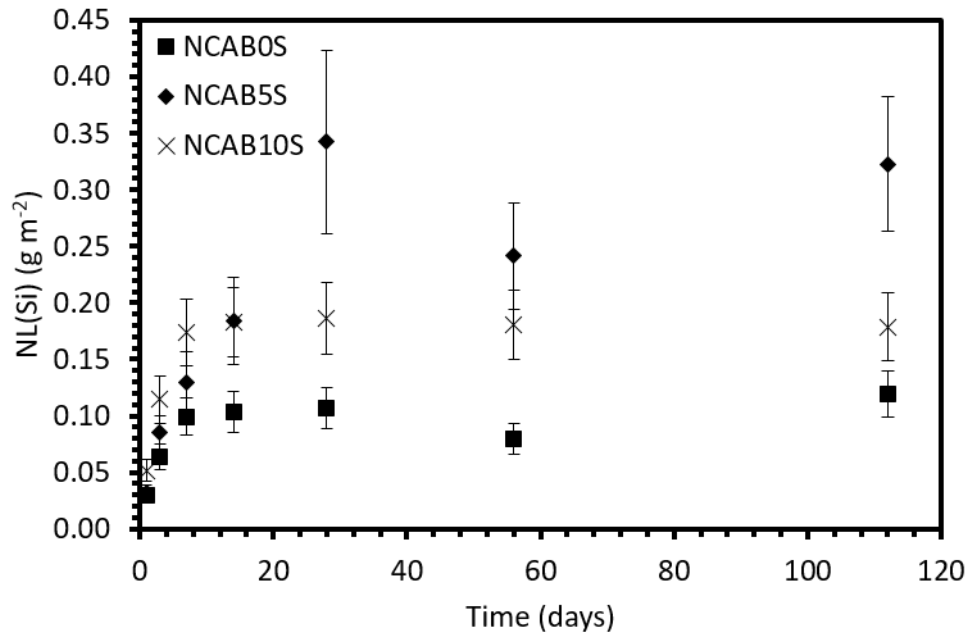


**Figure 5.33.** NL(Si) for NCAB<sub>x</sub>S glasses for KOH PCT-B experiments.

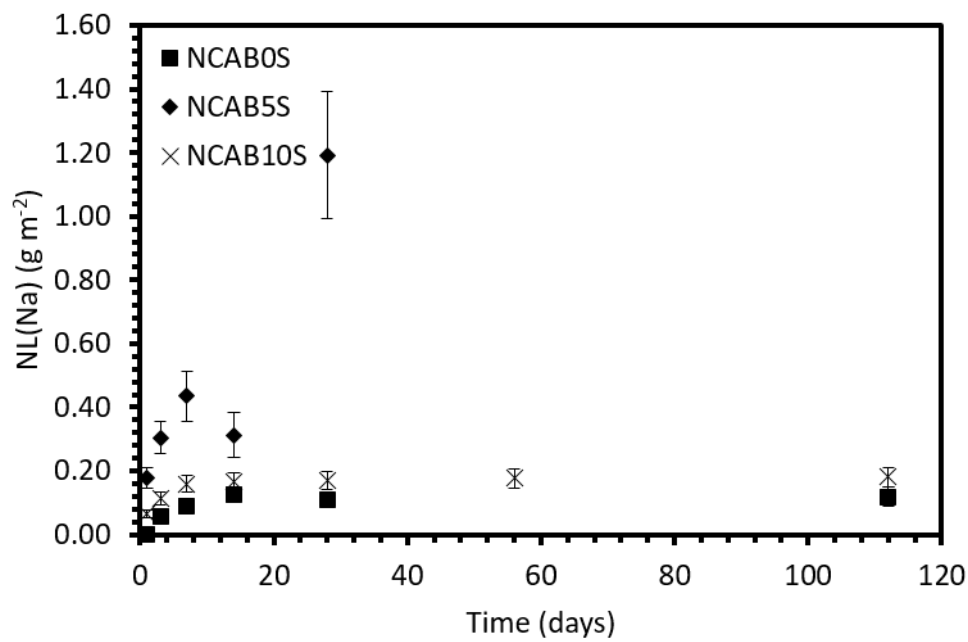


**Figure 5.34.** NL(Na) for NCAB<sub>x</sub>S glasses for KOH PCT-B experiments.

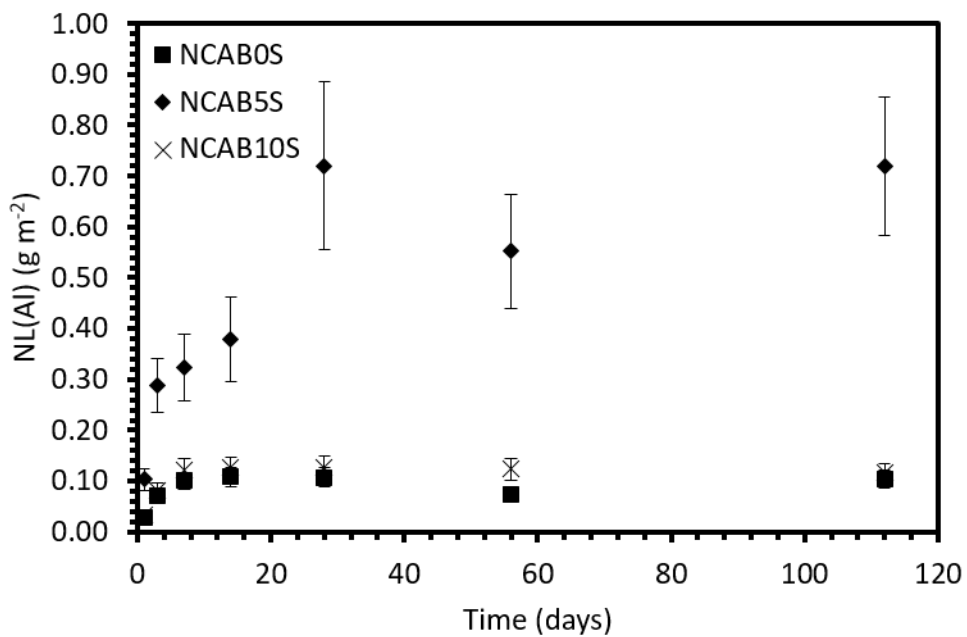


Figure 5.35. NL(Al) for NCAB<sub>x</sub>S glasses for KOH PCT-B experiments.

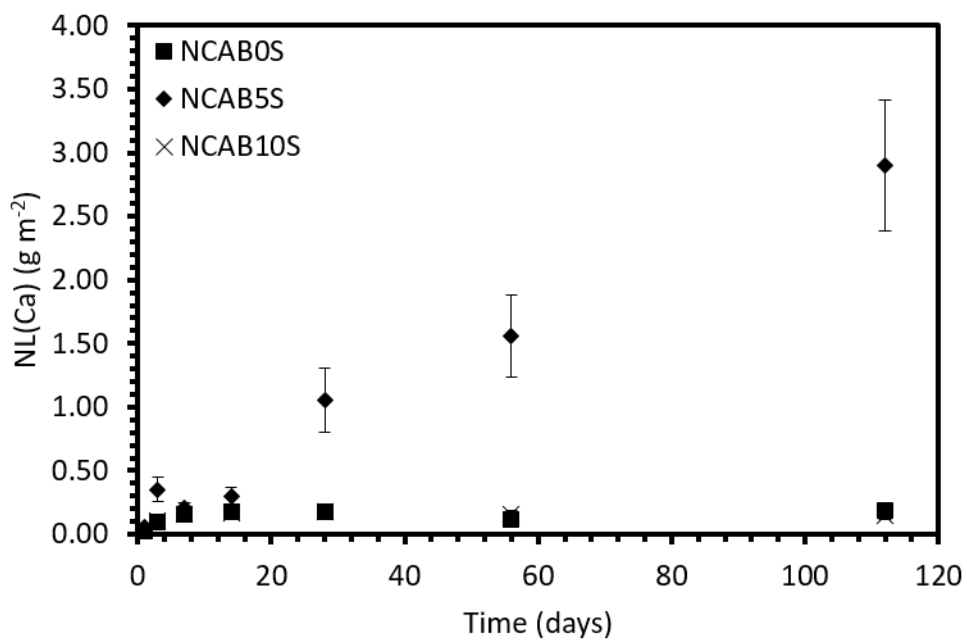


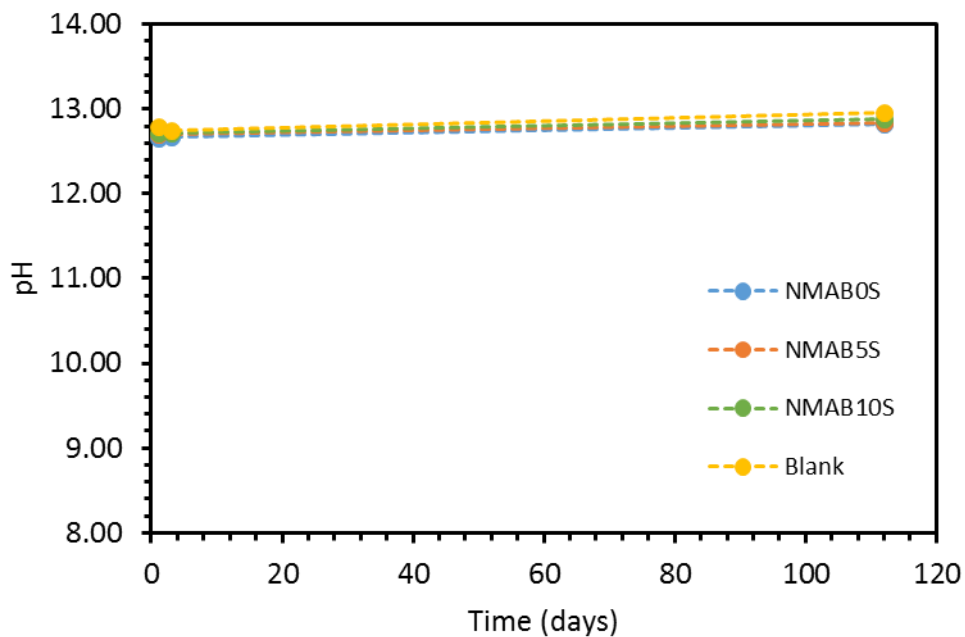
Figure 5.36. NL(Ca) for NCAB<sub>x</sub>S glasses for KOH PCT-B experiments.

#### 5.3.2.4 NMAB<sub>x</sub>S Glasses

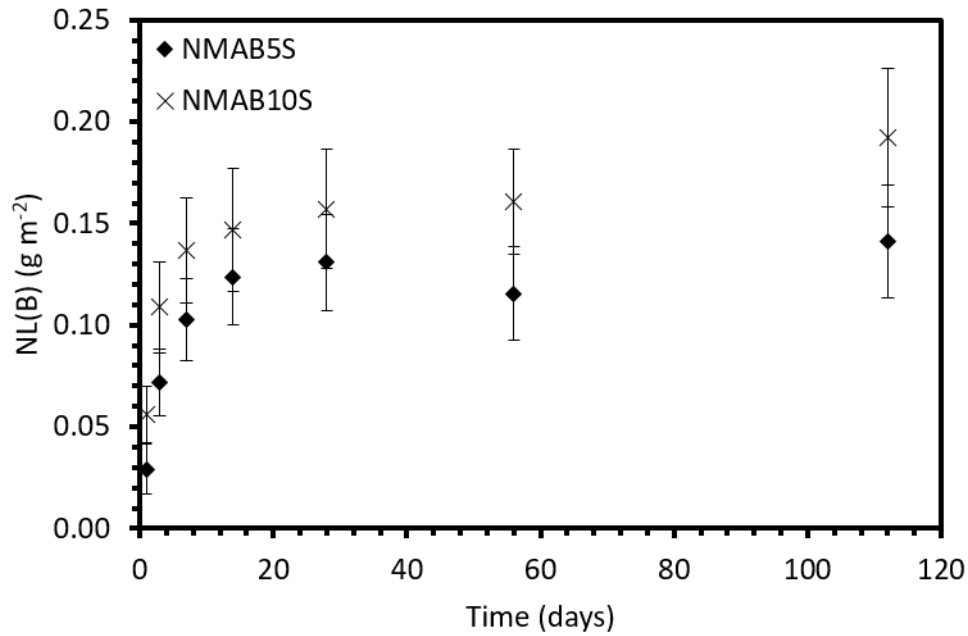
Figure 5.37 shows the pH values for the NMAB<sub>x</sub>S leachates. The blanks remained consistent, with an initial average of 12.80, and a final average of 12.96. Similarly, the NMAB0S, NMAB5S and NMAB10S samples maintained a high pH through the duration of the experiments, with respective initial values of 12.66, 12.70 and 12.72, and final values of 12.83, 12.84 and 12.89. Figure 5.38 shows the NL(B) data for the NMAB<sub>x</sub>S glasses (excluding NMAB0S which contains no boron) from 112-day PCT-B experiments using a KOH leachant. Initial and residual rates of B loss can be found in Table 5.8. The initial B loss rates for NMAB5S and NMAB10S were  $0.024 \pm 0.001$  and  $0.056 \pm 0.003 \text{ g m}^{-2} \text{ d}^{-1}$ , respectively. The data displayed the same turnover in mass loss rate as is seen in the other glasses, which occurred between 3 and 14 days for both glasses. NMAB10S had consistently higher NL(B) across all time-points, with a value after 112 days of  $0.19 \pm 0.03 \text{ g m}^{-2}$ , compared to  $0.14 \pm 0.03 \text{ g m}^{-2}$  for NMAB5S. NMAB10S also had a higher  $R_r(\text{B})$  at  $(4.0 \pm 0.2) \times 10^{-4} \text{ g m}^{-2} \text{ d}^{-1}$ , compared to  $(1.0 \pm 0.1) \times 10^{-4} \text{ g m}^{-2} \text{ d}^{-1}$  for NMAB5S. The normalised mass loss of silicon for the NMAB<sub>x</sub>S glasses is shown in Figure 5.39. The general trend of each of the glasses was similar; a high initial release rate –  $0.026 \pm 0.001$ ,  $0.035 \pm 0.001$  and  $0.056 \pm 0.003 \text{ g m}^{-2} \text{ d}^{-1}$  for NMAB0S, NMAB5S and NMAB10S, respectively – followed by a significant reduction between 3 and 14 days, leading to continued mass loss at a much lower rate than the initial rate after 28 days. NMAB10S had the highest NL(Si) at each sampling time, with NMAB5S having the second highest and NMAB0S the lowest. The final values of NL(Si) were  $0.15 \pm 0.03$ ,  $0.13 \pm 0.02$  and  $0.12 \pm 0.02 \text{ g m}^{-2}$ , and the  $R_r(\text{Si})$  values were  $(3.0 \pm 0.2) \times 10^{-4}$ ,  $(3.0 \pm 0.2) \times 10^{-4}$  and  $(3.0 \pm 0.2) \times 10^{-4}$ , for NMAB10S, NMAB5S and NMAB0S, respectively.

Figure 5.40 shows the NL(Na) values for the NMAB<sub>x</sub>S glasses. The general trend for each of the glasses follows those seen in the NL(B) and NL(Si) data. The initial Na loss rates were  $0.023 \pm 0.001$ ,  $0.026 \pm 0.001$  and  $0.034 \pm 0.002 \text{ g m}^{-2} \text{ d}^{-1}$  for NMAB0S, NMAB5S and NMAB10S, respectively, and the corresponding residual rates of release were  $(-2.0 \pm 0.1) \times 10^{-6}$ ,  $(3.0 \pm 0.2) \times 10^{-4}$  and  $(3.0 \pm 0.2) \times 10^{-4} \text{ g m}^{-2} \text{ d}^{-1}$ . The negative residual rate calculated for NMAB0S is unlikely to be significant as a positive value can be obtained from the data within error. Again, NMAB0S had the lowest NL(Na), followed by NMAB5S and NMAB10S, with final values of  $0.13 \pm 0.05$ ,  $0.16 \pm 0.05$  and  $0.17 \pm 0.05 \text{ g m}^{-2}$ , respectively. Figure 5.41 shows the normalised mass loss of aluminium for the three glasses. While the data exhibited the same overall

trends as in the NL(B) and NL(Si) data – high initial dissolution followed by a rate drop – the trends between the samples were reversed, i.e. NMAB0S had the highest NL(Al) and NMAB10S had the lowest. The  $R_0(\text{Al})$  values were  $0.020 \pm 0.001$ ,  $0.025 \pm 0.001$  and  $0.031 \pm 0.002 \text{ g m}^{-2} \text{ d}^{-1}$  for NMAB0S, NMAB5S and NMAB10S, respectively, whilst the  $R_r(\text{Al})$  values were  $(7.0 \pm 0.4) \times 10^{-5}$ ,  $(1.0 \pm 0.1) \times 10^{-4}$  and  $(3.0 \pm 0.2) \times 10^{-5} \text{ g m}^{-2} \text{ d}^{-1}$ . The final values of NL(Al) were  $0.104 \pm 0.017$ ,  $0.096 \pm 0.016$  and  $0.076 \pm 0.013 \text{ g m}^{-2}$  for NMAB0S, NMAB5S and NMAB10S, respectively. Figure 5.42 shows the NL(Mg) values for the NMAB $x$ S glasses. As with the Mg-containing borosilicate glasses, the magnesium mass loss was very low; below the detection limit for the ICP-OES for most of the data, which suggests that the magnesium leached from the glasses was incorporated into alteration phases during dissolution.



**Figure 5.37.** pH values for KOH PCT-B experiments on NMAB $x$ S glasses.



**Figure 5.38.** NL(B) for NMAB<sub>x</sub>S glasses for KOH PCT-B experiments.

**Table 5.8.** Initial ( $R_0(i)$ ) and residual ( $R_r(i)$ ) normalised mass loss rates for B, Na, Al and Si for the NMAB<sub>x</sub>S glasses in KOH.

Rate (g m <sup>-2</sup> d <sup>-1</sup> )	NMAB0S	NMAB5S	NMAB10S
$R_0(B)$	-	$0.024 \pm 0.001$	$0.056 \pm 0.003$
$R_r(B)$	-	$(1.0 \pm 0.1) \times 10^{-4}$	$(4.0 \pm 0.2) \times 10^{-4}$
$R_0(Na)$	$0.023 \pm 0.001$	$0.026 \pm 0.001$	$0.034 \pm 0.002$
$R_r(Na)$	$(-2.0 \pm 0.1) \times 10^{-6}$	$(3.0 \pm 0.2) \times 10^{-4}$	$(3.0 \pm 0.2) \times 10^{-4}$
$R_0(Al)$	$0.020 \pm 0.001$	$0.025 \pm 0.001$	$0.031 \pm 0.002$
$R_r(Al)$	$(7.0 \pm 0.4) \times 10^{-5}$	$(1.0 \pm 0.1) \times 10^{-4}$	$(3.0 \pm 0.2) \times 10^{-5}$
$R_0(Si)$	$0.026 \pm 0.001$	$0.035 \pm 0.001$	$0.056 \pm 0.003$
$R_r(Si)$	$(3.0 \pm 0.2) \times 10^{-4}$	$(3.0 \pm 0.2) \times 10^{-4}$	$(3.0 \pm 0.2) \times 10^{-4}$

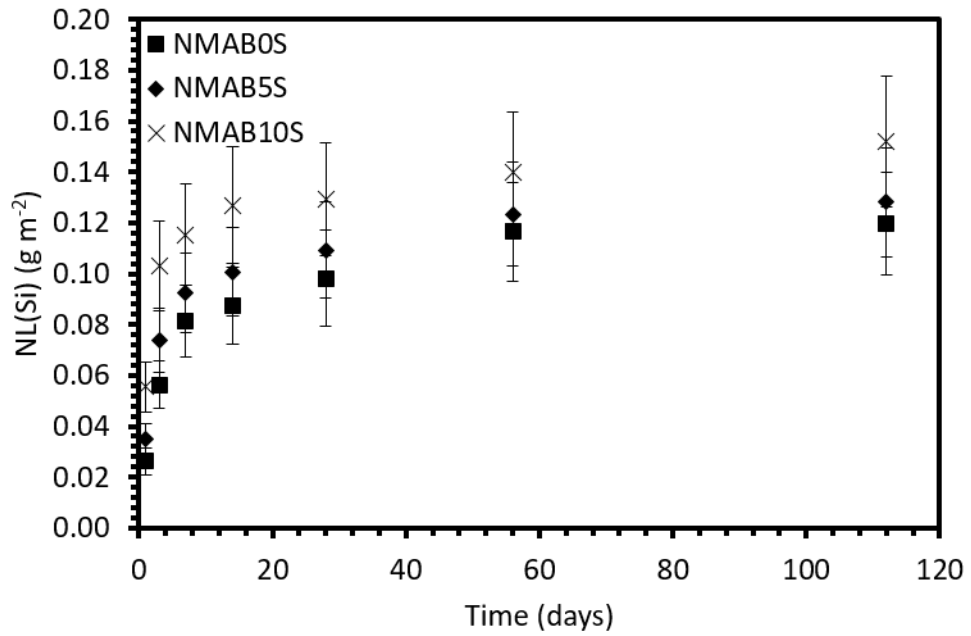


**Figure 5.39.** NL(Si) for NMAB<sub>x</sub>S glasses for KOH PCT-B experiments.

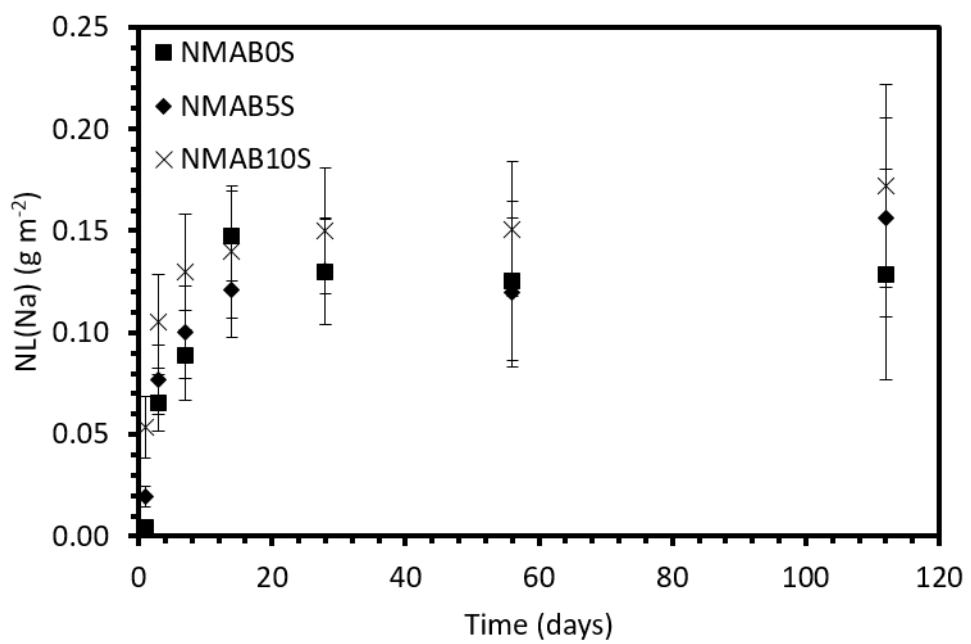


**Figure 5.40.** NL(Na) for NMAB<sub>x</sub>S glasses for KOH PCT-B experiments.

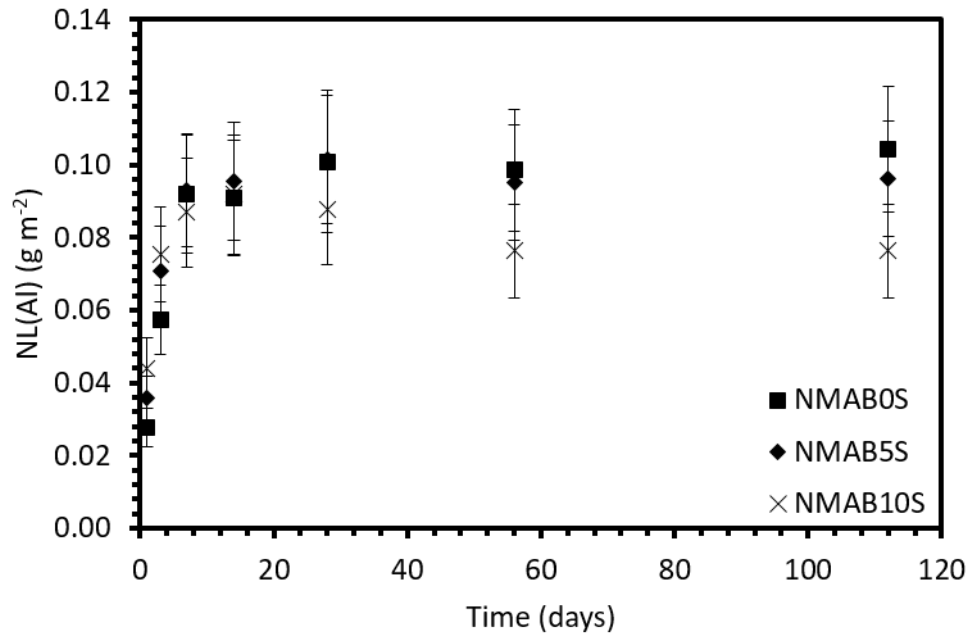


**Figure 5.41.** NL(Al) for NMAB<sub>x</sub>S glasses for KOH PCT-B experiments.

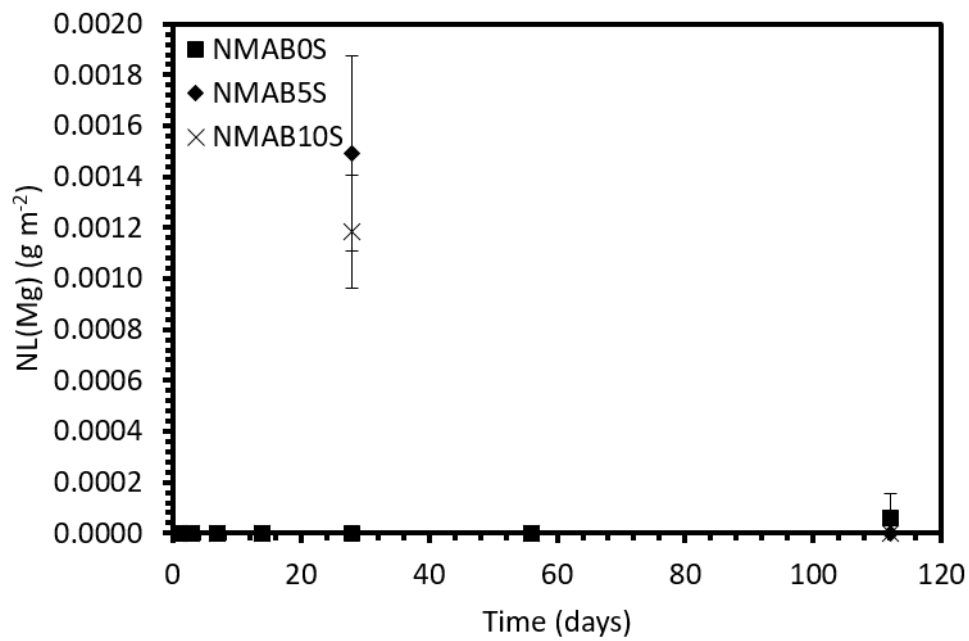


**Figure 5.42.** NL(Mg) for NMAB<sub>x</sub>S glasses for KOH PCT-B experiments.

## 5.4 Analysis of Alteration Product Formation

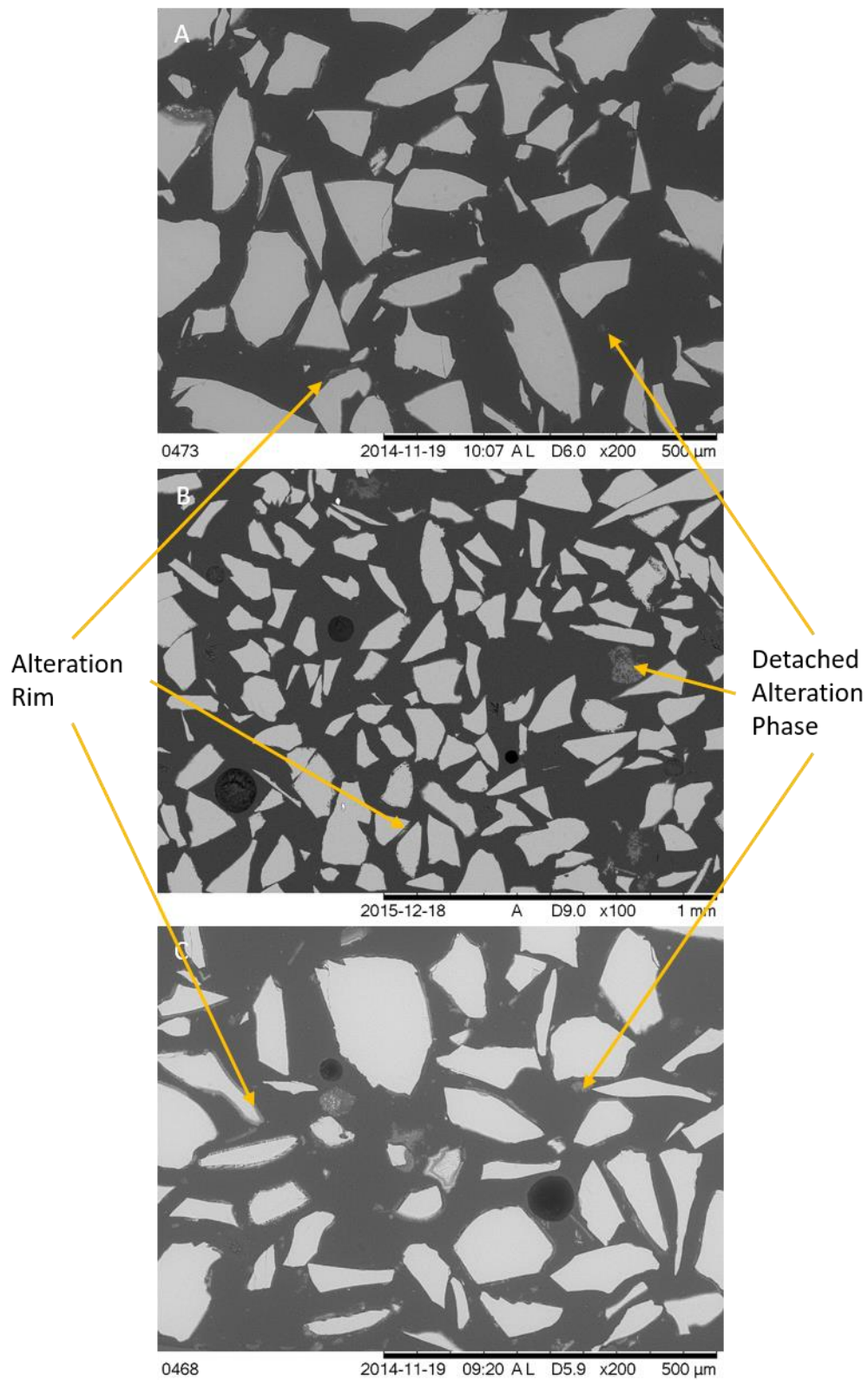
### 5.4.1 Ca(OH)<sub>2</sub>-leached Samples

#### 5.4.1.1 NC<sub>x</sub>BS Glasses

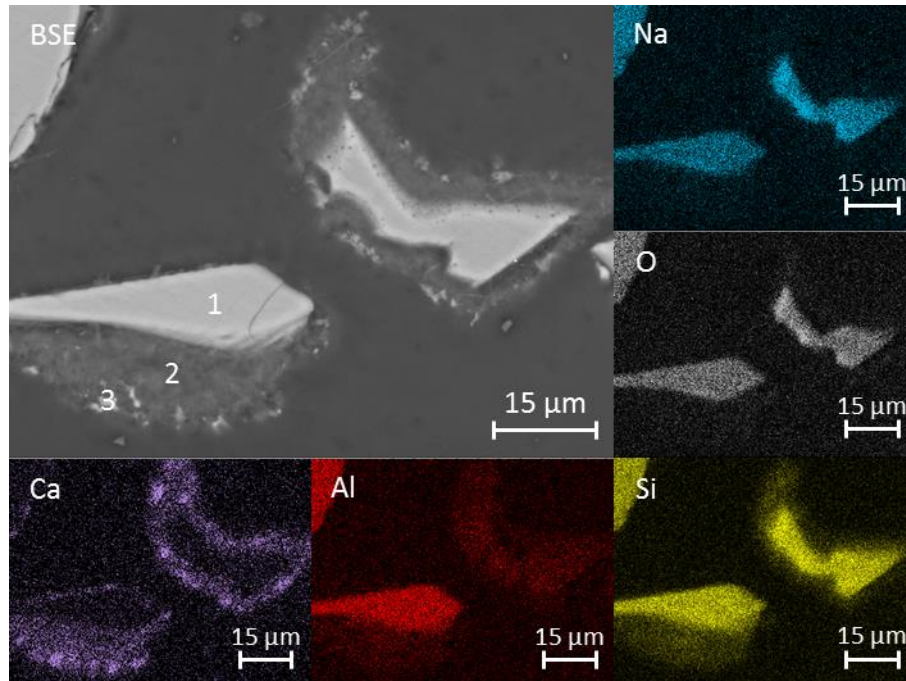
Figure 5.43 shows backscattered electron (BSE) images of cross-sectioned NC0BS, NC5BS and NC10BS glass particles which have undergone a PCT-B experiment with a Ca(OH)<sub>2</sub> leachant. Alteration layers can be seen in the form of ‘rims’ around the particles, and detached alteration phases, likely resulting from post-experiment handling, can also be observed. This is a phenomenon that was seen in the majority of the post-PCT-B powders analysed by SEM-EDS. EDS maps for the altered NC0BS particles are shown in Figure 5.44. The lighter region, denoted region ‘1’, is the glass particle, the dark region is the resin mounting and the middle region, denoted region ‘2’, is the alteration layer which formed during the PCT-B experiment. These data show that the glass phase corresponds to enrichment in Na, Si and O, and an absence of Ca. The alteration layer is rich in Ca, whilst also containing Si and Al, with a small amount of O and Na. There appear to be two distinct phases within the alteration layer: a brighter, Ca-rich phase, and a darker Ca-poor phase. This is evidenced by the EDS spectra of the different regions, shown in Figure 5.45.

Figure 5.46 shows the EDS maps for one of the NC5BS particles at higher magnification. The glass particle (1) is bounded by an alteration rim (2); the EDS spectra for these regions are shown in Figure 5.47. As with the alteration layers on the NC0BS particles, the alteration layer here was rich in Ca, whilst also containing Si, and was poor in Na and O. The difference is in the lack of Al in the NC5BS glass. The alteration layer is richer in Ca than the NC5BS glass itself, suggesting that the Ca(OH)<sub>2</sub> solution is the primary source of Ca for the alteration layer.

Elemental maps of one of the NC10BS particles are shown in Figure 5.48, and spectra for the glass and the alteration layer are shown in Figure 5.49. The alteration layer was rich in Ca and also contained Si, but was poor in Na and O, in keeping with the observations of the other NC<sub>x</sub>BS glasses. The alteration layer is enriched in Ca with respect to the particle, suggesting again that the solution is the primary source of Ca in the alteration layer, despite the glass containing 10.59 mol.% CaO.



**Figure 5.43.** BSE images of cross-sectioned NCxBS glass particles after a 112-day PCT-B experiment in  $\text{Ca}(\text{OH})_2$  (A) NC0BS, (B) NC5BS, (C) NC10BS.



**Figure 5.44.** BSE micrograph and elemental maps of NCOBS particles cross-section after a 112-day PCT-B experiment in  $\text{Ca}(\text{OH})_2$ , showing particle itself (point 1) and an alteration layer (2) with Ca-rich regions (3).

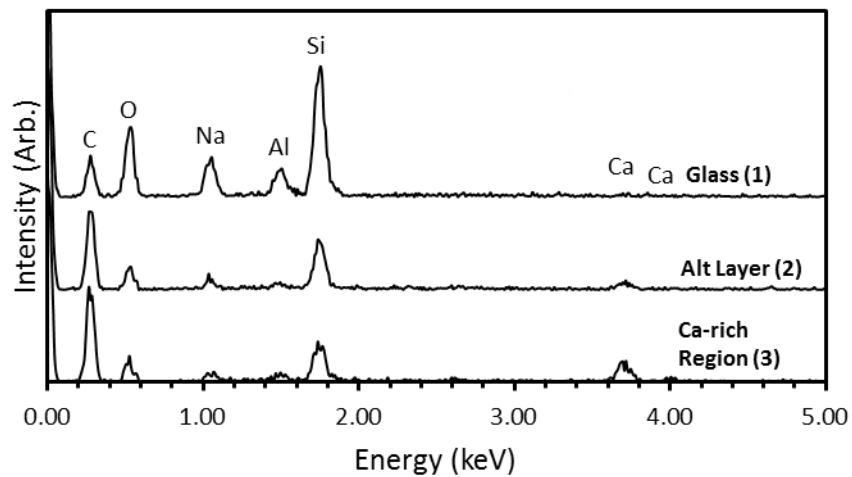


**Figure 5.45.** EDS spectra of NCOBS glass and alteration layer (with Ca-rich regions) after a 112-day PCT-B experiment in  $\text{Ca}(\text{OH})_2$ .

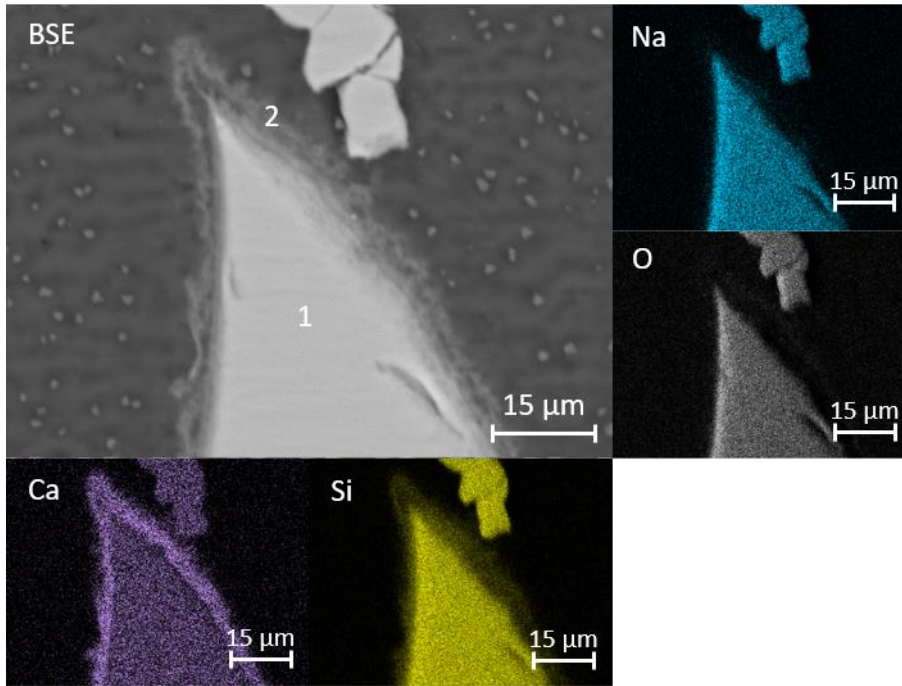


**Figure 5.46.** BSE micrograph and elemental maps of cross-sectioned NC5BS particle (1) after a 112-day PCT-B experiment in  $\text{Ca}(\text{OH})_2$ , showing alteration layer (2).

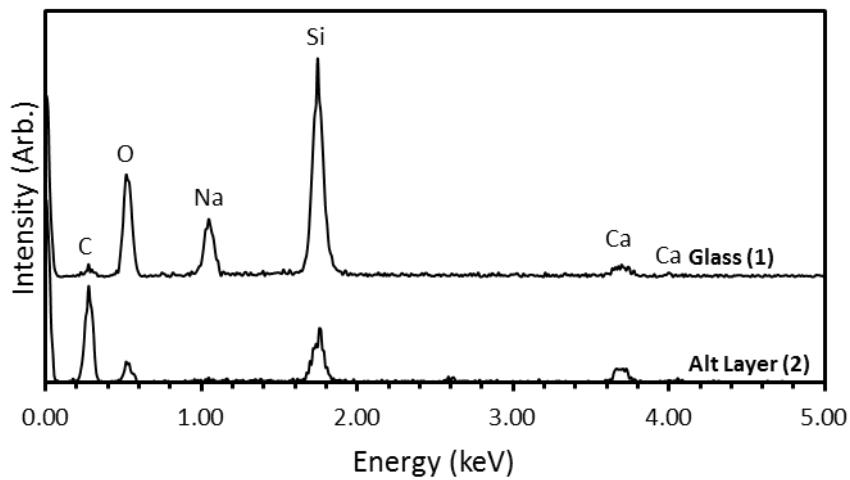


**Figure 5.37.** EDS spectra of NC5BS glass and alteration layer after a 112-day PCT-B experiment in  $\text{Ca}(\text{OH})_2$ .

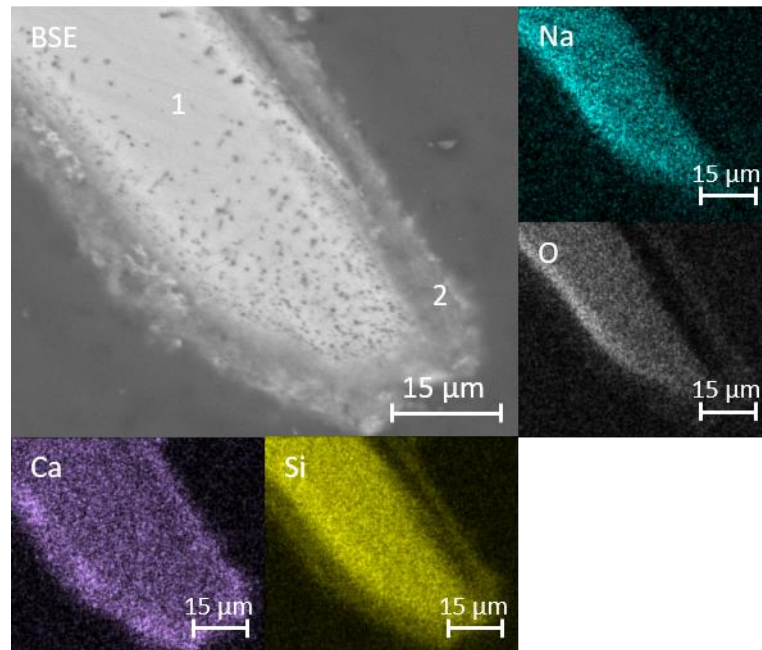


**Figure 5.48.** BSE micrograph and elemental maps of cross-sectioned NC10BS particle (1) after a 112-day PCT-B experiment in  $\text{Ca}(\text{OH})_2$ , showing alteration layer (2).

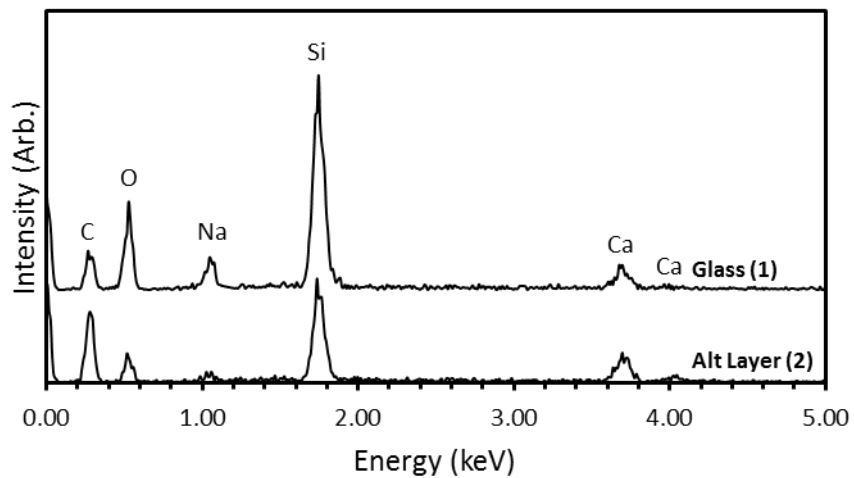
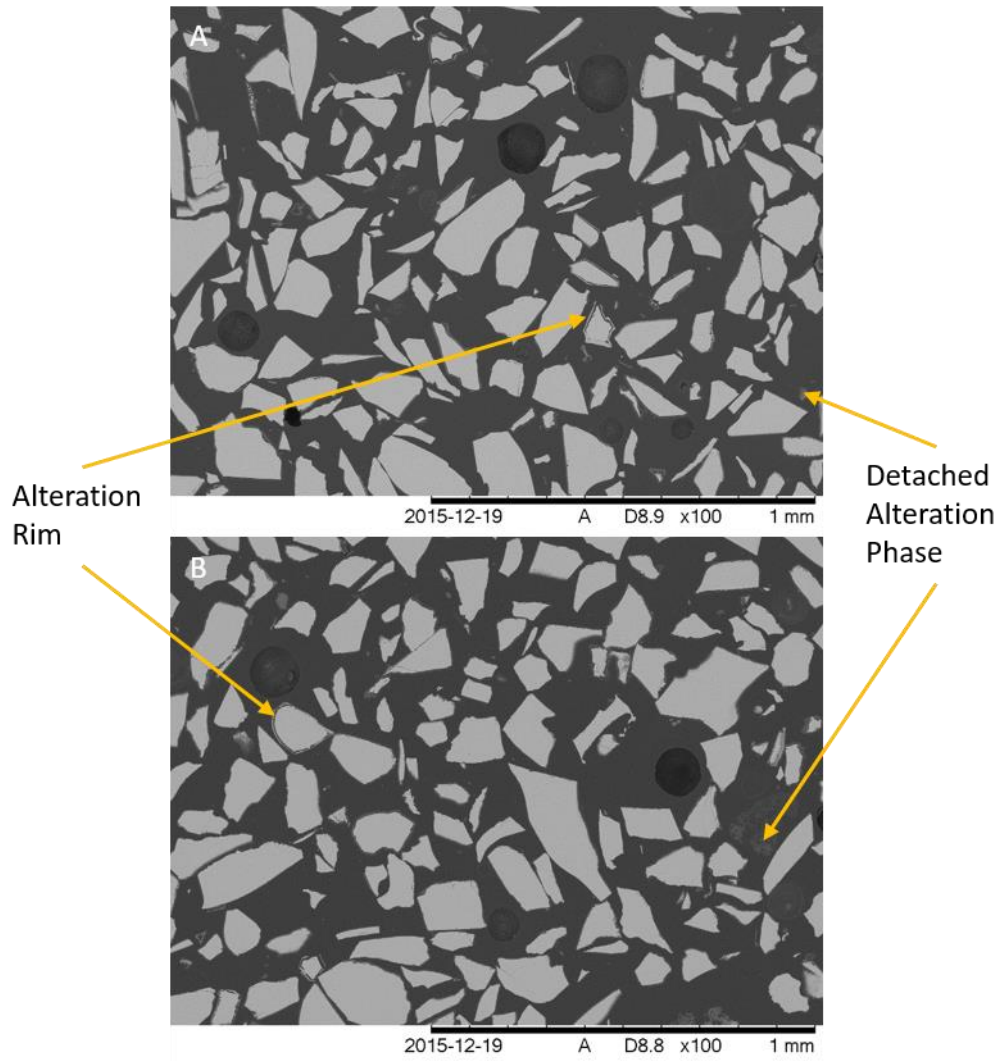


**Figure 5.49.** EDS spectra of NC10BS glass and alteration layer after a 112-day PCT-B experiment in  $\text{Ca}(\text{OH})_2$ .

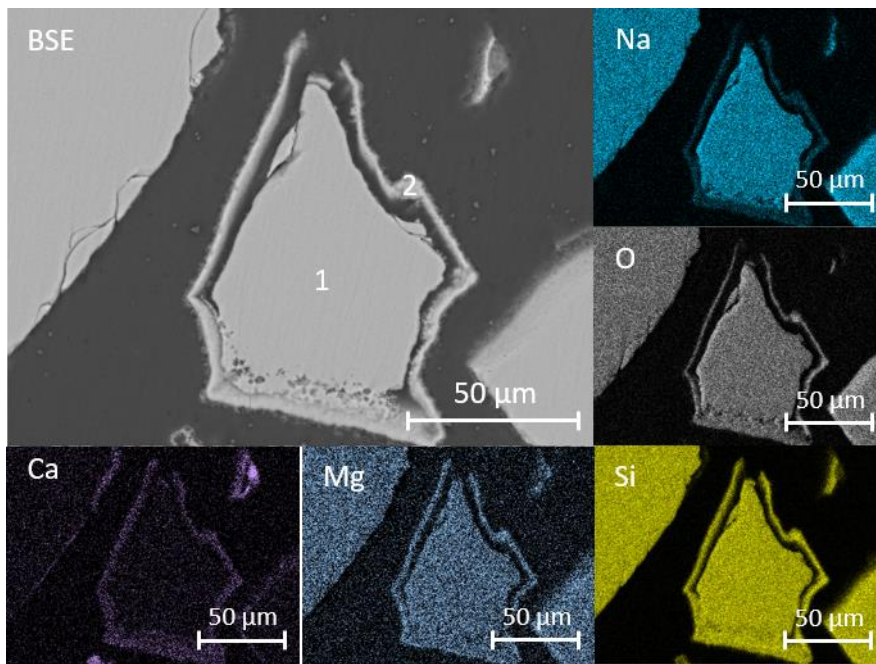
#### 5.4.1.2 NM<sub>x</sub>BS Glasses

Figure 5.50 shows BSE images of particles of NM<sub>x</sub>BS glasses altered in Ca(OH)<sub>2</sub>. Alteration rims were seen around many of the particles, with detached alteration phases also visible. Figure 5.51 shows EDS maps of an NM5BS particle at higher magnification. The alteration layer contained Ca, Mg, Si, O and Na. With respect to the glass particle, it was enriched in Ca and Mg, and depleted in Na (Figure 5.52). The only source of Ca in the alteration layer was the Ca(OH)<sub>2</sub> solution. The amount of Si in the alteration layer compared to that of the glass appeared to be higher than for the NC<sub>x</sub>BS glasses. The alteration layer was enriched in Mg compared to the glass, suggesting that the Mg that was leached was retained in the alteration layer, as also suggested by the low NL(Mg) levels for all Mg-containing glasses.

Figure 5.53 shows EDS maps of several of these particles and a piece of detached alteration phase (point 3). The alteration layer (point 2) contained Ca, Mg, Si, Na and O. With respect to the glass particle, the alteration layer was enriched in Ca, slightly depleted in Si and Mg, and significantly depleted in Na and O, as shown by the EDS spectra in Figure 5.54. The ratio of Mg in the alteration layer *versus* the Mg in the glass again suggests that most of the Mg was retained in the alteration layer, as with NM10BS. The detached alteration phase primarily consisted of Ca and Si, with significant Ca-enrichment compared to the glass and alteration layer.



**Figure 5.50.** BSE images of cross-sectioned  $\text{NM}_x\text{BS}$  glass particles after a 112-day PCT-B experiment in  $\text{Ca}(\text{OH})_2$  (A) NM5BS, (B) NM10BS.



**Figure 5.51.** BSE micrograph and elemental maps of cross-sectioned NM5BS particle (1) after a 112-day PCT-B experiment in  $\text{Ca}(\text{OH})_2$ , showing alteration layer (2).

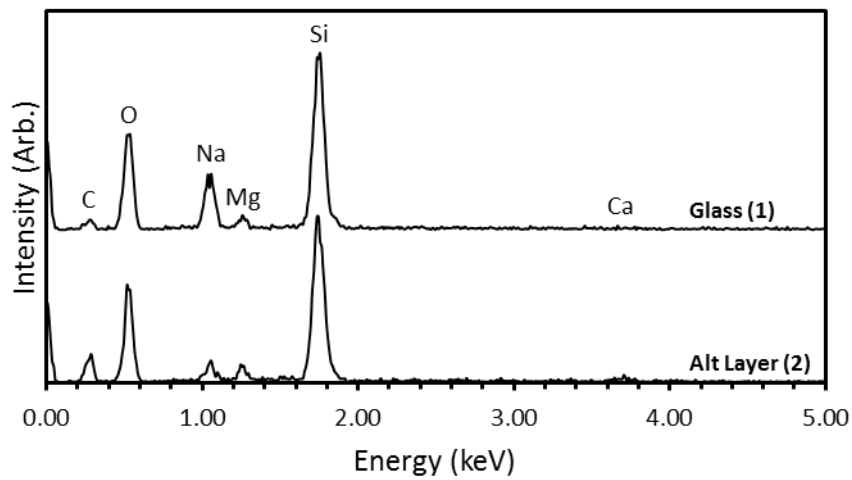


**Figure 5.52.** EDS spectra of NM5BS glass and alteration layer after a 112-day PCT-B experiment in  $\text{Ca}(\text{OH})_2$ .

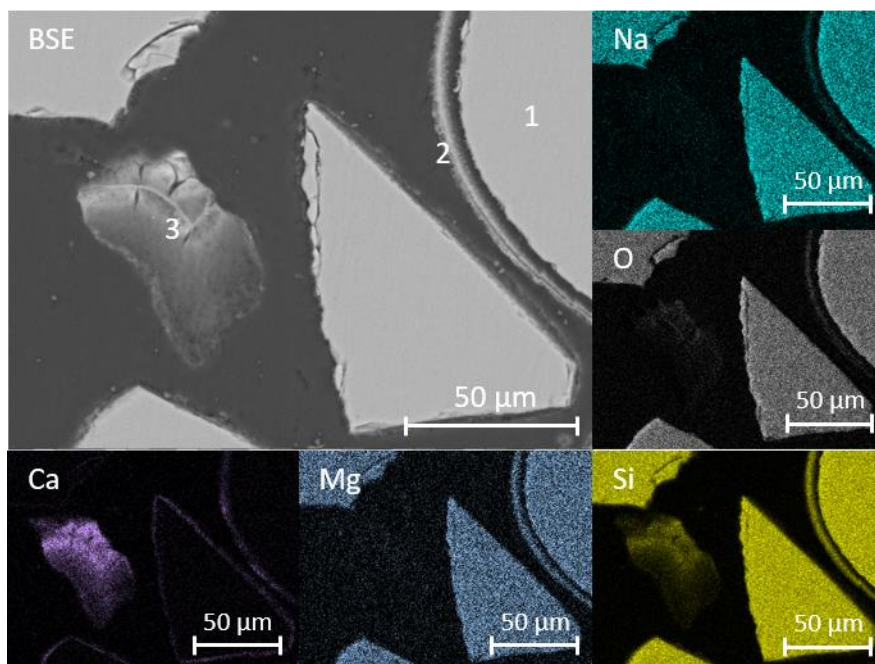


**Figure 5.53.** BSE micrograph and elemental maps of cross-sectioned NM10BS particle (1) after a 112-day PCT-B experiment in  $\text{Ca}(\text{OH})_2$ , showing alteration layer (2). A detached alteration phase can also be seen (3).

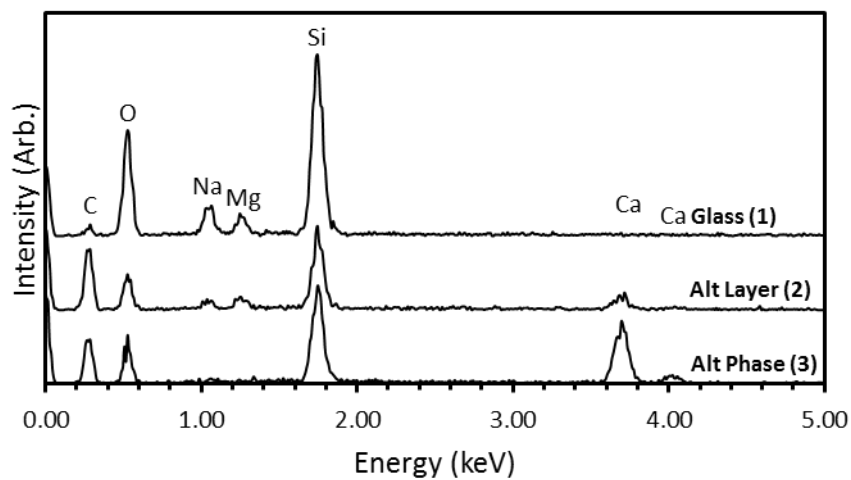


**Figure 5.54.** EDS spectra of NM5BS glass, alteration layer and detached alteration phase after a 112-day PCT-B experiment in  $\text{Ca}(\text{OH})_2$ .

#### 5.4.1.3 NCAB<sub>x</sub>S Glasses

BSE images of cross-sectioned NCAB<sub>x</sub>S particles which have undergone a PCT-B experiment with a Ca(OH)<sub>2</sub> leachant are shown in Figure 5.55. Detached alteration phases can be seen in these samples. Although alteration rims are not readily visible in Figure 5.55, they are readily visible in the higher magnification micrographs; Figures 5.56, 5.58 and 5.60. Figure 5.56 shows EDS maps of a cluster of several NCAB0S particles and a detached alteration phase. The maps suggest that small alteration layers were formed around some of the particles, primarily containing Ca and Si, with a minor amount of Al. The detached phase contained significantly more Ca than the alteration layer, as well as Si, Al and a small, but detectable, amount of Mg, per EDS spot analysis (Figure 5.57). The alteration layers were much less pronounced than for the NC<sub>x</sub>BS and NM<sub>x</sub>BS glasses.

A greater number of particles in the NCAB5S sample appeared to have alteration rims than for the NCAB0S glass, which could be due to the higher rate of dissolution; higher rates of dissolution are likely to lead to greater concentrations of alteration layer-forming elements, such as Si, in solution. The EDS maps in Figure 5.58 show that the alteration layer primarily consisted of Ca and Si, with Al and O. In comparison to the glass, the alteration layer is rich in Ca, but poor in the other 4 elements, as seen in the EDS spectra of the different phases in Figure 5.59. The detached alteration phase (3) consists of Ca and Si, with small amounts of Al and Mg, in line with the composition of the similar phase in the NCAB0S sample.

Alteration rims can be seen on many of the cross-sectioned altered NCAB10S particles in Figure 5.55, more so than on either the NCAB0S or NCAB5S particles. The elemental maps of one of these particles (Figure 5.60) show that the rim contained Ca, Si, Al and O, which is in line with what was seen for the NCAB0S and NCAB5S glasses. The EDS spectra of the glass and alteration layer (Figure 5.61) confirm this.

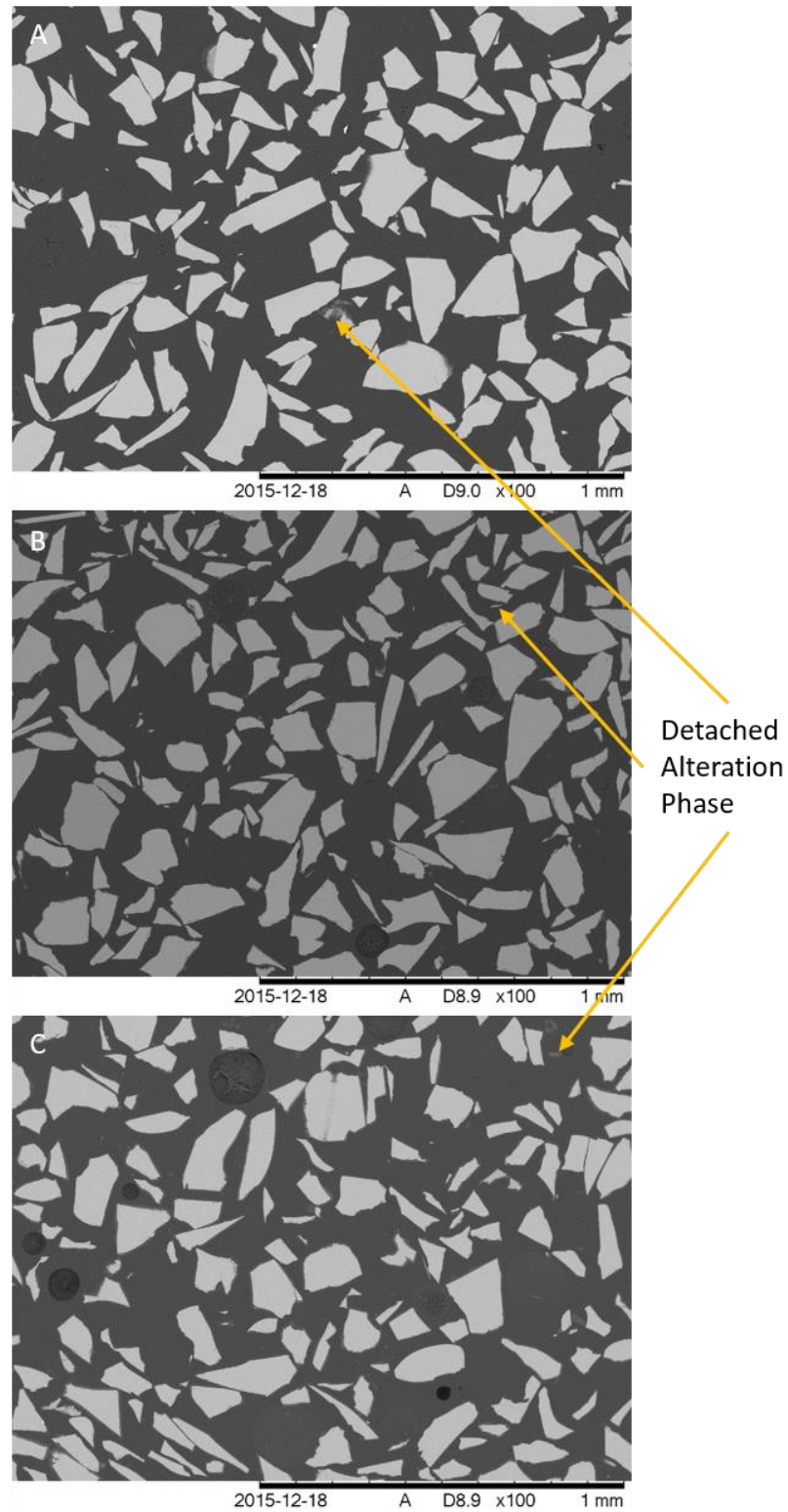


**Figure 5.55.** BSE images of cross-sectioned NCAB<sub>x</sub>S glass particles after a 112-day PCT-B experiment in Ca(OH)<sub>2</sub> (A) NCAB0S, (B) NCAB5S, (C) NCAB10S.

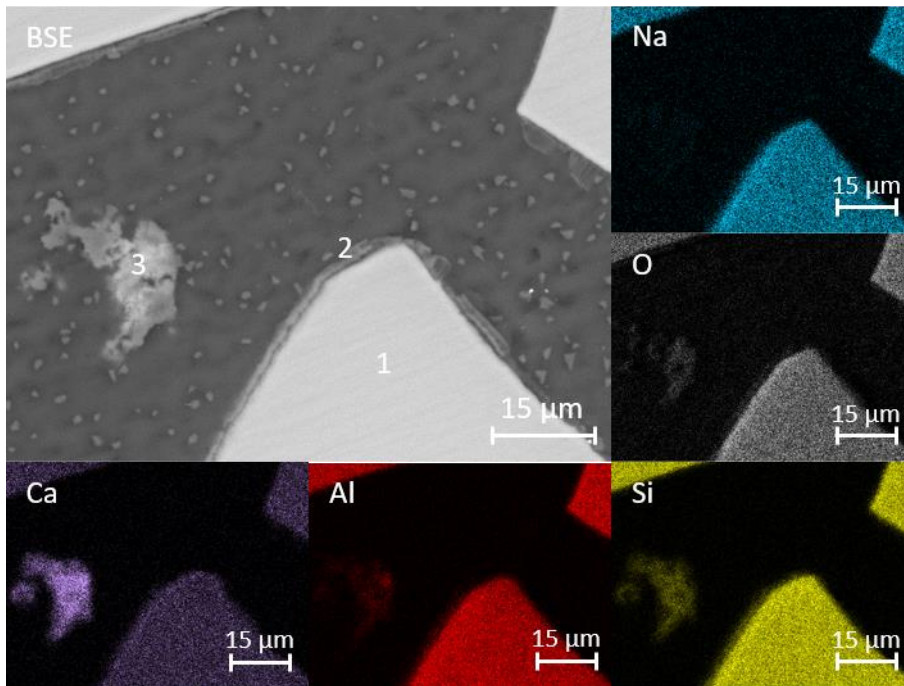


**Figure 5.56.** BSE micrograph and elemental maps of cross-sectioned NCABOS particles (1) after a 112-day PCT-B experiment in  $\text{Ca}(\text{OH})_2$ , showing alteration layer (2) and detached alteration phase (3).

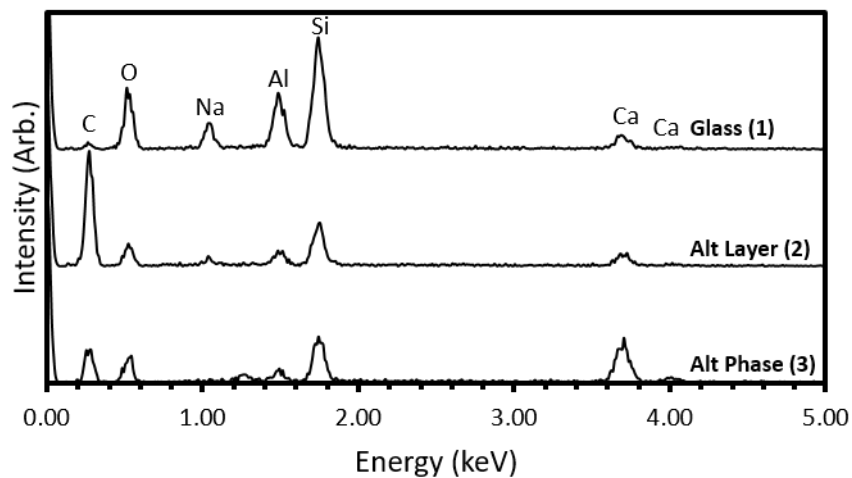


**Figure 5.57.** EDS spectra of NCABOS glass and alteration layer after a 112-day PCT-B experiment in  $\text{Ca}(\text{OH})_2$ .

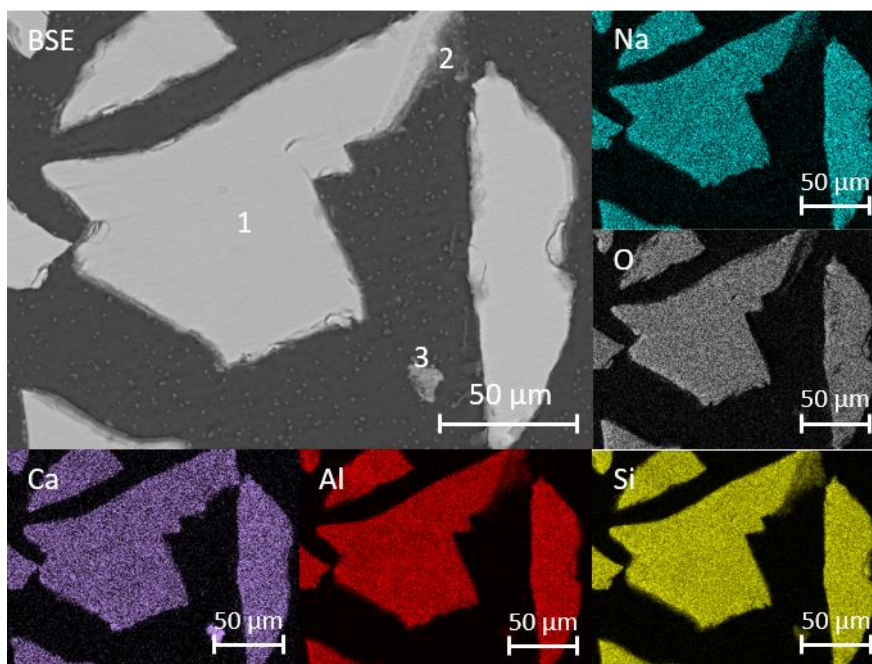


**Figure 5.58.** BSE micrograph and elemental maps of cross-sectioned NCAB5S particles (1) after a 112-day PCT-B experiment in  $\text{Ca}(\text{OH})_2$ , showing alteration layer (2). A detached alteration phase can also be seen (3).

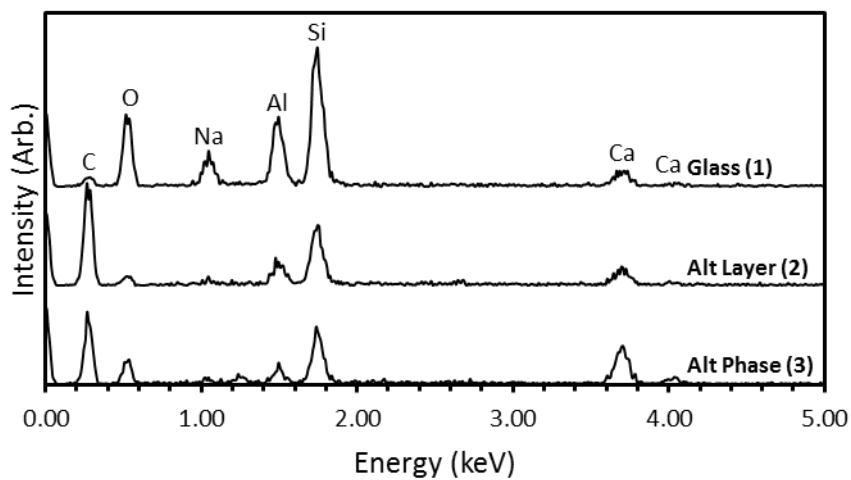


**Figure 5.59.** EDS spectra of NCAB5S glass, alteration layer and detached alteration phase after a 112-day PCT-B experiment in  $\text{Ca}(\text{OH})_2$ .

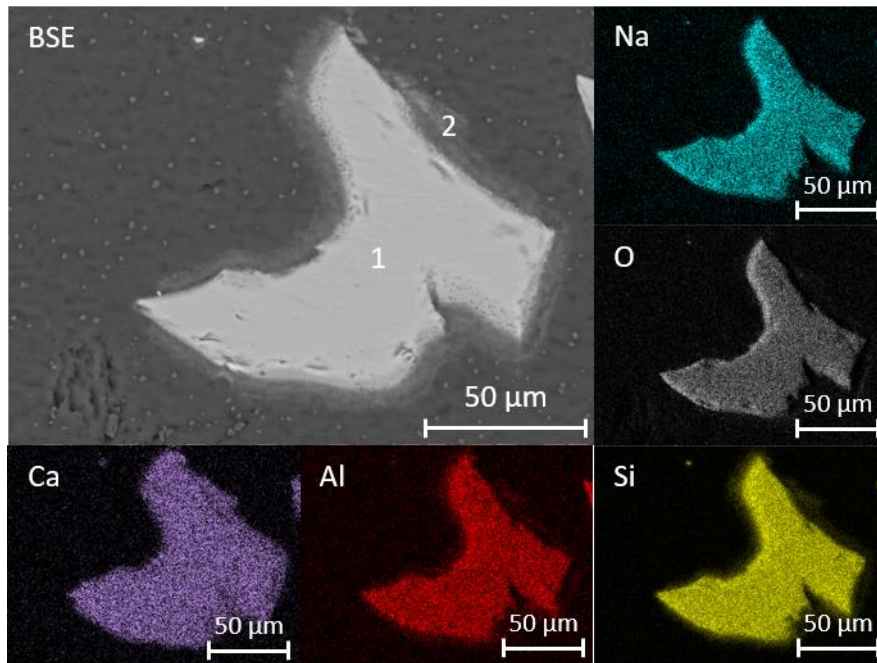


**Figure 5.60.** BSE micrograph and elemental maps of cross-sectioned NCAB10S particles (1) after a 112-day PCT-B experiment in  $\text{Ca}(\text{OH})_2$ , showing alteration layer (2).

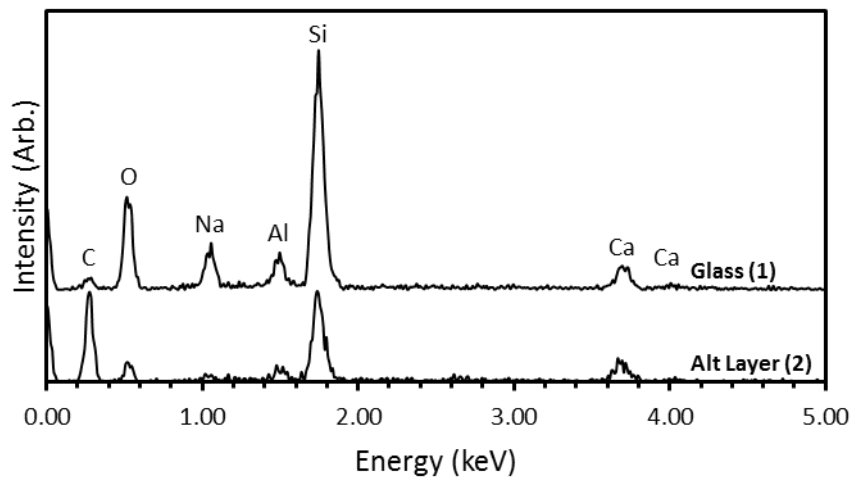


**Figure 5.61.** EDS spectra of NCAB10S glass and alteration layer after a 112-day PCT-B experiment in  $\text{Ca}(\text{OH})_2$ .

#### 5.4.1.3 NMABxS Glasses

Figure 5.62 shows cross-sectioned particles of NMABxS glasses which have been altered in  $\text{Ca}(\text{OH})_2$  for 112 days. Detached alteration phases can be seen in these samples. Alteration rims are not visible in the low magnification images, but are in the higher magnification images in Figures 5.63, 5.65 and 5.67. A BSE micrograph of one of the NMAB0S particles is shown in Figure 5.63. There was a small alteration rim around the particle, as well as a detached Ca- and Al-rich phase. The EDS spectra for these phases are shown in Figure 5.64.

A BSE micrograph and EDS maps of NMAB5S particles, showing alteration layers and detached alteration phases, are shown in Figure 5.65. As well as the alteration layer, which contains primarily Ca and Si with a small amount of Al, there were two distinct alteration phases: a Ca-Al phase (point 3); and a Ca-Si phase containing a significant amount of Mg (point 4). The Ca-Al phase appeared to be similar in morphology and composition to the Ca- and Al-rich phase observed on the NMAB0S sample. The EDS spectra for each of these phases, as well as the glass and alteration layer, are shown in Figure 5.66.

The alteration rims and detached alteration phases on the NMAB10S particles can be seen in more detail in the micrograph and EDS maps shown in Figure 5.67. Three different alteration phases were observed, characterised by their Mg content: a Ca-Si phase containing virtually no Mg (2); a phase containing an intermediate amount of Mg (3); and a phase containing a high amount of Mg (4). The EDS spectra for these phases and the glass are shown in Figure 5.68. Figure 5.69 shows a BSE micrograph of a Ca-Al phase similar to that observed in the NMAB0S and NMAB5S samples.

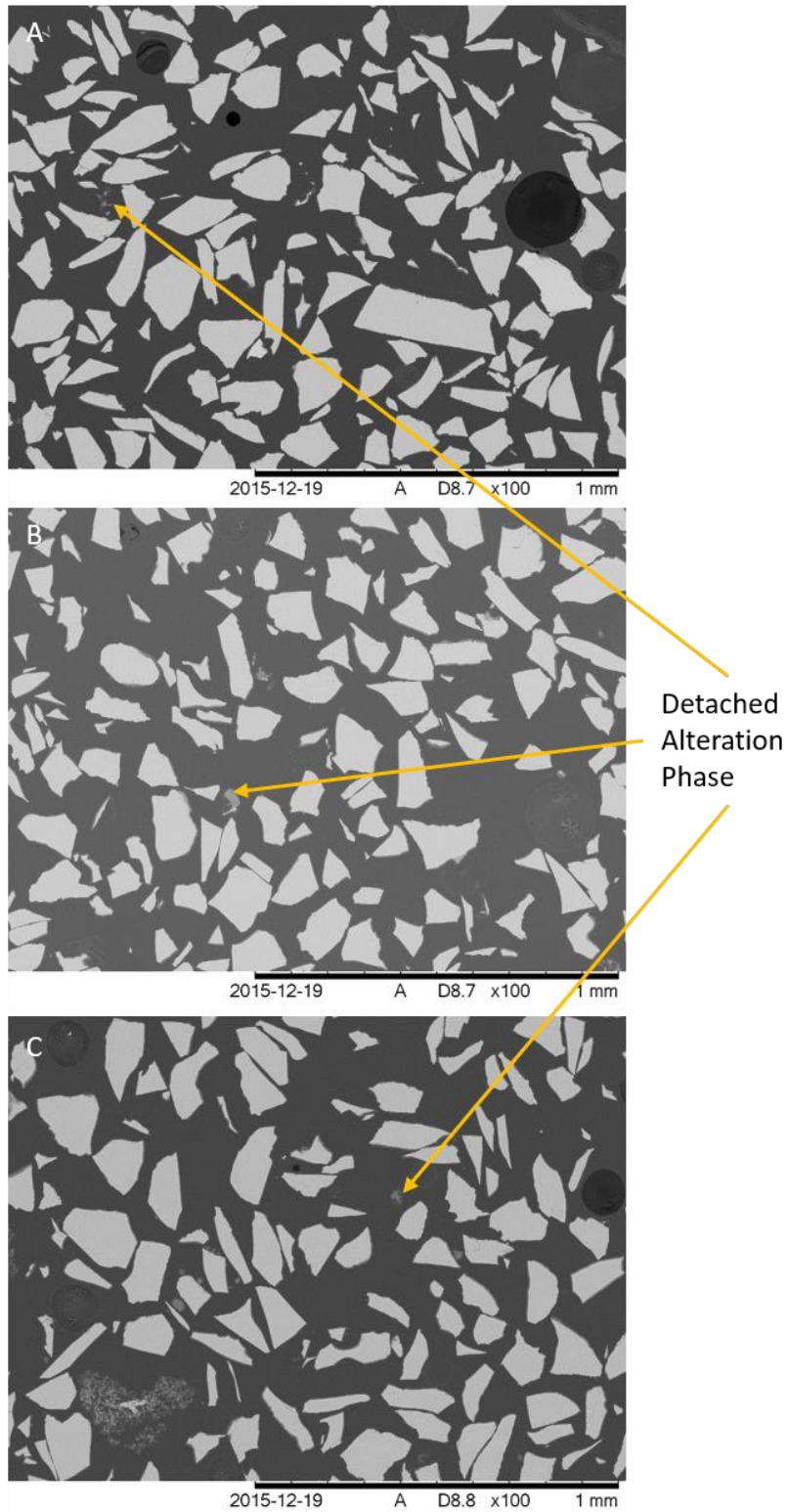


**Figure 5.62.** BSE images of cross-sectioned NMAB<sub>x</sub>S glass particles after a 112-day PCT-B experiment in Ca(OH)<sub>2</sub> (A) NMAB0S, (B) NMAB5S, (C) NMAB10S.

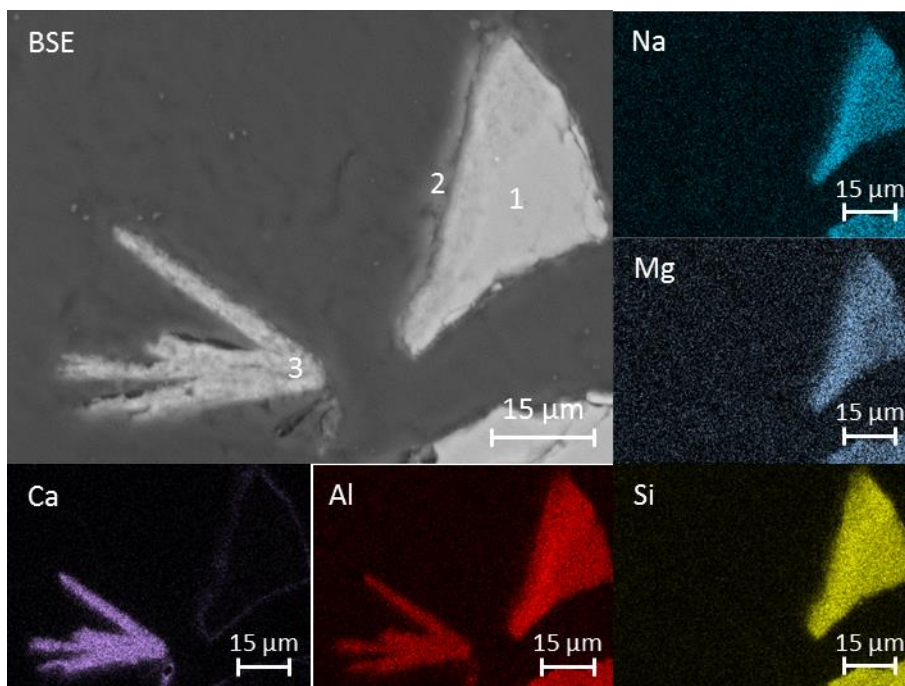


**Figure 5.63.** BSE micrograph and elemental maps of cross-sectioned NMABOS particles (1) after a 112-day PCT-B experiment in  $\text{Ca}(\text{OH})_2$ , showing alteration layer (2), and a detached alteration phase (3).

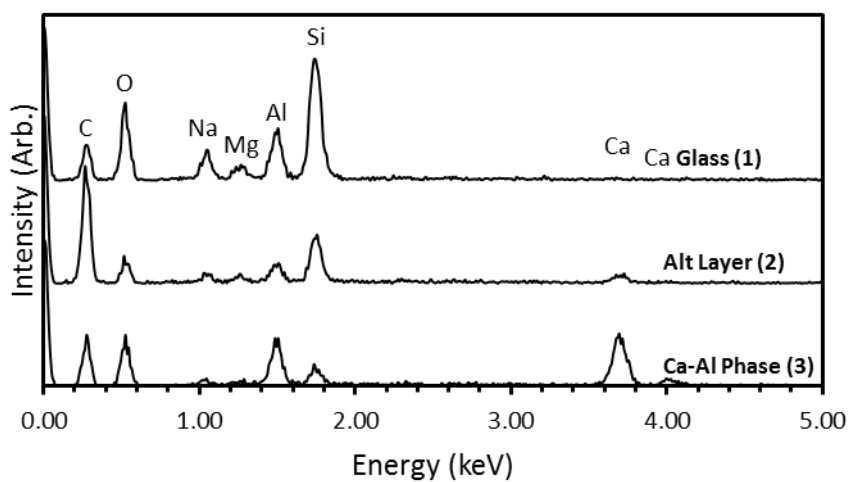


**Figure 5.64.** EDS spectra of NMABOS glass, alteration layer and alteration phase after a 112-day PCT-B experiment in  $\text{Ca}(\text{OH})_2$ .

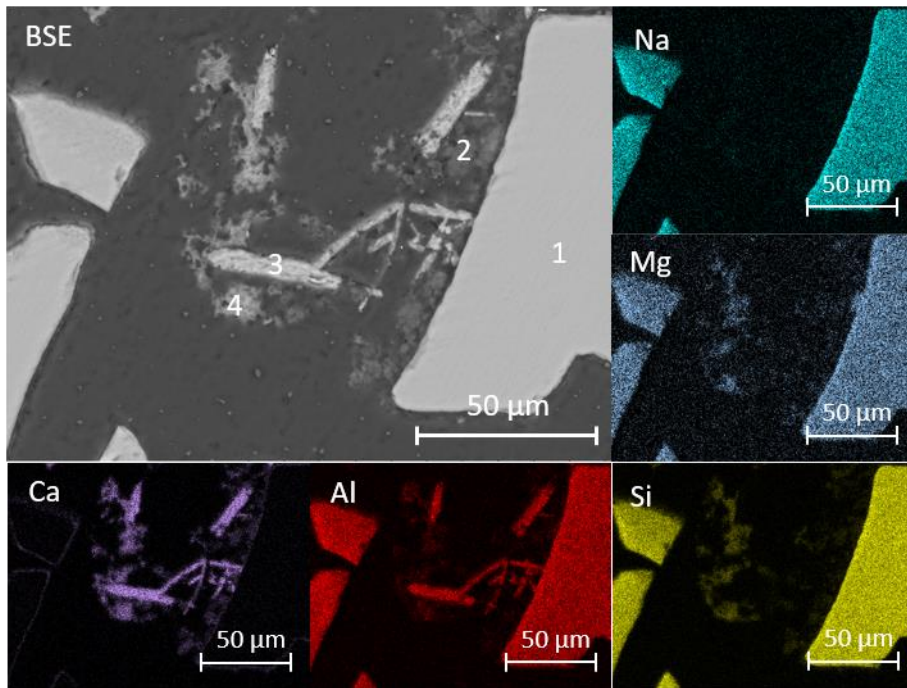


**Figure 5.65.** BSE micrograph and elemental maps of cross-sectioned NMAB5S particles (1) after a 112-day PCT-B experiment in  $\text{Ca}(\text{OH})_2$ , showing alteration layer (2), and detached alteration phases (3-4).

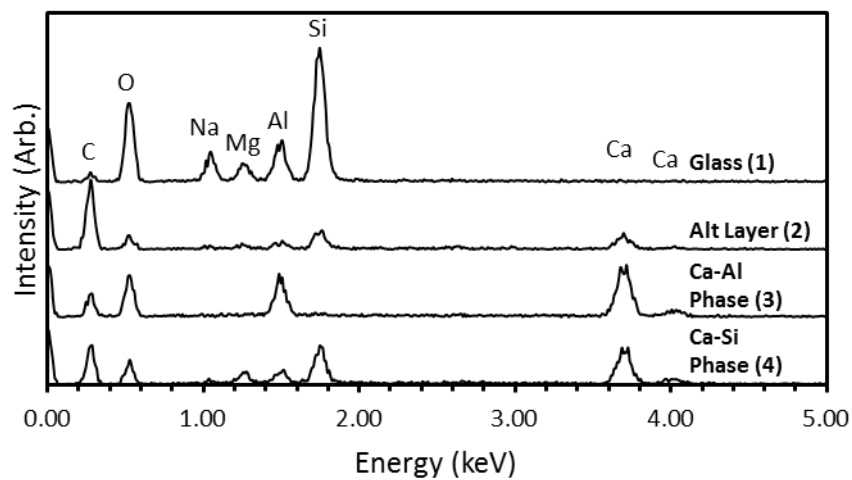


**Figure 5.66.** EDS spectra of NMAB5S glass and alteration products after a 112-day PCT-B experiment in  $\text{Ca}(\text{OH})_2$ .

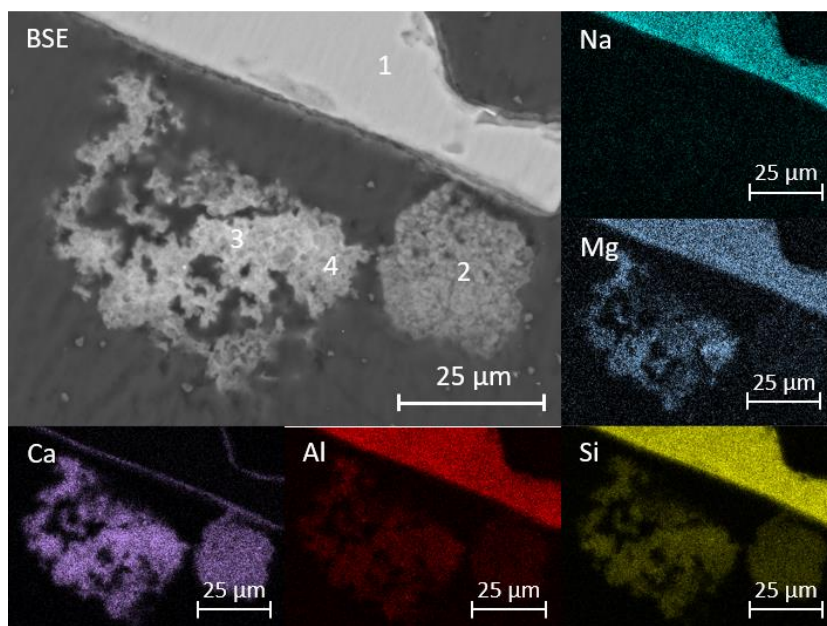


**Figure 5.67.** BSE micrograph and elemental maps of cross-sectioned NMAB10S particles (1) after a 112-day PCT-B experiment in  $\text{Ca}(\text{OH})_2$ , showing three alteration phases (2-4).

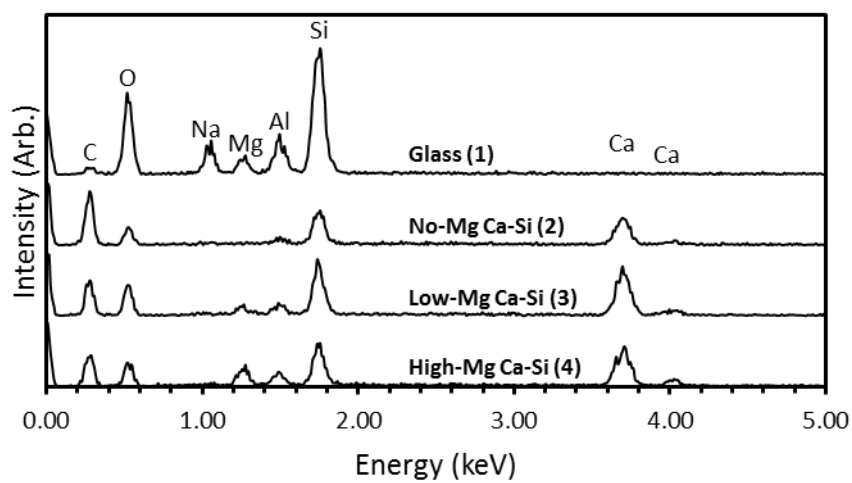


**Figure 5.68.** EDS spectra of NMAB10S glass and alteration products after a 112-day PCT-B experiment in  $\text{Ca}(\text{OH})_2$ .

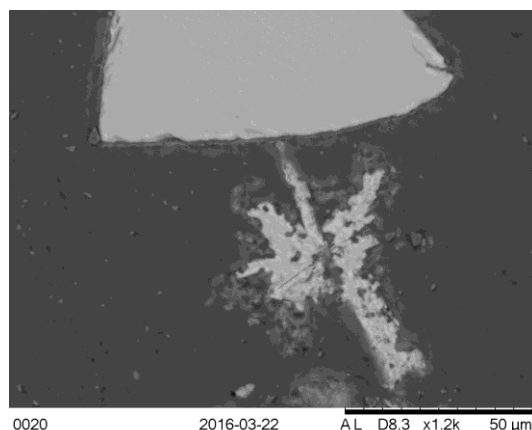


**Figure 5.69.** BSE image of Ca-Al phase observed in NMAB10S sample.

## 5.4.2 KOH-leached Samples

### 5.4.2.1 NCxBS Glasses

Figure 5.70 shows cross-sectioned particles of NC0BS, NC5BS and NC10BS that were leached in KOH for 112 days. Unlike the NC0BS and NC5BS particles leached in  $\text{Ca}(\text{OH})_2$ , no significant alteration layers were observed on these particles. However, alteration rims were observed on the NC10BS samples.

Although alteration rims were not visible on the NC5BS particles at lower magnification (Figure 5.70), at higher magnification they could be identified, as seen in Figure 5.71. The alteration rim primarily consisted of Ca, K and Si, as shown by the EDS spectra (Figure 5.72). Na was not retained in the alteration layer. There appeared to be a small gap between the glass and the alteration layer, most readily observed in the Si and O maps, which could be due to dehydration of the layer.

Significant alteration rims were visible on many of the NC10BS particles (Figure 5.70). Elemental maps of the alteration rim on one of these particles are shown in Figure 5.73. As with the alteration rim on the NC5BS particles, the alteration layer here consisted primarily of Ca, K and Si, and Na was not retained (Figure 5.74). There appeared to be some banding in the alteration layer, with alternating thick light phases and thin dark phases, although it was not possible to ascertain whether these were two different alteration phases, or a laminated layer with voids in between caused by dehydration.

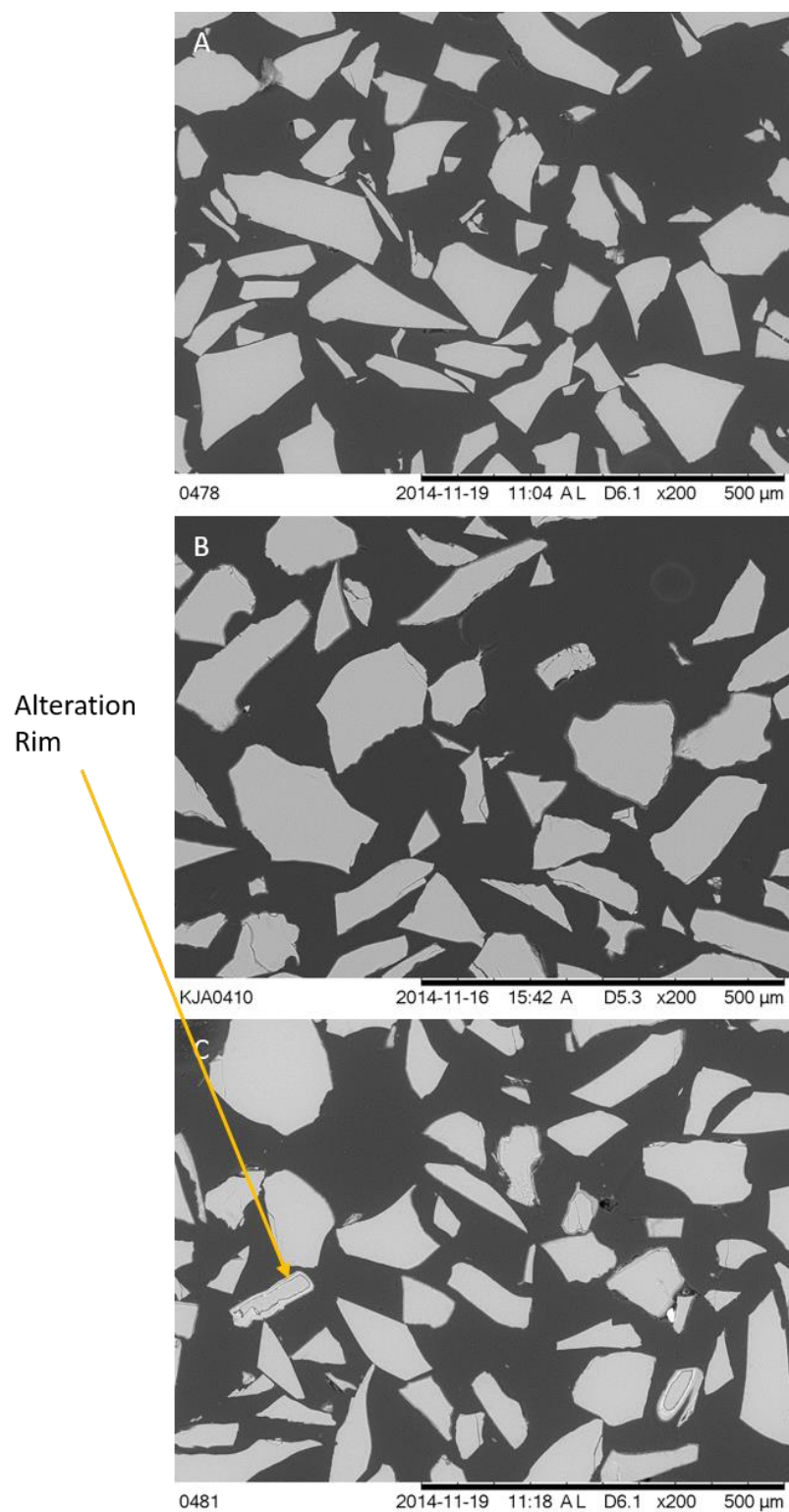


**Figure 5.70.** BSE images of cross-sectioned NCxBS glass particles after a 112-day PCT-B experiment in KOH (A) NC0BS, (B) NC5BS, (C) NC10BS.

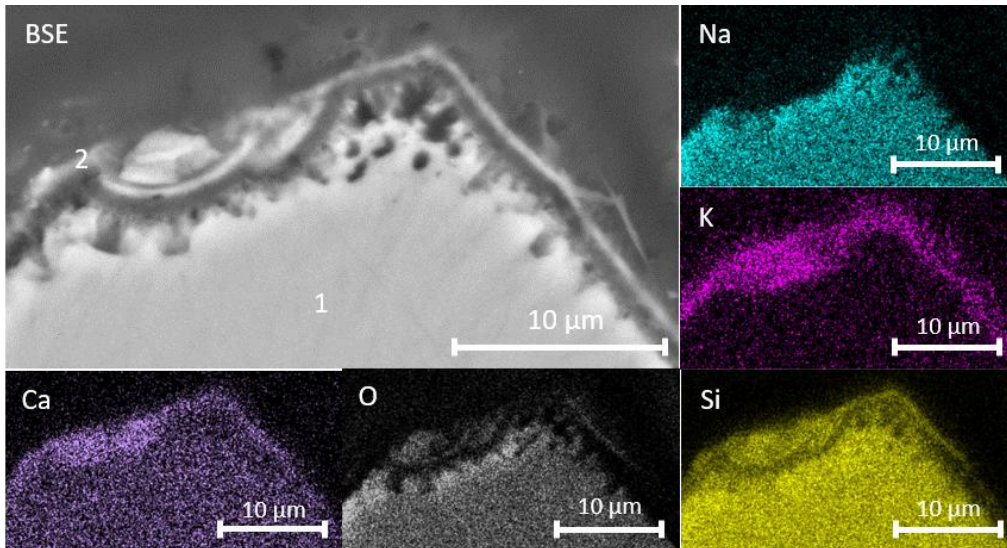


**Figure 5.71.** BSE micrograph and elemental maps of cross-sectioned NC5BS particle (1) after a 112-day PCT-B experiment in KOH, showing alteration layer (2).

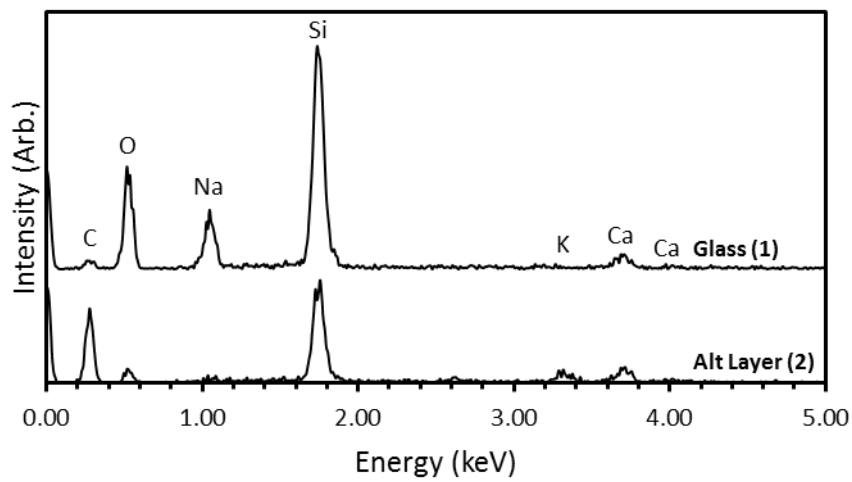


**Figure 5.72.** EDS spectra of NC5BS glass and alteration layer after a 112-day PCT-B experiment in KOH.

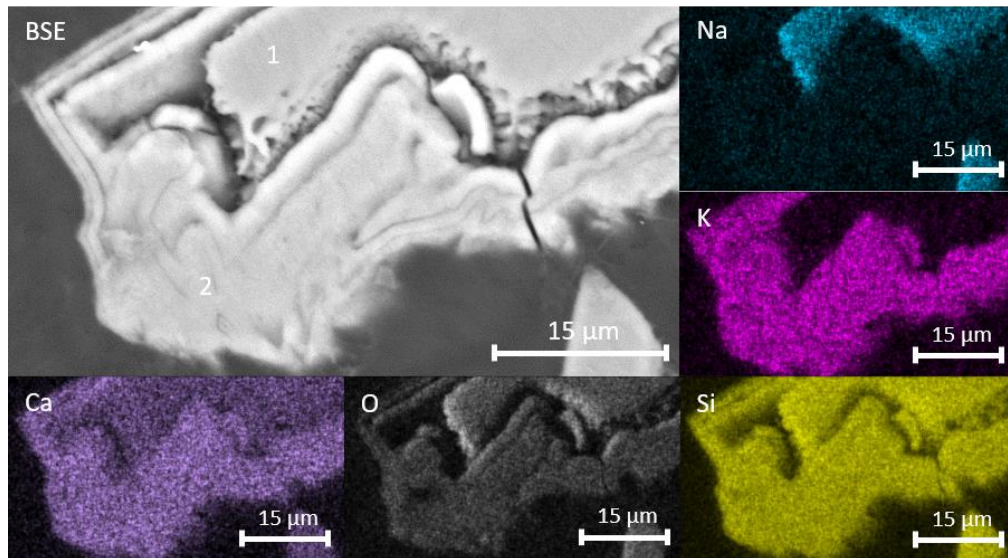


**Figure 5.73.** BSE micrograph and elemental maps of cross-sectioned NC10BS particle (1) after a 112-day PCT-B experiment in KOH, showing alteration layer (2).

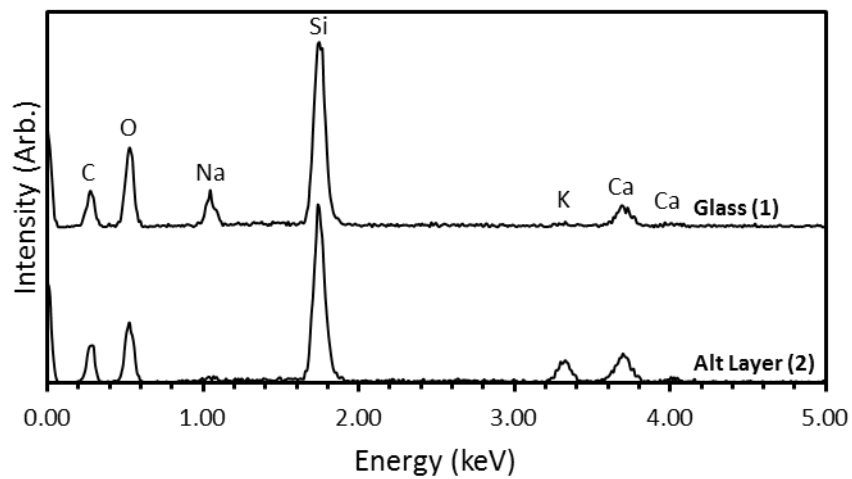


**Figure 5.74.** EDS spectra of NC10BS glass and alteration layer after a 112-day PCT-B experiment in KOH.

#### 5.4.2.2 *NM<sub>x</sub>BS Glasses*

Figure 5.75 shows cross-sectioned particles of NM5BS and NM10BS that have undergone alteration in KOH for 112 days. Alteration rims were observed on both samples, although they were more pronounced on the NM10BS particles.

Elemental maps of a NM5BS particle at higher magnification show the presence of an alteration rim (Figure 5.76), which had also penetrated into the particle. This could be due to a pre-existing crack leading to higher localised leaching rates. The EDS spectra of the particle and alteration layer (Figure 5.77) show that Mg and Si were retained in the alteration layer, along with a small amount of Na. A significant amount of K from solution was also incorporated into the alteration layer.

Figure 5.78 shows EDS maps for a particle of NM10BS altered in KOH for 112 days. As with the NM5BS particles, a significant alteration rim formed around the particle. K from solution was incorporated into the alteration rim, which consisted primarily of Si. Mg leached from the glass was also retained within the rim. The EDS spectra for the glass and the alteration rim are shown in Figure 5.79.

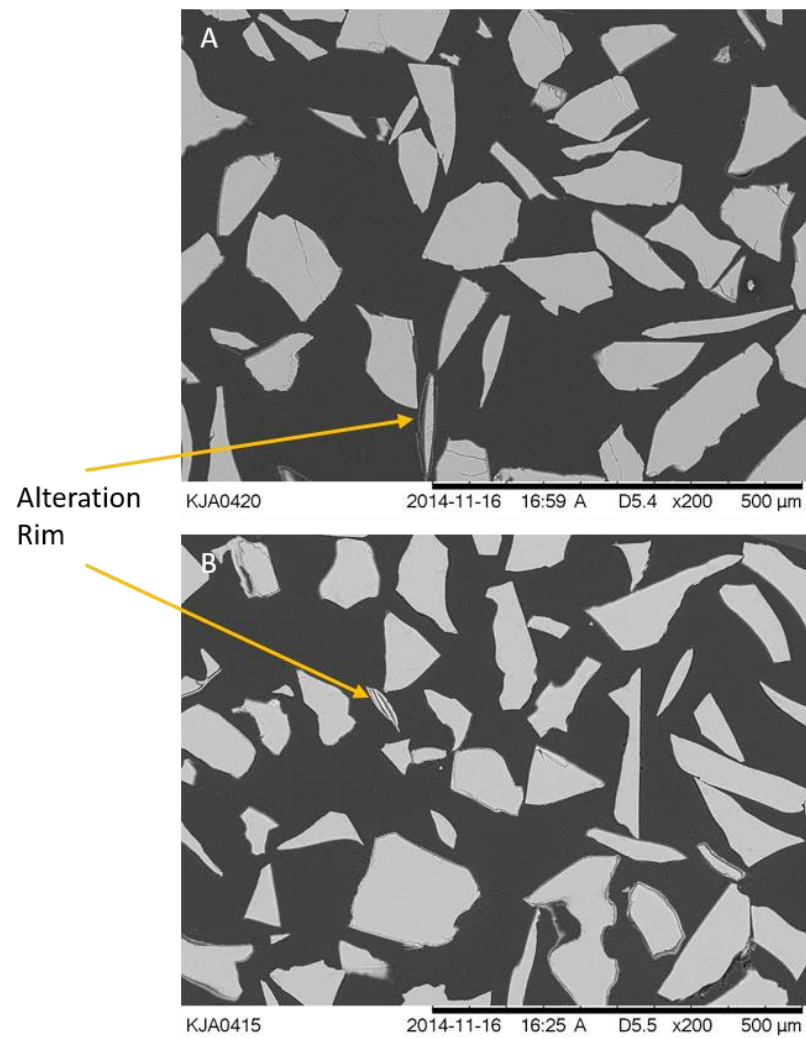


**Figure 5.75.** BSE images of cross-sectioned NMxBS glass particles after a 112-day PCT-B experiment in KOH (A) NM5BS, (B) NM10BS.

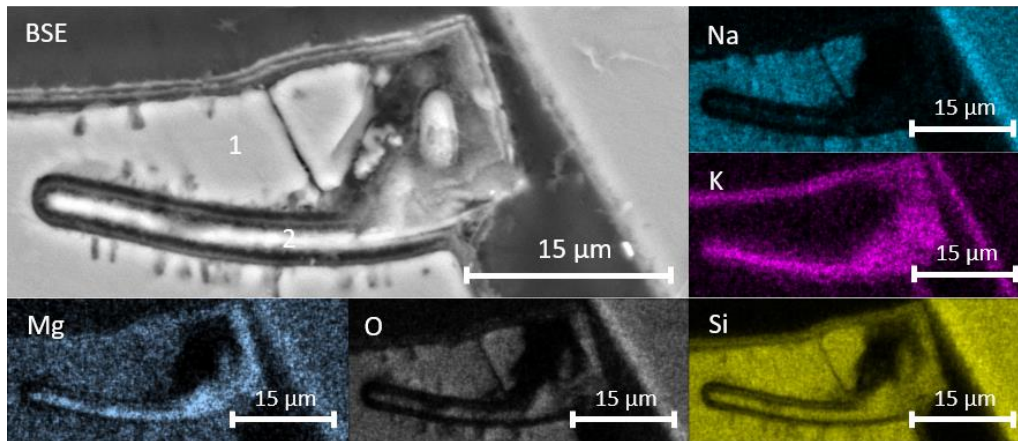


**Figure 5.76.** BSE micrograph and elemental maps of cross-sectioned NM5BS particle (1) after a 112-day PCT-B experiment in KOH, showing alteration (2).

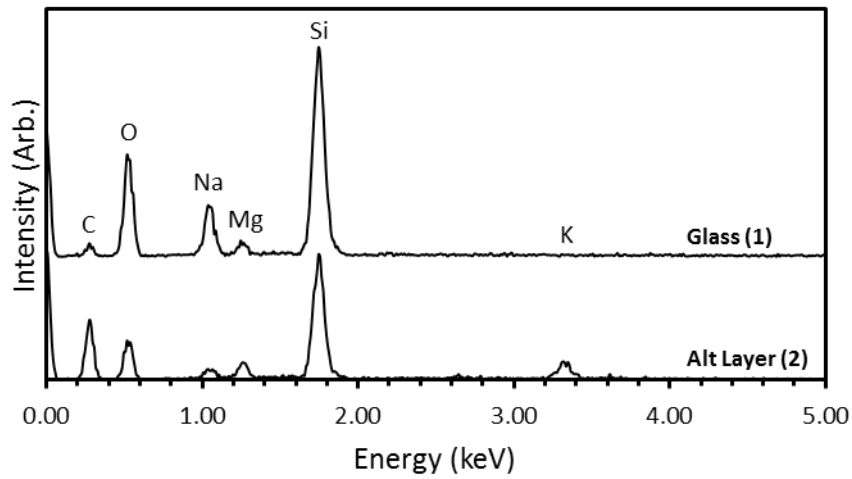


**Figure 5.77.** EDS spectra of NM5BS glass and alteration layer after a 112-day PCT-B experiment in KOH.

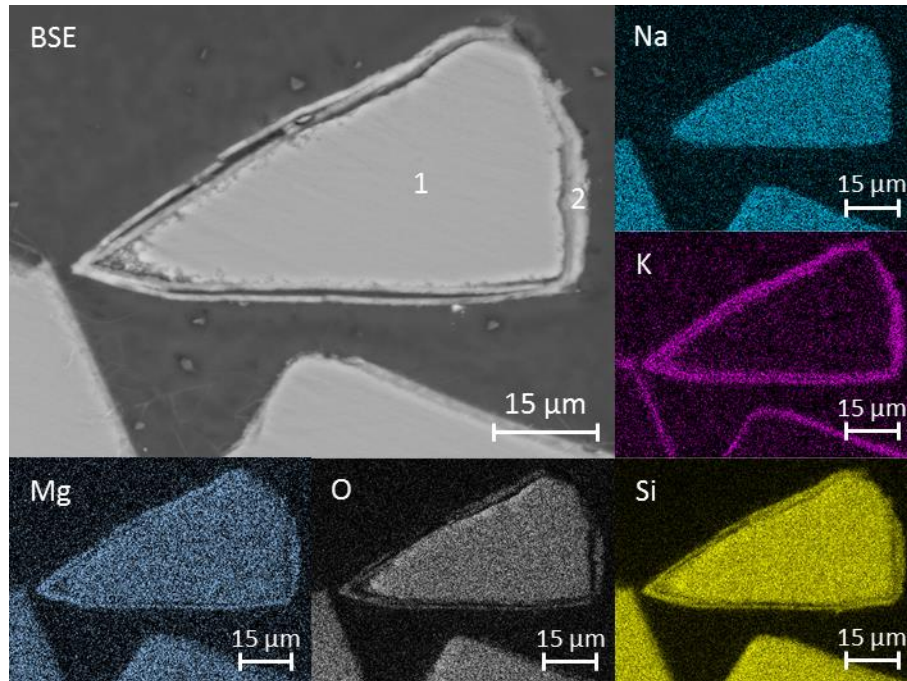


**Figure 5.78.** BSE micrograph and elemental maps of cross-sectioned NM10BS particle (1) after a 112-day PCT-B experiment in KOH, showing alteration layer (2).

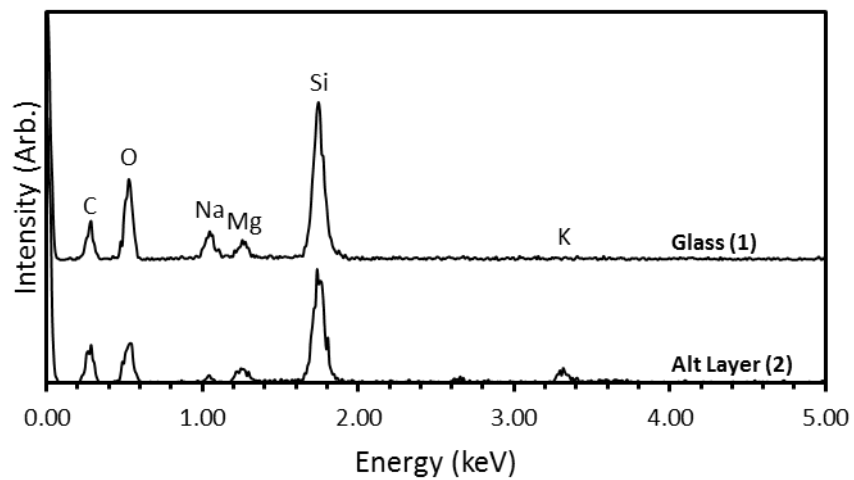


**Figure 5.79.** EDS spectra of NM10BS glass and alteration layer after a 112-day PCT-B experiment in KOH.

#### 5.4.2.3 NCAB<sub>x</sub>S Glasses

Figure 5.80 shows cross-sectioned particles of NCAB0S, NCAB5S and NCAB10S which have undergone alteration in KOH for 112 days. No alteration layers were observed on any of the particles examined. Figure 5.81 contains a BSE image of a particle of NCAB5S after dissolution, which is representative of the images taken of other particles of each of the glasses. No alteration layer was visible, although a bright phase was present on the surface of the particle. EDS analysis (Figure 5.82) confirmed this to be KCl, which was added to the KOH solution as a buffer, and precipitated from solution during the drying of the powder.

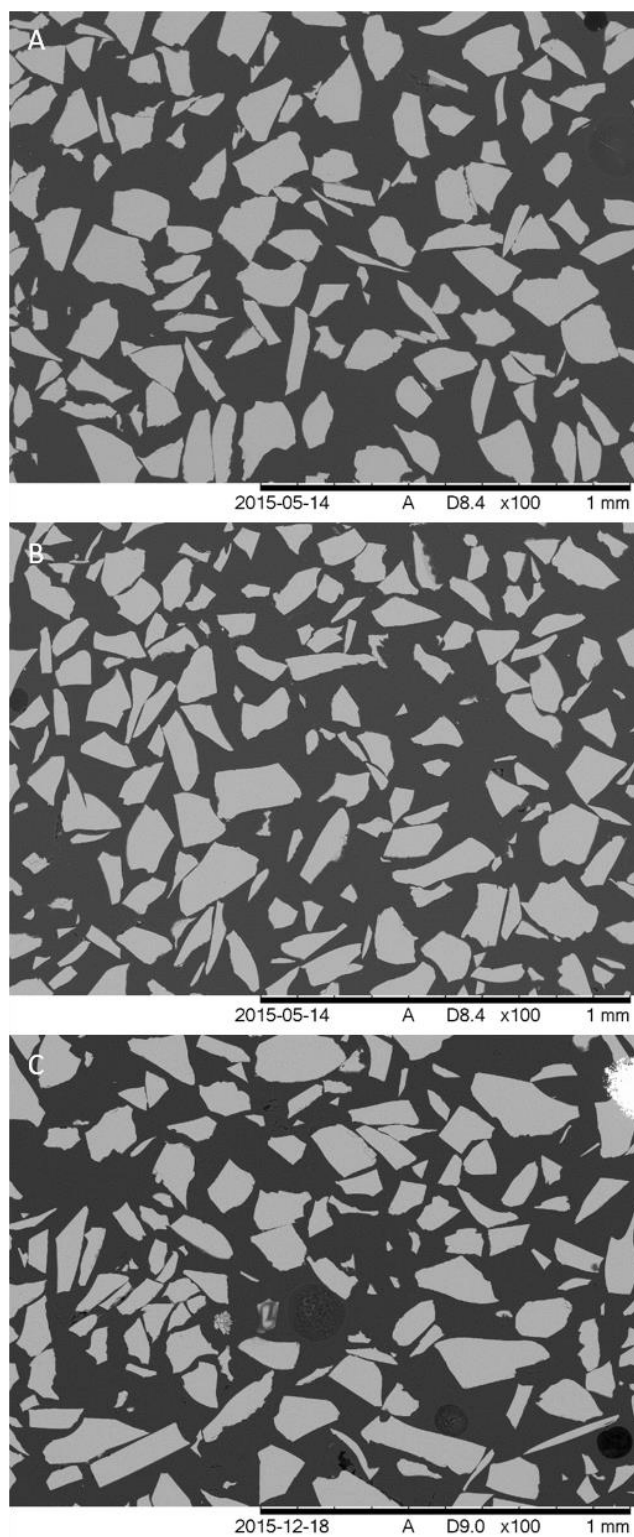


**Figure 5.80.** BSE images of cross-sectioned NCAB $x$ S glass particles after a 112-day PCT-B experiment in KOH (A) NCAB0S, (B) NCAB5S, (C) NCAB10S.

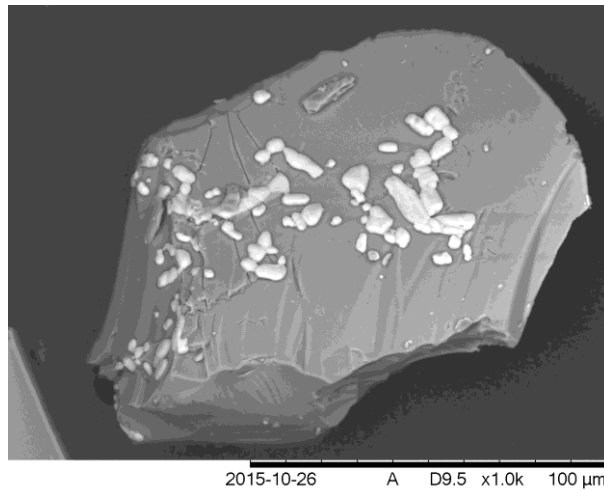


**Figure 5.81.** BSE images of NCAB5S glass particle after a 112-day PCT-B experiment in KOH.

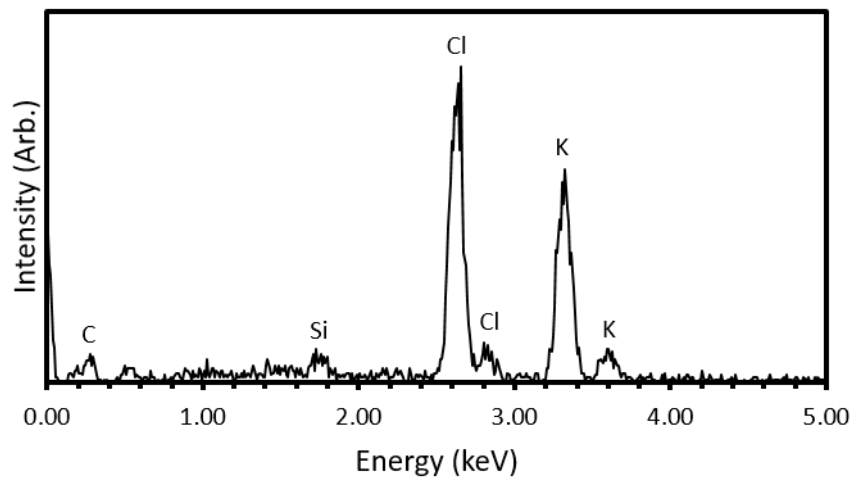


**Figure 5.82.** EDS spectrum of precipitate on NCAB5S particle after a 112-day PCT-B experiment in KOH.

#### 5.4.2.4 NMABxS Glasses

BSE images of cross-sectioned altered particles of NMAB0S, NMAB5S and NMAB10S are shown in Figure 5.83. As with the NCABxS glasses, no alteration layers were observed on any of these glasses. SEM analysis of the particles confirmed this lack of alteration layer. Figure 5.84 shows a BSE micrograph of an NMAB5S particle, which is representative of what was seen for particles of all three glasses. KCl precipitates were again observed on the surface of the glasses.

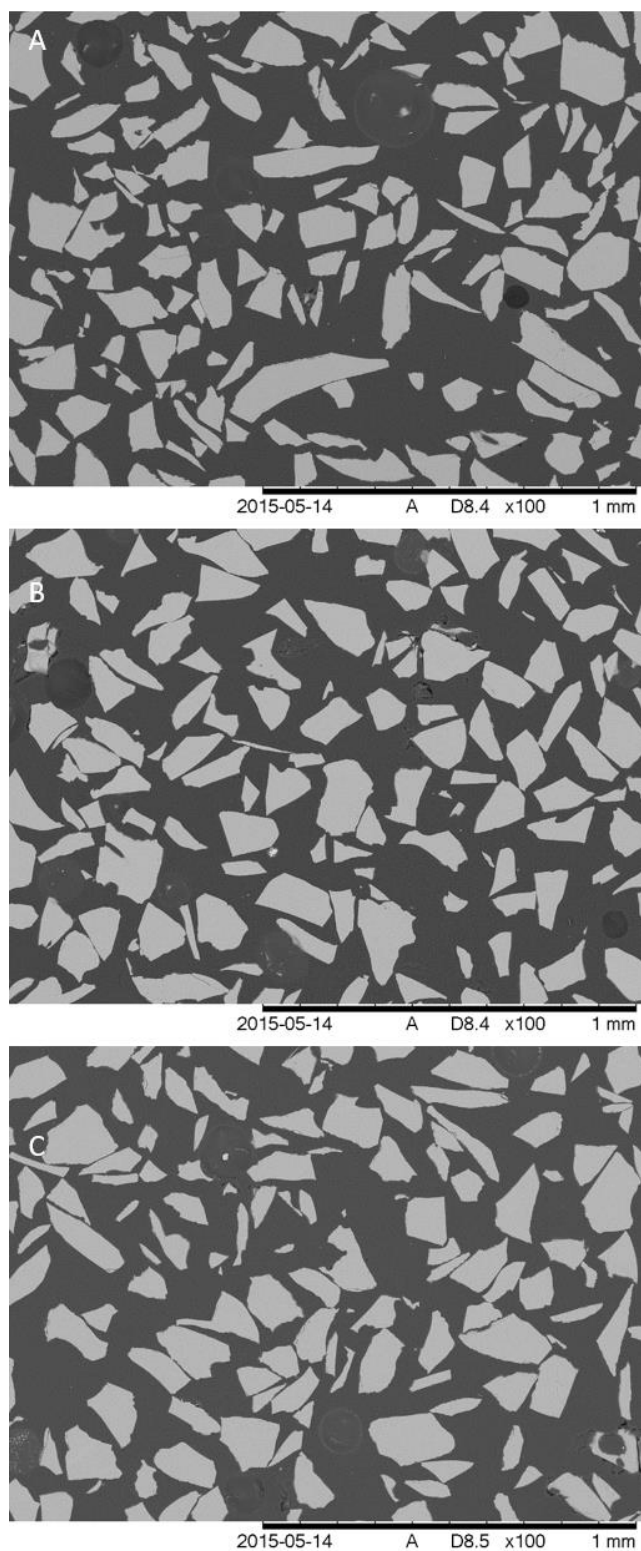


**Figure 5.83.** BSE images of cross-sectioned NMAB<sub>x</sub>S glass particles after a 112-day PCT-B experiment in KOH (A) NMAB0S, (B) NMAB5S, (C) NMAB10S.

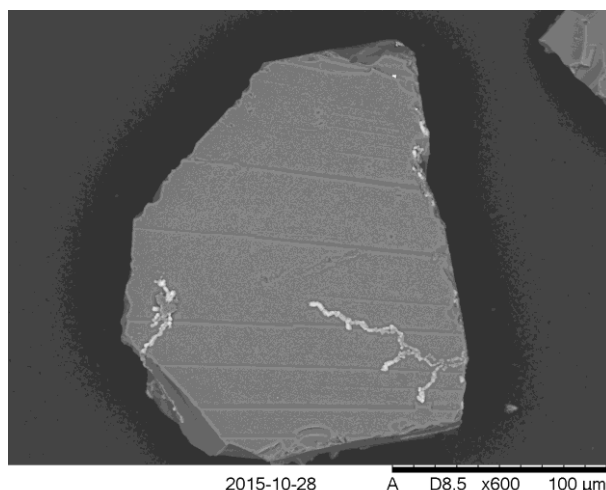


**Figure 5.84.** BSE image of an NMAB5S particle after a 112-day PCT-B experiment in KOH.

## 5.5 Discussion of Results

### 5.5.1. NCxBS Glasses

The final B, Na and Si mass losses for the NCxBS glasses, in both  $\text{Ca}(\text{OH})_2$  and KOH leachants, are shown in Figure 5.85. Figure 5.86 shows the initial ( $R_0(i)$ ) and residual ( $R_r(i)$ ) normalised mass loss rates for the three glasses in both  $\text{Ca}(\text{OH})_2$  and KOH. NC5BS consistently has the lowest mass loss of the three glasses. However, NC0BS and NC10BS appear to have artificially higher mass losses than the other glasses. These samples were analysed on the ICP-OES together, and there appears to have been a systematic error in the analysis increasing their mass loss values. Due to this, only the relative mass losses of NC0BS and NC10BS will be discussed here. In addition, data were only available for NC10BS up to 28 days in KOH due to test vessel failure, and so no residual rates are available for this sample in KOH. The trend appears to be different in the  $\text{Ca}(\text{OH})_2$  and KOH experiments; in  $\text{Ca}(\text{OH})_2$  NC10BS had higher  $NL(\text{B})$ ,  $NL(\text{Na})$ ,  $R_0(\text{B})$ ,  $R_0(\text{Na})$ ,  $R_r(\text{B})$  and  $R_r(\text{Na})$  values than NC0BS, whereas in KOH NC10BS had lower values of  $NL(\text{B})$ ,  $NL(\text{Na})$ ,  $R_0(\text{B})$  and  $R_0(\text{Na})$  than NC0BS. This is likely to be due to the role of Ca during dissolution. In the  $\text{Ca}(\text{OH})_2$  experiments, the role of Ca in forming a more passivating alteration layer was provided to all samples by the high Ca concentration in solution, regardless of the Ca content of the glass. However, in the KOH experiments, this effect was only available for those glasses containing Ca, which is borne out by the fact that no alteration layers were observed on NC0BS particles after dissolution in KOH (see

Section 5.4.2.1). Thus, in KOH the Ca-containing glass, NC10BS, had lower NL(B) and NL(Na) values than the glass which did not contain Ca, NC0BS, due to the formation of a passivating alteration layer around the glass particles. In  $\text{Ca}(\text{OH})_2$ , NC0BS was more resistant to dissolution than NC10BS, which could be due to the increased  $^{\text{IV}}\text{B}$  fraction (and decreased  $^{\text{III}}\text{B}$  fraction) in NC0BS compared to NC10BS, as found through  $^{11}\text{B}$  MAS-NMR experiments (see Section 4.4.1). An increased  $^{\text{IV}}\text{B}$  fraction could lead to a greater resistance of the B units to dissolution, due to the greater number of bond breakages required for release to solution.

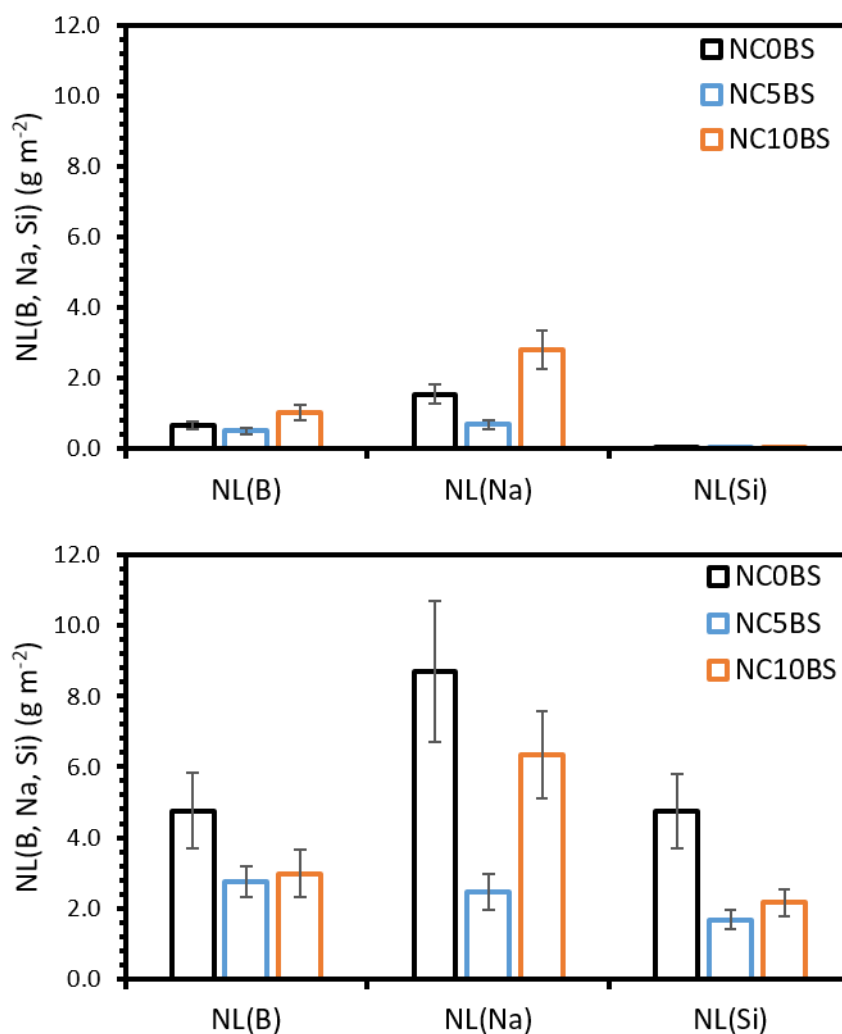


**Figure 5.85.** B, Na and Si normalised mass losses for NC<sub>x</sub>BS glasses after 112 day PCT tests in  $\text{Ca}(\text{OH})_2$  (top graph) and KOH (bottom graph).

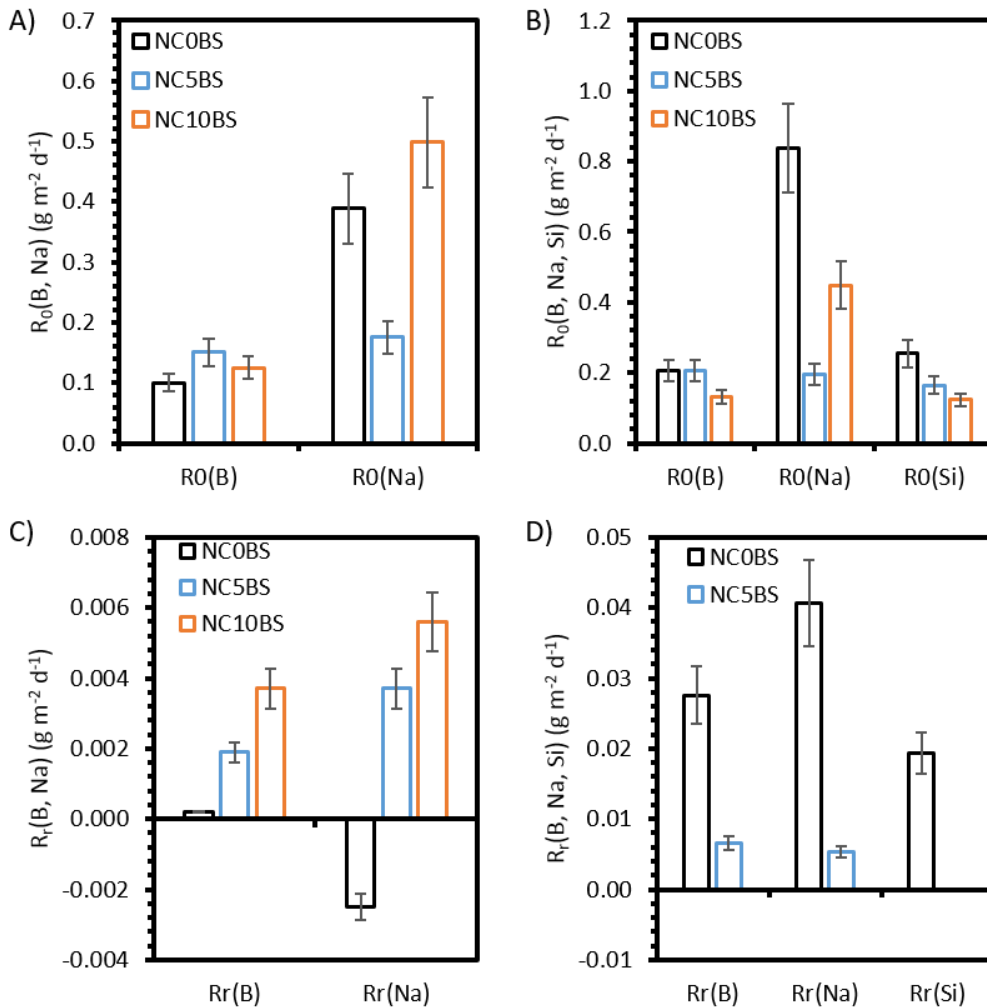


**Figure 5.86.** B, Na and Si normalised mass loss rates for NCxBS glasses after 112 day PCT tests: A) Initial rates,  $\text{Ca(OH)}_2$ ; B) Initial rates, KOH; C) Residual rates,  $\text{Ca(OH)}_2$ ; D) Residual rates, KOH.

Table 5.9 shows the ratio,  $R_{K/Ca}$ , of the normalised mass losses of B, Na and Si in KOH compared to those in  $\text{Ca(OH)}_2$ ;  $R_{K/Ca} > 1$  indicates that dissolution is higher in KOH, whereas  $R_{K/Ca} < 1$  indicates that dissolution is higher in  $\text{Ca(OH)}_2$ . These data show that the dissolution of the NCxBS glasses was significantly lower in  $\text{Ca(OH)}_2$  than in KOH. Previous work by Utton et al. [3] and Corkhill et al. [19] showed that the dissolution of nuclear waste glasses in a saturated  $\text{Ca(OH)}_2$  leachant was lower than in deionised water. This is in contradiction to other research, e.g. Abratis et al. [5], where dissolution of nuclear waste glasses was shown to increase with increased pH. Two potential causes of this phenomenon have been identified for the experiments performed in this investigation:

1. Due to the formation of secondary alteration products, the NCxBS particles

became significantly agglomerated during dissolution in  $\text{Ca}(\text{OH})_2$ , but not in KOH where fewer secondary phases were formed. This agglomeration led to a decrease in the effective surface area of the powdered sample (that was not possible to estimate accurately), thus lowering the apparent mass losses, which were normalised to the geometric surface area of the samples.

2. The alteration layers formed on the particles in  $\text{Ca}(\text{OH})_2$  were more passivating in nature than those formed in KOH. This was due to the high levels of  $\text{Ca}^{2+}$  ions in the  $\text{Ca}(\text{OH})_2$  alteration layers leading to a denser, less permeable layer than the high levels of  $\text{K}^+$  in the KOH layers.

Evidence for the former mechanism was found during observation of the post-dissolution powders. After the remaining leachate had been decanted, but before the samples were dried, visual observations were made of the consistency of the glass powder. In the  $\text{Ca}(\text{OH})_2$  samples, the powder had agglomerated to the point that it resembled a single monolithic ‘puck’, in contrast to the samples leached in KOH, which remained as free-flowing powders. Further evidence can be seen in the comparison of glass powder after alteration in the two leachants (Figure 5.87). The particles altered in KOH have KCl precipitates on the surface, but these are likely to have formed during drying of the powder, as the leachate was undersaturated with respect to KCl; the concentration of KCl in solution in the PCT-B experiments was  $15.66 \text{ g L}^{-1}$  (see Section 3.2.1), and the solubility of KCl in water at  $50 \text{ }^\circ\text{C}$  is  $300.94 \text{ g L}^{-1}$  [134]. Ca-rich precipitates formed on the particles altered in  $\text{Ca}(\text{OH})_2$ , which cemented the particles together, as postulated by Chave et al. [13] and Gin et al. [14]. These investigations suggest that the diffusion of ions through a Ca-rich silicate layer is up to four orders of magnitude lower than those through a Ca-free layer, due to the differences in structure and density caused by the presence of Ca, and by the ability of Ca to form strong complexes with  $\text{H}_2\text{O}$  molecules [66]. The SEM-EDS analysis of the alteration layers formed on the  $\text{NC}_x\text{BS}$  glasses in  $\text{Ca}(\text{OH})_2$  and KOH shows that the alteration layers formed in  $\text{Ca}(\text{OH})_2$  are significantly richer in Ca than those formed in KOH. This would explain the differences in the residual rates of the glasses in  $\text{Ca}(\text{OH})_2$  compared to KOH, e.g. the  $R_r(\text{B})$  and  $R_r(\text{Na})$  values for  $\text{NC}_5\text{BS}$  in  $\text{Ca}(\text{OH})_2$  were  $(1.9 \pm 0.3) \times 10^{-3}$  and  $(3.7 \pm 0.6) \times 10^{-3} \text{ g m}^{-2} \text{ d}^{-1}$ , respectively, compared to corresponding values of  $(6.6 \pm 1.0) \times 10^{-3}$  and  $(5.4 \pm 0.8) \times 10^{-3} \text{ g m}^{-2} \text{ d}^{-1}$  in KOH. It is likely that both of these mechanisms play a part in reducing the dissolution rate of the  $\text{NC}_x\text{BS}$  glasses in  $\text{Ca}(\text{OH})_2$  compared to KOH.

**Table 5.9.**  $R_{K/Ca}$  for each of the NC $x$ BS samples, as determined by ICP-OES analysis.

Sample	NL(B)	NL(Na)	NL(Si)
NC0BS	7.20	7.43	1223.7
NC5BS	5.42	3.56	1514.7
NC10BS	4.14	2.77	423.2

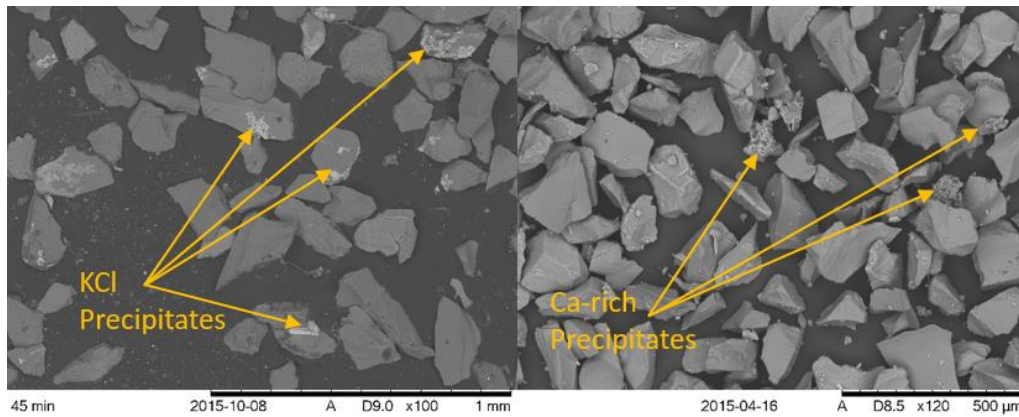


**Figure 5.87.** BSE micrographs of particles of NC5BS altered in KOH (left) and  $\text{Ca}(\text{OH})_2$  (right).

### 5.5.2 NM $x$ BS Glasses

Figure 5.88 shows the normalised mass losses of B, Na and Si for the NM $x$ BS glasses after 112 days of leaching in  $\text{Ca}(\text{OH})_2$  and KOH. Initial and residual normalised B, Na and Si mass loss rates are shown in Figure 5.89. As noted in the previous section, NC0BS appeared to have artificially high mass loss values, and so only NM5BS and NM10BS are compared in this section. In general, NM10BS had greater durability than NM5BS for both leachants, as evidenced by NM10BS having lower NL(B), NL(Na),  $R_r(\text{B})$  and  $R_r(\text{Na})$  values in  $\text{Ca}(\text{OH})_2$  and lower  $R_r(\text{B})$  and  $R_r(\text{Na})$  in KOH, while the  $R_0(\text{B})$  and  $R_0(\text{Na})$  values were similar in both leachants. Although NMR spectroscopy of these glasses, as described in Chapter 4, showed an increase in the connectivity of the silicate network with increasing Mg/Na, the fact that the initial rates, which should be most affected by structural changes, are very similar suggests that the primary cause of the difference in durability between the two glasses is related to the formation of alteration layers and other secondary products. This could be due

to a diffusion retardation mechanism, analogous to that suggested for the Ca-containing glasses.

For each of the glasses, the normalised mass losses for the elements were higher with KOH as the leachant than with  $\text{Ca}(\text{OH})_2$  as the leachant. The ratios of the final normalised mass loss for each element in KOH compared to that in  $\text{Ca}(\text{OH})_2$ ,  $R_{\text{K/Ca}}$ , are shown in Table 5.10. The mechanisms put forward to explain this phenomenon in the  $\text{NC}_x\text{BS}$  glasses are also applicable to the  $\text{NM}_x\text{BS}$  glasses. Agglomeration of the particles after the PCT experiments was observed for these glasses, and Ca-rich cementitious precipitates were identified (Figure 5.90).

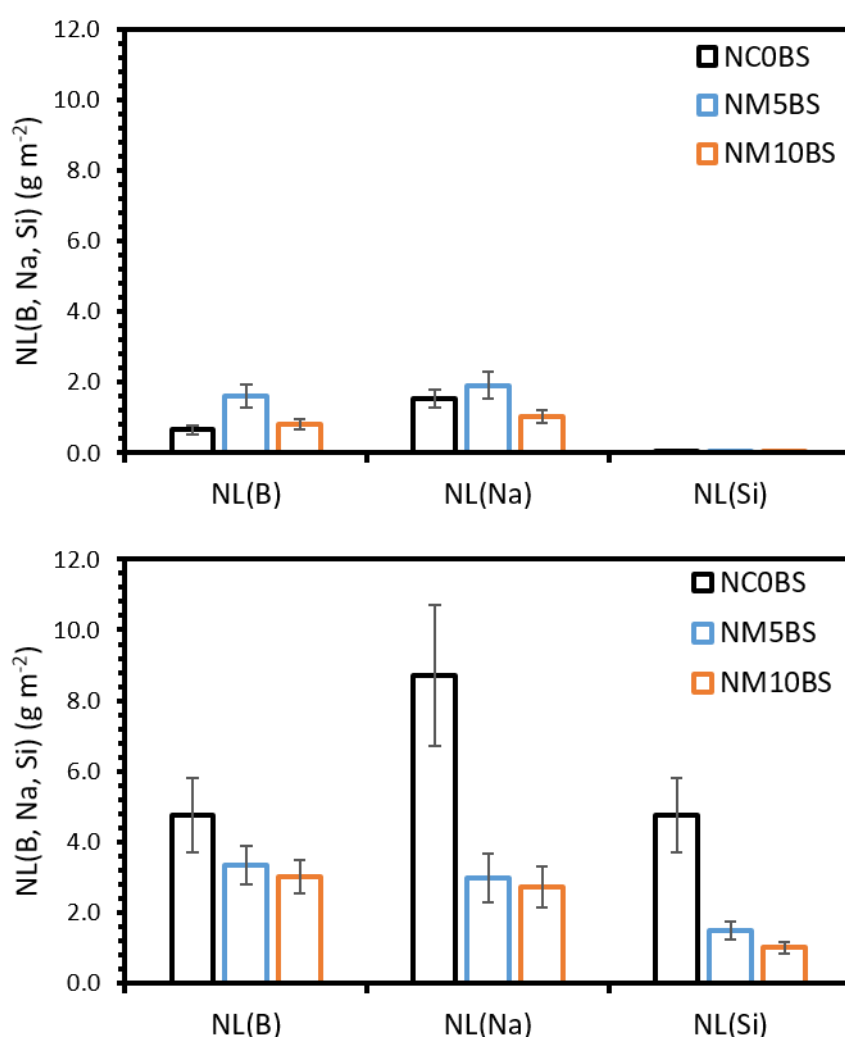


**Figure 5.88.** B, Na and Si normalised mass losses for  $\text{NM}_x\text{BS}$  glasses after 112 day PCT tests in  $\text{Ca}(\text{OH})_2$  (top graph) and KOH (bottom graph).

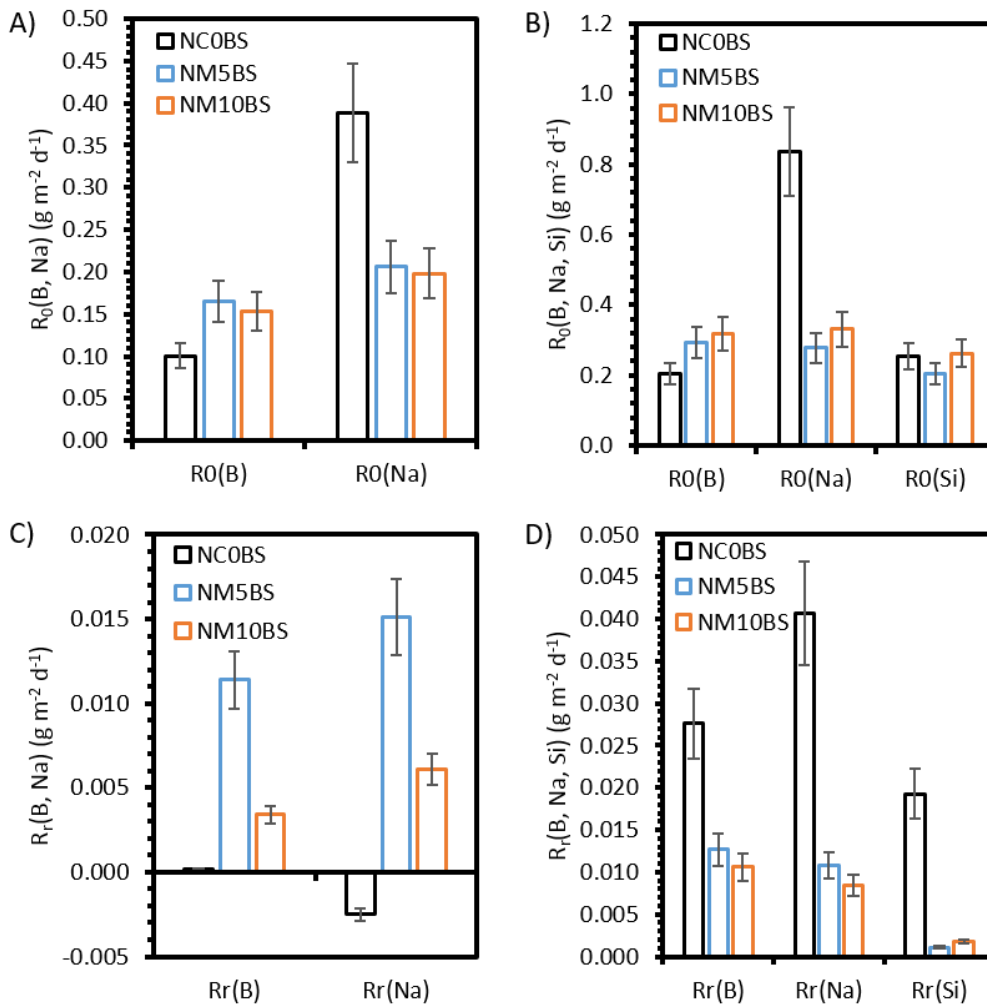


**Figure 5.89.** B, Na and Si normalised mass loss rates for NMxBS glasses after 112 day PCT tests: A) Initial rates, Ca(OH)<sub>2</sub>; B) Initial rates, KOH; C) Residual rates, Ca(OH)<sub>2</sub>; D) Residual rates, KOH.

**Table 5.10.**  $R_{K/Ca}$  for each of the NMxBS samples, as determined by ICP-OES analysis.

Sample	NL(B)	NL(Na)	NL(Si)
NC0BS	7.20	7.43	1223.7
NM5BS	2.08	1.55	230.9
NM10BS	3.71	2.61	249.4

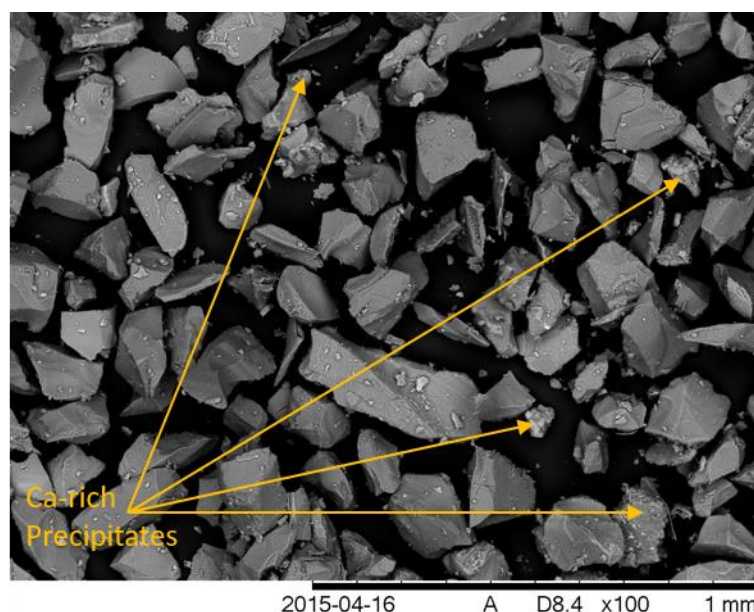


**Figure 5.90.** BSE micrograph of particles of NM5BS altered in  $\text{Ca}(\text{OH})_2$ .

### 5.5.3 NCABxS Glasses

As discussed in Section 5.1, NCAB5S is not included in this discussion due to the deviation of its CaO content from the targeted value. Figure 5.91 shows the final NL(B), NL(Al), NL(Na) and NL(Si) values for the NCABxS samples after 112 days of leaching in  $\text{Ca}(\text{OH})_2$  and KOH. Initial and residual normalised mass loss rates for both leachants are shown in Figure 5.92. In the KOH leachant, the chemical durability of the glasses decreased with increasing B/Al ratio (see Figure 5.93). The increase in the initial rate of dissolution from NCAB0S to NCAB10S in KOH suggests that  $\text{Al}_2\text{O}_3$  is more beneficial to the chemical durability of these glasses than  $\text{B}_2\text{O}_3$ . This is likely to be due to the fact that Si – O – Al bonds are more resistant to hydrolysis than Si – O – B bonds, leading to a slower glass dissolution rate [135]. It should be noted that the NC10BS glass is, in essence, NCAB15S, i.e. its nominal composition is  $10\text{Na}_2\text{O} \cdot 10\text{CaO} \cdot (15 - x)\text{Al}_2\text{O}_3 \cdot x\text{B}_2\text{O}_3 \cdot 65\text{SiO}_2$ , where  $x = 15$ . When the NL(B) and NL(Na) values of NCAB10S and NC10BS are compared (Figure 5.94), it can be seen that NC10BS continued the trend of increasing B/Al ratio leading to higher leaching levels in KOH. However, in  $\text{Ca}(\text{OH})_2$  it is difficult to identify an overall trend with varying B/Al ratio. NCAB0S, with B/Al = 0, had higher NL(Al),  $R_0(\text{Al})$ ,  $R_r(\text{Al})$  and  $R_r(\text{Na})$ , whilst the NL(Na) and  $R_0(\text{Na})$  values were the same, within error, for NCAB0S and NCAB10S. However, the NL(B),  $R_0(\text{B})$  and  $R_r(\text{B})$  values for NCAB10S (B/Al = 2.48) were higher than the equivalent NL(Al),  $R_0(\text{Al})$  and  $R_r(\text{Al})$  values for

NCAB0S. This suggests that the presence of alteration layers on the samples altered in  $\text{Ca}(\text{OH})_2$ , which were not observed on the particles altered in KOH, has a significant effect on the dissolution of the NCAB $x$ S glasses which masks the effect of the relative proportions of Si – O – Al and Si – O – B bonds.

The values of  $R_{\text{K/Ca}}$  for the NCAB $x$ S glasses are shown in Table 5.11. As with the NC $x$ BS and NM $x$ BS glasses, the NL(Al) and NL(Si) values are higher in KOH than in  $\text{Ca}(\text{OH})_2$  i.e.  $R_{\text{K/Ca}} > 1$ . This is attributed to the greater retention of these elements in alteration products in the Ca-rich system. However, the NL(B) and NL(Na) values for the NCAB $x$ S glasses were higher in  $\text{Ca}(\text{OH})_2$  than in KOH, suggesting that the durability of these glasses is higher in the latter system, in contrast with the borosilicate glasses. This is likely to be due to the precipitation of secondary phases during dissolution. The NCAB $x$ S glasses did not form significant alteration layers in either  $\text{Ca}(\text{OH})_2$  or KOH (although alteration layers were visible on some of the particles altered in  $\text{Ca}(\text{OH})_2$ ). However, in  $\text{Ca}(\text{OH})_2$  significant amounts of other secondary phases were observed, primarily rich in Ca and Si. Examples of these precipitates can be seen in the cross-sectioned sample of NCAB0S in Figure 5.56. In addition, Figure 5.95 shows these precipitates present in a non-cross-sectioned sample of NCAB10S. The precipitation of phases containing glass-formers such as Si and Al means that although the system reached saturation with respect to those elements, a driver for higher rates of dissolution remained due to the continued removal of Al and Si from solution. X-ray diffraction of the sample suggested that tobermorite-11Å (PDF [00-019-1364],  $\text{Ca}_5\text{Si}_6\text{O}_{17}\cdot 5\text{H}_2\text{O}$ ) may be present as one of these precipitates (Figure 5.96). The peak at around  $29.2^\circ 2\theta$  corresponds to the major reflection of the tobermorite-11Å phase. No other phases were present in high enough quantities ( $> 3 - 5$  wt.%) to be detected. In the KOH system, no precipitates were formed, as shown by SEM-EDS and XRD, although KCl precipitated from solution during the drying of the powder was observed (Figure 5.97). Despite the apparent lack of precipitates, PHREEQC modelling indicated that several phases, including tobermorite-9Å, tobermorite-11Å and tobermorite-14Å, were saturated with respect to the leachate, with Saturation Indices (SI) of 19.74, 20.23 and 17.11, respectively. This suggests that the solution was saturated with respect to Si- and Al-containing phases, which led to a significant decrease in dissolution rates for the NCAB $x$ S glasses in KOH.

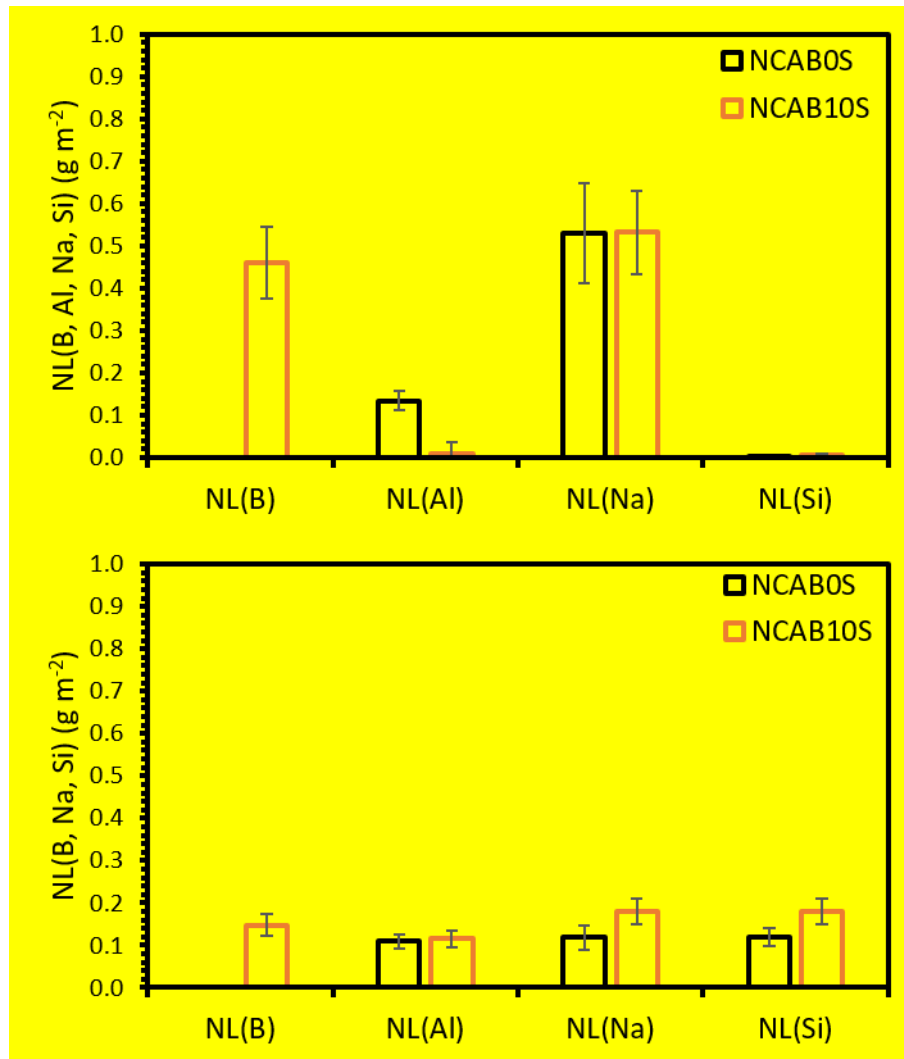


**Figure 5.91.** B, Al, Na and Si normalised mass losses for NCAB<sub>x</sub>S glasses after 112 day PCT tests in  $\text{Ca(OH)}_2$  (top graph) and  $\text{KOH}$  (bottom graph).

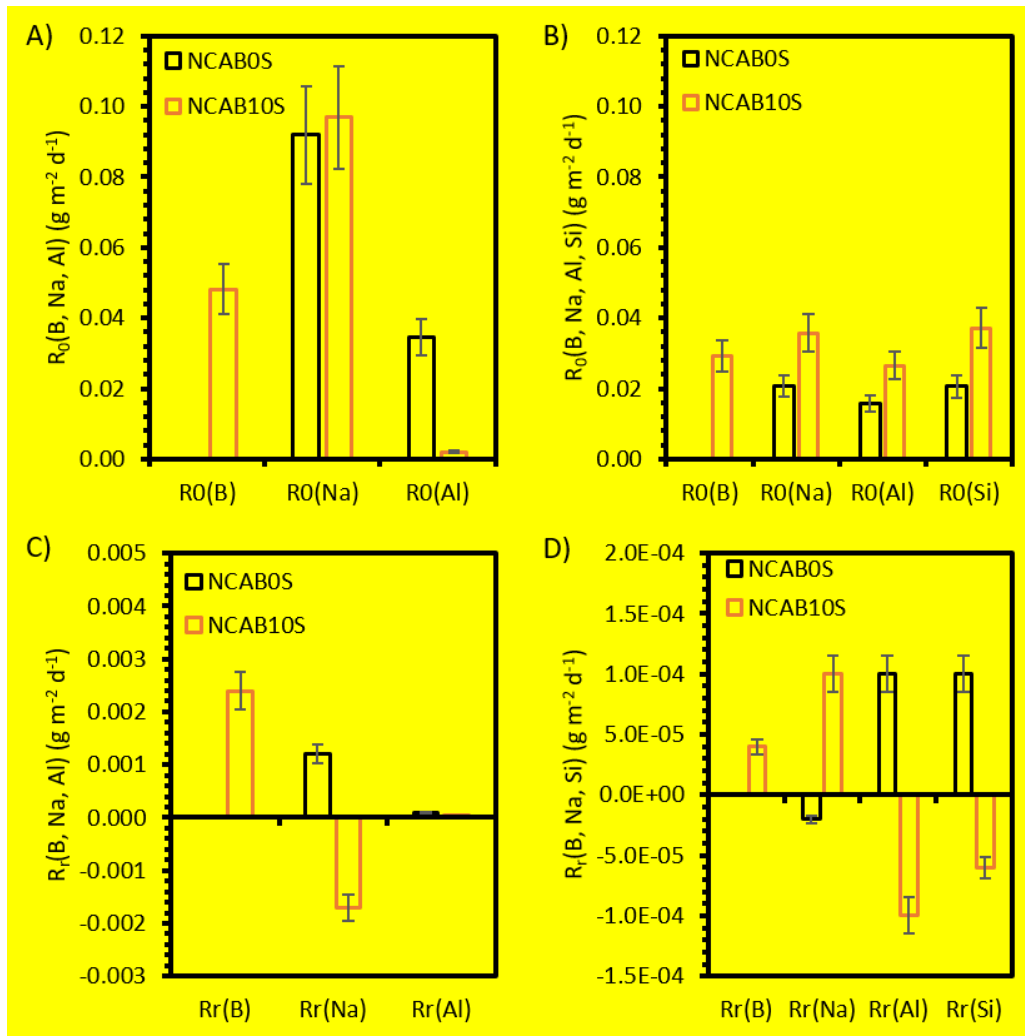


**Figure 5.92.** B, Na and Si normalised mass loss rates for NCAB $x$ S glasses after 112 day PCT tests: A) Initial rates,  $\text{Ca(OH)}_2$ ; B) Initial rates, KOH; C) Residual rates,  $\text{Ca(OH)}_2$ ; D) Residual rates, KOH (NCAB5S values not available).

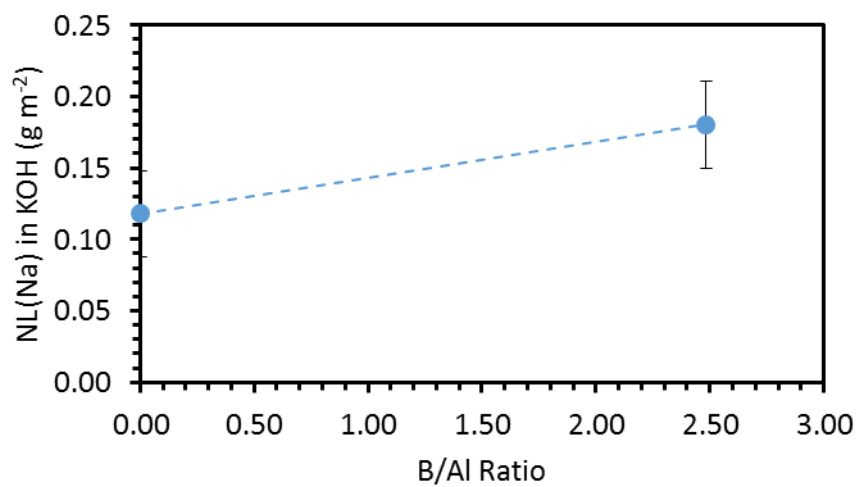


**Figure 5.93.**  $NL(\text{Na})$  in KOH PCT-B experiments as a function of B/Al ratio for NCAB0S and NCAB10S.

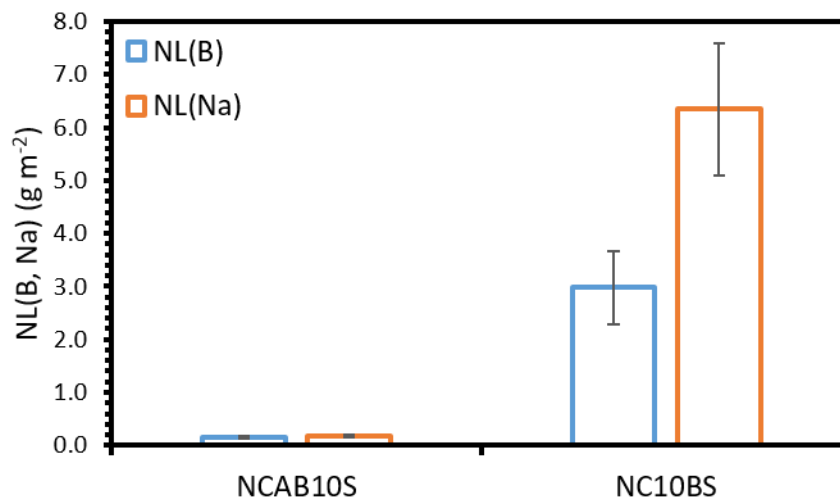


**Figure 5.94.** Comparison of NL(B) and NL(Na) for NCAB10S and NC10BS samples leached in KOH.

**Table 5.11.**  $R_{K/Ca}$  for each of the NCABxS samples, as determined by ICP-OES analysis.

Sample	NL(B)	NL(Al)	NL(Na)	NL(Si)
NCAB0S	N/A	0.81	0.22	2723.0
NCAB10S	0.32	14.15	0.34	23.48

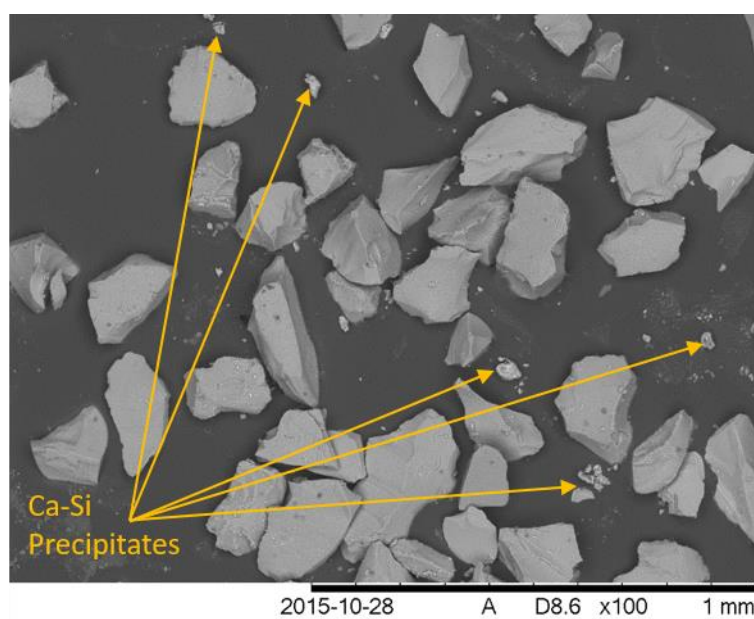


**Figure 5.95.** BSE micrograph of NCAB10S sample altered in  $\text{Ca}(\text{OH})_2$ , showing Ca-Si precipitates.

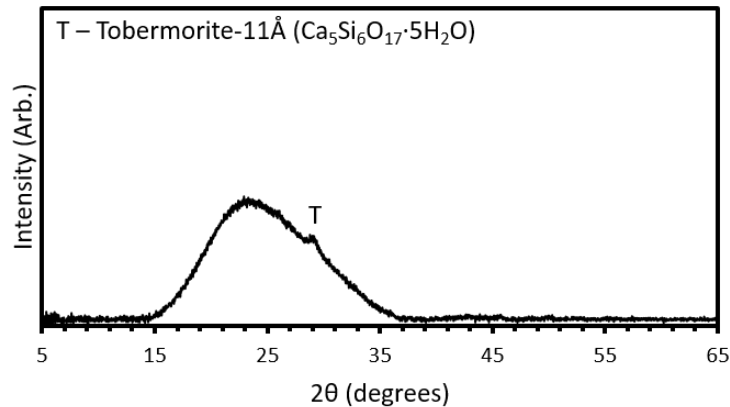


**Figure 5.96.** X-ray diffraction pattern for NCAB10S sample altered in  $\text{Ca}(\text{OH})_2$ .

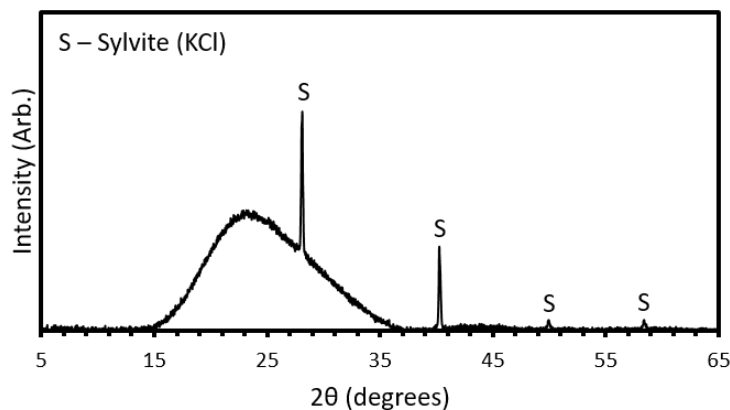


**Figure 5.97.** X-ray diffraction pattern for NCAB10S sample altered in KOH.

#### 5.5.4 NMAB<sub>x</sub>S Glasses

Figure 5.98 shows the normalised mass losses for the NMAB<sub>x</sub>S glasses after dissolution in  $\text{Ca}(\text{OH})_2$  and KOH. Figure 5.99 shows initial and residual normalised mass loss rates for these glasses in both leachants. A durability decrease was observed with increasing B/Al ratio for both leachants (see Figure 5.100), which is also attributed here to the higher resistance of the Si – O – Al bonds to hydrolysis, as with the NCAB<sub>x</sub>S glasses. This is supported by the increase in the initial mass loss rates of B and Na ( $R_0(\text{B})$  and  $R_0(\text{Na})$ ) with increasing B/Al ratio in both leachants (Figure 5.101). NM10BS was essentially NMAB15S in composition; see Section 5.5.1.3. Figure 5.102 shows the comparison of the NL(B) and NL(Na) values, after 112 days in  $\text{Ca}(\text{OH})_2$ , for the NMAB10S and NM10BS glasses. The values for the two glasses are similar. However, when the dissolution across the whole experiment is considered

(Figure 5.103), NM10BS had higher residual rates of B and Na mass loss, at  $(3.4 \pm 0.5) \times 10^{-3}$  and  $(6.1 \pm 0.9) \times 10^{-3} \text{ g m}^{-2} \text{ d}^{-1}$ , respectively, than NMAB10S which had values of  $(1.4 \pm 0.2) \times 10^{-3}$  and  $(3.0 \pm 0.5) \times 10^{-3} \text{ g m}^{-2} \text{ d}^{-1}$  for  $R_0(\text{B})$  and  $R_0(\text{Na})$ , respectively. This suggests again that the glass with the lower B/Al ratio was more durable over longer timescales.

The NMAB $x$ S glasses also exhibited similar behaviour to the NCAB $x$ S glasses with regard to the two leachants. As shown in Table 5.12, the NL(Al) and NL(Si) values for the glasses were higher in KOH, whereas the NL(B) and NL(Na) values, which are tracers for dissolution, were higher in Ca(OH)<sub>2</sub>. The mechanism for this is likely the same as for the NCAB $x$ S glasses; the formation of secondary phases in the Ca(OH)<sub>2</sub> leachate means that the solution does not remain saturated with respect to Al and Si, and so dissolution continued at an increased rate. X-ray diffraction (Figure 5.104) shows that in addition to the tobermorite-11Å (Ca<sub>5</sub>Si<sub>6</sub>O<sub>17</sub>·5H<sub>2</sub>O) phase seen in the NCAB $x$ S samples, a calcium borate hydrate phase (PDF [00-052-1654], Ca<sub>2</sub>B<sub>5</sub>O<sub>7</sub>(OH)<sub>5</sub>·H<sub>2</sub>O) may also be present. This would have significant implications for the use of B as a tracer for dissolution, as it is generally assumed to not be involved in the formation of secondary precipitates. The formation of calcium borate hydrates during the dissolution of B-containing glasses in Ca(OH)<sub>2</sub> has been postulated previously by Utton *et al.* to explain a delay in the initial hydration of borosilicate glass samples, referencing similar processes in cement chemistry [3]. However, as it is not possible to detect B with EDS, further analysis would be required to confirm this finding. The Ca- and Al-rich phase observed in the SEM-EDS analysis of all three samples (see Figs. 5.63, 5.65, 5.67), is likely to be a calcium aluminate hydrate phase, although, if crystalline, this phase did not appear to have been present in large enough quantities to be detected by the diffractometer. The Ca/Al ratio for this phase in each of the samples is given in Table 5.13. These suggest that this phase could be C<sub>4</sub>AH<sub>13</sub> (Ca<sub>4</sub>Al<sub>2</sub>O<sub>7</sub>·13H<sub>2</sub>O) or C<sub>4</sub>AH<sub>19</sub> (Ca<sub>4</sub>Al<sub>2</sub>O<sub>7</sub>·19H<sub>2</sub>O). However, PHREEQC calculations suggest that these phases might be unlikely to form in the presence of significant concentrations (> 10 ppm) of Mg and Si, with SI values after 112 days of -9.33 and -5.77 for C<sub>4</sub>AH<sub>13</sub> and C<sub>4</sub>AH<sub>19</sub>, respectively. However, the accuracy of PHREEQC is limited by the quality of thermodynamic data available on these phases. This might suggest that Mg-Si phases, such as those observed in Figures 5.65 and 5.67, may precipitate first, followed by a precipitation of calcium aluminate hydrate phases.

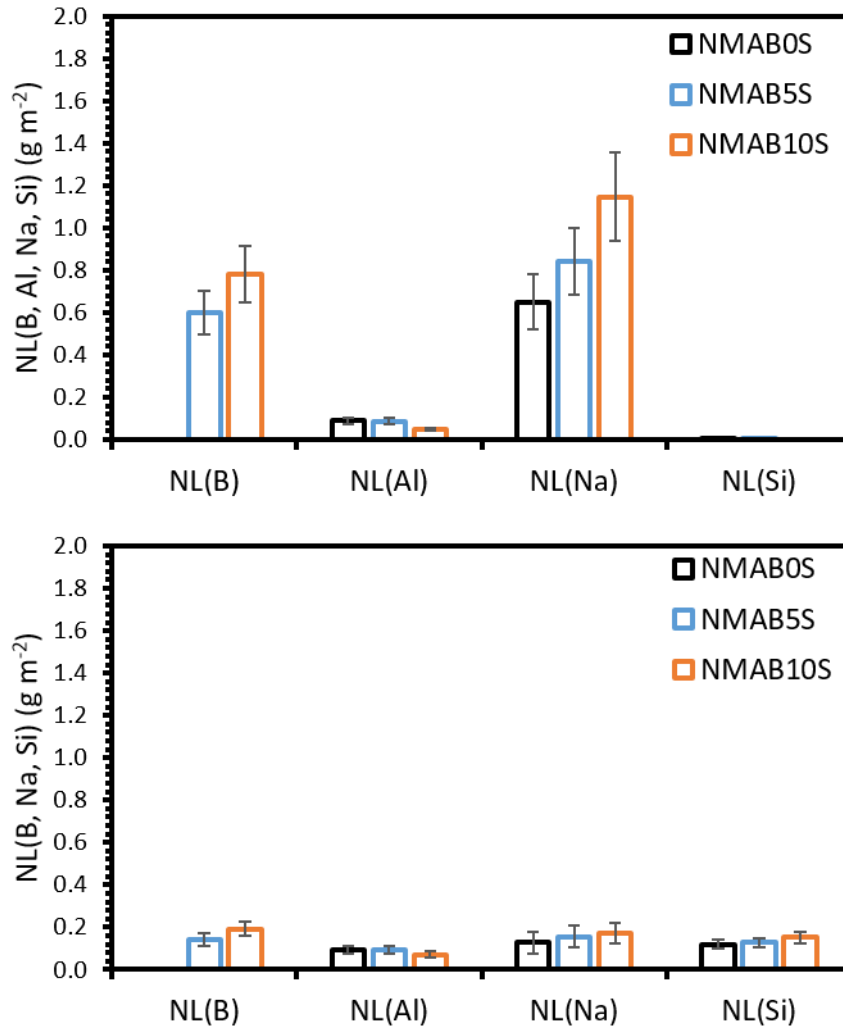


**Figure 5.98.** B, Al, Na and Si normalised mass losses for NMAB<sub>x</sub>S glasses after 112 day PCT tests in  $\text{Ca(OH)}_2$  (top graph) and  $\text{KOH}$  (bottom graph).

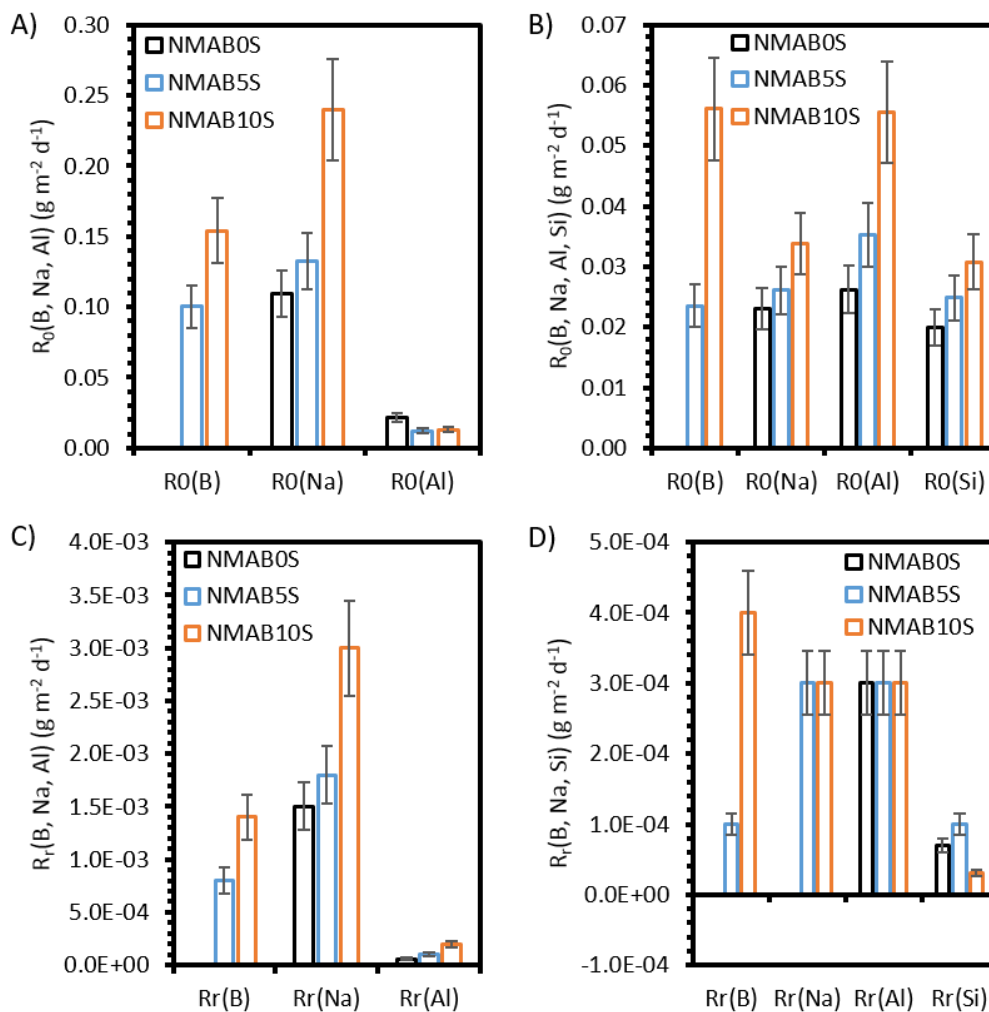


**Figure 5.99.** B, Na and Si normalised mass loss rates for NMAB<sub>x</sub>S glasses after 112 day PCT tests: A) Initial rates, Ca(OH)<sub>2</sub>; B) Initial rates, KOH; C) Residual rates, Ca(OH)<sub>2</sub>; D) Residual rates, KOH.

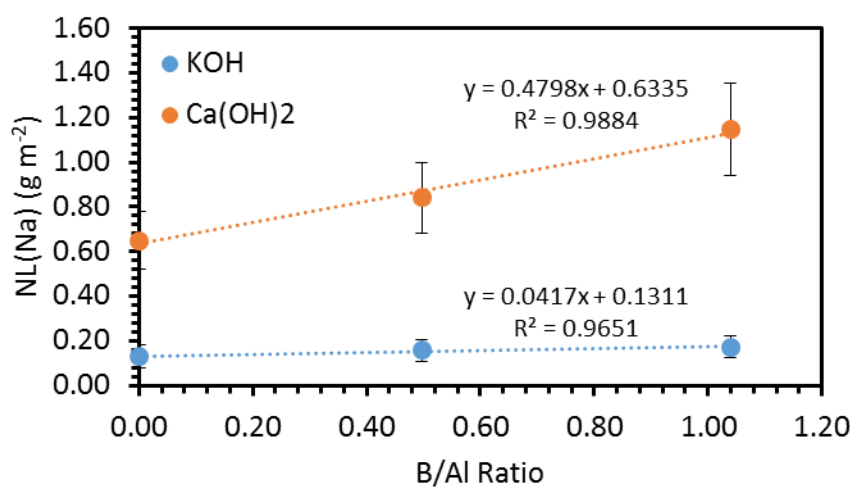


**Figure 5.100.** NL(Na) in KOH and Ca(OH)<sub>2</sub> PCT-B experiments as a function of B/Al ratio for NMAB0S, NMAB5S and NMAB10S.

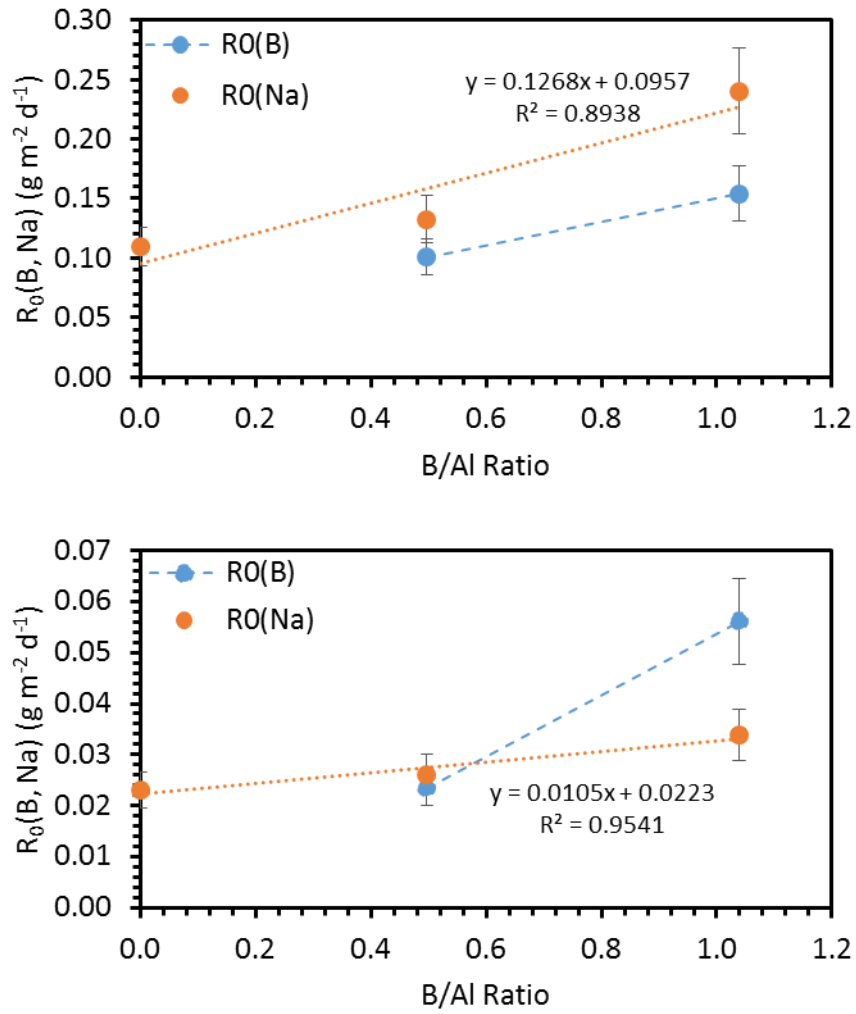


**Figure 5.101.**  $R_0(B)$  and  $R_0(Na)$  in  $\text{Ca(OH)}_2$  (top) and  $\text{KOH}$  (bottom) PCT-B experiments as a function of B/Al ratio for NMAB0S, NMAB5S and NMAB10S.

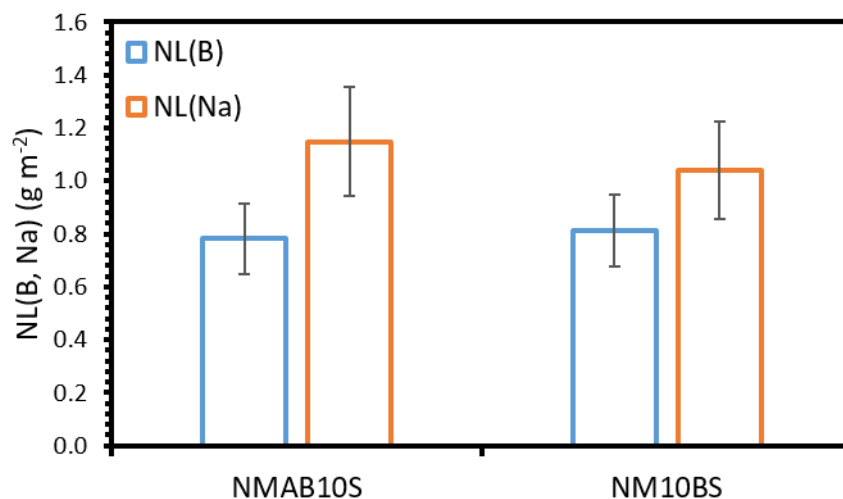


**Figure 5.102.** Comparison of NL(B) and NL(Na) for NMAB10S and NM10BS samples leached in  $\text{Ca}(\text{OH})_2$ .

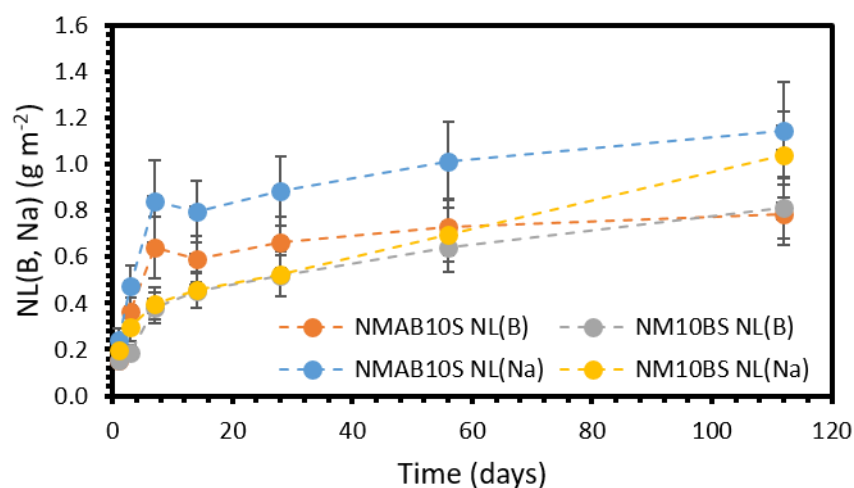


**Figure 5.103.** B and Na normalised mass losses for NMAB10S and NM10BS glasses during 112 day PCT tests in  $\text{Ca}(\text{OH})_2$ .

**Table 5.12.**  $R_{K/\text{Ca}}$  for each of the NMAB $x$ S samples, as determined by ICP-OES analysis.

Sample	NL(B)	NL(Al)	NL(Na)	NL(Si)
NMAB0S	N/A	1.06	0.20	142.3
NMAB5S	0.24	1.08	0.19	415.8
NMAB10S	0.26	1.47	0.15	604.0

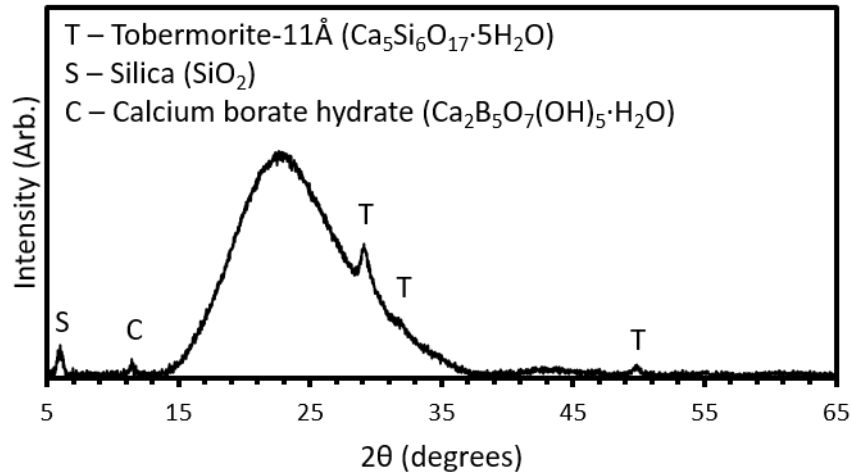


**Figure 5.104.** X-ray diffraction pattern for NMAB10S sample altered in  $\text{Ca}(\text{OH})_2$ .

**Table 5.13.** Ca/Al ratios for the calcium aluminate phases observed in the NMAB $x$ S samples, per triplicate EDS spot analysis.

Sample	Ca/Al (At. %)	Equivalent $\text{CaO}/\text{Al}_2\text{O}_3$
NMAB0S	$1.74 \pm 0.05$	$3.47 \pm 0.11$
NMAB5S	$2.42 \pm 0.25$	$4.83 \pm 0.51$
NMAB10S	$2.69 \pm 0.01$	$5.37 \pm 0.03$

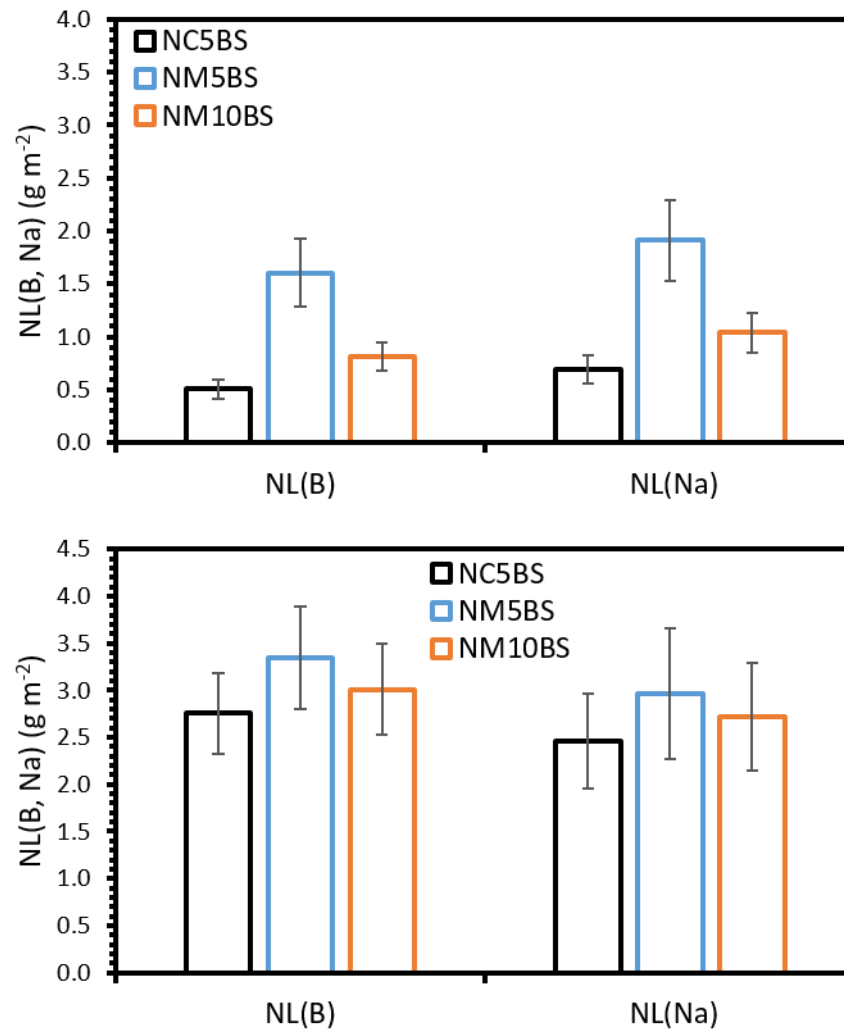
### 5.5.5 Effect of Ca vs Mg Addition on Glass Durability

The normalised mass losses of B and Na for NC5BS, NM5BS and NM10BS in both  $\text{Ca}(\text{OH})_2$  and KOH leachants are shown in Figure 5.105, and the initial and residual rates of B and Na mass loss are shown in Figure 5.106. These data show that the Ca-containing borosilicate had greater durability than the Mg-containing borosilicates in both leachants. Although the  $\text{NL}(\text{B})$  and  $\text{NL}(\text{Na})$  values for the three glasses were similar (within error) in KOH, the B and Na residual mass loss rates, which are more reliable as predictors of long-term durability, are significantly lower for NC5BS than NM5BS and NM10BS; the  $R_r(\text{B})$  values for NC5BS, NM5BS and NM10BS were  $(6.6 \pm 1.0) \times 10^{-3}$ ,  $0.013 \pm 0.002$  and  $0.011 \pm 0.002 \text{ g m}^{-2} \text{ d}^{-1}$ , respectively, and the corresponding  $R_r(\text{Na})$  values were  $(5.4 \pm 0.8) \times 10^{-3}$ ,  $0.011 \pm 0.002$  and  $(8.4 \pm 1.3) \times 10^{-3} \text{ g m}^{-2} \text{ d}^{-1}$ . In  $\text{Ca}(\text{OH})_2$ , the initial rates of mass loss are similar for the three glasses,

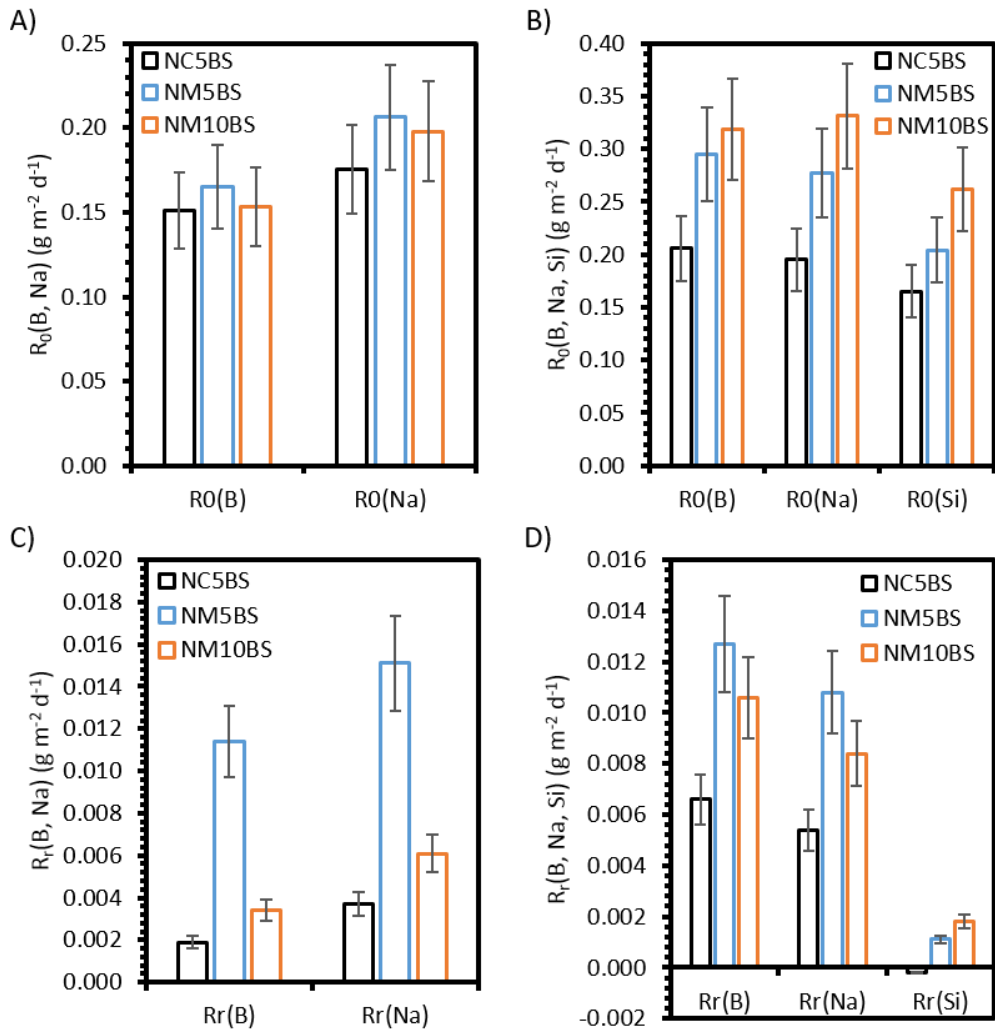
e.g.  $R_0(\text{B})$  was found to be  $0.151 \pm 0.023$ ,  $0.165 \pm 0.025$  and  $0.153 \pm 0.023 \text{ g m}^{-2} \text{ d}^{-1}$  for NC5BS, NM5BS and NM10BS, respectively. This suggests that the structural effects of the replacement of Na with Ca or Mg on the dissolution rate are similar, as the initial stage of dissolution is where these effects would be expected to be observed. However, the residual mass loss rates, as for the KOH leachant, were significantly lower for NC5BS compared to NM5BS and NM10BS, e.g. the  $R_r(\text{B})$  values for NC5BS, NM5BS and NM10BS were  $(1.9 \pm 0.3) \times 10^{-3}$ ,  $0.011 \pm 0.002$  and  $(3.4 \pm 0.5) \times 10^{-3} \text{ g m}^{-2} \text{ d}^{-1}$ , respectively. This suggests that the primary difference in the dissolution behaviour of the Ca- and Mg-containing glasses is likely to be due to differences in the formation of alteration layers and other secondary products. This could be due to the precipitation of secondary phases from solution. The Mg, Ca and Si normalised mass losses for the three glasses after dissolution for 112-days in KOH are shown in Figure 5.107. The  $NL(\text{Mg})$  for the Mg-containing glasses was much lower than the  $NL(\text{Ca})$  for NC5BS, suggesting that Mg was retained in secondary phases at a higher rate than Ca. As Ca-Si- and Mg-Si-rich phases have been observed to form in these samples, this would explain why the Mg-containing glasses were observed to have lower  $NL(\text{Si})$  values than NC5BS: more extensive formation of secondary phases in the Mg-containing glasses would have led to the significant removal of Si from the leachate, leading to higher levels of continued Si leaching than for NC5BS, which had less extensive secondary phase formation and hence a lower Si removal rate. An alternative explanation for these results is the nature of the Ca- and Mg-rich phases that are formed as part of the alteration layers. Protective C-S-H phases are likely to form in these high-pH conditions; however, it has been found that equivalent M-S-H phases do not form above pH 11 [136]. If the Mg-rich phases formed on the Mg-containing samples are significantly different to the C-S-H-like phases formed on the Ca-containing glasses, then the alteration layers of the Mg-containing glasses may not provide a decrease in the residual rate of the same magnitude.

Figure 5.108 shows the normalised mass losses of B and Na for NCAB0S, NCAB10S, NMAB0S, NMAB5S and NMAB10S after 112 days of alteration in  $\text{Ca}(\text{OH})_2$  and KOH, and the initial and residual normalised B and Na mass loss rates are shown in Figure 5.109. These data show that, as with the borosilicate glasses, the Ca-containing glasses were more chemically durable than their Mg-containing counterparts in  $\text{Ca}(\text{OH})_2$ . However, in KOH, the chemical durabilities of the Ca- and

Mg-containing glasses were approximately the same, within error. As secondary phases were not observed on these Ca- and Mg-containing aluminoborosilicate glasses in KOH, this suggests that the differences in chemical durability between the Ca- and Mg-containing glasses studied in this work are down to differences in the formation of secondary phases; when alteration layers and secondary precipitates were observed, the Ca-containing glasses, NC<sub>x</sub>BS and NCAB<sub>x</sub>S, had lower leach rates, but when no alteration layers and secondary precipitates were formed, the leach rates of the Ca-containing (NC<sub>x</sub>BS and NCAB<sub>x</sub>S) and Mg-containing (NM<sub>x</sub>BS and NMAB<sub>x</sub>S) glasses were similar, within error. This could be due to the precipitation of Mg-containing secondary phases being more likely than the precipitation of Ca-containing secondary phases, as suggested previously (Section 5.5.4). Precipitation of Mg-containing secondary phases during glass dissolution has been well documented in recent years [12], [21], [81], [137], although the precipitation of secondary phases in a mixed Ca and Mg system has not been investigated. PHREEQC calculations utilising solution data from the dissolution of NMAB10S in Ca(OH)<sub>2</sub> suggests that Mg-containing phases, such as saponite (Ca<sub>0.25</sub>(Mg,Fe)<sub>3</sub>((Si,Al)<sub>4</sub>O<sub>10</sub>)(OH)<sub>2</sub>·n(H<sub>2</sub>O), SI = 25.16 after 112 days) and sepiolite (Mg<sub>4</sub>Si<sub>6</sub>O<sub>15</sub>(OH), Si = 23.37 after 112 days), which are aluminosilicate and silicate clay minerals, respectively, have higher saturation indices in solution and are therefore more likely to form than Ca-containing phases such as tobermorite (SI values of 14.88, 17.74 and 18.71 for the 9Å, 11Å and 14Å versions). This is despite the calculations using Ca concentrations of 400 – 700 ppm, compared to Mg concentrations of 5 – 40 ppm. If the precipitation of Mg-containing (alumino)silicate phases occurs more rapidly than the precipitation of Ca-containing (alumino)silicate phases, then Si (and Al) will be removed more rapidly from systems containing Mg (and Ca), compared to those only containing Ca, and thus there will be a stronger continued driver for the continued dissolution of the glass. However, as discussed above, M-S-H has not been found to form above pH 11. This might suggest that the difference in behaviour between the Ca-containing and Mg-containing glasses is due to the differing nature of the Ca-rich (C-S-H) and Mg-rich (Mg(OH)<sub>2</sub> or other) and their different ability in retarding diffusion through the alteration layer.



**Figure 5.105.** B and Na normalised mass losses for NC5BS, NM5BS and NM10BS after 112-day PCT tests in  $\text{Ca(OH)}_2$  (top) and KOH (bottom).



**Figure 5.106.** B and Na normalised mass loss rates for NC5BS, NM5BS and NM10BS: A) Initial rates, Ca(OH)<sub>2</sub>; B) Initial rates, KOH; C) Residual rates Ca(OH)<sub>2</sub>; D) Residual rates, KOH.

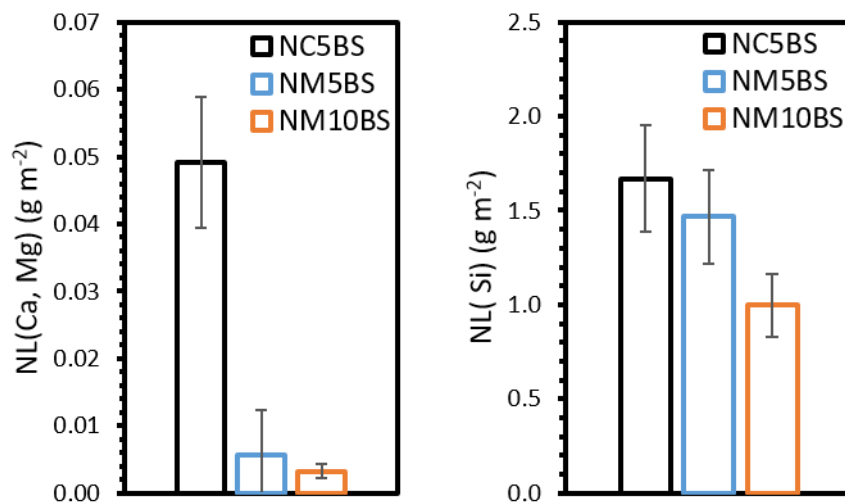


**Figure 5.107.** Ca, Mg and Si normalised mass losses for NC5BS, NM5BS and NM10BS after 112-day PCT tests KOH.

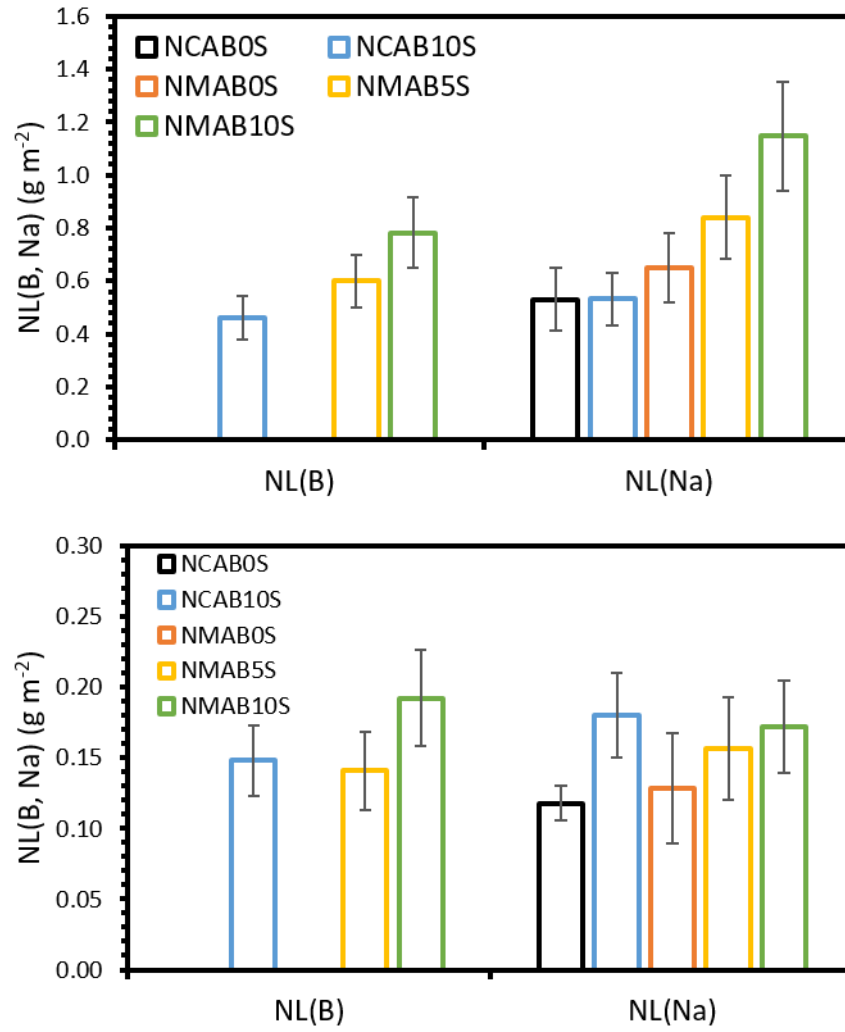


**Figure 5.108.** B and Na normalised mass losses for NCAB $x$ S and NMAB $x$ S after 112-day PCT tests in  $\text{Ca(OH)}_2$  (top) and  $\text{KOH}$  (bottom).

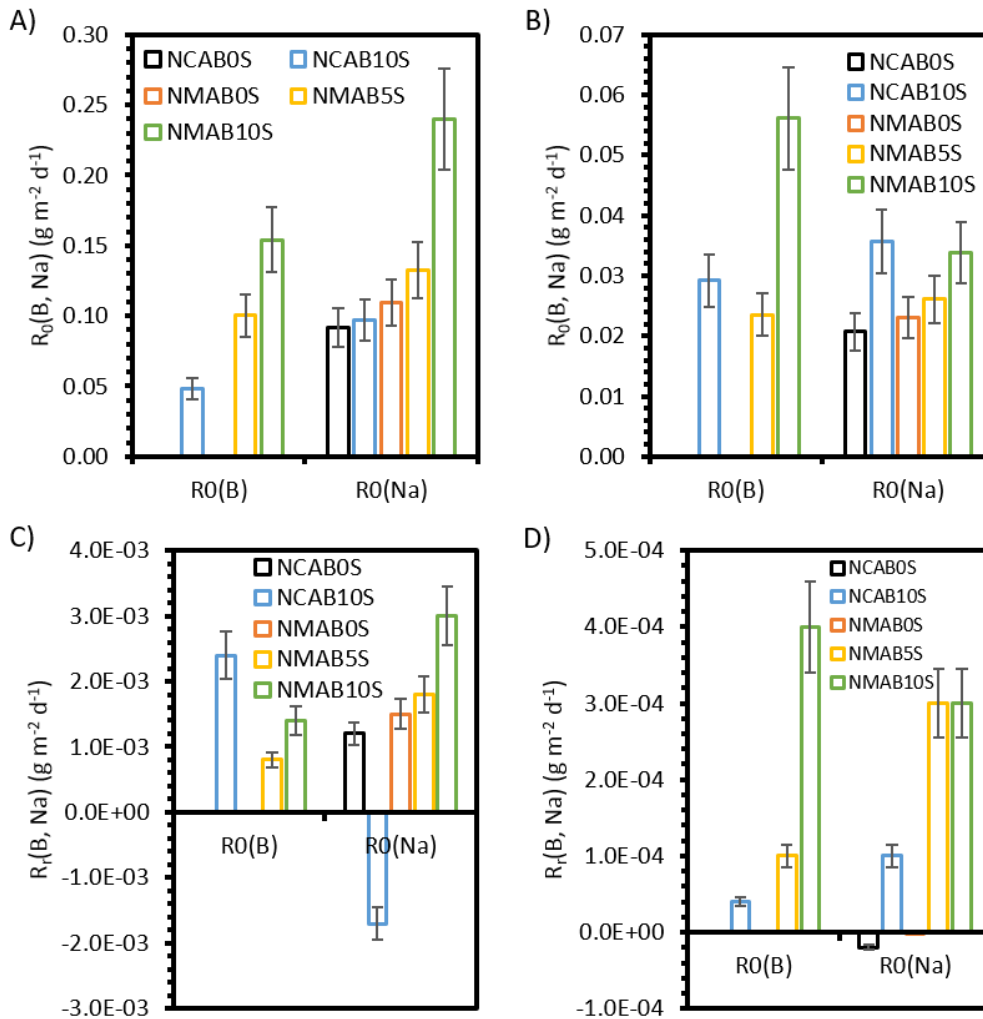


**Figure 5.109.** B and Na normalised mass loss rates for NCAB<sub>x</sub>S and NMAB<sub>x</sub>S after 112-day PCT tests: A) Initial rates, Ca(OH)<sub>2</sub>; B) Initial rates, KOH; C) Residual rates Ca(OH)<sub>2</sub>; D) Residual rates, KOH.

### 5.5.6 Summary

Dissolution experiments performed on a range of 3- to 5-oxide glasses, containing Na<sub>2</sub>O, CaO, MgO, Al<sub>2</sub>O<sub>3</sub>, B<sub>2</sub>O<sub>3</sub> and SiO<sub>2</sub>, have elucidated their leaching behaviour and the formation of alteration products during leaching, with respect to their composition. The key findings from these experiments are:

- Increasing the ratio of Ca/Na in borosilicate glasses leads to an increase in the chemical durability of the glasses in KOH, due to the formation of Ca-containing alteration layers which have a passivating effect on the dissolution.
- However, increasing the ratio of Ca/Na leads to a decrease in the chemical durability of the glasses in Ca(OH)<sub>2</sub>. The Ca(OH)<sub>2</sub> leachant enabled the

formation of Ca-containing passivating alteration layers on each glass, negating the effect of Ca in the glass. The increase in Ca/Na has been shown by NMR spectroscopy to lead to a lower proportion of <sup>IV</sup>B units present in the glass compared to <sup>III</sup>B units, which could have led to an increase in dissolution due to a reduction in the bond breakages required to release B into solution.

- Increasing the ratio of Mg/Na in borosilicate glasses leads to an increase in the chemical durability of the glasses, likely due to the formation of passivating alteration layers on the samples.
- Borosilicate glasses containing Ca were found to be more durable than those containing Mg. While the initial dissolution rates were similar, suggesting that this was not a structural effect, the residual dissolution rates were significantly different, likely due to either: Mg-containing precipitates forming more rapidly than Ca-containing precipitates, and thus removing Si (and possibly Al) from solution more rapidly, leading to an increased driver for further dissolution, or; different types of alteration layers forming on Ca-containing glasses (C-S-H) and Mg-containing glasses (Mg(OH)<sub>2</sub> or other) which are able to retard diffusion between the glass and leachate to greater or lesser extents.
- Increasing the B/Al ratio of Na-Ca aluminoborosilicate glasses leads to a decrease in their chemical durability in KOH due to the lower resistance of the Si – O – B bonds to hydrolysis, compared to Si – O – Al bonds.
- However, increasing the B/Al ratio of Na-Ca aluminoborosilicates leads to little change in their chemical durability in Ca(OH)<sub>2</sub>. This is likely due to the effect of passivating alteration layers, which were not present during dissolution in KOH, in reducing the dissolution rate in the higher B/Al glasses, negating the structural effects.
- Increasing the B/Al ratio of Na-Mg aluminoborosilicate glasses leads to a decrease in their durability, likely due to the lower resistance of Si – O – B bonds to hydrolysis compared to Si – O – Al bonds.
- Aluminoborosilicate glasses containing Ca are more durable than their Mg-containing counterparts. In KOH, their dissolution behaviour is similar, suggesting that there are no significant structural effects on dissolution resistance, but when the precipitation of secondary phases is taken into account, as seen in Ca(OH)<sub>2</sub>, the Ca-containing aluminoborosilicates are more

durable than the Mg-containing aluminoborosilicates. This could be due to the more rapid precipitation of Mg-containing secondary products leading to a higher rate of Si and Al removal from solution, creating a greater driver for continued dissolution, or due to the inability of Mg to form protective M-S-H phases at such high pH.

- The dissolution of the borosilicate glasses was lower in  $\text{Ca}(\text{OH})_2$  than in KOH, due to the agglomeration of particles caused by cementitious precipitates, and the formation of Ca-rich alteration layers which had a passivating effect on the particle surfaces.
- The dissolution of the aluminoborosilicate glasses was higher in  $\text{Ca}(\text{OH})_2$  than in KOH. In  $\text{Ca}(\text{OH})_2$ , secondary precipitates containing Si and Al were formed, so that, although the leachate became saturated with respect to these structural elements from the glass and alteration layer, they were continually removed from solution, leading to a continued driver for further dissolution. However, in KOH, although the leachate was saturated with respect to certain Si- and Al-containing phases, per PHREEQC calculations, no such precipitates were formed, and so the solution remained saturated with respect to both Si and Al, leading to a significantly decreased dissolution rate.

These results show the complexity of glass dissolution, even with relatively simple glass compositions, and that it is important to understand the effects of each component of a glass when considering its chemical durability. In order to obtain a fuller understanding of the effects of B/Al ratio and the effects of Ca vs Mg, it would be advantageous for similar experiments to be carried out on extended NCAB<sub>x</sub>S and NMAB<sub>x</sub>S glass series, e.g. 5 or more glasses of varying B/Al ratio. Experiments investigating the effects of other pertinent elements, e.g. Fe, on glass dissolution in these high-pH conditions would also be of value.



## 6. Dissolution Experiments on Literature Glass Compositions

### 6.1 Introduction

Dissolution experiments utilising the Materials Characterisation Center 1 (MCC-1) and Product Consistency Test B (PCT-B) protocols were performed on four glasses with relevance to UK vitrified waste disposal. As stated previously (Section 3.1.1), these glasses were: MW-25%, the inactive simulant of the UK HLW vitrified product; the International Simple Glass (ISG), an aluminoborosilicate glass developed as a reference for investigating the corrosion mechanisms of nuclear waste glasses [138]; BAS, a laboratory-made version of a natural basaltic glass [15]; and G73, a barium silicate glass developed as a potential matrix for vitrification of ILW, with a 30 wt.% waste-loading [2]. These experiments were performed to compare the resistance to dissolution of the existing and proposed UK nuclear waste glasses (MW-25% and G73) with a reference glass (ISG) and a suggested natural analogue (BAS), in conditions representing those possible in a UK Geological Disposal Facility (GDF).

### 6.2 Experimental Procedure

The glasses were produced or obtained as described in Section 3.1.1, and their compositions, as analysed by digestion and ICP-AES analysis, are shown in Table 6.1, along with their densities (measured by gas pycnometry). From these glasses, monoliths were produced following the method outlined in Section 3.1.2. MCC-1 experiments were set up as detailed in Section 3.2.2. Briefly, experiments were set up with durations of 30, 90, 180, 360, 540 and 720 days, and after the tests were complete, a 5 mL aliquot of solution was taken for analysis by inductively-coupled plasma optical emission spectrometry (ICP-OES) (Data shown in Appendix D). These concentration data from ICP-OES were used to calculate normalised mass losses and mass loss rates as described in Section 3.3. As detailed in Section 3.3, all ‘initial’ and ‘residual’ rates are apparent rates, rather than true rates. The glass monolith was removed and prepared for analysis by SEM-EDS. Powdered samples were also produced, as detailed in Section 3.1.2, and used in PCT-B experiments, which were set up as described in Section 3.2.1. The PCT-B experiments were conducted for a period of 112 days, with sampling points at 1, 3, 7, 14, 28, 56 and 112 days. Each

aliquot was used to measure pH and for elemental analysis of the solution.

**Table 6.1.** Compositions of literature glasses, analysed by digestion and ICP-AES. Glass density values from gas pycnometry

Oxide (mol. %)	ISG	MW-25%	BAS	G73
SiO <sub>2</sub>	53.55	47.67	52.39	62.06
Al <sub>2</sub> O <sub>3</sub>	3.95	2.55	10.67	2.85
B <sub>2</sub> O <sub>3</sub>	19.87	18.65	-	1.54
CaO	5.76	-	12.98	7.75
MgO	0.08	6.82	10.77	1.24
BaO	-	0.15	-	12.20
SrO	-	0.17	0.35	0.08
Na <sub>2</sub> O	14.77	9.57	3.01	3.68
Li <sub>2</sub> O	-	9.24	2.34	5.31
Cs <sub>2</sub> O	-	0.24	-	0.03
K <sub>2</sub> O	0.02	-	0.11	0.05
ZrO <sub>2</sub>	1.83	0.77	-	-
Fe <sub>2</sub> O <sub>3</sub>	0.02	1.31	5.26	2.91
CeO <sub>2</sub>	-	0.45	-	-
Cr <sub>2</sub> O <sub>3</sub>	-	0.29	0.01	-
Gd <sub>2</sub> O <sub>3</sub>	-	0.01	-	-
La <sub>2</sub> O <sub>3</sub>	-	0.13	-	-
Nd <sub>2</sub> O <sub>3</sub>	-	0.39	-	-
Pr <sub>2</sub> O <sub>3</sub>	-	0.12	-	-
Sm <sub>2</sub> O <sub>3</sub>	-	0.08	-	-
Y <sub>2</sub> O <sub>3</sub>	-	0.06	-	-
MnO <sub>2</sub>	-	-	0.20	0.01
RuO <sub>2</sub>	-	-	-	0.02
TeO <sub>2</sub>	-	-	-	-
TiO <sub>2</sub>	-	0.03	1.65	0.02
ZnO <sub>2</sub>	-	-	-	0.03
P <sub>2</sub> O <sub>5</sub>	-	0.09	0.06	0.04
CuO	-	-	-	0.01
NiO	0.16	0.48	0.15	0.12
MoO <sub>3</sub>	-	0.67	-	-
<b>Total</b>	<b>100.01</b>	<b>99.94</b>	<b>99.95</b>	<b>99.95</b>
<b>Density (g cm<sup>-3</sup>)</b>	<b>2.533</b>	<b>2.629</b>	<b>2.851</b>	<b>3.039</b>

## 6.3 Elemental Leaching Results

### 6.3.1 MCC-1 Leaching Results

Figure 6.1 shows the pH values of the leachates during the MCC-1 experiments. There was variation in the average pH of the blanks, from a minimum of 12.89 to a maximum of 13.81. However, in general, the pH of the leachates of the glass samples followed the variations in blank pH with time, suggesting that the variation was most likely due to variations in measurement accuracy. The consistency of the pH values for the glass samples with the pH of the blanks suggests that the addition of excess  $\text{Ca}(\text{OH})_2$  as a pH buffer was successful. Figure 6.2 shows the normalised mass loss of B for the glasses at 50 °C with an initial S/V of  $10 \text{ m}^{-1}$ . Initial ( $R_0(i)$ ) and residual ( $R_r(i)$ ) rates for these experiments are shown in Table 6.2. Out of the four glasses, boron was only detected in solution for ISG and MW-25%, and so NL(B) data are only presented for these samples. Initially, ISG had a higher NL(B), but it showed a more significant decrease in the mass loss rate with time, so that MW-25% had the higher mass loss after 180 - 360 days of dissolution. This is confirmed by their respective  $R_0(\text{B})$  and  $R_r(\text{B})$  values: ISG had a  $R_r(\text{B})$  value of  $(2.5 \pm 0.4) \times 10^{-3} \text{ g m}^{-2} \text{ d}^{-1}$  compared to a  $R_0(\text{B})$  value of  $0.146 \pm 0.022 \text{ g m}^{-2} \text{ d}^{-1}$ , a factor of  $\sim 60$  reduction; whereas MW-25% had only a factor of  $\sim 2$  reduction from the initial rate of  $0.087 \pm 0.013 \text{ g m}^{-2} \text{ d}^{-1}$  to the residual rate of  $0.047 \pm 0.007 \text{ g m}^{-2} \text{ d}^{-1}$ . Due to this, the final NL(B) for MW-25% was more than a factor of two greater than that for ISG, at  $41.2 \pm 7.0 \text{ g m}^{-2}$  compared to  $20.1 \pm 3.5 \text{ g m}^{-2}$  for MW-25%. The Si concentrations in solution were below the detection limits of the ICP-OES (i.e.  $<0.1$  ppm) for ISG, MW-25% and BAS (Figure 6.3). NL(Si) for G73 appeared to be relatively consistent at  $0.10 - 0.15 \text{ g m}^{-2}$ , with the exception for a peak of  $0.30 \text{ g m}^{-2}$  after 180 days, and a trough of  $0.02 \text{ g m}^{-2}$  after 720 days. The low Si concentrations in solution suggest that the Si was involved in the formation of alteration phases, as described previously in Chapter 5.

The normalised mass of Na for each of the four glasses is shown in Figure 6.4. As for the normalised mass loss of boron, ISG had the highest mass loss for the first 90 days, whereas the levels for the other three glasses remained similar: the initial rates were  $0.198 \pm 0.030$ ,  $0.132 \pm 0.020$ ,  $0.130 \pm 0.019$  and  $0.110 \pm 0.016 \text{ g m}^{-2} \text{ d}^{-1}$  for ISG, MW-25%, BAS and G73, respectively. With increasing time, each of the glasses, except MW-25%, underwent a ‘turnover’ of their normalised mass loss, moving from the high initial rates of mass loss, to a much lower residual rate. For BAS, this rate

transition occurred between 90 and 180 days, and for ISG and G73 this occurred between 180 and 360 days. MW-25% does not appear to undergo this transition to the same extent: the residual rates for ISG, BAS and G73 were  $(3.8 \pm 0.6) \times 10^{-3}$ ,  $(6.1 \pm 0.9) \times 10^{-3}$  and  $(2.9 \pm 0.4) \times 10^{-3} \text{ g m}^{-2} \text{ d}^{-1}$ , respectively, whereas the residual rate for MW-25% was  $0.054 \pm 0.008 \text{ g m}^{-2} \text{ d}^{-1}$ , approximately an order of magnitude higher. The value of NL(Na) for MW-25% after 720 days was  $49.2 \pm 8.4 \text{ g m}^{-2}$ , compared to values of  $25.2 \pm 4.4$ ,  $14.6 \pm 2.7$  and  $25.2 \pm 5.6 \text{ g m}^{-2}$  for ISG, BAS and G73, respectively. Figure 6.5 shows the ratio of NL(Na) to NL(B) for ISG and MW-25%. The values of NL(Na) seemed to closely follow the trends of those of NL(B) for ISG and MW-25%, as shown by the consistency of NL(Na)/NL(B) from 180 days onwards. However, as with the simple glasses (Chapter 5) the Na values were consistently higher than those for B, suggesting incongruent dissolution. This could be due to one or both of two possible causes: 1) Na ions are generally ionically-bonded to one oxygen, whereas  $\text{BO}_3$  and  $\text{BO}_4$  units are covalently bonded to 1 – 4 other structural units, and are hence more resistant to leaching; 2) The formation of borate precipitates, as suggested in Chapter 5 and later in this Chapter, means that less B is present in solution compared to Na.

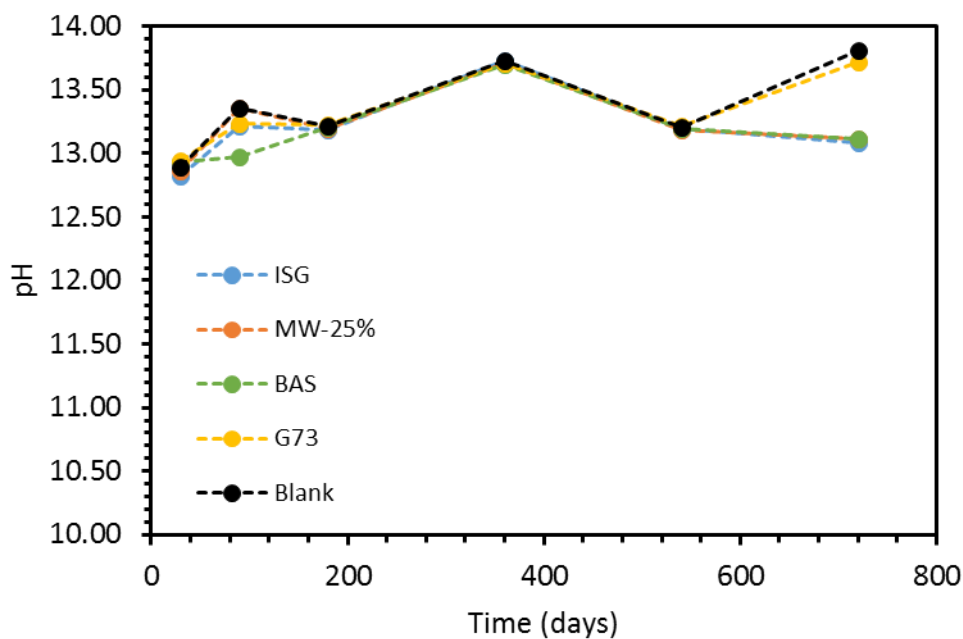


**Figure 6.1.** pH values for MCC-1 experiments on literature glasses.

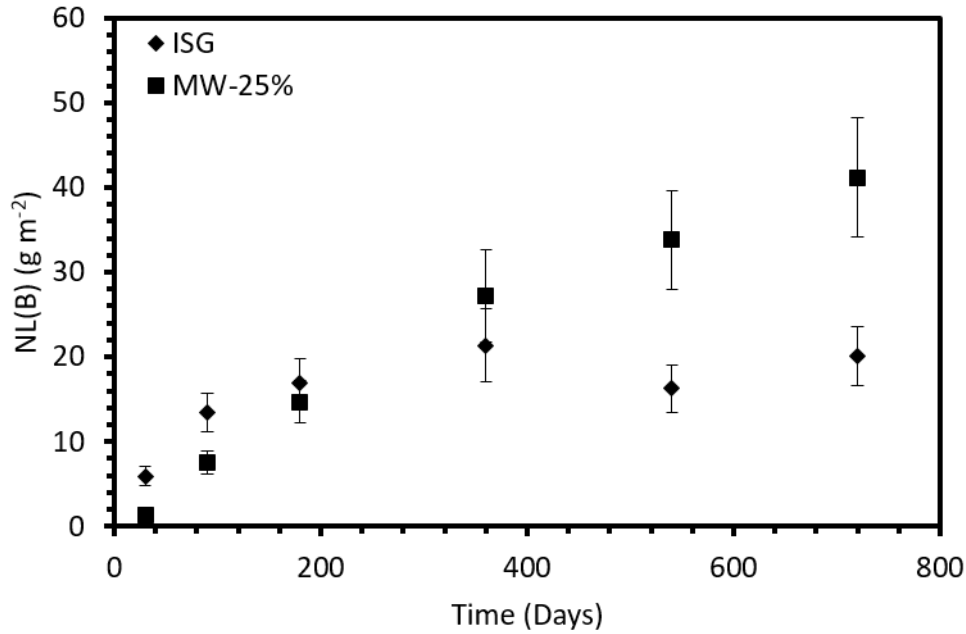


**Figure 6.2.** Normalised mass loss of boron in saturated  $\text{Ca}(\text{OH})_2$  solution using MCC-1 protocol.

**Table 6.2.** Initial ( $R_0(i)$ ) and residual ( $R_r(i)$ ) normalised mass loss rates for B and Na for MCC-1 dissolution experiments.

Rate ( $\text{g m}^{-2} \text{d}^{-1}$ )	ISG	MW-25%	BAS	G73
$R_0(\text{B})$	$0.146 \pm 0.022$	$0.087 \pm 0.013$	-	-
$R_r(\text{B})$	$(2.5 \pm 0.4) \times 10^{-3}$	$0.047 \pm 0.007$	-	-
$R_0(\text{Na})$	$0.198 \pm 0.030$	$0.132 \pm 0.020$	$0.130 \pm 0.019$	$0.110 \pm 0.016$
$R_r(\text{Na})$	$(2.9 \pm 0.4) \times 10^{-3}$	$0.054 \pm 0.008$	$(3.8 \pm 0.6) \times 10^{-3}$	$(6.1 \pm 0.9) \times 10^{-3}$
$R_0(\text{Ba})$	-	-	-	$0.133 \pm 0.020$
$R_r(\text{Ba})$	-	-	-	$(5.3 \pm 0.8) \times 10^{-3}$

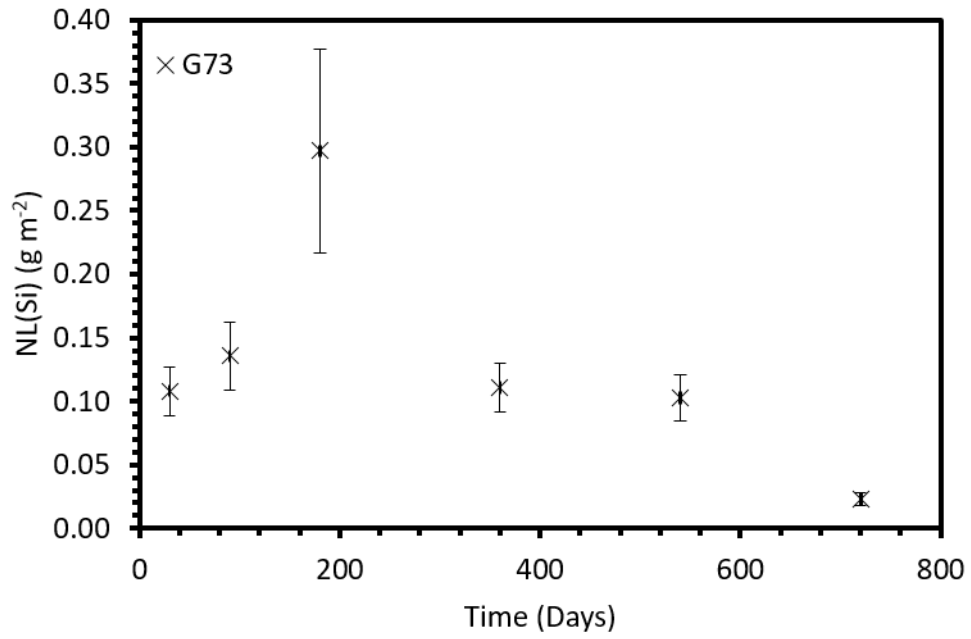


**Figure 6.3.** Normalised mass loss of silicon in saturated  $\text{Ca}(\text{OH})_2$  solution using MCC-1 protocol.

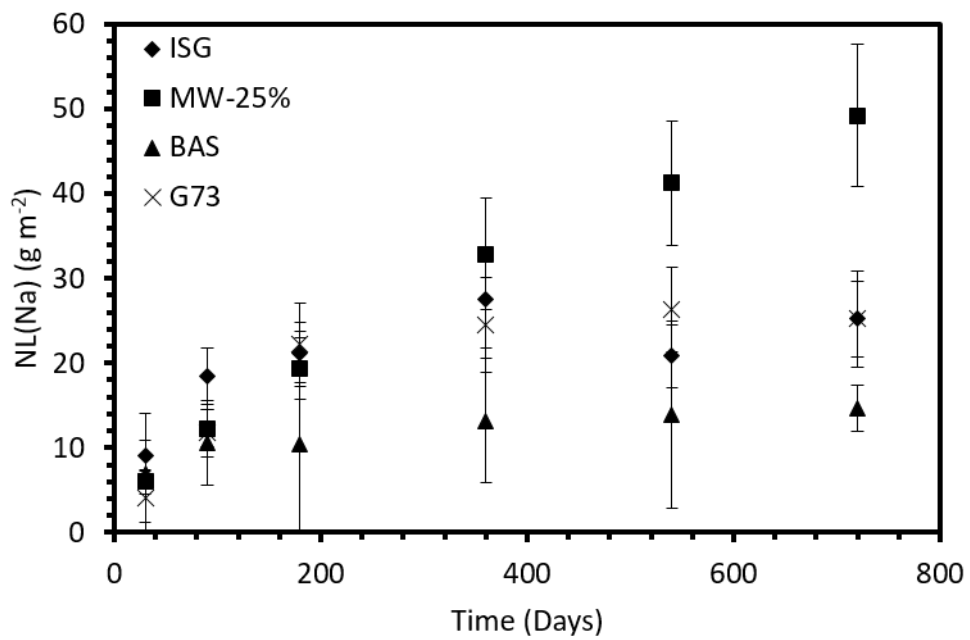


**Figure 6.4.** Normalised mass loss of sodium in saturated  $\text{Ca}(\text{OH})_2$  solution using MCC-1 protocol.

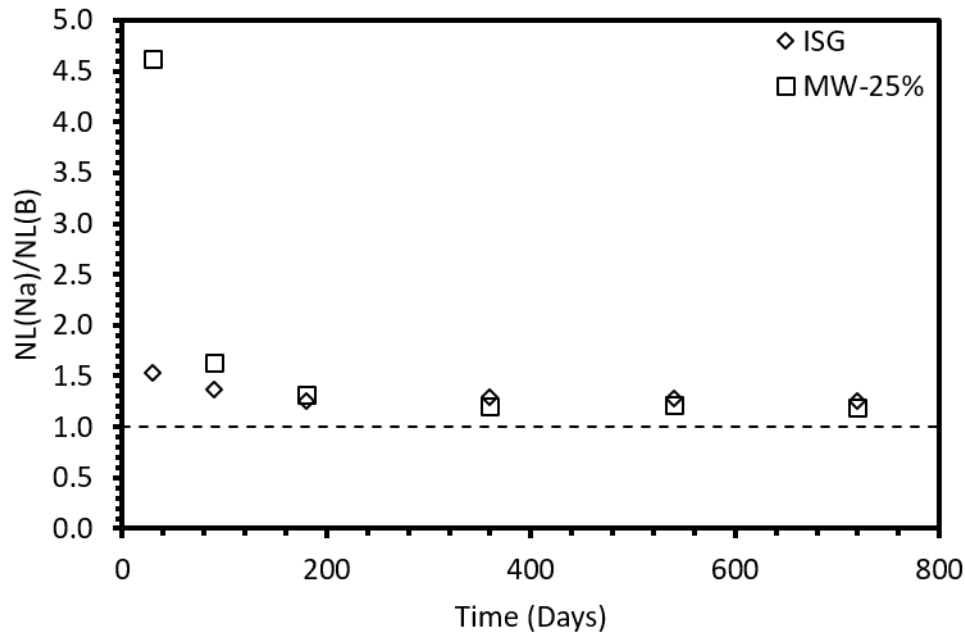


**Figure 6.5.** Ratio of Na mass loss to B mass loss for ISG and MW-25% during MCC-1 dissolution experiments.

Figure 6.6 shows the normalised mass loss of aluminium for the four glasses. As with silicon, the normalised mass loss of aluminium remained low at  $< 1 \text{ g m}^{-2}$  for the majority of data. Aluminium, like silicon, is involved in the formation of alteration products, both alteration layers and crystalline precipitates, and so the measured solution concentration is not equal to the amount of aluminium leached from the glass. It is not possible to relate these data to the dissolution of the glasses without also taking into account the formation of alteration products (Section 6.4.1).

The normalised mass losses of sodium and barium for G73 are compared in Figure 6.7. The barium release profile was similar to that of the sodium release, with  $R_0(\text{Na})$  and  $R_0(\text{Ba})$  values of  $0.110 \pm 0.016$  and  $0.133 \pm 0.020 \text{ g m}^{-2} \text{ d}^{-1}$ , respectively;  $R_r(\text{Na})$  and  $R_r(\text{Ba})$  values of  $(6.1 \pm 0.9) \times 10^{-3}$  and  $(5.3 \pm 0.8) \times 10^{-3} \text{ g m}^{-2} \text{ d}^{-1}$ , respectively; and  $NL(\text{Na})$  and  $NL(\text{Ba})$  values after 720 days of  $25.2 \pm 5.6 \text{ g m}^{-2}$  and  $23.0 \pm 3.9 \text{ g m}^{-2}$ , respectively. However, the behaviour of barium in G73 was markedly different to the behaviour of magnesium, also an alkaline-earth metal, in the other glasses. No magnesium was detected in solution through ICP-OES for either of the Mg-bearing glasses (MW-25% and BAS) at any time-point. ICP-MS analysis carried out on the 720-day samples showed the presence of a very low concentration of magnesium in solution – 66 ppb and 81 ppb for MW-25% and BAS, respectively. However, although

ISG contains only 0.08 mol. % MgO, the ICP-MS detected 68 ppb of Mg in solution for the ISG 720-day sample. It was not possible to determine the normalised mass loss of calcium in these experiments due to the use of a Ca-rich leachant solution, but in Chapter 5, it was shown that the behaviour of calcium during KOH leaching was similar to that of Mg. The differences in leaching behaviour between the alkaline earth metals are discussed in Section 6.5.1.

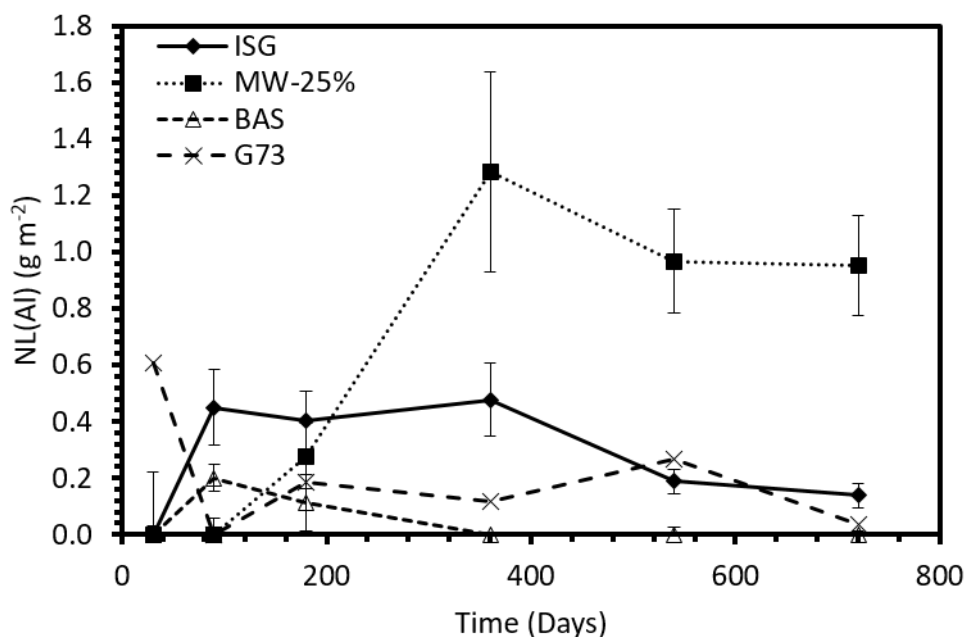


**Figure 6.6.** Normalised mass loss of aluminium in saturated  $\text{Ca}(\text{OH})_2$  solution using MCC-1 protocol (lines added as a guide to the eye).

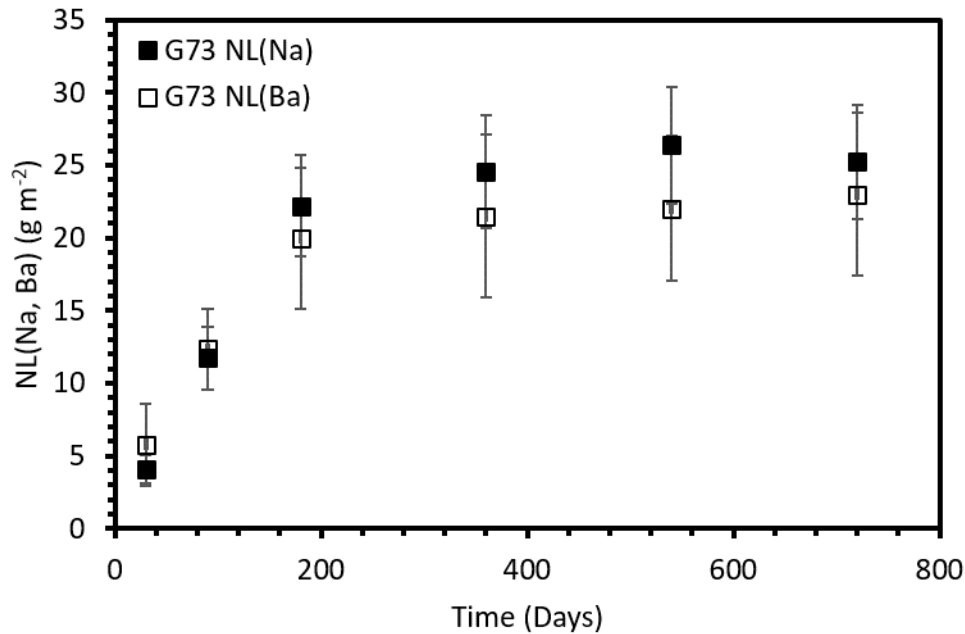


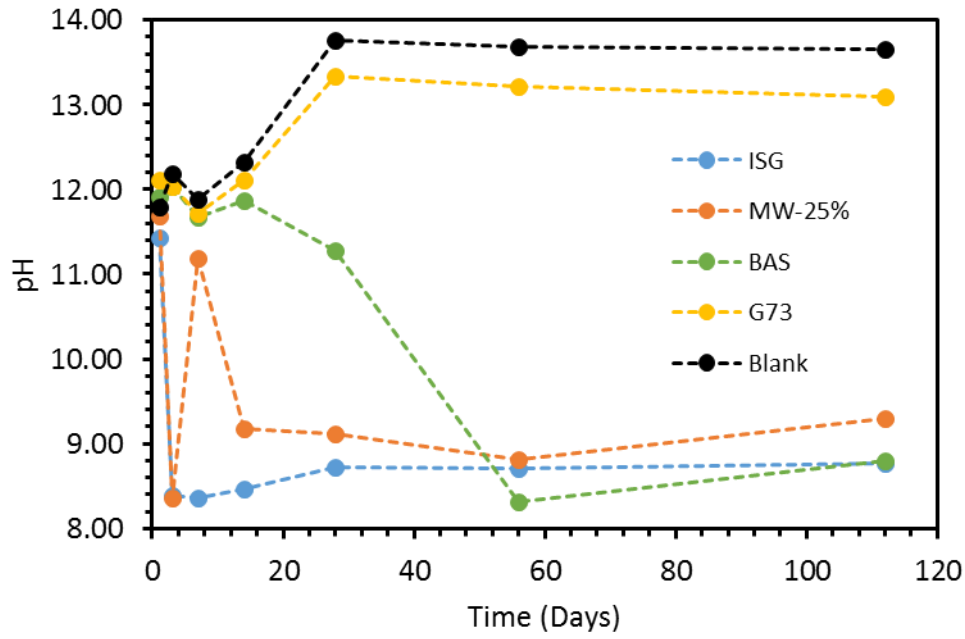
**Figure 6.7.** Comparison of the normalised mass losses of Na (filled symbols) and Ba (empty symbols) for G73 in saturated  $\text{Ca}(\text{OH})_2$  solution using the MCC-1 protocol.

### 6.3.2 PCT-B Leaching Results

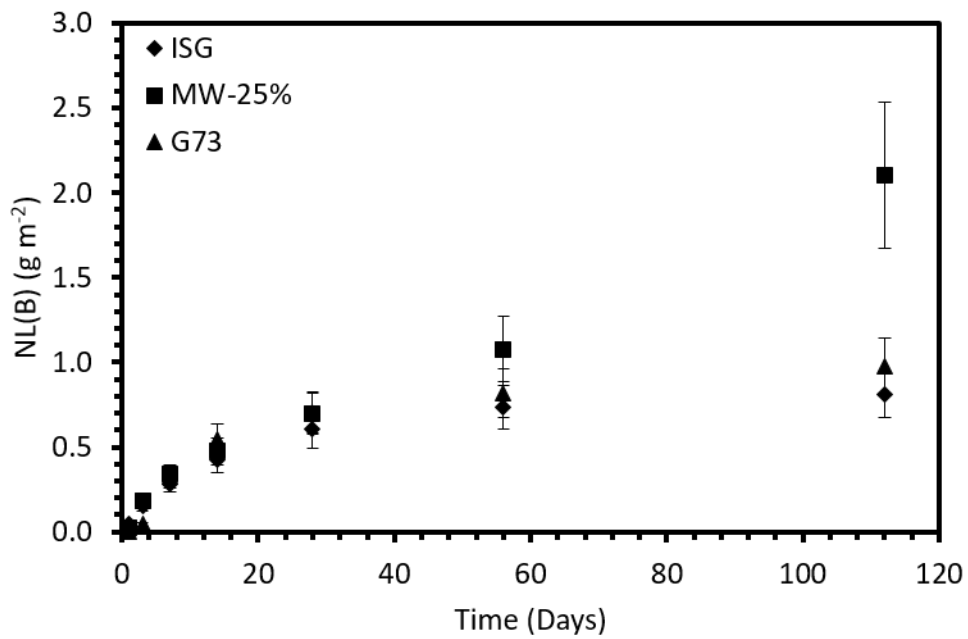
Figure 6.8 shows the average pH of the leachates during the PCT-B experiments. There were significant variations in pH for all samples, including the blanks, which suggests issues with carbonation of the samples after removal from the glovebox, as discussed in Section 5.3.1.1. However, it appears that the average pH for the G73 samples followed the variations in average pH of the blanks, which suggests that the solution remained buffered. It is not possible to draw any conclusions on the pH of the other three glasses. Figure 6.9 shows the normalised mass loss of boron for ISG, MW-25% and G73. Table 6.3 shows initial and residual normalised mass loss rates for each glass. The trends in the data were similar to those for the NL(B) data from the MCC-1 experiments. Initially, the normalised mass loss was similar for each of the glasses – ISG, MW-25% and G73 had  $R_0(\text{B})$  values of  $0.051 \pm 0.008$ ,  $0.062 \pm 0.009$  and  $0.046 \pm 0.007 \text{ g m}^{-2} \text{ d}^{-1}$ , respectively – but between 14 and 28 days, the NL(B) of ISG and G73 underwent a decrease in rate, whereas that of the MW-25% continued at a higher rate. This resulted in  $R_r(\text{B})$  values of  $(3.4 \pm 0.5) \times 10^{-3}$ ,  $(4.0 \pm 0.6) \times 10^{-3}$  and  $0.017 \pm 0.002 \text{ g m}^{-2} \text{ d}^{-1}$  for ISG, G73 and MW-25%, respectively. After 112 days, the NL(B) values were  $2.10 \pm 0.43 \text{ g m}^{-2}$ ,  $0.81 \pm 0.14 \text{ g m}^{-2}$  and  $0.97$

$\pm 0.17 \text{ g m}^{-2}$  for MW-25%, ISG and G73, respectively.

The normalised mass loss of silicon for each of the glasses is shown in Figure 6.10. For each of the glasses, there appears to be an incubation period at the start of the experiments, as evidenced by the lower initial mass loss rates ( $\sim 10^{-3} \text{ g m}^{-2} \text{ d}^{-1}$ ). The incubation period coincided with higher levels of Ca ( $> 200 \text{ ppm}$ ) in solution (see Figure 6.9). This can be seen more clearly when comparing Ca and Si concentrations in solution (Figure 6.12). This suggests that the presence of large amounts of Ca in solution increased the incorporation of Si into alteration phases. Once the Ca level had dropped below a certain threshold ( $\sim 200 \text{ ppm}$ ), the Si incorporation decreased leading to higher concentrations of Si in solution. This would explain why this incubation period was not observed in the monolithic experiments (Figure 6.3); the higher sample surface area in the powder experiments led to greater dissolution of Si and hence greater removal of Ca from solution compared to the monolithic experiments. This led to a drop in the Ca concentration below this threshold level, whereas the lower Ca removal from solution for the monolithic experiments meant that the Ca remained above the threshold level, as shown in Figure 6.13. After the incubation period, the NL(Si) for ISG increased rapidly, whereas that of the other glasses increased more slowly, with the exception of MW-25% between 56 and 112 days, which exhibited a sharp increase. The final values of NL(Si) were  $0.086 \pm 0.016 \text{ g m}^{-2}$ ,  $0.033 \pm 0.009 \text{ g m}^{-2}$ ,  $0.002 \pm 0.0005 \text{ g m}^{-2}$  and  $0.009 \pm 0.002 \text{ g m}^{-2}$  for ISG, MW-25%, BAS and G73, respectively.



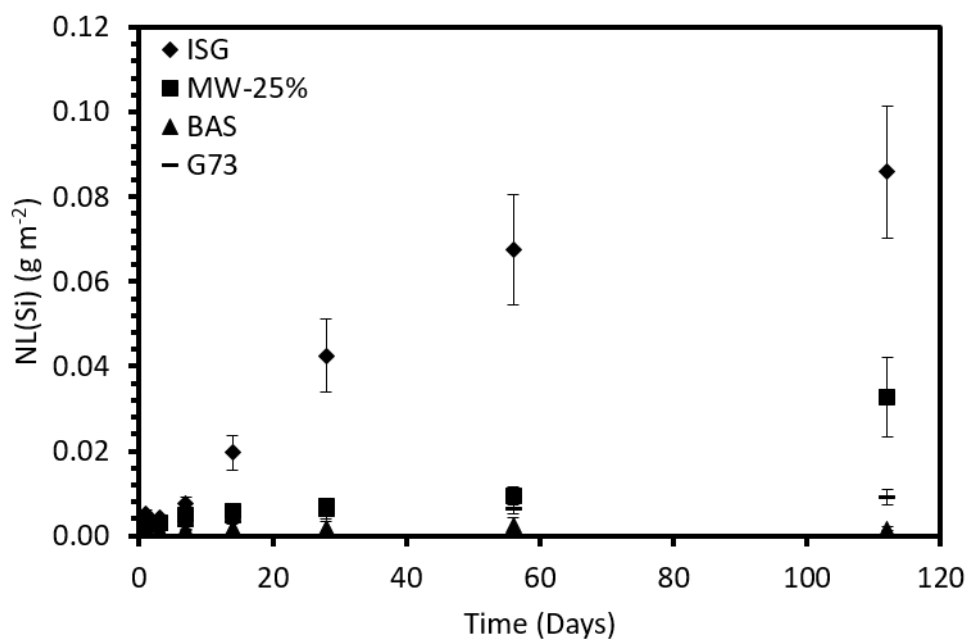
**Figure 6.8.** pH values for PCT-B experiments on literature glasses.



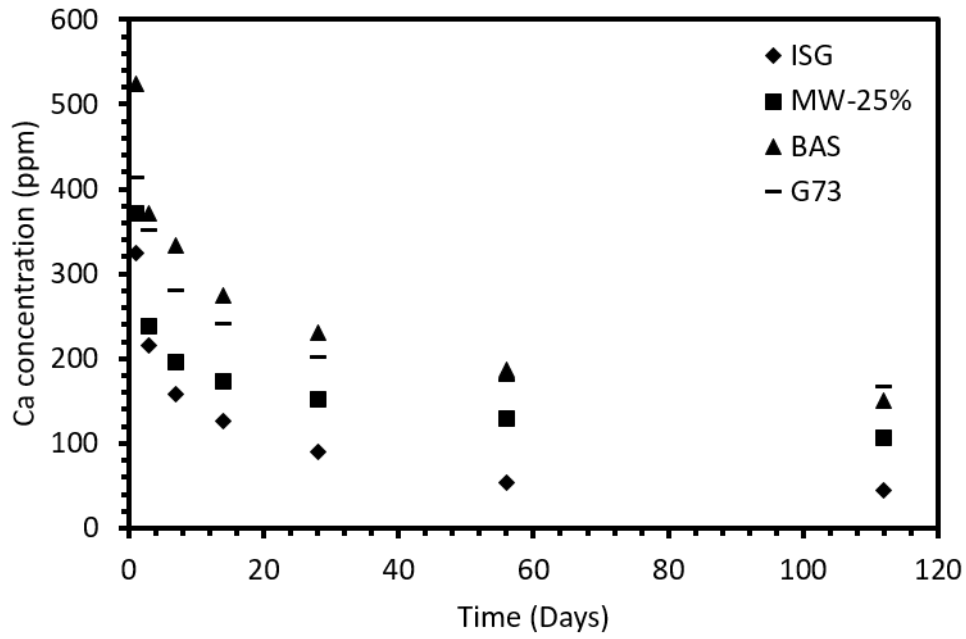
**Figure 6.9.** Normalised mass loss of boron (NL(B)) for ISG, MW-25% and G73 after 112-day PCT-B experiments with a saturated  $\text{Ca}(\text{OH})_2$  leachant.

**Table 6.3.** Initial ( $R_0(i)$ ) and residual ( $R_r(i)$ ) normalised mass loss rates for B and Na for PCT-B dissolution experiments.

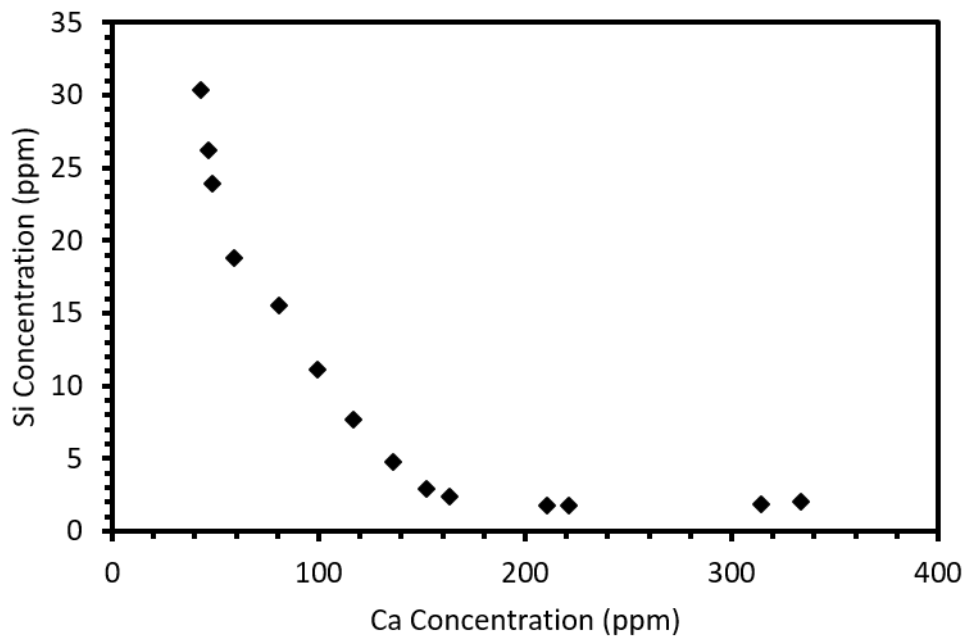
Rate ( $\text{g m}^{-2} \text{d}^{-1}$ )	ISG	MW-25%	BAS	G73
$R_0(\text{B})$	$0.051 \pm 0.008$	$0.062 \pm 0.009$	-	$0.046 \pm 0.007$
$R_r(\text{B})$	$(3.4 \pm 0.5) \times 10^{-3}$	$0.017 \pm 0.002$	-	$(4.0 \pm 0.6) \times 10^{-3}$
$R_0(\text{Na})$	$0.096 \pm 0.014$	$0.116 \pm 0.017$	$0.055 \pm 0.008$	$0.110 \pm 0.016$
$R_r(\text{Na})$	$(6.0 \pm 0.9) \times 10^{-3}$	$0.018 \pm 0.003$	$(5.4 \pm 0.8) \times 10^{-3}$	$(9.2 \pm 1.4) \times 10^{-3}$
$R_0(\text{Al})$	$0.013 \pm 0.002$	$(5.9 \pm 0.9) \times 10^{-3}$	$(6.5 \pm 1.0) \times 10^{-3}$	$(4.0 \pm 0.6) \times 10^{-4}$
$R_r(\text{Al})$	$(-4.0 \pm 0.6) \times 10^{-4}$	$(3.0 \pm 0.5) \times 10^{-4}$	$(6.0 \pm 0.9) \times 10^{-4}$	$(7.0 \pm 1.1) \times 10^{-6}$
$R_0(\text{Si})$	$(5.1 \pm 0.8) \times 10^{-3}$	$(2.7 \pm 0.4) \times 10^{-3}$	$(1.1 \pm 0.2) \times 10^{-3}$	$(9.0 \pm 1.4) \times 10^{-4}$
$R_r(\text{Si})$	$(6.0 \pm 0.9) \times 10^{-4}$	$(3.0 \pm 0.5) \times 10^{-4}$	$(-1.0 \pm 0.2) \times 10^{-7}$	$(6.0 \pm 0.9) \times 10^{-6}$
$R_0(\text{Ba})$	-	-	-	$0.104 \pm 0.016$
$R_r(\text{Ba})$	-	-	-	$(2.0 \pm 0.3) \times 10^{-3}$



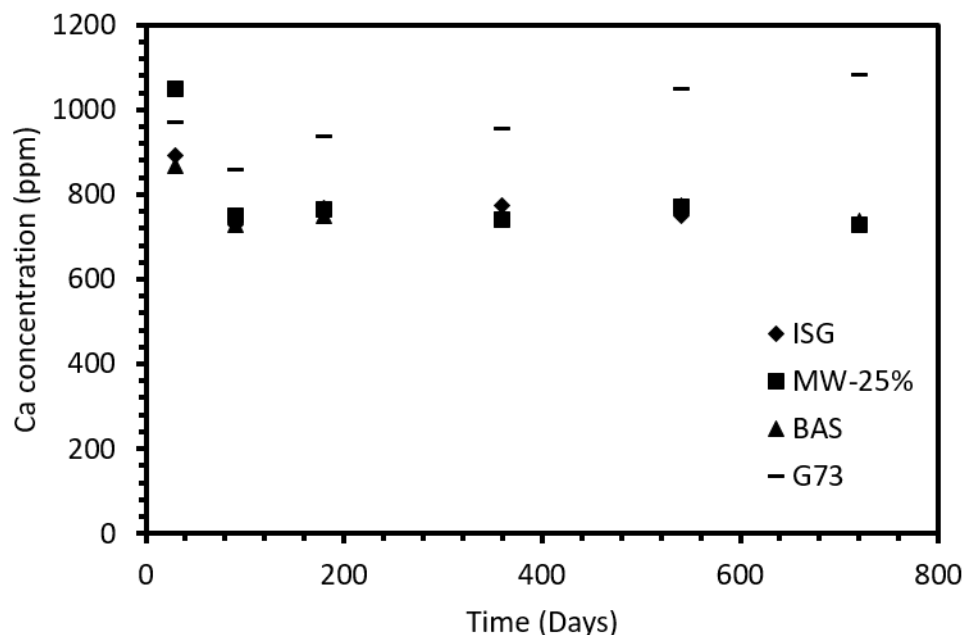
**Figure 6.10.** Normalised mass loss of silicon ( $NL(\text{Si})$ ) for ISG, MW-25%, BAS and G73 for 112-day PCT-B experiments with a saturated  $\text{Ca}(\text{OH})_2$  leachant.



**Figure 6.11.** Calcium concentration in solution for PCT-B experiments on literature glasses.



**Figure 6.12.** Ca vs Si concentration in solution for ISG duplicate samples during PCT-B dissolution experiments.



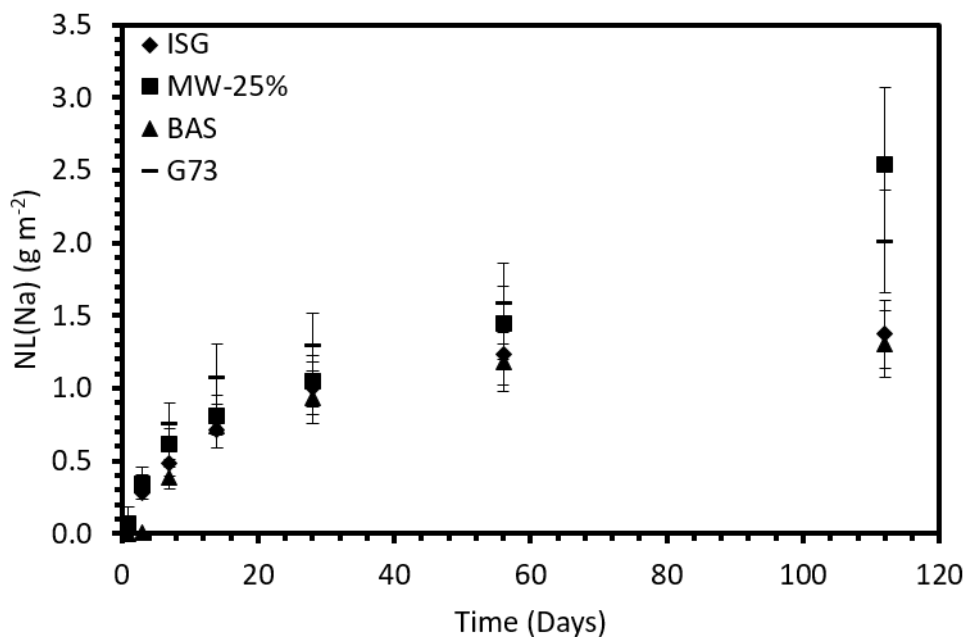
**Figure 6.13.** Calcium concentration in solution for MCC-1 experiments on literature glasses.

Figure 6.14 shows the normalised mass loss of sodium for each of the glasses. The initial mass losses were similar for each glass up to 3 days, with  $R_0(\text{Na})$  values of  $0.096 \pm 0.014$ ,  $0.116 \pm 0.017$ ,  $0.055 \pm 0.008$  and  $0.110 \pm 0.016 \text{ g m}^{-2} \text{ d}^{-1}$  for ISG, MW-25%, BAS and G73, respectively. As with the MCC-1 data, each of the glasses underwent a turnover in the rate of sodium release, with the exception of MW-25%. MW-25% had the highest  $R_r(\text{Na})$  value, at  $0.018 \pm 0.003 \text{ g m}^{-2} \text{ d}^{-1}$ , followed by G73, ISG and BAS with values of  $(9.2 \pm 1.4) \times 10^{-3}$ ,  $(6.0 \pm 0.9) \times 10^{-3}$  and  $(5.4 \pm 0.8) \times 10^{-3} \text{ g m}^{-2} \text{ d}^{-1}$ , respectively. After 112 days, MW-25% had the highest  $NL(\text{Na})$ , followed by G73, ISG and BAS, with values of  $2.54 \pm 0.52 \text{ g m}^{-2}$ ,  $2.01 \pm 0.35 \text{ g m}^{-2}$ ,  $1.37 \pm 0.23 \text{ g m}^{-2}$  and  $1.31 \pm 0.23 \text{ g m}^{-2}$ . As in the MCC-1 experiments,  $NL(\text{Na})$  was consistently higher than  $NL(\text{B})$ , as shown by Figure 6.15 (c.f. Figure 6.5 for MCC-1 data). The reasons for the variation in  $NL(\text{Na})/NL(\text{B})$  between the glasses are not known, but are likely due to the structural role that the  $\text{Na}^+$  ions are playing in each of the glasses, such as whether the  $\text{Na}^+$  cations are primarily associated with  $\text{AlO}_4$  or  $\text{SiO}_4$  tetrahedra, or with  $\text{BO}_4$  tetrahedra. The  $NL(\text{Na})/NL(\text{B})$  ratios were higher in the PCT-B experiments ( $\sim 1.7$  for ISG) than in the MCC-1 experiments ( $\sim 1.3$  for ISG). This might suggest that the cause of the higher  $NL(\text{Na})$  compared to  $NL(\text{B})$  could be the formation of secondary borate phases; the greater surface area for precipitation of the borate

phases in the PCT-B experiments might be expected to lead to higher NL(Na)/NL(B) ratios than for the MCC-1 experiments with lower sample surface areas.

NL(Al) values for the glasses are shown in Figure 6.16. With the exception of ISG, each of the glasses exhibited the same trend; an initially fast rate of mass loss, followed by a significant reduction in rate over longer time periods. The initial Al mass loss rates were  $0.013 \pm 0.002$ ,  $(5.9 \pm 0.9) \times 10^{-3}$ ,  $(6.5 \pm 1.0) \times 10^{-3}$  and  $(4.0 \pm 0.6) \times 10^{-4}$  for ISG, MW-25%, BAS and G73, respectively. However, after behaving similarly to the other glasses up to 28 days, NL(Al) for ISG decreased from a maximum of  $0.075 \pm 0.013 \text{ g m}^{-2}$  at 28 days, down to a value of  $0.033 \pm 0.007 \text{ g m}^{-2}$  after 112 days. The value of  $R_r(\text{Al})$  for ISG was  $(-4.0 \pm 0.6) \times 10^{-4} \text{ g m}^{-2} \text{ d}^{-1}$ , compared to  $(3.0 \pm 0.5) \times 10^{-4}$ ,  $(6.0 \pm 0.9) \times 10^{-4}$  and  $(7.0 \pm 1.1) \times 10^{-6} \text{ g m}^{-2} \text{ d}^{-1}$  for MW-25%, BAS and G73, respectively. The final NL(Al) values for MW-25%, BAS and G73 were  $0.061 \pm 0.011 \text{ g m}^{-2}$ ,  $0.208 \pm 0.037 \text{ g m}^{-2}$  and  $0.012 \pm 0.014 \text{ g m}^{-2}$ , respectively.

Figure 6.17 shows the comparison between the normalised mass losses of barium, sodium and boron for G73 over 112 days. NL(Na) was larger than NL(B) at all sampling intervals, with the difference increasing with time to a maximum of  $1.04 \pm 0.35 \text{ g m}^{-2}$  after 112 days (see also Figure 6.15). For the first 3 days the barium loss was similar to that of sodium, with values of  $R_0(\text{Na})$  and  $R_0(\text{Ba})$  of  $0.110 \pm 0.016$  and  $0.104 \pm 0.016 \text{ g m}^{-2} \text{ d}^{-1}$ , but over time the barium appeared to behave more similarly to boron, leading to values of NL(Ba) and NL(B) that are identical after 112 days (to 2 d.p.);  $0.97 \pm 0.17 \text{ g m}^{-2}$  compared to  $0.97 \pm 0.17 \text{ g m}^{-2}$ .



**Figure 6.14.** Normalised mass loss of sodium (NL(Na)) for ISG, MW-25%, BAS and G73 for PCT-B experiments with a saturated  $\text{Ca}(\text{OH})_2$  leachant.

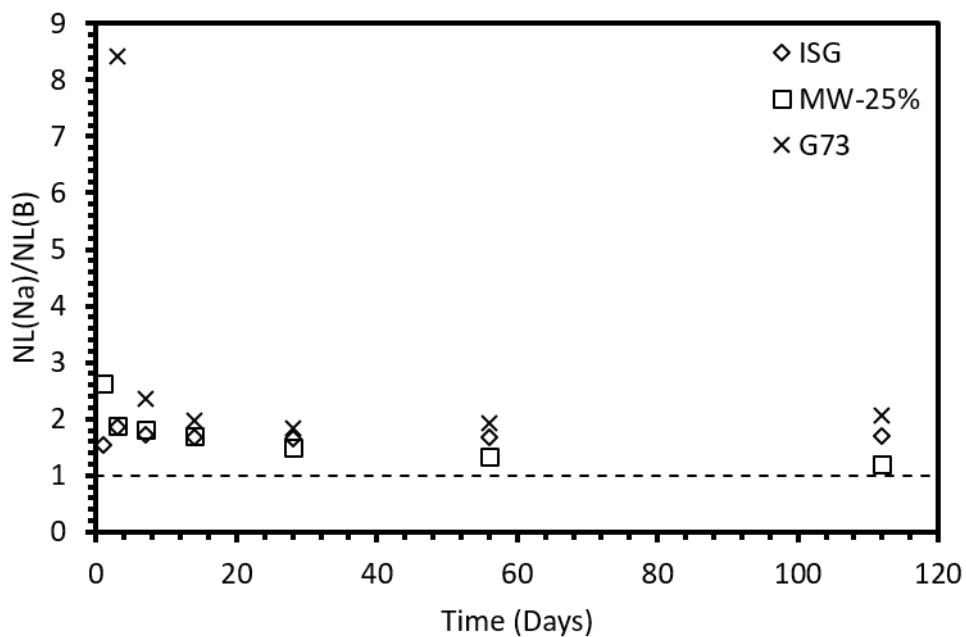


**Figure 6.15.** Ratio of Na mass loss to B mass loss for ISG, MW-25% and G73 during PCT-B dissolution experiments.

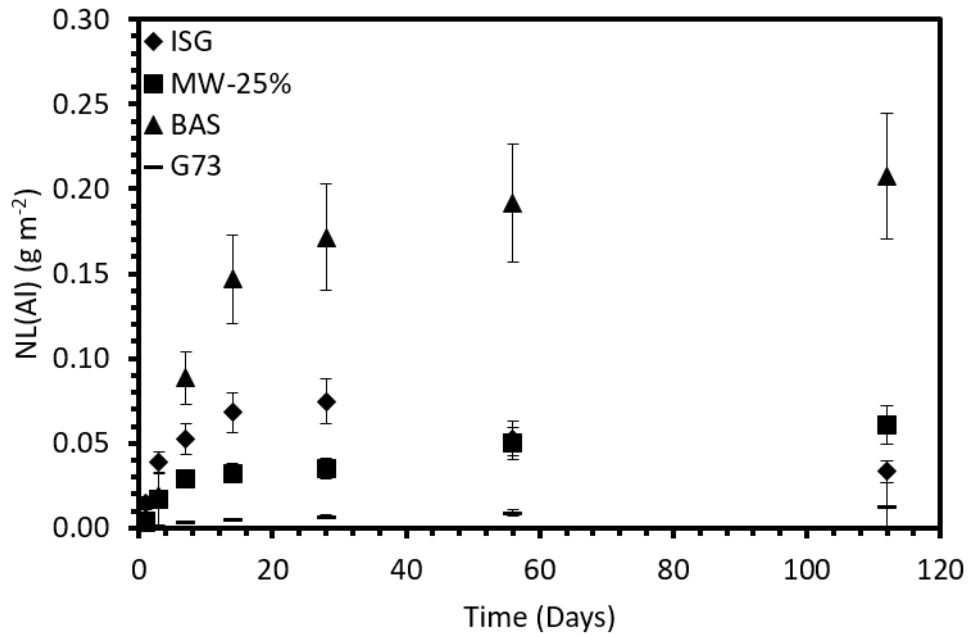


**Figure 6.16.** Normalised mass loss of aluminium (NL(Al)) for ISG, MW-25%, BAS and G73 for PCT-B experiments with a saturated  $\text{Ca}(\text{OH})_2$  leachant.

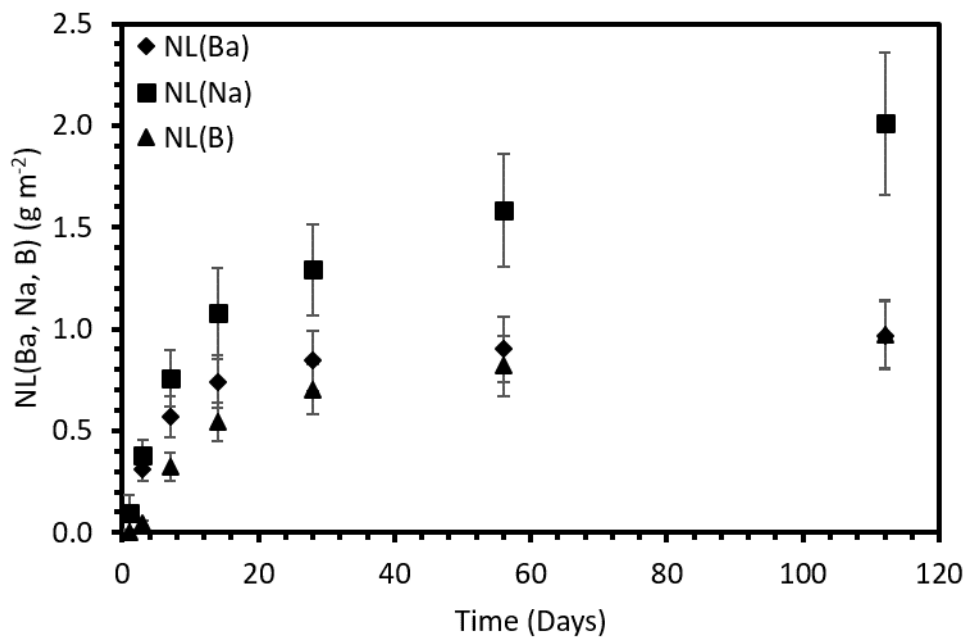


**Figure 6.17.** Normalised mass loss of Ba, Na and B for G73 using the PCT-B protocol with a saturated  $\text{Ca}(\text{OH})_2$  leachant.

## 6.4 SEM-EDS Analysis of Alteration Product Formation

### 6.4.1 Monoliths from MCC-1 Experiments

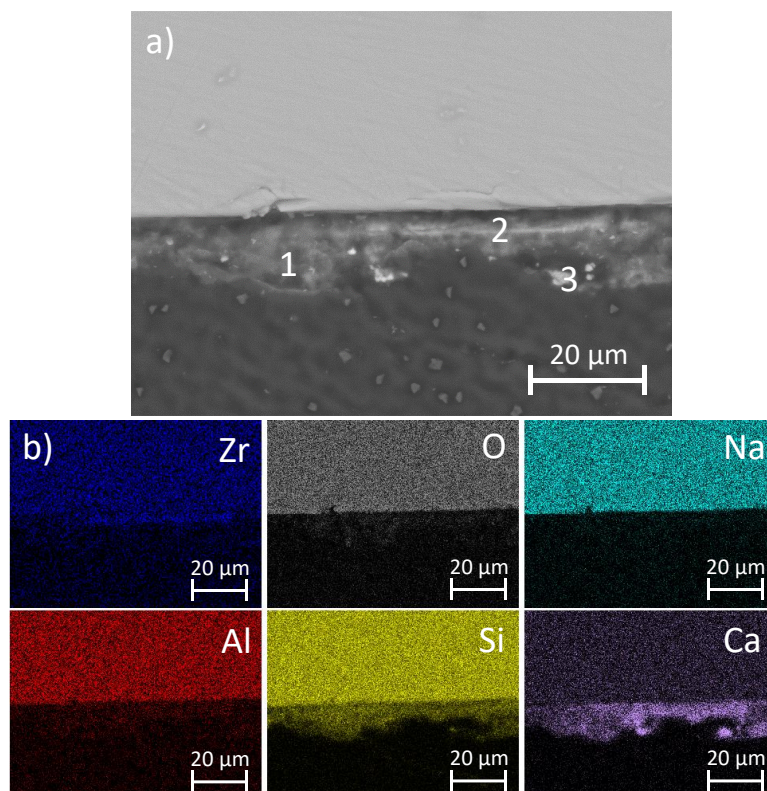
#### 6.4.1.1 ISG

Figure 6.18 shows a back-scattered electron (BSE) micrograph and EDS maps for an ISG sample leached for 30 days. A clear alteration layer was observed, with a thickness between 6 and 13  $\mu\text{m}$ . Three alteration phases were identified; 1) a Ca, Si and O containing phase, 2) a Zr-containing, Ca-enriched phase, 3) a Ca-O rich phase. EDS spot analyses taken at these points, and on the pristine glass, are shown in Figure 6.19. The lack of any elements except Ca, C and O suggests that Phase 3 was portlandite ( $\text{Ca}(\text{OH})_2$ ) or calcite ( $\text{CaCO}_3$ ), depending on whether the C signal is only from the carbon-coating of the sample or from the coating and the sample. Phase 1 appears to be mainly composed of Ca, Si and O, suggesting that it may be a poorly crystalline calcium silicate hydrate (C-S-H), e.g. tobermorite ( $\text{Ca}_5\text{Si}_6\text{O}_{16}(\text{OH})_2 \cdot 4\text{H}_2\text{O}$ ), which has been identified in a previous study of ISG by Abdelouas *et al.* [139]. Phase 2 also consists mostly of Ca, Si and O, and is therefore likely to be a C-S-H phase. There was a small, but detectable amount of Zr localised to this phase. Sodium leached from the glass was not retained in the alteration layer to any significant degree.

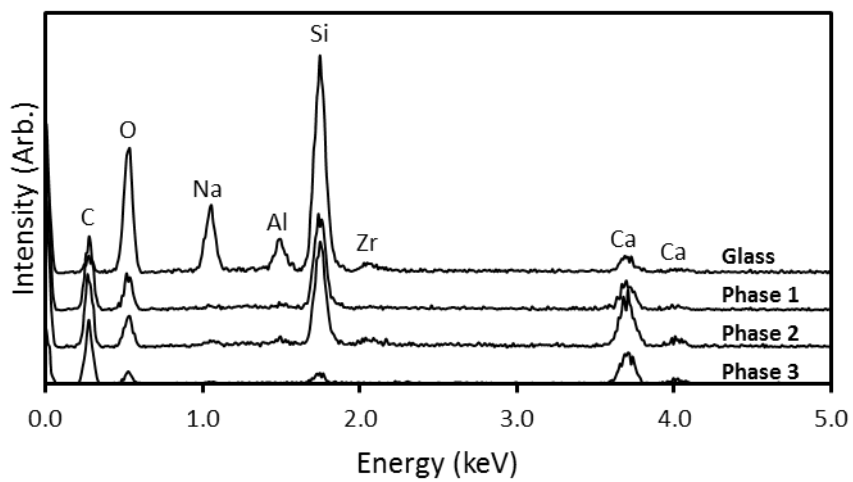
A BSE micrograph and EDS elemental maps for a sample of ISG altered for 90 days are shown in Figure 6.20. Measurement of the alteration layer at several positions on the surface of the monolith revealed a thickness in the range of 12-19  $\mu\text{m}$ . The sample displayed the same Ca-rich deposits (possible portlandite or calcite) as the 30-day sample (point 3 in Figure 6.18). The EDS maps and spot analyses (Figure 6.21) show the presence of three distinct phases within the alteration layer; a Ca- and Si-rich phase (point 1), a Zr-containing phase (point 2) and a second Ca- and Si-rich phase (point 4). A banding of alternating layers of the Ca-Si phase and the Zr-containing phases was observed. The alteration layer appeared to be more consistent in thickness and structure than for the 30-day sample.

Figure 6.22 shows SEM images for a sample altered in  $\text{Ca}(\text{OH})_2$  for 180 days. The alteration layer was approximately 9 – 12  $\mu\text{m}$  thick. Both Zr-containing and non-Zr phases (Phases 2 and 3, respectively, Figure 6.23) were present in the alteration layer, which was observed to have the same banded structure as the 90-day sample. The compositional difference between the phases is shown in Figure 6.23. Closest to the pristine glass, the alteration layer (Phase 1) appeared to have a different composition

to the banded region. The EDS analysis shows that it primarily consisted of Ca and Si, but unlike the other phases, Na was also detected, in addition to small concentrations of Al and Zr. Needle-like precipitates were observed on the surface of the alteration layer (Phase 4), in clusters 7 – 13  $\mu\text{m}$  in diameter. These clusters formed columns on the alteration layer which extended out 25  $\mu\text{m}$  from the outer surface of the alteration layer. EDS analysis of these precipitates showed the presence of primarily Ca and Si, suggesting that they are likely to be C-S-H phases, and the needle-like morphology suggests that they may be crystalline. These phases had a significantly higher Ca/Si ratio than the alteration layer, at  $2.19 \pm 0.11$  compared to  $1.36 \pm 0.09$  (see Section 6.5.2.1 for further discussion).



**Figure 6.18.** BSE image and elemental maps of alteration layer on a monolith of ISG altered for 30 days.



**Figure 6.19.** EDS spot analyses of alteration phases on a sample of ISG altered for 30 days.

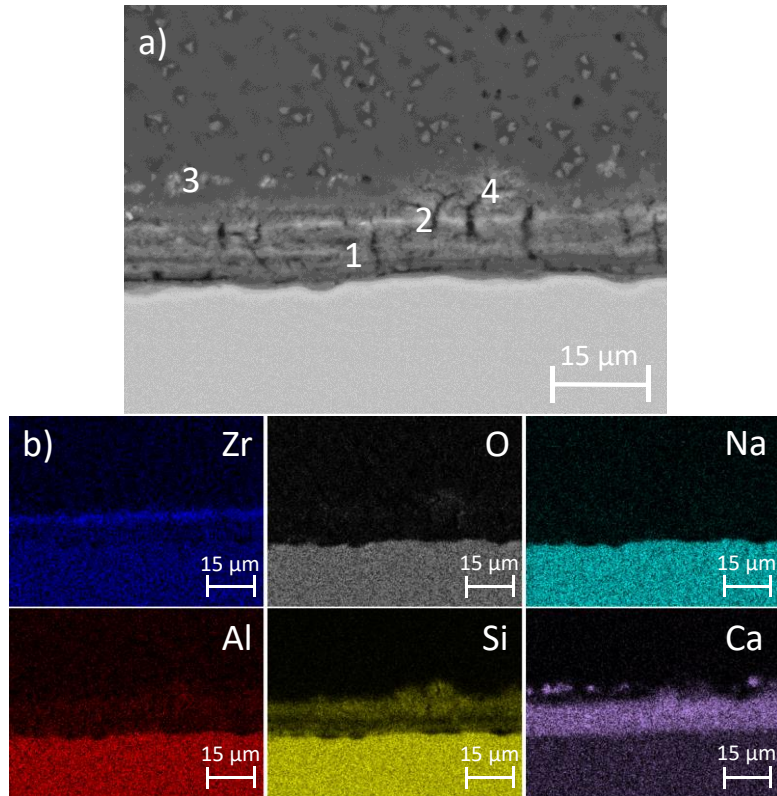


**Figure 6.20.** BSE image and elemental maps of alteration layer on a monolith of ISG altered for 90 days.

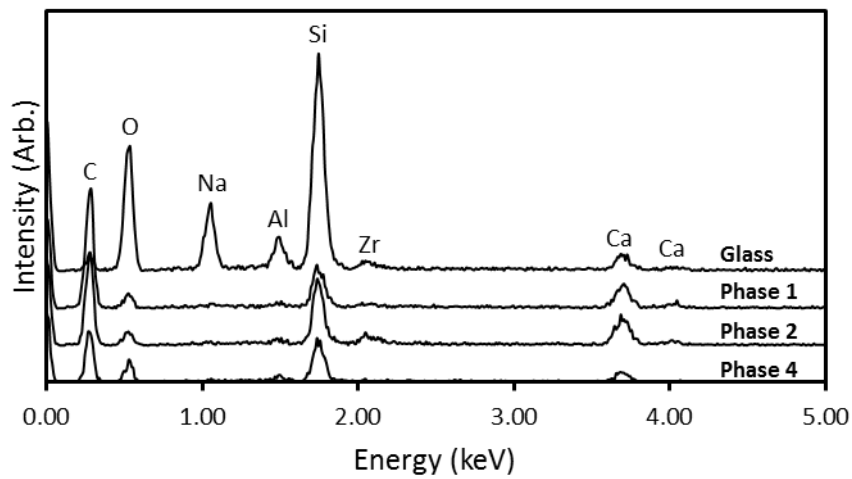


**Figure 6.21.** EDS spot analyses of alteration phases on a sample of ISG altered for 30 days.

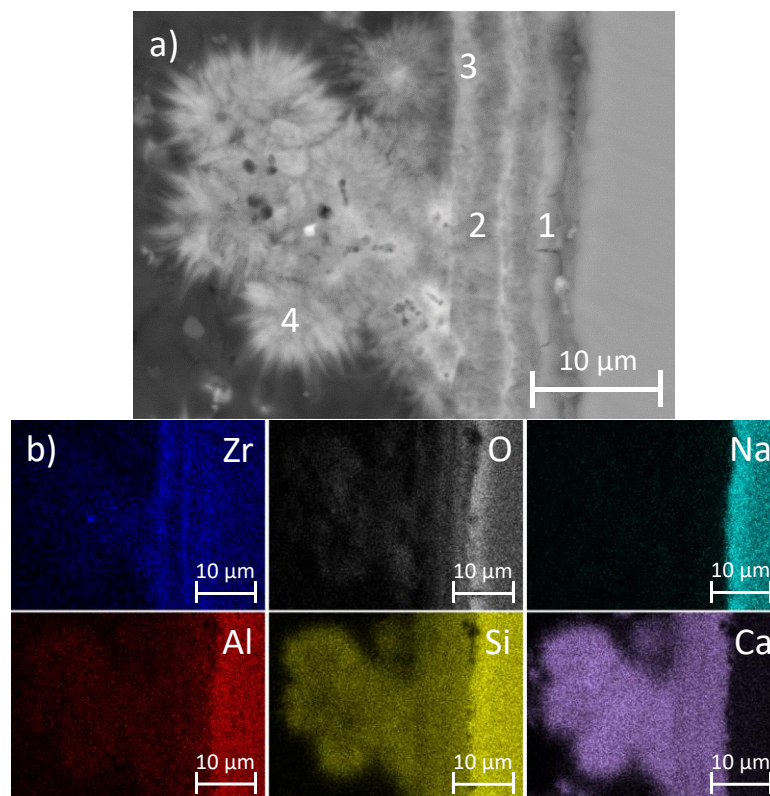


**Figure 6.22.** BSE image and elemental maps of alteration layer on a monolith of ISG altered for 180 days.

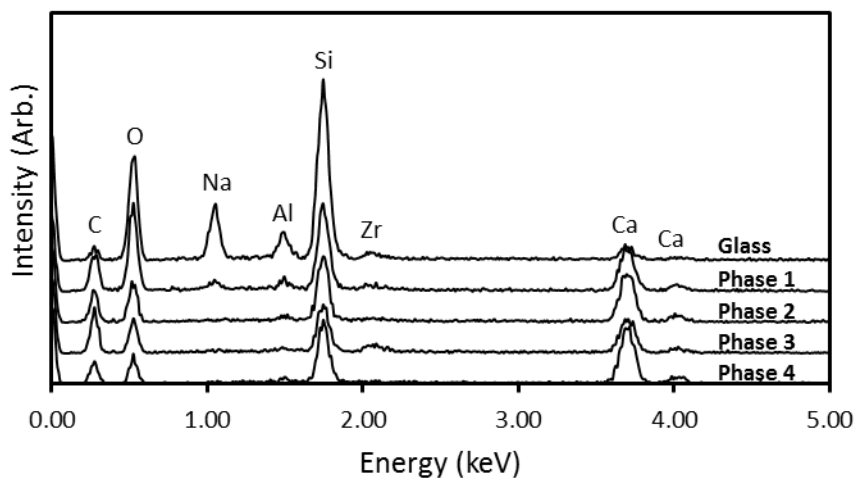


**Figure 6.23.** EDS spot analyses of alteration phases on a sample of ISG altered for 180 days.

The BSE micrograph and EDS elemental maps for a monolith of ISG altered in  $\text{Ca}(\text{OH})_2$  for 360 days are shown in Figure 6.24. The banding in the alteration layer detected for the 180-day sample was again observed. The thickness of the layer is 17 – 20 μm. Three distinct phases were observed: i) Zr-containing and; ii) non-Zr-

containing regions of the alteration layer; and iii) C-S-H-like precipitates. The precipitates were observed to form in clusters 9 – 12  $\mu\text{m}$  in diameter, in columns up to 40  $\mu\text{m}$  long. Figure 6.25 shows the relative compositions of the different phases. The C-S-H-like phase (Phase 3) had a greater Ca/Si ratio than the alteration layer, as for the 180-day sample, per EDS analysis (Figure 6.25).

The alteration layer banding was again present in the sample altered for 540 days (Figure 6.26). The thickness of the alteration layer varied between 11 and 14.5  $\mu\text{m}$ . Four primary distinct phases were observed in the EDS data on this sample (Figure 6.27): i) an O- and Zr-rich Ca-silicate adjacent to the glass surface (phase 1); then alternate bands of ii) an O- and Zr-poor Ca-silicate region (phase 2), and iii) an O-poor but Zr-rich Ca-silicate region (phase 3); iv) C-S-H-like precipitates (phase 4). In addition to these phases, there was a Ca-rich phase (phase 5), which is likely to be either portlandite ( $\text{Ca}(\text{OH})_2$ ) or calcite ( $\text{CaCO}_3$ ). The C-S-H-like precipitates formed clusters 6 – 13  $\mu\text{m}$  in diameter, extending outwards up to 38  $\mu\text{m}$  from the surface of the alteration layer. The EDS analysis (Figure 6.25) shows that the precipitates again had a higher Ca/Si ratio than the alteration layer.

Figure 6.28 shows a BSE micrograph and EDS elemental maps for a monolith of ISG altered for 720 days. The alteration phases (layer plus precipitates) were similar in structure to those of the 180-, 360- and 540-day samples; a Ca-Si alteration layer containing Zr-rich and Zr-poor regions (with a more O-rich region closer to the monolith surface), with C-S-H-like precipitates, with a higher Ca/Si ratio, deposited on the outside surface of the alteration layer. The alteration layer was 12 – 15  $\mu\text{m}$  thick, with the precipitates forming clusters 4 – 8  $\mu\text{m}$  in diameter which extended up to 17  $\mu\text{m}$  out from the surface of the alteration layer.

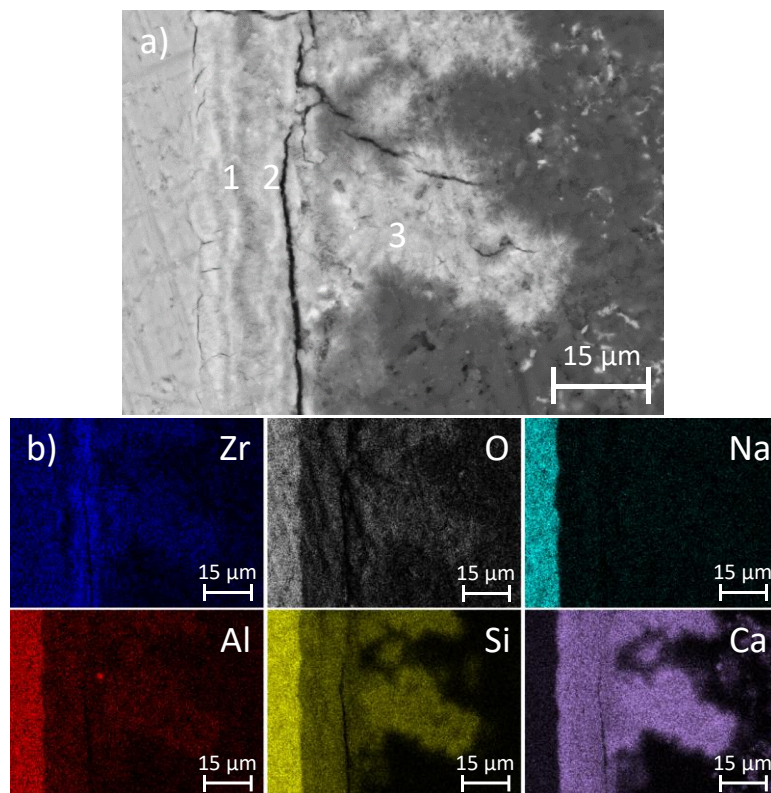


**Figure 6.24.** BSE image and elemental maps of alteration layer on a monolith of ISG altered for 360 days.

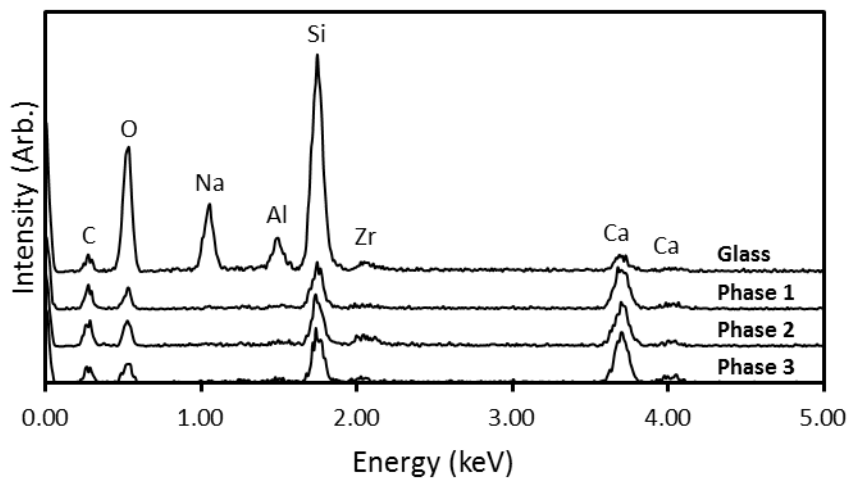


**Figure 6.25.** EDS spot analyses of alteration phases on a sample of ISG altered for 360 days.

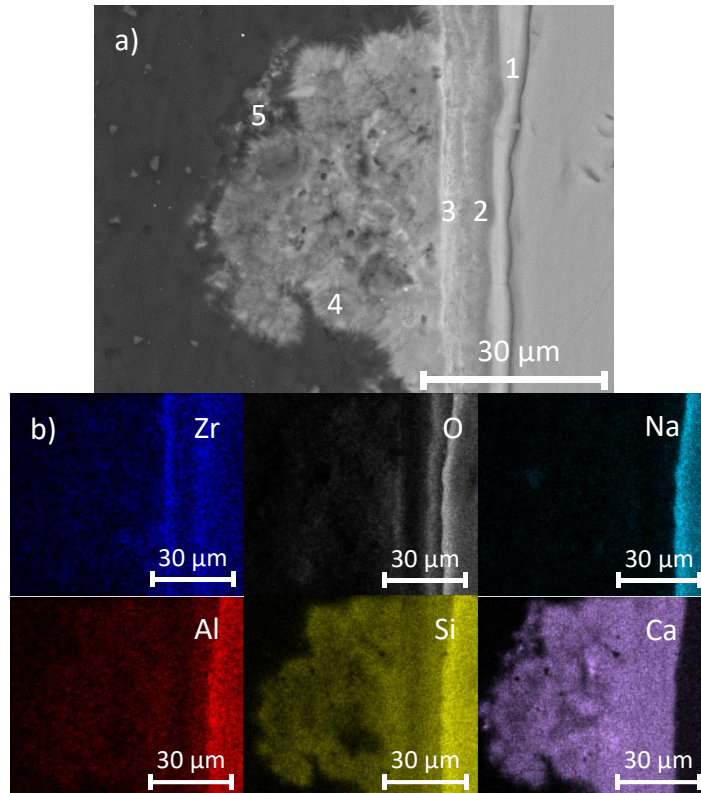


**Figure 6.26.** BSE image and elemental maps of alteration layer on a monolith of ISG altered for 540 days.

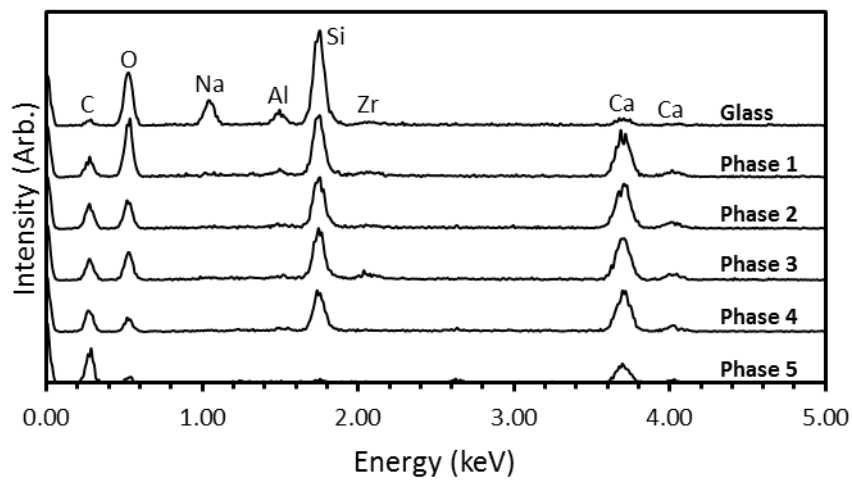


**Figure 6.27.** EDS spot analyses of alteration phases on a sample of ISG altered for 540 days.

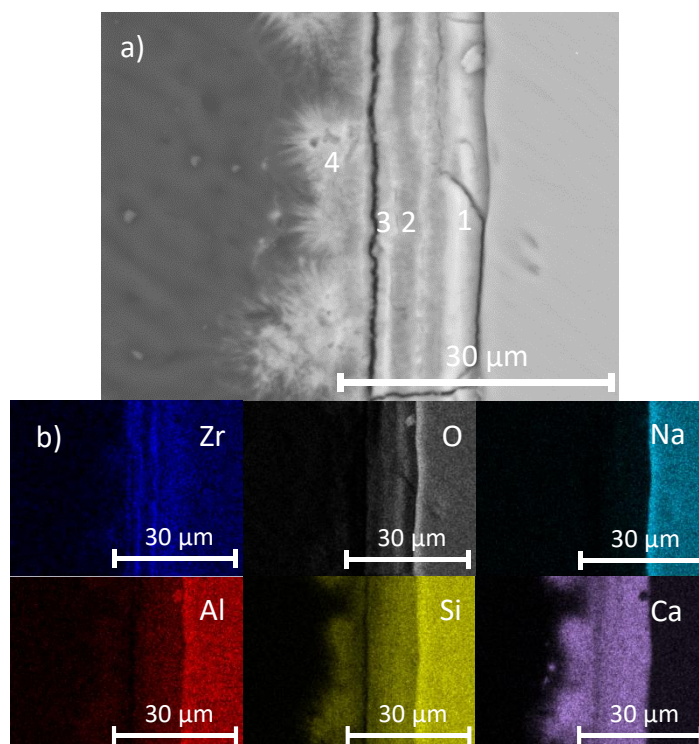


**Figure 6.28.** BSE image and elemental maps of alteration layer on a monolith of ISG altered for 720 days.

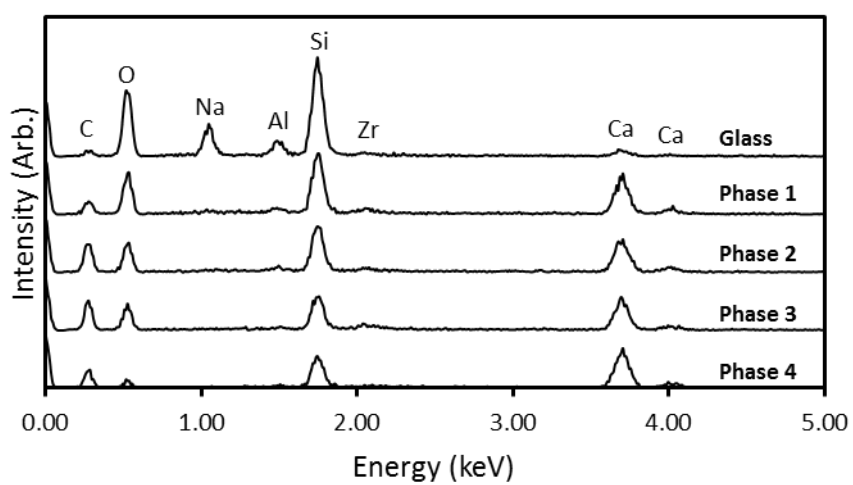


**Figure 6.29.** EDS spot analyses of alteration phases on a sample of ISG altered for 720 days.

#### 6.4.1.2 MW-25%

Figure 6.30 shows a BSE micrograph and elemental maps for a monolith of MW-25% that was altered in  $\text{Ca}(\text{OH})_2$  for 30 days. A small alteration layer (2 - 3  $\mu\text{m}$ ) was observed (point 1), which primarily contained Si, as shown by the EDS spot data in Figure 6.31. No incorporation of Ca into the alteration layer was observed, in contrast to the 30-day ISG sample (Figs. 6.18 & 6.19).

A BSE micrograph and EDS elemental maps of an MW-25% monolith altered for 90 days are shown in Figure 6.32. Three distinct phases were observed: 1) a phase that contained primarily Ca, Si, and O, with some Mg and Zr; 2) a phase with similar composition but with increased Mg content and decreased Zr content; and 3) a phase on the surface of the alteration layer composed of Ca, Si, and O with a small amount of Zr. This final phase had an acicular morphology, and was most likely a C-S-H-like phase. Ca was significantly incorporated into both the alteration layer and the secondary phase.

A BSE micrograph and EDS elemental maps of the alteration layer formed on a monolith of MW-25% altered for 180 days are shown in Figure 6.34. The alteration layer varied in thickness between 6 and 9  $\mu\text{m}$ , and consisted of several distinct phases, denoted by the number in the micrograph. The EDS spot spectra for these phases are shown in Figure 6.35. Phase 1 was a Ca-Mg-Si-O phase, which also contained Al and a small amount of Zr. A Ca-Si rich phase was also observed (Phase 2). At the edge of the alteration layer, a rim consisting of Fe-rich particles (bright phases in BSE micrograph) and a Mg- and Al-rich layer was observed (Phase 3). Precipitates containing Ca, Si, Mg and O were also observed on the surface of the alteration layer (Phase 4).

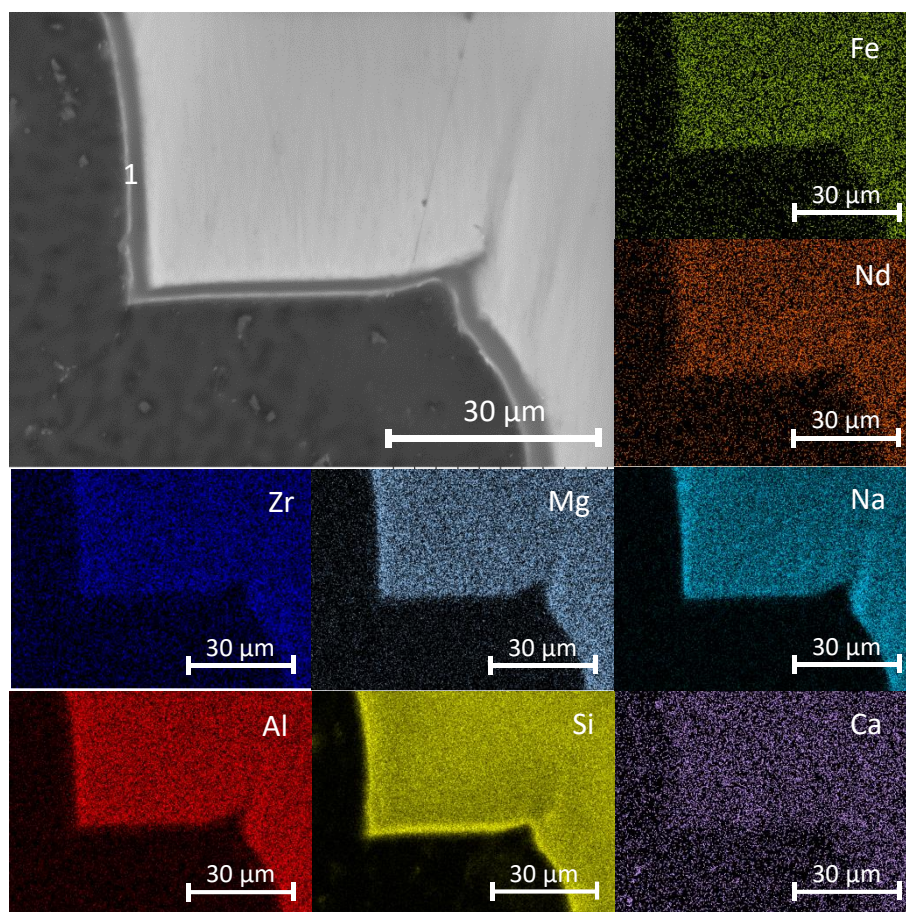


**Figure 6.30.** BSE image and elemental maps of alteration layer on a monolith of MW-25% altered for 30 days.

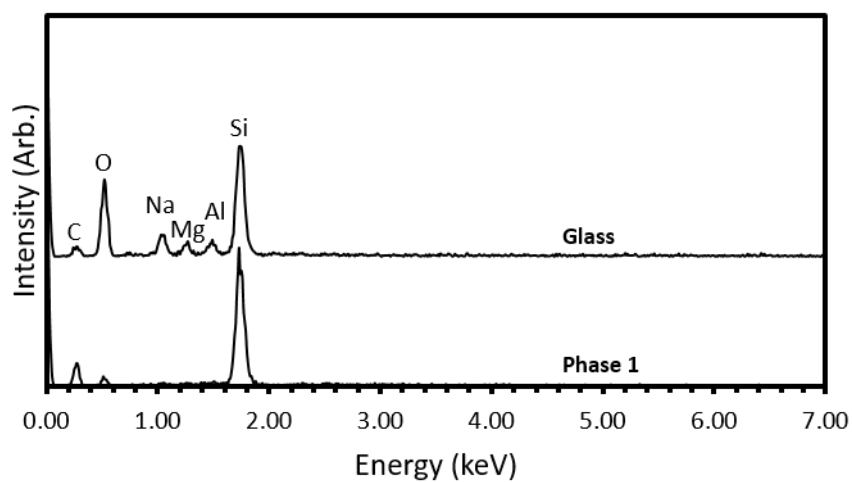


**Figure 6.31.** EDS spot analyses of alteration phases on a sample of MW-25% altered for 30 days.

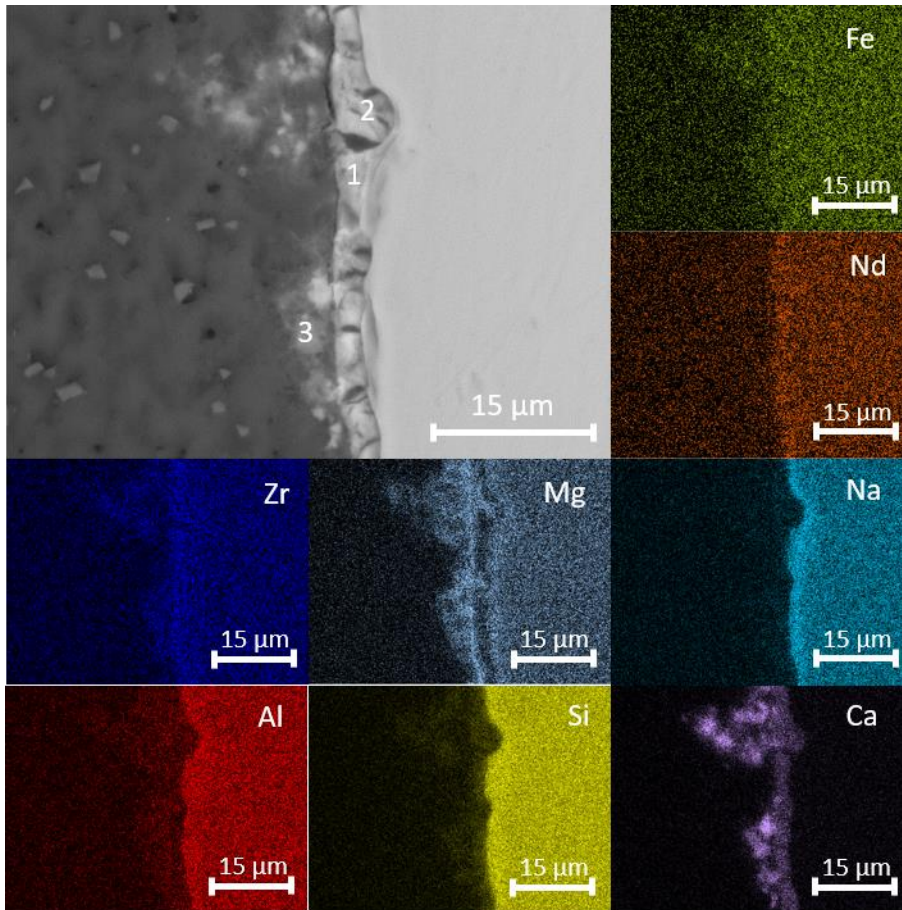


**Figure 6.32.** BSE image and elemental maps of alteration layer on a monolith of MW-25% altered for 90 days.

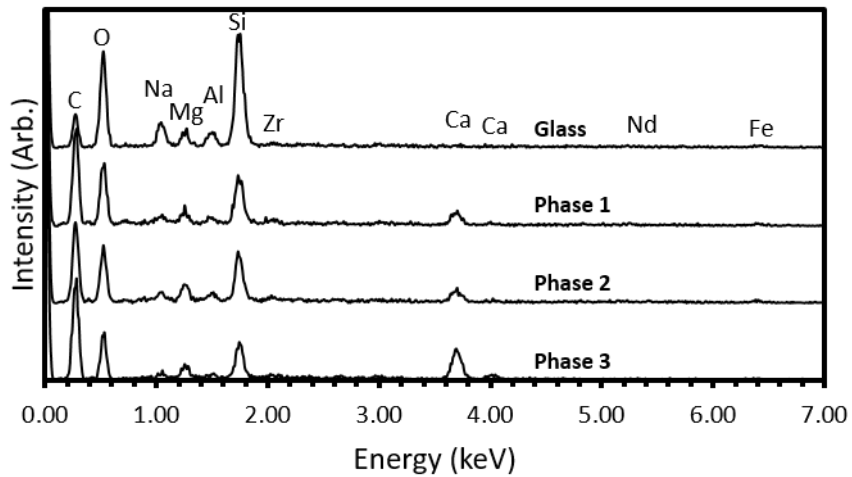


**Figure 6.33.** EDS spot analyses of alteration phases on a sample of MW-25% altered for 90 days.

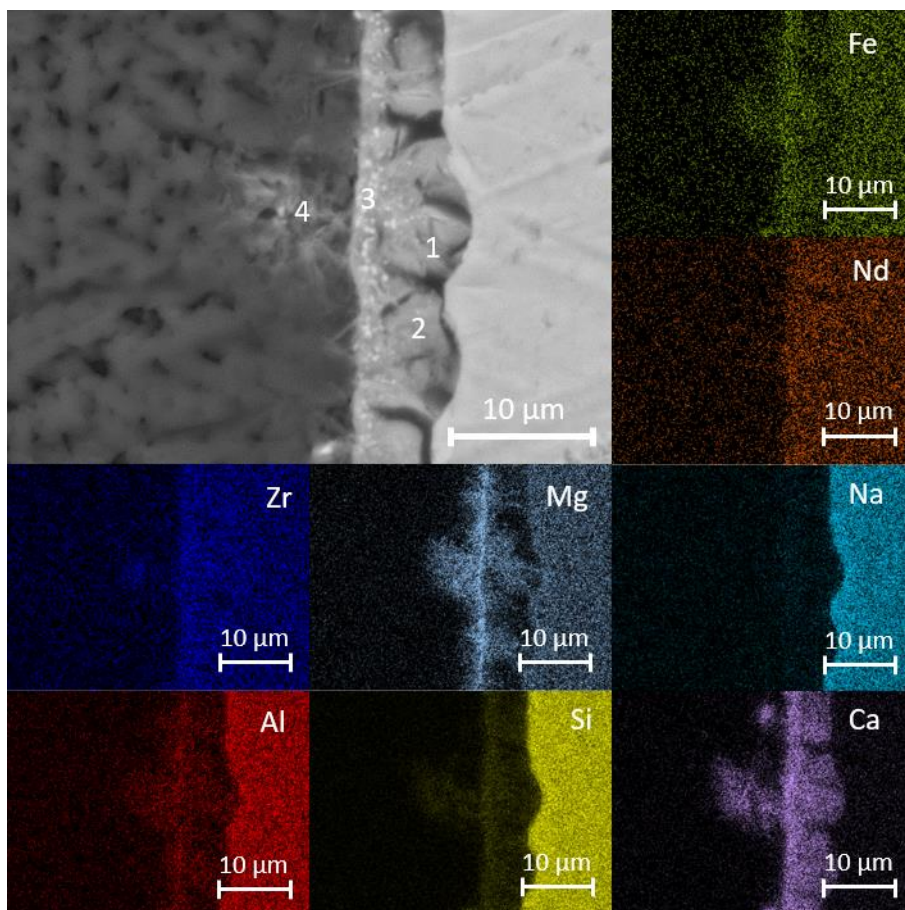


**Figure 6.34.** BSE image and elemental maps of alteration layer on a monolith of MW-25% altered for 180 days.

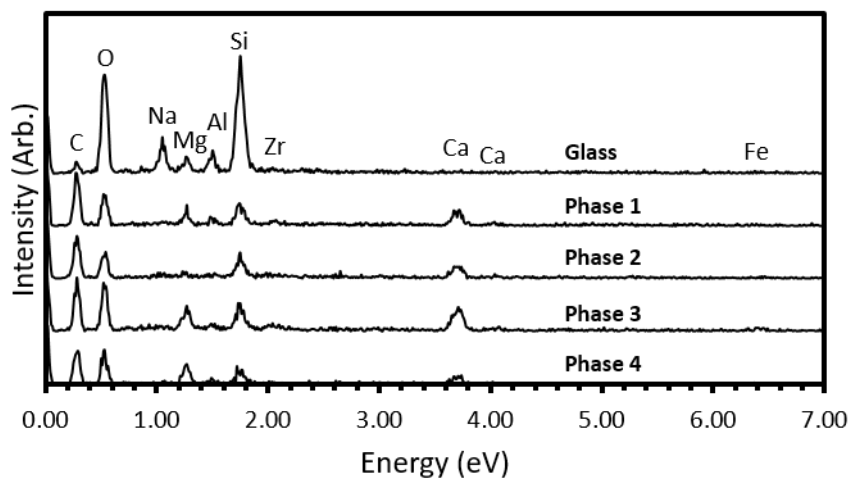


**Figure 6.35.** EDS spot analyses of alteration phases on a sample of MW-25% altered for 180 days.

Figure 6.36 shows a BSE micrograph and EDS elemental maps for a monolith of MW-25% altered in  $\text{Ca}(\text{OH})_2$  for 360 days. The alteration layer here was 11 to 14  $\mu\text{m}$  thick and was observed to be similar to that of the 180-day sample (Figure 6.34). There was a Ca- and Si-rich phase (Phase 1), a Mg- and Al-rich phase (2), a rim containing Fe-rich particles and a Mg- and Al-rich layer (3), and precipitates containing Ca, Si, Mg and O on the surface of the alteration layer. The Ca-Si phase was also enriched in Zr and Nd, compared to their levels in the glass. The Mg-Al phase (2) appeared to be localised as acicular, or possibly platy, forms, with enrichment in Mg relative to the glass. The precipitates, which could be C-S-H or M-S-H phases, formed clusters radiating from the surface of the alteration layer, similar to the arrangement of the C-S-H clusters on the ISG samples.

A BSE micrograph and EDS elemental maps for a 540-day MW-25% sample are shown in Figure 6.38. The alteration layer was  $\sim 18 \mu\text{m}$  thick. The alteration layer was similar in composition to the previous samples, with a primarily Ca- and Si-rich alteration layer (Phase 1), with Mg- and Al-rich needles (Phase 2), an Fe-enriched rim (Phase 3) (also containing Phase 2), and C-S-H-like precipitates (Phase 4). Figure 6.39 shows the EDS spectra for these phases. The C-S-H-like clusters of precipitates were more extensive than in previous samples.

Figure 6.40 contains a BSE micrograph and EDS elemental maps for a 720-day altered sample of MW-25%. The alteration layer was between 24 and 28  $\mu\text{m}$  thick. The morphology of the layer was similar to that of the samples altered for shorter durations, with: (1) a Ca-Si phase; (2) Mg-Al acicular cluster, (3) a multi-phase Fe-rich rim and (4) C-S-H and M-S-H-like precipitates. EDS spot analyses of these phases can be found in Figure 6.41. Nd in the alteration layer was primarily found within the Ca-Si phase, whereas the Zr was more prevalent in the Fe-rich rim, per the EDS maps in Figure 6.40.

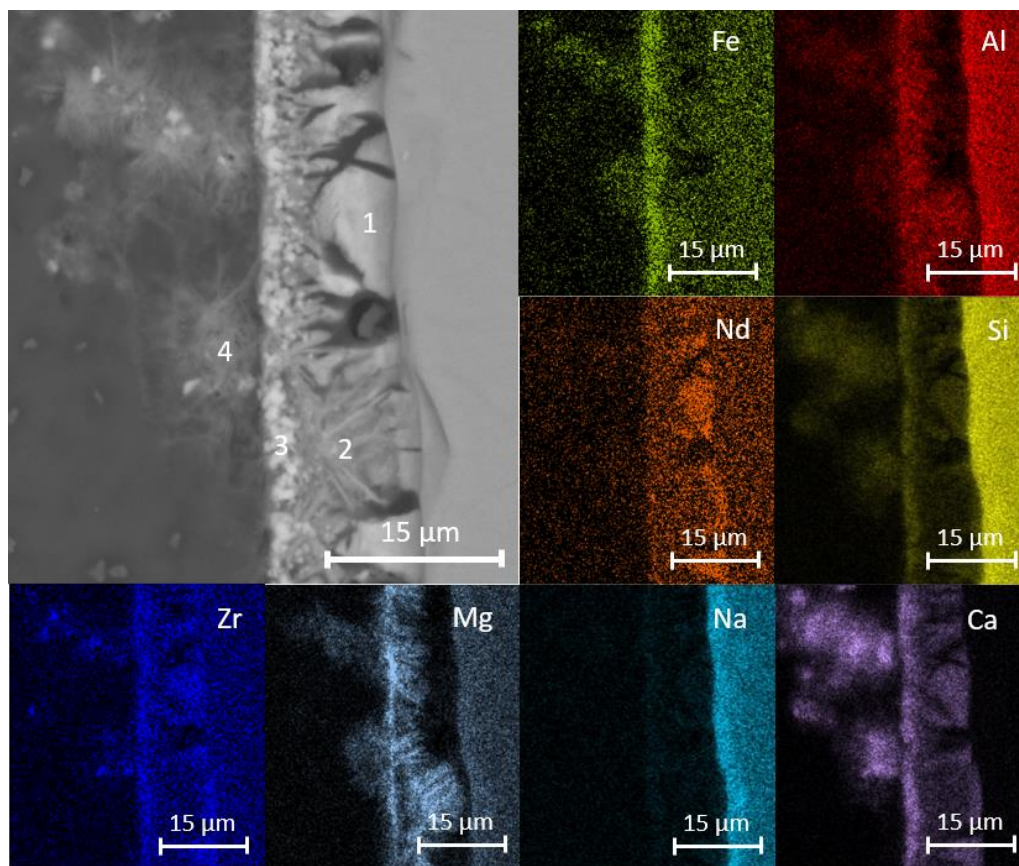


**Figure 6.36.** BSE image and elemental maps of alteration layer on a monolith of MW-25% altered for 360 days.

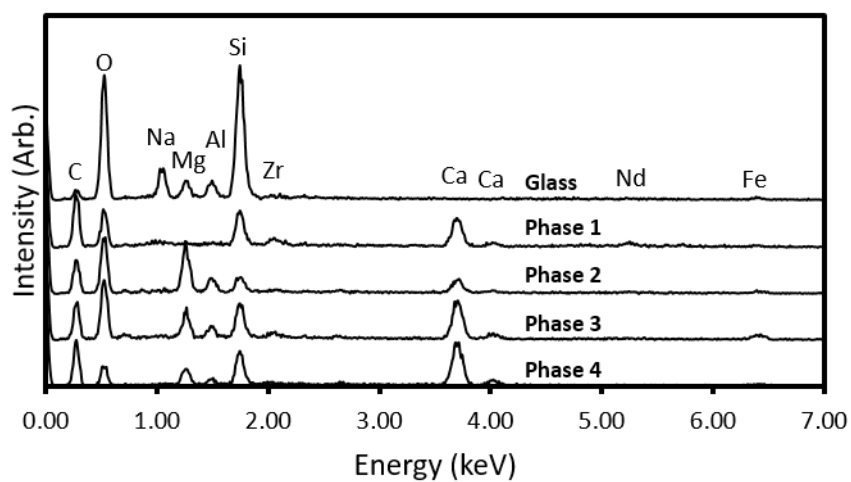


**Figure 6.37.** EDS spot analyses of alteration phases on a sample of MW-25% altered for 360 days.

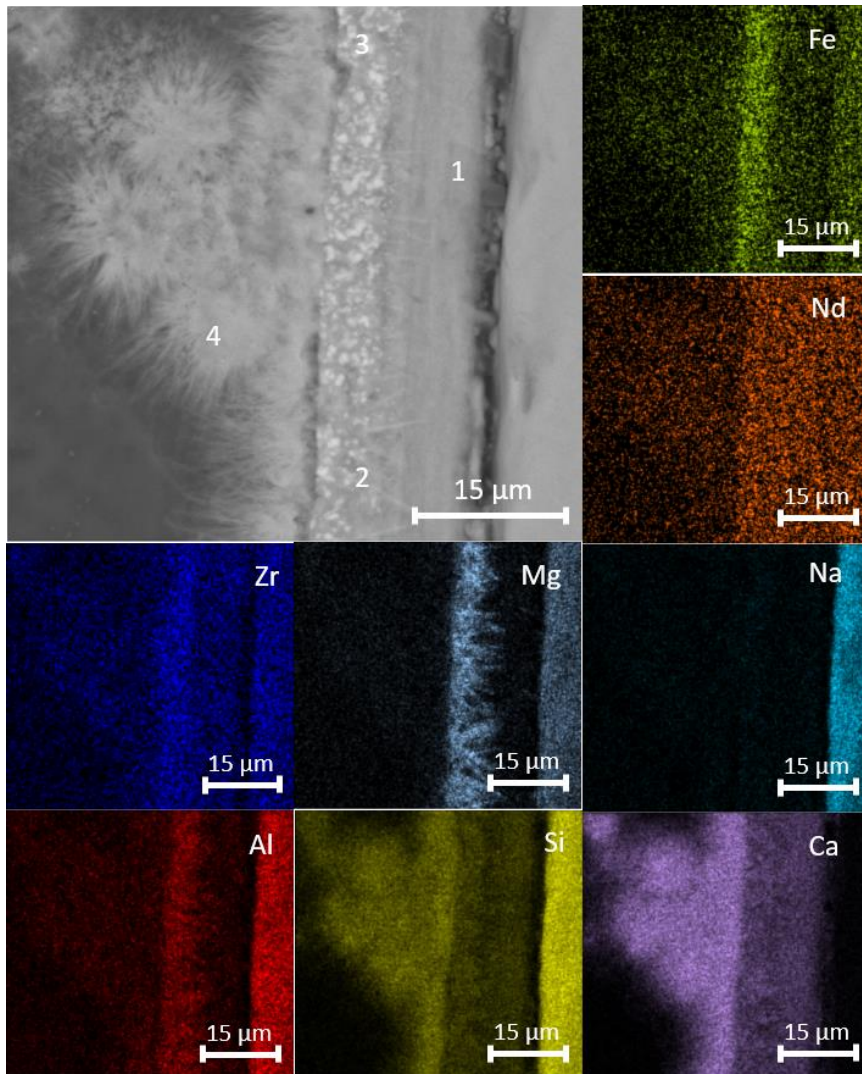


**Figure 6.38.** BSE image and elemental maps of alteration layer on a monolith of MW-25% altered for 540 days.

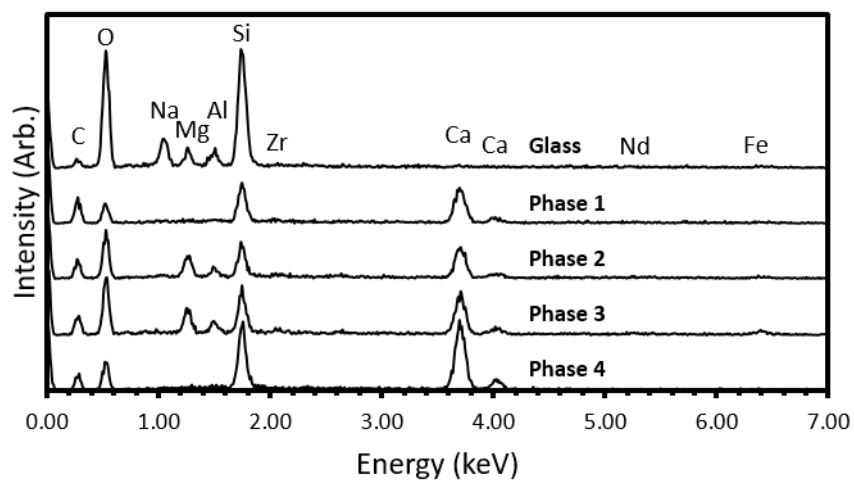


**Figure 6.39.** EDS spot analyses of alteration phases on a sample of MW-25% altered for 540 days.

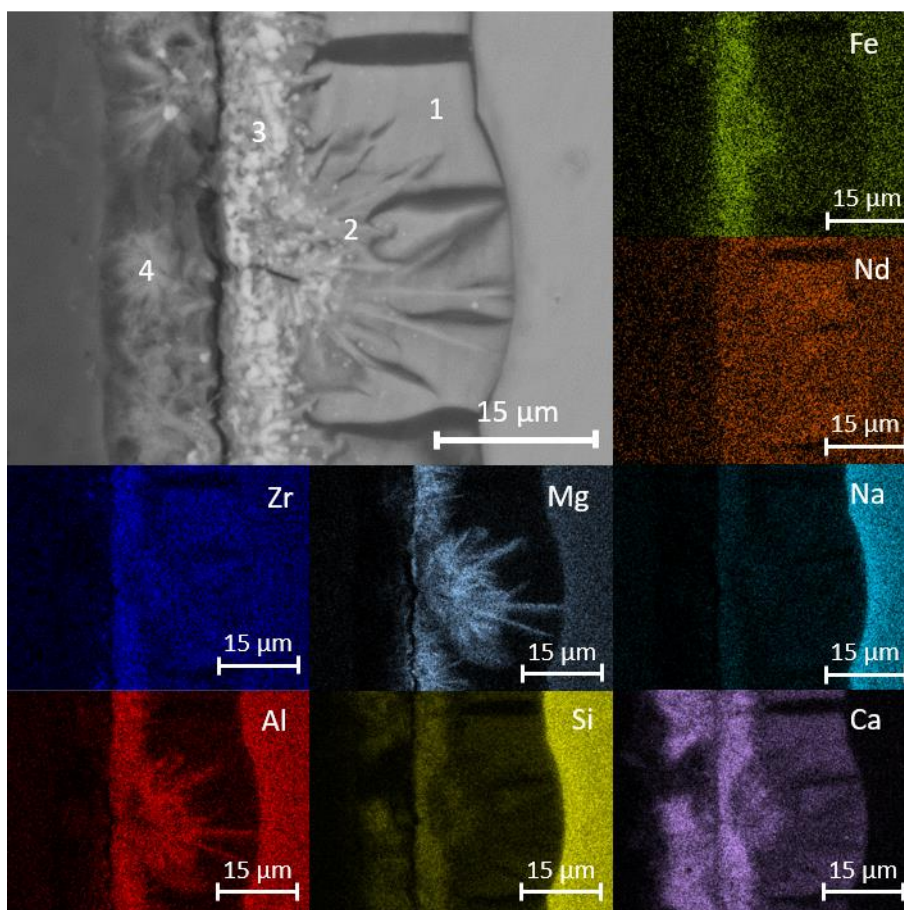


**Figure 6.40.** BSE image and elemental maps of alteration layer on a monolith of MW-25% altered for 720 days.

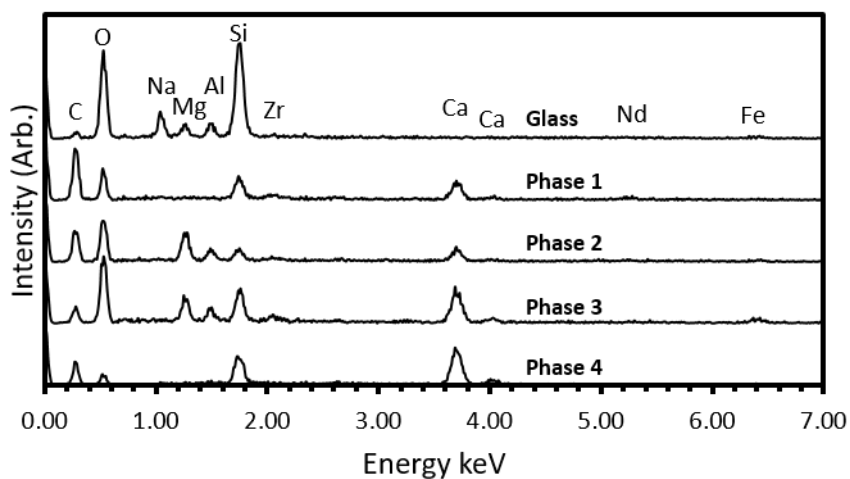


**Figure 6.41.** EDS spot analyses of alteration phases on a sample of MW-25% altered for 720 days.

### 6.4.1.3 BAS

Figure 6.42 shows a BSE micrograph and EDS elemental maps for the surface of a BAS monolith that was altered for 30 days. The alteration layer was approximately 10 to 12  $\mu\text{m}$  thick. EDS analysis (Figure 6.43) showed the presence of two distinct phases: 1) a Ca-Si rich phase that also contained small amounts of Mg, Al and Fe, and; 2) a Ca-rich phase similar to those observed on ISG and MW-25%, that is likely to be either portlandite ( $\text{Ca}(\text{OH})_2$ ) or calcite ( $\text{CaCO}_3$ ). Significant Ca incorporation into the alteration layer was observed, despite the short duration of dissolution.

A BSE micrograph and EDS elemental maps for a monolith of BAS altered for 90 days are shown in Figure 6.44. After this period of dissolution, the alteration layer was approximately 8.5 to 10.5  $\mu\text{m}$  thick. Several different phases were observed through EDS spot analysis (Figure 6.45): Phase 1 was rich in Mg, Ca, Al, Si and O, and also contained Fe; Phase 2 was similar in composition to Phase 1, but contained lower amounts of Mg and Al; Phase 3 was also Ca- and Si-rich, and also contained Al and small amounts of Mg and Fe; and Phase 4 was again Ca- and Si-rich and contained small amounts of Fe and Ti, but was poorest in Mg and Al.

Figure 6.46 shows a BSE micrograph and EDS elemental maps for a monolith of BAS altered for 180 days. The alteration layer is approximately 21  $\mu\text{m}$  thick. Three primary phases were observed: an acicular (or possibly platy) phase enriched in Mg (compared to the glass) which also contained Al, Si, Ca, Fe and O (Phase 1); a Ca- and Si-rich phase which also contained small amounts of Al and Fe (Phase 2); and a Ca-Si phase which was enriched in Fe compared to the glass and was observed to have a spherulitic morphology (Phase 3). The EDS spectra for these phases are shown in Figure 6.47.

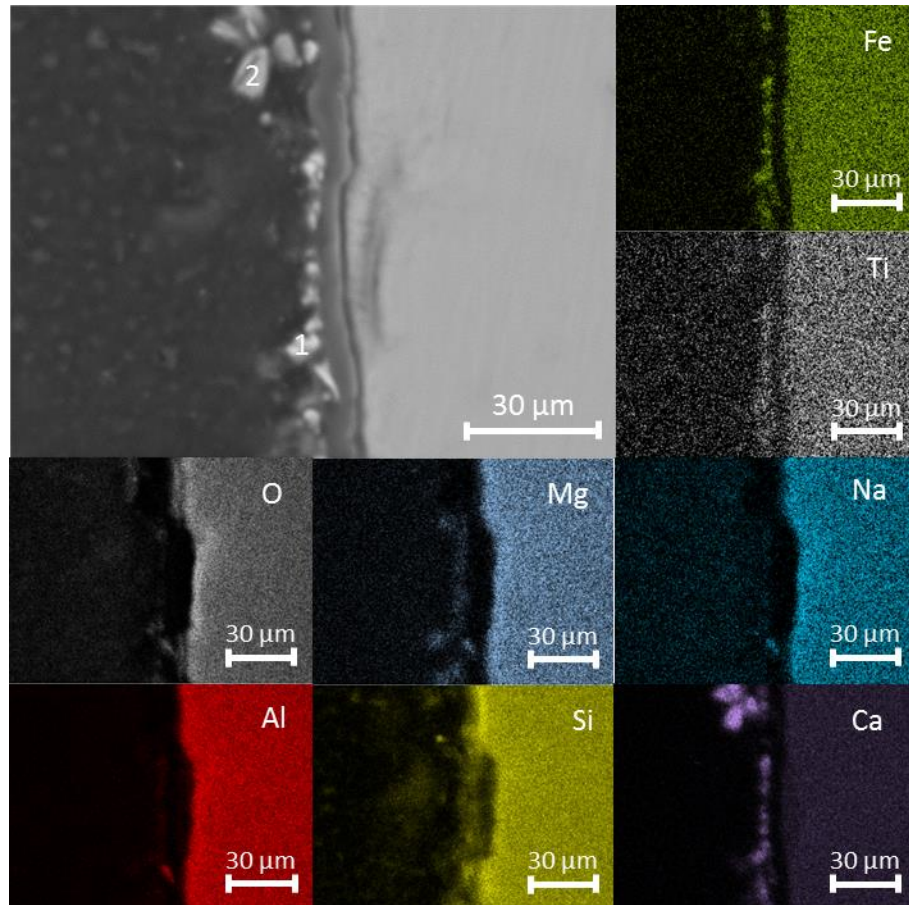


**Figure 6.42.** BSE image and elemental maps of alteration layer on a monolith of BAS altered for 30 days.

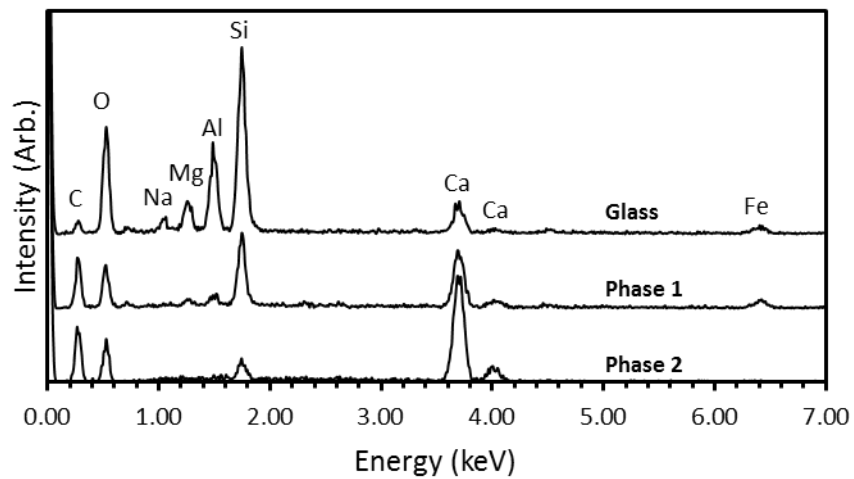


**Figure 6.43.** EDS spot analyses of alteration phases on a sample of BAS altered for 30 days.

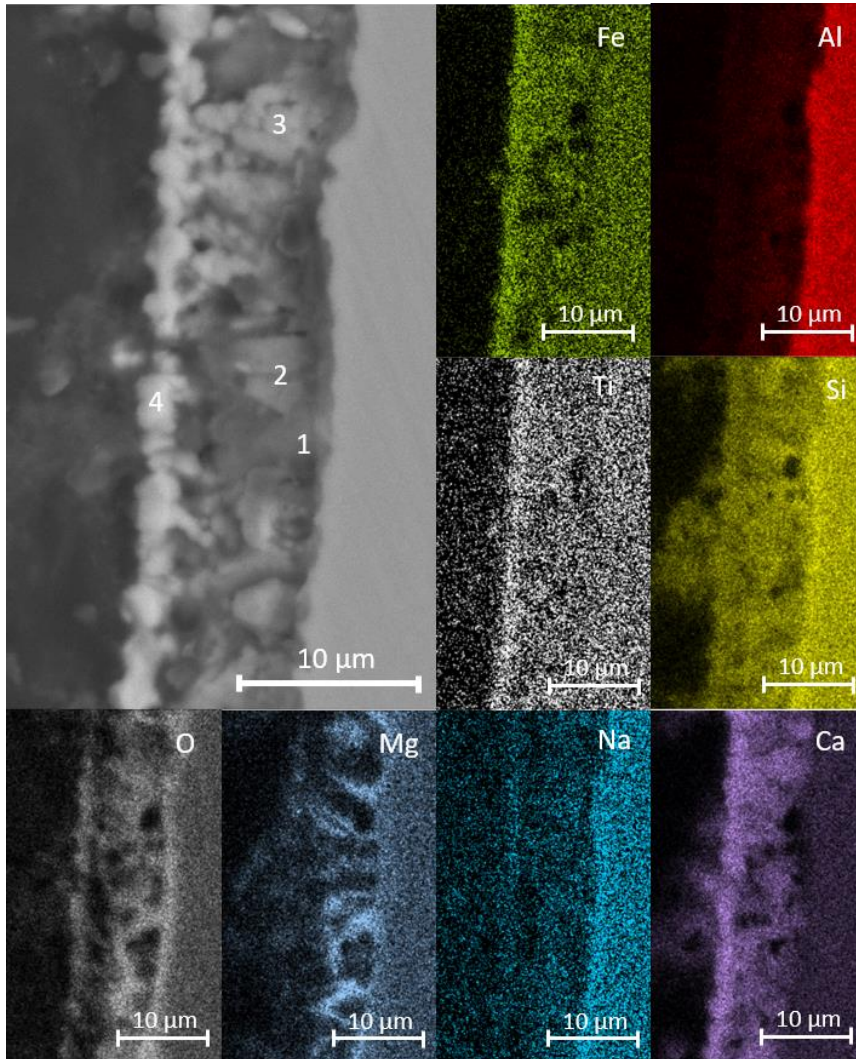


**Figure 6.44.** BSE image and elemental maps of alteration layer on a monolith of BAS altered for 90 days.

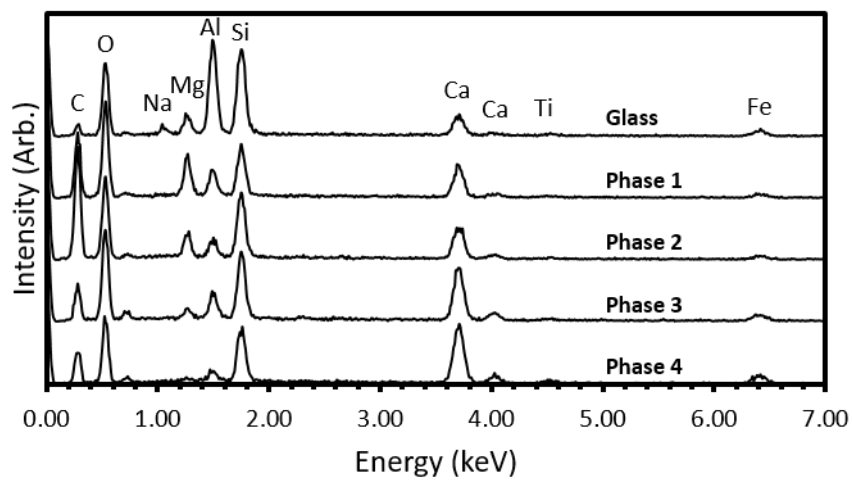


**Figure 6.45.** EDS spot analyses of alteration phases on a sample of BAS altered for 90 days.

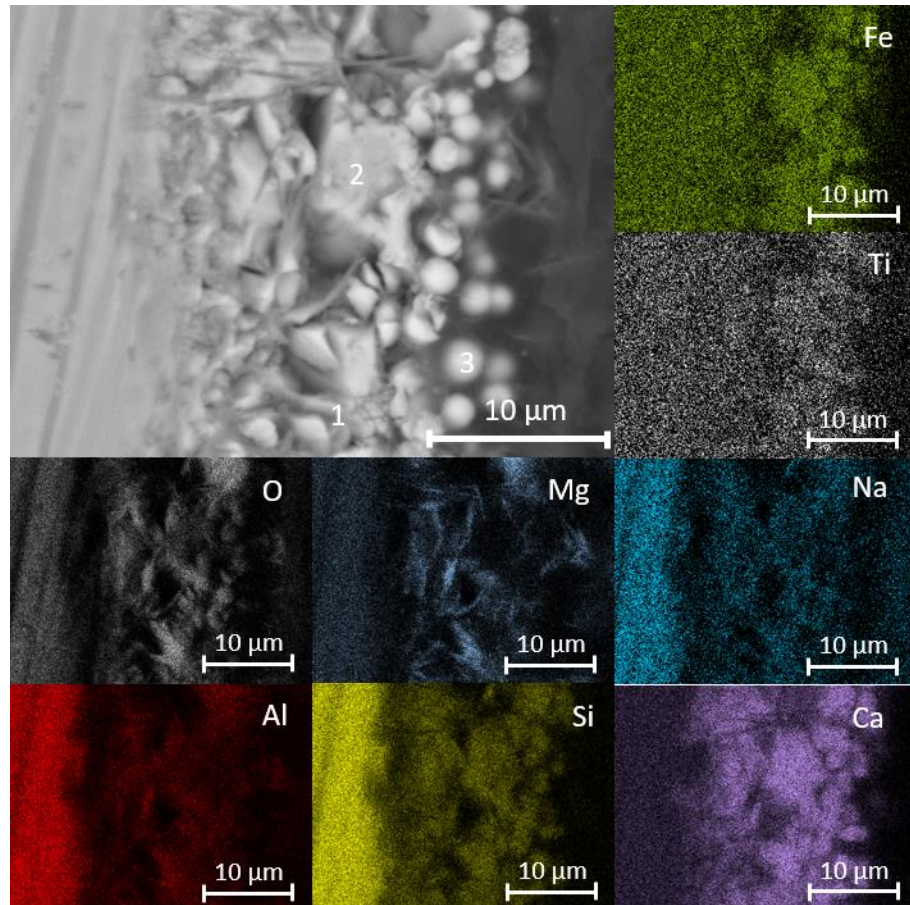


**Figure 6.46.** BSE image and elemental maps of alteration layer on a monolith of BAS altered for 180 days.

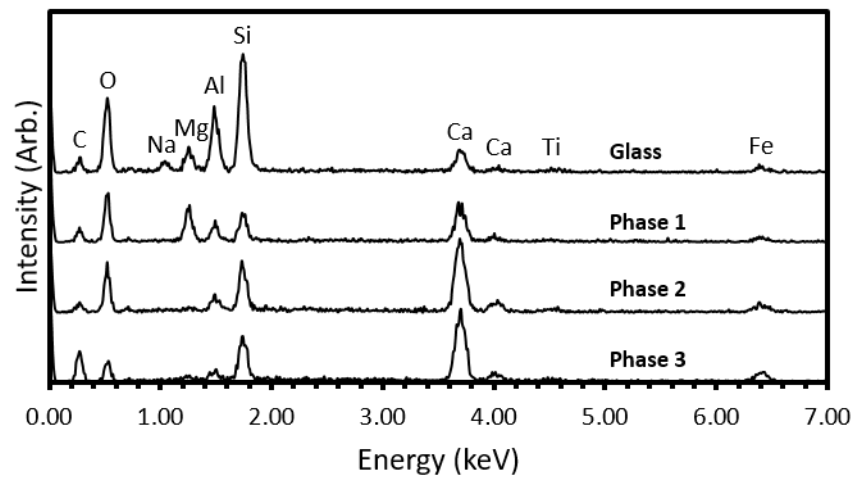


**Figure 6.47.** EDS spot analyses of alteration phases on a sample of BAS altered for 180 days.

Figure 6.48 shows a BSE micrograph and EDS maps for a monolith altered for 360 days. The alteration layer was between 4 and 7  $\mu\text{m}$  thick. Acicular clusters of precipitates were observed on the surface of the alteration layer. These precipitates consist primarily of Ca and Si, per EDS analysis (Figure 6.49, Phase 3), and appear similar to the precipitates observed on altered samples of both ISG and MW-25%. Within these precipitates, regions of significant Ca enrichment were observed (Phase 4), which could be portlandite ( $\text{Ca}(\text{OH})_2$ ) or calcite ( $\text{CaCO}_3$ ). The alteration layer itself appeared to consist of two primary phases: a Mg- and Al-rich Ca-Si phase with small amounts of Fe and Ti (Phase 1); and a Mg- and Al-poor Ca-Si phase with slightly increased levels of Fe, as well as small amount of Ti (Phase 2).

The alteration layer on a sample of BAS altered for 540 days in saturated  $\text{Ca}(\text{OH})_2$  is shown in Figure 6.50. The alteration layer was observed to be 8.5 to 12  $\mu\text{m}$  in thick, and was similar in composition to that of the 360-day sample, with a multi-phase alteration layer and precipitate clusters on the surface. The alteration layer consisted of three phases: a primarily Ca- and Si-containing phase (Phase 1); a Ca-Si phase with higher Mg and Al levels (Phase 2); and a Ca-Si phase with increased Fe content (Phase 3) (see EDS spectra in Figure 6.51).

Figure 6.52 shows the alteration layer on a monolith of BAS altered for 720 days, as observed by BSE imaging. This layer was approximately 9.5 to 16  $\mu\text{m}$  thick. The EDS analysis (Figure 6.53) supports the identification of two distinct regions within the alteration layer (Phases 1 & 2), as well as precipitates on the surface of the alteration layer (Phase 3). Phase 1 is localised to the inner part of the alteration layer, closer to the glass surface, and is richer in Mg, Al and Si than Phase 2, which is richer in Ca. Both phases contain Fe and Ti. The precipitates are primarily composed of Ca and Si, but also contain Mg.

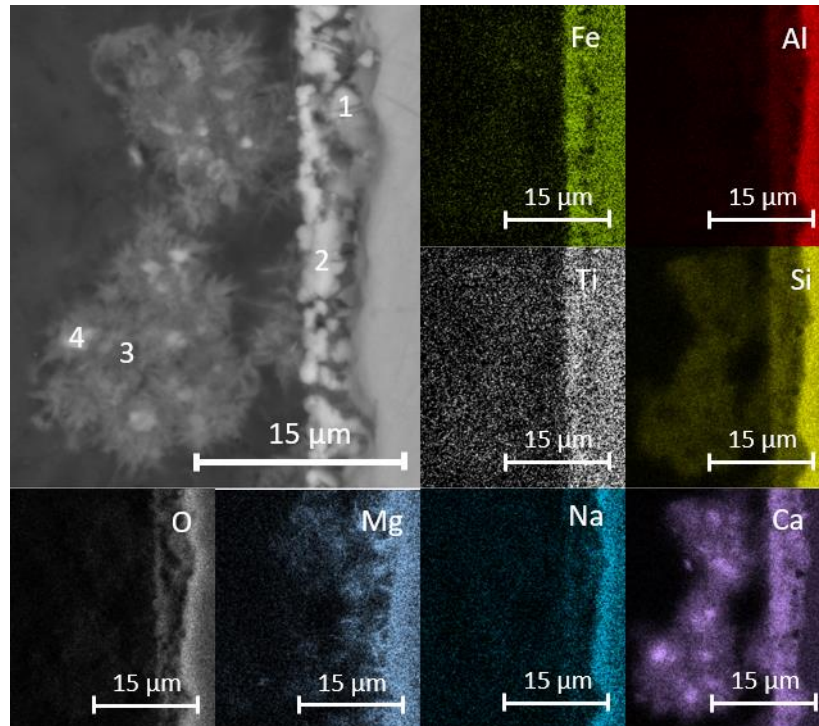


**Figure 6.48.** BSE image and elemental maps of alteration layer on a monolith of BAS altered for 360 days.

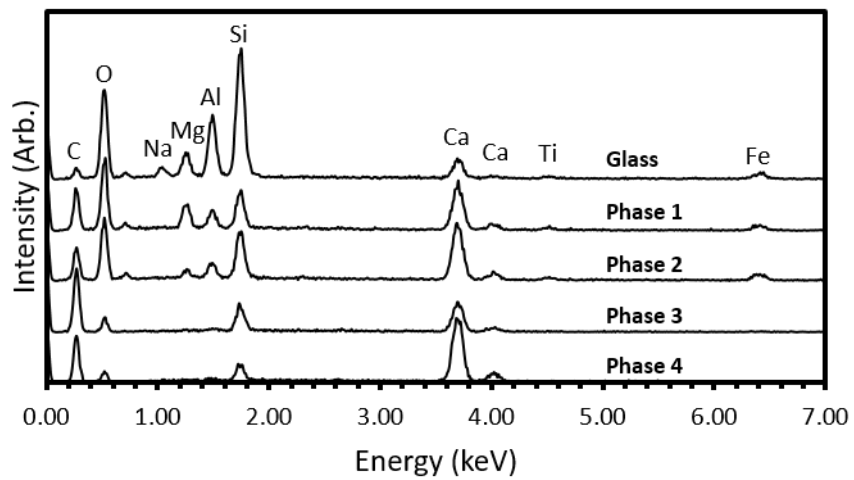


**Figure 6.49.** EDS spot analyses of alteration phases on a sample of BAS altered for 360 days.

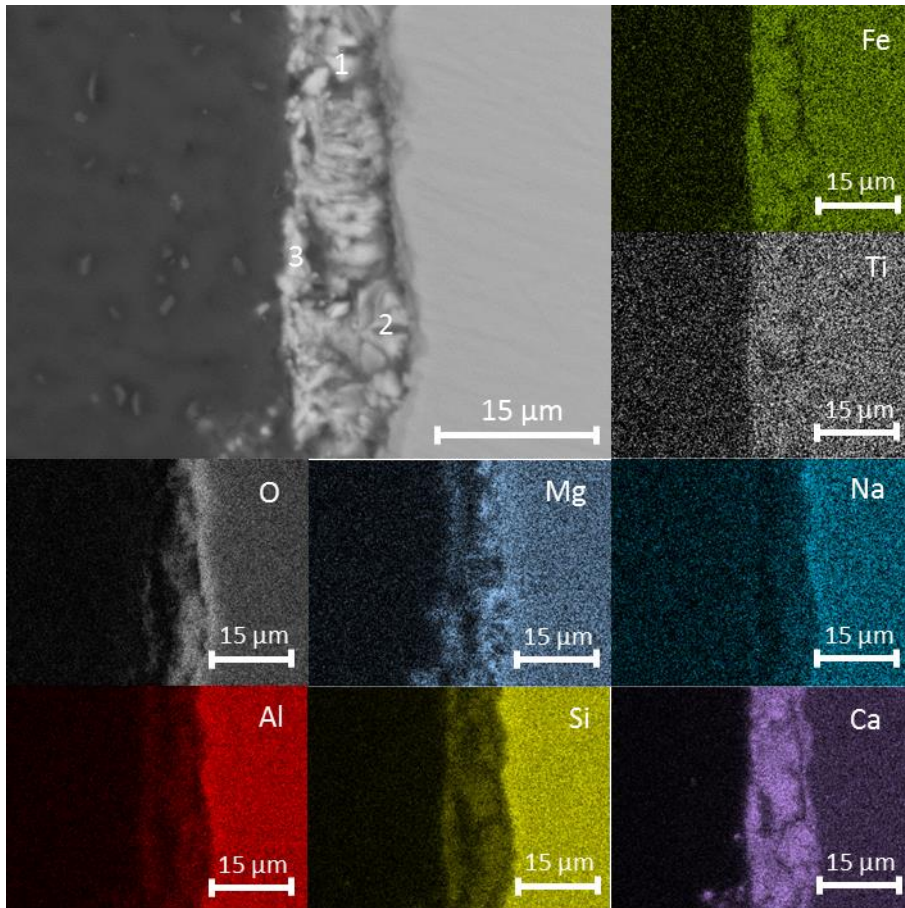


**Figure 6.50.** BSE image and elemental maps of alteration layer on a monolith of BAS altered for 540 days.

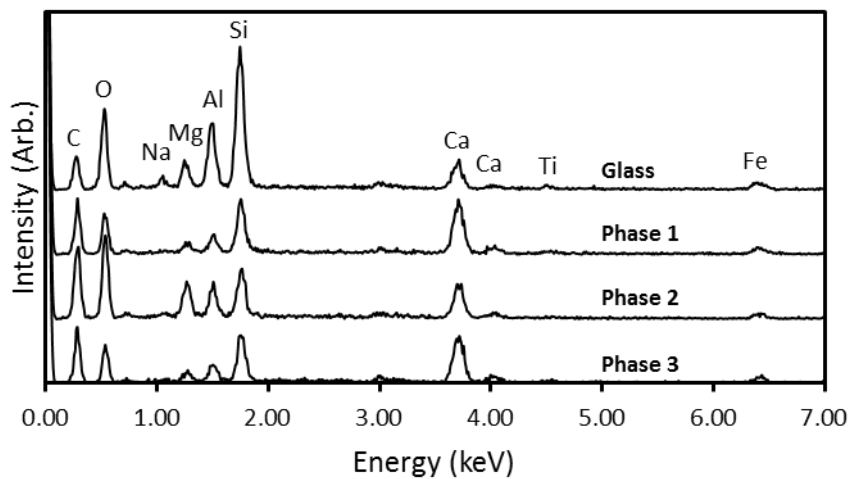


**Figure 6.51.** EDS spot analyses of alteration phases on a sample of BAS altered for 540 days.

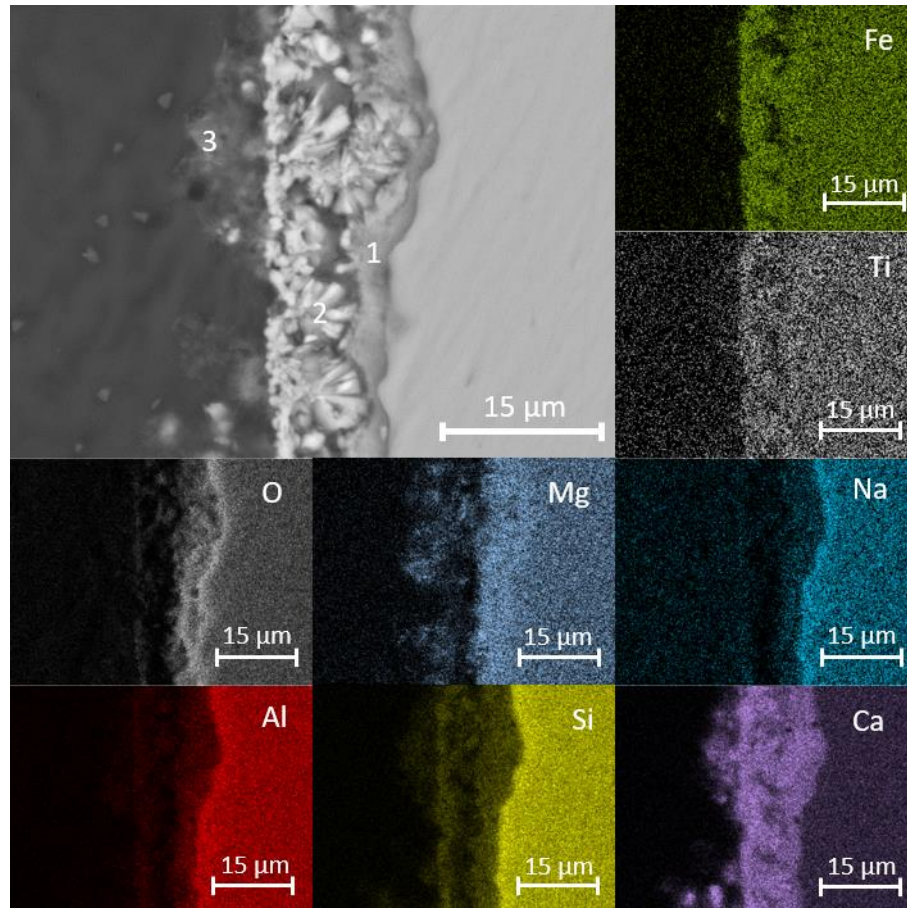


**Figure 6.52.** BSE image and elemental maps of alteration layer on a monolith of BAS altered for 720 days.

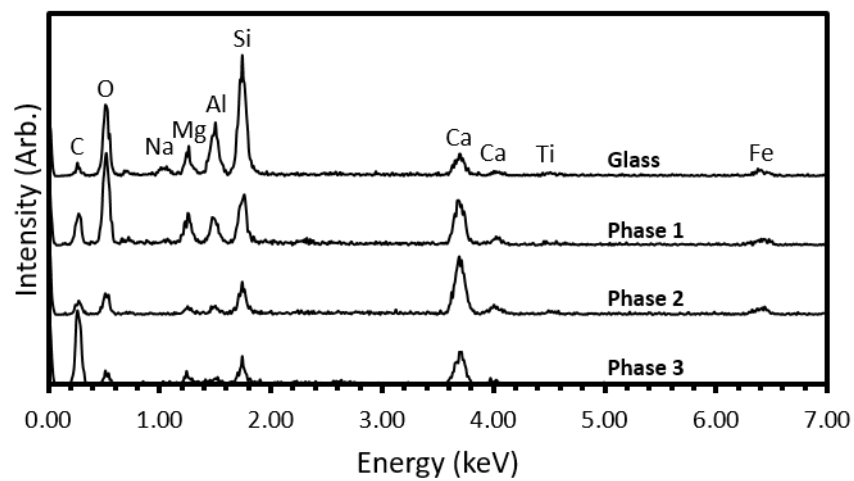


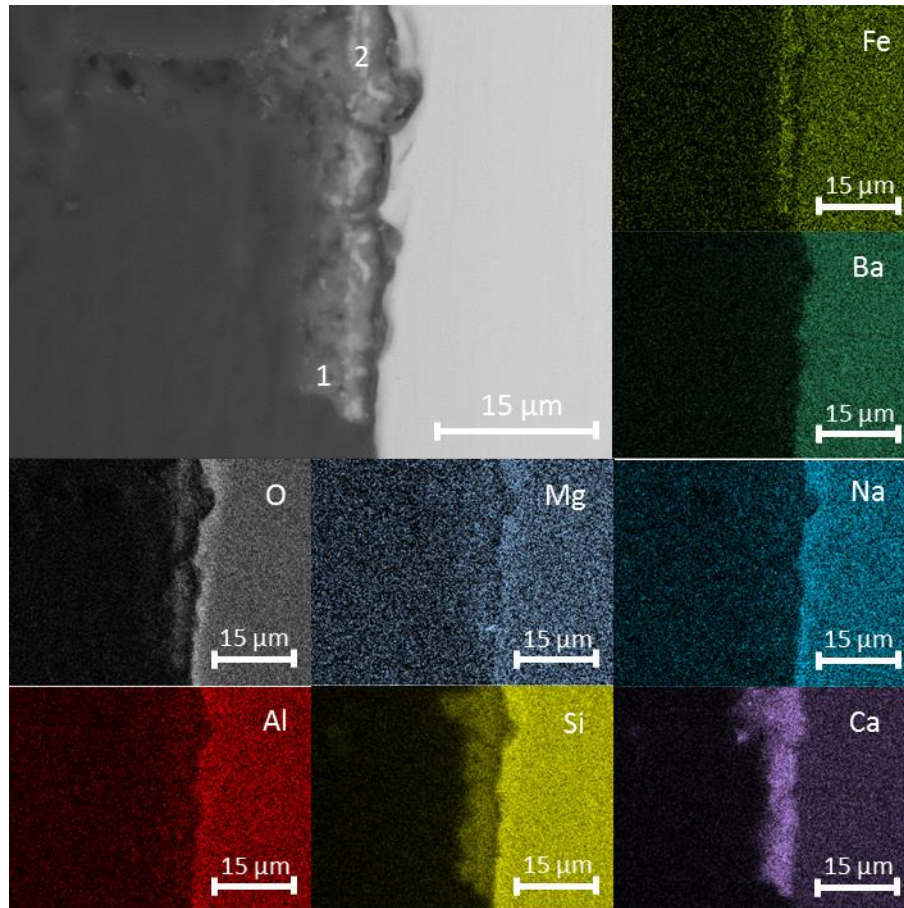
**Figure 6.53.** EDS spot analyses of alteration phases on a sample of BAS altered for 720 days.

#### 6.4.1.2 G73

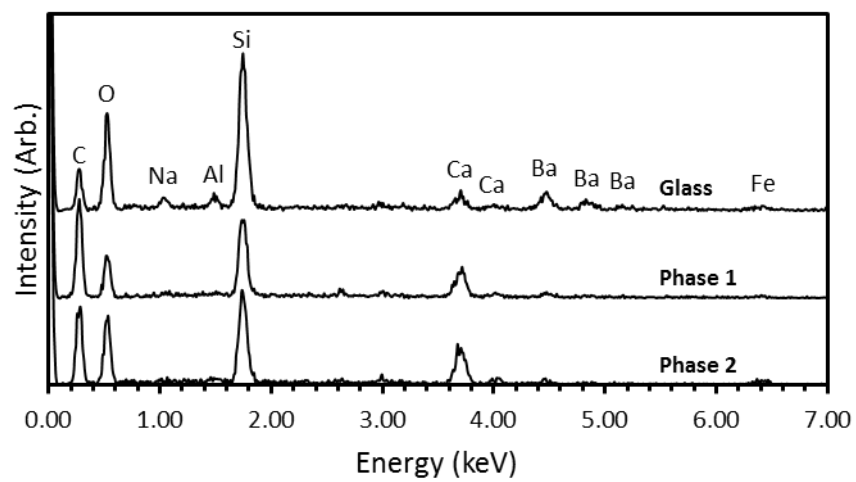
Figure 6.54 shows a BSE micrograph and EDS elemental maps for a monolith of G73 altered in  $\text{Ca}(\text{OH})_2$  for 30 days. The alteration layer was observed to be  $\sim 7 \mu\text{m}$  thick. Two different phases were observed within the alteration layer: 1) a Ca- and Si-rich phase; and 2) a similar phase containing a higher level of Fe. The EDS spectra for these two phases are shown in Figure 6.55.

Figure 6.56 shows a BSE micrograph and EDS elemental maps for a monolith of G73 altered in  $\text{Ca}(\text{OH})_2$  for 90 days. The alteration layer was approximately  $9 \mu\text{m}$  thick, and consisted of two primary phases, similar to those seen on the 30-day sample: a primarily Si-rich phase close to the glass (Phase 1); and a Ca- and Si-rich phase, also containing a significant amount of Fe (Phase 2). The EDS spectra for these phases are shown in Figure 6.57. Phase 2 formed in a layer parallel to the glass surface at the edge of the alteration layer, similar to the Fe-enriched alteration rim observed on the MW-25% and BAS samples. C-S-H-like precipitates were also observed on the surface of the alteration layer (Phase 3).

A BSE micrograph and EDS elemental maps of the alteration layer on a monolith of G73 altered for 180 days are shown in Figure 6.58. The alteration layer was in the range of  $13 - 17 \mu\text{m}$  thick. As with the 90-day sample, the alteration layer consisted of two primary phases: A Ca- and Si-rich phase (Phase 1); and a Ca-Si phase enriched in Fe (Phase 2). C-S-H-like precipitates were also observed (Phase 3). The EDS spectra for these phases are shown in Figure 6.59. The Fe-enriched phase tended to form away from the glass surface, although it did not form an unbroken rim in the same way as on the 90-day sample. A small region of Mg-rich alteration layer was present (Phase 4), which was also seen in the 90-day sample.



**Figure 6.54.** BSE image and elemental maps of alteration layer on a monolith of G73 altered for 30 days.



**Figure 6.55.** EDS spot analyses of alteration phases on a sample of G73 altered for 30 days.

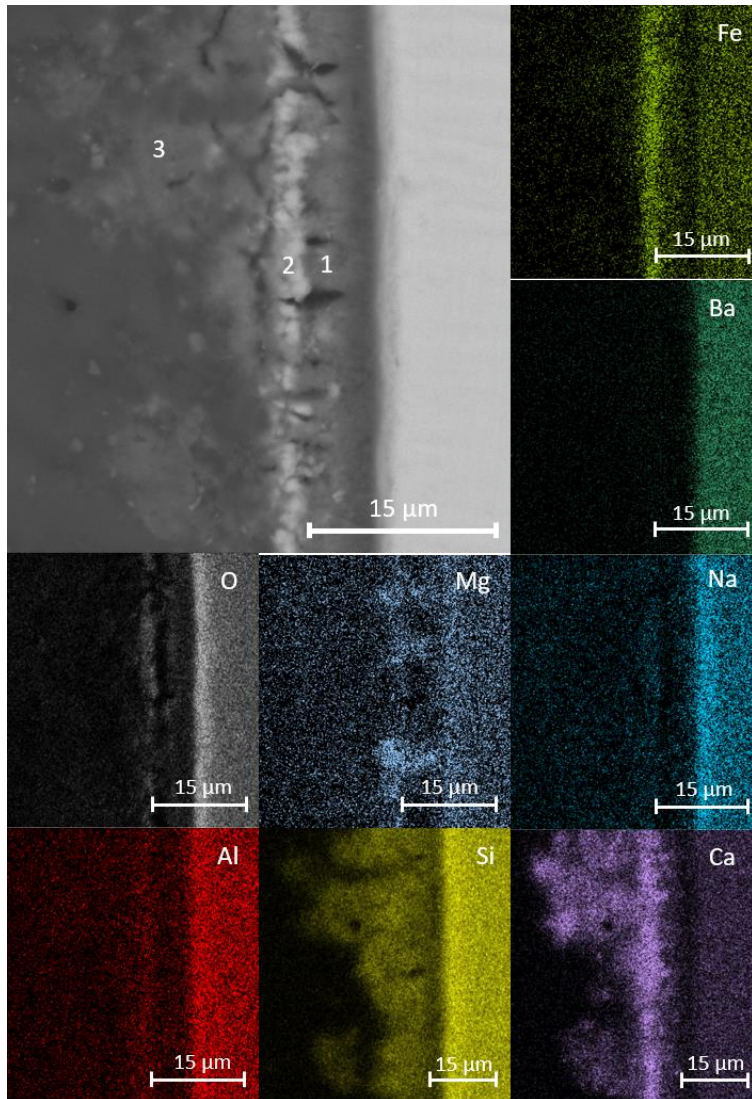


**Figure 6.56.** BSE image and elemental maps of alteration layer on a monolith of G73 altered for 90 days.

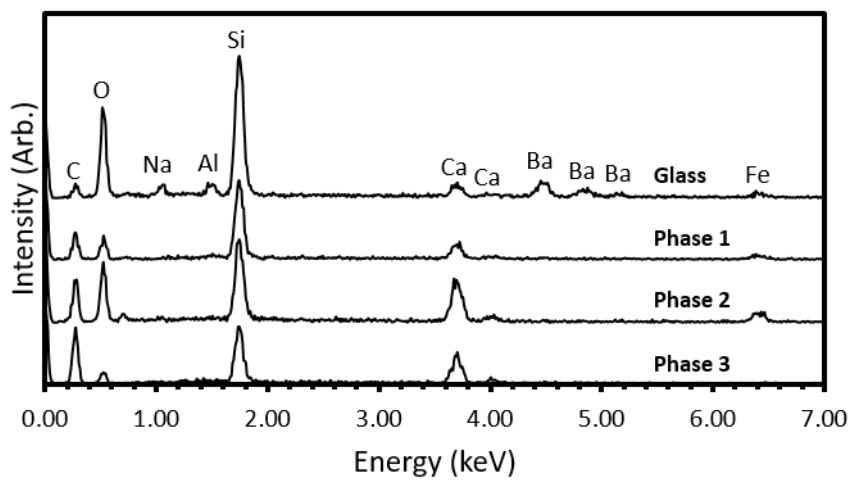


**Figure 6.57.** EDS spot analyses of alteration phases on a sample of G73 altered for 90 days.

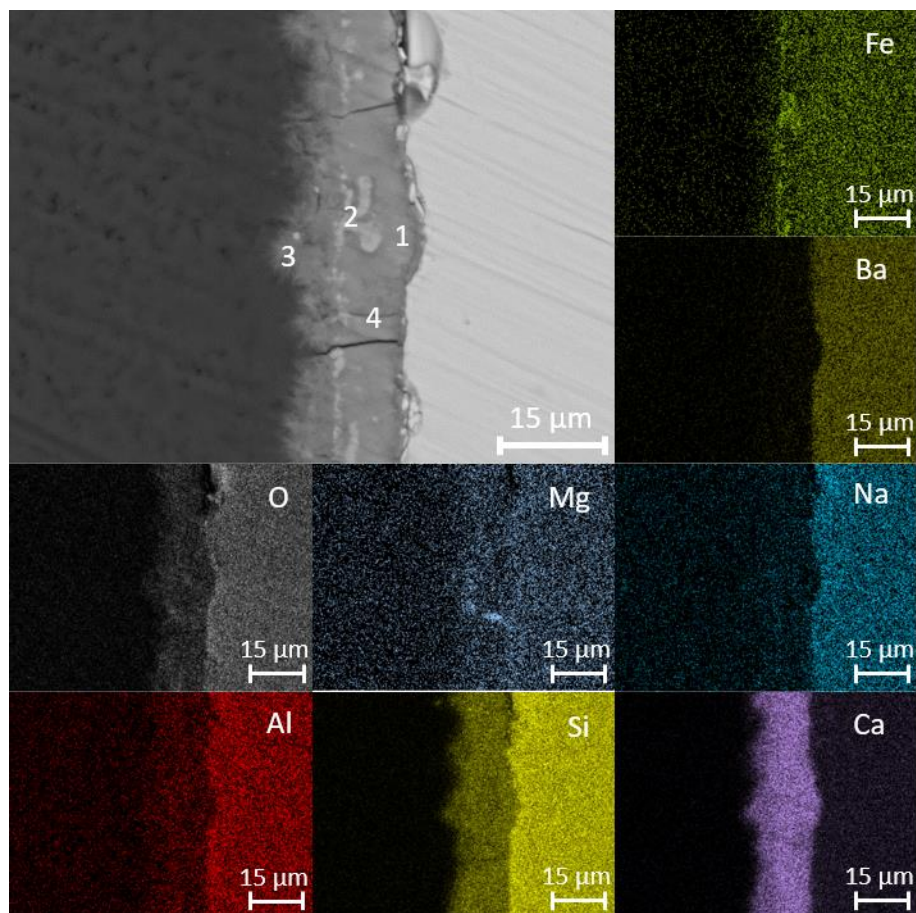


**Figure 6.58.** BSE image and elemental maps of alteration layer on a monolith of G73 altered for 180 days.

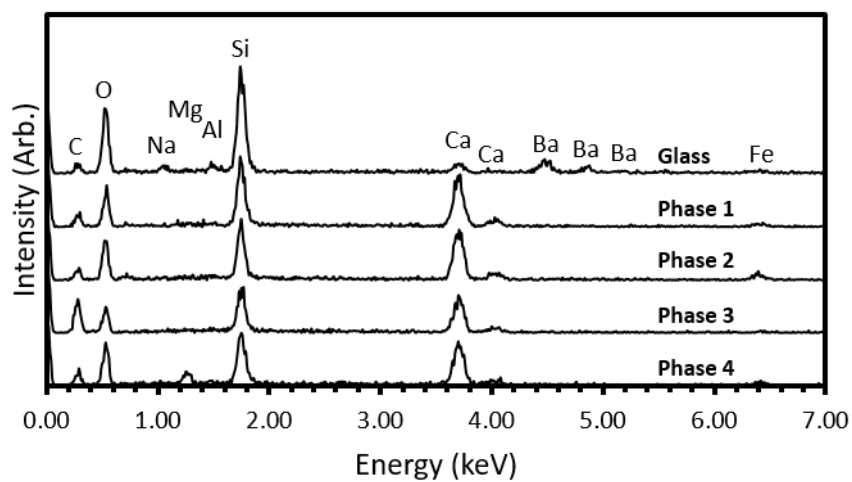
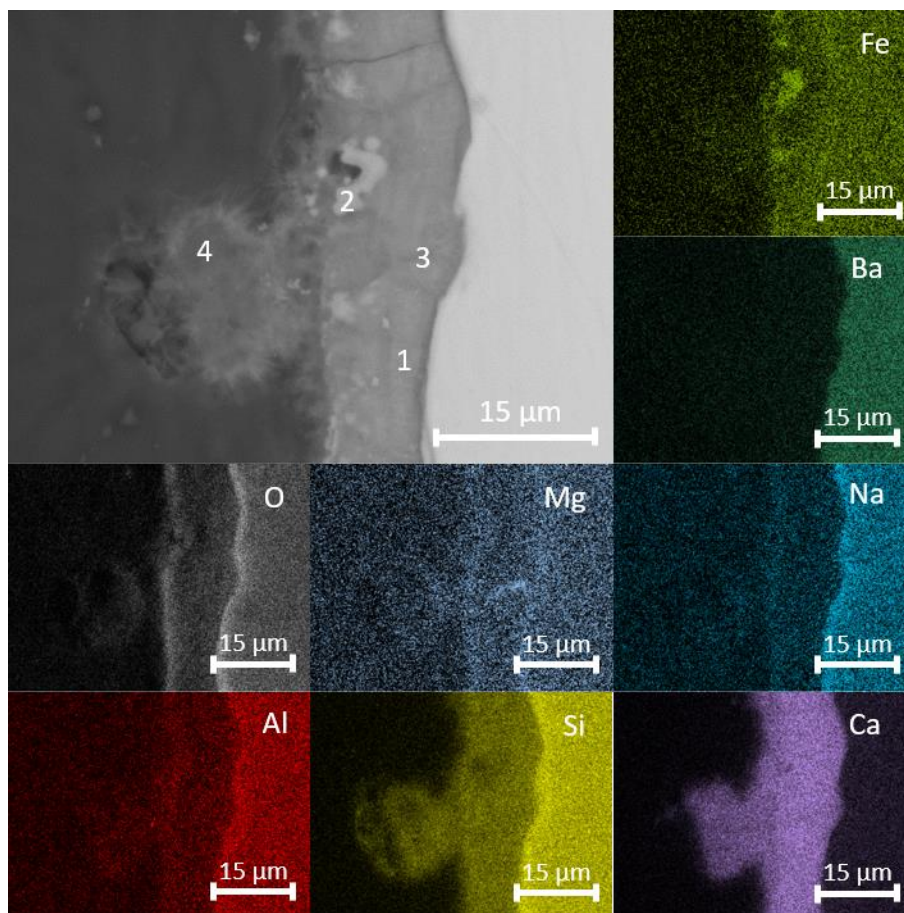


**Figure 6.59.** EDS spot analyses of alteration phases on a sample of G73 altered for 180 days.

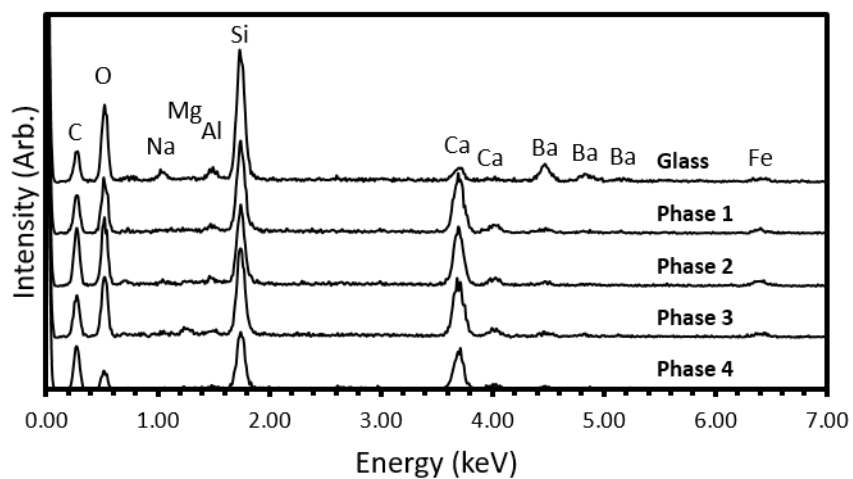
Figure 6.60 shows the alteration layer on a G73 monolith that was altered for 360 days. The alteration layer was 8.5 – 14.0  $\mu\text{m}$  thick, and its composition was very similar to that of the 180-day sample. The alteration layer itself primarily consisted of Ca and Si, with two distinct subphases with low and high Fe content (Phases 1 and 2, respectively). There was also a small region in the alteration layer that was significantly enriched in Mg (Phase 3), and C-S-H-like precipitates on the surface of the alteration layer (Phase 4). The EDS spectra for each of these phases are shown in Figure 6.61.

Figure 6.62 shows a BSE micrograph and EDS elemental maps for a G73 monolith leached for 540 days. The alteration layer was 21 – 24  $\mu\text{m}$  thick and was similar in composition to those of the earlier monoliths; a Ca- and S-rich primary phase (Phases 1 & 2), with a rim of an Fe-rich phase (Phase 3), and C-S-H-like precipitates on the surface of the layer (Phase 4). The EDS spectra for these phases are displayed in Figure 6.63. There was also a Mg-enriched phase within the alteration layer (Phase 5), which was present in other samples. There appeared to be two distinct regions within the Ca- and S-rich phase, characterised by higher (Phase 1) and lower (Phase 2) Ca/Si ratios.

Figure 6.64 shows the alteration layer for a monolith of G73 altered for 720 days in saturated  $\text{Ca}(\text{OH})_2$ . The alteration layer was between 12 and 15  $\mu\text{m}$  thickness. Figure 6.65 shows the relative elemental contents of the different alteration phases. As with the previous samples, the alteration layer primarily consisted of Ca and Si, with Fe-poor (Phase 1) and Fe-rich (Phase 2) regions and small regions of Mg-enrichment. C-S-H-like precipitate clusters were also observed on the surface of the alteration layer (Phase 4).



**Figure 6.60.** BSE image and elemental maps of alteration layer on a monolith of G73 altered for 360 days.



**Figure 6.61.** EDS spot analyses of alteration phases on a sample of G73 altered for 360 days.

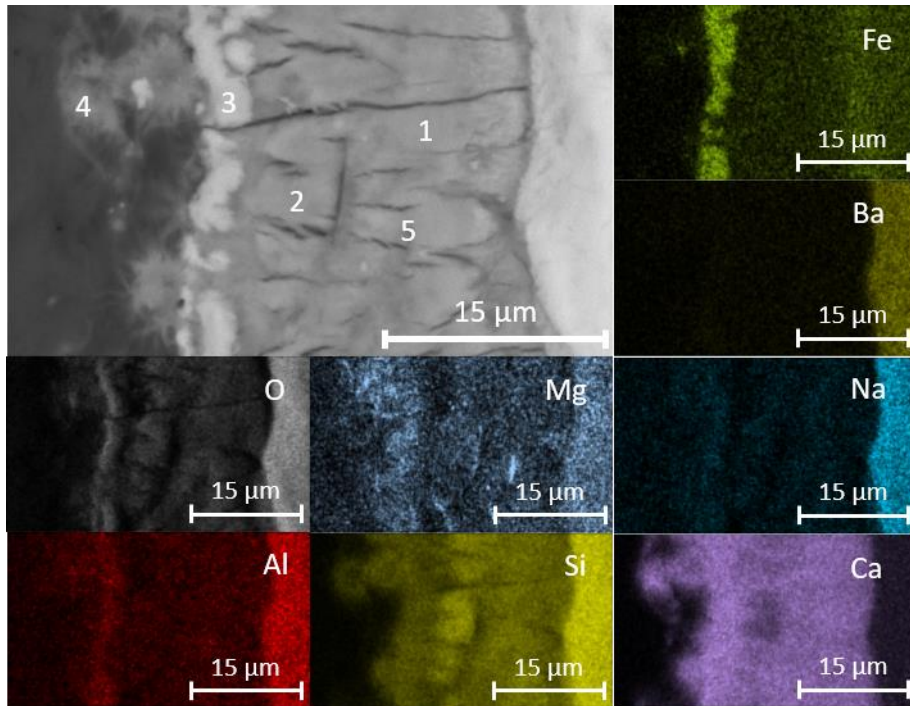


**Figure 6.62.** BSE image and elemental maps of alteration layer on a monolith of G73 altered for 540 days.

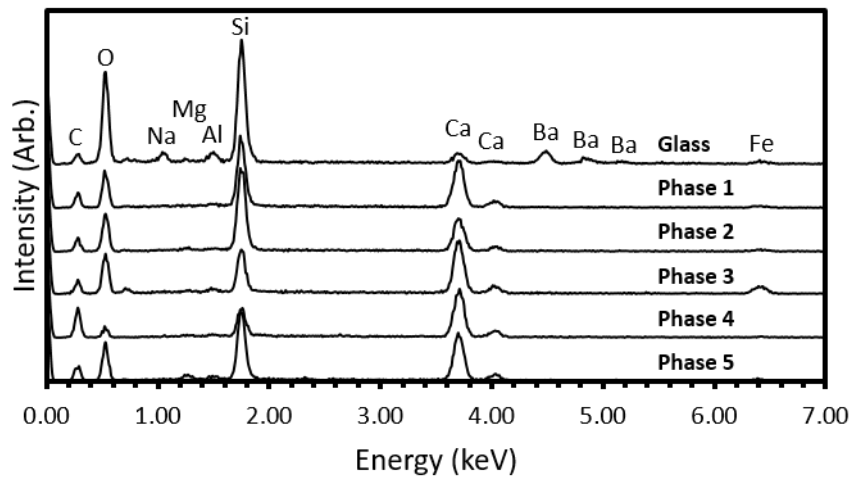


**Figure 6.63.** EDS spot analyses of alteration phases on a sample of G73 altered for 540 days.

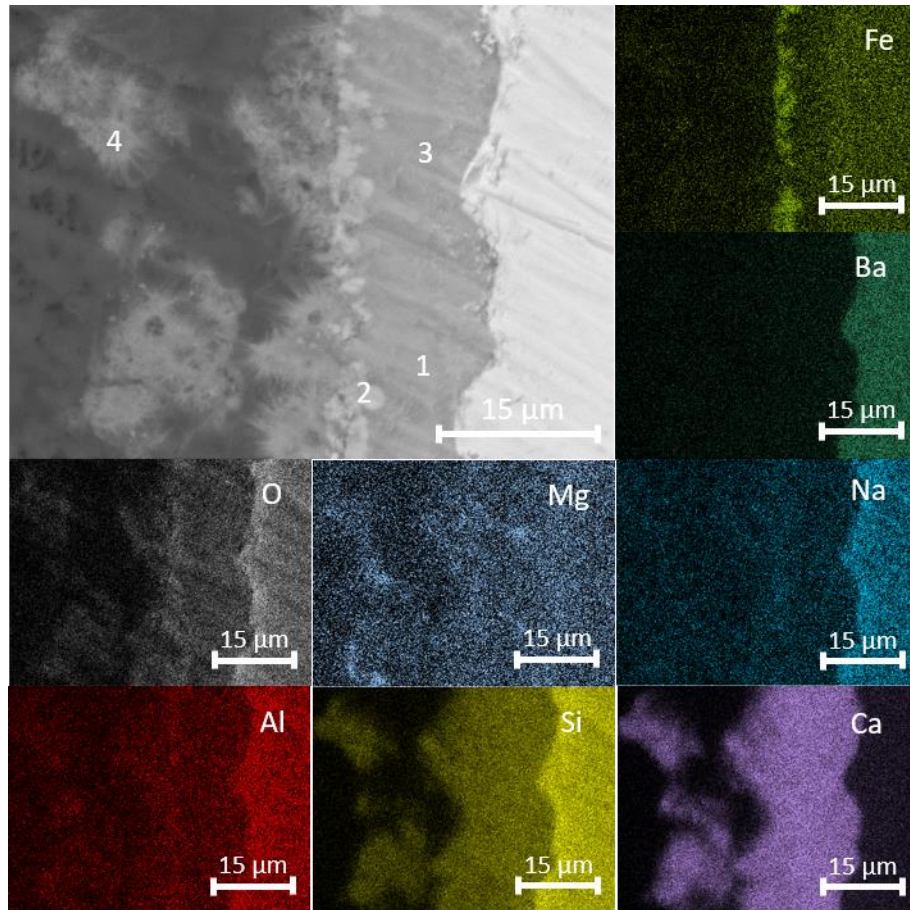


**Figure 6.64.** BSE image and elemental maps of alteration layer on a monolith of G73 altered for 720 days.

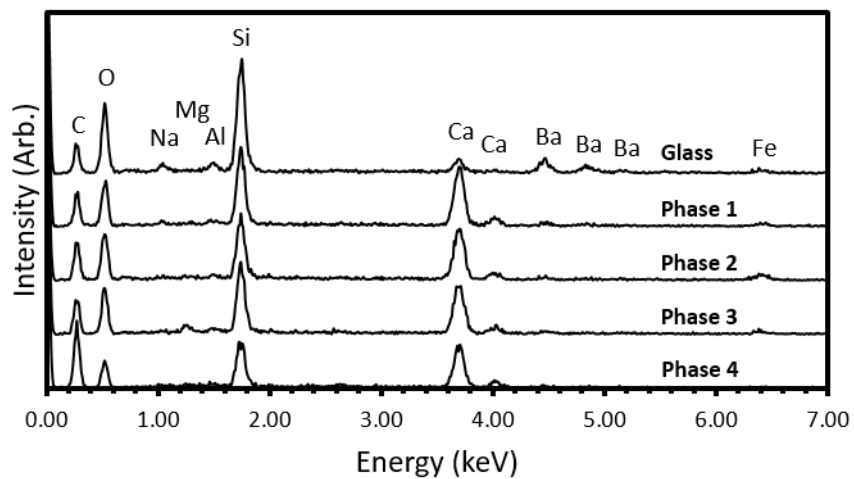


**Figure 6.65.** EDS spot analyses of alteration phases on a sample of G73 altered for 720 days.

## 6.5 Discussion of Results

### 6.5.1 Elemental Leaching Data

To use elemental leaching results to infer differences in chemical durability between samples, elements that remain mobile in solution during the process must be used. As boron is not thought to be retained in alteration phases during dissolution, it is generally used as a tracer for glass dissolution [13], [14], [140]. Sodium mass loss can also be used as a tracer for dissolution here, for two reasons: firstly, the NL(Na) values for each glass closely followed the trend of NL(B), suggesting that the leaching behaviour of Na and B was similar; and secondly, SEM studies of the glass alteration layers (see Section 6.4.1) show that sodium was not retained within alteration products in significant quantities. The final NL(B) and NL(Na) values obtained from both the PCT-B and MCC-1 experiments for the four literature glasses are shown in Figure 6.66 (N.B. no boron is present in the BAS sample). The initial and residual B and Na normalised mass loss rates for both sets of experiments are shown in Figure 6.67. These data suggest that the comparative durability of the four glasses, from most to least durable, is:

$$\text{BAS} > \text{ISG} > \text{G73} \gg \text{MW-25\%}$$

over the timescales used in these experiments (112 days for PCT-B and 720 days for MCC-1).

The finding that ISG is significantly more durable than MW-25% is consistent with the literature. The composition of ISG is based on that of SON68, an inactive simulant of French nuclear waste glass, although ISG is not waste-loaded. Previous work by Curti *et al.* showed that the durability of waste-loaded SON68 was up to a factor of 10 greater than that of waste-loaded MW-25% in unbuffered aqueous static dissolution tests at 90 °C [77]. As ISG (referred to as CJ4) has previously been shown to be less durable than SON68 [14], it is reasonable that ISG has been found here to be only twice as durable as MW-25%. This work shows that this trend holds for dissolution experiments carried out at 50 °C in a saturated Ca(OH)<sub>2</sub> leachant.

The dissolution behaviour of MW-25% deviated significantly from the other three glasses in that it did not appear to undergo a significant transition from the initial rate of dissolution to a significantly lower, residual rate of dissolution, which can be clearly seen in Figure 6.67. This suggests that there could be other mechanisms at work in the

dissolution of MW-25% compared to the other glasses. For example, it could be possible that continual precipitation of phases containing Si could negate the effect of silicic acid activity in reducing the dissolution rate, by causing the silicic acid to drop out of solution.

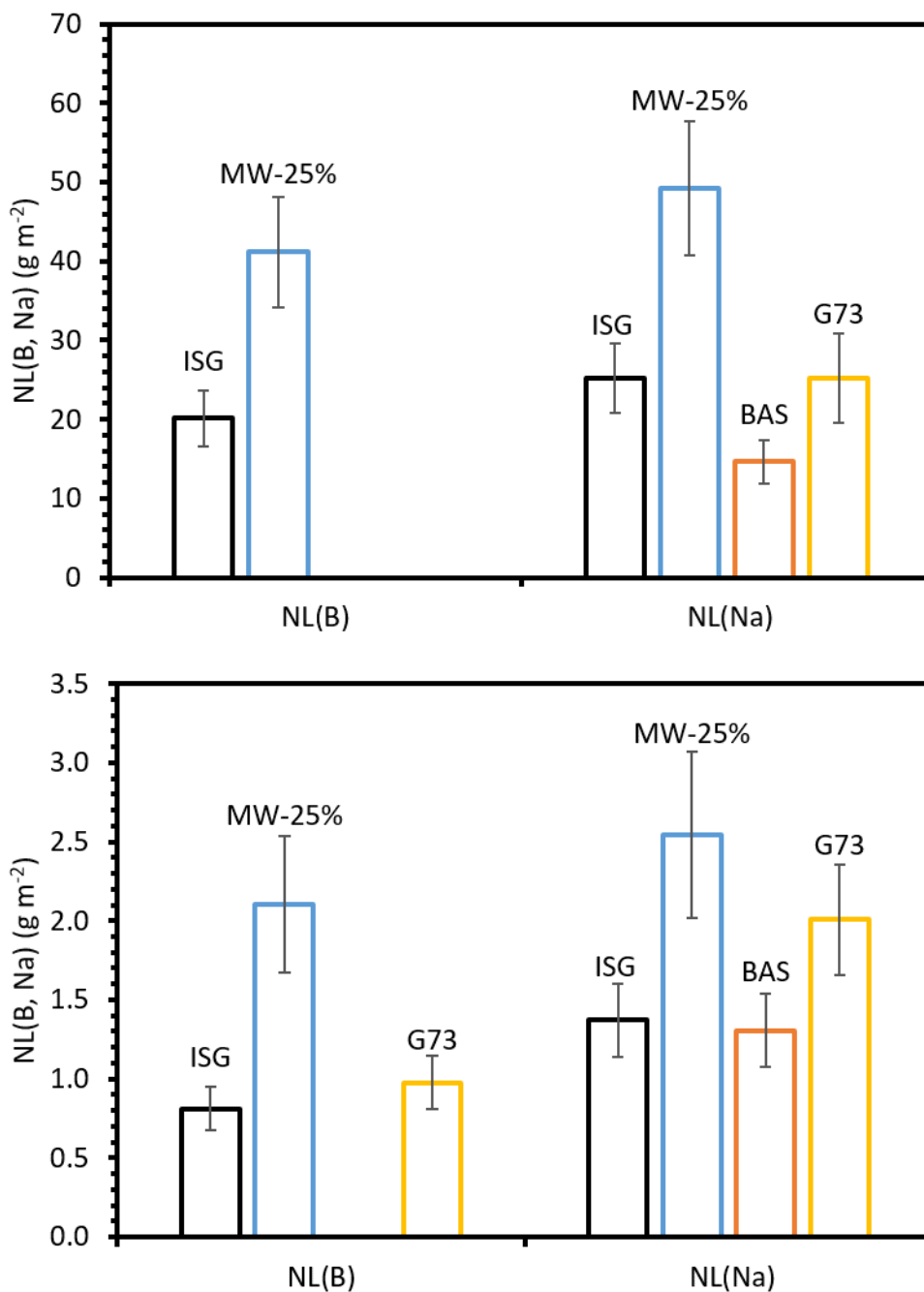


**Figure 6.66.** Final values of NL(B) and NL(Na) for the four literature glasses from the MCC-1 (upper graph) and PCT-B (lower graph) experiments.

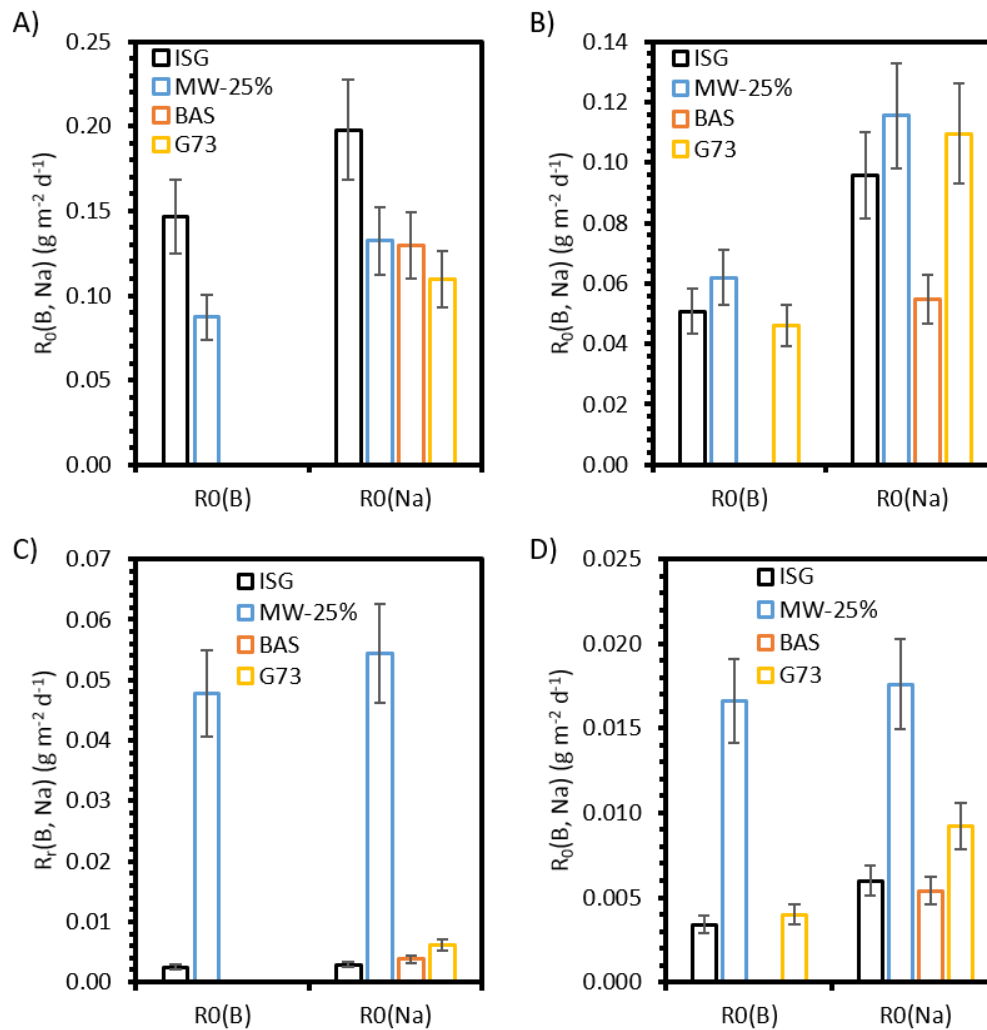


**Figure 6.67.** Initial and residual normalised B and Na mass loss rates for the four literature glasses: A) Initial rates, MCC-1; B) Initial rates, PCT-B; C) Residual rates, MCC-1; D) Residual rates, PCT-B.

The high observed durability of the laboratory-made basaltic glass (BAS) is also consistent with previous findings in the literature. Investigations comparing the dissolution of basaltic glasses with that of nuclear aluminoborosilicate glasses in unbuffered leachants have found that their durability is comparable over shorter timescales, but diverges significantly over time, with basaltic glasses becoming increasingly durable relative to the aluminoborosilicates [15], [103]. These investigations also showed that the alteration products formed on these two types of glasses during dissolution were comparable. This is partially borne out by the work conducted here, in that there are similarities in the alteration products of the MW-25% and BAS glasses, which both contain significant amounts of Fe, Mg and Al (see Section 6.5.2 for details). However, there is little correlation between the alteration

products formed on ISG and BAS, due to their differing compositions. As basaltic glasses have been repeatedly positioned as natural analogues for the dissolution of nuclear waste glasses [15], [103], [106]–[108], this is problematic. It appears that in high-pH, Ca-rich environments like those studied here, the behaviour of basaltic glasses is only partially comparable to the behaviour of aluminoborosilicate nuclear waste glasses.

The dissolution behaviour of G73 has not been studied previously. As it is essentially an alkali-alkaline earth silicate, with high Ba content, it is significantly different compositionally to the other three glasses. It was found to be intermediate in durability between the high durability (BAS and ISG) and low durability (MW-25%) glasses. This is likely due to it having the highest SiO<sub>2</sub> content (62.06 mol.%), which increased its durability, and having the highest modifier content (alkali and alkaline-earth oxides, 30.23 mol.%) which decreased it. Given that MW-25% is being used as a vitreous wasteform for UK HLW and is considered as fit for geological disposal, G73 must be considered to be an adequate vitreous matrix for the immobilisation of ILW, with respect to durability in high-pH, Ca-rich conditions.

The finding that MW-25% was the least chemically durable of the four literature glasses studied correlates with the findings of the dissolution experiments on simple glasses reported in Chapter 5. In the investigation of the dissolution behaviour of simple borosilicate and aluminoborosilicate glasses in Ca(OH)<sub>2</sub>, it was found that chemical durability decreased with B/Al ratio, that it increased with alkaline-earth oxide to alkali oxide ratio (MO/M<sub>2</sub>O), and that it was lower in Mg-containing glasses than Ca-containing glasses. Table 6.2 displays the B/Al, MO/M<sub>2</sub>O and MgO/(MgO + CaO) mol.% ratios for the four literature glasses. It is clear that MW-25% has the highest B/Al and MgO/(MgO + CaO) ratios, as well as the lowest MO/M<sub>2</sub>O ratio, all of which would indicate the glass having the lowest chemical durability based on the previous simple glass experiments. The (Na<sub>2</sub>O – Al<sub>2</sub>O<sub>3</sub>)/B<sub>2</sub>O<sub>3</sub> ratios of three of the four glasses (see Table 6.2, BAS excluded as it contains no boron) follows their durability trend, with ISG and G73 having similar ratios and similar dissolution resistance and MW-25% having the lowest ratio and lowest dissolution resistance. In Section 4.3.1, this ratio was shown to correlate with the <sup>IV</sup>B fraction of the boron-containing simple glasses, suggesting that glasses with a higher (Na<sub>2</sub>O – Al<sub>2</sub>O<sub>3</sub>)/B<sub>2</sub>O<sub>3</sub> ratio have greater network connectivity. This might imply a correlation between network connectivity and dissolution resistance. However, the literature glasses also

contain other alkali metals such as Li and K, and other intermediate elements such as cerium and lanthanum, which should be taken into account in this ratio. When this occurs, however, the ratio no longer shows a correlation with dissolution resistance. This might suggest that Na and Al have unique roles within the groups of alkali metals and intermediates.

A particular feature of note in the dissolution of these glasses is that none of them entered a stage of the resumption of alteration at an accelerated rate. The resumption of alteration, also known as Stage V or Stage III, depending on the schematic of dissolution used, is a phenomenon that has been observed in numerous nuclear waste glasses in a variety of conditions (including high-pH) [4], [84]–[88], as detailed in Section 2.4.3. The mechanism proposed for the resumption of alteration is that the formation of secondary crystalline products, generally silicates or aluminosilicates, removes network-forming elements, i.e. Si and Al, from both the passivating alteration layer and the glass itself, causing enhanced levels of degradation. The primary phases associated with this phenomenon are zeolites [88]. PHREEQC geochemical calculations suggest that zeolitic phases such as scolecite ( $\text{CaAl}_2\text{Si}_3\text{O}_{10}\cdot 3\text{H}_2\text{O}$ , SI after 720 days of 3.8, 4.05 and 3.7 for MW-25%, BAS and G73), gismondine ( $\text{CaAl}_2\text{Si}_2\text{O}_8\cdot 4\text{H}_2\text{O}$ , SI after 720 days of 1.66, 2.52 and 1.49 for MW-25%, BAS and G73) and mesolite ( $\text{Na}_2\text{Ca}_2(\text{Al}_2\text{Si}_3\text{O}_{10})_3\cdot 8\text{H}_2\text{O}$ , SI after 720 days of 4.15, 3.91 and 3.64 for MW-25%, BAS and G73) could be supersaturated in solution during the dissolution of MW-25%, BAS and G73 in  $\text{Ca}(\text{OH})_2$ . However, these phases have not yet been observed in these experiments, with the analysis techniques available. This might suggest that other Si- and Al-containing phases are precipitating preferentially over these zeolites. Geochemical modelling with PHREEQC also suggests that zeolitic phases might not be expected to be saturated during the dissolution of ISG in  $\text{Ca}(\text{OH})_2$  (negative Si values for all zeolites at all timepoints), although this could be due to insufficient thermodynamic data. This is in contrast to the work of Gin *et al.* [20] who observed the formation of zeolites on monolithic samples of ISG in a KOH leachant, and a consequent resumption of alteration.

**Table 6.2.** Comparison of literature glass compositions with respect to B/Al, alkaline earth oxide to alkali oxide, and MgO to MgO + CaO mol.% ratios.

Glass	B/Al	MO/M <sub>2</sub> O	MgO/ (MgO + CaO)	(Na <sub>2</sub> O - Al <sub>2</sub> O <sub>3</sub> )/ B <sub>2</sub> O <sub>3</sub>
ISG	5.03	0.39	0.00	0.54
MW-25%	7.30	0.38	0.999	0.38
BAS	0.00	4.38	0.45	0.38
G73	0.54	2.35	0.14	N/A

## 6.5.2 Alteration Layer Analysis

### 6.5.2.1 ISG

Three distinct phases were observed within the alteration layers formed on ISG monoliths during dissolution: A) a Ca- and Si-rich phase, with low Zr- and Al-content; B) a phase of similar composition but with a significant enrichment in Zr; and C) an inner layer with higher Ca and Al contents and intermediate Zr content. The relative composition for these phases are shown in Figure 6.68. Triplicate EDS measurements were taken for each phase for each timepoint. These data were then normalised to the triplicate EDS spectra of the glass composition. The normalised data for each phase were then averaged over all timepoints to give relative compositions of the phases across all samples. All of the phases had significantly elevated Ca contents compared to the glass, as well as elevated Zr contents, but similar or lower Si contents compared to the glass.

One of the features of interest in the evolution of the alteration layer on the monoliths between 30 and 720 days was the role of Zr in the alteration layer. For each of the ISG monoliths, the Zr in the alteration layer was not homogeneously distributed, but was concentrated in certain regions, creating Zr-rich (Phase B) and Zr-poor (Phase A) silicate regions that typically also contain Al (in lower amounts than the glass) and Ca (in higher amounts than the glass). This phenomenon was also recently observed by Gin *et al.* during dissolution of ISG in KOH, who suggested that this may have been due to a dissolution-reprecipitation mechanism [20]. The value of  $R_{Zr}$ , the ratio of Zr in the Zr-rich or Zr-poor silicate phases (at. %) compared to the Zr in the bulk glass (at. %) as calculated from EDS spot analyses for each sample, is shown in Table 6.3. For each sample, the concentration of Zr in the Zr-rich alteration layer phase was

found to be significantly greater than that of the bulk glass.  $R_{Zr}$  for the Zr-poor phases was generally  $< 1$ , with the exception of the 90-day sample. This suggests that either:

- the elements from the glass are leached into solution and are subsequently precipitated when their parent phases become supersaturated with respect to the leachate, or;
- there is significant rearrangement of elements during de-alkalisation (the set of processes whereby alkali elements leach to solution), requiring ‘uphill’ diffusion, in a similar fashion to that observed in spinodal decomposition [141].

The former is in line with the theory of Geisler *et al.*, where glass alteration is hypothesised to be governed by coupled dissolution and reprecipitation reactions [93]. In the current investigation, this is thought to be the more likely explanation, especially given the high Ca content of the alteration layers. For the post-30-day samples, the Zr-partitioning resulted in a pattern of banding within the alteration layer, consisting of alternating layers of Zr-rich and Zr-poor silicate phases again containing Al and Ca. Previous work by Arab *et al.* [142] has suggested that the presence of Zr in the glass has a two-fold effect on the glass dissolution: i) the presence of Zr in the glass matrix has a hardening effect on its nearest neighbour atoms, making them more resistant to leaching; ii) Zr in the alteration layer causes cross-linking, which retards or prevents the re-ordering and densification of the layer, leading to the retention of porosity and therefore percolation routes for further dissolution. However, the experiments performed in this investigation are not conducive to isolating the individual effect of Zr, and so further experiments would be required to determine whether Zr behaves in this way in the high-pH conditions used here, as compared to the buffered pH 8.2 solution used by Arab *et al.*

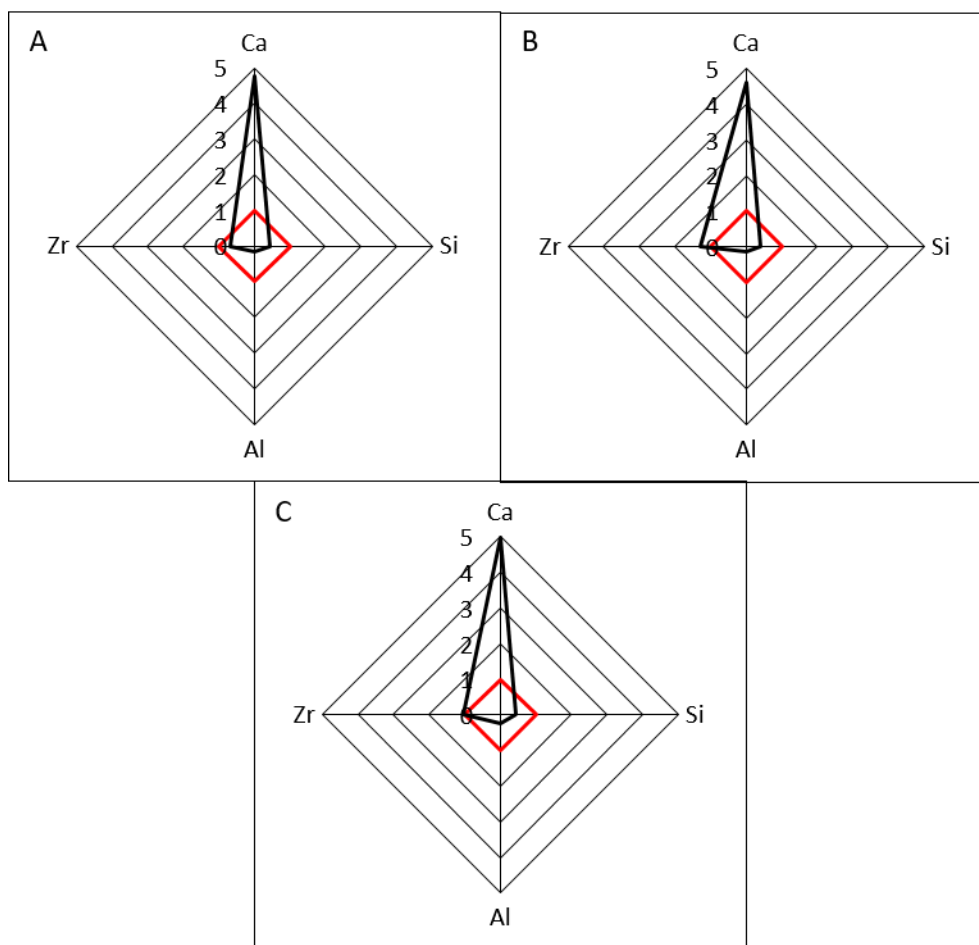


**Figure 6.68.** EDS-determined elemental concentration distributions for ISG alteration phases, normalised to monolith composition, phases A – C. The red diamond denotes the content of each of the elements in the glass.

**Table 6.3.**  $R_{Zr}$  for each of the ISG samples, as determined by triplicate EDS measurements. Errors shown are derived from the standard deviation of the triplicate measurements.

Phase	30 days	90 days	180 days	360 days	540 days	720 days
Phase B	$1.52 \pm 0.17$	$3.8 \pm 0.5$	$1.97 \pm 0.20$	$2.41 \pm 0.21$	$1.42 \pm 0.29$	$1.33 \pm 0.21$
Phase A	$0.82 \pm 0.16$	$1.7 \pm 0.4$	$0.59 \pm 0.11$	$0.84 \pm 0.16$	$0.77 \pm 0.28$	$0.99 \pm 0.08$

**Table 6.4.** Triplicate EDS-determined Ca/Si ratios for selected phases on altered ISG monoliths. Errors derived from standard deviation of triplicate measurements.

Phase	30 days	90 days	180 days	360 days	540 days	720 days
Alteration layer	0.63 ± 0.09	0.79 ± 0.11	1.36 ± 0.09	1.64 ± 0.36	1.59 ± 0.04	1.41 ± 0.20
C-S-H Precipitates	N/A	N/A	2.19 ± 0.11	1.81 ± 0.18	1.89 ± 0.21	1.73 ± 0.21

The two most significant changes in the ISG alteration layer with time were the change in the Ca/Si ratio of the alteration phases, and the appearance of C-S-H-like precipitates after 180 days. The Ca/Si values for different phases as a function of time are shown in Table 6.4. The general trend was for an increase in the Ca/Si ratio with time for the alteration layer up to 360 days, followed by a slow decrease between 360 and 720 days. The primary source of Ca in the alteration layer is the Ca(OH)<sub>2</sub> solution, whereas the primary source for Si is the glass monolith. A possible mechanism to explain the trends in the Ca/Si ratio is (schematic in Figure 6.69):

1. 0 – 180 days: Ca and Si leach from the glass and combine with Ca in solution to form the alteration layer. Over time, the greater concentration of Ca (from solution) compared to Si (from the glass) causes the Ca/Si ratio of the alteration layer to steadily increase.
2. 180 – 360 days: Ca and Si continue to leach from the glass. As the concentration of Ca in the alteration layer approaches that of the Ca in solution, the rate of change of Ca/Si slows.
3. 360 – 720 days: When the Ca concentration in the alteration layer reaches the concentration in solution, the leaching of Si from the glass becomes the dominant variable in the change of Ca/Si. As the rate of Si leaching is low, the Ca/Si ratio appears approximately stable with time.

The Ca/Si values suggest that tobermorite-type (Ca/Si = 0.83) phases might form at earlier times, with other phases, such as afwillite (Ca<sub>3</sub>(SiO<sub>3</sub>OH)<sub>2</sub>·2H<sub>2</sub>O, Ca/Si = 1.5) possibly becoming prevalent later on. However, PHREEQC geochemical modelling suggests that both afwillite (SI values of 0.36, 0.57, 1.00, 0.49 and 0.70 for 90, 180, 360, 540 and 720 days) and tobermorite (SI values of 11.61, 12.18, 13.44, 11.97 and

12.63 for tobermorite-11Å for 90, 180, 360, 540 and 720 days) should be supersaturated with respect to the leachate solution from 90 days onwards. The C-S-H precipitates have higher Ca/Si ratios than the alteration layers for each of the 180, 360, 540 and 720-day monoliths, with the ratio decreasing with time, as has been observed previously [19]. The high Ca/Si ratios ( $\sim 2$ ) suggest that the C-S-H phases may not be present on their own, as the formation of C-S-H phases with Ca/Si ratios  $\sim 2$  has not previously been observed. It is therefore likely that there are other, Ca-rich, phases present.

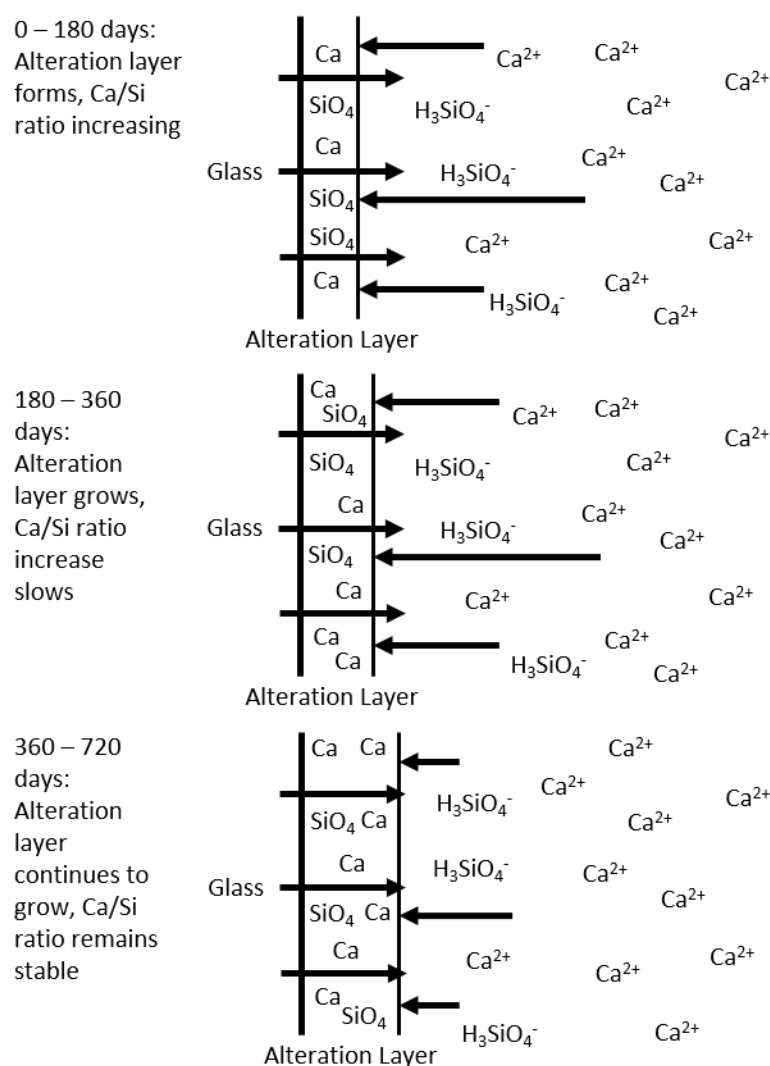


**Figure 6.69.** Schematic of mechanism of variation of Ca/Si ratio in alteration layer with time.

PHREEQC calculations indicate that the presence of crystalline C-S-H precipitates, particularly tobermorite-9Å, tobermorite-11Å and tobermorite-14Å, is thermodynamically favourable in Ca-rich systems with only a relatively small amount

of Si ( $< 10$  ppm) in solution, e.g. Si values of 2.98, 3.92 and 0.14 for 9Å, 11Å and 14Å after 30 days with a Si concentration of 1 ppm. However, despite all leached Si appearing to have precipitated out of solution, these precipitates do not appear at the microscale until the 180-day sample, where they are present in significant quantities. The precipitates were formed in radiating, acicular clusters from the surface of the alteration layer, and did not form a consistent layer around the whole sample. The cluster sizes ranged from 4 to 13  $\mu\text{m}$  across the four samples where they were observed (180, 360, 540 and 720 days). The precipitates always appeared on the outside of the sample, rather than within the alteration layer, or between the alteration layer and the glass surface. This suggests that they form only through direct precipitation from solution, rather than a re-ordering of the alteration layer.

Micro-focus X-Ray Diffraction ( $\mu\text{-XRD}$ ) data were collected on the 720-day monolith on the microXAS (X05LA) beamline at the Swiss Light Source, Paul Scherrer Institute, Switzerland. The data were collected at a monochromatic beam energy of 17.2 keV. A thin-section of the monolith was mounted onto a glass slide (see Figure 6.70), which was placed on a motorised stage positioned at an angle of  $25^\circ$  to the incident beam which had a spot size of 7  $\mu\text{m}$  by 2  $\mu\text{m}$ . The diffraction patterns were measured with a PILATUS 100K hybrid pixel array detector. This was mounted 46 mm behind the sample with a tungsten beamstop in place. A Si standard was used for calibration of the setup. The resulting diffraction data is shown in Figure 6.71. Portlandite ( $\text{Ca}(\text{OH})_2$ , PDF card [01-076-0571]) was readily identified from this diffraction pattern, which presumably had precipitated from the saturated  $\text{Ca}(\text{OH})_2$  leachant. This suggests that the Ca-rich phase observed on many of the monoliths was portlandite rather than calcite. This implies that carbonation of the samples has not occurred during the experiments, implying that the use of a  $\text{N}_2$  atmosphere glovebox to exclude  $\text{CO}_2$  was successful. Diffuse scattering is present from  $10$  to  $13^\circ 2\theta$ , which could be due to the monolith itself, or to an amorphous component of the alteration layer. Two further phases were identified: colemanite ( $\text{Ca}_2\text{B}_6\text{O}_{11}\cdot 5\text{H}_2\text{O}$ , PDF Card [00-006-0331]), a calcium borate hydrate mineral; and hibschite ( $\text{Ca}_3\text{Al}_2(\text{SiO}_4)_2(\text{OH})_4$ , PDF Card [00-042-0570]), a calcium aluminium silicate hydroxide. The presence of colemanite, a boron-containing mineral, casts some doubt on the validity of using boron as a tracer for glass dissolution in high-Ca solutions. The presence of calcium borate phases during glass dissolution at high-pH has previously been postulated by Utton *et al.* to explain an observed incubation period in

the release of boron [3]. A calcium borate precipitate was also tentatively identified on the altered NMAB10S sample in Section 5.5.4. However, assuming that the overall amount of colemanite present is small, NL(B) can still be used as an approximate measure of the dissolution of ISG. Any other phases present have not yet been identified, and further analysis work is needed for this to be achieved.

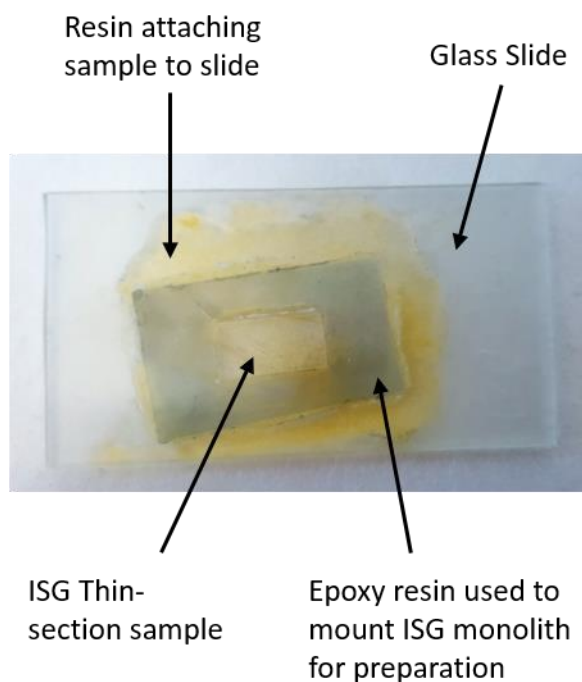


**Figure 6.70.** Thin-section sample of 720-day ISG monolith mounted on a glass slide for  $\mu$ -XRD analysis.

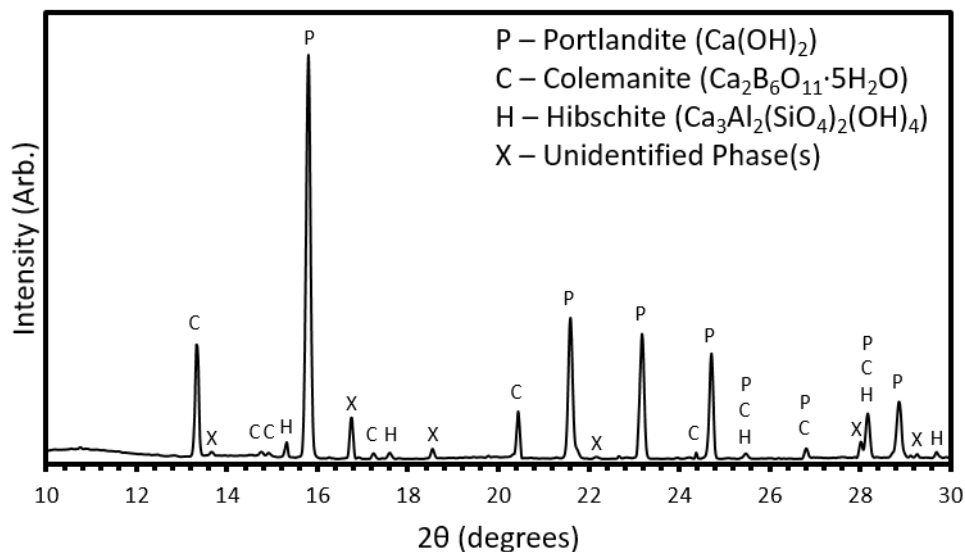


**Figure 6.71.**  $\mu$ -XRD data obtained on 720-day altered monolith of ISG, showing peaks associated with portlandite ( $\text{Ca}(\text{OH})_2$ ), colemanite ( $\text{Ca}_2\text{B}_6\text{O}_{11}\cdot 5\text{H}_2\text{O}$ ), hibschite ( $\text{Ca}_3\text{Al}_2(\text{SiO}_4)_2(\text{OH})_4$ ) and an unidentified phase or phases.

#### 6.5.2.2 MW-25%

Analysis of the alteration of the MW-25% monoliths revealed the presence of three distinct phases: A) a Ca- and Si- rich phase generally found closest to the surface of the glass; B) a Mg- and Al-rich phase present in an acicular form; and C) a spherical Fe-rich phase composing a rim in the alteration layer. The relative compositions on these phases are shown in Figure 6.72, and each of the phases can be seen in the BSE micrograph of the alteration layer on the 720-day monolith (Figure 6.73). All three phases appeared to be enriched in Ca with respect to the glass, and also enriched in Zr. Phase A was noticeably enriched in Nd with respect to the glass.

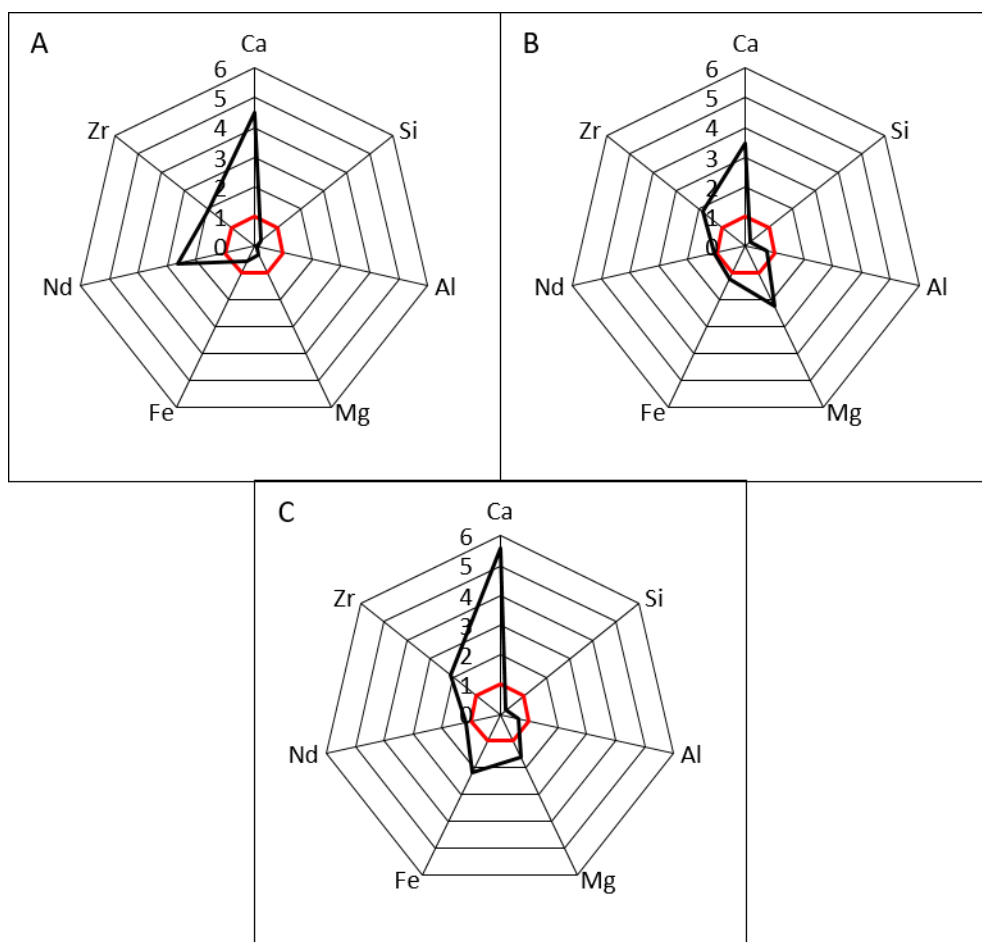


**Figure 6.72.** EDS-determined elemental concentration distributions for MW-25% alteration phases, normalised to monolith composition, phases A – C. The red heptagon denotes the content of each of the elements in the glass.

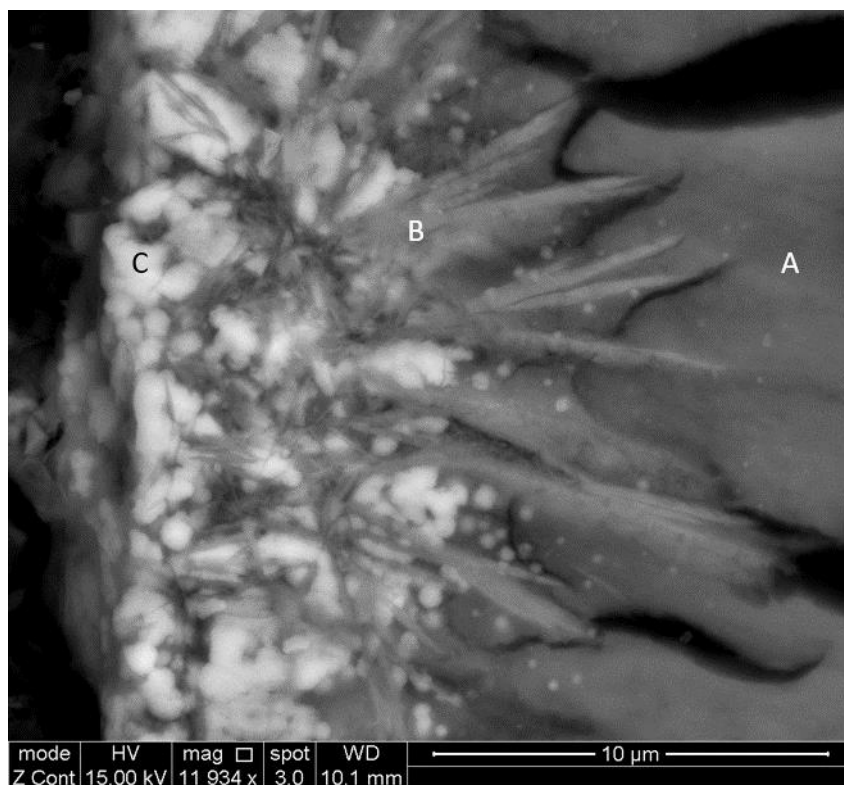


**Figure 6.73.** BSE image of alteration layer on a monolith of MW-25% altered for 720 days, showing 1) Dark-grey Ca-Si phase, 2) Light-grey Mg-Al phase and 3) White Fe-rich phase.

As with the ISG monoliths, changes were observed in the Ca/Si ratio of the alteration layers on the MW-25% monoliths with time (see Table 6.5) (N.B. No precipitates were observed until the 180-day monolith, and Ca was not observed in the alteration layer of the 30-day sample). The Ca/Si ratio increased up to the 540-day sample (c.f. 360 days for ISG), before decreasing slightly. The Ca/Si ratio of the precipitates was consistently higher than that of the alteration layer, as seen for the ISG samples.

**Table 6.5.** Triplicate EDS-determined Ca/Si ratios for selected phases on altered MW-25% monoliths. Errors derived from standard deviation of triplicate measurements.

Phase	30 days	90 days	180 days	360 days	540 days	720 days
Alteration layer	N/A	0.80 ± 0.07	1.10 ± 0.23	1.47 ± 0.16	1.58 ± 0.09	1.50 ± 0.08
C/M-S-H Precipitates	N/A	N/A	1.22 ± 0.31	2.32 ± 0.68	2.27 ± 0.22	2.61 ± 0.72

The behaviour of Mg in the formation of the alteration layer appeared to be significantly different to that of Ca. Mg leached from the glass was incorporated into the alteration layer, with negligible amounts remaining in solution (ICP-MS analysis of the 720-day leachate revealed a Mg concentration in solution of 66 ppb). The Mg was primarily found associated with Al in an acicular phase in the alteration layer (Phase B), as shown by Figure 6.73. These needles were observed from the 180-day sample onwards. The ratio of Mg (at. %) in the alteration phases to that in the glass, is significantly different for Phases A and B; 0.1 – 0.3 compared to 1.34 – 3.49. Micro-XRD data were collected on the 720-day monolith under the same conditions as the ISG data, at the Swiss Light Source, Paul Scherrer Institute. The diffraction data are shown in Figure 6.74. These data identified this phase as meixnerite ( $\text{Mg}_6\text{Al}_2(\text{OH})_{18}\cdot 4.5\text{H}_2\text{O}$ , PDF [00-035-0965]), a layered double hydroxide (LDH) which forms tabular crystals [143]. Meixnerite is not present in the PHREEQC LLNL database used in this work. Two other phases were identified from these data: brucite ( $\text{Mg}(\text{OH})_2$ , PDF Card [04-013-9512]) and portlandite ( $\text{Ca}(\text{OH})_2$ , PDF Card [01-073-6988]). It was not possible to identify the other phases present. Transmission Electron Microscopy was carried out on a thin-section of the alteration layer from the MW-25% sample altered in  $\text{Ca}(\text{OH})_2$  for 540 days (see Section 3.4.2 for experimental details). A TEM micrograph and Selective-Area Electron Diffraction (SAED) patterns from the sample are shown in Figure 6.75. Several different phases can be observed in the micrograph based on differences in contrast: a globular dark-grey phase, lighter-grey needle-like regions, a mid-grey phase pervading the sample, and a bright white phase. From the SAED patterns, it is clear that the dark-grey phase was amorphous, while the needle-like phase and white phases were at least partially crystalline. The morphology of the needle-like phase suggests that it may be meixnerite. This was confirmed by EDS analysis of the phases; the needle-like phase contained high levels of Mg and Al (Figure 6.76). The amorphous component in the meixnerite SAED pattern is likely due to the beam size being larger than the particular needle that was analysed, and so surrounding amorphous phases contributed to the diffraction pattern. The amorphous dark-grey phase contained primarily Ca, Si and O and is likely to correspond to Phase A, a Ca- and Si-rich phase, in Figure 6.72. The white phase would seem to correspond to the Fe-rich spherules seen in the SEM analysis of the MW-25% alteration layers. No Fe-containing phases were observed in the  $\mu$ -XRD data, most likely due to simple chance in not observing an Fe-rich area with the micro-focus X-

ray beam. Further investigation is needed in order to be able to identify this phase.

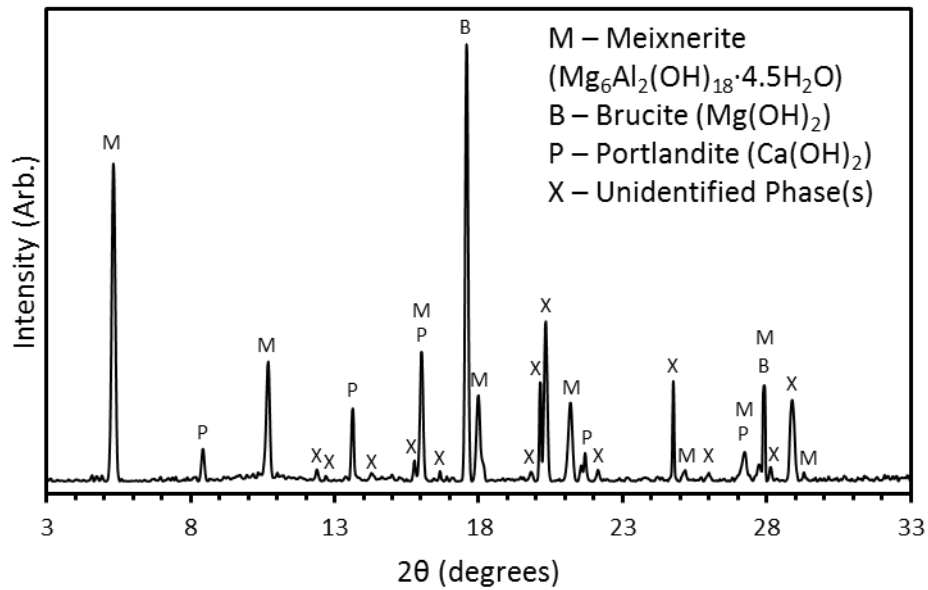


**Figure 6.74.**  $\mu$ -XRD data obtained on 720-day altered monolith of MW-25%, showing peaks associated with meixnerite  $(\text{Mg}_6\text{Al}_2(\text{OH})_{18} \cdot 4.5\text{H}_2\text{O})$  and an unidentified phase or phases.

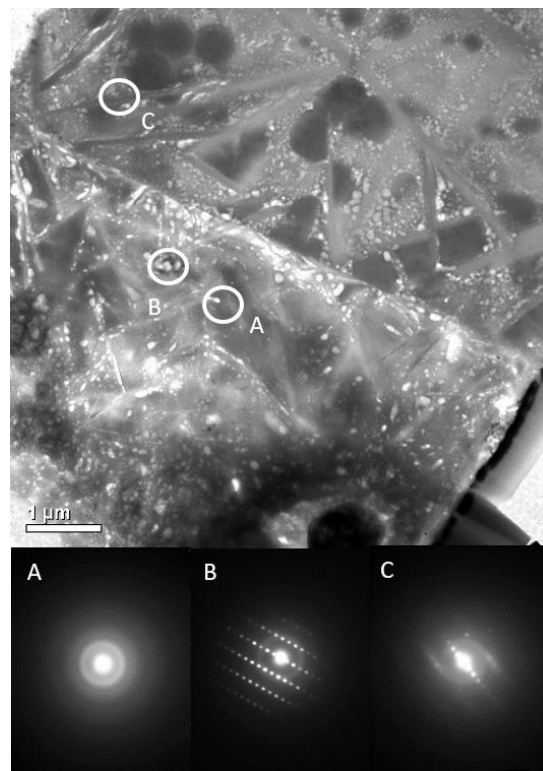


**Figure 6.75.** TEM micrograph and SAED patterns for a sample of alteration layer from MW-25% altered for 540 days in  $\text{Ca}(\text{OH})_2$ . Diffraction data were collected from the dark-grey region (A), the bright phase (B), and the needle-like phase (C).

Although meixnerite was seen in numerous locations on the glass surface, the most significant clusters of meixnerite were generally found at a point on the glass where there was a 'divot' in the glass surface, e.g. Figure 6.40. There are two possible explanations for this correlation:

- These divots are artifacts of glass production, e.g. bubbles trapped in the melt, which led to increased concentration of leached ions in solution (greater surface area to leachate volume within a small region) causing the formation of greater amounts of meixnerite locally (see schematic in Figure 6.77), or;
- An external stimulus, e.g. particulate matter in solution, caused the nucleation of meixnerite near to the surface of the glass. This led to increased dissolution in a localised region of the glass surface, forming the divot (see schematic in Figure 6.78).

The latter explanation is more likely, as although bubbles have been observed by visual inspection, none have been observed at the microscale by microscopy except at the surface in conjunction with the meixnerite clusters. This mechanism has been seen in weathered glass samples. The presence of these meixnerite crystals within the alteration layer itself suggests a dissolution-reprecipitation mechanism of alteration layer formation. It should be noted that in a review by Fournier *et al.* of the crystalline phases formed during the alteration of nuclear waste glasses [88], meixnerite was not observed in any of the experiments considered, and that none of the phases encountered in that work have been identified in the diffraction data here. However, MW-25% was not one of the glasses reported in the review.

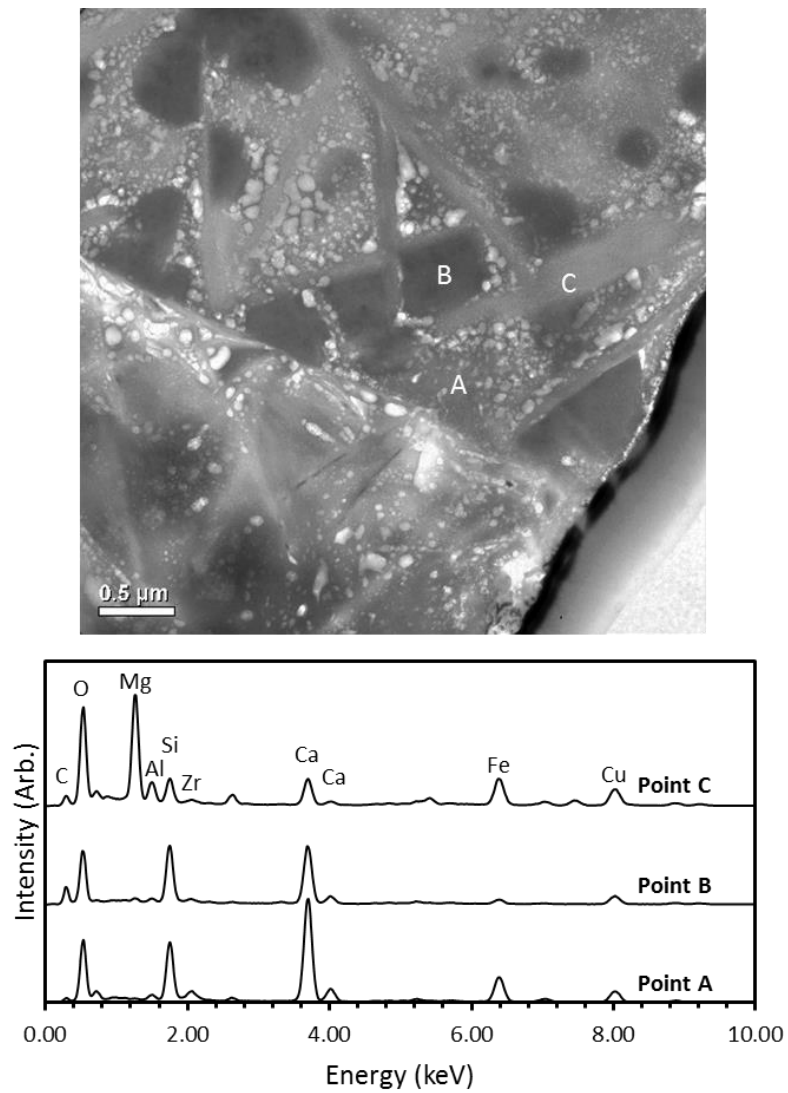
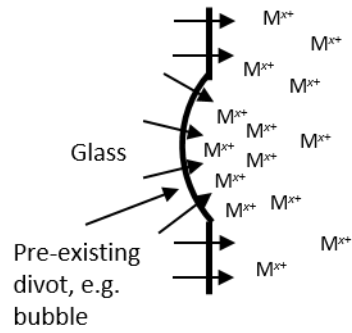
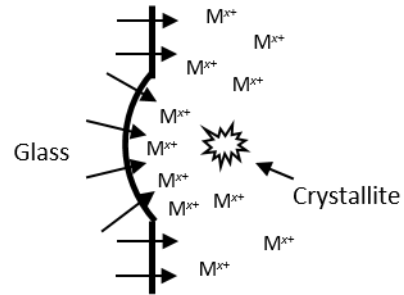


**Figure 6.76.** EDS point analysis for a sample of alteration layer from MW-25% altered for 540 days in  $\text{Ca}(\text{OH})_2$ . EDS spectra were collected from the mid-grey region (A), the dark-grey region (B), and the needle-like phase (C).

Leaching across glass surface  $\rightarrow$  higher leached species ( $M^{x+}$ ) concentration near divot



High local concentration of leached species leads to crystallite precipitation



Crystallite provides driver for leaching  $\rightarrow$  divot grows  $\rightarrow$  higher local concentration of leached species  $\rightarrow$  crystallite grows further

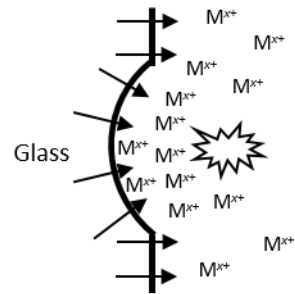


**Figure 6.77.** Schematic of mechanism of meixnerite crystal formation through presence of pre-existing surface defects.

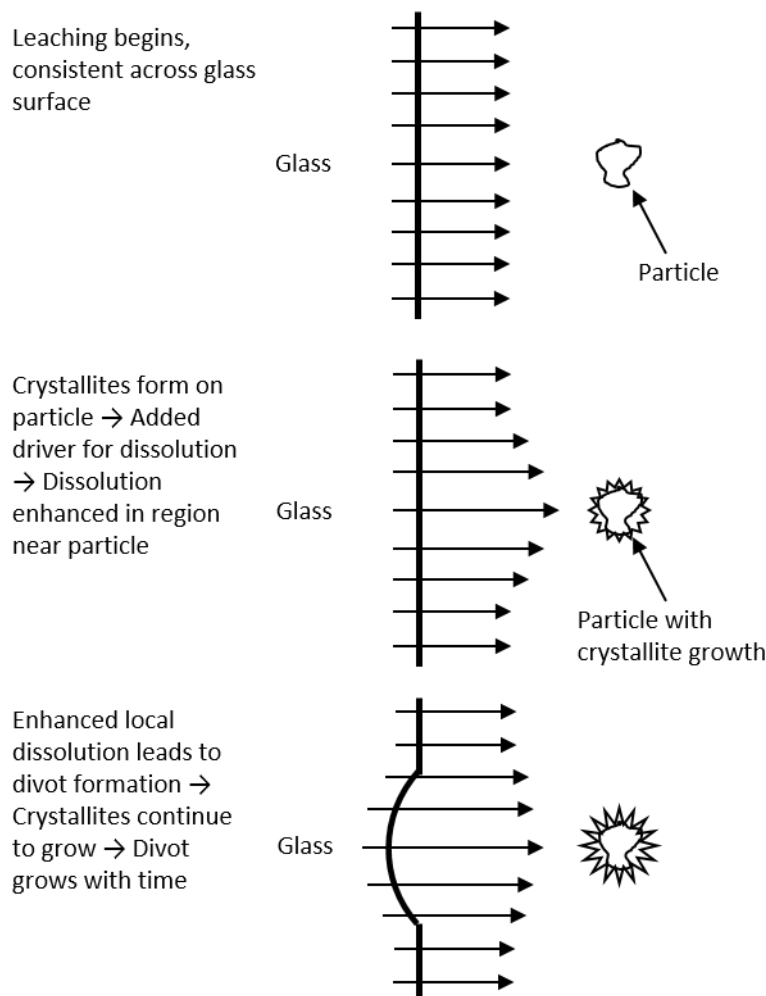


**Figure 6.78.** Schematic of mechanism of meixnerite crystal formation through presence of particulate matter in solution.

In MW-25%, rare-earth oxides are included as inactive surrogates of actinide (U, Pu, Np) oxides, in order to assess the likely behaviour of the actinides during dissolution. In this work, Nd has been chosen to represent the behaviour of all of the rare-earth oxides as it was the most abundant rare-earth in the glass and its distribution during dissolution was observed to be similar to that of the other rare-earths, per EDS analysis. Nd was not detected in any appreciable amount ( $> 10$  ppb) during ICP-OES analysis of the leachate samples, suggesting that if it had leached then it had been retained in the alteration layer. This was corroborated by ICP-MS analysis of the 720-day leachate, which showed that the amount in solution was  $< 0.05$  ppm. Further evidence of Nd retention in the alteration layer is that the concentrations of Nd in the alteration layer were higher than those in the glass, per EDS analysis (see Figure 6.72). Nd(III) has a larger ionic radius in glasses than any of the actinides;  $1.163 \text{ \AA}$  in nine-fold coordination, compared to  $0.76$ ,  $0.87$  and  $0.86 \text{ \AA}$  for octahedral U(V), Np(IV) and

Pu(IV), respectively. This larger size might suggest that it is more likely to be retained in the alteration layer, rather than percolating through. However, it is known from the literature that Layered Double Hydroxides (LDHs), such as the meixnerite observed in these samples, have capability for the sorption of both cationic and anionic radionuclides, including U(VI), whereas sorption of Nd(III) onto meixnerite was not observed in this investigation [144]–[146]. This has potential implications for the long-term fate of radionuclides in a GDF, and experiments investigating the potential of precipitated meixnerite to sorb radionuclides would be of interest. In addition to this, there are still many areas of further work required to fully understand the potential role of secondary precipitates on the sorption of radionuclides during long-term dissolution.

Fe was observed in the alteration layers for the MW-25% samples, and, as with Mg, it was not detected in significant amounts in solution (27 ppb detected in the 720-day leachate, using ICP-MS). The EDS analysis of the MW-25% samples (Figures 6.32 – 6.43) shows that the Fe was retained in the alteration layer. The Fe appeared to be concentrated in the outer region, or ‘Alteration Rim’, of the alteration layer, and tended to be present in spherical or globular forms, as shown by the micrographs in Figure 6.79. The morphology of these phases is similar to those of the goethite (FeOOH) crystals observed by Schwertmann and Carlson [147], suggesting that this is potentially the identity of the phase observed here. The partitioning of Fe into these phases within the rim of the alteration layer is clearly observed in Figure 6.72, which shows that the Fe concentration in the Ca-Si region of the alteration layer (Phase A) and in the alteration rim (Phase C) are significantly different.

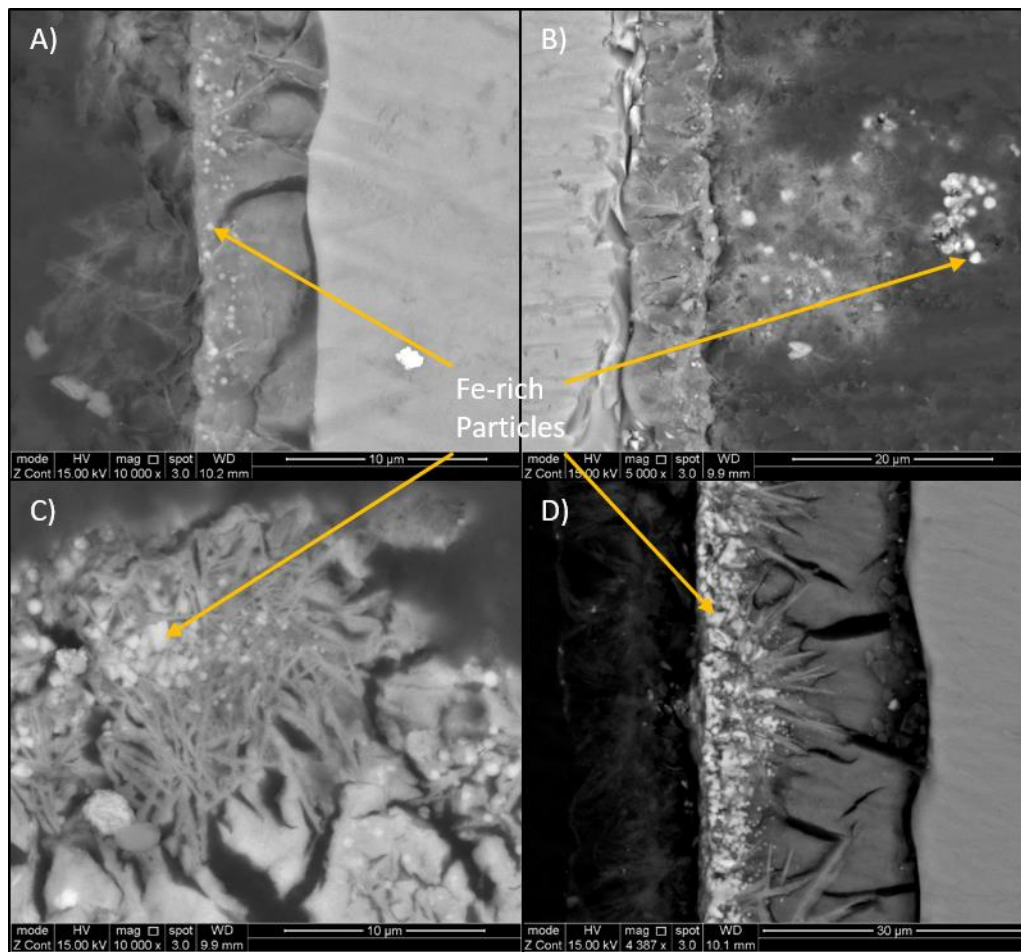


**Figure 6.79.** BSE micrographs showing Fe-rich particles on monoliths of MW-25% altered for: A) & B) 180 days; C) 360 days; D) 720 days.

As with the ISG samples, Zr leached from the glass appeared to be primarily retained by the alteration layer. However, the banded pattern of Zr-rich and Zr-poor regions that was observed in the ISG alteration layers was not observed on the MW-25% monoliths. This can potentially be explained by assuming that the method of alteration layer formation is a dissolution-precipitation mechanism. In this mechanism, elements leach from the glass until the leachate reaches saturation with respect to solid phases, at which point these phases can form, taking the solution below the saturation point again. The banded alteration layers in ISG are postulated to be caused by periodic repetition of this mechanism. In this theory, the concentrations of various elements in solution increase over time, with Si-containing phases precipitating from early on in dissolution. Eventually, the Zr concentration in solution reaches such a point that a Zr-containing phase precipitates, in a layer within the alteration layer. This process then occurs again until another layer of a Zr-containing phase precipitates, separated from its counterpart by a layer of more rapidly formed

Si-rich phase. As MW-25% contains significantly less  $\text{ZrO}_2$  than ISG (0.77 mol.% compared to 1.83 mol.%), the deposition of a Zr-rich layer will take considerably more time and thus may not occur twice within the timescales of these dissolution experiments. The Zr-containing phase(s) precipitating may also be different due to the differing compositions of ISG and MW-25%. This could also impact the formation of banding within the alteration layer. However, no Zr-containing phases have been identified on either of the glasses.

#### 6.5.2.3 BAS

Considering BAS monoliths of all dissolution durations, there appeared to be four discrete phases comprising the alteration layers (not necessarily all in the same sample), which all contain significant amounts of Ca and Si. The relative compositions of these phases are displayed in Figure 6.80. The four phases were: A) a phase that has low Mg, Al and O contents, but higher Fe and Ti contents; B) a phase with higher Mg, Al and O contents, but with decreased Fe and Ti contents; C) a phase with a similar composition to A, but with a greater Ti content, which formed as a rim on the alteration layer; and D) a phase with similar composition to A and C, albeit with higher Fe and lower Ti contents, but with a spherulitic morphology, which was primarily observed on the 180-day sample. All phases were enriched in Ca compared to the glass and A, C and D were also enriched in Ti and Fe. The formation of Fe-rich spherules was also observed for some of the MW-25% samples (Figure 6.79), where they were postulated to be composed of goethite ( $\text{FeOOH}$ ), although there is currently no direct evidence to support this.

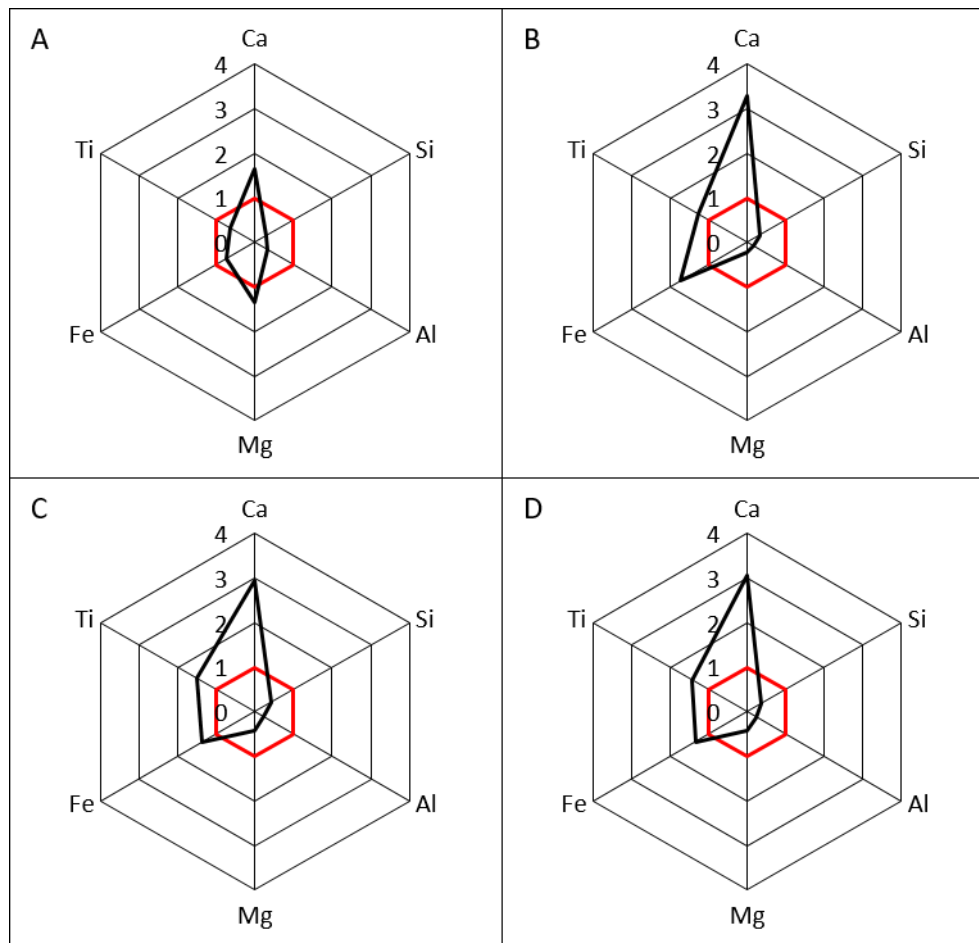


**Figure 6.80.** EDS-determined elemental concentration distributions for BAS alteration layers, normalised to monolith composition, phases A – D. The red hexagon denotes the content of the elements in the glass.

As with the ISG and MW-25% samples, there was a marked increase in the Ca/Si ratio with time (Table 6.6). The values at 180 days and 720 days were similar, suggesting that the system had reached stage 3 of the Ca/Si ratio evolution mechanism outlined in Section 6.5.2.1. However, the values at 360 and 540 days are significantly lower. This could be due to the difficulty of identifying the correct phase to measure for each sample, given the complex, multiphase nature of the alteration layer on the BAS samples. The Ca/Si ratio of the C-S-H precipitates was higher than that of the alteration layer, in common with the values observed for the ISG and MW-25% samples.

**Table 6.6.** Triplicate EDS-determined Ca/Si ratios for selected phases on altered BAS monoliths. Errors derived from standard deviation of triplicate measurements.

Phase	30 days	90 days	180 days	360 days	540 days	720 days
Phase A	N/A	1.67 ± 0.11	2.79 ± 0.67	2.24 ± 0.12	1.65 ± 0.22	3.19 ± 0.96
C-S-H Precipitates	N/A	N/A	N/A	2.40 ± 0.38	N/A	4.60 ± 1.12

The co-location of Mg and Al in the alteration layer is similar to that seen in the MW-25% samples, where this was due to the formation of meixnerite crystallites, as shown by  $\mu$ -XRD. The morphology of the two phases was similar, suggesting that the phase on the BAS monoliths could also be meixnerite.  $\mu$ -XRD data are not available for the BAS monoliths due to time constraints at the beamline.

When natural basaltic glasses undergo dissolution in the environment, a secondary phase known as palagonite is formed, which is the first stable alteration phase formed on volcanic glasses [148]. When investigating the dissolution behaviour of basaltic glasses as a potential natural analogue for nuclear waste glasses, it is important that the behaviour of basaltic glasses in laboratory experiments is comparable to their behaviour in the environment. The formation of palagonite is part of this comparison. There are two main types of palagonites: a mostly-amorphous, gel-like phase, and a more crystalline, smectite-like phase. The BAS glass leached in these experiments did appear to have both amorphous and crystalline contents, although without further investigation this cannot be confirmed. One feature often seen in palagonites is banding within the alteration phases, which was not observed during the experiments in this investigation. This could be due to the differing timescales of alteration of natural basaltic glasses: millions of years compared to 2 years for the BAS glass in these experiments.

#### 6.5.2.4 G73

Across all of the altered G73 monoliths, four different phases were identified; their relative compositions are shown in Figure 6.81. The four phases were: A) a primarily Ca- and Si- containing phase which constituted the majority of the alteration layer, also containing a small amount of Fe; B) an Fe-enriched, Ca- and Si-containing phase

which tended to be localised to a narrow region within the alteration layer; C) a Mg-enriched, Ca- and Si-containing phase which was present in highly-localised areas of the alteration layer; and D) a Ca- and Si-rich phase which had a significantly lower Ca/Si ratio than Phase A, and was only observed on the 540-day sample. As with the other three glasses, all observed alteration phases were significantly enriched in Ca compared to the glass. In addition, Phase B was enriched in Mg with respect to the glass, and Phase D was similarly enriched in Fe.

Although there was significant localisation of Mg within the alteration layer (Phase B contained, on average, 4 times the Mg of that in the glass), there wasn't evidence of co-location of Mg with Al, suggesting that it is unlikely that a phase such as mexinerite would form on this sample. This could be due to the low Mg-content of the glass (1.24 mol.% MgO) causing the leachate to have a low Mg/Al ratio compared to meixnerite, which requires 3 moles of Mg per mole of Al to form.

One of the key differences between G73 and the other glasses studied was that the primary alkaline-earth in the glass was Ba rather than Ca or Mg. The EDS data show that Ba was not significantly retained in the alteration layers, or other secondary products, of any of the G73 monoliths; the Ba concentration in the alteration phases was generally 2 - 4% of its concentration in the monoliths, although this increased to 10 - 20% for the 360- and 720-day samples. This behaviour was markedly different from that observed for Ca and Mg, which were consistently retained in alteration phases for all four glasses. This could have occurred due to:

- There being no Ba-containing phases that reached saturation point with respect to the leachate;
- The larger ionic radius of Ba (1.35 Å in sixfold coordination compared to 1.00 and 0.72 Å for Ca and Mg, respectively) meaning that it does not substitute easily into alkaline-earth-containing phases which have already precipitated.

PHREEQC modelling based on the presence of ~1 ppm S, as determined by ICP-MS, suggests that barite (BaSO<sub>4</sub>) may be saturated in the leachate (Si values of 0.18, 0.44, 0.45, 0.46 and 0.42 for 90 - 720 days), but no evidence of barite formation was observed by SEM-EDS. There is also little evidence in the literature that Ba substitutes into C-S-H and M-S-H phases [149], which indicates that the latter explanation has merit.

The Ca/Si ratios for Phase A and the C-S-H-like precipitates are shown in Table 6.7. The general trend appears to be a decrease in Ca/Si ratio with time up to 180 days, followed by a steady decline. This trend is similar to those shown by the ISG and MW-25% samples, albeit with an earlier time of peak Ca/Si (180 days compared to 360 and 540 days for ISG and MW-25%, respectively). As with the other glasses, the Ca/Si ratio in the C-S-H-like precipitates tended to be higher than that for the alteration layer, with the exception of the 180-day sample.

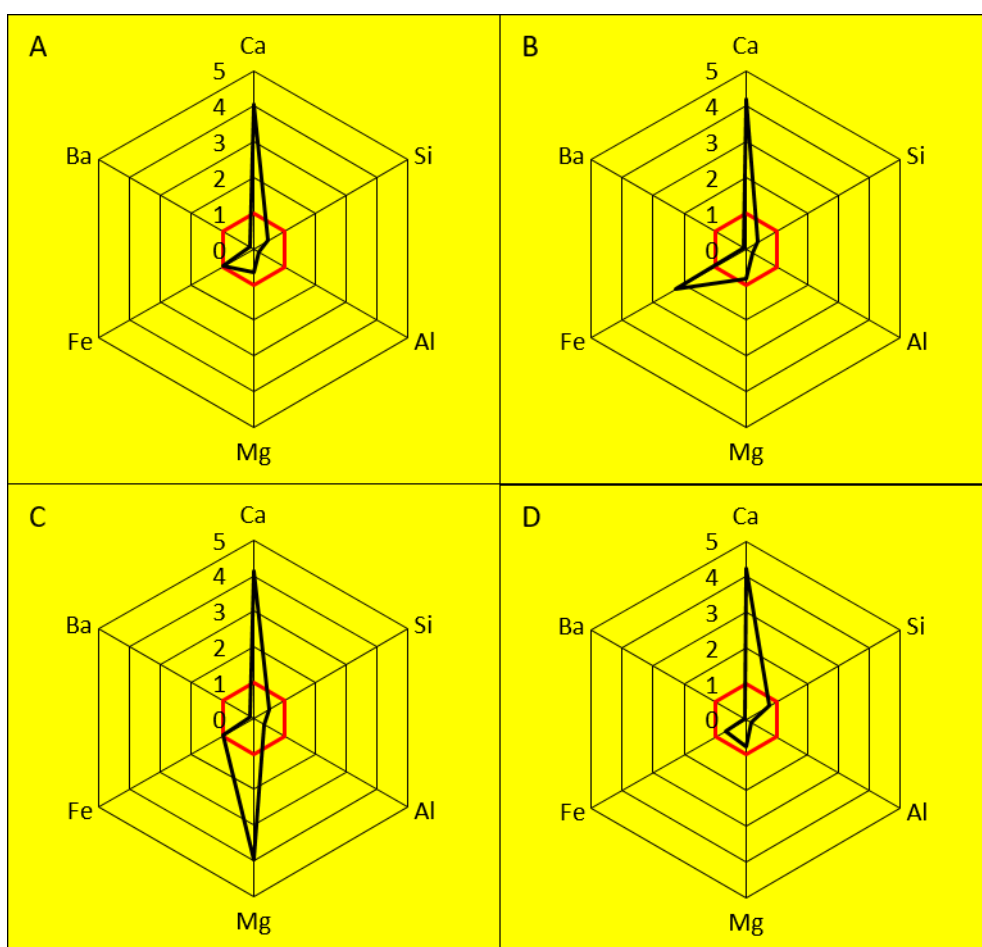


**Figure 6.81.** EDS-determined elemental concentration distributions for G73 alteration layers, normalised to monolith composition, phases A – D. The red hexagon denotes the contents of the elements within the glass.

**Table 6.7.** Triplicate EDS-determined Ca/Si ratios for selected phases on altered G73 monoliths. Errors derived from standard deviation of triplicate measurements.

Phase	30 days	90 days	180 days	360 days	540 days	720 days
Phase a)	0.55 ± 0.03	0.26 ± 0.04	1.49 ± 0.17	1.08 ± 0.04	1.38 ± 0.17	1.25 ± 0.05
C-S-H Precipitates	N/A	0.74 ± 0.24	1.43 ± 0.13	1.12 ± 0.23	1.81 ± 0.40	1.48 ± 0.08

#### 6.5.2.5 Alteration Layer Thickness

There are two primary methods for determining the thickness of the alteration layer on monolithic samples: 1) it can be calculated from the leaching data, or; 2) it can be estimated from analysis of the SEM images. The former method utilises the following equation:

$$AG_{th} = \frac{C_i}{\rho \times \frac{S}{V} \times x_i} \quad (\text{Equation 6.1})$$

Where:  $AG_{th}$  is the thickness of the alteration layer,  $C_i$  is the concentration of element  $i$  in solution,  $\rho$  is the density of the glass,  $S/V$  is the surface-area-to-volume ratio of the system and  $x_i$  is the fraction of element  $i$  in the glass. The calculated  $AG_{th}$  values for the glasses are shown in Table 6.8. Na leaching data was used for the calculations as it is present in all samples (unlike B) and seems to not be significantly retained in secondary phases.

The thicknesses of the alteration layers estimated from the SEM images are shown in Table 6.9. The actual thickness of the alteration layers varied with position across the sample surfaces, so a thickness range is given, rather than a specific thickness. It can be seen that the calculation method tends to underestimate the thickness of the alteration layers compared to the values measured from SEM. This could be due to the Na being retained in secondary phases, leading to an underestimation of the extent of alteration, or it could be due to the density of the alteration layer being less than the density of the bulk glass.

**Table 6.8.** Alteration layer thicknesses ( $AG_{th}$ ) for literature glasses, calculated using Na leaching data.

Day	$AG_{th}$ ( $\mu\text{m}$ )			
	ISG	MW-25%	BAS	G73
30	3.6	2.1	2.6	1.8
90	7.5	4.9	3.6	3.8
180	8.4	7.5	3.6	8.1
360	13.0	12.5	4.6	8.8
540	7.9	14.8	5.8	9.5
720	10.2	19.1	5.4	8.2

**Table 6.9.** Estimated alteration layer thicknesses for literature glasses, measured from SEM micrographs.

Day	Estimated alteration thickness ( $\mu\text{m}$ )			
	ISG	MW-25%	BAS	G73
30	6 - 13	2 - 3	10 - 12	5 - 13
90	12 - 19	3 - 6	8.5 - 10.5	8 - 9
180	9 - 12	6 - 9	21	12 - 15
360	17 - 20	11 - 14	4 - 7	8 - 14
540	11 - 14.5	18	8.5 - 12	21 - 25
720	12 - 15	24 - 28	9.5 - 16	11 - 15

### 6.5.3 Summary

Dissolution experiments carried out on four glasses, representing current and potential nuclear waste glasses and a natural analogue, have elucidated their leaching behaviour and the formation of alteration products during that leaching. The key findings from these experiments are:

- ISG and MW-25% have very different dissolution behaviours, both in terms of leaching and alteration products, and thus the research into the dissolution of ISG is of limited usefulness with regards to the disposal of vitrified waste in the UK, even when only mechanistic arguments are taken into account.
- The first observation of the formation of a Mg-Al Layered Double Hydroxide (LDH) is presented. This could have significant implications for the long-term fate of radionuclides during glass dissolution in a GDF, due to the ability of LDHs to sorb both cationic and anionic radionuclides, such as U and Tc.
- The dissolution behaviour of a laboratory-made basaltic glass (BAS) is only

partially comparable to that of aluminoborosilicate nuclear waste glasses and therefore the use of natural basaltic glasses as analogues of the long-term geological disposal of nuclear waste glasses must be carefully considered.

- Given its favorable performance in this investigation compared to MW-25%, G73 can be considered an adequate matrix for the disposal of UK ILW with regards to dissolution resistance.
- The use of a saturated  $\text{Ca}(\text{OH})_2$  solution as a leachant resulted in the significant precipitation of many of the elements leaching from the glasses, including Mg, Si, Fe, rare-earths and Zr. The retention of rare-earths is particularly important due to their role as surrogates of actinides within the glass.
- The development of significant localisation of various elements (Zr, Mg, Fe, Al) within the alteration layers suggests that the mechanism for dissolution of these glasses in these conditions is dissolution-reprecipitation.
- Secondary borate precipitates are potentially forming during the dissolution of borosilicate glasses at high-pH. If this is confirmed, it would mean that B cannot be considered a true tracer element for the dissolution of borosilicate glasses in these Ca-rich, high-pH conditions.
- Micro- and nano-focus techniques, such as  $\mu$ -XRD and TEM, are powerful tools for the identification of the secondary products of glass dissolution, and hence for the understanding of the mechanisms of glass dissolution.

To further this research, experiments performed in more complex solutions representative of a groundwater/cement-porewater mixed leachant should be investigated. The presence of significant concentrations of alkali (Na, Li), alkaline-earth (Ca, Mg) and other ions in solution could significantly affect the conditions for forming secondary phases, and thus affect the dissolution behaviour of these glasses. However, the immediate next steps in furthering this research should be to study the effect of other simple solutions, such as ones saturated with respect to Mg or Al, on the dissolution of nuclear waste glasses. Another area of importance is understanding the role of mineral precipitates on the resumption of alteration in these conditions. Extending the duration of the experiments in order to determine the onset of alteration resumption might provide information on precipitates which retard or enhance the onset of resumption of alteration. Further research into relevant glass compositions, e.g. Ca-Zn glass, is also of vital importance to the safety case for a UK GDF.



# 7. Discussion

## 7.1 Introduction

The stated aim of this work was to ‘...increase the knowledge base on the dissolution of nuclear waste glasses in Ca-rich, high-pH conditions, such as those that might be found in a UK Geological Disposal Facility.’ (Chapter 1). As discussed in Chapter 1, to fully understand glass dissolution, both the intrinsic dissolution resistance of the glass, related to its structure and composition, and the formation of secondary phases, which is dependent on glass composition and the physical and chemical conditions of the leachant, must be considered. With a view to achieving this aim, a range of glasses with varying CaO/Na<sub>2</sub>O, MgO/Na<sub>2</sub>O and B/Al ratios were produced. Their structures were analysed through Nuclear Magnetic Resonance (NMR) spectroscopy (Chapter 4), and their dissolution behaviours were investigated through static dissolution experiments (Chapter 5), in order to ascertain the effects of these compositional variables on the dissolution of glasses in high-pH conditions. In addition to this, the performance of existing UK nuclear waste glass, as well as reference compositions, was studied through static dissolution experiments (Chapter 6).

Discussions of the results have been included at the end of each chapter of this work. This chapter aims to distil, and bring together, these discussions in order to present a full picture of the contributions to the understanding of glass dissolution at high-pH from this work.

## 7.2 Effect of Glass Composition on Structure

### 7.2.1 Effect of Composition on B Coordination

In general, the addition of alkaline-earth oxides in replacement for soda was found to lead to a decrease in the fraction of <sup>IV</sup>B units, thought to be caused by the recalcitrance of the divalent Ca<sup>2+</sup> and Mg<sup>2+</sup> cations to charge-compensate two borate tetrahedra each. This finding is in line with that of Wu & Stebbins [150] and Quintas *et al.* [151], who both saw a decrease in the fraction of <sup>IV</sup>B units in aluminoborosilicate glasses with increasing CaO/Na<sub>2</sub>O ratios. It should also be noted that Wu & Stebbins and Quintas *et al.*, both found the relationship of composition to <sup>IV</sup>B fraction to be non-linear. However, in this investigation the relationship appears approximately linear, as shown by Figure 7.1. The effect of the alkaline earth on <sup>IV</sup>B fraction was stronger,

by a factor of  $\sim 1.5$ , for the Mg-containing glasses, as shown by Figure 4.12. This was attributed to the MgO behaving as an intermediate oxide, with a fraction of Mg being present as a network former in tetrahedral coordination. This leads to a two-fold effect in reducing the  ${}^{\text{IV}}\text{B}$  fraction: i) there are fewer  $\text{Mg}^{2+}$  cations available to charge-compensate for the  ${}^{\text{IV}}\text{B}$  tetrahedra, and; ii) the  ${}^{\text{IV}}\text{Mg}$  units require charge-compensation by other cations, further decreasing the total amount of cations available for charge-compensation of  ${}^{\text{IV}}\text{B}$  units. The presence of Mg in tetrahedral coordination has previously been observed in both silicate and aluminosilicate glasses [152], [153].

An increase in the ratio of B/Al in alkali-alkaline-earth aluminoborosilicates was found to lead to an increase in  ${}^{\text{IV}}\text{B}$  content, as shown by Figure 4.13b. This was due to the decreasing  $\text{Al}_2\text{O}_3$  content leading to an increase in the number of  $\text{Na}^+$  cations, which were preferentially associated with  ${}^{\text{IV}}\text{Al}$  tetrahedra, available for charge-compensation of the  ${}^{\text{IV}}\text{B}$  units. This is in agreement with previous studies; Geisinger *et al.* [131] and Yamashita *et al.* [55], [56] observed the same relationship in aluminoborosilicate glasses, and Bunker *et al.* [154] saw an equivalent relationship in alkaline-earth boroaluminate glasses. The  ${}^{\text{IV}}\text{B}$  fraction in the Mg-containing glasses was consistently lower than for the Ca-containing glasses, which is in agreement with a similar finding by Bunker *et al.* [155] in boroaluminate glasses. This is likely due to the increased ability of Mg to depress the  ${}^{\text{IV}}\text{B}$  fraction compared to Ca as a result of it behaving as an intermediate oxide with some network-forming capability, as outlined above.

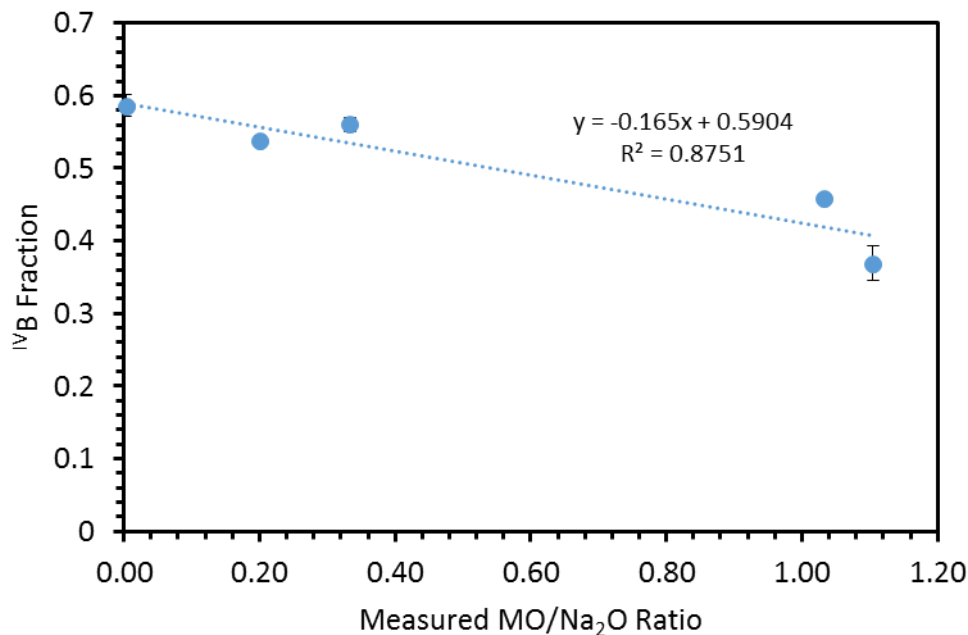


**Figure 7.1.** <sup>IV</sup>B fraction as a function of measured MO/Na<sub>2</sub>O ratio for the borosilicate (NC<sub>x</sub>BS and NM<sub>x</sub>BS) glasses.

### 7.2.2 Effect of Composition on Si Coordination

The replacement of soda with alkaline-earth oxides generally led to an increase in the fraction of symmetric Q<sub>4</sub> silicate units, as shown by Figure 7.2. This is thought to be due to a reduction in the number of Si – O – B bonds caused by the reduction in <sup>IV</sup>B units; <sup>IV</sup>B units have a greater number of potential bonds, and so are likely to lead to a greater number of Si – O – B bonds than <sup>III</sup>B units. This effect is significantly greater – by a factor of ~1.4 based on the gradients of the lines of best fit in Figure 4.16 – when the soda is replaced with MgO than when it is replaced with CaO. This can be attributed to the greater effect of the addition of MgO on the <sup>IV</sup>B fraction. For the MgO-containing glasses, the increase in symmetric Q<sub>4</sub> could also be due to a decrease in Q<sub>3</sub> units. If some of the Mg is present in tetrahedral coordination, as suggested above, then the total modifier content available to produce NBOs on silicate tetrahedra will be lower, as the <sup>IV</sup>Mg units would not be able to perform this role, and nor would the modifier cations required to charge-compensate said Mg tetrahedra.

An increase in B/Al ratio also led to an increase in symmetric Q<sub>4</sub> units, as inferred from the shift toward more negative relative frequencies (Figure 4.17). This is likely due to a decrease in Si – O – X bonds (X = B, Al), caused by the replacement of Al, which was found to be almost entirely in tetrahedral coordination, with B, of which a

maximum of ~40% was in tetrahedral coordination, with the rest in trigonal coordination. As stated above, tetrahedral <sup>IV</sup>B species can bond with four other units whereas trigonal <sup>III</sup>B units can only bond with three other units, leading to a decrease in Si – O – X bonds with decreasing <sup>IV</sup>B content. The effect was larger, by a factor of ~1.6, in the Mg-containing glasses than in the Ca-containing glasses. This is again attributed to the presence of a fraction of the Mg in tetrahedral coordination in the glass.

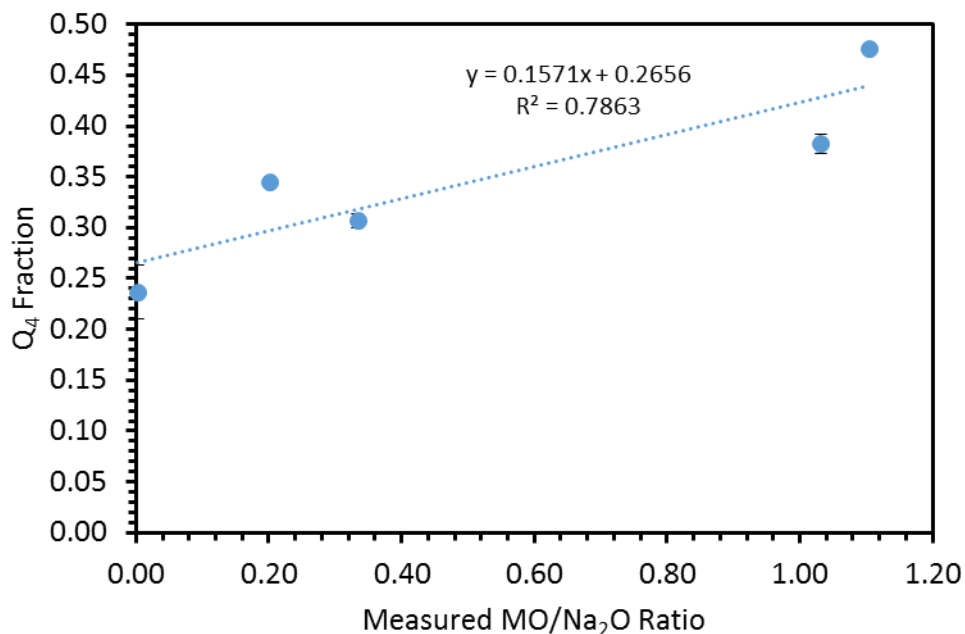


**Figure 7.2.** Q<sub>4</sub> fraction as a function of measured MO/Na<sub>2</sub>O ratio for the borosilicate (NC<sub>x</sub>BS and NM<sub>x</sub>BS) glasses.

### 7.2.3 Summary

In general, literature on the structural effects of the replacement of Na<sub>2</sub>O with alkaline-earth oxides is scarce for both silicates and borosilicates. Most studies focus on the addition of alkaline-earth oxides in replacement of: other alkaline-earth oxides [152], [156]; SiO<sub>2</sub> [157], or the base glass [158]–[160]. The results from this work, therefore, help to bridge a gap in knowledge with regards to glass structure. These results are also important in the context of UK vitrified nuclear waste. As the UK has a large inventory of Mg-containing waste from its fleet of now-decommissioned Magnox reactors, the effect of Mg presence on glass structure is of relevance. However, the vitrified waste containing Mg also tends to contain significant amounts of Fe, the paramagnetic effects of which make analysis by NMR spectroscopy difficult.

Obtaining NMR spectra on Fe-free, Mg-containing glasses is, therefore, helpful. The NMR spectroscopy carried out in this work suggests that the presence of Mg in glass leads to a decrease in the overall polymerisation of the glass structure and an increase in its heterogeneity, despite it behaving as a partial network former. This is likely to have detrimental effects on the dissolution resistance of the glass, and is important to take into account when comparing UK Mg-rich glasses to other international nuclear waste glasses which contain significant amounts of Ca, such as the French SON68.

Investigations into the effect of compositional variance on the structure of aluminoborosilicate glasses have tended to focus on the variation of the  $\text{Al}_2\text{O}_3/\text{SiO}_2$  ratio [161]–[163], or the variation of the  $\text{B}_2\text{O}_3/\text{SiO}_2$  ratio [164]–[166], with the exception of two studies by Yamashita *et al.* [55], [56]. Investigations into the effects of varying the B/Al ratio are important in the field of nuclear waste glasses as natural aluminosilicate glasses, such as basaltic glasses, which contain no B, have been suggested as natural analogues for the geological disposal of nuclear waste glasses, which are generally borosilicate or aluminoborosilicate glasses. The significant structural differences observed with varying B/Al ratio in this work suggest that one must be wary when comparing glasses with different network formers. The glasses containing more B were found to be less well polymerised than those containing larger amounts of Al, which led to a reduction in their dissolution resistance (see Section 7.3.2).

## **7.3 Effect of Glass Composition on Durability in High-pH Environments**

### **7.3.1 Effect of Alkaline-Earth Oxide Replacement for Soda**

Increasing the ratio of  $\text{MO}/\text{Na}_2\text{O}$  in borosilicate glasses led to an increase in their dissolution resistance in the KOH leachant. The mechanism for this was likely the increased ability of the glasses to produce protective alteration layers when they contained alkaline-earths. In the  $\text{Ca}(\text{OH})_2$  leachant, increasing  $\text{MgO}/\text{Na}_2\text{O}$  led to an increase in the dissolution resistance of the  $\text{NM}_x\text{BS}$  glasses, but an increase in  $\text{CaO}/\text{Na}_2\text{O}$  led to a decrease in the dissolution resistance of the  $\text{NC}_x\text{BS}$  glasses. The discrepancy between the two glass series here could be due to the role of Ca during dissolution. As stated, the presence of Ca in the glass in KOH leachant is likely to lead to a more protective alteration layer than for the base  $\text{NC0BS}$  glass, which does not

contain Ca. However, in a  $\text{Ca}(\text{OH})_2$  leachant, this effect is provided for all samples by the high Ca concentration in solution, regardless of Ca content in the glass. This might suggest that the NC0BS glass was inherently more durable than the NC10BS glass, but the difference between the two glasses was primarily seen in their residual rates of dissolution ( $R_r(\text{B})$  values were  $(2.0 \pm 1.0) \times 10^{-4}$  and  $(3.7 \pm 0.2) \times 10^{-3} \text{ g m}^{-2} \text{ d}^{-1}$  for NC0BS and NC10BS, respectively) which are not likely to be significantly affected by glass structure. This indicates that this trend may be due to the behaviour of the alteration layer or the precipitation of secondary crystalline phases. A possible explanation for this could be that the rate of formation of secondary precipitates was faster for NC10BS compared to NC0BS, which led to a continued removal of Si from solution, leading to a higher residual rate of dissolution. Evidence for the former explanation was seen during SEM analysis of the samples, where a greater amount of secondary precipitates were observed in the NC10BS sample than the NC0BS sample (see Figure 5.43 in Section 5.4.1.1). The fact that the same trend of increasing dissolution with increasing  $\text{MO}/\text{Na}_2\text{O}$  was not observed in the  $\text{NM}_x\text{BS}$  glasses also lends weight to this theory, as there was no significant difference in precipitate formation observed in NM5BS and NM10BS compared to NC0BS (see Figure 5.50 in Section 5.4.1.2).

No linear correlations were found between the initial rate of dissolution of the  $\text{NC}_x\text{BS}$  and  $\text{NM}_x\text{BS}$  glasses and their  $\text{MO}/\text{Na}_2\text{O}$  ratio. This might suggest that the effect of varying the  $\text{MO}/\text{Na}_2\text{O}$  is more complicated than a linear relation.

The Ca-containing glasses had higher chemical durability than the Mg-containing glasses, which is in line with broadly similar comparisons of Ca- and Mg-containing glasses in the literature [12], [77]. The initial rates of dissolution for the two series were found to be similar, within error, suggesting that structural differences identified by NMR spectroscopy did not play a significant role in altering the dissolution rate. Instead, it is likely that it is the differences in the precipitation of Ca- and Mg-containing phases from solution that are important. The  $\text{NL}(\text{Mg})$  values for the  $\text{NM}_x\text{BS}$  glasses, e.g. a maximum of  $(1.11 \pm 0.22) \times 10^{-2} \text{ g m}^{-2}$  for NM5BS in KOH, were much lower than the  $\text{NL}(\text{Ca})$  values for the equivalent Ca-containing glasses, e.g. a maximum of  $0.149 \pm 0.036 \text{ g m}^{-2}$  for NC5BS in KOH, which suggests that Mg was precipitating at a higher rate than Ca. As most of the observed precipitated Ca- and Mg-containing phases contained Si and/or Al, this suggests that Si and Al also precipitate from solution at a higher rate for the Mg-containing glasses. This was also

indicated by PHREEQC modelling which showed that the leachate might be expected to become saturated with respect to Mg-containing phases more rapidly than with respect to Ca-containing phases. This would lead to the leachate being further from saturation with respect to Mg and Si and so Mg and Si leaching continued at a higher rate than for Ca and Si from the Ca-containing glasses. The difference in behaviour between the Ca-containing and Mg-containing glasses could also be explained by the fact that M-S-H has not been found to form at such high pH values previously [136]. Any structural differences between C-S-H and the Mg-rich phases that formed could result in a difference in their ability to retard diffusion between the glass and the leachate, i.e. the Mg-rich phase alteration layer may not be as protective of the glass as a C-S-H-based alteration layer.

Although similar to the behaviour of the Ca- and Mg-borosilicate glasses in the  $\text{Ca(OH)}_2$  leachant, the behaviour of the Ca- and Mg-aluminoborosilicate glasses appeared to be slightly different to the borosilicate glasses in the KOH leachant. The NL(B) and NL(Na) values for the Mg-aluminoborosilicates were higher than for the equivalent Ca glasses, but the NL(Al) and NL(Si) values were similar or lower. This could be evidence for increased heterogeneity of the glass structure in the Mg-aluminoborosilicates, with partitioning of Na and B into a borate sub-network, and Al and Si into the primary glass network, as postulated from the NMR spectra of the glasses. This would suggest that the borate sub-network was significantly less durable than the Al and Si glass network.

A linear increase in the initial rate of dissolution with increasing MO/Na<sub>2</sub>O ratio was observed for the NMAB<sub>x</sub>S glasses (Figure 7.3). However, this is likely to be a coincidence with the increasing B/Al ratio of the NMAB<sub>x</sub>S series; increasing B/Al ratio was observed to increase the initial rate of dissolution (see Section 7.3.2)

Comparisons of the dissolution behaviour of Ca- and Mg-containing glasses are few and far-between in the literature, and studies carried out in high-pH conditions are of even greater rarity. The direct comparison of the dissolution of equivalent Ca- and Mg-containing glasses in high-pH conditions in this work is of great relevance to the planned geological disposal of UK vitrified waste, due to the presence of significant quantities of Mg in a large section of the inventory. This work suggests that in the context of UK geological disposal, with potential for the formation of a Ca-rich, highly-alkaline plume, the presence of Mg in a glass is detrimental to its chemical durability compared to the presence of Ca.

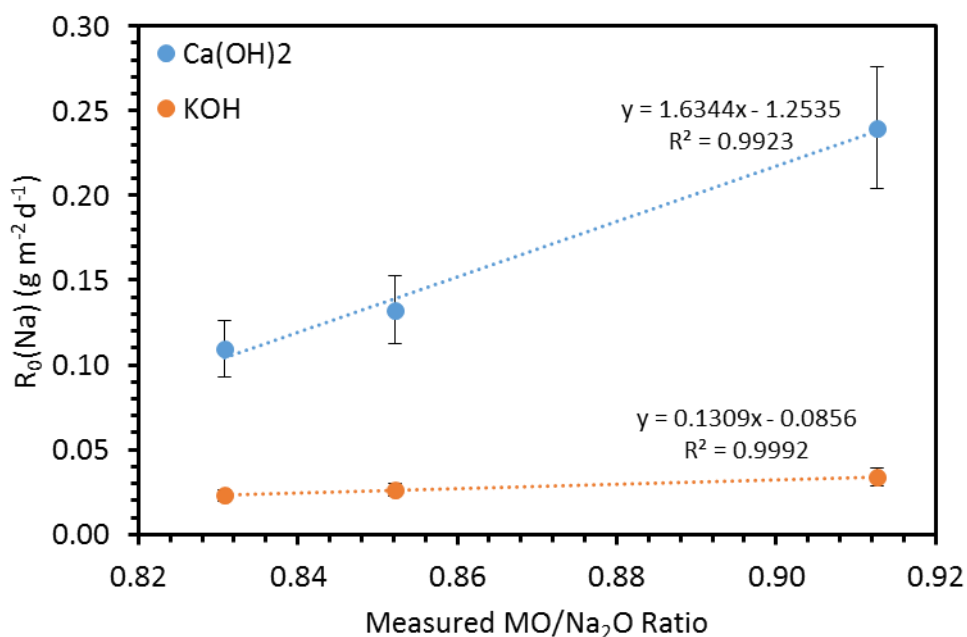


**Figure 7.3.**  $R_0(\text{Na})$  as a function of measured  $\text{MO}/\text{Na}_2\text{O}$  ratio for the  $\text{NMAB}_x\text{S}$  glasses in  $\text{Ca}(\text{OH})_2$  and  $\text{KOH}$ .

### 7.3.2 Effect of Varying B/Al Ratio

Increasing the ratio of B/Al in aluminoborosilicate glasses led to a decrease in their dissolution resistance in both leachants. This is attributed to the lower resistance of Si – O – B bonds to hydrolysis compared to Si – O – Al bonds, and also to the decrease in non-silicate tetrahedral units ( $^{\text{IV}}\text{B} + ^{\text{IV}}\text{Al}$ ), due to the replacement of tetrahedral Al on a molar basis by B, of which <40% is in tetrahedral coordination. Previous work by Pierce *et al.* [167] suggested that the initial rate of dissolution of sodium aluminoborosilicate glasses, as calculated from dynamic, Single-Pass Flow-Through (SPFT) dissolution experiments, remained approximately constant with varying B/Al ratio, even at pH values of around 12. However, this investigation found a significant correlation between B/Al ratio and the initial rate of dissolution, in contrast to the results reported by Pierce *et al.* This is illustrated by Figure 7.4, which shows the initial rate of dissolution for the  $\text{NMAB}_x\text{S}$  series as a function of measured B/Al ratio in both  $\text{Ca}(\text{OH})_2$  and  $\text{KOH}$  leachants (N.B.  $R_0(\text{B})$  values are not included as there were not enough data points for a line of best fit). This could be due to the presence of

alkaline-earths having an effect on the behaviour of the glasses with varying B/Al ratio, or it could be that the conditions in the PCT-B experiments, even at the earliest sampling points, are not far enough from equilibrium to negate solution saturation effects on the dissolution rate.

As mentioned in Section 7.2.3, any differences in the behaviour of glasses with different B/Al ratios are important due to the potential use of natural aluminosilicate glasses as analogues for the geological disposal of (alumino)borosilicate nuclear waste glasses. The results presented here, which show increased dissolution with increasing B/Al, suggest again that this is a comparison that must be considered carefully, as natural glasses do not contain  $B_2O_3$ .

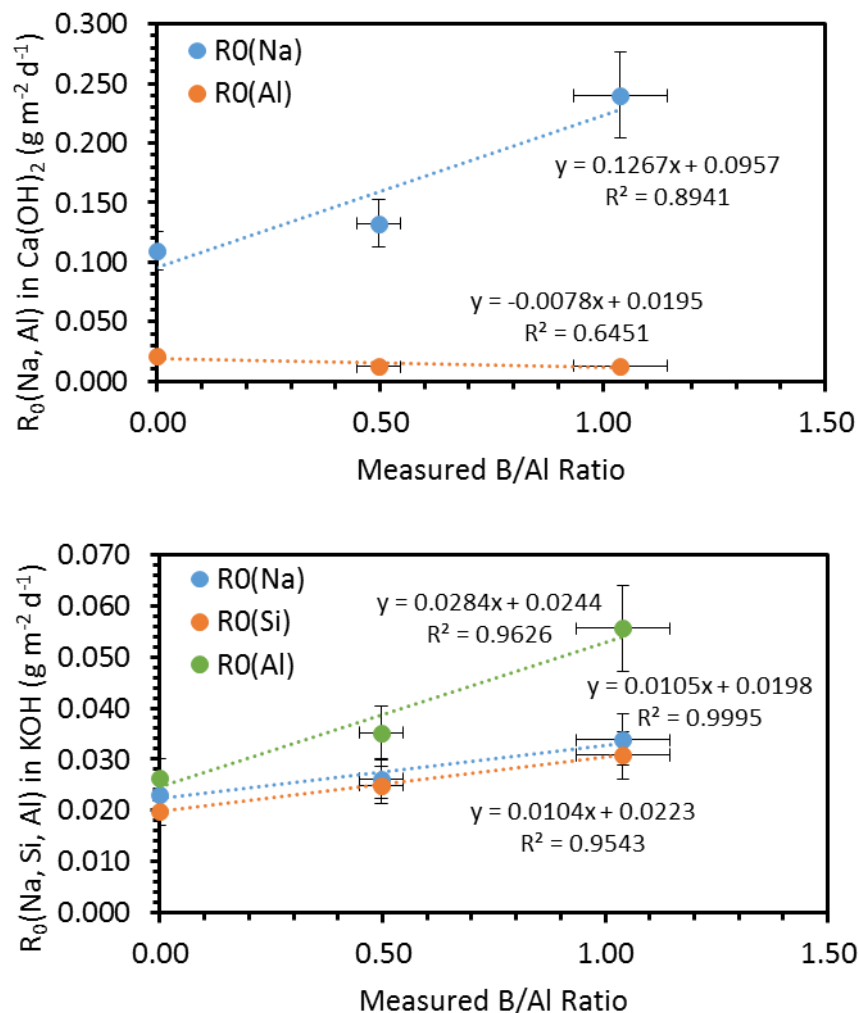


**Figure 7.4.**  $R_0(\text{Na})$ ,  $R_0(\text{Si})$  and  $R_0(\text{Al})$  as a function of measured B/Al ratio for the NMAB<sub>x</sub>S glasses in  $\text{Ca}(\text{OH})_2$  (Top) and  $\text{KOH}$  (Bottom).

## 7.4 Effect of Glass Structure on Durability in High-pH Environments

The structure of glasses is expected to affect their initial rate of dissolution, before solution saturation effects become significant. No significant linear correlations were observed for any structural parameters, e.g.  $N_4$  or  $^{29}\text{Si}$  chemical shift, when comparing to all glasses. This is likely due to the variation of several different compositional parameters across the four glass series, which obscures the effect of individual parameter variation. When the data are split into the individual series, a linear correlation between  $^{29}\text{Si}$  relative frequency and the initial rate of dissolution is apparent for the NMAB $x$ S series (it should be noted that the NMAB $x$ S series is the only series with enough data points for a line of best fit to be drawn). This correlation is shown in Figure 7.5. As values of  $^{29}\text{Si}$  relative frequency which are more negative indicate a higher degree of polymerisation of the glass network, this correlation suggests that the more polymerised the glass was, the less durable it was. This runs contrary to the traditional view of glass dissolution and suggests that this correlation is a coincidence. Indeed, when the  $^{29}\text{Si}$  relative frequency of the NMAB $x$ S glasses is plotted against their B/Al ratios, there is a strong linear correlation (Figure 7.6). As seen in Figure 7.4 in the previous section, the B/Al ratio is strongly correlated with initial dissolution rate for the NMAB $x$ S glasses, and thus the correlation between the initial rate of dissolution and the  $^{29}\text{Si}$  relative frequency is probably a coincidence due to the correlation between B/Al and  $^{29}\text{Si}$  relative frequency.

The effect of the variation of B/Al ratio, discussed in Section 7.3.2, does not seem to be due to the associated changes in the fraction of  $^{\text{IV}}\text{B}$  units present in the glass ( $N_4$ ). No correlations were observed between the initial dissolution rate and  $N_4$  (e.g.  $R_0(\text{Na})$  in  $\text{Ca}(\text{OH})_2$  versus  $N_4$ , Figure 7.7). This suggests that the effect of varying B/Al ratio is likely to be dominated by the relative resistances to hydrolysis of the Si – O – Al and Si – O – B bonds.

In order to fully investigate the effect of the structure of the glasses on their durability resistance, more datapoints for the NC $x$ BS, NM $x$ BS and NCAB $x$ S series are required.

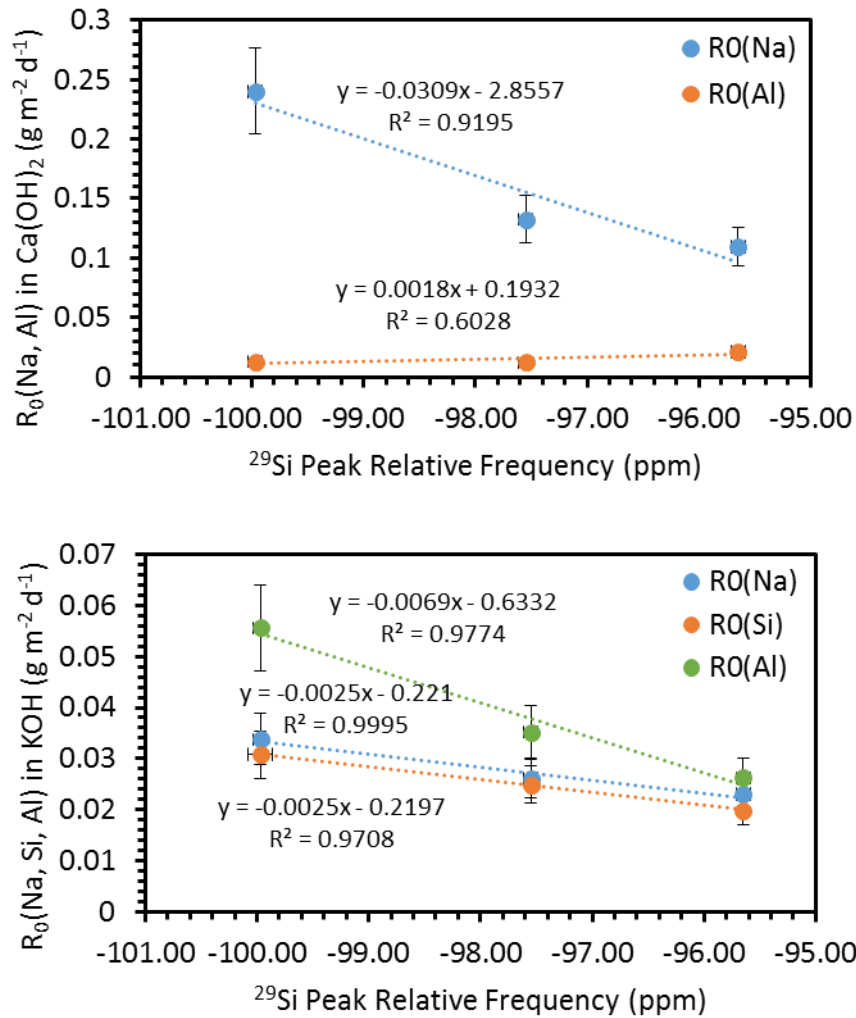


**Figure 7.5.**  $R_0(\text{Na})$ ,  $R_0(\text{Si})$  and  $R_0(\text{Al})$  as a function of measured  $^{29}\text{Si}$  relative frequency for the NMAB $x$ S glasses in  $\text{Ca}(\text{OH})_2$  (Top) and  $\text{KOH}$  (Bottom).

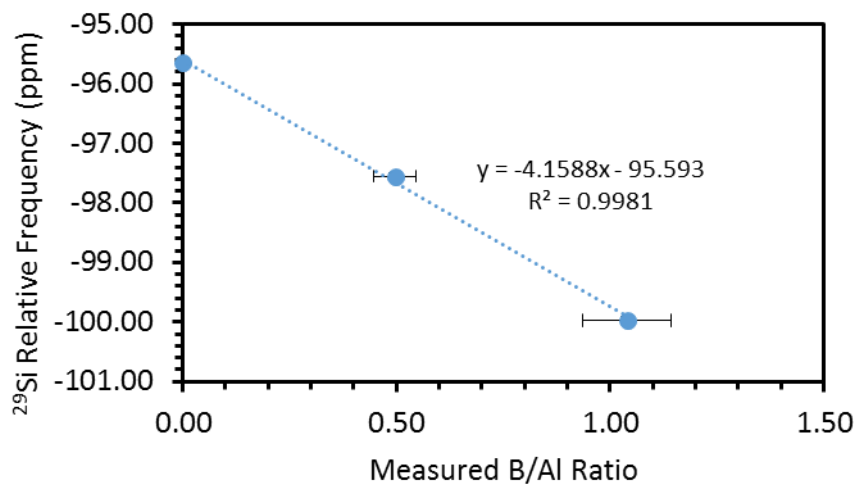


**Figure 7.6.**  $^{29}\text{Si}$  relative frequency for the NMAB $x$ S glasses as a function of measured B/Al ratio.

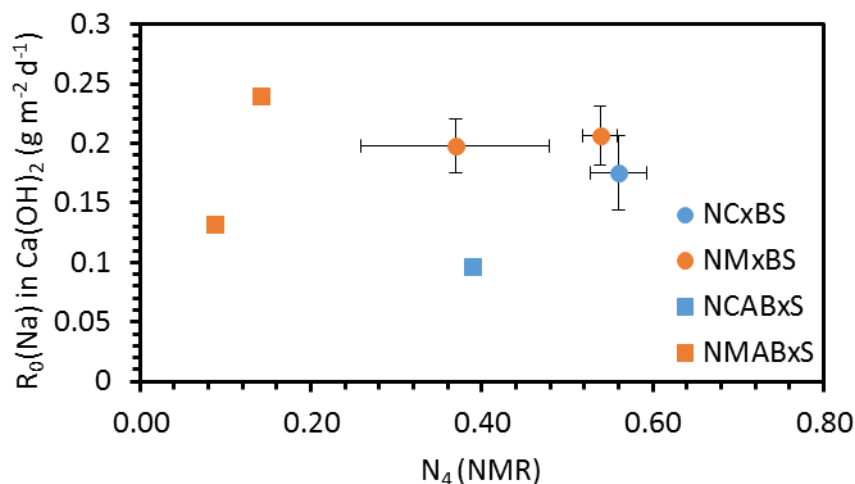


**Figure 7.7.**  $R_0(\text{Na})$  as a function of  $N_4$  during dissolution in  $\text{Ca}(\text{OH})_2$ .

## 7.5 Effect of Leachant Cation on Dissolution in High-pH Environments

The dissolution of the simple glasses in  $\text{Ca}(\text{OH})_2$  versus KOH, in the form of the comparison of  $R_0(\text{Na})$ ,  $R_r(\text{Na})$  and the ratio of the two,  $R_{0/r}(\text{Na})$ , are shown in Figure 7.8. Both the Ca-containing and Mg-containing borosilicate glasses had higher levels of dissolution in the KOH leachant than in the  $\text{Ca}(\text{OH})_2$  leachant, with the exception of the residual rate for NM5BS, confirming previous studies in the literature which showed lower-than-expected dissolution in  $\text{Ca}(\text{OH})_2$  leachants [3], [19]. This is attributed to the formation of cementitious materials causing agglomeration of the particles and hence a lower effective surface area for leaching, and to the formation of Ca-rich alteration layers, seen on all samples, which had a passivating effect on the particle surfaces. In contrast, the Ca- and Mg-containing aluminoborosilicate glasses were observed to have lower levels of dissolution in the KOH leachant compared to the  $\text{Ca}(\text{OH})_2$  leachant. This is attributed to the precipitation of secondary phases: in  $\text{Ca}(\text{OH})_2$ , secondary precipitates containing Al and Si were formed (likely  $\text{Ca}_4\text{AH}_{13}$  or  $\text{C}_4\text{AH}_{19}$ , see Section 5.5.4) which meant that although the leachate reached saturation with respect to Si and Al, these elements were continually removed from solution by the precipitation of these phases and so the glasses continued to leach at a significant rate; in KOH, no evidence of the formation of such precipitates was observed, possibly due to the lower Ca concentrations in solution, and so the leachate

remained saturated with respect to Al and Si, leading to a much decreased level of leaching.

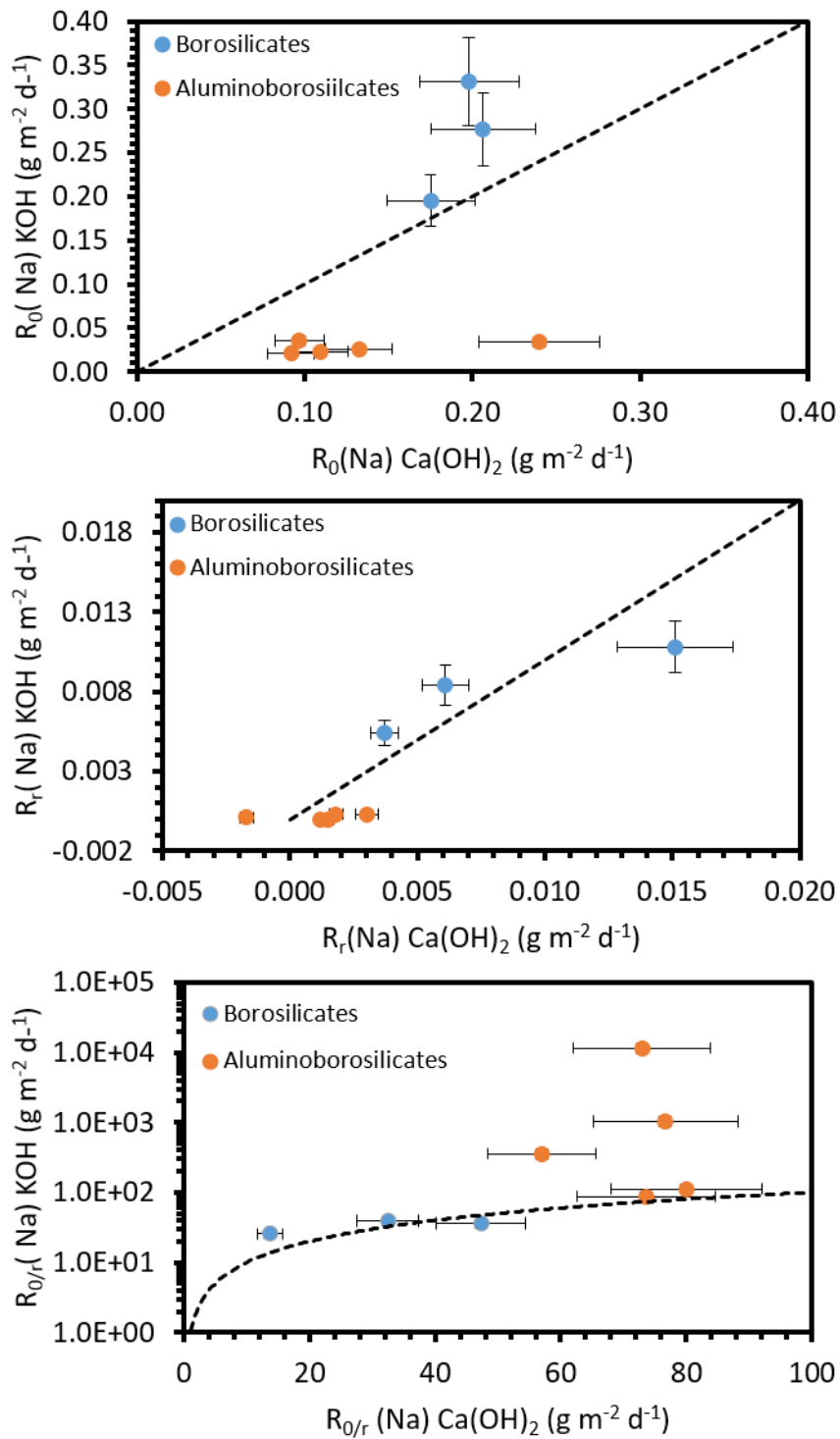


**Figure 7.8.**  $R_0(\text{Na})$  (Top),  $R_r(\text{Na})$  (Middle) and  $R_{0/r}(\text{Na})$  (Bottom) in KOH vs  $\text{Ca(OH)}_2$  for the simple glasses

The identification of significant differences in the dissolution behaviour of glasses with leachant cation affirms the importance of a full understanding of the geochemical environment during geological disposal, including knowledge of the groundwater composition, the surrounding geology and man-made environment (e.g. construction and backfill materials).

## 7.6 Dissolution Congruency in High-pH Environments

The dissolution of the simple glasses in  $\text{Ca}(\text{OH})_2$  did not appear to be congruent, based on the initial rates of release of the different elements. Figure 7.9 shows  $R_0(\text{Na})$  and  $R_0(\text{Al})$  for a range of glasses as a function of  $R_0(\text{B})$  in  $\text{Ca}(\text{OH})_2$ . The  $R_0(\text{Al})$  values were significantly lower than the  $R_0(\text{B})$  values, suggesting that B is leached much more rapidly than Al in the initial stages of dissolution. This is in agreement with the suggestion that Si – O – Al bonds are more resistant to dissolution than Si – O – B bonds. The  $R_0(\text{Na})$  values were slightly higher than the  $R_0(\text{B})$  values, which is consistent with the Na being more easily released from the network due to its single bond, compared to 3-4 bonds for B. Figure 7.10 shows  $R_0(\text{Al})$  for the NCAB $x$ S and NMAB $x$ S glasses (excl. NCAB5S) as a function of  $R_0(\text{Na})$  during dissolution in  $\text{Ca}(\text{OH})_2$ . The  $R_0(\text{Al})$  values were significantly lower than the  $R_0(\text{Na})$  values, with poor correlation ( $R^2 = 0.06$ ). This suggests that either the majority of the Na leached was not associated with  $^{\text{IV}}\text{Al}$  tetrahedra in the glass, or that Al-containing phases had already begun to precipitate at this early stage.

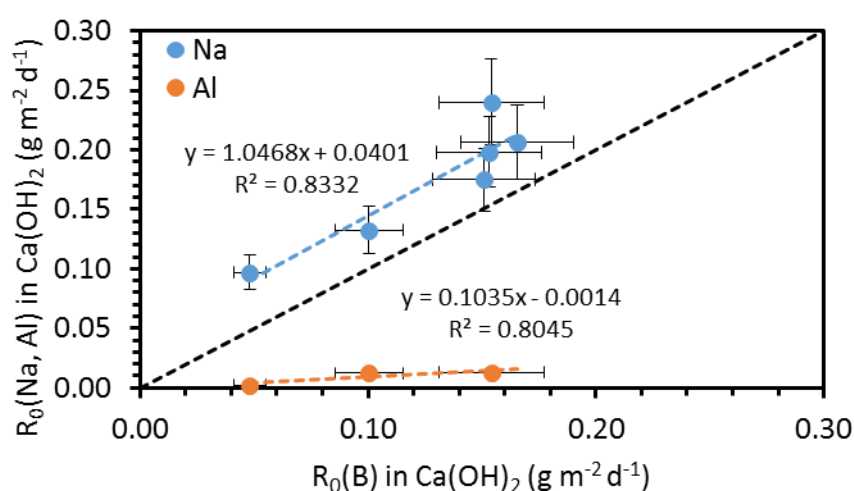


**Figure 7.9.**  $R_0(\text{Na})$  (for NC5BS, NM $x$ BS, NCAB10S, NMAB5S, NMAB10S) and  $R_0(\text{Al})$  (for NCAB10S, NMAB5S, NMAB10S) as a function of  $R_0(\text{B})$  during dissolution in  $\text{Ca}(\text{OH})_2$  for. Dotted line indicates congruent dissolution.

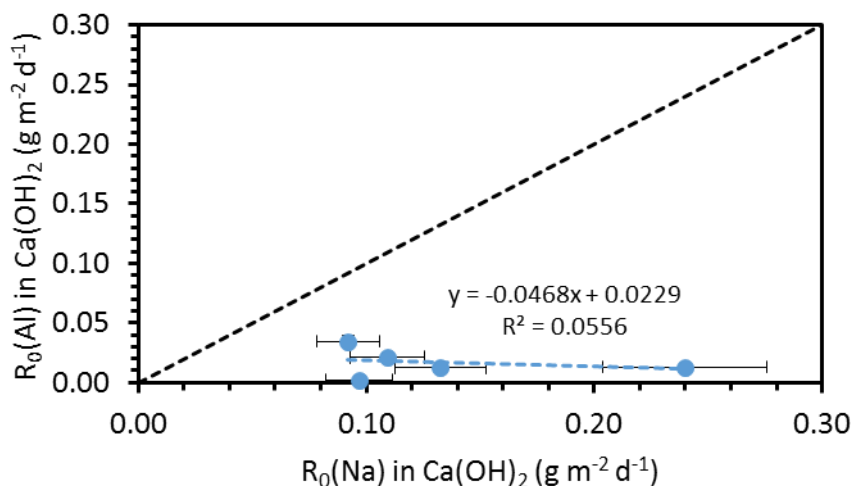


**Figure 7.10.**  $R_0(\text{Al})$  (for NCAB $_x$ S excl. NCAB5S, and NMAB $_x$ S) as a function of  $R_0(\text{Na})$  during dissolution in  $\text{Ca}(\text{OH})_2$ .

The dissolution of the simple glasses in KOH appeared to be congruent, with the exception of the release of Al. Figure 7.11 shows  $R_0(\text{Na})$  (for NC5BS, NM5BS, NM10BS, NCAB10S, NMAB5S, NMAB10S) as a function of  $R_0(\text{B})$  for dissolution in KOH. The data fall along the line denoting congruence and have a strong linear correlation ( $R^2 = 0.99$ ), suggesting congruent release of Na and B. The  $R_0(\text{Si})$  values for the same glasses correlate well with both the  $R_0(\text{B})$  and  $R_0(\text{Na})$  values, but are lower than would be expected for congruent dissolution (Figure 7.12). This might suggest that most of the Na in the glasses is not associated with creating NBOs on  $\text{SiO}_4$  tetrahedra, which is in line with simple charge compensation calculations ( $[\text{Na}_2\text{O}] \leq [\text{B}_2\text{O}_3] + [\text{Al}_2\text{O}_3]$  for all glasses). It could also indicate that B is more readily liberated from the glass structure than Si, or that there some precipitation of Si-containing phases was occurring even during the first few days of dissolution. The behaviour of Al in relation to Na is less straightforward. When data for all the glasses are included, there is no correlation between  $R_0(\text{Al})$  and  $R_0(\text{Na})$ . However, when the data are split into separate NCAB $_x$ S and NMAB $_x$ S series (Figure 7.13), a pattern emerges. The  $R_0(\text{Al})$  and  $R_0(\text{Na})$  values are well correlated ( $R^2 > 0.999$ ) for the NMAB $_x$ S series, with  $R_0(\text{Al})$  values significantly greater than would be expected for congruent dissolution. The NCAB $_x$ S series, on the other hand, has  $R_0(\text{Al})$  values that are lower than would be expected for congruent dissolution. This suggests that the dissolution behaviour of the Ca- and Mg-containing glasses is fundamentally different, which might explain why the Mg-containing glasses have been found to be

less dissolution resistant than those containing Ca (see Section 7.3.1). This same pattern is seen when comparing the  $R_0(\text{Al})$  and  $R_0(\text{Si})$  values of the  $\text{NCAB}_x\text{S}$  and  $\text{NMAB}_x\text{S}$  glasses (Figure 7.14), which suggests that the difference lies with the behaviour of the Al. Either the Al is more easily released from the Mg-containing glasses, or it is more readily precipitated from solution for the Ca-containing glasses. If the latter was true, it might be expected that the distance from congruence would increase as the overall rate of dissolution increased, however this does not seem to be the case for the  $\text{NCAB}_x\text{S}$  glasses. This would suggest that the discrepancy in the behaviour of the glasses is down to the Al being more readily released to solution for the Mg-containing glasses. Given that all the Al appears to be present in tetrahedral coordination for both glass series (see Section 4.2.3), this is not due to variations in Al coordination. This could be due to the different cationic field strengths of the  $\text{Mg}^{2+}$  and  $\text{Ca}^{2+}$  ions. The small radius of the  $\text{Mg}^{2+}$  cation means that fewer oxygens can surround it for charge-balancing, compared to the larger  $\text{Ca}^{2+}$  cation which can have a greater number of oxygen nearest neighbours. This means that the average negative charge on the oxygen ions must be higher for  $\text{Mg}^{2+}$  than for  $\text{Ca}^{2+}$ , which requires the presence of species such as  $^{\text{IV}}\text{Al} - \text{O} - ^{\text{IV}}\text{Al}$ , whereas the  $\text{Ca}^{2+}$  cation can be charge-balanced by  $\text{Si} - \text{O} - ^{\text{IV}}\text{Al}$  species [129]. This is confirmed by recent NMR data from Lee *et al.* which shows that the  $^{\text{IV}}\text{Al} - \text{O} - ^{\text{IV}}\text{Al}$  avoidance of Mg-aluminosilicates is much lower than for equivalent Ca-aluminosilicates [168]. The energetically unfavourable nature of the  $^{\text{IV}}\text{Al} - \text{O} - ^{\text{IV}}\text{Al}$  bond, as evinced by the Loewenstein Avoidance Principle [133], might lead to an increase in the release of Al from the glass by two mechanisms:

- The  $^{\text{IV}}\text{Al} - \text{O} - ^{\text{IV}}\text{Al}$  bonds are more easily broken during dissolution compared to the stronger  $\text{Si} - \text{O} - ^{\text{IV}}\text{Al}$  bonds, leading to a higher rate of Al release in the Mg-containing glasses, which have greater  $^{\text{IV}}\text{Al} - \text{O} - ^{\text{IV}}\text{Al}$  populations than the Ca-containing glasses
- As the  $\text{Mg}^{2+}$  ions leach to solution, they leave behind clusters of  $^{\text{IV}}\text{Al} - \text{O} - ^{\text{IV}}\text{Al}$  bonds, which rapidly dissolve, whereas when  $\text{Ca}^{2+}$  ions are leached, they leave behind  $\text{Si} - \text{O} - ^{\text{IV}}\text{Al}$  bonds which remain as part of the glass matrix.

Either of these mechanisms, or a combination of the two, could account for the discrepancy in behaviour between the  $\text{NMAB}_x\text{S}$  and  $\text{NCAB}_x\text{S}$  glasses, including having an effect on their overall dissolution resistances.

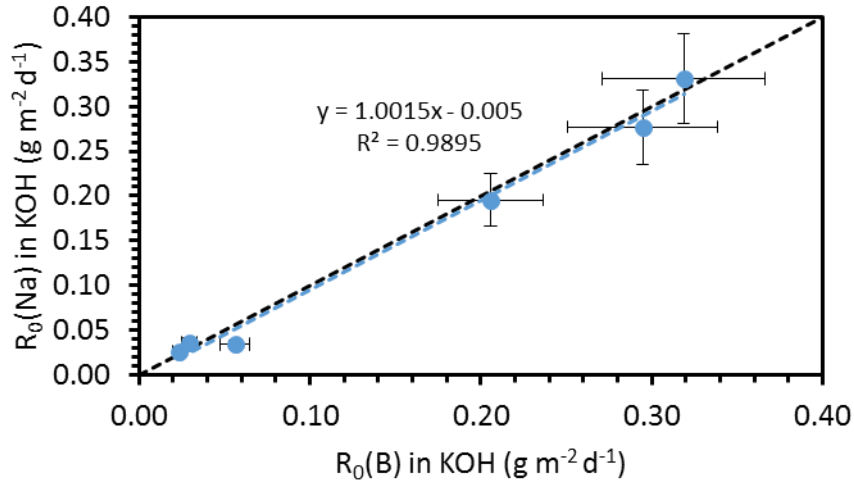


**Figure 7.11.**  $R_0(\text{Na})$  (for NC5BS, NM5BS, NM10BS, NCAB10S, NMAB5S, NMAB10S) as a function of  $R_0(\text{B})$  during dissolution in KOH.

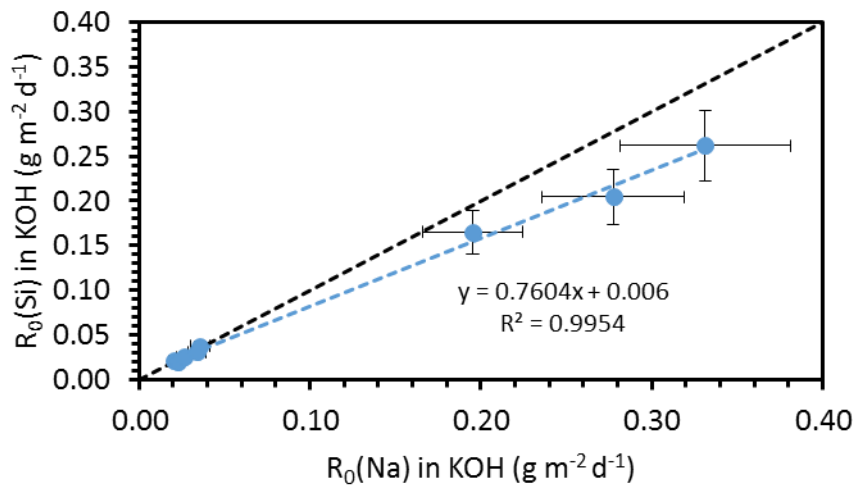
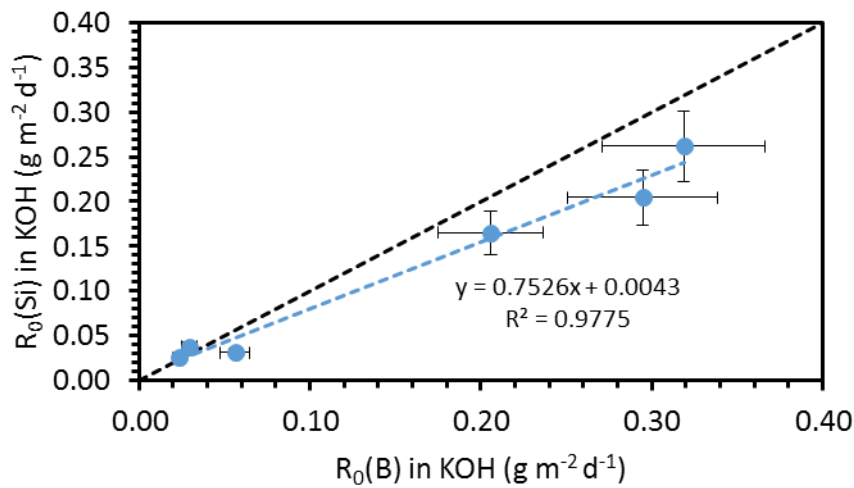


**Figure 7.12.**  $R_0(\text{Si})$  as a function of  $R_0(\text{B})$  (Top) and  $R_0(\text{Na})$  (Bottom) during dissolution in KOH (for same glasses as in Figure 7.11).

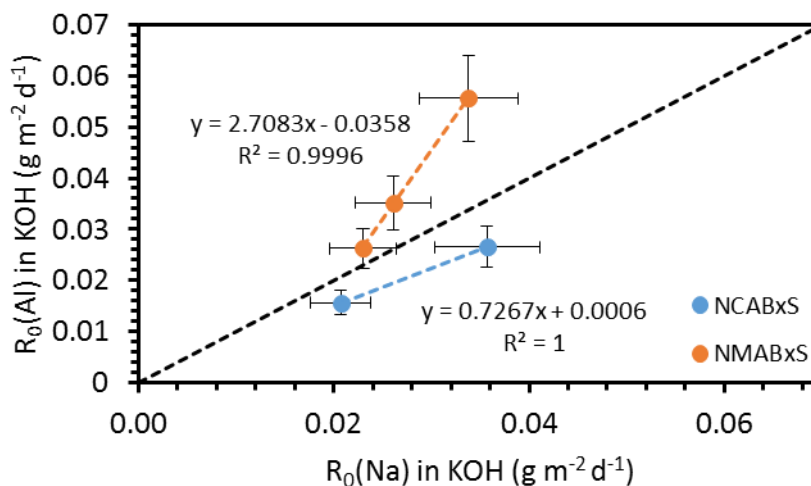


**Figure 7.13.**  $R_0(\text{Al})$  as a function of  $R_0(\text{Na})$  during dissolution in KOH.

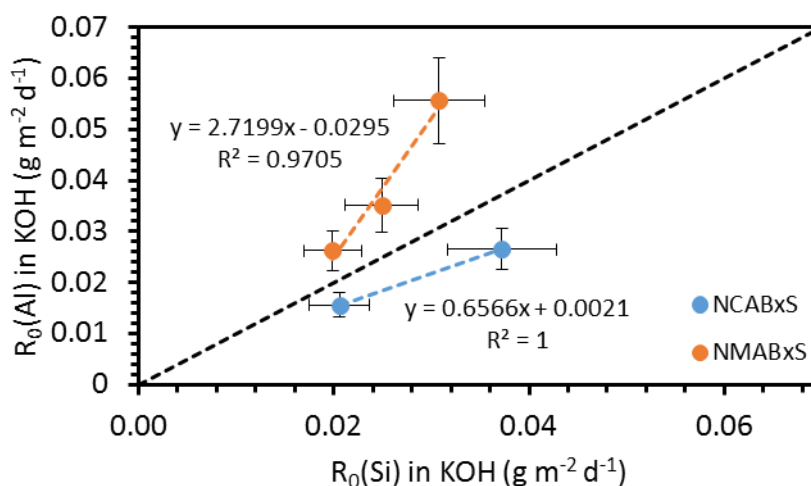


**Figure 7.14.**  $R_0(\text{Al})$  as a function of  $R_0(\text{Si})$  during dissolution in KOH.

## 7.7 Dissolution Performance of Current and Proposed UK Nuclear Waste and Reference Glasses

Dissolution tests utilising the PCT-B and MCC-1 protocols, on powdered and monolithic samples, respectively, were carried out using a  $\text{Ca}(\text{OH})_2$  leachant on 4 known glasses: MW-25%, an inactive simulant of UK HLW vitrified product; International Simple Glass (ISG), a reference glass for international HLW glass dissolution; BAS, a laboratory version of a natural basaltic glass; and G73, a proposed glass for the immobilisation of ILW, waste-loaded with 30 wt.% ILW simulant. Solution analysis was performed using ICP-OES, while analysis of the secondary phases formed was carried out using SEM, EDS, Transmission Electron Microscopy

(TEM) and micro-focus XRD. The results of these experiments are presented in Chapter 6. The aim of these experiments was to measure the resistance to dissolution of the different glasses, and to assess whether ISG and BAS can be used as analogues for UK nuclear waste glass dissolution.

### 7.7.1 Validity of ISG as an Analogue for the Dissolution of UK HLW Vitrified Product

It was found that MW-25% and ISG have very different dissolution behaviour. ISG was found to be significantly more durable than MW-25%; the final NL(B) and NL(Na) values for MW-25% were found to be 1.85 – 2.60 times higher than those for ISG, in both the PCT-B and MCC-1 experiments. The composition of ISG is based on that of SON68, the inactive simulant of French HLW glass, which has been previously shown to be significantly more durable than MW-25% [77], in agreement with the results presented in this work. The increased durability of ISG is also in line with the results from the dissolution of simple glasses: ISG is a Ca-containing glass (5.76 mol.% CaO), whereas MW-25% is a Mg-containing glass (6.82 mol.% MgO), and ISG also has a lower B/Al ratio than MW-25%; 5.03 compared to 7.30. Both of these factors suggest that ISG should be more chemically durable than MW-25%.

The secondary phases formed during dissolution of ISG were identified as portlandite ( $\text{Ca}(\text{OH})_2$ ), colemanite ( $\text{Ca}_2\text{B}_6\text{O}_{11}\cdot 5\text{H}_2\text{O}$ ) and hibschite ( $\text{Ca}_3\text{Al}_2(\text{SiO}_4)_2(\text{OH})_4$ ), whereas those identified for MW-25% were portlandite ( $\text{Ca}(\text{OH})_2$ ), brucite ( $\text{Mg}(\text{OH})_2$ ) and meixnerite ( $\text{Mg}_6\text{Al}_2(\text{OH})_{18}\cdot 4.5\text{H}_2\text{O}$ ). This suggests that the presence of Mg in MW-25% is central to the formation of secondary products during the dissolution of MW-25%, and that the differences in the dissolution behaviour of Ca-containing and Mg-containing glasses extend beyond structural considerations. Of particular note is the formation of meixnerite, a layered double hydroxide, which has not previously been observed to form during glass dissolution. Layered double hydroxides can sorb both cationic and anionic species, and hydrotalcite ( $\text{Mg}_6\text{Al}_2\text{CO}_3(\text{OH})_{16}\cdot 4(\text{H}_2\text{O})$ ), the carbonated form of meixnerite, has been postulated as phase of interest for the sequestration of  $^{129}\text{I}$ , a problematic anionic radionuclide [169].

In general, these results suggest that ISG is not a useful analogue for comparison to Mg-containing UK HLW. In addition to the differences in leaching rate and secondary phase precipitation, the behaviour of Zr during the dissolution of ISG is

also an issue. Zr was found to form bands within the alteration layer, giving it a significantly different structure to that seen for MW-25%. This Zr banding has also been suggested in a previous study by Gin *et al.* [20].

### **7.7.2 Validity of Basaltic Glasses as Natural Analogues for the Dissolution of Nuclear Waste Glasses**

The dissolution behaviour of BAS was found to be only partially comparable to that of aluminoborosilicate nuclear waste glasses. It had the highest chemical durability of the four glasses, and other studies have shown that this difference increases with length of experiment [13], [15]. The secondary precipitates that were formed during its dissolution were similar to those for MW-25%, which also contains significant amounts of Fe, Mg and Al, but different to those formed on ISG, which has a significantly different composition. This suggests that natural basaltic glasses could potentially be used as natural analogues for nuclear waste glass dissolution, but only when the compositions of the glasses are similar, i.e. when the nuclear waste glasses contain little or no B<sub>2</sub>O<sub>3</sub>.

### **7.7.3 Roles of Different Elements During High-pH Dissolution**

Throughout the experiments, near-total precipitation of many elements leaching from the glasses, including Mg, Si, Fe, Zr and the rare-earths, was observed. This is attributed to the use of a saturated Ca(OH)<sub>2</sub> leachant, as highly-alkaline solutions promote precipitation of secondary phases. Of particular note is the retention of the rare-earth elements in alteration products during the dissolution of MW-25%. The rare-earth elements are present in this glass as surrogates for the actinides, e.g. U, Pu and Am, which are present in the full-scale waste glass. The retention of these elements suggests that leaching of nuclear waste glasses in a GDF would not necessarily lead to the immediate release of actinides to the environment. However, as the rare-earth elements were only present in MW-25%, it cannot be concluded that this would occur for any glass in these conditions.

### **7.7.4 Mechanism of Dissolution in High-pH Environments**

During the dissolution of these glasses, significant localisations of various elements were observed in the alteration products, e.g. for ISG there was localisation of Zr, in the form of banding within the alteration layer (see Sections 6.4.1.1 & 6.5.2.1), and

there were significant localisations of Mg, Al and Fe in MW-25%, BAS and G73. The presence of these localisations suggests that the mechanism of dissolution in these Ca-rich, high-pH conditions is similar to the coupled dissolution-precipitation mechanism proposed and developed by Geisler *et al.* [61], [93], rather than the creation of a gel layer through de-alkalisation and re-structuring. An implication of this mechanism of glass dissolution is the formation of lamellar (banded) alteration layers over time, such as those seen on ISG in this investigation. These lamellar layers could have a significant impact on the dissolution behaviour of glasses on the timescales associated with geological disposal, due to their effect on the diffusion of ions.

#### **7.7.5 Precipitation of B-containing Phases During Dissolution**

Micro-focus XRD on an altered sample of ISG showed the possible presence of colemanite ( $\text{Ca}_2\text{B}_6\text{O}_{11}\cdot 5\text{H}_2\text{O}$ ), a calcium borate hydrate. Further work is required to confirm this finding but, if accurate, it would cast significant doubt on the use of B as a tracer for glass dissolution in Ca-rich, high-pH conditions. B is chosen as a tracer for glass dissolution as it is generally believed to remain in solution once leached and not to precipitate in secondary phases. The involvement of B in the precipitation of secondary phases under high-pH conditions, specifically calcium borates, was previously postulated by Utton *et al.* [3] as an explanation for an apparent incubation period in the normalised mass loss of B.

#### **7.7.6 Summary**

The results produced from this investigation show that there are important issues with the use of natural glasses as analogues for modelling the long-term dissolution behaviour of nuclear waste glasses; the use of ISG as an analogue for the dissolution of Mg-rich UK HLW glass; and also, potentially, in the use of B as a tracer for glass dissolution.



## 8. Conclusions and Further Work

### 8.1 Conclusions

In general, the findings of this work are:

1. The addition of CaO and MgO, in replacement for Na<sub>2</sub>O, to glasses has a significant effect on their structure; a decrease in the fraction of <sup>IV</sup>B units, leading to fewer available bonds to B units and hence fewer Si – O – B bonds. However, the dissolution of these glasses at high-pH is lower than that of glass with no CaO or MgO, likely due to the increased passivating effects of alteration layers containing Ca and Mg.
2. Increasing the B/Al ratio of alkali-alkaline-earth aluminoborosilicate glasses leads to an overall decrease in the proportion of non-silicate tetrahedral species (<sup>IV</sup>Al + <sup>IV</sup>B), also with an increase in the proportion of borate-rich sub-networks and a decrease in Si – O – X bonds (X = B, Al). This depolymerisation of the network leads to decreasing dissolution resistance of aluminoborosilicate glasses in high-pH as their B/Al ratio increases.
3. The nature of the cation in highly-alkaline solutions has a significant effect on the dissolution rate of glasses attacked by it. Ca-rich solutions cause greater dissolution in glasses containing significant amounts of Al, whereas K-rich solutions cause greater dissolution in borosilicate glasses.
4. ISG is not a valid analogue for the dissolution of Mg-containing UK HLW glasses, due to their significantly different compositions. Dissolution experiments on ISG are useful in trying to further understand the roles of elements such as Ca and Zr during dissolution, but the data cannot be used as a comparison for MW-25% and other UK nuclear waste glasses.
5. MW-25% has relatively poor durability in Ca-rich, high-pH solutions. This is likely due to its high Mg content leading to increased borate-silicate segregation and its high B/Al ratio leading to depolymerisation of the glass network and an increase in the presence of borate-rich sub-networks. In contrast to this, G73, proposed as an immobilisation matrix for UK ILW, was found to have dissolution resistance on a par with ISG in these conditions, suggesting that it could be a viable solution for the vitrification and long-term disposal of ILW.

6. The dissolution of natural basaltic glasses is only partially comparable to the dissolution of aluminoborosilicate nuclear waste glasses. They are primarily comparable when the compositions of the natural glass and nuclear waste glass are very similar, but caution must still be exercised due to the differences in behaviour between natural and laboratory basaltic glasses.
7. The analysis of alteration layer formation by micro- and nano-focus techniques, such as  $\mu$ -XRD and TEM, can provide vital information on the mechanisms of glass dissolution.

## 8.2 Further Work

Although this work has sought to add to the body of work in the dissolution of UK nuclear waste glasses, there are still many questions to be answered:

- What are the specific roles of Ca and Mg in the structure of borosilicate and aluminoborosilicate glasses? –  $^{25}\text{Mg}$  and  $^{43}\text{Ca}$  MAS-NMR spectroscopy is required to help answer this question.
- What is the potential long-term fate of actinides during nuclear waste glass dissolution? Would they be retained in alteration phases, as with the rare-earth elements seen in this work? – Dissolution experiments on glasses doped with actinides would be helpful to answer these questions. Full-scale active UK HLW vitrified product is likely to be too radiologically hot for experiments to be safely carried out.

As well as these questions arising directly from this work, there are also many natural points of progression from this research:

- Investigating the effect of leachate solution rich in Mg or Al on the dissolution of nuclear waste glasses
- Investigating the effect of using more complex solutions, such as a simulant groundwater or simulant cement porewaters, on the dissolution of UK nuclear waste glasses
- Further research into the correlation of dissolution data from glasses altered in natural conditions to data collected in the laboratory.
- Investigating the effect of the presence of steel corrosion products on glass dissolution, in order to obtain a more accurate view of glass dissolution in the presence of steel waste canisters

- Investigations into the dissolution resistance of active UK HLW vitrified product, to investigate the effects of radiation on aqueous dissolution, namely radiolysis of the attacking solution and the presence of decay products.



## Appendix A – XRD of Pristine Glasses

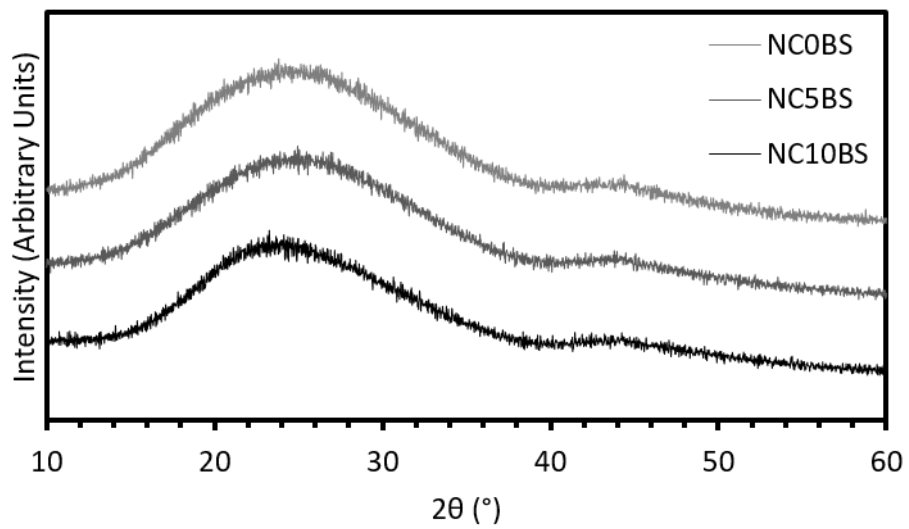


**Figure A1.** X-ray diffraction patterns for NCxBS glass powders before alteration.

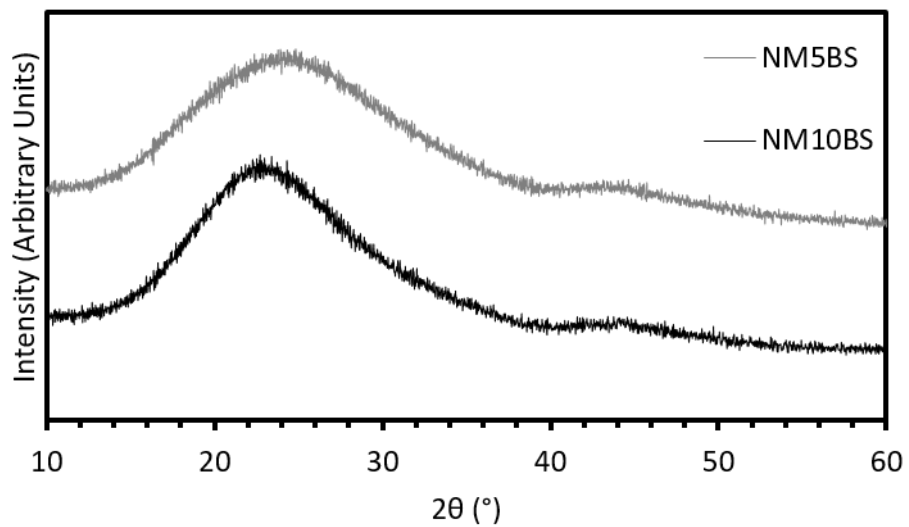


**Figure A2.** X-ray diffraction patterns for NMxBS glass powders before alteration.

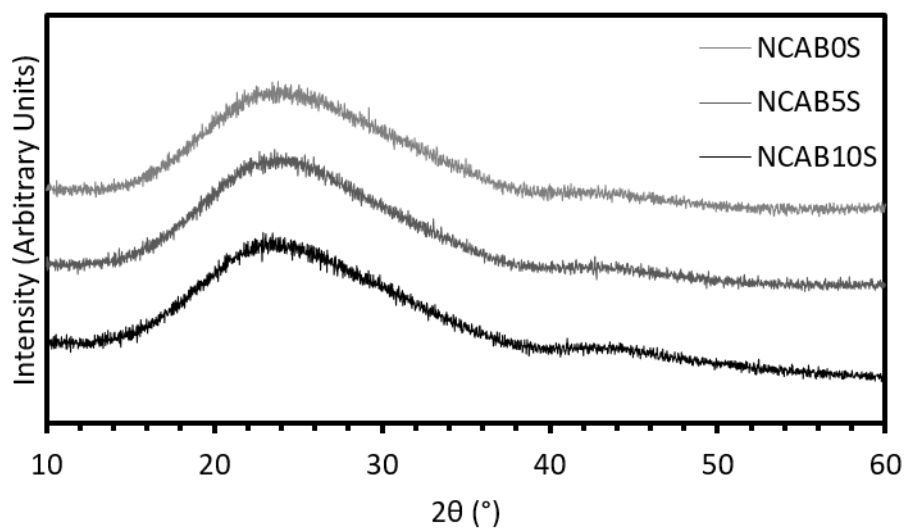


**Figure A3.** X-ray diffraction patterns for NCAB<sub>x</sub>S glass powders before alteration.

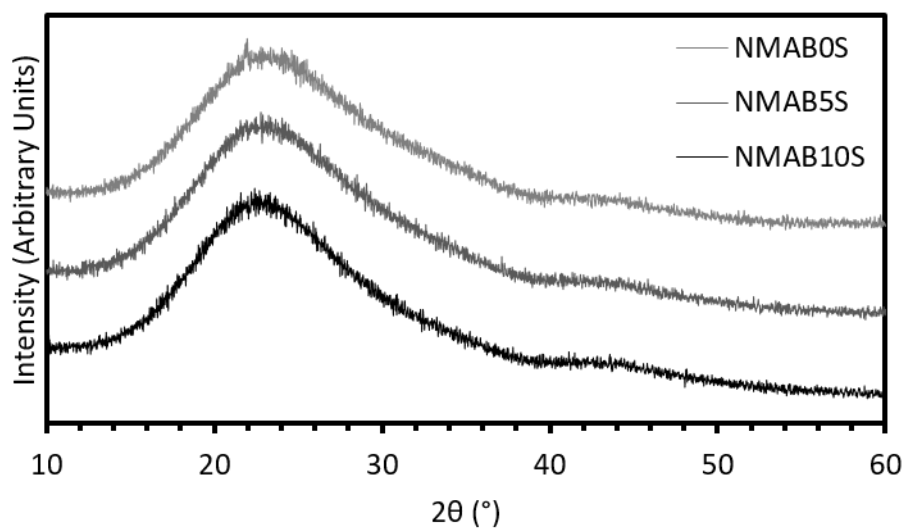


**Figure A4.** X-ray diffraction patterns for NMAB<sub>x</sub>S glass powders before alteration.

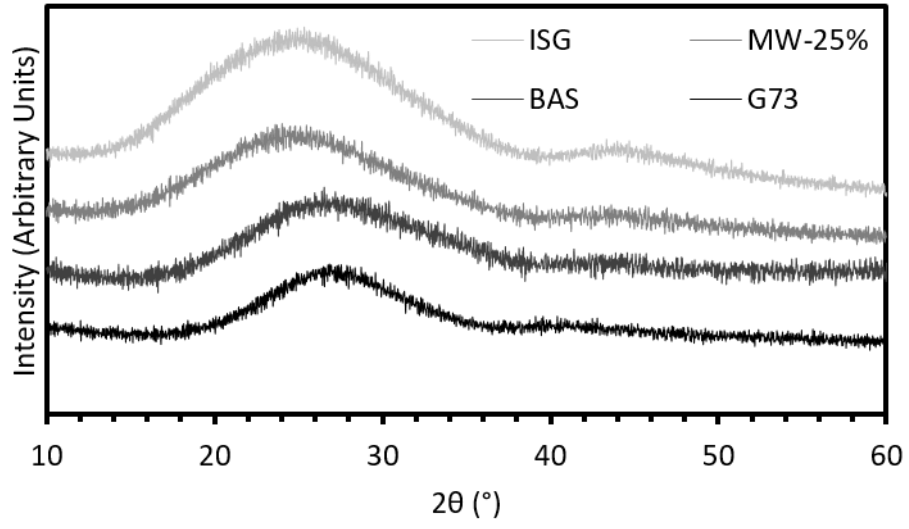


**Figure A5.** X-ray diffraction patterns for literature glass powders before alteration.



## Appendix B – Fitting of NMR Spectra

Example fits for the  $^{11}\text{B}$  and  $^{29}\text{Si}$  MAS-NMR data discussed in Chapter 4.

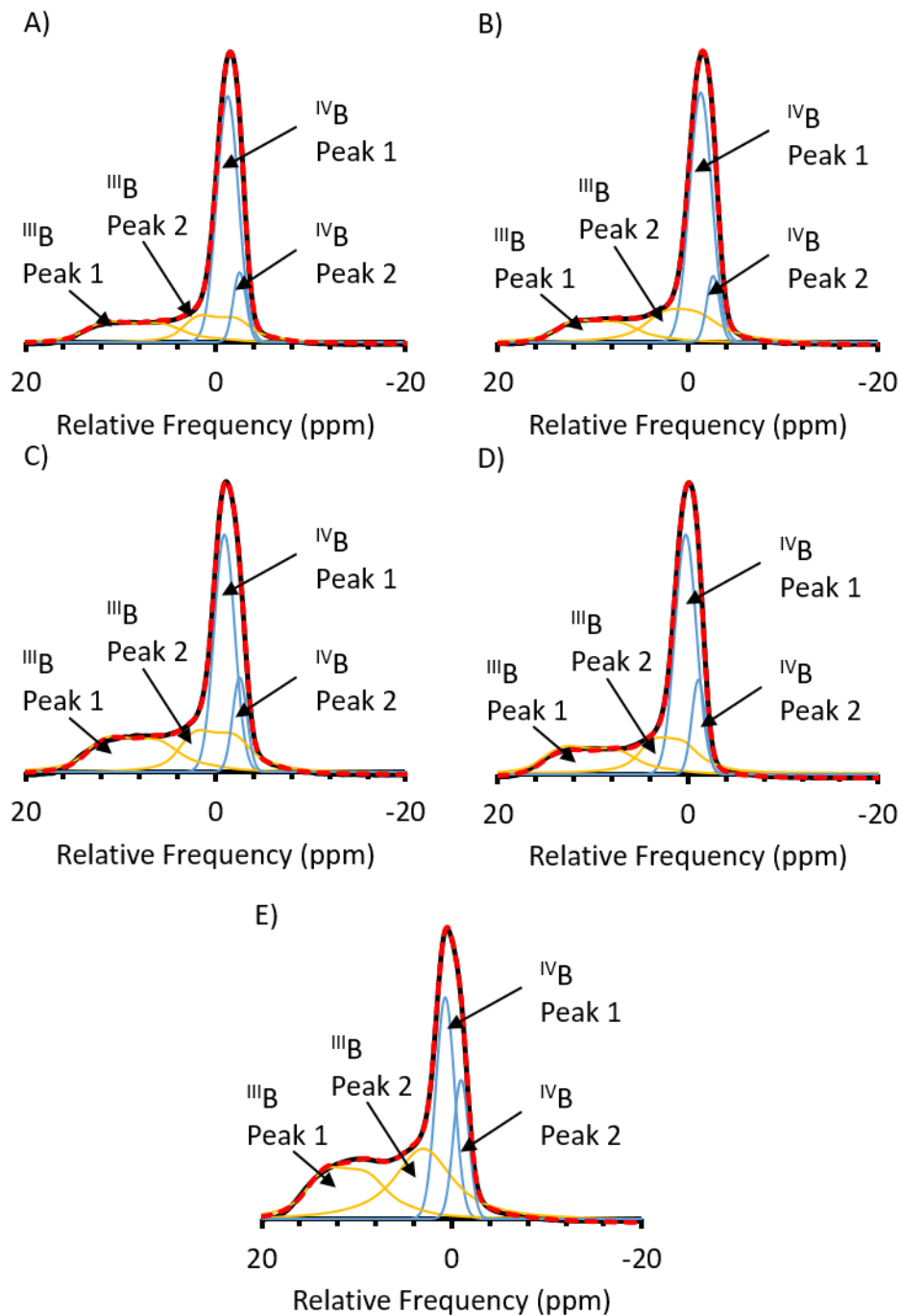


**Figure B1.** Fits for  $^{11}\text{B}$  MAS-NMR spectra of: A) NC0BS; B) NC5BS; C) NC10BS; D) NM5BS and E) NM10BS.

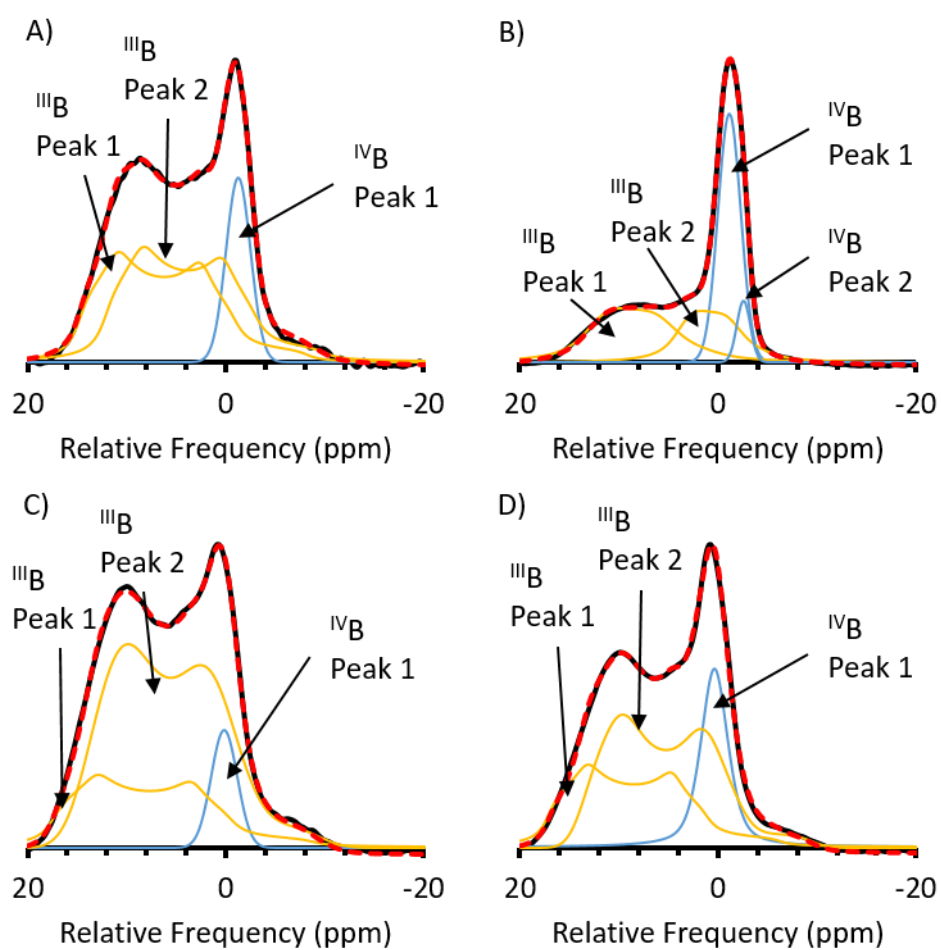


**Figure B2.** Fits for  $^{11}\text{B}$  MAS-NMR spectra of: A) NCAB5S; B) NCAB10S; C) NMAB5S and D) NMAB10S.

**Table B1.** Calculated peak areas for deconvolutions of  $^{11}\text{B}$  MAS-NMR spectra

<b>Sample</b>	<b><math>^{\text{III}}\text{B}</math> Peak 1 Area (%)</b>	<b><math>^{\text{III}}\text{B}</math> Peak 2 Area (%)</b>	<b><math>^{\text{IV}}\text{B}</math> Peak 1 Area (%)</b>	<b><math>^{\text{IV}}\text{B}</math> Peak 2 Area (%)</b>
<b>NC0BS</b>	19.8 ± 0.3	17.6 ± 1.2	54.1 ± 2.4	8.4 ± 0.9
<b>NC5BS</b>	18.0 ± 0.7	22.0 ± 1.6	52.7 ± 1.4	7.3 ± 0.4
<b>NC10BS</b>	25.8 ± 0.6	24.5 ± 0.9	38.9 ± 0.7	10.9 ± 0.5
<b>NM5BS</b>	22.3 ± 0.3	19.8 ± 0.3	46.7 ± 0.2	11.4 ± 0.1
<b>NM10BS</b>	31.3 ± 3.0	26.9 ± 5.1	29.0 ± 3.0	12.8 ± 0.8
<b>NCAB5S</b>	43.2 ± 1.2	40.3 ± 1.7	16.5 ± 0.8	N/A
<b>NCAB10S</b>	35.1 ± 2.3	22.1 ± 2.4	37.8 ± 0.6	5.1 ± 0.5
<b>NMAB5S</b>	N/A	N/A	N/A	N/A
<b>NMAB10S</b>	N/A	N/A	N/A	N/A

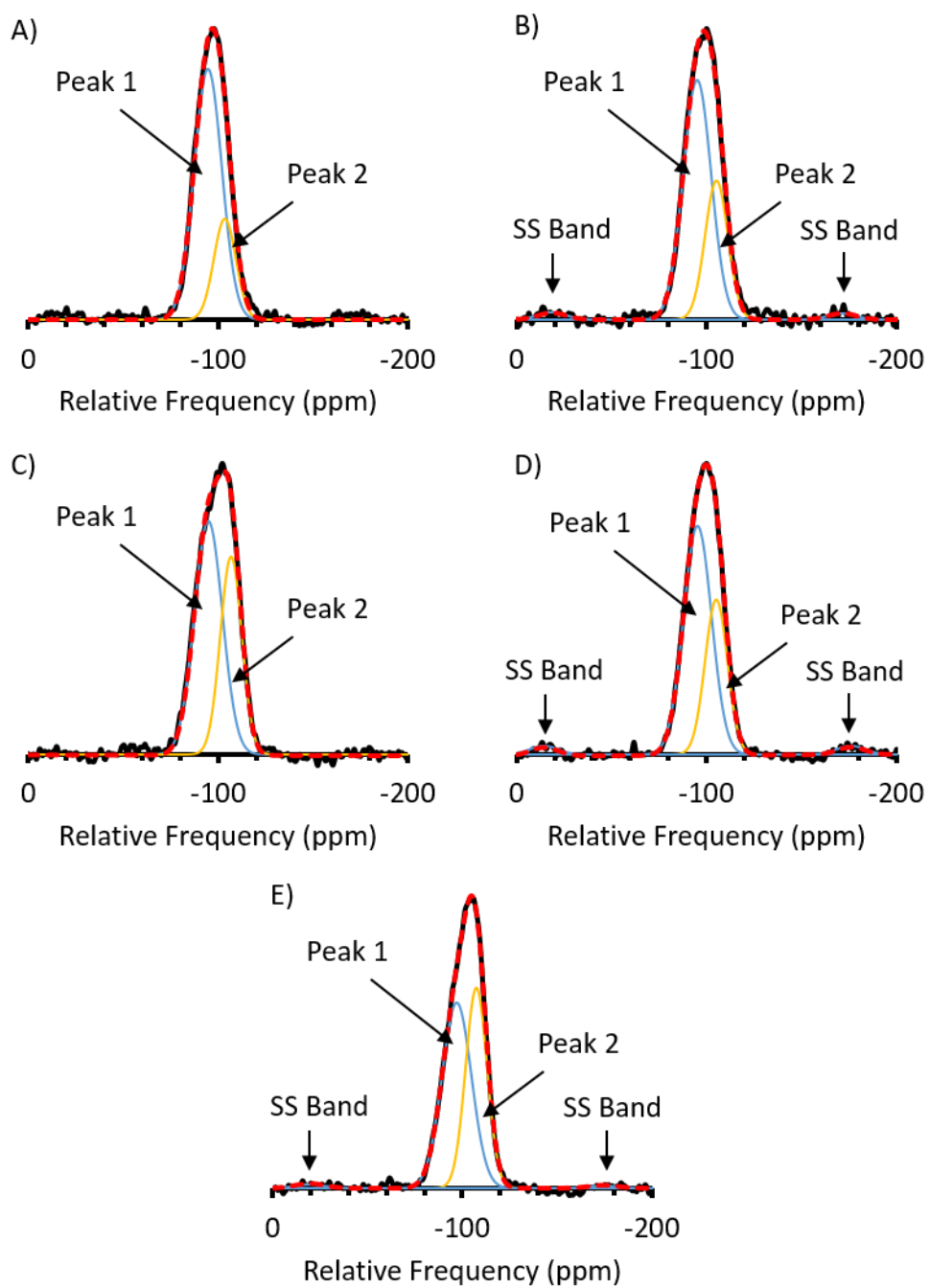


**Figure B3.** Fits for  $^{29}\text{Si}$  MAS-NMR spectra of: A) NC0BS; B) NC5BS; C) NC10BS; D) NM5BS and E) NM10BS.

**Table B2.** Calculated peak areas for deconvolutions of  $^{29}\text{Si}$  MAS-NMR spectra

<b>Sample</b>	<b>Peak 1 Area (%)</b>	<b>Peak 2 Area (%)</b>	<b>Spinning Sideband 1 Area (%)</b>	<b>Spinning Sideband 2 Area (%)</b>
<b>NC0BS</b>	$76.32 \pm 2.59$	$23.68 \pm 2.59$	N/A	N/A
<b>NC5BS</b>	$65.76 \pm 0.68$	$30.70 \pm 0.68$	$1.84 \pm 0.00$	$1.70 \pm 0.00$
<b>NC10BS</b>	$61.76 \pm 0.92$	$38.24 \pm 0.92$	N/A	N/A
<b>NM5BS</b>	$61.14 \pm 0.89$	$34.57 \pm 0.90$	$2.23 \pm 0.00$	$2.05 \pm 0.01$
<b>NM10BS</b>	$50.26 \pm 2.73$	$47.61 \pm 2.79$	$1.29 \pm 0.05$	$0.83 \pm 0.03$
<b>NCAB5S</b>	N/A	N/A	N/A	N/A
<b>NCAB10S</b>	N/A	N/A	N/A	N/A
<b>NMAB5S</b>	N/A	N/A	N/A	N/A
<b>NMAB10S</b>	N/A	N/A	N/A	N/A



## Appendix C – ICP-OES Data (Chap. 5)

**Table C1.** ICP-OES elemental concentration data for NCxBS and NMxBS glass powders altered in KOH. N.P. = Not Present in sample; M.E. = Measurement Error on ICP-OES; B.D.L. = Below Detection Limit.

Sample	Average elemental concentration across duplicates							
	Time (Days)	B (ppm)	Al (ppm)	Na (ppm)	Si (ppm)	Ca (ppm)	K (ppm)	Mg (ppm)
NC0BS	1	19.03	0.51	184.20	95.61	N.P.	5401.50	N.P.
	3	49.42	0.45	443.45	256.03	N.P.	6230.00	N.P.
	7	92.82	0.47	650.46	483.22	N.P.	6499.50	N.P.
	14	115.42	0.19	768.17	683.85	N.P.	4823.40	N.P.
	28	186.03	2.14	1064.65	1103.33	N.P.	6497.37	N.P.
	56	218.62	0.93	1139.66	1227.73	N.P.	6661.00	N.P.
	112	319.77	1.56	1624.10	1697.98	N.P.	8941.00	N.P.
NC5BS	1	13.17	N.P.	22.53	48.99	4.20	9435.00	N.P.
	3	43.02	N.P.	88.27	172.37	4.51	6590.60	N.P.
	7	102.61	N.P.	205.14	413.49	6.59	7000.10	N.P.
	14	157.76	N.P.	302.64	617.88	4.36	6849.29	N.P.
	28	154.26	N.P.	303.46	624.58	6.28	6764.95	N.P.
	56	M.E.	N.P.	M.E.	323.96	0.96	M.E.	N.P.
	112	210.59	N.P.	399.16	634.22	2.52	8805.07	N.P.
NC10BS	1	11.42	N.P.	62.76	62.86	6.25	1031.95	N.P.
	3	27.94	N.P.	131.84	133.88	9.34	1068.20	N.P.
	7	44.11	N.P.	112.95	208.18	18.03	1195.29	N.P.
	14	135.28	N.P.	394.57	512.47	22.33	1238.87	N.P.
	28	217.72	N.P.	626.86	788.32	36.96	1518.91	N.P.
	56	M.E.	N.P.	M.E.	M.E.	M.E.	M.E.	N.P.
	112	M.E.	N.P.	M.E.	M.E.	M.E.	M.E.	N.P.
NM5BS	1	20.49	N.P.	49.94	60.40	N.P.	6872.50	0.16
	3	66.43	N.P.	131.44	227.53	N.P.	4990.01	0.05
	7	112.57	N.P.	212.60	420.79	N.P.	5047.55	0.37
	14	161.91	N.P.	300.82	523.88	N.P.	5085.52	0.08
	28	180.16	N.P.	342.39	542.08	N.P.	4942.04	0.21
	56	M.E.	N.P.	M.E.	550.84	N.P.	M.E.	0.01
	112	270.57	N.P.	496.61	576.89	N.P.	5862.74	0.10
NM10BS	1	13.57	N.P.	17.70	35.64	N.P.	5485.63	0.05
	3	132.95	N.P.	160.91	314.21	N.P.	5612.58	0.10
	7	132.37	N.P.	159.89	310.59	N.P.	5591.51	0.33
	14	141.13	N.P.	182.73	261.98	N.P.	5626.18	0.06
	28	187.35	N.P.	242.79	321.38	N.P.	6080.89	0.14
	56	M.E.	N.P.	M.E.	376.69	N.P.	M.E.	B.D.L
	112	245.46	N.P.	299.44	398.24	N.P.	6720.88	0.21

**Table C2.** ICP-OES elemental concentration data for NCABxS and NMABxS glass powders altered in KOH. N.P. = Not Present in sample; M.E. = Measurement Error on ICP-OES; B.D.L. = Below Detection Limit.

Sample	Average elemental concentration across duplicates							
	Time (Days)	B (ppm)	Al (ppm)	Na (ppm)	Si (ppm)	Ca (ppm)	K (ppm)	Mg (ppm)
NCAB0S	1	N.P.	3.92	B.D.L.	8.84	1.65	10337.50	N.P.
	3	N.P.	9.41	4.95	19.44	6.74	6501.66	N.P.
	7	N.P.	13.68	7.77	30.78	11.25	6560.58	N.P.
	14	N.P.	14.90	11.04	32.40	12.22	7344.02	N.P.
	28	N.P.	15.04	9.89	33.90	12.35	6519.15	N.P.
	56	N.P.	10.58	M.E.	25.83	8.25	M.E.	N.P.
	112	N.P.	15.16	10.82	39.29	13.59	8484.62	N.P.
NCAB5S	1	0.21	11.08	11.62	10.75	1.99	4083.00	N.P.
	3	1.07	31.44	28.05	29.72	13.69	11044.50	N.P.
	7	1.98	35.79	32.58	45.67	8.11	4543.50	N.P.
	14	2.58	21.22	29.64	65.14	12.02	3069.00	N.P.
	28	7.75	82.08	114.81	123.76	42.96	11440.50	N.P.
	56	M.E.	63.97	M.E.	89.27	64.34	33857.75	N.P.
	112	M.E.	43.11	M.E.	66.59	72.14	2277.22	N.P.
NCAB10S	1	1.88	1.59	5.95	16.70	3.82	7521.25	N.P.
	3	4.16	3.78	10.55	37.65	8.77	7430.00	N.P.
	7	6.36	5.79	15.05	57.75	13.39	7466.25	N.P.
	14	6.80	6.02	16.05	61.52	14.21	7288.75	N.P.
	28	7.06	6.16	16.37	63.70	15.13	7205.00	N.P.
	56	7.11	6.07	17.40	62.78	13.83	7301.25	N.P.
	112	7.33	5.75	18.04	62.84	12.97	7250.00	N.P.
NMAB0S	1	N.P.	4.10	1.06	9.46	N.P.	6262.10	B.D.L.
	3	N.P.	8.58	6.81	20.56	N.P.	6398.66	B.D.L.
	7	N.P.	13.94	9.40	30.21	N.P.	6414.73	B.D.L.
	14	N.P.	14.00	15.87	32.92	N.P.	6579.90	B.D.L.
	28	N.P.	15.76	14.13	37.54	N.P.	6439.37	B.D.L.
	56	N.P.	15.66	13.89	45.27	N.P.	8270.92	B.D.L.
	112	N.P.	16.89	14.54	47.39	N.P.	7690.64	0.00
NMAB5S	1	0.72	4.46	2.01	12.71	N.P.	6925.19	B.D.L.
	3	1.80	8.97	8.12	26.99	N.P.	6958.08	B.D.L.
	7	2.62	11.94	10.70	34.38	N.P.	7041.83	B.D.L.
	14	3.21	12.43	13.15	38.06	N.P.	7141.16	B.D.L.
	28	3.44	13.43	14.36	41.93	N.P.	7134.74	0.07
	56	3.09	12.77	13.43	48.12	N.P.	8501.78	B.D.L.
	112	3.84	13.14	17.86	51.19	N.P.	8381.34	0.00
NMAB10S	1	2.47	4.66	5.04	19.99	N.P.	8513.78	B.D.L.
	3	4.86	8.07	10.10	37.54	N.P.	8744.74	B.D.L.
	7	6.20	9.45	12.63	42.72	N.P.	8656.25	B.D.L.
	14	6.76	10.14	13.80	47.74	N.P.	8536.41	B.D.L.
	28	7.34	9.84	15.05	49.39	N.P.	8611.16	0.06
	56	7.64	8.72	15.40	54.44	N.P.	10237.27	B.D.L.
	112	14.90	8.92	27.03	60.36	N.P.	17057.79	B.D.L.

**Table C3.** ICP-OES elemental concentration data for NCxBS and NMxBS glass powders altered in Ca(OH)<sub>2</sub>. N.P. = Not Present in sample; M.E. = Measurement Error on ICP-OES; B.D.L. = Below Detection Limit.

Sample	Average elemental concentration across duplicates						
	Time (Days)	B (ppm)	Al (ppm)	Na (ppm)	Si (ppm)	Ca (ppm)	Mg (ppm)
NC0BS	1	6.24	1.40	67.10	0.28	371.75	N.P.
	3	13.36	1.83	135.70	0.36	318.35	N.P.
	7	21.65	1.80	167.00	0.62	281.30	N.P.
	14	30.58	1.99	216.00	0.78	254.45	N.P.
	28	41.93	2.43	313.85	1.39	348.70	N.P.
	56	46.25	2.33	340.90	1.66	314.55	N.P.
	112	45.06	1.82	290.90	1.40	235.10	N.P.
NC5BS	1	9.93	N.P.	24.52	1.00	418.20	N.P.
	3	14.81	N.P.	34.23	0.58	411.40	N.P.
	7	17.69	N.P.	39.42	0.52	385.44	N.P.
	14	20.67	N.P.	45.25	0.49	354.13	N.P.
	28	23.77	N.P.	55.71	0.43	318.63	N.P.
	56	28.49	N.P.	73.11	0.51	269.63	N.P.
	112	36.15	N.P.	104.42	0.40	192.25	N.P.
NC10BS	1	8.77	N.P.	47.32	0.34	433.55	N.P.
	3	17.43	N.P.	93.92	0.44	342.45	N.P.
	7	24.83	N.P.	107.00	0.81	300.75	N.P.
	14	38.07	N.P.	163.95	1.02	268.15	N.P.
	28	53.27	N.P.	229.10	1.86	305.40	N.P.
	56	63.99	N.P.	270.65	3.89	201.85	N.P.
	112	79.11	N.P.	290.00	13.31	93.18	N.P.
NM5BS	1	11.58	N.P.	29.93	0.50	430.20	0.09
	3	13.48	N.P.	28.60	0.61	385.47	0.01
	7	25.44	N.P.	51.22	0.62	373.18	0.01
	14	31.74	N.P.	64.38	0.49	329.00	0.05
	28	45.82	N.P.	95.63	0.62	283.13	0.03
	56	80.55	N.P.	179.39	0.84	193.49	0.03
	112	122.79	N.P.	302.96	2.43	101.54	0.05
NM10BS	1	10.94	N.P.	19.08	0.38	494.20	0.08
	3	13.66	N.P.	28.88	0.46	383.01	0.01
	7	27.92	N.P.	39.49	0.51	399.02	0.03
	14	33.83	N.P.	46.14	0.45	350.00	0.02
	28	39.04	N.P.	53.61	0.48	296.63	0.04
	56	49.16	N.P.	71.81	0.68	229.53	0.03
	112	63.23	N.P.	109.42	1.53	134.55	0.06

**Table C4.** ICP-OES elemental concentration data for NCABxS and NMABxS glass powders altered in Ca(OH)<sub>2</sub>. N.P. = Not Present in sample; M.E. = Measurement Error on ICP-OES; B.D.L. = Below Detection Limit.

Sample	Average elemental concentration across duplicates						
	Time (Days)	B (ppm)	Al (ppm)	Na (ppm)	Si (ppm)	Ca (ppm)	Mg (ppm)
NCAB0S	1	N.P.	4.33	7.37	0.48	492.00	N.P.
	3	N.P.	8.06	15.46	0.31	431.00	N.P.
	7	N.P.	10.50	25.01	0.33	368.98	N.P.
	14	N.P.	13.62	32.24	0.29	317.75	N.P.
	28	N.P.	16.12	36.17	0.19	280.75	N.P.
	56	N.P.	17.52	41.76	0.13	250.26	N.P.
	112	N.P.	18.35	46.25	0.01	225.85	N.P.
NCAB5S	1	0.92	9.03	17.64	0.13	539.20	N.P.
	3	2.98	17.57	50.89	0.09	463.60	N.P.
	7	5.30	26.63	72.65	0.14	400.35	N.P.
	14	9.62	45.72	130.60	0.25	387.80	N.P.
	28	11.38	56.78	157.00	0.51	461.05	N.P.
	56	11.44	54.92	159.85	0.76	379.80	N.P.
	112	12.57	50.84	149.40	1.20	359.90	N.P.
NCAB10S	1	4.20	0.09	8.96	0.78	259.00	N.P.
	3	7.90	0.05	15.78	0.97	243.53	N.P.
	7	9.56	0.02	19.22	1.13	238.10	N.P.
	14	10.73	0.04	23.00	1.21	223.65	N.P.
	28	12.49	0.00	26.50	1.33	200.01	N.P.
	56	16.02	0.10	37.42	1.88	155.80	N.P.
	112	22.86	0.41	53.31	2.68	110.14	N.P.
NMAB0S	1	N.P.	2.95	10.54	0.20	632.60	0.01
	3	N.P.	5.90	19.89	0.27	472.19	B.D.L.
	7	N.P.	8.30	38.99	0.25	443.40	B.D.L.
	14	N.P.	10.52	47.64	0.24	379.00	B.D.L.
	28	N.P.	12.01	52.47	0.18	326.50	B.D.L.
	56	N.P.	12.81	61.36	0.20	279.63	B.D.L.
	112	N.P.	13.26	68.28	0.31	244.50	B.D.L.
NMAB5S	1	2.24	1.37	12.55	0.13	786.60	B.D.L.
	3	6.90	3.06	37.62	0.41	632.20	B.D.L.
	7	9.77	5.95	52.70	0.19	520.40	B.D.L.
	14	11.29	7.79	61.30	0.17	456.63	B.D.L.
	28	12.57	8.98	68.00	0.11	400.50	B.D.L.
	56	13.89	10.05	80.34	0.14	338.75	B.D.L.
	112	14.77	10.63	86.88	0.11	288.13	0.01
NMAB10S	1	5.98	1.21	20.01	0.16	713.40	0.04
	3	14.23	2.20	40.17	0.37	651.20	B.D.L.
	7	25.45	2.43	71.56	0.21	815.80	B.D.L.
	14	23.82	2.31	68.99	0.08	599.75	B.D.L.
	28	27.14	3.27	77.76	0.01	530.00	B.D.L.
	56	30.26	4.18	90.26	B.D.L.	440.38	B.D.L.
	112	33.03	4.96	103.93	B.D.L.	363.88	B.D.L.

# Appendix D – ICP-OES Data (Chap. 6)

**Table D1.** ICP-OES elemental concentration data for ISG and MW-25% glass powders altered in Ca(OH)<sub>2</sub>. N.P. = Not Present in sample; M.E. = Measurement Error on ICP-OES; B.D.L. = Below Detection Limit.

Sample	Time (Days)	Average elemental concentration across duplicates (ppm)												
		B	Al	Na	Si	Ca	Mg	Zr	Ce	Nd	Fe	La	Ba	
ISG	1	3.59	0.59	8.72	1.44	323.88	N.P.	0.08	N.P.	N.P.	N.P.	N.P.	N.P.	
	3	12.40	1.57	36.56	1.23	215.68	N.P.	B.D.L.	N.P.	N.P.	N.P.	N.P.	N.P.	
	7	23.22	2.18	63.10	2.20	157.83	N.P.	B.D.L.	N.P.	N.P.	N.P.	N.P.	N.P.	
	14	35.91	2.85	94.84	5.76	126.44	N.P.	B.D.L.	N.P.	N.P.	N.P.	N.P.	N.P.	
	28	51.90	3.17	134.86	12.69	89.80	N.P.	B.D.L.	N.P.	N.P.	N.P.	N.P.	N.P.	
	56	63.56	2.28	169.17	20.50	53.65	N.P.	B.D.L.	N.P.	N.P.	N.P.	N.P.	N.P.	
	112	71.26	1.46	190.57	26.44	44.63	N.P.	B.D.L.	N.P.	N.P.	N.P.	N.P.	N.P.	
	MW-25%	1	2.00	0.10	5.75	0.68	371.63	B.D.L.	0.01	B.D.L.	B.D.L.	0.02	0.01	N.P.
		3	13.70	0.45	28.15	0.81	238.44	B.D.L.	B.D.L.	0.01	0.00	0.11	0.04	N.P.
		7	26.31	0.78	52.00	1.28	196.30	B.D.L.	B.D.L.	0.02	B.D.L.	B.D.L.	0.03	N.P.
		14	37.44	0.87	69.66	1.48	173.38	B.D.L.	B.D.L.	0.05	B.D.L.	B.D.L.	0.02	N.P.
28		55.33	0.96	90.81	1.86	152.61	B.D.L.	0.00	0.08	0.00	B.D.L.	0.01	N.P.	
56		87.13	1.38	127.79	2.56	128.90	B.D.L.	B.D.L.	0.06	B.D.L.	B.D.L.	0.03	N.P.	
112	172.84	1.70	227.88	8.99	106.35	B.D.L.	0.02	0.06	B.D.L.	0.01	0.01	N.P.		



**Table D3.** ICP-OES elemental concentration data for literature glass monoliths altered in  $\text{Ca}(\text{OH})_2$ . N.P. = Not Present in sample; M.E. = Measurement Error on ICP-OES; B.D.L. = Below Detection Limit.

Sample	Time (Days)	Average elemental concentration across duplicates (ppm)											
		B	Al	Na	Si	Ca	Mg	Zr	Ce	Nd	Fe	La	Ba
ISG	30	4.07	B.D.L.	9.86	B.D.L.	892.29	N.P.	B.D.L.	N.P.	N.P.	N.P.	N.P.	N.P.
	90	8.87	0.14	19.17	B.D.L.	729.60	N.P.	B.D.L.	N.P.	N.P.	N.P.	N.P.	N.P.
	180	11.37	0.13	22.55	B.D.L.	767.80	N.P.	B.D.L.	N.P.	N.P.	N.P.	N.P.	N.P.
	360	14.53	0.16	29.61	B.D.L.	774.32	N.P.	B.D.L.	N.P.	N.P.	N.P.	N.P.	N.P.
	540	10.97	0.06	22.20	B.D.L.	750.44	N.P.	B.D.L.	N.P.	N.P.	N.P.	N.P.	N.P.
	720	13.30	0.05	26.32	B.D.L.	730.65	N.P.	B.D.L.	N.P.	N.P.	N.P.	N.P.	N.P.
MW-25%	30	0.83	B.D.L.	4.18	B.D.L.	1050.09	B.D.L.	B.D.L.	B.D.L.	B.D.L.	B.D.L.	B.D.L.	N.P.
	90	4.72	B.D.L.	8.37	B.D.L.	748.20	B.D.L.	B.D.L.	B.D.L.	B.D.L.	B.D.L.	B.D.L.	N.P.
	180	8.88	0.06	12.73	B.D.L.	765.32	B.D.L.	B.D.L.	B.D.L.	B.D.L.	B.D.L.	B.D.L.	N.P.
	360	16.49	0.27	21.75	B.D.L.	739.94	B.D.L.	B.D.L.	B.D.L.	B.D.L.	B.D.L.	B.D.L.	N.P.
	540	20.69	0.20	27.53	B.D.L.	770.97	B.D.L.	B.D.L.	B.D.L.	B.D.L.	B.D.L.	B.D.L.	N.P.
	720	25.03	0.20	32.66	B.D.L.	728.79	B.D.L.	B.D.L.	B.D.L.	B.D.L.	B.D.L.	B.D.L.	N.P.
BAS	30	N.P.	B.D.L.	1.47	B.D.L.	867.93	B.D.L.	N.P.	N.P.	N.P.	B.D.L.	N.P.	N.P.
	90	N.P.	0.17	2.12	B.D.L.	728.83	B.D.L.	N.P.	N.P.	N.P.	B.D.L.	N.P.	N.P.
	180	N.P.	0.10	2.19	B.D.L.	751.04	B.D.L.	N.P.	N.P.	N.P.	B.D.L.	N.P.	N.P.
	360	N.P.	B.D.L.	2.85	B.D.L.	746.59	B.D.L.	N.P.	N.P.	N.P.	B.D.L.	N.P.	N.P.
	540	N.P.	B.D.L.	2.89	B.D.L.	773.49	B.D.L.	N.P.	N.P.	N.P.	B.D.L.	N.P.	N.P.
	720	N.P.	B.D.L.	3.01	B.D.L.	736.21	B.D.L.	N.P.	N.P.	N.P.	B.D.L.	N.P.	N.P.
G73	30	B.D.L.	0.13	0.95	0.26	970.75	B.D.L.	N.P.	N.P.	N.P.	B.D.L.	N.P.	13.35
	90	B.D.L.	0.00	2.66	0.32	857.38	B.D.L.	N.P.	N.P.	N.P.	B.D.L.	N.P.	27.73
	180	B.D.L.	0.04	4.93	0.68	937.38	B.D.L.	N.P.	N.P.	N.P.	B.D.L.	N.P.	43.96
	360	B.D.L.	0.02	5.65	0.26	956.00	B.D.L.	N.P.	N.P.	N.P.	B.D.L.	N.P.	48.98
	540	B.D.L.	0.06	6.05	0.24	1048.38	B.D.L.	N.P.	N.P.	N.P.	B.D.L.	N.P.	50.09
	720	B.D.L.	0.01	5.68	0.05	1082.75	B.D.L.	N.P.	N.P.	N.P.	B.D.L.	N.P.	51.31



# Appendix E – PHREEQC Phases

**Table E1.** List of phases included in LLNL database in PHREEQC calculations, showing their assigned thermodynamic constants. N.D. = Not in Database.

Phase	Chemical Formula	Log k	-ΔH (Enthalpy of Reaction) (kJ/mol)	Enthalpy of Formation (kcal/mol)
Afwillite	Ca <sub>3</sub> Si <sub>2</sub> O <sub>4</sub> (OH) <sub>6</sub>	60.0452	-316.0590	-1143.3100
Akermanite	Ca <sub>2</sub> MgSi <sub>2</sub> O <sub>7</sub>	45.3190	-288.5750	-926.4970
Albite	NaAlSi <sub>3</sub> O <sub>8</sub>	2.7645	-51.8523	-939.6800
Albite_high	NaAlSi <sub>3</sub> O <sub>8</sub>	4.0832	-62.8562	-937.0500
Albite_low	NaAlSi <sub>3</sub> O <sub>8</sub>	2.7645	-51.8523	-939.6800
Amesite-14A	Mg <sub>4</sub> Al <sub>4</sub> Si <sub>2</sub> O <sub>10</sub> (OH) <sub>8</sub>	75.4571	-797.0980	-2145.6700
Analcime	Na <sub>96</sub> Al <sub>96</sub> Si <sub>2.04</sub> O <sub>6</sub> :H <sub>2</sub> O	6.1396	-75.8440	-3296.8600
Analcime-dehy	Na <sub>96</sub> Al <sub>96</sub> Si <sub>2.04</sub> O <sub>6</sub>	12.5023	-116.6410	-2970.2300
Andalusite	Al <sub>2</sub> SiO <sub>5</sub>	15.9445	-235.2330	-615.8660
Andradite	Ca <sub>3</sub> Fe <sub>2</sub> (SiO <sub>4</sub> ) <sub>3</sub>	33.3352	-301.1730	-1380.3500
Anorthite	CaAl <sub>2</sub> (SiO <sub>4</sub> ) <sub>2</sub>	26.5780	-303.0390	-1007.5500
Anthophyllite	Mg <sub>7</sub> Si <sub>8</sub> O <sub>22</sub> (OH) <sub>2</sub>	66.7965	-483.4860	-2888.7500
Antigorite	Mg <sub>48</sub> Si <sub>34</sub> O <sub>85</sub> (OH) <sub>62</sub>	477.1943	-3364.4300	-17070.9000
B <sub>2</sub> O <sub>3</sub>	B <sub>2</sub> O <sub>3</sub>	5.5464	-18.0548	-1273.5000
Baddeleyite	ZrO <sub>2</sub>	-7.9405	9.7201	-1100.5600
Beidellite-Ca	Ca <sub>1.165</sub> Al <sub>2.33</sub> Si <sub>3.67</sub> O <sub>10</sub> (OH) <sub>2</sub>	5.5914	-162.4030	-1370.6600
Beidellite-H	H <sub>33</sub> Al <sub>2.33</sub> Si <sub>3.67</sub> O <sub>10</sub> (OH) <sub>2</sub>	4.6335	-154.6500	-1351.1000
Beidellite-Mg	Mg <sub>1.165</sub> Al <sub>2.33</sub> Si <sub>3.67</sub> O <sub>10</sub> (OH) <sub>2</sub>	5.5537	-165.4550	-1366.8900
Beidellite-Na	Na <sub>33</sub> Al <sub>2.33</sub> Si <sub>3.67</sub> O <sub>10</sub> (OH) <sub>2</sub>	5.6473	-155.8460	-1369.7600
Boehmite	AlO <sub>2</sub> H	7.5642	-113.2820	-238.2400
Borax	Na <sub>2</sub> (B <sub>4</sub> O <sub>5</sub> (OH) <sub>4</sub> ):8H <sub>2</sub> O	12.0395	80.5145	-6288.4400
Boric_acid	B(OH) <sub>3</sub>	-0.1583	20.2651	-1094.8000
Brucite	Mg(OH) <sub>2</sub>	16.2980	-111.3400	-221.3900
Ca-Al_Pyroxene	CaAl <sub>2</sub> SiO <sub>6</sub>	35.9759	-361.5480	-783.7930
Ca <sub>2</sub> Al <sub>2</sub> O <sub>5</sub> :8H <sub>2</sub> O	Ca <sub>2</sub> Al <sub>2</sub> O <sub>5</sub> :8H <sub>2</sub> O	59.5687	N.D.	N.D.
Ca <sub>3</sub> Al <sub>2</sub> O <sub>6</sub>	Ca <sub>3</sub> Al <sub>2</sub> O <sub>6</sub>	113.0460	-833.3360	-857.4920
Ca <sub>4</sub> Al <sub>2</sub> Fe <sub>2</sub> O <sub>10</sub>	Ca <sub>4</sub> Al <sub>2</sub> Fe <sub>2</sub> O <sub>10</sub>	140.5050	-1139.8600	-1211.0000
Ca <sub>4</sub> Al <sub>2</sub> O <sub>7</sub> :13H <sub>2</sub> O	Ca <sub>4</sub> Al <sub>2</sub> O <sub>7</sub> :13H <sub>2</sub> O	107.2537	N.D.	N.D.
Ca <sub>4</sub> Al <sub>2</sub> O <sub>7</sub> :19H <sub>2</sub> O	Ca <sub>4</sub> Al <sub>2</sub> O <sub>7</sub> :19H <sub>2</sub> O	103.6812	N.D.	N.D.
CaAl <sub>2</sub> O <sub>4</sub>	CaAl <sub>2</sub> O <sub>4</sub>	46.9541	-436.9520	-555.9960
CaAl <sub>2</sub> O <sub>4</sub> :10H <sub>2</sub> O	CaAl <sub>2</sub> O <sub>4</sub> :10H <sub>2</sub> O	37.9946	N.D.	N.D.
CaAl <sub>4</sub> O <sub>7</sub>	CaAl <sub>4</sub> O <sub>7</sub>	68.6138	-718.4640	-951.0260
CaZrO <sub>3</sub>	CaZrO <sub>3</sub>	-148.5015	801.2820	-650.3450
Ce(OH) <sub>3</sub>	Ce(OH) <sub>3</sub>	19.8852	N.D.	N.D.
Ce(OH) <sub>3</sub> (am)	Ce(OH) <sub>3</sub>	21.1852	N.D.	N.D.
Ce <sub>2</sub> O <sub>3</sub>	Ce <sub>2</sub> O <sub>3</sub>	62.3000	N.D.	N.D.
CeO <sub>2</sub>	CeO <sub>2</sub>	-8.1600	N.D.	N.D.
Chalcedony	SiO <sub>2</sub>	-3.7281	31.4093	-217.2820

<b>Chamosite-7A</b>	Fe <sub>2</sub> Al <sub>2</sub> Si <sub>5</sub> O <sub>5</sub> (OH) <sub>4</sub>	32.8416	-364.2130	-902.4070
<b>Chrysotile</b>	Mg <sub>3</sub> Si <sub>2</sub> O <sub>5</sub> (OH) <sub>4</sub>	31.1254	-218.0410	-1043.1200
<b>Clinochlore-14A</b>	Mg <sub>5</sub> Al <sub>2</sub> Si <sub>3</sub> O <sub>10</sub> (OH) <sub>8</sub>	67.2391	-612.3790	-2116.9600
<b>Clinochlore-7A</b>	Mg <sub>5</sub> Al <sub>2</sub> Si <sub>3</sub> O <sub>10</sub> (OH) <sub>8</sub>	70.6124	-628.1400	-2113.2000
<b>Clinoptilolite-Ca</b>	Ca <sub>1.7335</sub> Al <sub>3.45</sub> Fe <sub>.017</sub> Si <sub>14.533</sub> O <sub>36</sub> :10.922H <sub>2</sub> O	-7.0095	-74.6745	-4919.8400
<b>Clinoptilolite-dehy-Ca</b>	Ca <sub>1.7335</sub> Al <sub>3.45</sub> Fe <sub>.017</sub> Si <sub>14.533</sub> O <sub>36</sub>	28.6255	-329.2780	-4112.8300
<b>Clinoptilolite-dehy-Na</b>	Na <sub>3.467</sub> Al <sub>3.45</sub> Fe <sub>.017</sub> Si <sub>14.533</sub> O <sub>36</sub>	28.4987	-253.7980	-4104.9800
<b>Clinoptilolite-hy-Ca</b>	Ca <sub>1.7335</sub> Al <sub>3.45</sub> Fe <sub>.017</sub> Si <sub>14.533</sub> O <sub>36</sub> :11.645H <sub>2</sub> O	-7.0108	-65.4496	-4971.4400
<b>Clinoptilolite-hy-Na</b>	Na <sub>3.467</sub> Al <sub>3.45</sub> Fe <sub>.017</sub> Si <sub>14.533</sub> O <sub>36</sub> :10.877H <sub>2</sub> O	-7.1384	1.8817	-4909.1800
<b>Clinoptilolite-Na</b>	Na <sub>3.467</sub> Al <sub>3.45</sub> Fe <sub>.017</sub> Si <sub>14.533</sub> O <sub>36</sub> :10.922H <sub>2</sub> O	-7.1363	2.3282	-4912.3600
<b>Clinozoisite</b>	Ca <sub>2</sub> Al <sub>3</sub> Si <sub>3</sub> O <sub>12</sub> (OH)	43.2569	-457.7550	-1643.7800
<b>Coesite</b>	SiO <sub>2</sub>	-3.1893	28.6144	-216.6140
<b>Colemanite</b>	Ca <sub>2</sub> B <sub>6</sub> O <sub>11</sub> :5H <sub>2</sub> O	21.5148	N.D.	N.D.
<b>Cordierite_anhyd</b>	Mg <sub>2</sub> Al <sub>4</sub> Si <sub>5</sub> O <sub>18</sub>	52.3035	-626.2190	-2183.2000
<b>Cordierite_hydr</b>	Mg <sub>2</sub> Al <sub>4</sub> Si <sub>5</sub> O <sub>18</sub> :H <sub>2</sub> O	49.8235	-608.8140	-2255.6800
<b>Corundum</b>	Al <sub>2</sub> O <sub>3</sub>	18.3121	-258.6260	-400.5000
<b>Cristobalite(alpha)</b>	SiO <sub>2</sub>	-3.4488	29.2043	-216.7550
<b>Cristobalite(beta)</b>	SiO <sub>2</sub>	-3.0053	24.6856	-215.6750
<b>Cronstedtite-7A</b>	Fe <sub>2</sub> Fe <sub>2</sub> Si <sub>5</sub> O <sub>5</sub> (OH) <sub>4</sub>	16.2603	-244.2660	-697.4130
<b>Daphnite-14A</b>	Fe <sub>5</sub> AlAlSi <sub>3</sub> O <sub>10</sub> (OH) <sub>8</sub>	52.2821	-517.5610	-1693.0400
<b>Daphnite-7A</b>	Fe <sub>5</sub> AlAlSi <sub>3</sub> O <sub>10</sub> (OH) <sub>8</sub>	55.6554	-532.3260	-1689.5100
<b>Diaspore</b>	AlHO <sub>2</sub>	7.1603	-110.4200	-238.9240
<b>Dicalcium_silicate</b>	Ca <sub>2</sub> SiO <sub>4</sub>	37.1725	-217.6420	-2317.9000
<b>Diopside</b>	CaMgSi <sub>2</sub> O <sub>6</sub>	20.9643	-133.7750	-765.3780
<b>Enstatite</b>	MgSiO <sub>3</sub>	11.3269	-82.7302	-369.6860
<b>Epidote</b>	Ca <sub>2</sub> FeAl <sub>2</sub> Si <sub>3</sub> O <sub>12</sub> OH	32.9296	-386.4510	-1543.9900
<b>Epidote-ord</b>	FeCa <sub>2</sub> Al <sub>2</sub> (OH)(SiO <sub>4</sub> ) <sub>3</sub>	32.9296	-386.3510	-1544.0200
<b>Fayalite</b>	Fe <sub>2</sub> SiO <sub>4</sub>	19.1113	-152.2560	-354.1190
<b>Fe(OH)2</b>	Fe(OH) <sub>2</sub>	13.9045	-95.4089	-568.5250
<b>Fe(OH)3</b>	Fe(OH) <sub>3</sub>	5.6556	-84.0824	-823.0130
<b>FeO</b>	FeO	13.5318	-106.0520	-65.0200
<b>Ferrite-Ca</b>	CaFe <sub>2</sub> O <sub>4</sub>	21.5217	-264.7380	-363.4940
<b>Ferrite-Dicalcium</b>	Ca <sub>2</sub> Fe <sub>2</sub> O <sub>5</sub>	56.8331	-475.2610	-2139.2600
<b>Ferrite-Mg</b>	MgFe <sub>2</sub> O <sub>4</sub>	21.0551	-280.0560	-1428.4200
<b>Ferrosilite</b>	FeSiO <sub>3</sub>	7.4471	-60.6011	-285.6580
<b>Forsterite</b>	Mg <sub>2</sub> SiO <sub>4</sub>	27.8626	-205.6140	-520.0000
<b>Foshagite</b>	Ca <sub>4</sub> Si <sub>3</sub> O <sub>9</sub> (OH) <sub>2</sub> :0.5H <sub>2</sub> O	65.9210	-359.8390	-1438.2700
<b>Gehlenite</b>	Ca <sub>2</sub> Al <sub>2</sub> SiO <sub>7</sub>	56.2997	-489.9340	-951.2250
<b>Gibbsite</b>	Al(OH) <sub>3</sub>	7.7560	-102.7880	-309.0650
<b>Gismondine</b>	Ca <sub>2</sub> Al <sub>4</sub> Si <sub>4</sub> O <sub>16</sub> :9H <sub>2</sub> O	41.7170	N.D.	N.D.
<b>Goethite</b>	FeOOH	0.5345	-61.9291	-559.3280
<b>Greenalite</b>	Fe <sub>3</sub> Si <sub>2</sub> O <sub>5</sub> (OH) <sub>4</sub>	22.6701	-165.2970	-787.7780
<b>Grossular</b>	Ca <sub>3</sub> Al <sub>2</sub> (SiO <sub>4</sub> ) <sub>3</sub>	51.9228	-432.0060	-1582.7400
<b>Gyrolite</b>	Ca <sub>2</sub> Si <sub>3</sub> O <sub>7</sub> (OH) <sub>2</sub> :1.5H <sub>2</sub> O	22.9099	-82.8620	-1176.5500
<b>Hatrurite</b>	Ca <sub>3</sub> SiO <sub>5</sub>	73.4056	-434.6840	-700.2340
<b>Hedenbergite</b>	CaFe(SiO <sub>3</sub> ) <sub>2</sub>	19.6060	-124.5070	-678.2760
<b>Hematite</b>	Fe <sub>2</sub> O <sub>3</sub>	0.1086	-129.4150	-197.7200
<b>Hercynite</b>	FeAl <sub>2</sub> O <sub>4</sub>	28.8484	-345.9610	-1966.4500

<b>Hillebrandite</b>	Ca <sub>2</sub> SiO <sub>3</sub> (OH) <sub>2</sub> :0.17H <sub>2</sub> O	36.8190	-203.0740	-637.4040
<b>Hydroboracite</b>	MgCaB <sub>6</sub> O <sub>11</sub> :6H <sub>2</sub> O	20.3631	N.D.	N.D
<b>Jadeite</b>	NaAl(SiO <sub>3</sub> ) <sub>2</sub>	8.3888	-84.4415	-722.1160
<b>Kaolinite</b>	Al <sub>2</sub> Si <sub>2</sub> O <sub>5</sub> (OH) <sub>4</sub>	6.8101	-151.7790	-982.2210
<b>Katoite</b>	Ca <sub>3</sub> Al <sub>2</sub> H <sub>12</sub> O <sub>12</sub>	78.9437	N.D.	N.D
<b>Kyanite</b>	Al <sub>2</sub> SiO <sub>5</sub>	15.6740	-230.9190	-616.8970
<b>La(OH)<sub>3</sub></b>	La(OH) <sub>3</sub>	20.2852	N.D.	N.D
<b>La(OH)<sub>3</sub>(am)</b>	La(OH) <sub>3</sub>	23.4852	N.D.	N.D
<b>La<sub>2</sub>O<sub>3</sub></b>	La <sub>2</sub> O <sub>3</sub>	66.2000	N.D.	N.D
<b>Larnite</b>	Ca <sub>2</sub> SiO <sub>4</sub>	38.4665	-227.0610	-551.7400
<b>Laumontite</b>	CaAl <sub>2</sub> Si <sub>4</sub> O <sub>12</sub> :4H <sub>2</sub> O	13.6667	-184.6570	-1728.6600
<b>Lawsonite</b>	CaAl <sub>2</sub> Si <sub>2</sub> O <sub>7</sub> (OH) <sub>2</sub> :H <sub>2</sub> O	22.2132	-244.8060	-1158.1000
<b>Lime</b>	CaO	32.5761	-193.8320	-151.7900
<b>Magnetite</b>	Fe <sub>3</sub> O <sub>4</sub>	10.4724	-216.5970	-267.2500
<b>Margarite</b>	CaAl <sub>4</sub> Si <sub>2</sub> O <sub>10</sub> (OH) <sub>2</sub>	41.0658	-522.1920	-1485.8000
<b>Mayenite</b>	Ca <sub>12</sub> Al <sub>14</sub> O <sub>33</sub>	494.2199	-4056.7700	-4644.0000
<b>Merwinite</b>	MgCa <sub>3</sub> (SiO <sub>4</sub> ) <sub>2</sub>	68.5140	-430.0690	-1090.8000
<b>Mesolite</b>	Na.676Ca.657Al <sub>1.99</sub> Si <sub>3.01</sub> O <sub>10</sub> :2.647H <sub>2</sub> O	13.6191	-179.7440	-5947.0500
<b>Minnesotaite</b>	Fe <sub>3</sub> Si <sub>4</sub> O <sub>10</sub> (OH) <sub>2</sub>	13.9805	-105.2110	-1153.3700
<b>Monticellite</b>	CaMgSiO <sub>4</sub>	29.5852	-195.7110	-540.8000
<b>Montmor-Ca</b>	Ca.165Mg.33Al <sub>1.67</sub> Si <sub>4</sub> O <sub>10</sub> (OH) <sub>2</sub>	2.4952	-100.1540	-1361.5000
<b>Montmor-Mg</b>	Mg.495Al <sub>1.67</sub> Si <sub>4</sub> O <sub>10</sub> (OH) <sub>2</sub>	2.3879	-102.6080	-1357.8700
<b>Montmor-Na</b>	Na.33Mg.33Al <sub>1.67</sub> Si <sub>4</sub> O <sub>10</sub> (OH) <sub>2</sub>	2.4844	-93.2165	-1360.6900
<b>Mordenite</b>	Ca.2895Na.361Al.94Si <sub>5.06</sub> O <sub>12</sub> :3.468H <sub>2</sub> O	-5.1969	16.7517	-6736.6400
<b>Mordenite-dehy</b>	Ca.2895Na.361Al.94Si <sub>5.06</sub> O <sub>12</sub>	9.9318	-86.1590	-5642.4400
<b>Na<sub>2</sub>O</b>	Na <sub>2</sub> O	67.4269	-351.6360	-99.1400
<b>Na<sub>2</sub>SiO<sub>3</sub></b>	Na <sub>2</sub> SiO <sub>3</sub>	22.2418	-82.7093	-373.1900
<b>Na<sub>4</sub>SiO<sub>4</sub></b>	Na <sub>4</sub> SiO <sub>4</sub>	70.6449	-327.7790	-497.8000
<b>Na<sub>6</sub>Si<sub>2</sub>O<sub>7</sub></b>	Na <sub>6</sub> Si <sub>2</sub> O <sub>7</sub>	101.6199	-471.9510	-856.3000
<b>NaFeO<sub>2</sub></b>	NaFeO <sub>2</sub>	19.8899	-163.3390	-698.2180
<b>Natrolite</b>	Na <sub>2</sub> Al <sub>2</sub> Si <sub>3</sub> O <sub>10</sub> :2H <sub>2</sub> O	18.5204	-186.9710	-5718.5600
<b>Natrosilite</b>	Na <sub>2</sub> Si <sub>2</sub> O <sub>5</sub>	18.1337	-51.7686	-590.3600
<b>Nd(OH)<sub>3</sub></b>	Nd(OH) <sub>3</sub>	18.0852	N.D.	N.D
<b>Nd(OH)<sub>3</sub>(am)</b>	Nd(OH) <sub>3</sub>	20.4852	N.D.	N.D
<b>Nd(OH)<sub>3</sub>(c)</b>	Nd(OH) <sub>3</sub>	15.7852	N.D.	N.D
<b>Nd<sub>2</sub>O<sub>3</sub></b>	Nd <sub>2</sub> O <sub>3</sub>	58.6000	N.D.	N.D
<b>Nepheline</b>	NaAlSiO <sub>4</sub>	13.8006	-135.0680	-500.2410
<b>Nontronite-Ca</b>	Ca.165Fe <sub>2</sub> Al <sub>3.33</sub> Si <sub>3.67</sub> H <sub>2</sub> O <sub>12</sub>	-11.5822	-38.1380	-1166.7000
<b>Nontronite-H</b>	H.33Fe <sub>2</sub> Al <sub>3.33</sub> Si <sub>3.67</sub> H <sub>2</sub> O <sub>12</sub>	-12.5401	-30.4520	-1147.1200
<b>Nontronite-Mg</b>	Mg.165Fe <sub>2</sub> Al <sub>3.33</sub> Si <sub>3.67</sub> H <sub>2</sub> O <sub>12</sub>	-11.6200	-41.1779	-1162.9300
<b>Nontronite-Na</b>	Na.33Fe <sub>2</sub> Al <sub>3.33</sub> Si <sub>3.67</sub> H <sub>2</sub> O <sub>12</sub>	-11.5263	-31.5687	-1165.8000
<b>Okenite</b>	CaSi <sub>2</sub> O <sub>4</sub> (OH) <sub>2</sub> :H <sub>2</sub> O	10.3816	-19.4974	-749.6410
<b>Paragonite</b>	NaAl <sub>3</sub> Si <sub>3</sub> O <sub>10</sub> (OH) <sub>2</sub>	17.5220	-275.0560	-1416.9600
<b>Pargasite</b>	NaCa <sub>2</sub> Al <sub>3</sub> Mg <sub>4</sub> Si <sub>6</sub> O <sub>22</sub> (OH) <sub>2</sub>	101.9939	-880.2050	-3016.6200
<b>Periclase</b>	MgO	21.3354	-150.1390	-143.8000
<b>Portlandite</b>	Ca(OH) <sub>2</sub>	22.5552	-128.6860	-986.0740
<b>Pr(OH)<sub>3</sub></b>	Pr(OH) <sub>3</sub>	19.5852	N.D.	N.D
<b>Pr(OH)<sub>3</sub>(am)</b>	Pr(OH) <sub>3</sub>	21.0852	N.D.	N.D
<b>Pr<sub>2</sub>O<sub>3</sub></b>	Pr <sub>2</sub> O <sub>3</sub>	61.4000	N.D.	N.D

<b>Prehnite</b>	Ca <sub>2</sub> Al <sub>2</sub> Si <sub>3</sub> O <sub>10</sub> (OH) <sub>2</sub>	32.9305	-311.8750	-1481.6500
<b>Pseudowollastonite</b>	CaSiO <sub>3</sub>	13.9997	-79.4625	-388.9000
<b>Pyrophyllite</b>	Al <sub>2</sub> Si <sub>4</sub> O <sub>10</sub> (OH) <sub>2</sub>	0.4397	-102.1610	-1345.3100
<b>Quartz</b>	SiO <sub>2</sub>	-3.9993	32.9490	-217.6500
<b>Rankinite</b>	Ca <sub>3</sub> Si <sub>2</sub> O <sub>7</sub>	51.9078	-302.0890	-941.7000
<b>Ripidolite-14A</b>	Mg <sub>3</sub> Fe <sub>2</sub> Al <sub>2</sub> Si <sub>3</sub> O <sub>10</sub> (OH) <sub>8</sub>	60.9638	-572.4720	-1947.8700
<b>Ripidolite-7A</b>	Mg <sub>3</sub> Fe <sub>2</sub> Al <sub>2</sub> Si <sub>3</sub> O <sub>10</sub> (OH) <sub>8</sub>	64.3371	-586.3250	-1944.5600
<b>Saponite-Ca</b>	Ca <sub>1.165</sub> Mg <sub>3</sub> Al <sub>1.33</sub> Si <sub>3.67</sub> O <sub>10</sub> (OH) <sub>2</sub>	26.2900	-207.9710	-1436.5100
<b>Saponite-H</b>	H <sub>0.33</sub> Mg <sub>3</sub> Al <sub>1.33</sub> Si <sub>3.67</sub> O <sub>10</sub> (OH) <sub>2</sub>	25.3321	-200.2350	-1416.9400
<b>Saponite-Mg</b>	Mg <sub>3.165</sub> Al <sub>1.33</sub> Si <sub>3.67</sub> O <sub>10</sub> (OH) <sub>2</sub>	26.2523	-210.8220	-1432.7900
<b>Saponite-Na</b>	Na <sub>0.33</sub> Mg <sub>3</sub> Al <sub>1.33</sub> Si <sub>3.67</sub> O <sub>10</sub> (OH) <sub>2</sub>	26.3459	-201.4010	-1435.6100
<b>Scolecite</b>	CaAl <sub>2</sub> Si <sub>3</sub> O <sub>10</sub> :3H <sub>2</sub> O	15.8767	-204.9300	-6048.9200
<b>Sepiolite</b>	Mg <sub>4</sub> Si <sub>6</sub> O <sub>15</sub> (OH) <sub>2</sub> :6H <sub>2</sub> O	30.4439	-157.3390	-2418.0000
<b>Sillimanite</b>	Al <sub>2</sub> SiO <sub>5</sub>	16.3080	-238.4420	-615.0990
<b>SiO<sub>2</sub>(am)</b>	SiO <sub>2</sub>	-2.7136	20.0539	-214.5680
<b>Spinel</b>	Al <sub>2</sub> MgO <sub>4</sub>	37.6295	-398.1080	-546.8470
<b>Talc</b>	Mg <sub>3</sub> Si <sub>4</sub> O <sub>10</sub> (OH) <sub>2</sub>	21.1383	-148.7370	-1410.9200
<b>Tobermorite-11A</b>	Ca <sub>5</sub> Si <sub>6</sub> H <sub>11</sub> O <sub>22.5</sub>	65.6121	-286.8610	-2556.4200
<b>Tobermorite-14A</b>	Ca <sub>5</sub> Si <sub>6</sub> H <sub>21</sub> O <sub>27.5</sub>	63.8445	-230.9590	-2911.3600
<b>Tobermorite-9A</b>	Ca <sub>5</sub> Si <sub>6</sub> H <sub>6</sub> O <sub>20</sub>	69.0798	-329.5570	-2375.4200
<b>Tremolite</b>	Ca <sub>2</sub> Mg <sub>5</sub> Si <sub>8</sub> O <sub>22</sub> (OH) <sub>2</sub>	61.2367	-406.4040	-2944.0400
<b>Tridymite</b>	SiO <sub>2</sub>	-3.8278	31.3664	-909.0650
<b>Wairakite</b>	CaAl <sub>2</sub> Si <sub>4</sub> O <sub>10</sub> (OH) <sub>4</sub>	18.0762	-237.7810	-1579.3300
<b>Wollastonite</b>	CaSiO <sub>3</sub>	13.7605	-76.5756	-389.5900
<b>Wustite</b>	Fe <sub>0.947</sub> O	12.4113	-102.4170	-266.2650
<b>Xonotlite</b>	Ca <sub>6</sub> Si <sub>6</sub> O <sub>17</sub> (OH) <sub>2</sub>	91.8267	-495.4570	-2397.2500
<b>Zircon</b>	ZrSiO <sub>4</sub>	-15.4193	64.8635	-2033.4000
<b>Zoisite</b>	Ca <sub>2</sub> Al <sub>3</sub> (SiO <sub>4</sub> ) <sub>3</sub> OH	43.3017	-458.1310	-1643.6900
<b>Anatase</b>	TiO <sub>2</sub>	-8.5586	N.D.	-939.9420
<b>Eucryptite</b>	LiAlSiO <sub>4</sub>	13.6106	-141.8180	-2124.4100
<b>Ilmenite</b>	FeTiO <sub>3</sub>	0.9046	N.D.	-1236.6500
<b>Petalite</b>	LiAlSi <sub>4</sub> O <sub>10</sub>	-3.8153	-13.1739	-4886.1500
<b>Rutile</b>	TiO <sub>2</sub>	-9.6452	N.D.	-226.1070
<b>Spodumene</b>	LiAlSi <sub>2</sub> O <sub>6</sub>	6.9972	-89.1817	-3054.7500
<b>Ti<sub>2</sub>O<sub>3</sub></b>	Ti <sub>2</sub> O <sub>3</sub>	42.9866	N.D.	-1520.7800
<b>Ti<sub>3</sub>O<sub>5</sub></b>	Ti <sub>3</sub> O <sub>5</sub>	34.6557	N.D.	-2459.2400
<b>TiO(alpha)</b>	TiO	61.1282	N.D.	-519.8350
<b>Titanite</b>	CaTiSiO <sub>5</sub>	719.5839	N.D.	N.D.
<b>Ba(OH)<sub>2</sub>:8H<sub>2</sub>O</b>	Ba(OH) <sub>2</sub> :8H <sub>2</sub> O	24.4911	-55.4363	-3340.5900
<b>Ba<sub>2</sub>Si<sub>3</sub>O<sub>8</sub></b>	Ba <sub>2</sub> Si <sub>3</sub> O <sub>8</sub>	23.3284	-95.3325	-4184.7300
<b>Ba<sub>2</sub>SiO<sub>4</sub></b>	Ba <sub>2</sub> SiO <sub>4</sub>	44.5930	-237.2060	-2287.4600
<b>BaO</b>	BaO	47.8036	-270.1840	-553.2980
<b>Sanbornite</b>	BaSi <sub>2</sub> O <sub>5</sub>	9.4753	-31.0845	-2547.8000

# Bibliography

- [1] Department of Energy and Climate Change, “Implementing Geological Disposal,” July 2014.
- [2] P. A. Bingham, N. C. Hyatt, and R. J. Hand, “Vitrification of UK intermediate level radioactive wastes arising from site decommissioning: Property modelling and selection of candidate host glass compositions,” *Glas. Technol. Eur. J. Glas. Sci. Technol. Part A*, vol. 53, no. 3, pp. 83–100, 2012.
- [3] C. A. Utton, R. J. Hand, P. A. Bingham, N. C. Hyatt, S. W. Swanton, and S. J. Williams, “Dissolution of vitrified wastes in a high-pH calcium-rich solution,” *J. Nucl. Mater.*, vol. 435, no. 1–3, pp. 112–122, 2013.
- [4] S. Gin and J. P. Mestre, “SON 68 nuclear glass alteration kinetics between pH 7 and pH 11.5,” *J. Nucl. Mater.*, vol. 295, no. 1, pp. 83–96, 2001.
- [5] P. K. Abraitis *et al.*, “The kinetics and mechanisms of simulated British Magnox waste glass dissolution as a function of pH, silicic acid activity and time in low temperature aqueous systems,” *Appl. Geochemistry*, vol. 15, no. 9, pp. 1399–1416, 2000.
- [6] J. P. Hamilton, S. L. Brantley, C. G. Pantano, L. J. Criscenti, and J. D. Kubicki, “Dissolution of nepheline, jadeite and albite glasses: Toward better models for aluminosilicate dissolution,” *Geochim. Cosmochim. Acta*, vol. 65, no. 21, pp. 3683–3702, 2001.
- [7] E. M. Pierce, E. A. Rodriguez, L. J. Calligan, W. J. Shaw, and B. Pete McGrail, “An experimental study of the dissolution rates of simulated aluminoborosilicate waste glasses as a function of pH and temperature under dilute conditions,” *Appl. Geochemistry*, vol. 23, no. 9, pp. 2559–2573, 2008.
- [8] M. T. Harrison, B. F. Dunnett, S. Morgan, C. R. Scales, and J. S. Small, “International research on vitrified HLW long-term behaviour: State of the art,” NNL (09)8864, no. 4. 2009.
- [9] B. Thien, N. Godon, F. Hubert, F. Angéli, S. Gin, and A. Ayrál, “Structural identification of a trioctahedral smectite formed by the aqueous alteration of a nuclear glass,” *Appl. Clay Sci.*, vol. 49, no. 3, pp. 135–141, 2010.
- [10] B. M. J. Thien, N. Godon, A. Ballesteró, S. Gin, and A. Ayrál, “The dual effect of Mg on the long-term alteration rate of AVM nuclear waste glasses,” *J. Nucl. Mater.*, vol. 427, no. 1–3, pp. 297–310, 2012.
- [11] E. Curti, R. Dähn, F. Farges, and M. Vespa, “Na, Mg, Ni and Cs distribution and speciation after long-term alteration of a simulated nuclear waste glass: A micro-XAS/XRF/XRD and wet chemical study,” *Geochim. Cosmochim. Acta*, vol. 73, no. 8, pp. 2283–2298, 2009.
- [12] P. Frugier, C. Martin, I. Ribet, T. Advocat, and S. Gin, “The effect of composition on the leaching of three nuclear waste glasses: R7T7, AVM and VRZ,” *J. Nucl. Mater.*, vol. 346, no. 2–3, pp. 194–207, 2005.

- [13] T. Chave, P. Frugier, S. Gin, and A. Ayrat, "Glass-water interphase reactivity with calcium rich solutions," *Geochim. Cosmochim. Acta*, vol. 75, no. 15, pp. 4125–4139, 2011.
- [14] S. Gin, X. Beaudoux, F. Angéli, C. Jégou, and N. Godon, "Effect of composition on the short-term and long-term dissolution rates of ten borosilicate glasses of increasing complexity from 3 to 30 oxides," *J. Non. Cryst. Solids*, vol. 358, no. 18–19, pp. 2559–2570, 2012.
- [15] I. Techer, T. Advocat, J. Lancelot, and J. M. Liotard, "Basaltic glass: Alteration mechanisms and analogy with nuclear waste glasses," *J. Nucl. Mater.*, vol. 282, no. 1, pp. 40–46, 2000.
- [16] D. M. Wellman, J. P. Icenhower, and W. J. Weber, "Elemental dissolution study of Pu-bearing borosilicate glasses," *J. Nucl. Mater.*, vol. 340, no. 2–3, pp. 149–162, 2005.
- [17] B. P. McGrail et al., "Near-field performance assessment for a low-activity waste glass disposal system: Laboratory testing to modeling results," *J. Nucl. Mater.*, vol. 298, no. 1–2, pp. 95–111, 2001.
- [18] C. M. Jantzen, D. I. Kaplan, N. E. Bibler, D. K. Peeler, and M. John Plodinec, "Performance of a buried radioactive high level waste (HLW) glass after 24 years," *J. Nucl. Mater.*, vol. 378, no. 3, pp. 244–256, 2008.
- [19] C. L. Corkhill, N. J. Cassingham, P. G. Heath, and N. C. Hyatt, "Dissolution of UK high-level waste glass under simulated hyperalkaline conditions of a colocated geological disposal facility," *Int. J. Appl. Glas. Sci.*, vol. 4, no. 4, pp. 341–356, 2013.
- [20] S. Gin et al., "The fate of silicon during glass corrosion under alkaline conditions: A mechanistic and kinetic study with the International Simple Glass," *Geochim. Cosmochim. Acta*, vol. 151, pp. 68–85, Feb. 2015.
- [21] M. Debure, P. Frugier, L. De Windt, and S. Gin, "Dolomite effect on borosilicate glass alteration," *Appl. Geochemistry*, vol. 33, pp. 237–251, 2013.
- [22] "CoRWM Doc 700 July 2006," July 2006.
- [23] T. W. Hicks et al., "Concepts for the Geological Disposal of Intermediate-Level Radioactive Waste," vol. 44, no. 1572, pp. 1–66, 2008.
- [24] T. Baldwin, N. Chapman, and F. Neall, "Geological Disposal Options for High-Level Waste and Spent Fuel Report for the UK Nuclear Decommissioning Authority," Sci. York, January 2008.
- [25] I. W. Donald, B. L. Metcalfe, and R. N. J. Taylor, "The immobilization of high level radioactive wastes using ceramics and glasses," *J. Mater. Sci.*, vol. 32, no. 22, pp. 5851–5887, 1997.
- [26] M. I. Ojovan and W. E. Lee, "Glassy wastefoms for nuclear waste immobilization," *Metall. Mater. Trans. A Phys. Metall. Mater. Sci.*, vol. 42, no. 4, pp. 837–851, 2011.
- [27] A. A. Lebedev, *Abr. Staatl. Opt. Inst. Leningr.*, vol. 2, no. 10, 1921.
- [28] J. E. Shelby, *Introduction to Glass Science and Technology*, 2nd ed. Cambridge: The Royal Society of Chemistry, 2005.

- [29] K. S. Evstropiev and E. A. Porai-Koshits, "Discussion on the modern state of the crystallite hypothesis of glass structure," *J. Non. Cryst. Solids*, vol. 11, pp. 170–172, 1972.
- [30] W. H. Zachariasen, "The atomic arrangement in glass," *J. Am. Chem. Soc.*, vol. 54, no. 10, pp. 3841–3851, 1932.
- [31] B. E. Warren, "SUMMARY OF WORK ON ATOMIC ARRANGEMENT IN GLASS\*," *J. Am. Ceram. Soc.*, vol. 24, no. 8, pp. 256–261, 1941.
- [32] G. N. Greaves, A. Fontaine, P. Lagarde, D. Raoux, and S. J. Gurman, "Local structure of silicate glasses," *Nature*, vol. 293, pp. 611–616, 1981.
- [33] G. N. Greaves, "EXAFS and the structure of glass," *J. Non. Cryst. Solids*, vol. 71, no. 1–3, pp. 203–217, 1985.
- [34] A. G. Smekal, "On the structure of glass," *J. Soc. Glas. Technol.*, vol. 35, pp. 392–395, 1951.
- [35] U. Voigt, H. Lammert, H. Eckert, and A. Heuer, "Cation clustering in lithium silicate glasses: Quantitative description by solid-state NMR and molecular dynamics simulations," *Phys. Rev. B*, vol. 72, no. 6, p. 64207, 2005.
- [36] C. Huang and A. N. Cormack, "The structure of sodium silicate glass," *J. Chem. Phys.*, vol. 93, no. 11, pp. 8180–8186, 1990.
- [37] A. C. Wright, "Borate structures: crystalline and vitreous," *Phys. Chem. Glas. - Eur. J. Glas. Sci. Technol. Part B*, vol. 51, no. 1, pp. 1–39, 2010.
- [38] T. Abe, "Borosilicate Glasses," *J. Am. Ceram. Soc.*, vol. 35, no. 11, pp. 284–299, 1952.
- [39] P. Beekenkamp, in *Physics of Non-Crystalline Solids*, J. A. Prins, Ed. Amsterdam: North-Holland Publishing Co., 1965, pp. 512–518.
- [40] P. K. Gupta, in *Collected Paper: XIV International Congress on Glass*, 1986, p. 1.
- [41] A. C. Wright, N. Vedischeva, and B. A. Shakhmatkin, "Vitreous borate networks containing superstructural units: A challenge to the random network theory?," *J. Non. Cryst. Solids*, vol. 192, pp. 92–97, 1995.
- [42] J. Krogh-Moe, *Phys. Chem. Glas.*, vol. 3, p. 101, 1962.
- [43] D. L. Griscom, "Borate Glass Structure," in *Borate Glasses: Structure, Properties and Applications*, 1st ed., L. D. Pye, V. D. Frechette, and N. J. Kreidl, Eds. New York: Springer US, 1978, pp. 11–138.
- [44] Y. H. Yun and P. J. Bray, "Nuclear magnetic resonance studies of the glasses in the system Na<sub>2</sub>O-B<sub>2</sub>O<sub>3</sub>-SiO<sub>2</sub>," *J. Non. Cryst. Solids*, vol. 27, no. 3, pp. 363–380, 1978.
- [45] Y. H. Yun, S. A. Feller, and P. J. Bray, "Correction and Addendum to "Nuclear Magnetic Resonance Studies of the Glasses in the System Na<sub>2</sub>O-B<sub>2</sub>O<sub>3</sub>-SiO<sub>2</sub>," *J. Non. Cryst. Solids*, vol. 33, pp. 273–277, 1979.
- [46] W. J. Dell, P. J. Bray, and S. Z. Xiao, "<sup>11</sup>B NMR studies and structural modeling of Na<sub>2</sub>O-B<sub>2</sub>O<sub>3</sub>-SiO<sub>2</sub> glasses of high soda content," *J. Non. Cryst. Solids*, vol. 58, no. 1, pp. 1–16, 1983.
- [47] S. Sen, "Temperature induced structural changes and transport mechanisms in borate, borosilicate and boroaluminate liquids: High-resolution and high-

- temperature NMR results,” *J. Non. Cryst. Solids*, vol. 253, no. 1–3, pp. 84–94, 1999.
- [48] R. Martens and W. Müller-Warmuth, “Structural groups and their mixing in borosilicate glasses of various compositions - an NMR study,” *J. Non. Cryst. Solids*, vol. 265, no. 1, pp. 167–175, 2000.
- [49] D. Manara, A. Grandjean, and D. R. Neuville, “Advances in understanding the structure of borosilicate glasses: A Raman spectroscopy study,” *Am. Mineral.*, vol. 94, pp. 777–784, 2009.
- [50] S. A. Brawer and W. B. White, “Raman spectroscopic investigation of the structure of silicate glasses (II). Soda-alkaline earth-alumina ternary and quaternary glasses,” *J. Non. Cryst. Solids*, vol. 23, no. 2, pp. 261–278, 1977.
- [51] H. Scholze, *Glass: Nature, Structure and Properties*, Third. London: Springer-Verlag, 1991.
- [52] J. F. Stebbins and Z. Xu, “NMR evidence for excess non-bridging oxygen in an aluminosilicate glass,” *Nature*, vol. 390, no. 6655, pp. 60–62, 1997.
- [53] C. Huang and E. C. Behrman, “Structure and properties of calcium aluminosilicate glasses,” *J. Non. Cryst. Solids*, vol. 128, no. 3, pp. 310–321, 1991.
- [54] L. Cormier, D. R. Neuville, and G. Calas, “Structure and properties of low-silica calcium aluminosilicate glasses,” *J. Non. Cryst. Solids*, vol. 274, no. 1, pp. 110–114, 2000.
- [55] H. Yamashita, H. Yoshino, K. Nagata, H. Inoue, T. Nakajin, and T. Maekawa, “Nuclear magnetic resonance studies of alkaline earth phosphosilicate and aluminoborosilicate glasses,” *J. Non. Cryst. Solids*, vol. 270, no. 1, pp. 48–59, 2000.
- [56] H. Yamashita, K. Inoue, T. Nakajin, H. Inoue, and T. Maekawa, “Nuclear magnetic resonance studies of 0.139MO (or  $M'_2O$ )·0.673SiO<sub>2</sub>·(0.188– $x$ )Al<sub>2</sub>O<sub>3</sub>· $x$ B<sub>2</sub>O<sub>3</sub> (M=Mg, Ca, Sr and Ba, M'=Na and K) glasses,” *J. Non. Cryst. Solids*, vol. 331, no. 1, pp. 128–136, 2003.
- [57] Q. J. Zheng *et al.*, “Structure of boroaluminosilicate glasses: Impact of [Al<sub>2</sub>O<sub>3</sub>]/[SiO<sub>2</sub>] ratio on the structural role of sodium,” *Phys. Rev. B*, vol. 86, no. 5, p. 54203, Aug. 2012.
- [58] A. M. Bevilacqua, N. B. Messi de Bernasconi, D. O. Russo, M. A. Audero, M. E. Sterba, and A. D. Heredia, “Section 5. Nuclear waste immobilization: Immobilization of simulated high-level liquid wastes in sintered borosilicate, aluminosilicate and aluminoborosilicate glasses,” *J. Nucl. Mater.*, vol. 229, pp. 187–193, 1996.
- [59] G. Leturcq, G. Berger, T. Advocat, and E. Vernaz, “Initial and long-term dissolution rates of aluminosilicate glasses enriched with Ti, Zr and Nd,” *Chem. Geol.*, vol. 160, no. 1–2, pp. 39–62, 1999.
- [60] C. Jégou, S. Gin, and F. Larché, “Alteration kinetics of a simplified nuclear glass in an aqueous medium: Effects of solution chemistry and of protective gel properties on diminishing the alteration rate,” *J. Nucl. Mater.*, vol. 280, no. 2, pp. 216–229, 2000.

- [61] T. Geisler, A. Janssen, D. Scheiter, T. Stephan, J. Berndt, and A. Putnis, "Aqueous corrosion of borosilicate glass under acidic conditions: A new corrosion mechanism," *J. Non. Cryst. Solids*, vol. 356, no. 28–30, pp. 1458–1465, 2010.
- [62] D. Rébiscoul, F. Bruguier, V. Magnin, and S. Gin, "Impact of soda-lime borosilicate glass composition on water penetration and water structure at the first time of alteration," *J. Non. Cryst. Solids*, vol. 358, no. 22, pp. 2951–2960, 2012.
- [63] A. C. Buechele, D. A. McKeown, W. W. Lukens, D. K. Shuh, and I. L. Pegg, "Tc and Re behavior in borosilicate waste glass vapor hydration tests II," *J. Nucl. Mater.*, vol. 429, no. 1–3, pp. 159–165, 2012.
- [64] ASTM, "Standard Test Method for Static Leaching of Monolithic Waste Forms for Disposal of Radioactive Waste", C1220-10, 2010.
- [65] ASTM International, "Standard Practice for Measurement of the Glass Dissolution Rate Using the Single-Pass Flow-Through Test Method", C1662-10, 2010.
- [66] N. Rajmohan, P. Frugier, and S. Gin, "Composition effects on synthetic glass alteration mechanisms: Part 1. Experiments," *Chem. Geol.*, vol. 279, no. 3–4, pp. 106–119, 2010.
- [67] J. P. Icenhower and C. I. Steefel, "Experimentally determined dissolution kinetics of SON68 glass at 90 °C over a silica saturation interval: Evidence against a linear rate law," *J. Nucl. Mater.*, vol. 439, no. 1–3, pp. 137–147, 2013.
- [68] S. R. Gislason and E. H. Oelkers, "Mechanism, rates, and consequences of basaltic glass dissolution: II. An experimental study of the dissolution rates of basaltic glass as a function of pH and temperature," *Geochim. Cosmochim. Acta*, vol. 67, no. 20, pp. 3817–3832, 2003.
- [69] X. Feng and I. L. Pegg, "A glass dissolution model for the effects of S/V on leachate pH," *J. Non. Cryst. Solids*, vol. 175, no. 2–3, pp. 281–293, 1994.
- [70] P. Van Iseghem *et al.*, "A Critical Evaluation of the Dissolution Mechanisms of High-level Waste Glasses in Conditions of Relevance for Geological Disposal (GLAMOR)," 2008.
- [71] P. Frugier *et al.*, "SON68 nuclear glass dissolution kinetics: Current state of knowledge and basis of the new GRAAL model," *J. Nucl. Mater.*, vol. 380, no. 1–3, pp. 8–21, 2008.
- [72] A. Paul, *Chemistry of Glasses*, 2nd ed. London: Chapman and Hall Ltd, 1990.
- [73] D. Gelder and S. Fearn, "Anomalous diffusion in the hydration of glass surfaces," *Eur. J. Glas. Sci. Technol., Part A*, vol. 53, pp. 46–52, 2012.
- [74] R. H. Doremus, "Interdiffusion of hydrogen and alkali ions in a glass surface," *J. Non. Cryst. Solids*, vol. 19, pp. 137–144, 1975.
- [75] T. Maeda, K. Hotta, H. Usui, and T. Banba, "Characteristics of alteration layers formed on simulated HLW glass under silica-saturated solutions," *J. Aust. Ceram. Soc.*, vol. 48, no. 1, pp. 90–95, 2012.

- [76] B. Grambow and R. Müller, “First-order dissolution rate law and the role of surface layers in glass performance assessment,” *J. Nucl. Mater.*, vol. 298, no. 1–2, pp. 112–124, 2001.
- [77] E. Curti, J. L. Crovisier, G. Morvan, and A. M. Karpoff, “Long-term corrosion of two nuclear waste reference glasses (MW and SON68): A kinetic and mineral alteration study,” *Appl. Geochemistry*, vol. 21, no. 7, pp. 1152–1168, 2006.
- [78] R. Hellmann *et al.*, “Nanometre-scale evidence for interfacial dissolution–reprecipitation control of silicate glass corrosion,” *Nat. Mater.*, vol. 14, no. January, pp. 307–311, 2015.
- [79] P. Frugier, T. Chave, S. Gin, and J. E. Lartigue, “Application of the GRAAL model to leaching experiments with SON68 nuclear glass in initially pure water,” *J. Nucl. Mater.*, vol. 392, no. 3, pp. 552–567, 2009.
- [80] Y. Minet, B. Bonin, S. Gin, and P. Frugier, “Analytic implementation of the GRAAL model: Application to a R7T7-type glass package in a geological disposal environment,” *J. Nucl. Mater.*, vol. 404, no. 3, pp. 178–202, 2010.
- [81] M. Debure, L. De Windt, P. Frugier, and S. Gin, “HLW glass dissolution in the presence of magnesium carbonate: Diffusion cell experiment and coupled modeling of diffusion and geochemical interactions,” *J. Nucl. Mater.*, vol. 443, no. 1–3, pp. 507–521, 2013.
- [82] H. Rawson, *Properties and Applications of Glass: Glass Science and Technology*, 1st ed. Amsterdam, 1980.
- [83] R. W. Douglas and T. M. M. El-Shamy, “Reactions of Glasses with Aqueous Solutions,” *J. Am. Ceram. Soc.*, vol. 50, no. 1, pp. 1–8, 1967.
- [84] C. A. Utton, R. J. Hand, N. C. Hyatt, S. W. Swanton, and S. J. Williams, “Formation of alteration products during dissolution of vitrified ILW in a high-pH calcium-rich solution,” *J. Nucl. Mater.*, vol. 442, no. 1–3, pp. 33–45, 2013.
- [85] K. Ferrand, S. Liu, and K. Lemmens, “The interaction between nuclear waste glass and ordinary portland cement,” *Int. J. Appl. Glas. Sci.*, vol. 4, no. 4, pp. 328–340, 2013.
- [86] B. Fleury, N. Godon, A. Ayrat, and S. Gin, “SON68 glass dissolution driven by magnesium silicate precipitation,” *J. Nucl. Mater.*, vol. 442, no. 1–3, pp. 17–28, 2013.
- [87] S. Ribet and S. Gin, “Role of neoformed phases on the mechanisms controlling the resumption of SON68 glass alteration in alkaline media,” *J. Nucl. Mater.*, vol. 324, no. 2–3, pp. 152–164, 2004.
- [88] M. Fournier, S. Gin, and P. Frugier, “Resumption of nuclear glass alteration: State of the art,” *J. Nucl. Mater.*, vol. 448, no. 1–3, pp. 348–363, 2014.
- [89] Z. Andriambololona, “R7T7 Glass Alteration in the presence of mortar; effect of the cement grade,” in *Scientific Basis for Nuclear Waste Management XV, MRS Proc.*, vol. 257, 1992, pp. 151–158.
- [90] R. Hellmann *et al.*, “Unifying natural and laboratory chemical weathering with interfacial dissolution-reprecipitation: A study based on the nanometer-scale

- chemistry of fluid-silicate interfaces,” *Chem. Geol.*, vol. 294–295, pp. 203–216, 2012.
- [91] S. Mercado-Depierre, F. Angeli, F. Frizon, and S. Gin, “Antagonist effects of calcium on borosilicate glass alteration,” *J. Nucl. Mater.*, vol. 441, no. 1–3, pp. 402–410, 2013.
- [92] R. Hellmann *et al.*, “Nanometre-scale evidence for interfacial dissolution–reprecipitation control of silicate glass corrosion,” *Nat. Mater.*, vol. 14, no. January, pp. 307–311, 2015.
- [93] T. Geisler *et al.*, “The mechanism of borosilicate glass corrosion revisited,” *Geochim. Cosmochim. Acta*, vol. 158, pp. 112–129, 2015.
- [94] L. Dohmen *et al.*, “Pattern formation in silicate glass corrosion zones,” *Int. J. Appl. Glas. Sci.*, vol. 4, no. 4, pp. 357–370, 2013.
- [95] I. Hasdemir, S. Striepe, J. Deubener, and B. C. Schmidt, “Micromechanical properties of banded alterations of archaeological glass fragments,” *J. Non. Cryst. Solids*, vol. 376, pp. 126–132, 2013.
- [96] T. Lombardo *et al.*, “Characterisation of complex alteration layers in medieval glasses,” *Corros. Sci.*, vol. 72, pp. 10–19, 2013.
- [97] R. C. Ewing, “Natural Glasses: Analogues for Radioactive Waste Forms,” in *Scientific Basis for Nuclear Waste Management*, vol. 1, 1979, pp. 57–68.
- [98] S. N. Karkhanis, G. M. Bancroft, W. S. Fyfe, and J. D. Brown, “Leaching behaviour of rhyolite glass,” *Nature*, vol. 284, no. 5755, pp. 435–437, 1980.
- [99] G. Malow and R. C. Ewing, in *Scientific Basis for Nuclear Waste Management Vol. 3*, 1981, pp. 315–322.
- [100] A. P. Dickin, “Hydrothermal leaching of rhyolite glass in the environment has implications for nuclear waste disposal,” *Nature*, vol. 294, no. 5839, pp. 342–347, Nov. 1981.
- [101] J. K. Bates, L. J. Jardine, and M. J. Steindler, “Hydration Aging of Nuclear Waste Glass,” *Science*, vol. 218, no. 4567, pp. 51–54, Oct. 1982.
- [102] A. Barkatt *et al.*, “The chemical durability of tektites—A laboratory study and correlation with long-term corrosion behavior,” *Geochim. Cosmochim. Acta*, vol. 48, no. 2, pp. 361–371, 1984.
- [103] G. Malow, W. Lutze, and R. C. Ewing, “Alteration effects and leach rates of basaltic glasses: Implications for the long-term stability of nuclear waste form borosilicate glasses,” *J. Non. Cryst. Solids*, vol. 67, no. 1–3, pp. 305–321, 1984.
- [104] W. Lutze, G. Malow, R. C. Ewing, M. J. Jercinovic, and K. Keil, “Alteration of basalt glasses: Implications for modelling the long-term stability of nuclear waste glasses,” *Nature*, vol. 314, no. 6008, pp. 252–255, 1985.
- [105] M. C. Magonthier, J. C. Petit, and J. C. Dran, “Rhyolitic glasses as natural analogues of nuclear waste glasses: behaviour of an Icelandic glass upon natural aqueous corrosion,” *Appl. Geochemistry Suppl.*, vol. 1, pp. 83–93, 1992.

- [106] I. Techer, T. Advocat, J. Lancelot, and J. M. Liotard, "Dissolution kinetics of basaltic glasses: Control by solution chemistry and protective effect of the alteration film," *Chem. Geol.*, vol. 176, no. 1–4, pp. 235–263, 2001.
- [107] I. Techer, J. Lancelot, N. Clauer, J. M. Liotard, and T. Advocat, "Alteration of a basaltic glass in an argillaceous medium: The Salagou dike of the lodève Permian (France). Analogy with an underground nuclear waste repository," *Geochim. Cosmochim. Acta*, vol. 65, no. 7, pp. 1071–1086, 2001.
- [108] J. L. Crovisier, T. Advocat, and J. L. Dussossoy, "Nature and role of natural alteration gels formed on the surface of ancient volcanic glasses (Natural analogs of waste containment glasses)," *J. Nucl. Mater.*, vol. 321, no. 1, pp. 91–109, 2003.
- [109] J. L. Crovisier, J. H. Thomassin, T. Juteau, J. P. Eberhart, J. C. Touray, and P. Baillif, "Experimental seawater-basaltic glass interaction at 50°C: Study of early developed phases by electron microscopy and X-ray photoelectron spectrometry," *Geochim. Cosmochim. Acta*, vol. 47, no. 3, pp. 377–387, 1983.
- [110] M. T. Harrison, C. J. Steele, and A. D. Riley, "The effect on long term aqueous durability of variations in the composition of UK vitrified HLW product," *Glas. Technol. Eur. J. Glas. Sci. Technol. Part A*, vol. 53, no. 5, pp. 211–216, 2012.
- [111] N. E. Ahmad, S. Fearn, J. R. Jones, and W. E. Lee, "Preliminary Surface Study of Short Term Dissolution of UK High Level Waste Glass," *Procedia Mater. Sci.*, vol. 7, pp. 230–236, 2014.
- [112] E. Curti, D. Grolimund, and C. N. Borca, "A micro-XAS/XRF and thermodynamic study of Ce III/IV speciation after long-term aqueous alteration of simulated nuclear waste glass: Relevance for predicting Pu behavior?," *Appl. Geochemistry*, vol. 27, no. 1, pp. 36–63, 2012.
- [113] A. Kingsbury, L. Rust, and D. North, "Final Simulant Record for the ISL Glass Formulation Trials for the Hinkley Point 'A' Wet Intermediate Level Waste Thermal Vitrification Project", 2009.
- [114] ASTM, "Standard Test Methods for Determining Chemical Durability of Nuclear, Hazardous, and Mixed Waste Glasses and Multiphase Glass Ceramics: The Product Consistency Test (PCT)" C1285-14, 2014.
- [115] G. M. Hieftje, "Introduction - A Forward-Looking Perspective," in *Inductively Coupled Plasma Spectrometry and its Applications*, Second., S. J. Hill, Ed. Oxford: Blackwell Publishing Ltd, 2007, p. 22.
- [116] M. Thompson and J. N. Walsh, *Handbook of Inductively Couple Plasma Spectrometry*, 2nd ed. Glasgow: Blackie Academic & Professional, 1989.
- [117] L. Reimer, *Scanning Electron Microscopy: Physics of Image Formation and Microanalysis*, Second. Heidelberg, 1998.
- [118] P. J. Goodhew, J. Humphreys, and R. Beanland, *Electron Microscopy and Analysis*, 3rd ed. London: Taylor & Francis, 2001.
- [119] J. C. Russ, *Fundamentals of Energy Dispersive X-Ray Analysis*, 1st ed. Bodmin: Butterworths & Co Ltd., 1984.

- [120] B. Cowan, *Nuclear Magnetic Resonance and Relaxation*, 1st ed. Cambridge: Cambridge University Press, 1997.
- [121] D. C. Apperley, R. K. Harris, and P. Hodgkinson, *Solid-State NMR: Basic Principles & Practice*, 1st ed. New York: Momentum Press, LLC, 2012.
- [122] D. Massiot *et al.*, “Modelling one- and two-dimensional solid-state NMR spectra,” *Magn. Reson. Chem.*, vol. 40, no. 1, pp. 70–76, 2002.
- [123] B. G. Parkinson, D. Holland, M. E. Smith, A. P. Howes, and C. R. Scales, “Effect of minor additions on structure and volatilization loss in simulated nuclear borosilicate glasses,” *J. Non. Cryst. Solids*, vol. 353, no. 44–46, pp. 4076–4083, 2007.
- [124] G. Czjzek *et al.*, “Atomic coordination and the distribution of electric field gradients in amorphous solids,” *Phys. Rev. B*, vol. 23, no. 6, pp. 2513–2530, 1981.
- [125] J. B. d’Espinoise de Lacaille, C. Fretigny, and D. Massiot, “MAS-NMR spectra of quadrupolar nuclei in disordered solids: The Czjzek model,” *J. Magn. Reson.*, vol. 192, no. 2, pp. 244–251, 2008.
- [126] A. R. West, *Basic Solid State Chemistry*, Second. Chichester: John Wiley & Sons, Ltd., 1999.
- [127] D. L. Parkhurst and C. A. J. Appelo, “Description of Input and Examples for PHREEQC Version 3 — A Computer Program for Speciation, Batch-Reaction, One-Dimensional Transport, and Inverse Geochemical Calculations. U.S. Geological Survey Techniques and Methods, Book 6, Chapter A43, 497 p.,” U.S. Geol. Surv. Tech. Methods, B. 6, chapter A43, p. 6–43A, 2013.
- [128] K. J. D. Mackenzie and M. E. Smith, *Multinuclear Solid-State NMR of Inorganic Materials*, First., Amsterdam: Pergamon, 2002.
- [129] M. M. Smedskjaer, R. E. Youngman, and J. C. Mauro, “Impact of ZnO on the structure and properties of sodium aluminosilicate glasses: Comparison with alkaline earth oxides,” *J. Non. Cryst. Solids*, vol. 381, pp. 58–64, 2013.
- [130] S. J. Watts, R. G. Hill, M. D. O’Donnell, and R. V. Law, “Influence of magnesia on the structure and properties of bioactive glasses,” *J. Non. Cryst. Solids*, vol. 356, no. 9–10, pp. 517–524, 2010.
- [131] K. L. Geisinger, R. Oestrike, A. Navrotsky, G. L. Turner, and R. J. Kirkpatrick, “Thermochemistry and structure of glasses along the join NaAlSi<sub>3</sub>O<sub>8</sub>-NaBSi<sub>3</sub>O<sub>8</sub>,” *Geochim. Cosmochim. Acta*, vol. 52, no. 10, pp. 2405–2414, 1988.
- [132] S. K. Lee and J. F. Stebbins, “The Structure of Aluminosilicate Glasses: High-Resolution <sup>17</sup>O and <sup>27</sup>Al MAS and 3QMAS NMR Study,” *J. Phys. Chem. B*, vol. 104, no. 17, pp. 4091–4100, 2000.
- [133] W. Loewenstein, “The distribution of aluminum in the tetrahedra of silicates and aluminates,” *Am. Mineral.*, vol. 39, pp. 92–96, 1954.
- [134] S. P. Pinho and E. A. Macedo, “Solubility of NaCl, NaBr, and KCl in water, methanol, ethanol, and their mixed solvents,” *J. Chem. Eng. Data*, vol. 50, no. 1, pp. 29–32, 2005.

- [135] B. C. Bunker and W. H. Casey, *The Aqueous Chemistry of Oxides*, First. New York: Oxford University Press, 2016.
- [136] B. Lothenbach, D. Nied, E. L'Hôpital, G. Achiedo, and A. Dauzères, "Magnesium and calcium silicate hydrates," *Cem. Concr. Res.*, vol. 77, pp. 60–68, 2015.
- [137] M. Debure, L. De Windt, P. Frugier, S. Gin, and P. Vieillard, "Mineralogy and thermodynamic properties of magnesium phyllosilicates formed during the alteration of a simplified nuclear glass," *J. Nucl. Mater.*, vol. 475, pp. 255–265, 2016.
- [138] S. Gin *et al.*, "An international initiative on long-term behavior of high-level nuclear waste glass," *Mater. Today*, vol. 16, no. 6, pp. 243–248, 2013.
- [139] A. Abdelouas *et al.*, "A Preliminary Investigation of the ISG Glass Vapor Hydration," *Int. J. Appl. Glas. Sci.*, vol. 4, no. 4, pp. 307–316, Dec. 2013.
- [140] B. E. Scheetz, W. P. Freeborn, D. K. Smith, C. Anderson, M. Zolensky, and W. B. White, "The Role of Boron in Monitoring the Leaching of Borosilicate Glass Waste Forms," *Mater. Res. Soc. Symp. Proc.*, vol. 44, pp. 129–134, 1985.
- [141] J. W. Cahn, "On spinodal decomposition," *Acta Metall.*, vol. 9, no. 9, pp. 795–801, 1961.
- [142] M. Arab, C. Cailleteau, F. Angeli, F. Devreux, L. Girard, and O. Spalla, "Aqueous alteration of five-oxide silicate glasses: Experimental approach and Monte Carlo modeling," *J. Non. Cryst. Solids*, vol. 354, pp. 155–161, 2008.
- [143] M. Fleischer, A. Pabst, J. A. Mandarino, G. Y. Chao, and L. J. Cabri, "New Mineral Names," *Am. Mineral.*, vol. 61, pp. 174–176, 1976.
- [144] S. A. Kulyukhin, E. P. Krasavina, I. A. Rumer, and I. V. Klimovich, "Sorption of strontium and yttrium radionuclides from aqueous solutions onto layered double hydroxides of various compositions," *Radiochemistry*, vol. 56, no. 6, pp. 593–606, 2014.
- [145] X. Zhang *et al.*, "Removal of uranium(VI) from aqueous solutions by magnetic Mg–Al layered double hydroxide intercalated with citrate: Kinetic and thermodynamic investigation," *Colloids Surfaces A Physicochem. Eng. Asp.*, vol. 414, pp. 220–227, Nov. 2012.
- [146] M. J. Kang, K. S. Chun, S. W. Rhee, and Y. Do, "Comparison of sorption behavior of I<sup>-</sup> and TcO<sup>4-</sup> on Mg/Al layered double hydroxide," *Radiochim. Acta*, vol. 85, no. 1–2, pp. 57–63, 1999.
- [147] U. Schwertmann and L. Carlson, "The pH-dependent transformation of schwertmannite to goethite at 25°C," *Clay Miner.*, vol. 40, no. 1, pp. 63–66, 2005.
- [148] N. A. Stroncik and H. U. Schmincke, "Palagonite - A review," *Int. J. Earth Sci.*, vol. 91, no. 4, pp. 680–697, 2002.
- [149] M. L. D. Gougar, B. E. Scheetz, and D. M. Roy, "Ettringite and C-S-H portland cement phases for waste ion immobilization: A review," *Waste Manag.*, vol. 16, no. 4, pp. 295–303, 1996.

- [150] J. Wu and J. F. Stebbins, "Effects of cation field strength on the structure of aluminoborosilicate glasses: High-resolution  $^{11}\text{B}$ ,  $^{27}\text{Al}$  and  $^{23}\text{Na}$  MAS NMR," *J. Non. Cryst. Solids*, vol. 355, no. 9, pp. 556–562, 2009.
- [151] A. Quintas, T. Charpentier, O. Majerus, D. Caurant, J. L. Dussossoy, and P. Vermaut, "NMR study of a rare-earth aluminoborosilicate glass with varying Ca-to- $\text{Na}_2\text{O}$  ratio," *Appl. Magn. Reson.*, vol. 32, no. 4, pp. 613–634, 2007.
- [152] S. J. Watts, R. G. Hill, M. D. O'Donnell, and R. V. Law, "Influence of magnesia on the structure and properties of bioactive glasses," *J. Non. Cryst. Solids*, vol. 356, no. 9–10, pp. 517–524, 2010.
- [153] M. M. Smedskjaer, R. E. Youngman, and J. C. Mauro, "Impact of ZnO on the structure and properties of sodium aluminosilicate glasses: Comparison with alkaline earth oxides," *J. Non. Cryst. Solids*, vol. 381, pp. 58–64, 2013.
- [154] B. C. Bunker, R. J. Kirkpatrick, R. K. Brow, G. L. Turner, and C. Nelson, "Local Structure of Alkaline-Earth Boroaluminate Crystals and Glasses: II.  $^{11}\text{B}$  and  $^{27}\text{Al}$  MAS-NMR Spectroscopy of Alkaline-Earth Boroaluminate Glasses," *J. Am. Ceram. Soc.*, vol. 74, no. 6, pp. 1430–1438, 1991.
- [155] B. C. Bunker, R. J. Kirkpatrick, R. K. Brow, G. L. Turner, and C. Nelson, "Local Structure of Alkaline-Earth Boroaluminate Crystals and Glasses: II,  $^{11}\text{B}$  and  $^{27}\text{Al}$  MAS NMR Spectroscopy of Alkaline-Earth Boroaluminate Glasses," *J. Am. Ceram. Soc.*, vol. 74, no. 6, pp. 1430–1438, 1991.
- [156] S. Deriano *et al.*, "Structure and mechanical properties of alkali – alkaline earth – silicate glasses," vol. 45, no. 1, pp. 37–44, 2004.
- [157] S. Liu, G. Zhao, H. Ying, J. Wang, and G. Han, "Effects of mixed alkaline earth oxides additive on crystallization and structural changes in borosilicate glasses," *J. Non. Cryst. Solids*, vol. 354, no. 10–11, pp. 956–961, 2008.
- [158] H. Miyoshi, D. Chen, H. Masui, T. Yazawa, and T. Akai, "Effect of calcium additive on structural changes under heat treatment in sodium borosilicate glasses," *J. Non. Cryst. Solids*, vol. 345–346, pp. 99–103, 2004.
- [159] M. M. Islam, D. Holland, A. P. Howes, and C. R. Scales, "The effect of divalent additions on the structure of a mixed alkali borosilicate glass for high level waste immobilisation," *Phys. Chem. Glas. Eur. J. Glas. Sci. Technol. Part B*, vol. 51, no. 3, pp. 137–145, 2010.
- [160] D. Holland *et al.*, "NMR insights into wasteforms for the vitrification of high-level nuclear waste," *Appl. Magn. Reson.*, vol. 32, no. 4, pp. 483–497, 2007.
- [161] M. Potuzak and M. M. Smedskjaer, "Physical properties of boroaluminosilicate glasses: Effect of modifier cation field strength," *Phys. Chem. Glas. Eur. J. Glas. Sci. Technol. Part B*, vol. 55, no. 1, pp. 18–24, 2014.
- [162] Q. Zheng, M. Potuzak, J. C. Mauro, M. M. Smedskjaer, R. E. Youngman, and Y. Yue, "Composition–structure–property relationships in boroaluminosilicate glasses," *J. Non. Cryst. Solids*, vol. 358, no. 6–7, pp. 993–1002, Apr. 2012.
- [163] Q. J. Zheng *et al.*, "Structure of boroaluminosilicate glasses: Impact of  $[\text{Al}_2\text{O}_3]/[\text{SiO}_2]$  ratio on the structural role of sodium," *Phys. Rev. B*, vol. 86, no. 5, p. 54203, Aug. 2012.

- [164] J. Ramkumar *et al.*, “Structural studies on boroaluminosilicate glasses,” *J. Non. Cryst. Solids*, vol. 354, no. 15–16, pp. 1591–1597, Mar. 2008.
- [165] E. I. Morin, J. Wu, and J. F. Stebbins, “Modifier cation (Ba, Ca, La, Y) field strength effects on aluminum and boron coordination in aluminoborosilicate glasses: the roles of fictive temperature and boron content,” *Appl. Phys. A*, vol. 116, no. 2, pp. 479–490, Apr. 2014.
- [166] E. I. Morin and J. F. Stebbins, “Separating the effects of composition and fictive temperature on Al and B coordination in Ca, La, Y aluminosilicate, aluminoborosilicate and aluminoborate glasses,” *J. Non. Cryst. Solids*, vol. 432, pp. 384–392, Jan. 2016.
- [167] E. M. Pierce *et al.*, “Experimental determination of the effect of the ratio of B/Al on glass dissolution along the nepheline (NaAlSiO<sub>4</sub>)-malinkoite (NaBSiO<sub>4</sub>) join,” *Geochim. Cosmochim. Acta*, vol. 74, no. 9, pp. 2634–2654, 2010.
- [168] S. K. Lee, H. I. Kim, E. J. Kim, K. Y. Mun, and S. Ryu, “Extent of Disorder in Magnesium Aluminosilicate Glasses: Insights from <sup>27</sup>Al and <sup>17</sup>O NMR,” *J. Phys. Chem. C*, vol. 120, no. 1, pp. 737–749, 2016.
- [169] G. Fetter, E. Ramos, M. T. Olguin, P. Bosch, T. López, and S. Bulbulian, “Sorption of <sup>131</sup>I<sup>-</sup> by hydrotalcites,” *J. Radioanal. Nucl. Chem.*, vol. 221, no. 1, pp. 63–66, 1997.
- [170] C. A. Utton, N. C. Hyatt, and S. W. Swanton, “Interactions of vitrified wastes with NRVB: A report to NDA RWMD,” 2012.